14th International Conference on CFD in
Oil & Gas, Metallurgical and Process Industries
SINTEF, Trondheim, Norway, October 12–14, 2020

SINTEF
PROCEEDINGS 6

Proceedings from the 14th International Conference on CFD in Oil & Gas, Metallurgical and Process Industries

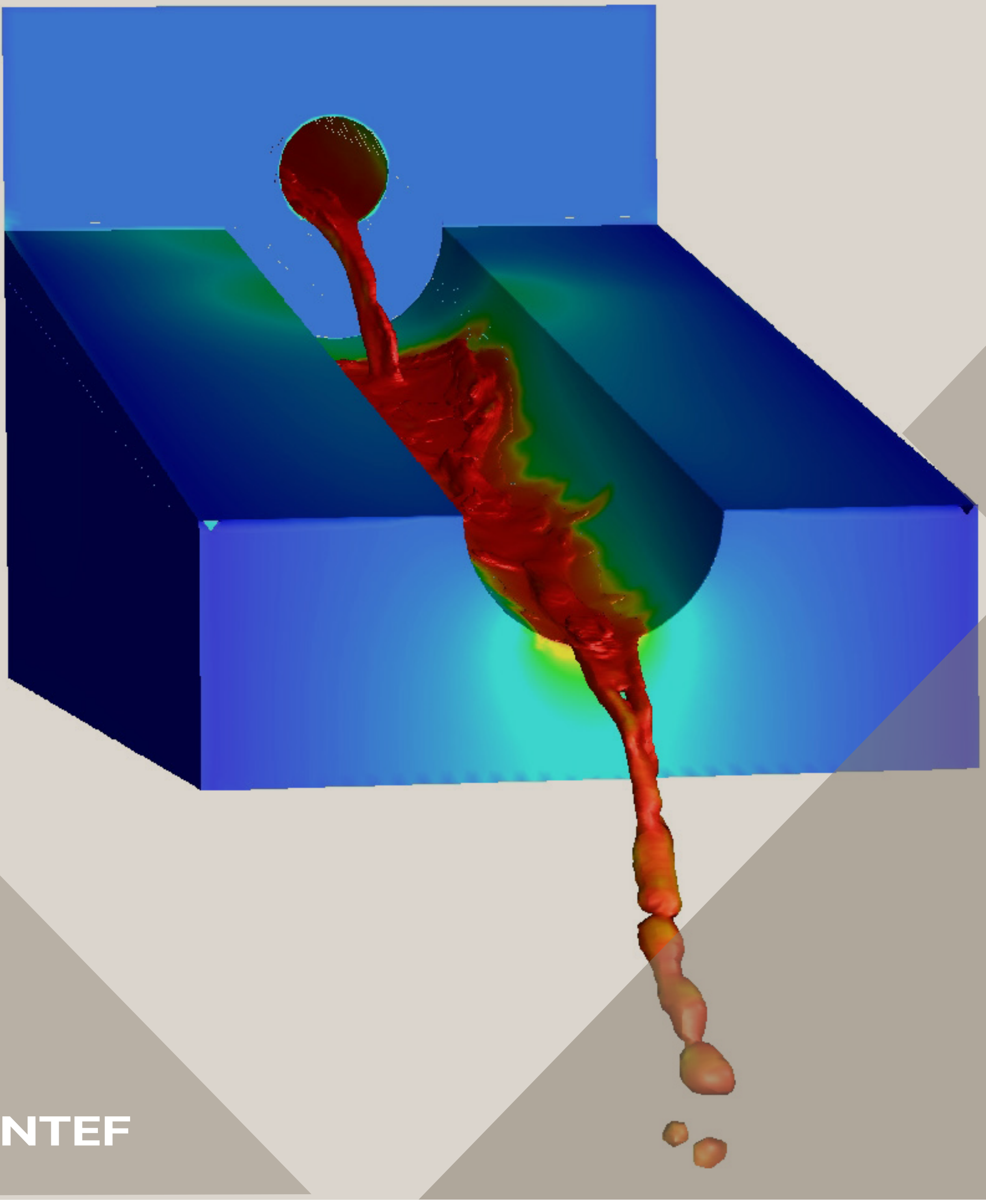

SINTEF

SINTEF Proceedings

Editors:
Jan Erik Olsen, Jan Hendrik Cloete and Stein Tore Johansen

Proceedings from the 14th International Conference on CFD in Oil & Gas, Metallurgical and Process Industries

SINTEF, Trondheim, Norway
October 12–14, 2020

SINTEF Academic Press

SINTEF Proceedings 6
Editors: Jan Erik Olsen, Jan Hendrik Cloete and Stein Tore Johansen

Proceedings from the 14th International Conference on CFD in Oil &
Gas, Metallurgical and Process Industries, SINTEF, Trondheim,
Norway, October 12–14, 2020

Keywords:
CFD, fluid dynamics, modelling

Cover illustration: Tapping of metal by Jan Erik Olsen

ISSN 2387-4295 (online)
ISBN 978-82-536-1684-1 (pdf)

SINTEF Academic Press
Address: Børrestuveien 3
PO Box 124 Blindern
N-0314 OSLO
Tel: +47 40 00 51 00

www.sintef.no/community
www.sintefbok.no

SINTEF Proceedings
SINTEF Proceedings is a serial publication for peer-reviewed conference proceedings on a variety of scientific topics.
The processes of peer-reviewing of papers published in SINTEF Proceedings are administered by the conference organizers and proceedings editors. Detailed procedures will vary according to custom and practice in each scientific community.

Preface

This book contains manuscripts from the 14th International Conference on Computational Fluid Dynamics in the Oil & Gas, Metallurgical and Process Industries. The conference was organized by SINTEF in collaboration with NTNU, MINTEK and CSIRO. The conference series was initiated by CSIRO and Phil Schwarz in 1997. So far, the conference has been alternating between CSIRO in Melbourne and SINTEF in Trondheim. The conferences focus on the application of CFD in the oil and gas industries, metal production, mineral processing, power generation, chemicals and other process industries. 2020 was a remarkable year with a worldwide pandemic due to the Covid-19 virus. This led to travel restrictions and a decision to host the conference as a virtual conference. The conference was hosted online through Microsoft Teams on October 12-14, 2020.

At the conference 61 technical studies and 6 keynotes were presented from Europe, Asia, Australia, Africa and North America. Of these 22 was papers was submitted for the conference proceedings. The conference papers undergo a review process involving two experts.

The organizing committee would like to thank everyone who has helped with review of manuscripts, all those who helped to promote the conference and all authors who have submitted scientific contributions. We are also grateful for the support from the conference sponsors: EDR Medeso and SFI Metal Production.

Jan Erik Olsen, Jan Hendrik Cloete & Stein Tore Johansen

Organizing Committee:

Stein Tore Johansen, SINTEF/NTNU (Conference chairman)

Jan Erik Olsen, SINTEF (Conference coordinator)

Henri Cloete, SINTEF

Shahriar Amini, SINTEF

Bernhard Müller, NTNU

Janikke Solsvik, NTNU

Kristian Etienne Einarsrud, NTNU

Quinn Reynolds, MINTEK

Paal Skjetne, SINTEF

Sverre Gullikstad Johnsen, SINTEF

Peter Witt, CSIRO

Scientific Committee:

Niels Deen, TU Eindhoven

Omar Matar, Imperial College

Dirk Lucas, HZDR

Jiyuan Tu, RMIT

Bernhard Müller, NTNU

Rajat Mittal, Johns Hopkins University

Pär Jönsson, KTH

Jos Derksen, University of Aberdeen

Stefan Pirker, Johannes Kepler University

Hans Kuipers, TU Eindhoven

Dmitry Eskin, Skolkovo Institute of Science & Technology

Josip Zoric, SINTEF

Markus Braun, ANSYS

Phil Schwarz, CSIRO

Harald Laux, Osram

Olivier Simonin, INP Toulouse

Djamel Lakehal, Pöyry Schweiz AG

Contents

IMPROVEMENT OF EULER-EULER SIMULATION OF TWO-PHASE FLOW BY PARTICLE-CENTER-AVERAGED METHOD

Hongmei Lyu[1, 2]* , Fabian Schlegel, Roland Rzehak, Dirk Lucas

[1]Helmholtz-Zentrum Dresden - Rossendorf, Institute of Fluid Dynamics, Bautzner Landstrasse 400, D-01328 Dresden, Germany

[2]Technische Universität Dresden, Faculty of Mechanical Engineering, Institute of Power Engineering, D-01062 Dresden, Germany

* E-mail: h.lyu@hzdr.de

ABSTRACT

The standard Euler-Euler modelling is based on the phase-averaged method and the forces of the bubble are the function of gas volume fraction. However, the closure models for the forces are developed based on the measured bubble trajectory and the assumption that the forces act on bubble center. This inconsistency can lead to a nonphysical gas concentration in the center or in the near wall region of a pipe if the bubble diameter is larger than the mesh size. In addition, mesh independent solutions may not exist in these cases.

In the present contribution, particle-center-averaged method is used in the average of the parameters for the disperse phase and the forces for bubble is changed to act on the bubble center. In this approach, the number density of the bubble centers is one of the solution variables. The gas volume fraction can be calculated from the number density by a diffusion-based method, which is much easier to implement in the CFD codes using the unstructured grids like OpenFOAM. A physically motivated model for the wall-contact force is introduced to ensure that the bubble centers cannot come arbitrarily close to walls.

The remedy of the issues with the conventional phase-averaged two-fluid model is demonstrated using a simplified two-dimensional test case. Furthermore, a comparison is made for pipe flow cases where experimental data are available. The results show that the particle-center-averaged method can help to decrease the over-prediction of the peaks in the gas volume fraction profiles and obtain the mesh independent solutions in the Euler-Euler modelling.

Keywords: Particle-center-average, number density, bubble dimension, diffusion equation, deformation force model, equation of motion.

NOMENCLATURE

Greek Symbols

α	Volume fraction, [-].
β	Bubble volume fraction attaching all bubble volume to its center, [-].
ρ	Mass density, [kg·m^{-3}].
τ	Diffusion time, [s].
σ	Surface tension coefficient, [N·m^{-1}].

Latin Symbols

d	Bubble diameter, [m].
$\boldsymbol{f}$	Interfacial forces, [N·m^{-3}].
$\boldsymbol{g}$	Acceleration of gravity, [m·s^{-2}].
J	Superficial velocity, [m·s^{-1}].
n	Number density of bubble centers, [m^{-3}].
N	The number of bubbles in the system, [-].
p	Pressure, [Pa].
r	Bubble radial, [m].
$\mathbf{S}$	Viscous stress tensor, [N·m^{-2}].
$\mathbf{T}$	Reynold stress tensor, [N·m^{-2}].
t	Time, [s].
$\boldsymbol{u}$	Velocity, [m·s^{-1}].
V	Bubble volume, [m^{3}].
X	Phase indicator function, [-].

Sub/superscripts

air	Air.
B	Bubble.
c	Continuous phase.
d	Disperse phase.
diff	diffusion
deformation	Deformation force.
i	Index *i*.
interfacial	Interfacial force.
lift	Lift force.
water	Water.

INTRODUCTION

Two-phase flows are widely encountered in chemical engineering, energy production and conversion, oil and gas industries and biotechnology (Lucas et al., 2010). However, many flow mechanisms are still unclear due to their high complexity. Experimental investigations on the two-phase flows are challenging, costly and time-consuming due to the need to discriminate the two phases. In comparison, simulations provide a more accessible way to study these flows, but they invariably rely on models. Among the simulation methods, the Eulerian two-fluid model shows the advantages for the simulation of the bubbly flows up to the industrial dimensions.

In the standard Eulerian framework, the fluids are treated as the interpenetrating continua using a phase indicator function to identify each phase. In this way, the forces acting on the bubble are distributed to the entire region covered by it. As a consequence, the coherent motion of the bubble as a whole is not enforced. As a result, some unphysical phenomena appear in the simulation results of the standard Euler-Euler modelling. For example, an over-prediction of the peak of the gas volume fraction can appear in the pipe center if the bubble diameter is larger than the mesh size (Tomiyama et al., 2003). A similar phenomenon can occur in the near wall region such that the peak of gas volume fraction locates directly on the wall (Rzehak et al., 2017).

A feasible way to recover the inconsistencies in the two-fluid model is by using the particle-center-averaged method to average the parameters of disperse phase. This approach has been applied to introduce bubble geometry in the simulation of the wall-bounded bubbly flow (Moraga et al., 2006). In this method, the delta function indicating the location of the bubble center is involved explicitly (Biesheuvel et al., 1989, Biesheuvel et al., 1990, Sangani et al., 1993, Moraga et al., 2006) or implicitly (Zhang et al., 1994a, Prosperetti, 1998) in the averaging. As a result, the mass and momentum of each bubble are assigned to its center. Also the forces act in the bubble center. In addition, the number density of the bubble centers is the primary variable and the gas volume fraction is derived from it.

The calculation of the gas volume fraction is a key issue in the two-fluid modelling based on the particle-center-averages. The coarse graining methods in the CFD-DEM modelling (Khawaja et al., 2012, Peng et al., 2014) and the interphase coupling methods of the Euler-Lagrange modelling (Kitagawa et al., 2001, Hu et al., 2008) can be borrowed to deal with this issue. Among these methods, the “small particle approximation” used in Zhang and Prosperetti’s research (Zhang et al., 1994a, Prosperetti, 1998) assigns all the volume of the disperse element to the mesh cell containing its center. This is not appropriate for the case of interest in the present study where the bubble size exceeds the spacing of the numerical mesh. Analytical approaches, which compute the volume of the overlapped region between the bubble and the Euler mesh are easy to implement for the structured meshes but difficult to use on the unstructured ones. Moreover, the analytical method can cause large fluctuations in the distribution of the gas volume fraction when the mesh spacing is smaller than the bubble diameter (Sun et al., 2015b). The convolution method (Kitagawa et al., 2001, Xiao et al., 2011) and the diffusion-based method (Sun et al., 2015b, Sun et al., 2015a) are two promising approaches for the calculation of the gas volume fraction. In the convolution method, the gas volume fraction is calculated as a weighted average by using a kernel function as the weight factor. However, it is complicated to deal with the kernel function near the curved boundaries or in corners of the domain where boundaries meet non-orthogonally and to implement it in a code for the unstructured meshes and parallel computation (Sun et al., 2015b). In the diffusion-based method, the gas volume fraction is the solution of a diffusion equation. This method is easy to implement for the cases using the structured or unstructured meshes and serial or parallel processing. In addition, it gives similar results as the convolution method with a Gaussian kernel function by selecting a suitable diffusion time (Sun et al., 2015b). Hence, it is used for the calculation of the gas volume fraction in this study.

When the particle-center-averaged method is used, the averaged momentum equation obtained for the disperse phase is slightly different. In the standard Euler-Euler modelling, this equation is derived by averaging the local instantaneous momentum equation of the disperse phase. In contrast, Zhang and Prosperetti et al. (Zhang et al., 1994a, Zhang et al., 1994b, Prosperetti, 1998) derived this equation by averaging the particle equation of motion directly. The disperse phase momentum equations derived by these two methods have slightly different meanings. In the standard Euler-Euler modelling, the equation shows the momentum balance of the disperse phase material entirely contained inside the control volume. The equation derived by Zhang and Prosperetti et al. instead displays the momentum balance of the disperse phase material, which belongs to the particles with their centers located inside the control volume. For the gas-liquid bubbly flow, since the mass and viscosity of the disperse bubbles are small, the latter method is recommended (Zhang et al., 1994a, Zhang et al., 1994b, Zhang et al., 1995) to avoid involving the constitutive equations of the gas material. Therefore, the momentum equation derived by the latter method is used for gas phase in present study.

In this work, the particle-center-averaging is applied to the dispersed phase and the phase-averaging is used for the continuous phase. The idea of using the different averaging approaches for the various phases was introduced in the study of two-phase flow before (Zhang et al., 1994a, Prosperetti, 1998, Moraga et al., 2006). The momentum equation for the disperse phase derived from the equation of motion of the bubbles shows explicitly that the bubbles respond to pressure and stress of the continuous phase. Furthermore, the models for interfacial forces are changed to be functions of the number density of the bubble centers. In addition, to avoid the bubble centers to come arbitrarily close to walls, a wall-contact force is introduced. The deformation force model of Lucas et al. (Lucas et al., 2007) is adapted for oblate ellipsoidal bubbles and used in the simulation.

In present study, the particle-center-averaged method and the deformation force model are implemented in OpenFOAM-6. In order to evaluate the Euler-Euler modelling based on the particle-center-averages, a simple two-dimensional test case is used first and then comparisons between predictions and experimental measurements are made. The novelty of this research lies in combining the particle-center-averaged method with the Helmholtz-Zentrum Dresden-Rossendorf baseline closure model (Rzehak et al., 2017) for the Euler-Euler modelling and determining the gas volume fraction based on a diffusion equation.

TWO-FLUID MODEL FRAMEWORK BASED ON PARTICLE-CENTER-AVERAGED METHOD

This section introduces the theory of the applied Euler-Euler model. As mentioned before, the phase-average and the particle-center-average are used to average the continuous and the disperse phases respectively. The difference between this method and the standard Euler-Euler method employing the phase-average for both phases will be explained in detail. Both phases are taken as incompressible and a fixed monodisperse bubble size is assumed.

Continuity equations

Since the continuous phase uses the phase-average method, its continuity equation remains the same as in the standard Euler-Euler modelling (Drew et al., 1998, Prosperetti, 1998)

$$\frac{\partial \alpha_c}{\partial t} + \nabla \cdot \alpha_c \overline{\boldsymbol{u}_c}^x = 0. \tag{1}$$

In this equation, the volume fraction is defined as

$$\alpha_c = \int_{C^N} X_c P^N dC^N \ , \tag{2}$$

while the ensemble phase-averaged velocity of the continuous phase $\overline{\boldsymbol{u}_c}^x$ is given by

$$\overline{\boldsymbol{u}_c}^x = \frac{\int_{C^N} \boldsymbol{u}_c X_c P^N dC^N}{\alpha_c} \ . \tag{3}$$

In these equations, X_c is the phase-indicator function for the continuous phase. P^N is the probability density function of the set of all possible states of N bubbles, C^N. Here and the following, the notation with an overbar and nearby x is used to indicate ensemble phase-averaged variables.

Employing particle-center-averages, the continuity equation for the disperse phase is a transport equation for the number density of the bubble centers (Prosperetti, 1998)

$$\frac{\partial n}{\partial t} + \nabla \cdot (n\langle \boldsymbol{u}_d \rangle) = 0. \tag{4}$$

The definition of this number density is

$$n(\boldsymbol{x}, t) = \int P(\boldsymbol{x}, \boldsymbol{u}_d, t)\, d\boldsymbol{u}_d \ , \tag{5}$$

where $P(\boldsymbol{x}, \boldsymbol{u}_d, t)$ is the probability of finding a bubble centered at $\boldsymbol{x}$ with center-of-mass velocity $\boldsymbol{u}_d$ at time *t*. It is related to P^N as the integral over all bubbles except one. From the definition, we can see that the number density is non-zero only for those control volumes that may contain a bubble center.

In Eq. (4), $\langle \boldsymbol{u}_d \rangle$ is the particle-center-averaged velocity of the bubbles. It is defined as

$$\langle \boldsymbol{u}_d \rangle(\boldsymbol{x}, t) = \frac{\int P(\boldsymbol{x}, \boldsymbol{u}_d, t)\boldsymbol{u}_d \, d\boldsymbol{u}_d}{n(\boldsymbol{x}, t)} . \tag{6}$$

By using Eq. (4) as the continuity equation, information on the bubble centres will be accessible.

Momentum equations

For incompressible Newtonian flow, the momentum equation for the continuous phase is (Prosperetti, 1998)

$$\begin{aligned} \frac{\partial \alpha_c \rho_c \overline{\boldsymbol{u}_c}^x}{\partial t} &+ \nabla \cdot (\alpha_c \rho_c \overline{\boldsymbol{u}_c}^x \overline{\boldsymbol{u}_c}^x) \\ &= -\alpha_c \nabla \overline{p_c}^x + \alpha_c \nabla \cdot \overline{\boldsymbol{S}_c}^x \\ &+ \nabla \cdot \alpha_c \overline{\boldsymbol{T}_c}^x + \overline{\boldsymbol{f}_c^{\text{interfacial}}}^x \\ &+ \alpha_c \rho_c \boldsymbol{g} \ . \end{aligned} \tag{7}$$

The momentum equation for the disperse phase is (Prosperetti, 1998)

$$\begin{aligned} \frac{\partial (\beta_d \rho_d \langle \boldsymbol{u}_d \rangle)}{\partial t} &+ \nabla \cdot (\beta_d \rho_d \langle \boldsymbol{u}_d \rangle \langle \boldsymbol{u}_d \rangle) \\ &= -\beta_d \nabla \overline{p_c}^x + \beta_d \nabla \cdot \overline{\boldsymbol{S}_c}^x \\ &+ \nabla \cdot (\beta_d \langle \boldsymbol{T}_d \rangle) + \beta_d \rho_d \boldsymbol{g} \\ &+ \langle \boldsymbol{f}_d^{\text{interfacial}} \rangle \ , \end{aligned} \tag{8}$$

where

$$\beta_d = n V_d \ . \tag{9}$$

It is important to note that β_d is not the disperse phase volume fraction. The latter is related to the bubble number density by a convolution

$$\alpha_d(\boldsymbol{x}) = \iiint n(\boldsymbol{x_0}) X_d(\boldsymbol{x_0}) d\boldsymbol{x_0} \ , \tag{10}$$

where $X_d(\boldsymbol{x_0})$ is the phase indicator function in the location of $\boldsymbol{x} = \boldsymbol{x_0}$.

The difference between above momentum equations and those in the standard Euler-Euler modelling lies in the following aspects.

1) In the viscous stress term, the parameters related to the volume fraction (α_c and β_d) are outside of the divergence operator.

2) The momentum equation of the disperse phase explicitly shows the response of the bubbles to the pressure and viscous stress of the continuous phase, since the equation is derived from the bubble equation of motion. In this condition, no additional closure model for the pressure or stress of gas phase is required.

3) The momentum equation of the disperse phase is related to the bubble number density instead of the gas volume fraction.

Models for Interfacial forces and turbulence

The relation of the interfacial forces in Eqs. (7) and (8) is

$$\overline{\boldsymbol{f}_c^{\text{interfacial}}}^x = -\langle \boldsymbol{f}_d^{\text{interfacial}} \rangle \ . \tag{11}$$

The selected correlations for the interfacial forces according to the HZDR baseline model (Rzehak et al., 2017) are listed in Table 1. In the simulations using the standard Euler-Euler modelling in OpenFOAM-6, it was found necessary to apply a damping for the lift force within the distance of one bubble diameter from the wall (see Fig. 1 below). For comparability, this wall-damped lift force is used for the particle-center-averaged simulations as well throughout this study except where specifically noted elsewise. No such damping was mentioned in previous simulations with the HZDR baseline model using ANSYS CFX.

Table 1: Selected models for interfacial forces in simulation

Interfacial force	Selected model
Drag force	Ishii et al. (1979)
(Shear-) lift force	Tomiyama et al. (2002) with cosine wall damping
Turbulent dispersion force	Burns et al. (2004)
Wall (-lift) force	Hosokawa et al. (2002)
Virtual mass force	Constant coefficient, $C_{vm} = 0.5$

The interfacial force models in the Euler-Euler simulations based on the particle-center-averaged method should be expressed as functions of the number density of the bubble centers rather the gas volume fraction. This conversion is achieved by the following formulation

$$f(n) = \frac{nV_d}{\alpha} f(\alpha), \qquad (12)$$

where $f(n)$ and $f(\alpha)$ are the interfacial forces as functions of the number density of the bubble centers and the gas volume fraction, respectively.

Furthermore, an additional wall-contact force must be introduced to avoid the bubble centers coming unphysically close to the wall. The deformation force model proposed by Lucas et al. (Lucas et al., 2007) is changed to be applicable for the bubbles with a more general oblate ellipsoidal shape and used in the simulation. The model reads

$$\begin{aligned} f_{\text{deformation}} &= -2\pi r_B \sigma n \left[-\frac{1}{x^2} \right. \\ &+ \frac{1}{1-x^3} \left(2x\sqrt{1-x^3} \operatorname{arctanh} \sqrt{1-x^3} \right. \\ &\left. \left. - \frac{3}{2}x + \frac{3}{2}x^4 \frac{\operatorname{arctanh}\sqrt{1-x^3}}{\sqrt{1-x^3}} \right) \right]. \end{aligned} \qquad (13)$$

Both laminar and turbulent flows of the continuous phase are considered. In the turbulent case, the turbulent dispersion force and the *k-ω* SST turbulent model are employed together with the bubble-induced turbulence model of Ma et al. (Ma et al., 2017). The flow of the disperse phase is assumed to be laminar because the gas viscosity and density are much smaller than those of the liquid.

Diffusion-based method for gas volume fraction calculation

In this study, a diffusion-based method (Sun et al., 2015b, Sun et al., 2015a) is used to compute the gas volume fraction from the number density of the bubble centers. In this method, the gas volume fraction is calculated by solving a diffusion equation

$$\frac{\partial \alpha_d}{\partial \tau} - \nabla \cdot \left(C_{diff} \nabla \alpha_d \right) = 0 \qquad (14)$$

with an initial condition

$$\alpha_d(x, \tau = 0) = n(x, \tau = 0)V_d. \qquad (15)$$

The diffusion coefficient C_{diff} is set to $1 \text{m}^2 \cdot \text{s}^{-1}$ in this study. The variable τ is a pseudo-time, independent of physical time and the diffusion time $\tau = T$ up to which Eq. (13) is integrated determines the size of the diffusion domain.

The appropriate size of the diffusion domain remains an open question. Previously, it has been set to be 3 to 6 times the diameters of disperse element (Deen et al., 2004, Sun et al., 2015b, Sun et al., 2015a). This size can exceed the bubble size since the paths of the bubble motions may exhibit oscillations. In this study, an optimal diffusion time is determined by comparing the theoretical distribution of the gas volume fraction for a stream of spherical bubbles and the distribution of the gas volume fraction calculated by the diffusion equation.

The theoretical gas volume fraction distribution for a stream of spherical bubbles is (Lubchenko et al., 2018)

$$\alpha_d(x) = \alpha_{max} - \frac{\alpha_{max}}{r_B^2}(x - x_0)^2 \qquad (16)$$

where the peak of the gas volume fraction, α_{max}, is related to the frequency of bubble injection.

The one-dimensional solution of Eq. (14) is (Haberman, 2012)

$$\begin{aligned} &\alpha_d(x, \tau) \\ &= \int_{-\infty}^{+\infty} nV_d \delta(x - x_0) \\ &\times \frac{1}{\sqrt{4\pi\tau}} \exp\left[-\frac{(x - x_0)^2}{4\tau} \right] dx_0, \end{aligned} \qquad (17)$$

which is seen to be the convolution of the initial δ –gas volume distribution with a Gaussian kernel.

An optimal diffusion time is determined by minimizing the root-mean-square deviation between $\alpha_d(x)$ and $\alpha_d(x, \tau)$ given by Eqs. (16) and (17), respectively. The Matlab optimization function *fminbnd( )* is used for this purpose. The resulting optimized diffusion time is

$$T = \frac{d_B^2}{30C_{diff}}. \qquad (18)$$

The gas volume fraction calculated using this optimized time is expected to have the most similar shape as the theoretical distribution (Eq. (16)).

ILLUSTRATION OF THE EULER-EULER MODELLING METHOD BASED ON THE PARTICLE-CENTER-AVERAGES

In this section, the advantages of the Euler-Euler simulation based on the particle-center-averaged method over the standard Euler-Euler modelling are illustrated by a simplified test case. Gas and liquid are taken to be air and water from here on and the indices denoting the phases are adapted accordingly.

Geometry and simulation set up

A two-dimensional test case similar to that used in Tomiyama et al (2003) is employed. The domain is a rectangle with a size of 0.03 m×0.5 m (see Fig. **1** a)).

A stream of bubbles is injected from the center of the shorter side. The gas volume fraction at inlet for the cases simulated by the standard Euler-Euler modelling can be seen in Fig. **1** b)). The lateral length covered by the gas volume fraction at the inlet shows the dimension of one bubble. The inlet liquid velocity is a parabolic profile (see Fig. **1** c)) to introduce a shear flow field. The inlet gas velocity is uniform with a value of 0.18 $\text{m} \cdot \text{s}^{-1}$.

For Euler-Euler simulations based on the particle-center-averages, the inlet number density of the bubble centers is non-zero only in the center mesh. Its value is calculated to obtain the same inlet gas flow rate as the cases simulated by the standard Euler-Euler modelling. For a uniform mesh and uniform inlet gas velocity, it is given by

$$n = \frac{1}{V_d} \sum_{i=1}^{M} \alpha_{air,i} \ , \qquad (19)$$

where M is the number of mesh cells at the inlet and V_d is the volume of the bubble.

Mesh sensitivity analysis

To reveal the numerical problems caused by the inconsistencies in the standard Euler-Euler modelling, the mesh sensitivity is analyzed in the simulation using the standard Euler-Euler modelling and the Euler-Euler simulation based on the particle-center-averaged method.

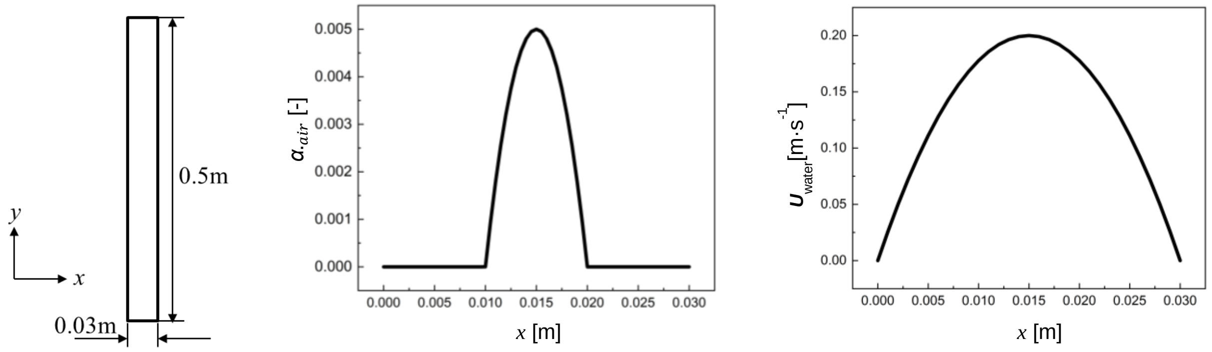

a) Geometry b) Inlet gas volume distribution c) Inlet liquid velocity distribution

Figure 1: Geometry and inlet settings

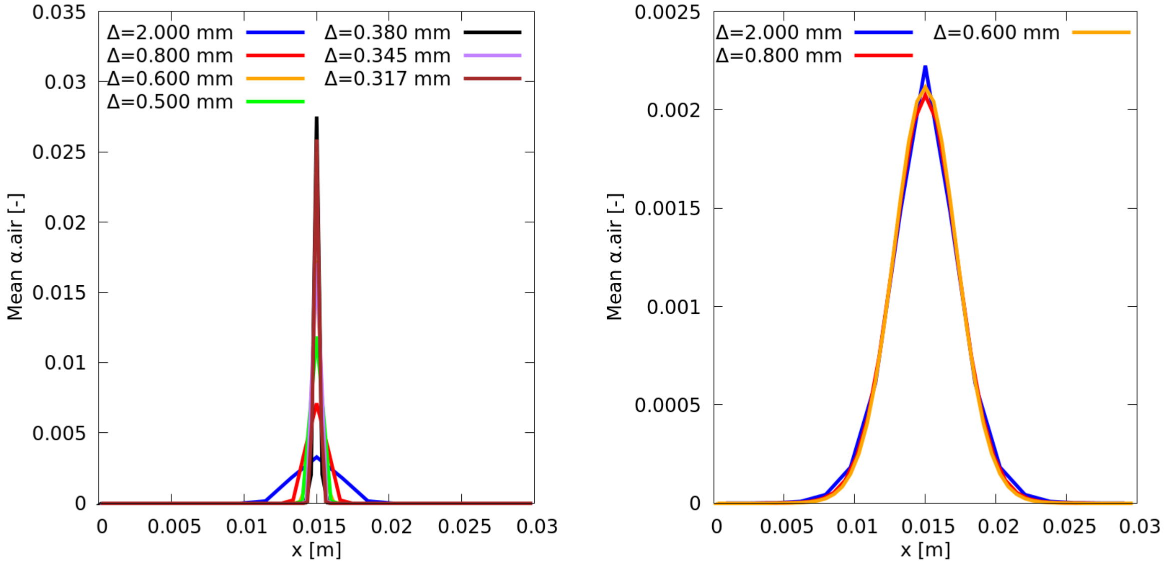

a) Standard Euler-Euler modelling b) Euler-Euler modelling based on particle-center-averages

Figure 2: Mesh sensitivity analysis in laminar flow case at a height y = 0.4 m (Δ : mesh size)

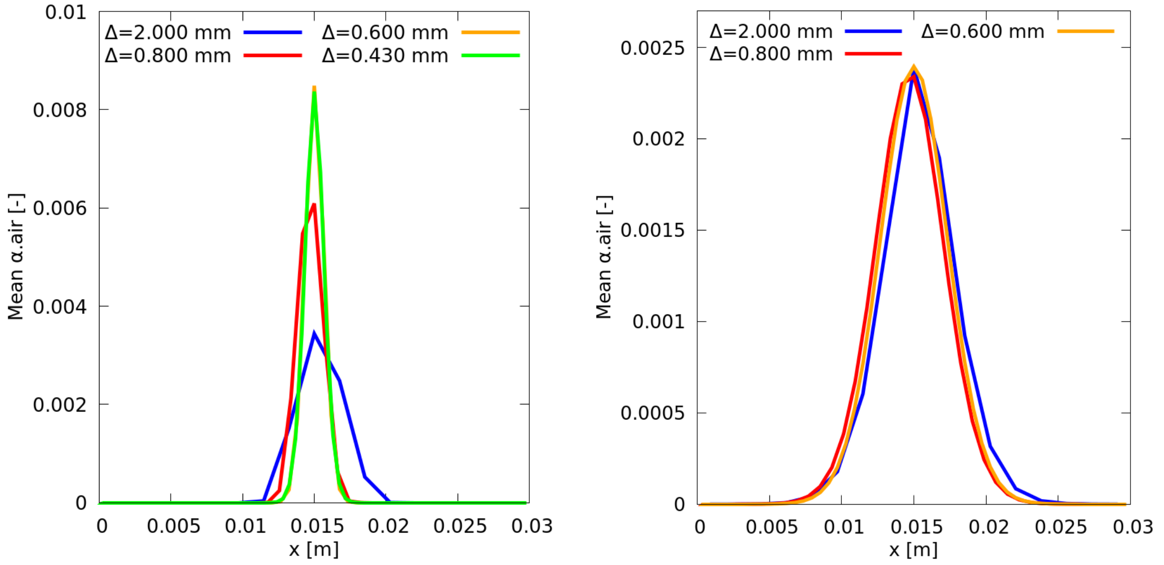

a) Standard Euler-Euler modelling b) Euler-Euler modelling based on particle-center-average

Figure 3: Mesh sensitivity analysis in turbulent flow case at a height y = 0.4 m (Δ : mesh size)

In this analysis, the bubble diameter is taken as 10 mm, while the coarsest spacing of the numerical grids $\Delta = 2$ mm. The simulation results at a height y = 0.4 m above the inlet are shown.

Laminar flow

The mesh sensitivity analysis of laminar simulation results can be seen in Fig. 2. In the results for the standard Euler-Euler modelling, the peak of the gas volume fraction increases continuously with decreasing mesh size (see Fig. 2 a)). Therefore, the mesh independent results are not found. This reason for the phenomenon is that the lift force is distributed to the cells of the numerical mesh covered by the bubble, which drives the gas in the mesh cells located at the bubble edge towards the bubble center, even though the bubble center does not move in the lateral direction. This phenomenon becomes more significant when the mesh is refined.

In comparison, in the results of the Euler-Euler simulation based on the particle-center-averaged method, the peak of the gas volume fraction does not increase upon refining the mesh (see Fig. 2 b)) since the lift force acts on the bubble center. As a result, the solution obtained with a mesh size of 0.8mm can be regarded as mesh independent solution. This means that in the laminar flow condition, the particle-center-averaged method remedies the numerical deficiency of the standard Euler-Euler approach and provides a mesh independent solution.

Turbulent flow

Upon including the turbulent dispersion force, the mesh independent solutions exist in both cases (see Fig. 3) since this force smoothes the nonphysical peak of gas volume fraction in the standard Euler-Euler modelling. The solutions for meshes with 0.6 mm and 0.8 mm can be regarded as mesh independent for the standard Euler-Euler modelling and the particle-center-average based Euler-Euler simulations, respectively. However, the nonphysical behaviours are still visible in the results of the standard Euler-Euler modelling.

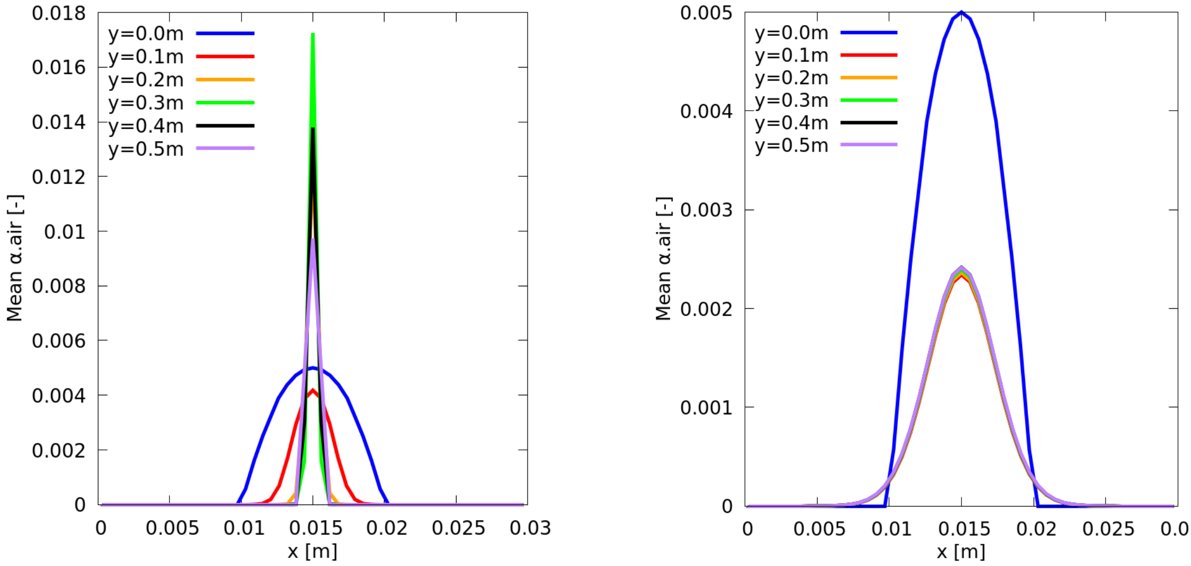

a) Standard Euler-Euler modelling

b) Euler-Euler simulation based on particle-center-average

Figure 4: Lateral gas volume fraction distribution in laminar flow case

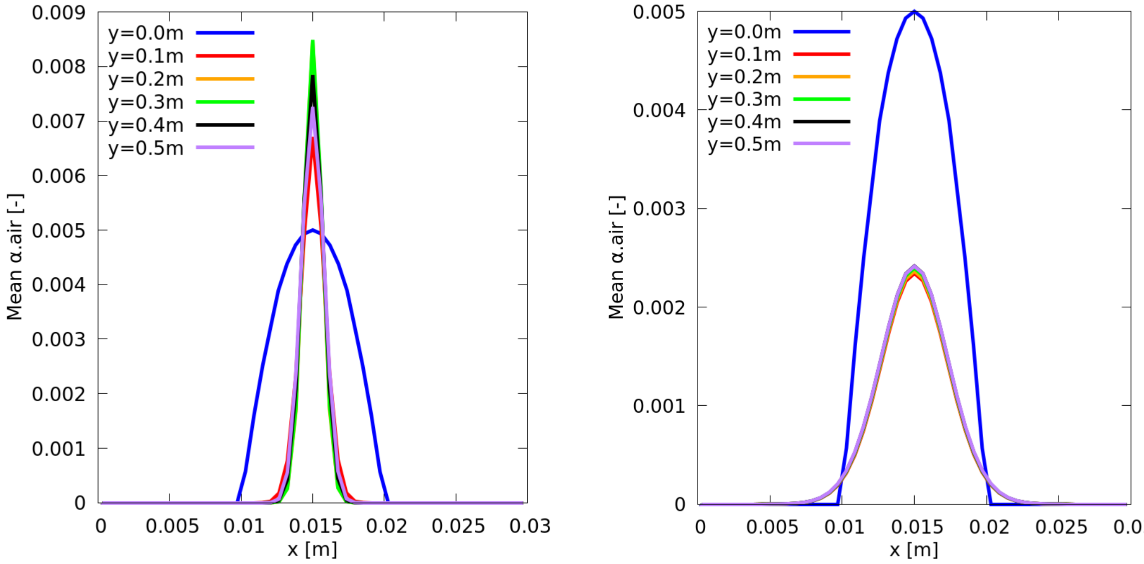

a) Standard Euler-Euler modelling

b) Euler-Euler simulation based on particle-center-averaging

Figure 5: Lateral gas volume fraction distribution in turbulent flow case

When the grids are refined from 2 mm to 0.6 mm, the peak of the gas volume fraction increases and the lateral region covered by the gas decreases significantly (see Fig. 3 a)).

Axial development of gas volume fraction

In this section, the axial development of the distribution of the gas volume fraction in the two-dimensional test case is analyzed to show the improvement of the predictions obtained by the particle-center-averaged method. The mesh size for all the simulation cases in this section is 0.6 mm. It should be noted that for the inlet conditions as described above, the relative velocity between gas and liquid has a value of $-0.02\ \mathrm{m{\cdot}s^{-1}} \sim 0.18\mathrm{m{\cdot}s^{-1}}$. However, the terminal velocity, which will be approached by the bubble as it rises is about $0.23\ \mathrm{m{\cdot}s^{-1}}$ according to the correlation of Mendelson (Mendelson, 1967). Hence, the relative velocity will increase within a certain distance from the inlet.

Laminar flow case

In the simulations of the laminar flow case by the standard Euler-Euler modelling (see Fig. 4 a)), the gas moves to the channel center downstream of the inlet. A nonphysical peak of the gas volume fraction appears with an increasing distance. In addition, the lateral region covered by the gas becomes smaller than the bubble diameter and its extent decreases further downstream. This is nonphysical since the bubble size is expected to remain unchanged. As mentioned before, these phenomena are caused by the lift force being distributed to the bubble volume instead of acting on the bubble center.

In contrast, by using the particle-center-average based Euler-Euler modelling, the distribution of gas volume fraction remains almost unchanged after a short transient next to the inlet (see Fig. 4 b)). Further downstream, the lateral region covered by the gas has a size close to the bubble diameter. The increase of relative velocity right after the inlet causes the decrease of the peak of gas volume fraction. In conclusion, the predictions of the distributions of the gas volume fraction using the particle-center-averages are considered more reasonable.

Turbulent flow case

If the turbulent dispersion force is included, the nonphysical behaviours in the standard Euler-Euler modelling are weakened but remain visible in the results (see Fig. 5 a)). The lateral region covered by the gas downstream of the inlet is still smaller than the bubble diameter. Additionally, the peak of the gas volume fraction downstream is higher than that at the inlet. However, it should be lower than that at the inlet because of the increase of relative velocity with increasing distance from the inlet. In comparison, upon using simulation based on the particle-center-averages (see Fig. 5 b)), after a short distance downstream of the inlet, the distribution of the gas volume fraction remains almost unchanged and the size of the lateral region covered by the gas is close to the bubble diameter and remains constant. The simulation results of the gas volume fraction using the particle-center-averages are more physical because the lift force acts only on the bubble center.

In conclusion, the particle-center-averaging can help to avoid the overconcentration of gas around the location of the bubble center and provide a mesh independent solution.

COMPARISON OF SIMULATION RESULTS AND EXPERIMENTAL DATA IN PIPE FLOW

In order to evaluate the particle-center-averaged method in the Euler-Euler modelling, the simulation results of the standard Euler-Euler modelling and the Euler-Euler simulation based on the particle-center-averages are compared with measurement data from the MTLoop experiment (Lucas et al., 2005).

The test section in the MTLoop facility is a vertical pipe. Its inner diameter is 51.2 mm. The temperature of air and water in the experiment is 30℃ and the pressure is atmospheric pressure. The data used for comparison are measured at a distance of 3.03 m from the location of the gas injection. The ratio between the distance from the inlet and the pipe diameter (L/D) is about 59. Therefore, fully-developed flow is expected at the measurement location.

The inlet velocities and the volume fractions are uniform for disperse and continuous phases in the simulation. They are calculated from the superficial air and water velocities in the experiment. The parameters of the selected cases are listed in Table 2.

Table 2: Parameters of selected MTLoop cases

Test No.	$J_{\mathrm{air}}\ [\mathrm{m \cdot s^{-1}}]$	$J_{\mathrm{water}}\ [\mathrm{m \cdot s^{-1}}]$	d_B [mm]
017	0.0040	0.4050	4.865
019	0.0040	1.0170	4.697
042	0.0096	1.6110	4.151
043	0.0096	2.5540	2.918
047	0.0151	0.1020	7.442
048	0.0151	0.1610	6.486
064	0.0235	1.6110	4.661

The bubble diameters listed in this table are the Sauter mean diameters at the height of 3.03 m. In the simulation, the radial mesh size is 0.512 mm. It is uniform and finer than the bubble diameter.

First of all, the necessity of damping the lift force near wall in the simulations using the standard Euler-Euler modelling is illustrated. The radial distribution of the lift forces with and without near wall damping are shown in Fig. 6. As can be seen, without damping the lift force assumes extremely large values near the wall. This is due to the fine grid with a spacing smaller than the bubble size.

The effects of damping the lift force near wall on the distribution of the gas volume fraction in the cases simulated by the standard Euler-Euler modelling can be seen in Fig. 7. Without damping the lift, the peaks of the gas volume fraction in the simulation results can be much higher than the experimental data and locate directly on the wall. These peaks should locate at about one bubble radius away from the wall in the condition without considering bubble deformations. The reason for this unphysical phenomenon is that the lift force is too high in near wall region. In comparison, the peak value and location simulated by damping the lift force have a better agreement with the experimental data. As a consequence, the wall-damping lift force is used in the following simulations.

The comparison of the radial distributions of the gas volume fraction to those simulated by the particle-center-averaged Euler-Euler modelling and the standard Euler-Euler modelling and the experimental data is shown in Fig. 8. The over-prediction of the peak of the gas volume fraction in the results calculated by the standard Euler-Euler modelling can be seen in these figures. The extent of the over-prediction is more severe for the cases with smaller bubble Sauter mean diameters.

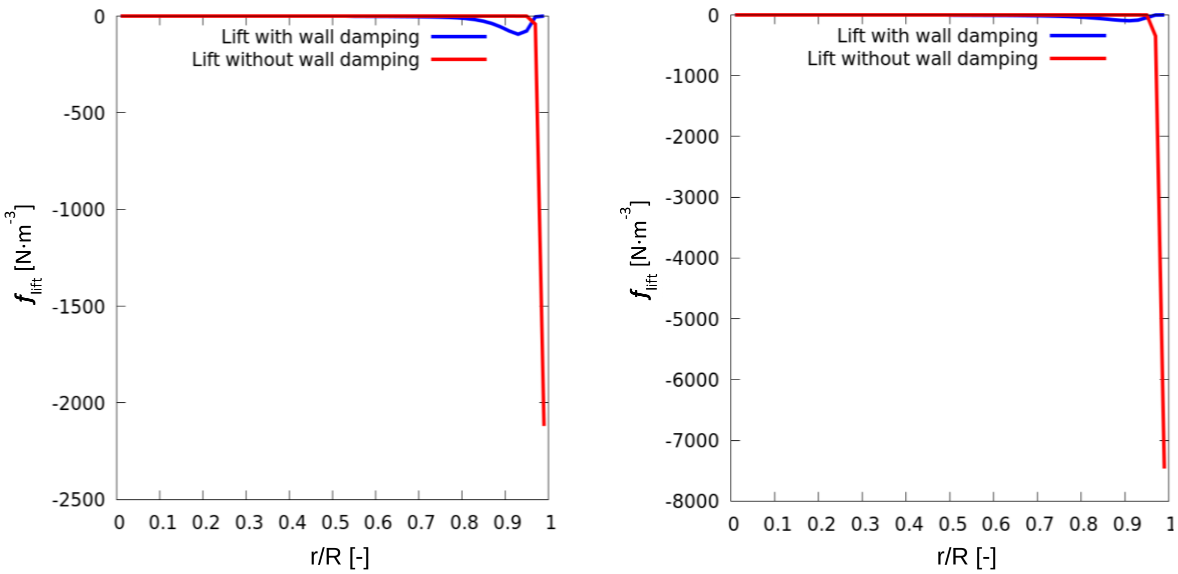

a) MTLoop 042 b) MTLoop 064

Figure 6: Radial distribution of lift force in cases simulated by standard Euler-Euler modelling

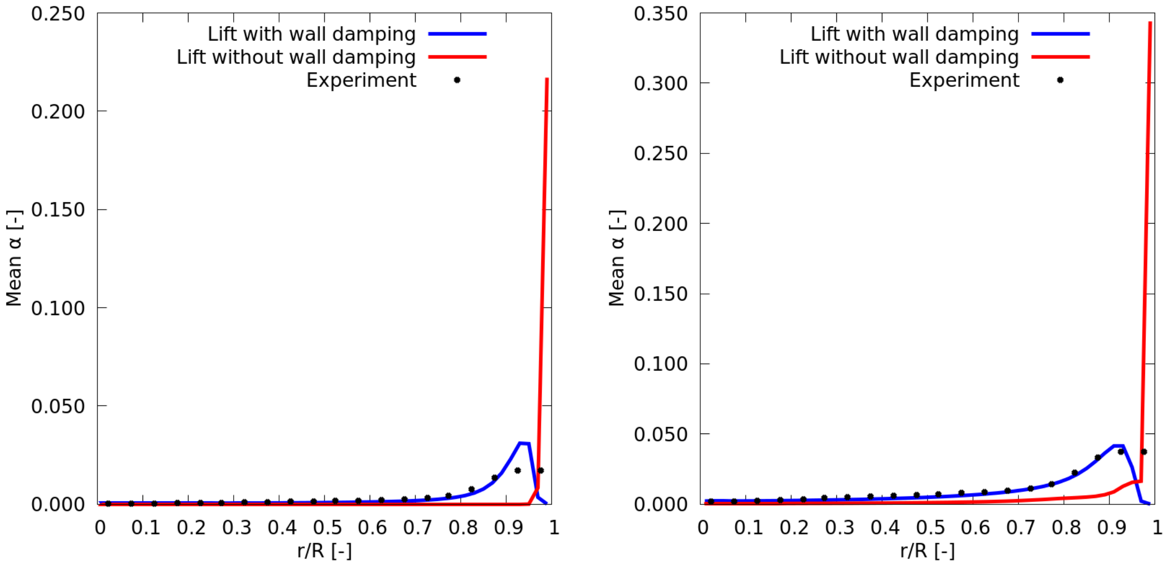

a) MTLoop 042 b) MTLoop 064

Figure 7: Radial distribution of gas volume fraction in cases simulated by standard Euler-Euler modelling

For case MTLoop 043, the peak value of gas volume fraction in the simulation result is about 10 times higher as in the experimental data. The over-prediction of the peak value for the gas volume fraction can be caused by the distributed lift force over the bubble volume in the standard Euler-Euler modelling. Furthermore, the reason of more significant over-prediction of the peak for smaller bubbles where the ratio of bubble diameter and mesh size is smaller can be that with the presently applied lift force correlation, the smaller bubble in these simulation cases experiences a higher lift force.

In comparison, the particle-center-averaged method displays its ability to avoid the over-prediction of the peak of the gas volume fraction in the near wall region. The peaks of the gas volume fraction simulated by the Euler-Euler based on the particle-center-averaged method fit the experimental data well in the majority of cases. The most notable deviation in these results is that the peak location is further away from the wall compared to the experimental data and the simulation results of the standard Euler-Euler modelling. This may result from using wall-lift and wall-contact forces at the same time could drive too much gas away from the wall.

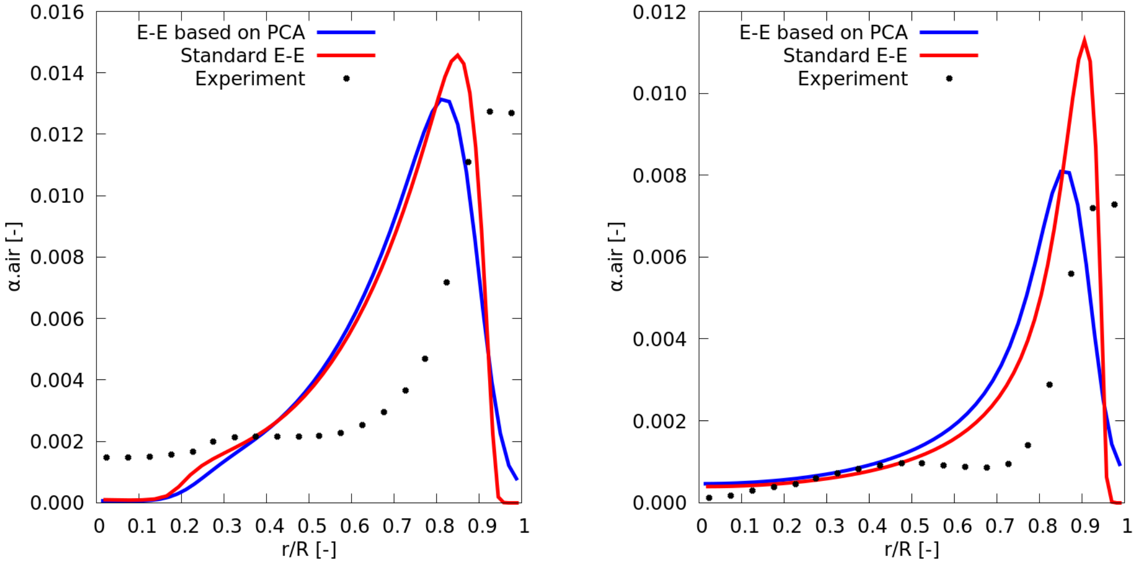

a) MTLoop 017 b) MTLoop 019

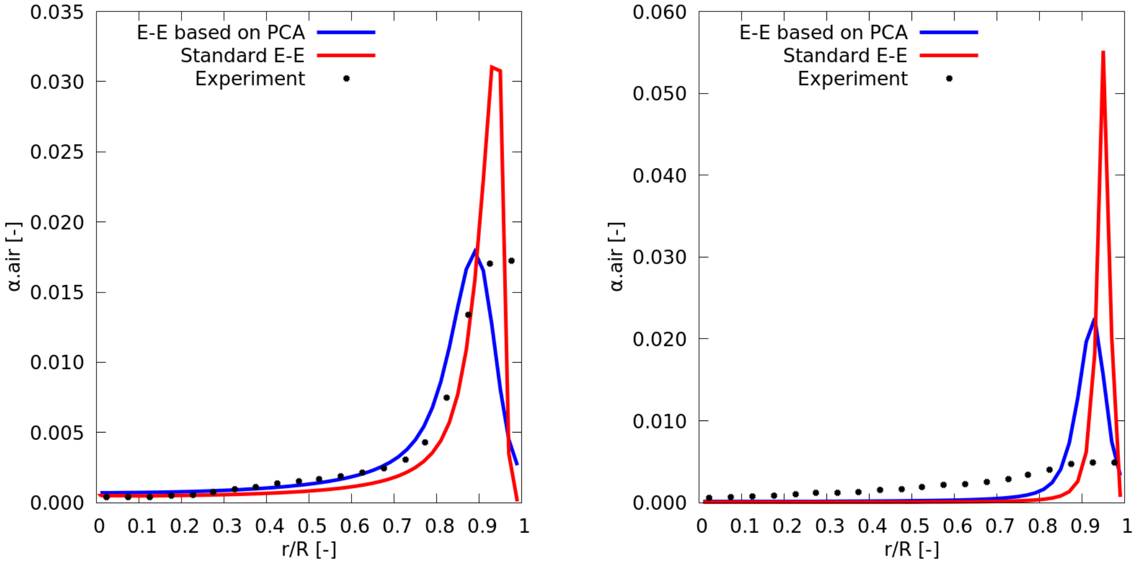

c) MTLoop 042 d) MTLoop 043

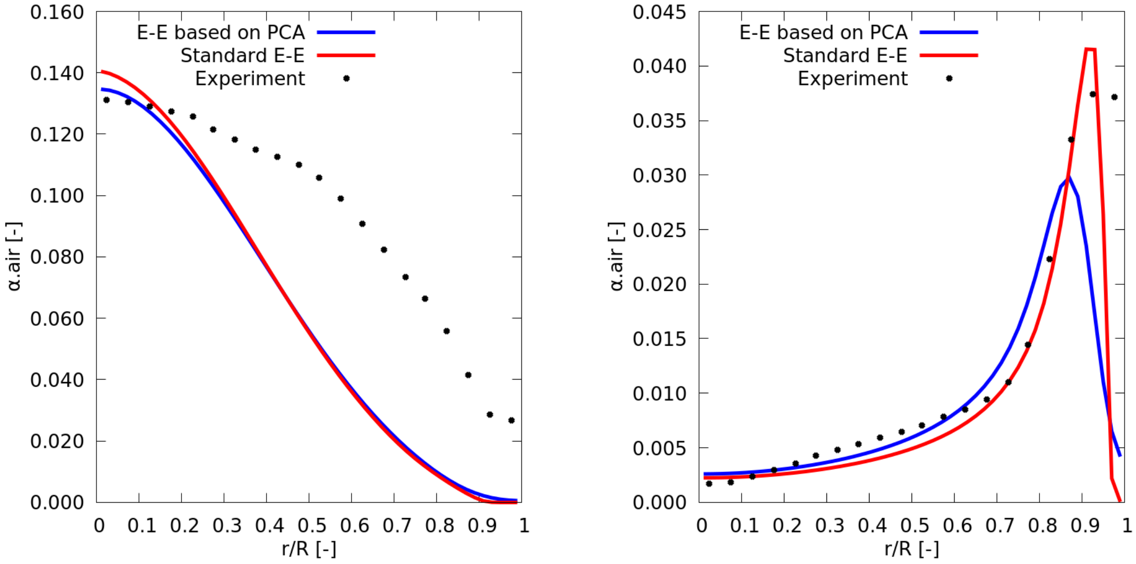

e) MTLoop 047 f) MTLoop 064

Figure 8: Radial distribution of gas volume fraction at 3.03 m downstream of the inlet with wall-damping lift force (E-E: Euler-Euler, PCA: particle-center-average)

CONCLUSION AND OUTLOOK

Inconsistencies exist in the standard Euler-Euler modelling based on the phase-averages since the forces of bubble are the function of gas volume fraction. When the bubble size exceeds that of the numerical mesh, the distributed lift force in bubble volume can lead to an over-prediction of the peak of the gas volume fraction. Refining the numerical mesh may lead to the increasing over-prediction of the peak value and mesh independent solution may not exist.

The diffusion-based particle-center-averaged method has been shown to remedy these inconsistencies. In this method, the forces act on the bubble center and the bubble dimension is considered in the process of using the diffusion-based method to transfer the number density of bubble canters into the gas volume fraction. A deformation force is employed to prevent the bubble centers to come arbitrarily close to the walls. As a result, the unphysical over-predictions of the peak value of the gas volume fraction near a wall or in the pipe center are alleviated or eliminated compared to the results of the standard Euler-Euler modelling. Numerically, the benefit of using this method is that the mesh-independent solutions exist.

In the Euler-Euler simulations based on the particle-center-averaged method, the forces acting on the continuous phase should still be distributed to the region covered by the bubble. Since this work is still in process, it has not been shown here. Furthermore, the future work should be focused on the research of near wall forces to avoid driving too much gas away from the wall.

REFERENCES

Biesheuvel, A. and W. Gorissen (1990), “Void fraction disturbances in a uniform bubbly fluid”, *International Journal of Multiphase Flow*, **16**, 211-231.

Biesheuvel, A. and S. Spoelstra (1989), “The added mass coefficient of a dispersion of spherical gas bubbles in liquid”, *International journal of multiphase flow*, **15**, 911-924.

Deen, N. G., M. van Sint Annaland, et al. (2004), “Multi-scale modeling of dispersed gas–liquid two-phase flow”, *Chemical Engineering Science*, **59**, 1853-1861.

Drew, D. A. and S. L. Passman (1998). Theory of multicomponent fluids, Springer Science & Business Media.

Haberman, R. (2012). Applied partial differential equations with Fourier series and boundary value problems, Pearson Higher Ed.

Hu, G. and I. Celik (2008), “Eulerian–Lagrangian based large-eddy simulation of a partially aerated flat bubble column”, *Chemical Engineering Science*, **63**, 253-271.

Khawaja, H. A., S. A. Scott, et al. (2012), “Quantitative analysis of accuracy of voidage computations in CFD-DEM simulations”, *The Journal of Computational Multiphase Flows*, **4**, 183-192.

Kitagawa, A., Y. Murai, et al. (2001), “Two-way coupling of Eulerian–Lagrangian model for dispersed multiphase flows using filtering functions”, *International journal of multiphase flow*, **27**, 2129-2153.

Lubchenko, N., B. Magolan, et al. (2018), “A more fundamental wall lubrication force from turbulent dispersion regularization for multiphase CFD applications”, *International Journal of Multiphase Flow*, **98**, 36-44.

Lucas, D., M. Beyer, et al. (2010), “A new database on the evolution of air–water flows along a large vertical pipe”, *International Journal of Thermal Sciences*, **49**, 664-674.

Lucas, D., E. Krepper, et al. (2005), “Development of co-current air–water flow in a vertical pipe”, *International Journal of Multiphase Flow*, **31**, 1304-1328.

Lucas, D., E. Krepper, et al. (2007), “Use of models for lift, wall and turbulent dispersion forces acting on bubbles for poly-disperse flows”, *Chemical Engineering Science*, **62**, 4146-4157.

Ma, T., C. Santarelli, et al. (2017), “Direct numerical simulation–based Reynolds-averaged closure for bubble-induced turbulence”, *Physical Review Fluids*, **2**, 034301.

Mendelson, H. D. (1967), “The prediction of bubble terminal velocities from wave theory”, *AIChE Journal*, **13**, 250-253.

Moraga, F., A. Larreteguy, et al. (2006), “A center-averaged two-fluid model for wall-bounded bubbly flows”, *Computers Fluids*, **35**, 429-461.

Peng, Z., E. Doroodchi, et al. (2014), “Influence of void fraction calculation on fidelity of CFD‐DEM simulation of gas‐solid bubbling fluidized beds”, *AIChE Journal*, **60**, 2000-2018.

Prosperetti, A. (1998), Ensemble averaging techniques for disperse flows, *Particulate Flows*, Springer, 99-136.

Rzehak, R., T. Ziegenhein, et al. (2017), “Unified modeling of bubbly flows in pipes, bubble columns, and airlift columns”, *Chemical Engineering Science*, **157**, 147-158.

Sangani, A. S. and A. Didwania (1993), “Dispersed-phase stress tensor in flows of bubbly liquids at large Reynolds numbers”, *Journal of Fluid Mechanics*, **248**, 27-54.

Sun, R. and H. Xiao (2015a), “Diffusion-based coarse graining in hybrid continuum–discrete solvers: Applications in CFD–DEM”, *International Journal of Multiphase Flow*, **72**, 233-247.

Sun, R. and H. Xiao (2015b), “Diffusion-based coarse graining in hybrid continuum–discrete solvers: Theoretical formulation and a priori tests”, *International Journal of Multiphase Flow*, **77**, 142-157.

Tomiyama, A., N. Shimada, et al. (2003), “Application of Number Density Transport Equation for the Recovery of Consistency in Multi-Field Model”, *ASME/JSME 2003 4th Joint Fluids Summer Engineering Conference*, American Society of Mechanical Engineers.

Xiao, H. and J. Sun (2011), “Algorithms in a robust hybrid CFD-DEM solver for particle-laden flows”, *Communications in Computational Physics*, **9**, 297-323.

Zhang, D. and A. Prosperetti (1994a), “Averaged equations for inviscid disperse two-phase flow”, *Journal of Fluid Mechanics*, **267**, 185-219.

Zhang, D. and A. Prosperetti (1994b), “Ensemble phase‐averaged equations for bubbly flows”, *Physics of Fluids*, **6**, 2956-2970.

Zhang, D. and A. Prosperetti (1995), “Energy and momentum equations for disperse two-phase flows and their closure for dilute suspensions”, *J. Fluid Mech*.

14th International Conference on CFD in Oil & Gas, Metallurgical and Process Industries
SINTEF, Trondheim, NORWAY
October 12-14, 2020

ON MODELLING ELECTROCHEMICAL GAS EVOLUTION USING THE VOLUME OF FLUID METHOD

Kurian J. VACHAPARAMBIL[1*], **Kristian Etienne EINARSRUD**[1†]

[1]Department of Materials Science and Engineering, Norwegian University of Science and Technology (NTNU), Trondheim 7491, Norway

[*] E-mail: kurian.j.vachaparambil@ntnu.no
[†] E-mail: kristian.e.einarsrud@ntnu.no

ABSTRACT

In this work we describe the various building block relevant in simulating electrochemical gas evolution using Volume of Fluid (VOF) method. These building blocks are implemented in the VOF solver available in OpenFOAM® and its predictions are compared to the theoretical models reported in literature. The fully coupled solver to model electrochemical gas evolution is used to model the case of a bubble evolving on a vertical electrode under constant potential condition to showcase its ability.

Keywords: VOF, Surface tension modelling, Interfacial mass transfer, Bubble growth, Gauss's law, Dissolved gas transport, Electrochemical systems .

NOMENCLATURE

Greek Symbols

ρ Density, $[{}^{kg}/_{m^3}]$
μ Dynamic viscosity, $[{}^{kg}/_{ms}]$
ν Kinematic viscosity, $[{}^{m^2}/_{s}]$
σ Surface tension, $[{}^{N}/_{m}]$
κ Interfacial curvature, $[{}^{1}/_{m}]$
α Volume fraction, $[-]$
ϕ Potential, $[V]$
β Growth coefficient, $[-]$
$\mathcal{F}$ Fraction of electrode area covered by bubble, $[-]$

Latin Symbols

D Diffusion coefficient, $[{}^{m^2}/_{s}]$.
$\vec{g}$ Acceleration due to gravity, $[{}^{m}/_{s^2}]$.
k Conductivity, $[{}^{S}/_{m}]$.
p Pressure, $[Pa]$.
C Molar concentration, $[{}^{mol}/_{m^3}]$.
$\vec{x}$ Position vector, $[m]$.
$\vec{U}$ Velocity vector, $[{}^{m}/_{s}]$.
$\vec{i}$ Current density vector, $[{}^{A}/_{m^2}]$.
$\vec{S}$ Individual cell face surface area vector, $[m^2]$.
He Jump condition across the interface, $[-]$.
f Void fraction, $[-]$.
R Bubble radius, $[m]$.
I Current when no bubbles are present, $[A]$.
d Interelectrode distance, $[m]$.
A Total electrode area, $[m^2]$.
M Molar mass, $[{}^{kg}/_{mol}]$.
F Faraday's constant (=96485), $[{}^{As}/_{mol}]$.

Sub/superscripts

1 Liquid or phase 1.
2 Bubble or phase 2.
i Dissolved gas species.
0 Operating condition.
s Saturation condition.
e Averaged or effective value.
$'$ Initial/starting condition.
m Modified.
∞ At bulk.
$\hat{}$ Harmonic average.

INTRODUCTION

Electrochemical gas evolution is relevant in a variety of industrial processes such as water-splitting, chloralkaline and Hall–Héroult. Bubble evolution in these systems involve nucleation, growth, coalescence and detachment from electrode. The dynamic behaviour of bubbles causes overpotential changes due to supersaturation, ohmic resistance and electrode screening, as well as enhanced mass transfer (Zhao *et al.*, 2019). Due to the complex and coupled nature of electrochemical gas evolution (Taqieddin *et al.*, 2018), numerical modelling of the system is an ideal way to understand its physics and develop strategies to efficiently remove these bubbles.

In literature, the numerical models used to simulate the continuum scale processes in electrochemical gas evolution can be broadly divided into dispersed and interface-resolving approaches. The dispersed approaches, like Euler-Euler, Mixture and Euler-Lagrange models, relies on a priori knowledge of flow to select interphase closure terms (Hreiz *et al.*, 2015). These approaches do not resolve the dispersed bubbles and are typically used to simulate industrial scale electrochemical systems (Hreiz *et al.*, 2015). On the other hand, interface-resolving approaches, like Volume of Fluid (VOF) (Einarsrud and Johansen, 2012; Einarsrud *et al.*, 2017; Sun *et al.*, 2018) and phase-field (Zhang *et al.*, 2020), resolve individual bubbles and is typically used to study in detail the dynamic behaviour of few bubbles. Although these studies have provided knowledge relevant to simulate the multiphysics nature of electrochemical gas evolution, there is still a lack research that addresses the coupled multiphysics as well as the multiscale nature of the process as highlighted by Taqieddin *et al.* (2018)

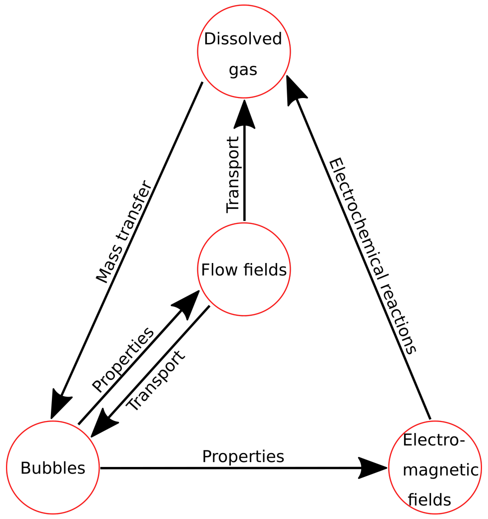

Figure 1: Schematic of the coupling between various modules of the proposed solver proposed to model electrochemical gas evolution.

In this work, we highlight various modules required to simulate electrochemical gas evolution, see Fig.1, to partly address the knowledge gap highlighted by Taqieddin *et al.* (2018). The decoupled modules are developed on the VOF solver available on OpenFOAM® 6, interFoam (Deshpande *et al.*, 2012). These modules are individually verified by comparison to relevant theoretical models available in literature and finally the potential of the fully coupled solver is discussed.

THE DECOUPLED MODEL DESCRIPTION

In this section, we introduce the various modules that are relevant in modelling electrochemical gas evolution: reliable small (sub-millimeter) bubbles, transport of dissolved gas, supersaturation driven bubble growth and ohmic resistance associated with bubble evolution. Before these individual modules are described, the VOF model as implemented in interFoam is introduced, for further details please refer Deshpande *et al.* (2012). The VOF model uses a scalar function known as volume fraction of liquid (α_1) which takes a value equal to unity in the liquid, zero in the gas phase and $0 < \alpha_1 < 1$ in the interface. The volume fraction of gas is calculated as $\alpha_2 = 1 - \alpha_1$. The advection of the volume fraction of liquid is computed as

$$\frac{\partial \alpha_1}{\partial t} + \nabla \cdot (\alpha_1 \vec{U}) + \nabla \cdot (\alpha_1(1-\alpha_1)\vec{U}_r) = 0, \quad (1)$$

where $\vec{U}$ is the velocity in domain and $\vec{U}_r$ is the compressive velocity computed based on a user-defined compression factor (C_α), see Deshpande *et al.* (2012). The fluid properties, like density (ρ) and viscosity (μ), are computed as $\chi = \alpha_1\chi_1 + \alpha_2\chi_2$. The mass conservation equation of the phases, described using continuity equation, is

$$\nabla \cdot \vec{U} = 0. \quad (2)$$

The momentum equation is written using a modified pressure, $p_m = p - \rho\vec{g}\cdot\vec{x}$, as

$$\begin{aligned}\frac{\partial \rho \vec{U}}{\partial t} + \nabla \cdot (\rho \vec{U}\vec{U}) =& \nabla \cdot (\mu \nabla \vec{U}) + \nabla \vec{U} \cdot \nabla \mu + \vec{F}_{ST} \\ & - \nabla p_m - \vec{g}\cdot\vec{x}\nabla\rho,\end{aligned} \quad (3)$$

where $\vec{F}_{ST}$ is the surface tension force is treated using the Continuum Surface Force (CSF) model (Brackbill *et al.*, 1992) and viscous term, usually written as $\nabla\cdot\mu(\nabla\vec{U}+\nabla\vec{U}^T)$ can be expressed as $\nabla\cdot(\mu\nabla\vec{U}) + \nabla\vec{U}\cdot\nabla\mu$ using Eq.2, see Deshpande *et al.* (2012).

Modelling sub-millimeter bubbles

One of the main well known problems associated with VOF approach is the errors in determining the local curvature used in surface tension modelling. These errors generate spurious velocities near the interface that can cause non-physical flow in the computational domain (Popinet, 2018; Vachaparambil and Einarsrud, 2019). The spurious velocities tend to become stronger with smaller length scales or lower Capillary number and it can sometimes be strong enough to generate nonphysical random walk of the bubbles. One of the approaches to reduce spurious velocities is to replace the commonly used CSF model with the Sharp Surface Force (SSF) model, proposed by Raeini *et al.* (2012), other advances has been reviewed in Popinet (2018). The work by Vachaparambil and Einarsrud (2019), has shown the ability of SSF to successfully simulate capillary rise and rising bubbles as well as reduce spurious velocities compared to CSF model.

The SSF model, based on the work of Raeini *et al.* (2012); Vachaparambil and Einarsrud (2019), describes $\vec{F}_{ST}$ as

$$\vec{F}_{ST} = \sigma \kappa_{final} \nabla \alpha_{sh}, \quad (4)$$

where κ_{final} is obtained using a three step smoothing of curvature and α_{sh} is calculated as

$$\alpha_{sh} = \frac{1}{1-C_{sh}}\left[\min\left(\max\left(\alpha_1, \frac{C_{sh}}{2}\right), 1-\frac{C_{sh}}{2}\right) - \frac{C_{sh}}{2}\right], \quad (5)$$

where C_{sh} is the user-defined sharpening coefficient which must satisfy $0 \leq C_{sh} < 1$. To model sub-millimeter bubble, the sharpening coefficient is set to 0.3 (Vachaparambil and Einarsrud, 2020b).

Transport of dissolved gas

Compared to single phase flows, the transport of species in a two phase flow requires the treatment of the interfacial conditions i.e. concentration jump across the interface and continuity of diffusive fluxes, see Maes and Soulaine (2018) or Deising *et al.* (2018). These interfacial conditions are incorporated into a single unified transport equation which solves for the concentration field in both liquid and the gas in the Compressive Continuous Species Transfer (CCST) model, developed by Maes and Soulaine (2018). The governing equation for C_i, in CCST model, is

$$\begin{aligned}\frac{\partial C_i}{\partial t} + \nabla \cdot (\vec{U}C_i) =& \nabla \cdot (\hat{D}_i \nabla C_i - \hat{D}_i B C_i \nabla \alpha_1) \\ & - \nabla \cdot (B\alpha_1\alpha_2\vec{U}_r C_i),\end{aligned} \quad (6)$$

where $\vec{U}_r$ is the compressive velocity (used in Eq.1), B is the defined as $(1-He)/(\alpha_1+\alpha_2 He)$, where He describes the concentration jump across the interface (also known as partition coefficient), and $\hat{D}_i$ is the harmonic averaging of the diffusion coefficients, see Maes and Soulaine (2018) for further details. Inorder to simulate the transport of dissolved gas, which should only be in the liquid, we use He equal to a value near zero (like 10^{-4}), to minimize the transport of dissolved gas into the bubble which is accounted for by the CCST model based on the defined value of He (Maes and Soulaine, 2018; Vachaparambil and Einarsrud, 2020b). As He is a small number (10^{-4}), C_i obtained from Eq.6 can be interpreted as $C_i = \overline{C}_i - \overline{C}_s$, where $\overline{C}_i$ is the actual concentration and $\overline{C}_s$ represents the saturation concentration, based on Vachaparambil and Einarsrud (2020a,b).

Supersaturation driven bubble growth

When modelling interfacial mass transfer phenomena and the associated bubble growth, Sherwood number based correlations are widely used in CFD simulations (Einarsrud and Johansen, 2012; Einarsrud *et al.*, 2017). The drawback of these correlations is its limited applicability, due to its dependence on the bubble shape and relevant Reynolds and Schmidt number (Deising *et al.*, 2018). A more universal approach is to use the Fick's 1^{st} law, which is the governing equation used in deriving Sherwood number correlations (Bird *et al.*, 2007). To the best of the authors knowledge there are only two very recent works that has used Fick's 1^{st} law to model bubble evolution: Vachaparambil and Einarsrud (2020a,b) and Maes and Soulaine (2020).

In order to model the growth of bubble driven by the supersaturated electrolyte, we use the approach proposed by Vachaparambil and Einarsrud (2020a,b). In this work, the phenomenological Fick's 1^{st} law, the driving force for bubble growth, is coupled to CCST, described based on Eq.6, with relevant source terms for species transport (Eq.6), advection of α_1 (Eq.1) and continuity (Eq.2) equations is implemented by extending the work of Hardt and Wondra (2008). For information about the relevant governing equations and source terms, please refer to Vachaparambil and Einarsrud (2020b).

Modelling electromagnetic effects

To model the electromagnetic effects, we use Gauss's law which can be described mathematically as

$$\nabla \cdot \vec{i} = 0, \tag{7}$$

where the current density ($\vec{i}$) can be expressed using the gradient of potential (ϕ) as

$$\vec{i} = -k\nabla\phi, \tag{8}$$

where k is the conductivity, calculated as an algebraic averaging of conductivities, i.e. $\alpha_1 k_1 + \alpha_2 k_2$. This approach has been used in literature to describe the evolution of carbon dioxide bubbles in aluminum reduction process (Einarsrud and Johansen, 2012).

SOLVER SETTINGS

Due to the coupled nature of momentum and pressure equations, the equations are computed using the PISO algorithm, see Deshpande *et al.* (2012). The governing equations are discretized with first order schemes for time and second order schemes in space, for details please refer to Vachaparambil and Einarsrud (2020b). The convergence criterion used solve governing equations for p_{rgh} and other variables (like ϕ, $\vec{U}$, C_i and others) are 10^{-20} and 10^{-10} respectively. When surface tension is relevant in the simulations, a constraint on time step constraint described in Deshpande *et al.* (2012); Vachaparambil and Einarsrud (2019) is used to prevent the growth of spurious velocities.

VERIFICATION OF THE DECOUPLED SOLVER

In this section, we verify the individual modules implemented in interFoam using theoretical models described in literature.

On sub-millimeter bubbles

The ability of the SSF model to reliably simulate sub-millimeter bubbles is demonstrated by a simulation of a stationary bubble. Without body forces, i.e. gravity, in the domain, any velocities present in the simulation can be attributed to spurious velocities. As electrochemically generated bubbles can be present on both the electrode surface and in the bulk (after detachment), it is necessary to reliably simulate sub-millimeter bubbles for both cases.

The properties of the liquid and gas used in the simulation are $\rho_1 = 1000$kg/m^3, $\rho_2 = 1$kg/m^3, $\nu_1 = 10^{-6}$m^2/s, $\nu_2 = 1.48\times10^{-5}$m^2/s and $\sigma = 0.07$N/m. Two test cases, where the bubble is available in the bulk (SBC1) and attached to the electrode surface (SBC2), where the stationary bubble has a diameter ($2R$) of 0.5mm are simulated in a 2D domain of dimensions $4R \times 4R$. Both SBC1 and SBC2 are meshed using a hexahedral grid with 120×120 cells. For SBC1, all the boundaries are assigned zeroGradient for both $\vec{U}$ and α_1 but the p_{rgh} is assigned fixedValue of 101325Pa. In the case of SBC2, where the left and right boundaries are defined as walls, $\vec{U}$ uses no-slip condition at the walls and zeroGradient at the other boundaries along with α_1 uses zeroGradient on all boundaries (with a default contact angle of 90° at the walls) and p_{rgh} as fixedValue (equal to 0Pa) at the top wall and fixedFluxPressure (Greenshields, 2019) on the other boundaries. Due to the surface tension, the maximum time step allowed is manually limited to 0.6μs (see Deshpande *et al.* (2012); Vachaparambil and Einarsrud (2019)) and the simulations are run until 0.05s.

The accuracy of these simulations are estimated using Laplace pressure and magnitude spurious velocities, like in Vachaparambil and Einarsrud (2019). The Laplace pressure in a 2D bubble can be calculated based on Young-Laplace equation as $\Delta p_c = \sigma/R$ and the spurious velocities (U_{sc}) is estimated as max($|\vec{U}|$). The Laplace pressure in the bubble, from the simulations, is calculated as

$$\Delta p = \frac{\int_V \alpha_2 p dV}{\int_V \alpha_2 dV} - p_0, \tag{9}$$

where p_0 is the operating pressure used in the simulations. The associated error in Laplace pressure (E) is calculated as $(\overline{\Delta p} - \Delta p_c)/\Delta p_c$, where the overbar indicates the averaged value over the simulation time.

Table 1: Time averaged values of spurious velocities, Laplace pressure and its error obtained while simulating a stationary sub-millimeter bubble.

Case	$\overline{U_{sc}}$ (m/s)	$\overline{\Delta p}$ (Pa)	E
SBC1	0.0108	255.35	−0.088
SBC2	0.0198	253.91	−0.093

As shown in Fig.2, the spurious velocities generated are present on both sides of the interface (for both TC1 and

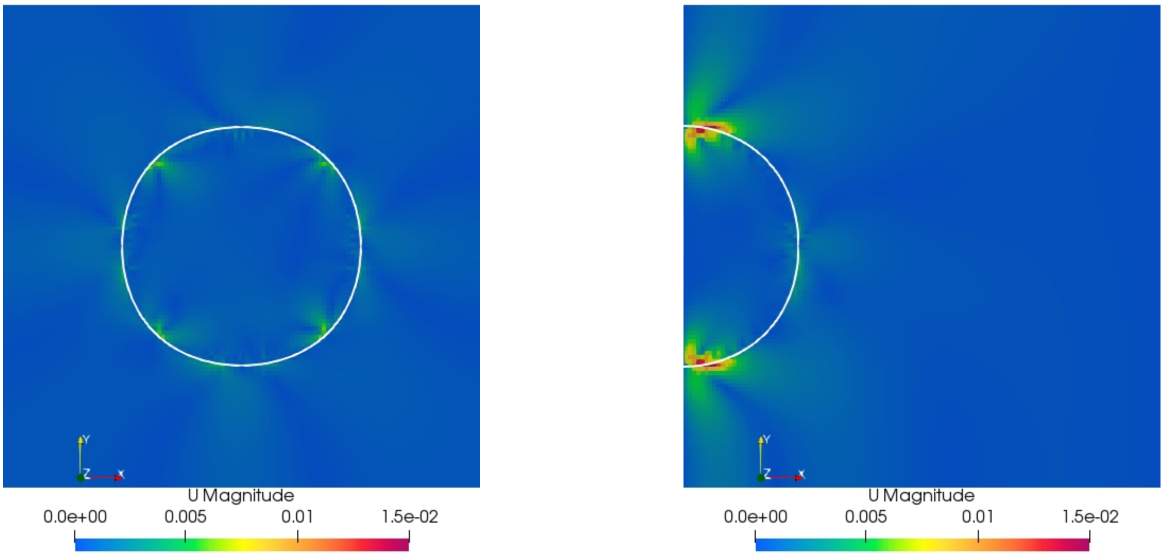

(a) Bubble in the bulk (SBC1).

(b) Bubble on the wall (SBC2).

Figure 2: Comparison of the spurious velocities (m/s) generated while modelling stationary bubbles at $t = 0.05$s with interface (at $\alpha_1 = 0.5$) represented by the white contour.

TC2). Interestingly, the spurious velocities generated are quite different in both TC1 and TC2, with the latter generating strong spurious velocities near the foot of the bubble. These time averaged spurious velocities and error in estimating the Laplace pressure of the bubble quantified in Table.1.

On the transport of dissolved gas

In order to show that Eq.6 with $He = 10^{-4}$ can model the transport of dissolved gas reasonably well, we take a hypothetical case where a rising bubble moves through a region of supersaturation. The fluid properties used in the simulations, which are adapted from Hysing *et al.* (2009), are $\rho_1 = 1000$kg/m^3, $\rho_2 = 1$kg/m^3, $\nu_1 = 0.01$m^2/s, $\nu_2 = 0.1$m^2/s, $\sigma = 1.96$N/m and $|\vec{g}| = 0.98$m/s^2 along with $D_1 = 10^{-9}$m^2/s and $D_2 = 10^{-5}$m^2/s. A bubble of diameter 0.5m is initialized such that its center is 0.5m from the bottom and side boundaries in a domain of dimensions 1m×2m. The simulation is run with hexahedral mesh with 160×320 cells. The region of supersaturation, $C_i = 10$mol/m^3, is initialized in an area of 1m×0.7m from a distance of 0.8m from the bottom wall. All four boundaries are assigned the zeroGradient condition for C_i and α_1. The boundary conditions for $\vec{U}$ are assigned slip conditions at the side walls and remaining walls are set as no-slip. For p_{rgh}, the top wall is assigned the fixedValue (equal to zero) but the other walls are described using fixedFluxPressure (Greenshields, 2019).

The spatial distribution of the dissolved gas as the bubble rises and deforms is illustrated in Fig.3. The convection induced by the rising bubble does not advect the dissolved gas into the bubble. Due to the use of a non-zero He, to prevent B in Eq.6 from becoming infinity, dissolved gas does numerically drift into the bubble but this is negligible (lower than 0.01% of the amount of dissolved gas).

On supersaturation driven bubble growth

Adapted fromVachaparambil and Einarsrud (2020a,b), the fluid properties used in the simulation are $\rho_1 = 997.08$kg/m^3, $\rho_2 = 1.81$kg/m^3, $\nu_1 = 8.92 \times 10^{-7}$m^2/s, $\nu_2 = 8.228 \times 10^{-6}$m^2/s, $D_1 = 1.94 \times 10^{-9}$m^2/s, $D_2 = 9.18 \times 10^{-6}$m^2/s and $M = 44 \times 10^{-3}$kg/mol. Both surface tension and gravity are neglected in the simulations. The parameters used in the solver are defined based on the work by Vachaparambil and Einarsrud (2020b). The domain used for the computation is 3cm×3cm which is meshed with 4000×4000 cells, the pre-existing bubble (of diameter equal to 0.5mm) is initialized at the center of the domain. The liquid phase is initialized with a concentration of dissolved gas at 200.64mol/m^3. The boundary conditions used are described in Vachaparambil and Einarsrud (2020b).

The approach to describe the growth of a pre-existing bubble in a supersaturated solution can be verified by the Extended Scriven model proposed by Hashemi and Abedi (2007) (based on the work by Scriven (1959)):

$$R = 2\beta\sqrt{D_1\left(t + \frac{R'^2}{4D_1\beta^2}\right)}, \tag{10}$$

where β is the growth coefficient and R' is the radius of the pre-existing bubble. The growth coefficient for 2D bubbles, derived in Vachaparambil and Einarsrud (2020b), is

$$\beta_{2D} = \frac{a + \sqrt{a^2 + 4a}}{2\sqrt{2}}, \tag{11}$$

where a is equal to $M\Delta C/\rho_2$ and ΔC is equal to the concentration of the dissolved gas that is over the saturation condition (equal to 200.64mol/m^3). Fig.4 shows that the evolution of bubble radius predicted by the model agrees reasonably with the Extended Scriven with β_{2D}. The discrepancy between the simulation and the Extended Scriven model can be explained by the discontinuous nature of dissolved gas concentration at $t = 0$s (Vachaparambil and Einarsrud, 2020a,b).

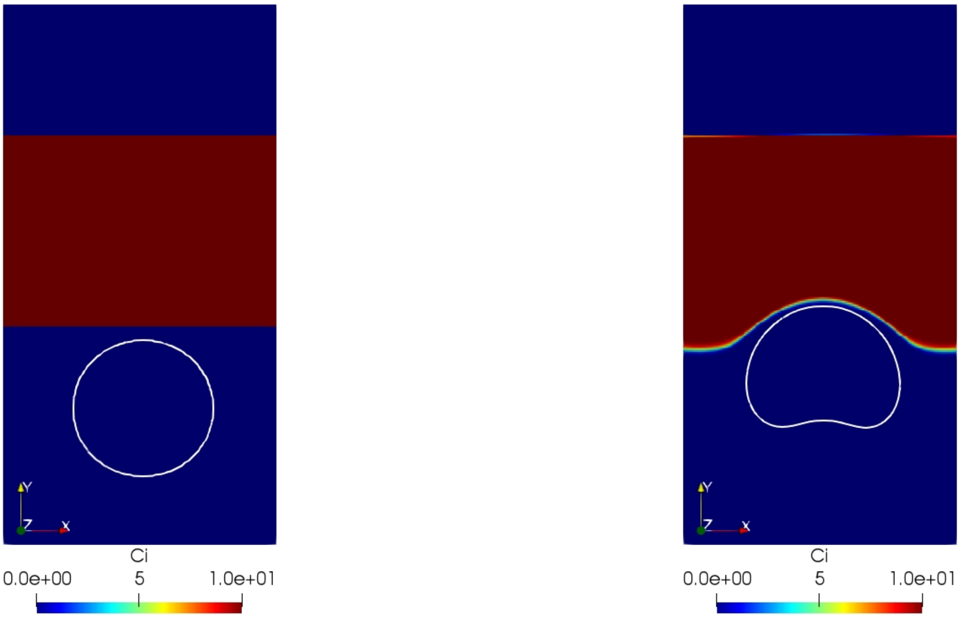

(a) $t = 0$s.

(b) $t = 1$s.

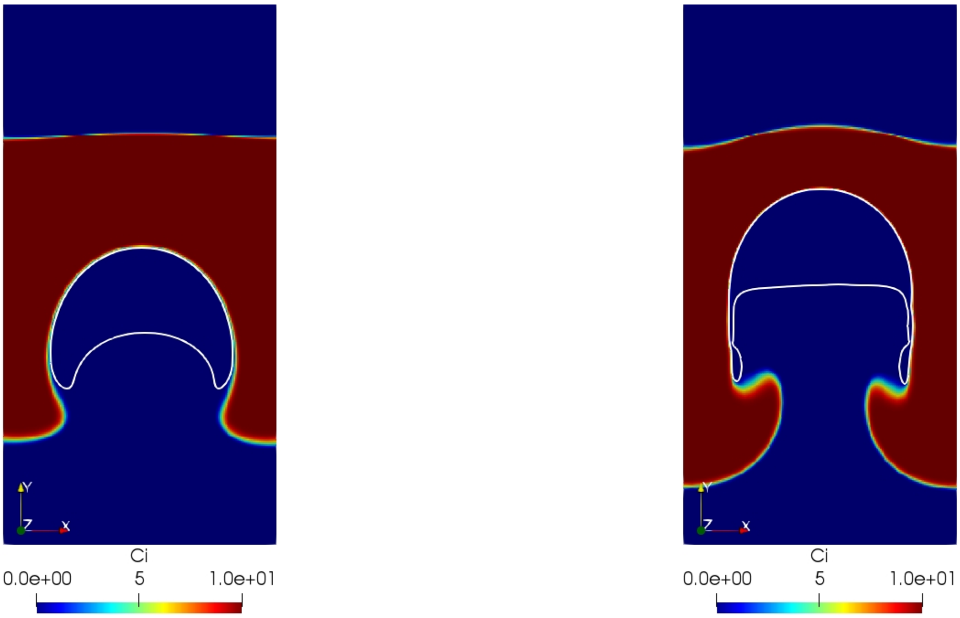

(c) $t = 2$s.

(d) $t = 3$s.

Figure 3: The concentration of dissolved gas (mol/m^3) around a rising bubble (interface, at $\alpha_1 = 0.5$, is represented by white contour) modelled based on Eq.6.

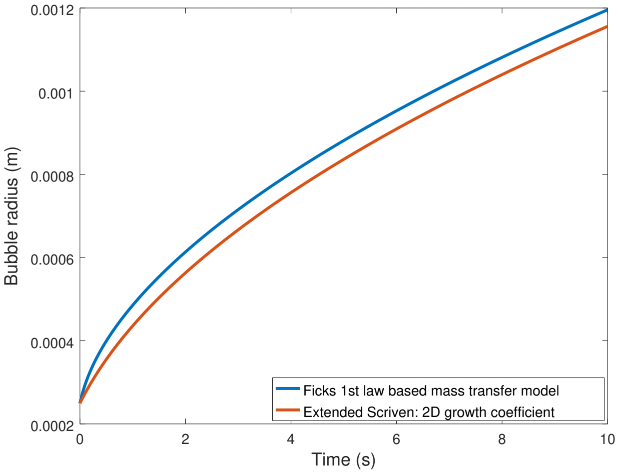

Figure 4: Comparison of the bubble growth predicted by Fick's 1^{st} law based model (based on the work by Vachaparambil and Einarsrud (2020b)) and the the Extended Scriven model (Eq.10) using $\beta_{2D} = 4.0509$.

On electromagnetism and its effects

In the case of constant potential difference across the electrodes, the current varies due to the bubble evolution. The effect of bubbles can be divided based on its position, i.e. in the bulk and attached to the electrode, which is investigated in this subsection.

The fluid parameters used for these simulations are $\rho_1 = 1000$kg/m^3, $\rho_2 = 1$kg/m^3, $\nu_1 = 10^{-6}$m^2/s, $\nu_2 = 1.48 \times 10^{-5}$m^2/s, $k_1 = 100$S/m and $k_2 = 10^{-13}$S/m. Both gravity and surface tension are neglected in these simulations. Assuming that the electrolyte is bubble free, for an inter-electrode gap of 1cm and the difference in potential between the electrode is 0.01V corresponds to a current density of 100A/m^2. Any change in current density can be attributed to the presence of bubbles in the computational domain.

When bubbles are attached on the electrode surface

When bubbles are present on the electrode surface, it increases the resistance in the system due to volume of the bubble and electrode screening. If an area of 2D bubble, which is present in the bulk, is redistributed on the surface such that the effective area is the same, the current reduces due to the increase in effective resistance at the electrode (due to electrode screening). This is showcased by considering two cases: EC1 (bubble is present in the bulk) and EC2 (bubble is attached to the electrode), see Fig.5.

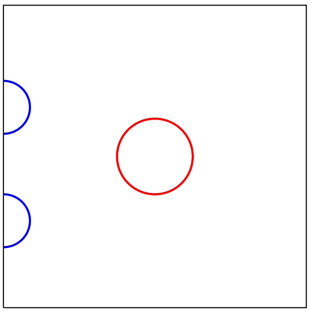

Figure 5: Illustration of the cases, EC1 and EC2, considered to showcase the effect electrode screening. EC1, represented by 🟥, considers a bubble of radius 1mm at the center of domain. EC2, represented by 🟦, considers two equally sized bubbles (semicircles with radii equal to 1mm) whose centers are 2.5mm and 6.5mm away from the bottom wall.

The computational domain, of dimensions 1cm×1cm, is meshed by 200×200 cells. The left and right boundaries, which are the electrodes, are assigned as no-slip conditions for velocity and fixedFluxPressure (Greenshields, 2019) for pressure. The top and bottom boundaries are assigned fixedValue (equal to 0Pa) for p_{rgh} and zeroGradient for velocity. All the boundaries are assigned zeroGradient for α_1. For ϕ, left and right walls are assigned 0V and 0.01V respectively, whereas the remaining boundaries are set as zeroGradient. The initial conditions for the α_1, are set as described in Fig.5.

The reduction of the current due to the presence of the bubble on the electrode surface is shown in Table.2.

Table 2: Reduction of current due to the presence of bubble on the electrode.

Case	$\mathcal{F}^a$	Area of 2D bubbles (m^2)	Current^b (A)
EC1	1	3.16 $\times10^{-6}$	9.384$\times10^{-7}$
EC2	0.6	3.16 $\times10^{-6}$	9.306$\times10^{-7}$

[a] $\mathcal{F}$ represents the fraction of the left electrode area in contact with electrolyte, [b] Current is calculated as $\sum \vec{i}.\vec{S}$ where $\vec{S}$ is the face surface area of individual cell on the left electrode.

When bubbles are present in the bulk

The 2D simulations use the a domain, of size 1cm×1cm, which is meshed with 200×200 cells. The left and right boundaries use no-slip, fixedFluxPressure (Greenshields, 2019) and fixedValue (equal to 0V and 0.01V) for $\vec{U}$, p_{rgh} and ϕ respectively. The other boundaries are assigned zeroGradient for both $\vec{U}$ and ϕ whereas p_{rgh} use fixedValue (equal to 0V). For α_1, all the boundaries are assigned the zeroGradient condition. For 3D simulations, the domain of size 1cm×1cm×1cm is meshed with 200×200×200 cells. The left and right boundaries are set according to the analogous conditions for 2D simulations whereas the remaining boundaries are treated like the top/bottom boundaries used in 2D simulations. The initial conditions used for α_1 is chosen so that bubble, with a range of sizes, are randomly placed in the bulk, as shown in Fig.A1 and Fig.A2 for 2D and 3D simulations respectively.

The bubbles change the effective conductivity of the electrolyte (k_e) which can be theoretically estimated using the Bruggermann's correlation (valid for polydispersed spherical bubbles (Bruggeman, 1935)) as

$$k_e/k_1 = (1 - f)^{1.5}, \tag{12}$$

where f is the void fraction (calculated as the ratio of total volume of the bubble to the volume of the domain). Once the k_e is computed, the resistance is computed as $d/(k_e A)$, where d is the interelectrode distance (equal to 1cm) and A is the area of the 3D electrode (equal to 0.01×0.01m^2), and current in the system and current density are determined based on Ohm's law with cell voltage computed as the difference between the right and left boundary conditions for ϕ (equal to 0.01V). As expected, Fig.6 shows that 3D simulations provides a better agreement to the current density obtained from Bruggermann correlations than the 2D simulations. Further the solver successfully predicts the

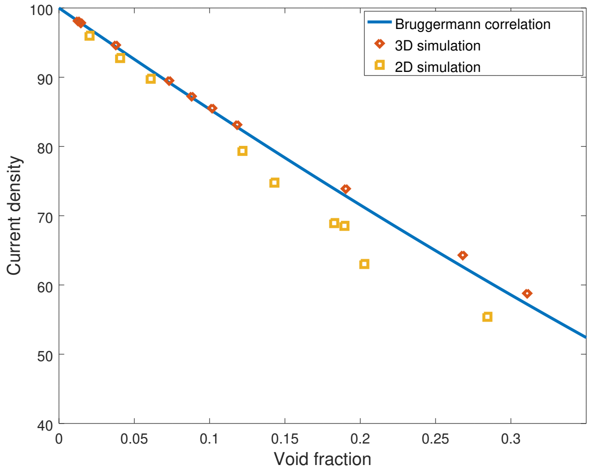

Figure 6: Comparison of the current density (A/m^2) reduction with increase in void fraction of bubbles (in bulk) predicted by the simulations (for 2D and 3D) and Bruggermann's correlation.

reduction of current density with the increase in the void fraction of bubbles.

ON THE FULLY COUPLED SOLVER

For the fully coupled solver, the solution is obtained by solving the volume fraction equation, then calculating the relevant source terms, the coupled momentum and continuity equations, then the Gauss'law and finally the transport of dissolved gas using CCST model at each time step.

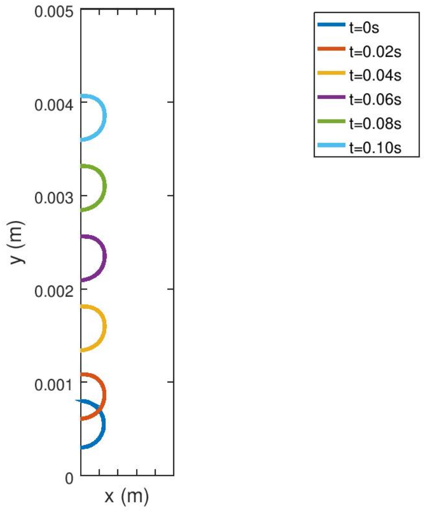

Figure 7: Comparison interface morphology and position with time in the computational domain.

In order to showcase the ability of the solver, we simulate the growth of a pre-existing bubble due to electrochemical reactions occurring at a vertical electrode-electrolyte interface. The occurrence of pre-existing bubbles at surface imperfections, for instance from previous nucleation events, can reduce the energy required for nucleation to values as low as zero (Vachaparambil and Einarsrud, 2018). This approximation, which is physically reasonable as bubble has been observed to generate from the same site on the electrode for a range of current densities (Westerheide and Westwater, 1961; bo Liu *et al.*, 2019), enables direct modelling of the growth of the bubble without the need to treat bubble nucleation. In order to treat bubble nucleation in a CFD framework, algorithms like the one proposed by Damme *et al.* (2010) are required.

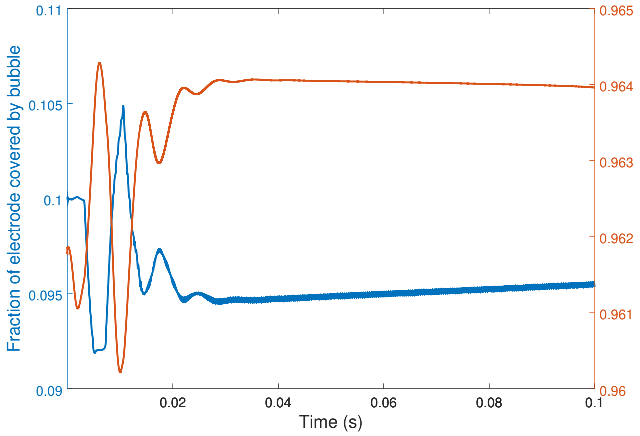

Figure 8: Comparison change in footprint of the bubble on the electrode (fraction of bubble covered electrode) and the associated change in normalized current (calculated as $(\sum \vec{i}\cdot\vec{S})/(I)$, where I is the current when no bubbles are present, i.e. 100A/m^2 ×(5×10^{-9}m^2)) with time.

The computational domain used for the simulation is 1mm×5mm which is meshed by 200×1000 cells. The left and right boundaries are set as walls and the boundary conditions are described based on the individual modules in the decoupled solver except for the the C_i at the left wall which is computed using the Faraday's law of electrolysis, as $\partial_n C_i = |\vec{i}|\alpha_1/(2FD_1)$, and ϕ is assigned a fixedValue of 0V and 10^{-3}V at left and right walls respectively. The pre-existing bubble, of radius equal to 0.25mm, is initialized as that its center is on the left wall at a distance of 0.55mm from the lower boundary. The fluid properties used in the proof of concept simulation are: $\rho_1 = 1000\text{kg/m}^3$, $\rho_2 = 1\text{kg/m}^3$, $\nu_1 = 10^{-6}\text{m}^2/\text{s}$, $\nu_2 = 1.48\times10^{-5}\text{m}^2/\text{s}$, $D_1 = 10^{-9}\text{m}^2/\text{s}$, $D_2 = 10^{-5}\text{m}^2/\text{s}$, $\sigma = 0.003\text{N/m}$, $M = 44\times10^{-3}\text{kg/mol}$, $k_1 = 100\text{S/m}$, $k_2 = 10^{-13}\text{S/m}$ and $|\vec{g}| = 9.81\text{m/s}^2$. Due to the use of surface tension, the maximum time step allowed is manually limited to 8μs (see Deshpande *et al.* (2012); Vachaparambil and Einarsrud (2019)) and the simulations are run until 0.1s.

The concentration distribution of the dissolved gas generated by the electrochemical reactions and the current density distribution around the rising bubble attached to the electrode at $t = 0.1$s is shown in Fig.9. As the bubble rises up, the growth rate and the effective radius of the bubble increases as seen in Fig.10 which is associated with the increase in the bubble footprint after the initial transient behaviour of the bubble, see Fig.8. The change in current obtained directly correlates with the footprint and size of the bubble, see Fig.8 and Fig.10.

CONCLUSION

We implemented the individual models relevant in modelling an electrochemical gas evolution in the VOF solver available in OpenFOAM® 6. The modules added into interFoam are: SSF (for surface tension modelling), C-CST

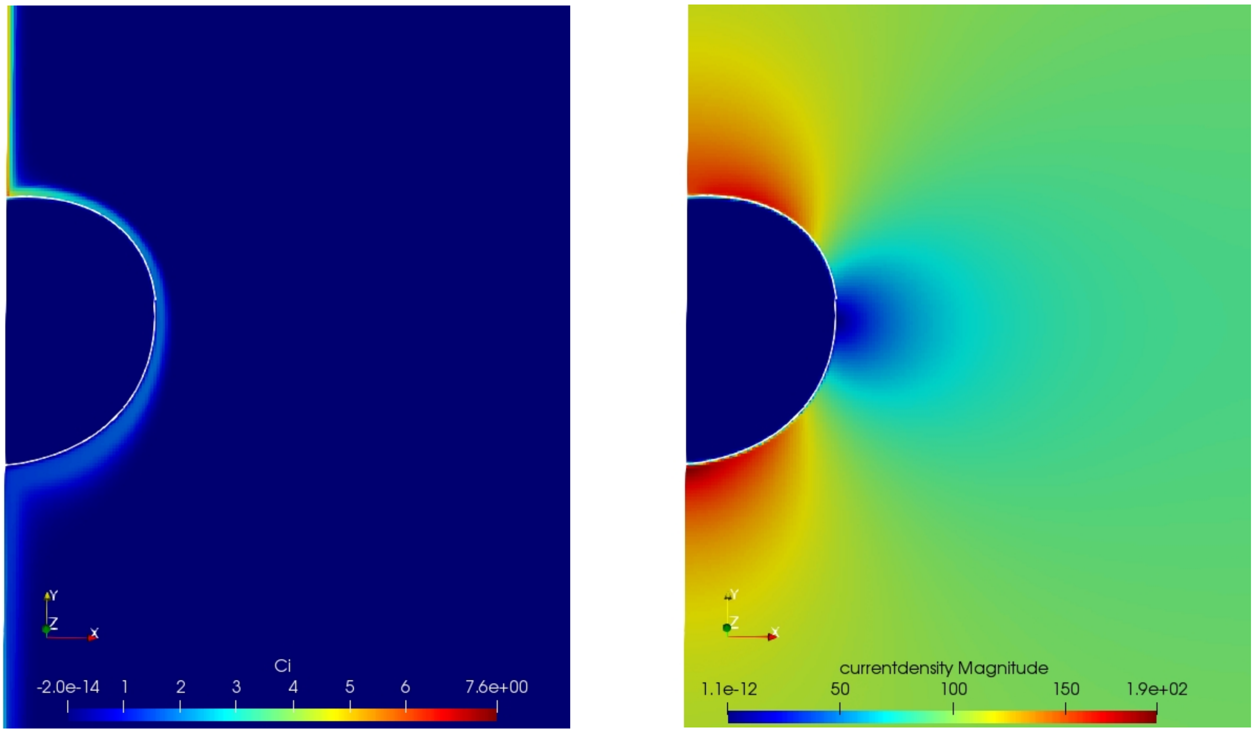

(a) C_i (mol/m^3).

(b) $|\vec{i}|$ (A/m^2).

Figure 9: Comparison of the distribution of dissolved gas and current density (magnitude) around the bubble (whose interface, at $\alpha_1 = 0.5$, is represented by the white contour) at $t = 0.1$s.

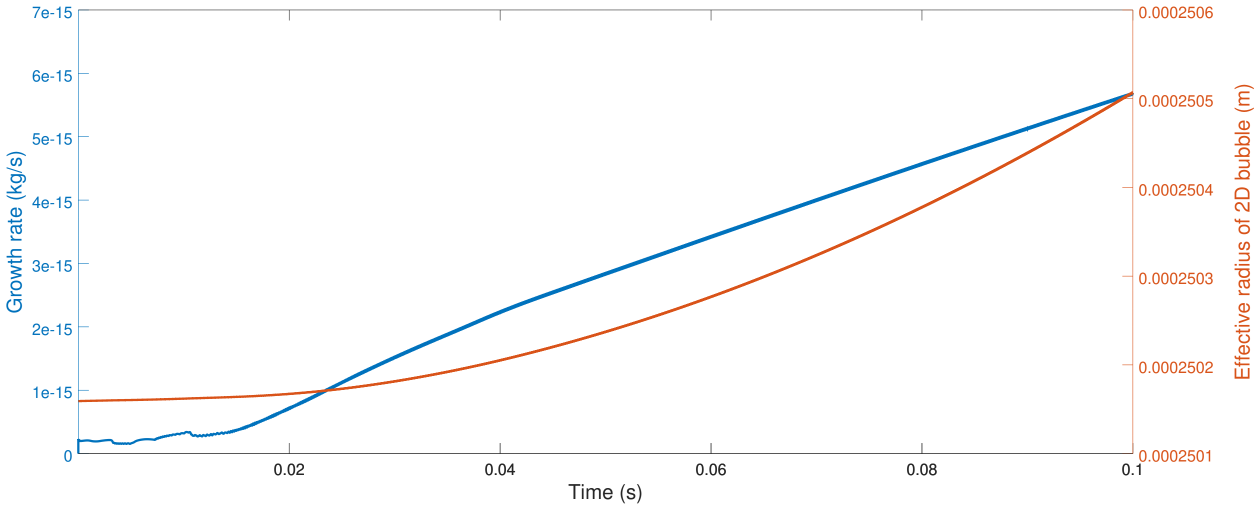

Figure 10: Comparison of the growth rate and the effective radius of the bubble as it evolves.

(transport of dissolved gas), supersaturation driven bubble growth model and Gauss's law. The predictions from these decoupled modules agree quite reasonably with relevant theoretical models available in literature. The bubble evolution, under constant potential condition, as predicted by the fully coupled solver is also discussed to showcase the ability of the proposed solver to handle electrochemical gas evolution. The proposed fully coupled solver, unlike other works reported in literature, can 'theoretically' be applied to simulate a variety of flow configuration (current density and electrode orientations) as well as the impact of bubble detachment in electrochemical systems due to the use of phenomenological models.

ACKNOWLEDGEMENTS

This work was funded by the Department of Materials Science and Engineering at NTNU. The authors would also like to thank UNINETT Sigma2 for providing necessary computational resources through grant NN9741K.

REFERENCES

BIRD, R., STEWART, W. and LIGHTFOOT, E. (2007). *Transport Phenomena: Revised Second Edition*. Wiley, New York.

BO LIU, H., HU, Q., MING PAN, L., WU, R., LIU, Y. and ZHONG, D. (2019). "Electrode-normal magnetic field facilitating neighbouring electrochemical bubble release from hydrophobic islets". *Electrochimica Acta*, **306**, 350 – 359.

BRACKBILL, J., KOTHE, D. and ZEMACH, C. (1992). "A continuum method for modeling surface tension". *Journal of Computational Physics*, **100(2)**, 335 – 354.

BRUGGEMAN, D.A.G. (1935). "Berechnung verschiedener physikalischer konstanten von heterogenen substanzen. i. dielektrizitätskonstanten und leitfähigkeiten der mischkörper aus isotropen substanzen". *Annalen der Physik*, **416(7)**, 636–664.

DAMME, S.V., MACIEL, P., PARYS, H.V., DECONINCK, J., HUBIN, A. and DECONINCK, H. (2010). "Bubble nucleation algorithm for the simulation of gas evolving electrodes". *Electrochemistry Communications*, **12(5)**, 664 – 667.

DEISING, D., BOTHE, D. and MARSCHALL, H. (2018). "Direct numerical simulation of mass transfer in bubbly flows". *Computers & Fluids*, **172**, 524 – 537.

DESHPANDE, S.S., ANUMOLU, L. and TRUJILLO, M.F. (2012). "Evaluating the performance of the two-phase flow solver interFoam". *Computational Science & Discovery*, **5(1)**, 014016.

EINARSRUD, K.E. and JOHANSEN, S.T. (2012). "Modelling of bubble behaviour in aluminium reduction cells". *Progress in Computational Fluid Dynamics, an International Journal*, **12(2-3)**, 119–130.

EINARSRUD, K.E., EICK, I., BAI, W., FENG, Y., HUA, J. and WITT, P.J. (2017). "Towards a coupled multi-scale, multi-physics simulation framework for aluminium electrolysis". *Applied Mathematical Modelling*, **44**, 3 – 24.

GREENSHIELDS, C.J. (2019). "Openfoam user guide version 7". URL `http://foam.sourceforge.net/docs/Guides-a4/OpenFOAMUserGuide-A4.pdf`.

HARDT, S. and WONDRA, F. (2008). "Evaporation model for interfacial flows based on a continuum-field representation of the source terms". *Journal of Computational Physics*, **227(11)**, 5871 – 5895.

HASHEMI, S.J. and ABEDI, J. (2007). "Advances in modeling of new phase growth". *Energy & Fuels*, **21(4)**, 2147–2155.

HREIZ, R., ABDELOUAHED, L., FÜNFSCHILLING, D. and LAPICQUE, F. (2015). "Electrogenerated bubbles induced convection in narrow vertical cells: A review". *Chemical Engineering Research and Design*, **100**, 268 – 281.

HYSING, S., TUREK, S., KUZMIN, D., PAROLINI, N., BURMAN, E., GANESAN, S. and TOBISKA, L. (2009). "Quantitative benchmark computations of two-dimensional bubble dynamics". *International Journal for Numerical Methods in Fluids*, **60(11)**, 1259–1288.

MAES, J. and SOULAINE, C. (2018). "A new compressive scheme to simulate species transfer across fluid interfaces using the volume-of-fluid method". *Chemical Engineering Science*, **190**, 405 – 418.

MAES, J. and SOULAINE, C. (2020). "A unified single-field volume-of-fluid-based formulation for multi-component interfacial transfer with local volume changes". *Journal of Computational Physics*, **402**, 109024.

POPINET, S. (2018). "Numerical models of surface tension". *Annual Review of Fluid Mechanics*, **50(1)**, 49–75.

RAEINI, A.Q., BLUNT, M.J. and BIJELJIC, B. (2012). "Modelling two-phase flow in porous media at the pore scale using the volume-of-fluid method". *Journal of Computational Physics*, **231(17)**, 5653 – 5668.

SCRIVEN, L. (1959). "On the dynamics of phase growth". *Chemical Engineering Science*, **10(1)**, 1 – 13.

SUN, M., LI, B. and LI, L. (2018). "A multi-scale mathematical model of growth and coalescence of bubbles beneath the anode in an aluminum reduction cell". *Metallurgical and Materials Transactions B*, **49(5)**, 2821–2834.

TAQIEDDIN, A., ALLSHOUSE, M.R. and ALSHAWABKEH, A.N. (2018). "Editors' choice—critical review—mathematical formulations of electrochemically gas-evolving systems". *Journal of The Electrochemical Society*, **165(13)**, E694–E711.

VACHAPARAMBIL, K.J. and EINARSRUD, K.E. (2018). "Explanation of bubble nucleation mechanisms: A gradient theory approach". *Journal of The Electrochemical Society*, **165(10)**, E504–E512.

VACHAPARAMBIL, K.J. and EINARSRUD, K.E. (2019). "Comparison of surface tension models for the volume of fluid method". *Processes*, **7(8)**, 542.

VACHAPARAMBIL, K.J. and EINARSRUD, K.E. (2020a). "Modeling interfacial mass transfer driven bubble growth in supersaturated solutions". *AIP Advances*, **10(10)**, 105024.

VACHAPARAMBIL, K.J. and EINARSRUD, K.E. (2020b). "Numerical simulation of bubble growth in a supersaturated solution". *Applied Mathematical Modelling*, **81**, 690 – 710.

WESTERHEIDE, D.E. and WESTWATER, J.W. (1961). "Isothermal growth of hydrogen bubbles during electrolysis". *AIChE Journal*, **7(3)**, 357–362.

ZHANG, Z., LIU, W. and FREE, M.L. (2020). "Phase-field modeling and simulation of gas bubble coalescence and detachment in a gas-liquid two-phase electrochemical system". *Journal of The Electrochemical Society*, **167(1)**.

ZHAO, X., REN, H. and LUO, L. (2019). "Gas bubbles in electrochemical gas evolution reactions". *Langmuir*, **35(16)**, 5392–5408.

APPENDIX A

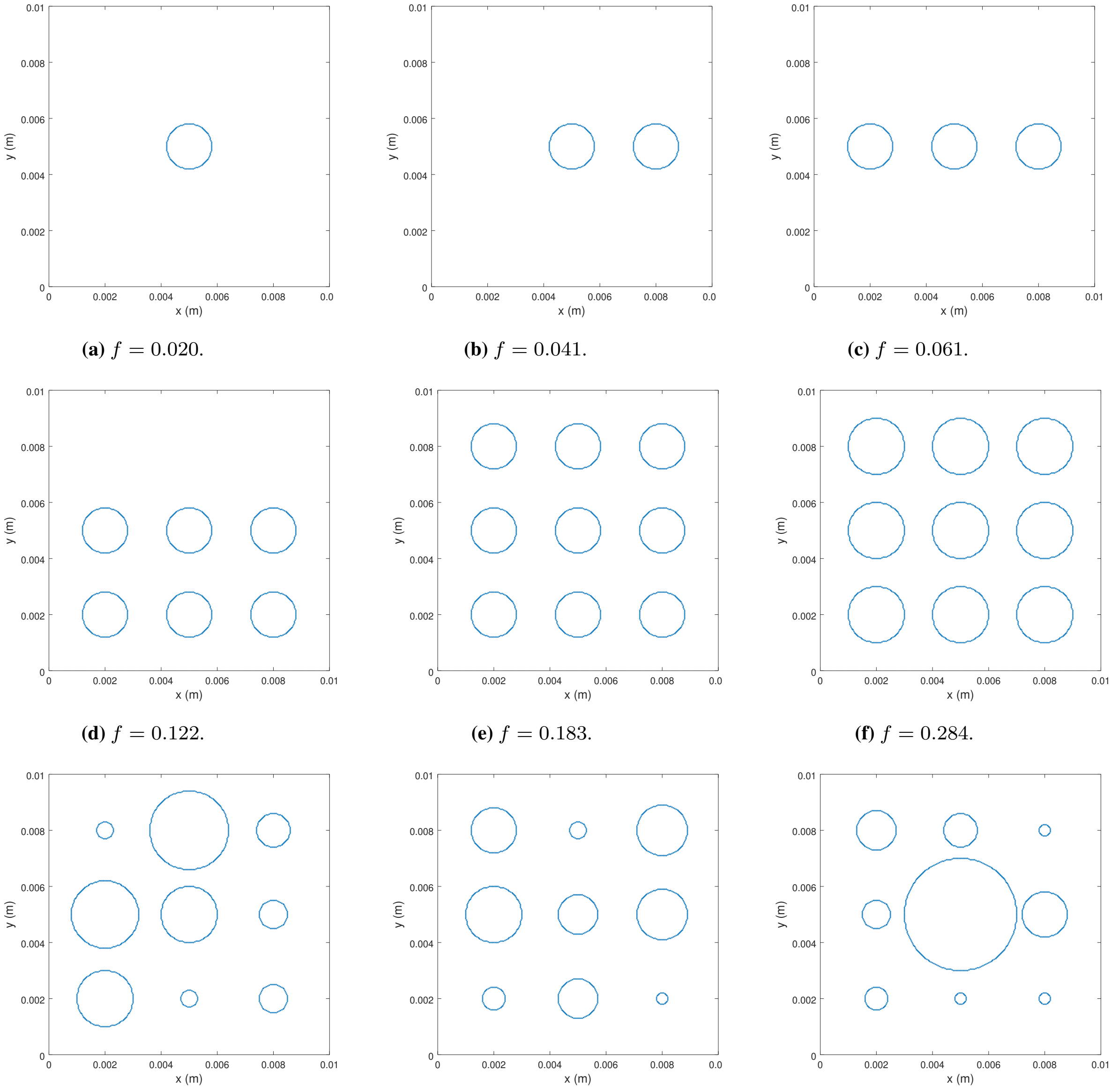

(a) $f = 0.020$. **(b)** $f = 0.041$. **(c)** $f = 0.061$.

(d) $f = 0.122$. **(e)** $f = 0.183$. **(f)** $f = 0.284$.

(g) $f = 0.203$. **(h)** $f = 0.143$. **(i)** $f = 0.190$.

Figure A1: The distribution of the 2D bubbles in the computational domain.

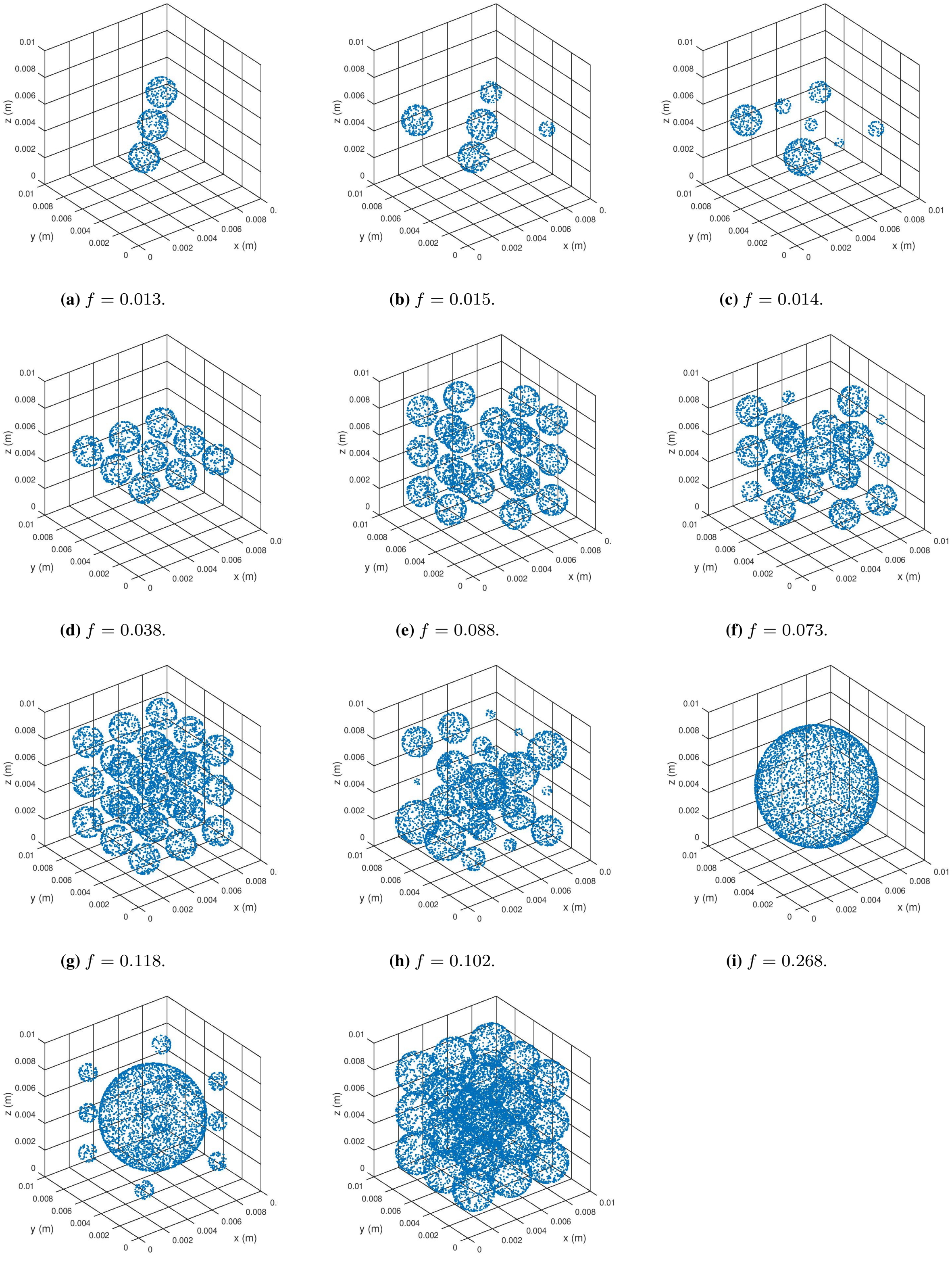

(a) $f = 0.013$.

(b) $f = 0.015$.

(c) $f = 0.014$.

(d) $f = 0.038$.

(e) $f = 0.088$.

(f) $f = 0.073$.

(g) $f = 0.118$.

(h) $f = 0.102$.

(i) $f = 0.268$.

(j) $f = 0.190$.

(k) $f = 0.311$.

Figure A2: The distribution of the 3D bubbles in the computational domain.

14th International Conference on CFD In Oil & Gas, Metallurgical and Process Industries
SINTEF, Trondheim, NORWAY
October 12-14, 2020

INVERSE MODELLING OF INTERFACIAL TENSION BETWEEN FERROALLOY AND SLAG USING OPENFOAM

Sergey BUBLIK[1*], **Kristian Etienne EINARSRUD**[1†]
[1]Department of Materials Science and Engineering, Norwegian University of Science and Technology
(NTNU), Trondheim, NORWAY

[*] E-mail: sergey.bublik@ntnu.no
[†] E-mail: kristian.e.einarsrud@ntnu.no

ABSTRACT

The entrainment of molten ferroalloy droplets in slag during tapping operations is strongly related to turbulence and interfacial forces between alloy and slag. Therefore, interfacial phenomena are of great importance for the ferroalloys industry and a better understanding of entrainment mechanisms can reduce ferroalloy losses with slag flow. The interfacial tension plays an important role in the interaction between ferroalloy and slag due to the ability to modify droplets shape and the flow regime. However, the measurement of interfacial tension between two molten phases is challenging due to high temperatures and complex composition. In particular, surface active elements significantly influence the interfacial tension. Available methods for determining the interfacial tension are often based on using complex equipment (e.g. a furnace equipped with an X-ray camera) and tend to have significant uncertainty in measurements. In this study, a methodology for inverse modelling of interfacial tension between ferroalloys and slag was developed and investigated by combining experimental measurements, reduced order modelling and simulations in OpenFOAM. The proposed method relies upon experimental determination of the shape of single droplets, from which surface tension can be determined using numerical procedures such as elliptic fitting and the low-bond axisymmetric drop shape technique. Given relevant material properties for single phases, parameters governing the interactions between the phases, e.g. interfacial tension, can be determined by comparing parametric simulations to experiments in which interactions are present. Simulations are realized using multiphaseInterFoam for a slag droplet at rest on molten metal in an inert atmosphere. The current work describes the modelling strategy and demonstrates its applicability to recent experiments for the FeMn-slag system. The uncertainty and sensibility of the method are assessed by comparing different available simulation settings, resolution and the uncertainty in the experimental data.

Keywords: Inverse modelling, interfacial phenomena, interfacial tension, slag metal separation.

NOMENCLATURE

Greek Symbols

α	Phase fraction within the range $0 < \alpha < 1$.
γ	Surface or interfacial tension, $[N/m]$.
θ	Contact angle, [°].
μ	Dynamic viscosity, $[Pa \cdot s]$.
ν	Kinematic viscosity, $[m^2/s]$.
ρ	Density, $[kg/m^3]$.
$\Delta\rho$	Density difference between two phases, $[kg/m^3]$.

Latin Symbols

a	Length of the semi-major axis of an ellipse, $[m]$.
b	Length of the semi-minor axis of an ellipse, $[m]$.
c	Capillary constant, $[m^{-2}]$.
g	Gravitational acceleration, 9,81, $[m/s^2]$.
h	Height, $[m]$.
m	Weight, $[kg]$.
P	Pressure, $[Pa]$.
ΔP	Pressure difference across the interface, $[Pa]$.
ΔP_0	Pressure difference at a reference plane, $[Pa]$.
R_0	Radius of curvature at the droplet apex, $[m]$.
R_1, R_2	Principal radii of curvature, $[m]$.
U	Fluid velocity, $[m/s]$.
U_r	Compression velocity, $[m/s]$.
V	Volume, $[m^3]$.
x	Position vector, $[m]$.

Sub/superscripts

n	Phase.
exp	Corresponding to experiments.
sim	Corresponding to simulations.
vis	Visible.
$non-vis$	Non-visible.
$slag$	Corresponding to slag.
$FeMn$	Corresponding to FeMn.
Ar	Corresponding to argon atmosphere.
$slag-Ar$	Interface between slag and Ar.
$FeMn-Ar$	Interface between FeMn and Ar.
$FeMn-slag$	Interface between FeMn and slag.

INTRODUCTION

Ferroalloys are widely used to improve various properties of steels and alloys, for example, hardness, ductility and corrosion resistance (Holappa, 2013). Ferroalloys are produced mainly by carbothermic reduction in submerged arc furnaces (SAFs), where raw materials are heated up by applying the electric current to electrodes. Raw materials in the production of ferroalloys are complex in chemical composition and therefore all other elements, which do not end up in the alloy phase, need to be separated from the alloy and removed as the slag. The removal of molten material (a mixture of slag and alloy) is carried out through an operation which is called tapping. During this operation, the SAF is opened by a drilling machine and thereafter the molten material comes out from the furnace into a cascade of ladles (Tangstad, 2013). The first ladle in the cascade is used for separation of slag and alloy due to the density differences, and storing the alloy, while the following ladles are used only for the slag (Fig. 1). The molten flow typically disintegrates after the impact with either the surface of the alloy ladle or the molten material due to turbulence and interfacial forces between alloy and slag (Lee, 2016). It results in the formation and entrainment of small alloy droplets in slag phase, which then overflows to slag ladles, contributing to the alloy losses. For this reason, the interfacial phenomena are vital for the ferroalloys industry and a better understanding of entrainment mechanisms can reduce ferroalloy losses with slag flow.

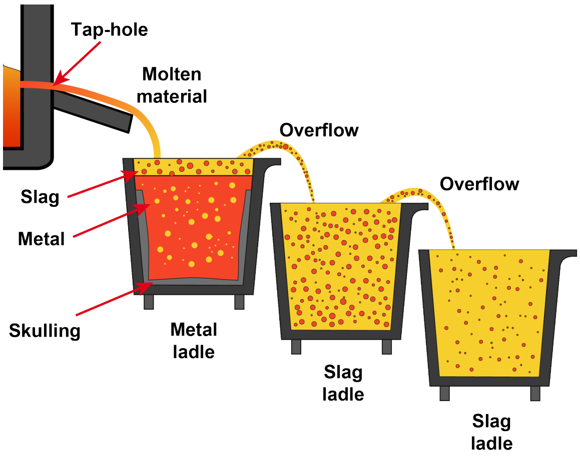

Figure 1: Tapping of the SAF.

The interfacial tension characterizes the interaction between slag and metal and the stability of the interface between slag and alloy (Ooi *et al.*, 1974). High interfacial tension results in better separation, while its lower values promote the formation of slag-metal emulsion. Furthermore, surface active elements, which can significantly reduce the interfacial tension, are typically present in molten systems (Li *et al.*, 2003). In ferroalloys production, the surface active elements are represented by sulphur and oxygen. The thermodynamic equilibrium between alloy and slag is described by the reaction (Saridikmen *et al.*, 2007):

$$[S] + (O^{2-}) \Leftrightarrow (S^{2-}) + [O], \tag{1}$$

where $[S], [O]$ are sulphur and oxygen in alloy, $(S^{2-}), (O^{2-})$ are sulphur and oxygen in slag.

In addition, the interfacial tension can affect the terminal (settling) velocity of alloy droplets in slag phase. Droplets can have various regimes (Clift *et al.*, 1978), which are based on physical properties such as density, interfacial tension and viscosity. Hence, depending on the regime, the surface area of a droplet can be significantly different from its initial shape, meaning that the drag force which acts in the flow direction will also be affected by the regime.

Experimentally, surface and interfacial tension between two molten materials are determined by melting materials in a furnace equipped with an X-ray camera (Jakobsson *et al.*, 2000) or by applying the sessile drop technique with a digital camera (Kim *et al.*, 2010). After recording images from interfacial interaction between two different phases and a gas, surface or interfacial tension are obtained by the numerical solution of the Young-Laplace equation. However, in most cases, the measurement of interfacial/surface tension is extremely complicated due to high temperatures and complex composition of materials.

The equilibrium in the three-fluid interaction is described schematically as shown in Fig. 2a and consequently the surface and interfacial tension vectors are characterized by applying the Neumann vectorial triangle (Fig. 2b). At the equilibrium the sum of surface forces equals to zero, therefore the force balance for all interfaces (αβ, αδ, βδ) is written as (Rowlinson and Widom, 2002):

$$\begin{aligned} \gamma_{\alpha\beta} + \gamma_{\beta\delta}\cos\beta + \gamma_{\alpha\delta}\cos\alpha &= 0 \\ \gamma_{\alpha\beta}\cos\beta + \gamma_{\beta\delta} + \gamma_{\alpha\delta}\cos\delta &= 0 \\ \gamma_{\alpha\beta}\cos\alpha + \gamma_{\beta\delta}\cos\delta + \gamma_{\alpha\delta} &= 0, \end{aligned} \tag{2}$$

where $\gamma_{\alpha\beta}$, $\gamma_{\alpha\delta}$, $\gamma_{\beta\delta}$ is the tension of the $\alpha\beta$, $\alpha\delta$, $\beta\delta$ interface, respectively.

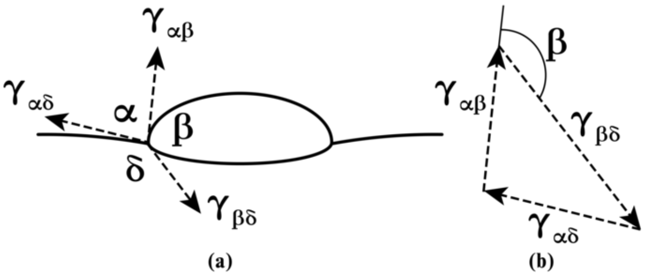

Figure 2: (a) The equilibrium between a fluid droplet, resting on the interface between two fluids of different densities, (b) the Neumann's triangle; $\gamma_{\alpha\beta}$ corresponds to surface tension between slag and gas, $\gamma_{\alpha\delta}$ corresponds to surface tension between FeMn alloy and gas, $\gamma_{\beta\delta}$ corresponds to interfacial tension between FeMn alloy and slag.

Based on the law of cosines, the force balance can be rewritten in order to obtain a numerical value of $\cos\beta$:

$$\cos\beta = \frac{\gamma_{\alpha\delta}^2 - \gamma_{\alpha\beta}^2 - \gamma_{\beta\delta}^2}{2\gamma_{\alpha\beta}\gamma_{\beta\delta}}. \tag{3}$$

A methodology allowing for the observations of interfacial flow between ferromanganese alloys (FeMn) and slag, was developed by the authors (Bublik *et al.*, 2019), based on experiments using a sessile drop furnace and recording of images.

In this work, the interfacial tension between FeMn alloy and slag has been determined based on a new inverse modelling strategy, combining simulations with analysis of images from the sessile drop furnace. The model applicability and sensibility has been studied and discussed by comparing different settings in OpenFOAM and the uncertainty in experimental data.

METHOD DESCRIPTION

A. Materials preparation

The synthetic FeMn alloy and slag for experiments in the sessile drop furnace were prepared from pure powders according to the industrial composition (Table 1). The powders were mixed and melted separately in a graphite crucible in an induction furnace in Ar atmosphere at 1773 K, 60 min of holding for FeMn and 5 min of holding for slag. After the first melting, both FeMn and slag were removed from the crucible, ground into small pieces in a ball mill and then remelted in the graphite crucible in the induction furnace at the same operational parameters.

Table 1: Chemical composition of materials used for the experiments in the sessile drop furnace.

Material	Chemical composition, wt. %							
	Mn	Fe	C	MnO	CaO	MgO	SiO_2	Al_2O_3
HC FeMn	78	15	7	-	-	-	-	-
FeMn slag	-	-	-	38	23	6	23	10

B. Experimental setup

The sessile drop technique was applied in order to determine surface tension of alloy/slag and to investigate the interfacial behaviour between FeMn and slag:

- In experiments, where *surface tension* was measured, a piece of slag or FeMn alloy was placed on a graphite substrate (ISO-88) as shown in Fig. 3 and Fig. 4, the furnace is heated up and images of interaction between slag-graphite or alloy-graphite were recorded. Thereafter, the images were analyzed by means of the Young-Laplace equation.

- In experiments for measurement of *interfacial interaction*, small FeMn pieces were placed in a graphite cup (Fig. 5) and a slag piece was placed on top of the FeMn layer. Subsequently, the interfacial tension is measured by inverse modelling in OpenFOAM.

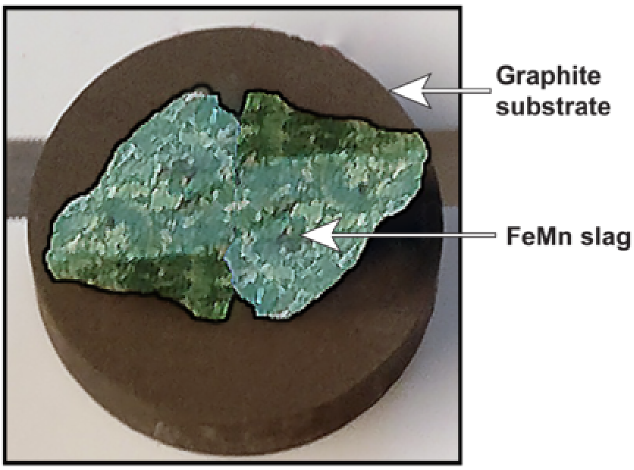

Figure 3: Slag on a graphite substrate before experiments for measurement of surface tension in the sessile drop furnace.

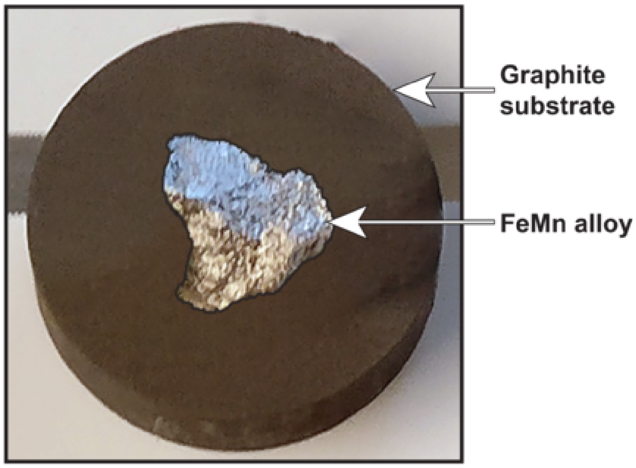

Figure 4: FeMn alloy on a graphite substrate before experiments for measurement of surface tension in the sessile drop furnace.

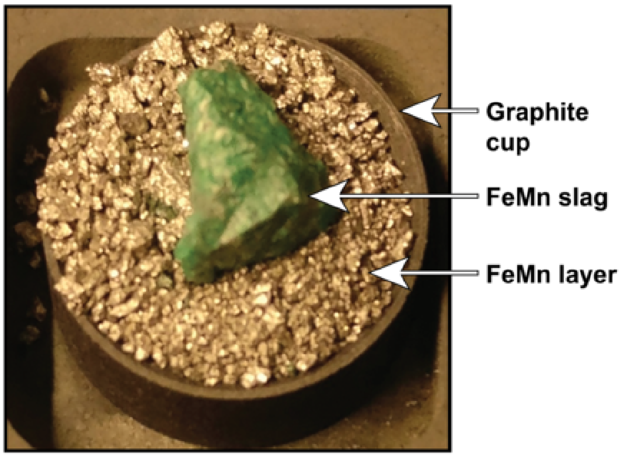

Figure 5: Slag on top of FeMn pieces in a graphite cup before experiments for measurement of interfacial tension in the sessile drop furnace.

The sessile drop furnace (Fig. 6) was equipped with a digital video camera (Sony XCD-SX910CR, Sony Corporation, Millersville, MD) with a telecentric lens (Navitar 1-50993D) to record images from the molten samples with the resolution of 1280x1024 pixels. The experiments were done at the maximum temperature of 1623, 1673, 1723 K and holding time of 5, 10, 15 min.

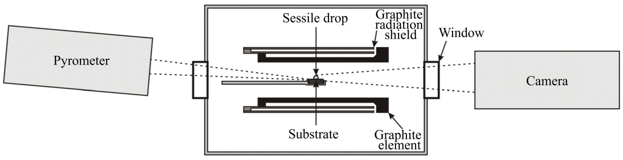

Figure 6: Schematic illustration of the sessile drop furnace.

C. Methodology for inverse modelling

The methods consist of the followings steps:

a) Conduct experiments with a single slag or FeMn alloy droplet and determine the *surface tension* of each phase.

b) Conduct experiments in the sessile drop furnace with FeMn layer and a slag piece on top.

c) Conduct simulations in OpenFOAM for a certain range of interfacial tension using densities of FeMn alloy and slag in the molten state, weight of the slag droplet and surface tensions determined from step *a)*.

d) Calculate visible (or non-visible) height of the slag droplet (in %) both for experiments and simulations. Compare experimental and simulation values to determine *interfacial tension*.

Determination of surface tension

The Young-Laplace equation describes the relationship between the curvature of a droplet and surface tension:

$$\Delta P = \gamma\left(\frac{1}{R_1} + \frac{1}{R_2}\right). \tag{4}$$

If external forces are not applied on a droplet, except of the gravity, the pressure difference is expressed as:

$$\begin{aligned}\Delta P &= \Delta P_0 + \Delta\rho g h\\ &= \frac{2\gamma}{R_0} + \Delta\rho g h.\end{aligned} \tag{5}$$

a) Surface tension of slag is determined by the elliptic solution of the Young-Laplace equation (Hernandez-Baltazar and Gracia-Fadrique, 2005), implemented in MATLAB. Surface tension (in N/m) is determined from the expression:

$$\gamma = \frac{a^2(\rho_{slag} - \rho_{Ar})g}{\frac{a^3}{b^3} + \frac{a}{b} - 2}, \tag{6}$$

where the values of the semi-major axis a and the semi-minor axis b are obtained from image analysis of slag droplets in experiments, after fitting an ellipse to the slag curvature (Fig. 7). The elliptic solution fails if contact angle (θ) between the droplet and the substrate is lower than 90°, giving wrong values for surface tension. In addition, there is a significant uncertainty in measurements by this method if droplet's surface during experiments is rough.

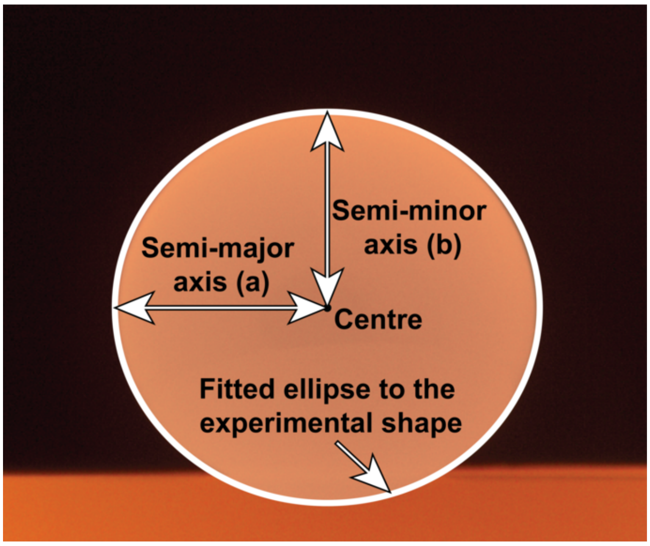

Figure 7: Ellipsoidal fitting to the slag droplet during experiments in the sessile drop furnace.

b) The contact angle between FeMn alloy and the graphite substrate is lower than 90°, and the surface roughness is high (Fig. 8). For this reason, surface tension of FeMn alloy is measured by a plugin for ImageJ (Rueden *et al.*, 2017), which is based on the low-bond axisymmetric drop shape analysis (LBADSA) (Stalder *et al.*, 2010). The plugin extracts parameters of droplet's contour after the fitting of the Young-Laplace equation to the image data (Fig. 9). The output from the plugin is the capillary constant c, which is related to surface tension of FeMn (γ) through the equation:

$$c = \frac{(\rho_{FeMn} - \rho_{Ar})g}{\gamma}. \tag{7}$$

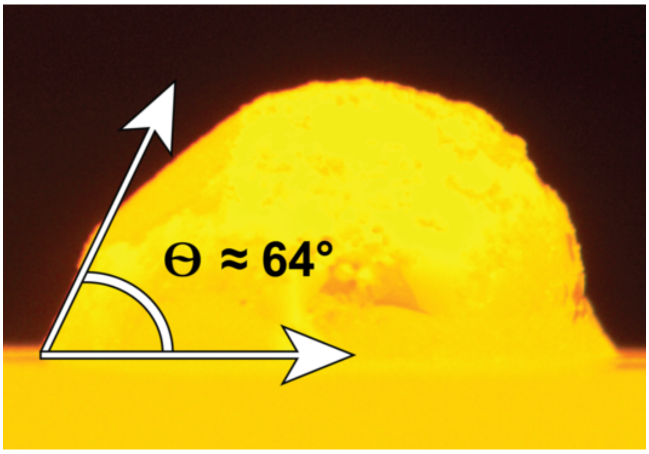

Figure 8: FeMn alloy surface during experiments in the sessile drop furnace.

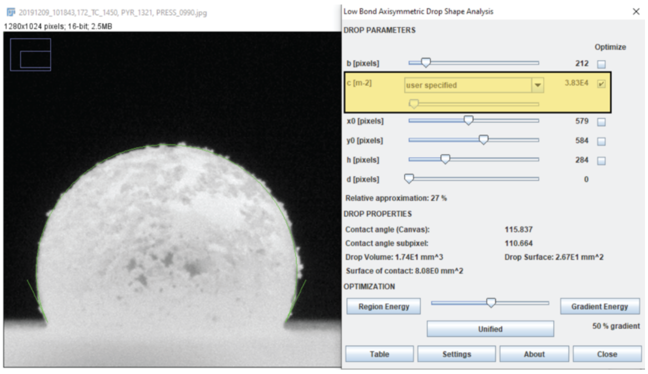

b [pixels] 212 ☐
c [m-2] user specified 3.83E4 ☑
x0 [pixels] 579 ☐
y0 [pixels] 584 ☐
h [pixels] 284 ☐
d [pixels] 0
Relative approximation: 27 %
Contact angle (Canvas): 115.837
Contact angle subpixel: 110.664
Drop Volume: 1.74E1 mm^3
Drop Surface: 2.67E1 mm^2
Surface of contact: 8.08E0 mm^2
50 % gradient

Figure 9: Fitting and measurement of parameters of a FeMn droplet from the image data by LBADSA plugin for ImageJ.

Simulations using multiphaseInterFoam

Simulations were carried out in OpenFOAM 6 (Weller *et al.*, 1998) using *multiphaseInterFoam*, a solver for N incompressible fluids which captures the interfaces and includes surface tension and contact angle effect for each phase, with optional mesh motion and topology changes.

multiphaseInterFoam is based on the volume-of-fluid (VOF) method (Hirt and Nichols, 1981), where a transport equation is applied to define the volume fraction α_n of each of the phases (Andersson, 2010). The transport equation is solved with the continuity and momentum equation for each phase (Damian, 2012). The continuity equation is defined as:

$$\nabla \cdot \mathbf{U} = 0. \tag{8}$$

The transport equation for α is:

$$\frac{\partial \alpha}{\partial t} + \nabla \cdot (\mathbf{U}\alpha) + \nabla \cdot [\mathbf{U}_r \alpha(1-\alpha)] = 0, \tag{9}$$

and the momentum equation is expressed as:

$$\begin{aligned} \frac{\partial(\rho \mathbf{U})}{\partial t} + \nabla \cdot (\rho \mathbf{U}\mathbf{U}) &= -\nabla p + \mathbf{g} \cdot \mathbf{x} \nabla \rho \\ &+ \mu \left[\nabla \mathbf{U} + (\nabla \mathbf{U})^T\right] + \gamma \kappa \nabla \alpha, \end{aligned} \tag{10}$$

where $\mu \left[\nabla \mathbf{U} + (\nabla \mathbf{U})^T\right]$ is the viscous term, $\gamma \kappa \nabla \alpha$ is surface tension force per unit volume, which is based on the continuum surface force model (Berberovic *et al.*, 2009), κ is the mean curvature of the free surface:

$$\kappa = -\nabla \cdot \left(\frac{\nabla \alpha}{|\nabla \alpha|} \right). \tag{11}$$

The mixture density (ρ) and viscosity (μ) are calculated as weighted averages based on the phase fraction in a control volume, i.e.:

$$\rho = \sum_n \rho_n \alpha_n \tag{12}$$

and

$$\mu = \sum_n \mu_n \alpha_n. \tag{13}$$

Evidently, cells with only a single phase, retain the material properties of the phase in question.

Reduced order modelling

In order to determine the interfacial tension between slag and alloy, the non-visible height of droplets (in %) both in experiments and simulations was calculated by the following procedure:

A. Procedure for slag droplets in experiments

1. Measure the weight of the slag droplet before experiments, m_{slag}.

2. Calculate the (total) volume of the slag droplet in molten state, V_{total}^{slag}:

$$V_{total}^{slag} = \frac{m_{slag}}{\rho_{slag}}. \tag{14}$$

3. The slag droplet resting on top of the FeMn layer is assumed to be a spherical cap both above and below the FeMn-Ar interface as shown in Fig. 10. According to the geometric properties of the spherical cap, a and h_{vis}^{exp} can be obtained directly by measuring corresponding distances, while the height below the interface, $h_{non-vis}^{exp}$, is unknown, and therefore it has to be determined via additional calculations.

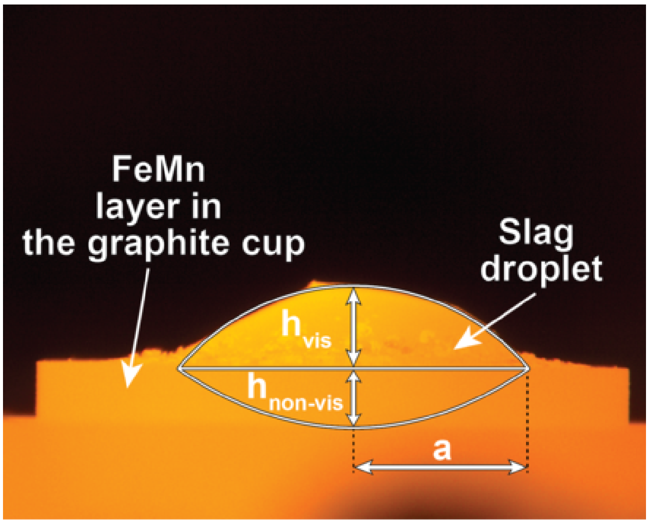

Figure 10: Slag droplet on top of FeMn layer in experiments: a is the base radius of the spherical cap, h_{vis} and $h_{non-vis}$ are the height of the spherical cap above and below the interface, respectively.

4. Calculate the visible volume of the slag droplet, V_{vis}^{slag}:

$$V_{vis}^{slag} = \frac{1}{6}\pi h_{vis}^{exp}\left(3(a^{exp})^2 + (h_{vis}^{exp})^2\right). \tag{15}$$

5. Calculate the non-visible volume of the slag droplet, $V_{non-vis}^{slag}$:

$$V_{non-vis}^{slag} = V_{total}^{slag} - V_{vis}^{slag}. \tag{16}$$

6. Determine the height of the spherical cap below the interface in *meters*, $h_{non-vis}^{exp}$. In this study, a MATLAB script has been developed, allowing to solve the equation for the volume of a spherical cap (eq. 17) and calculate $h_{non-vis}^{exp}$, given that a, h_{vis}^{exp}, $V_{non-vis}^{slag}$ are known.

$$V_{non-vis}^{slag} = \frac{1}{6}\pi h_{non-vis}^{exp}\left(3(a^{exp})^2 + (h_{non-vis}^{exp})^2\right). \tag{17}$$

7. Calculate the non-visible height of the slag droplet in %:

$$h_{non-vis}^{exp}(\%) = \frac{h_{non-vis}^{exp}}{h_{non-vis}^{exp} + h_{vis}^{exp}} \cdot 100. \tag{18}$$

B. Procedure for slag droplets in simulations

1. In simulations, the height of slag droplets both below and above the interface can be obtained directly from measuring distances as shown in Fig. 11.

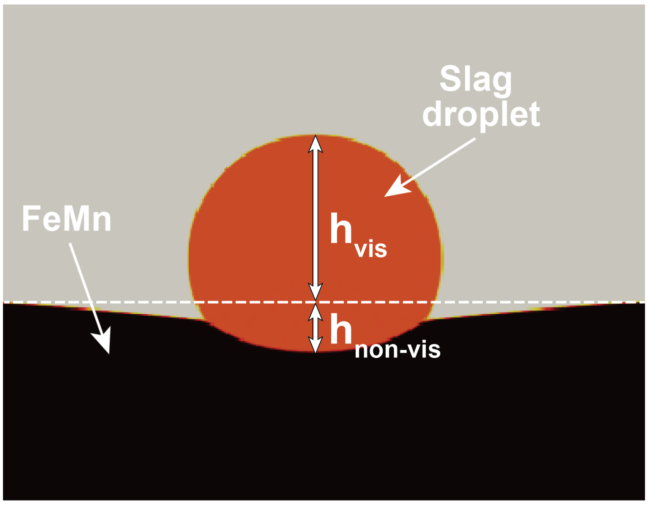

Figure 11: Slag droplet on top of FeMn bath in simulations.

2. Calculate the non-visible height of the slag droplet in %:

$$h^{sim}_{non-vis}(\%) = \frac{h^{sim}_{non-vis}}{h^{sim}_{non-vis} + h^{sim}_{vis}} \cdot 100. \qquad (19)$$

3. The non-visible height of the slag droplet in simulations obtained from equation *19* is compared with experimental values from equation *18* to find the corresponding non-visible height and thereby also the corresponding interfacial tension, which in the simulations was varied according to a range of expected values.

EXPERIMENTAL CONDITIONS AND NUMERICAL SETTINGS

Experimental conditions

The experimental parameters used in experiments in the sessile drop furnace are shown in Table 2.

Table 2: Experimental conditions in the sessile drop furnace.

Parameter	**Value in measurement of**	
	Surface tension	**Interfacial tension**
m_{slag}, g	0,120	≈0,050 - 0,060
m_{FeMn}, g	0,120	≈0,300 - 0,350
Ar flow, NLPM	0,1	0,1
Pressure inside the chamber, Pa	101325	101325
Maximum temperature, K	1723	1623, 1673, 1723
Holding time at maximum temperature, min	5	5, 10, 15
Heating rate to 1473 K, K/min	300	300
Heating rate from 1473 K to maximum temperature, K/min	≈25	≈25

Numerical settings and simulation procedure

Simulations were carried out on an axisymmetric 2D geometry as shown in Fig. 12, where the following boundary conditions were applied:

- Left wall - symmetry.
- Right, top and lower wall - no-slip condition with a fixed flux pressure (P = 0 Pa).

The initial number of cells in the simulations was 5000. In order to increase the resolution at the interfaces (slag-Ar, FeMn-Ar, FeMn-slag), 2D dynamic mesh refinement (CFD Online Discussion Forums, 2018) was applied, which allows increasing the number of cells up to 20000 for the given simulation setup. All simulations were performed on resourses provided by the NTNU IDUN computing cluster (Sjalander *et al.*, 2019) using modified settings for damBreak4phase tutorial case (cf. The OpenFOAM Foundation, 2016) with multiphaseInterFoam solver, as shown in Table 3. The presence of so-called spurious currents in VOF simulations results in considerable challenges when aiming to reach a static steady state and therefore low values of under-relaxation factors were applied to reduce spurious currents as it was proposed by Vachaparambil and Einarsrud, 2019. Simulations were aiming to reach steady state conditions corresponding to a droplet at rest. As multiphaseInterFoam is a transient solver, transient simulations with dynamic time stepping from 10^{-5} to 10^{-6} s and the maximum Courant number of 0,25 until 1 s flow time was attained - sufficient to obtain a (quasi) steady state for all simulations considered. The simulations were initialized with a slag droplet with radius from 1,47 to 1,63 mm, depending on the weight of the slag droplet, initially positioned 1,50 mm above the alloy interface.

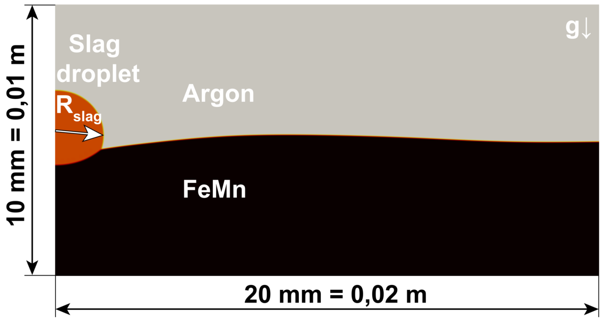

Figure 12: 2D axisymmetric geometry applied in simulations. R_{slag} varies from 0,00147 to 0,00163 m (from 1,47 to 1,63 mm), depending on the weight of a slag droplet, and g is the gravity, acting in y-direction.

In addition, a numerical calculation using equation *3* has been carried out to evaluate a relevant range of interfacial tension for the simulations. Values of $\cos\beta$, as illustrated in Fig. 13, are greater than 1 when interfacial tension is smaller than 0,85 N/m. Interfacial tension of 0,85 N/m has therefore been used as the minimum value in simulations, while the maximum interfacial tension is assumed to be identical to surface tension of FeMn - 1,50 N/m.

The physical parameters used in simulations are shown in Table 4.

In order to reduce the effects of spurious currents even more, the viscosity was set to an (artificial) elevated value. Since the steady state is static - the actual value of the viscosity should not impact the final converged result. In order to determine a suitable value for the viscosity - a parametric study was performed, in which the steady state solutions (if found) were compared, according to the values indicated below.

- $10^{-6} \leq \nu_{FeMn} \leq 10^{-2}$ m^2/s.

Table 3: Numerical solution parameters used in the simulation setup.

Solution and algorithm control settings (fvSolution)

Parameter	Field					
	alpha	**pcorr**	**p_rgh**	**p_rghFinal**	**U**	**UFinal**
tolerance	10^{-6}	10^{-8}	10^{-8}	10^{-9}	10^{-6}	10^{-8}
relTor	0	0	0	0	0	0
maxIter	100	-	-	50	-	-
nAlphaSubCycles	2	-	-	-	-	-
nAlphaCorr	2	-	-	-	-	-
MULESCorr	false	-	-	-	-	-
cAlpha	1	-	-	-	-	-
nLimiterIter	3	-	-	-	-	-
smoother	GaussSeidel	-	-	-	-	-
nSweeps	1	-	-	-	-	-
solver	smoothSolver	-	-	-	-	-
relaxationFactors	-	0,3	0,3	0,9	0,3	-

PIMPLE loop

Parameter	Value
nCorrectors	1
nOuterCorrectors	1
momentumPredictor	false

Numerical schemes settings (fvSchemes)

Time derivatives	Value
ddtSchemes	CrankNicolson 0,50

Time and data input/output control settings (controlDict)

Parameter	Value
deltaT	10^{-6}
maxDeltaT	10^{-5}
maxCo	0,25
maxAlphaCo	0,25

- $10^{-5} \leq \nu_{slag} \leq 10^{-3}$ m^2/s.
- $10^{-5} \leq \nu_{Ar} \leq 10^{-3}$ m^2/s.

In addition, a parametric study of the mesh resolution, quality of the dynamic mesh refinement (DMR) and geometry size has been carried out to determine the most appropriate parameters to be used in simulations without affecting the results and changing the convergence time significantly. For all simulations in the parametric study, $\gamma_{slag-Ar}$, $\gamma_{FeMn-Ar}$ and $\gamma_{FeMn-slag}$ were 0,70, 1,00 and 0,70 N/m, respectively.

RESULTS AND DISCUSSION

A. Surface tension of FeMn alloy and slag

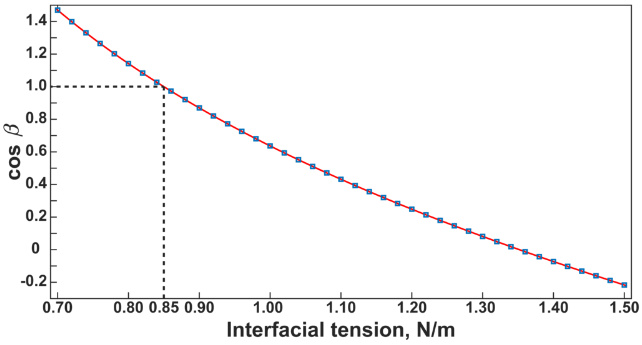

Figure 13: Values of cos β calculated by equation *3*.

Table 4: Physical parameters applied in simulations.

Parameter	Value
ρ_{slag}, kg/m^3	3300*
ρ_{FeMn}, kg/m^3	5612*
ρ_{Ar}, kg/m^3	1,66
ν_{slag}, m^2/s	varied
ν_{FeMn}, m^2/s	varied
ν_{Ar}, m^2/s	varied
$\gamma_{slag-Ar}$, N/m	0,65
$\gamma_{FeMn-Ar}$, N/m	1,50
$\gamma_{FeMn-slag}$, N/m	0,85 - 1,50

*Density of slag and FeMn alloy in molten state (Muller *et al.*, 2015)

The values surface tension of FeMn alloy and slag, obtained after the experimental measurement, are shown in Fig. 14. Surface tension of FeMn alloy was found to be 1,50 ± 0,05 N/m, while surface tension of slag was considerably lower (0,65 ± 0,01 N/m). From the confidence intervals, it is evident that the LBADSA methodology, which was applied for the measurement of surface tension of FeMn has higher deviation (±0,05 N/m), that the ellipsoidal solution of the Young-Laplace equation, where the confidence interval for surface tension of slag was ±0,01 N/m.

B. Parametric study: influence of viscosity

For simulations with $\nu_{FeMn} \leq 10^{-6}$ m^2/s, the alloy interface failed to stabilize as indicated in Fig. 15. For values of $10^{-4} \leq \nu_{FeMn} \leq 10^{-2}$ m^2/s, the interface was stable, also for a wide range of viscosities for the remaining phases; $10^{-4} \leq \nu_{slag} \leq 10^{-5}$ m^2/s and $10^{-3} \leq \nu_{Ar} \leq 10^{-5}$ m^2/s, indicated in Fig. 16. Increasing the viscosity further led to unphysical numerical artifacts.

From the parametric study, it was concluded to choose $\nu_{FeMn} = 10^{-4}$ m^2/s, $\nu_{slag} = 10^{-5}$ m^2/s and $\nu_{Ar} = 10^{-5}$ m^2/s. The kinematic viscosity of FeMn differs from the real kinematic viscosity of FeMn, which is usually in the order of 10^{-6} m^2/s; however, the assumed kinematic viscosity of FeMn should not influence the steady state of the simulations as discussed earlier.

C. Parametric study: influence of mesh resolution and geometry size

Studied settings of DMR and mesh resolution, total number

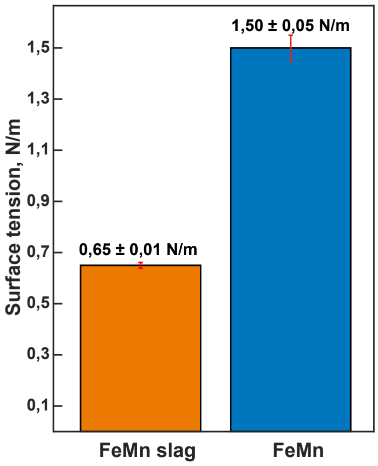

Figure 14: Surface tension of FeMn alloy and slag measured experimentally in the sessile drop furnace. Red lines on top of bars are 95 % confidence intervals.

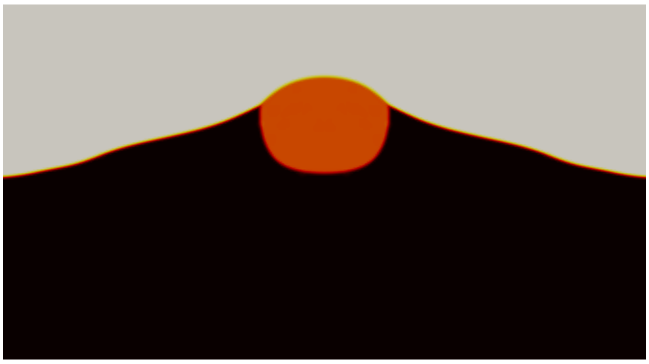

Figure 15: Surface instabilities induced by spurious currents.

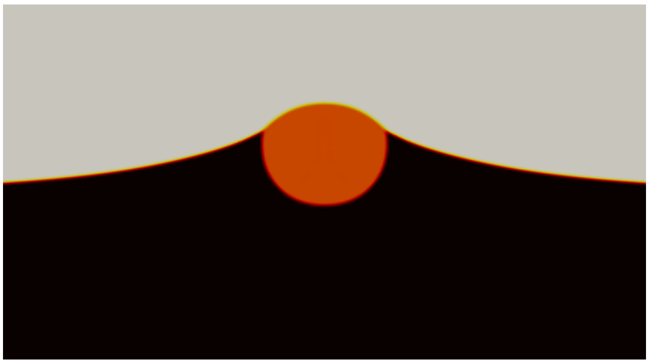

Figure 16: The simulation results for the kinematic viscosity: $\nu_{FeMn} = 10^{-4}$ m^2/s, $\nu_{slag} = 10^{-4}$-10^{-5} m^2/s, $\nu_{Ar} = 10^{-3}$-10^{-5} m^2/s.

of cells before and after DMR as well as maximum time step and convergence time are presented in Table 5. In addition, the influence of geometry size has been studied with the parameters as shown in Table 6. Since the non-visible height of the slag droplet is crucial for obtaining the interfacial tension based on the inverse modelling strategy, it has been applied for comparing the steady state in various simulations.

The non-visible height obtained at different time steps in tests of different mesh resolution and DMR quality is shown in Fig. 17. In test A1 and A2, the slag droplet has reached a steady state as represented in Fig. 18, while the convergence time increases with increasing the quality of DMR as well as the total number of mesh cells after DMR increases up to 2,0 and 3,6 times for low (A1) and average (A2) quality of DMR, respectively. On the contrary, test A3 with the highest quality of DMR and test A5 with the highest number of cells after DMR, have instabilities in achieving the steady state, which leads to higher values of the average non-visible height. Similarly to tests A1 and A2, the increasing of mesh resolution in test A4 does not have any influence on the simulation results, however, the convergence time increases to 24784 s. For the proposed simulation setup, the settings from test A2 with average quality of DMR has been chosen as optimal since it requires slightly higher convergence time compared to test A1 with low quality.

The influence of geometry size in x- and y-direction on the non-visible height of the slag droplet is demonstrated in Fig. 19. Tests B2-B5 have shown similar steady results with relatively close values of the average non-visible height, while test B1 has instabilities at the FeMn-Ar interface, resulting in the average non-visible height two times higher compared to other simulations. Test B2 has been chosen as optimal since it requires the lowest convergence time compared to tests B3-B5 with higher geometry size.

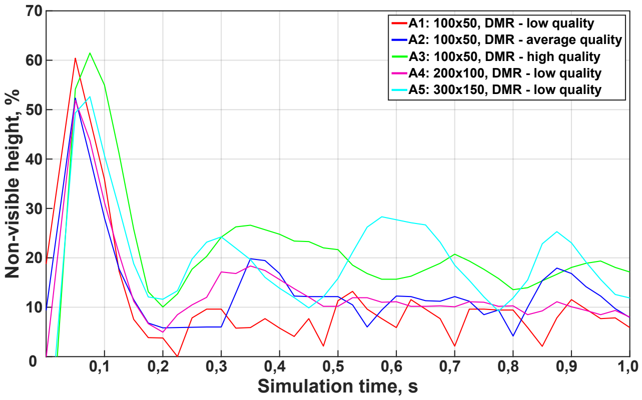

Figure 17: Effect of mesh resolution and DMR quality on the non-visible height of slag droplet in the parametric study. The average non-visible height in percent at the steady state (after 0,2 s of simulation time) for each test is: A1 - 7,4; A2 - 11,2; A3 - 18,9; A4 - 11,2; A5 - 18,4.

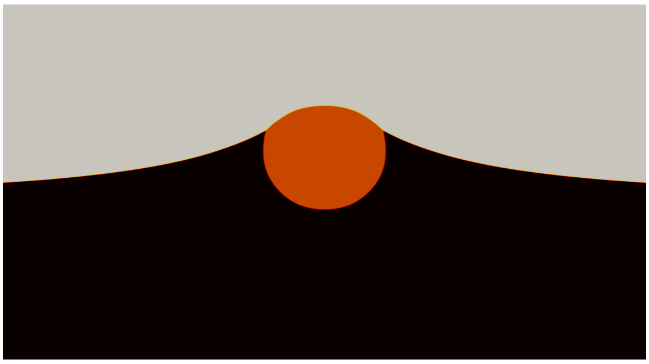

Figure 18: The steady state of slag droplet reached in simulations in the parametric study.

D. Interfacial tension between FeMn alloy and slag

Fig. 20 shows the simulation matrix obtained after performing simulations with various values of interfacial tension and parameters as shown in Table 4, with viscosities and resolution as determined in previous sections. The corresponding non-visible height to the values of interfacial tension from 0,85 to 1,50 N/m is illustrated in Fig. 21. The results demon-

Table 5: Settings for mesh resolution and DMR quality used in the parametric study.

Mesh	DMR quality	Mesh resolution, mm^2	Initial total number of cells	Total number of cells after DMR	Maximum time step, s	Convergence time, s
A1	Low	0,200 x 0,200	5000	10000	10^{-5}	8541
A2	Average	0,200 x 0,200	5000	18000	10^{-5}	14009
A3	High	0,200 x 0,200	5000	44000	10^{-5}	52366
A4	Low	0,100 x 0,100	20000	31800	10^{-5}	24784
A5	Low	0,066 x 0,066	45000	66500	10^{-5}	64886

Table 6: Geometry size used in the parametric study.

Mesh	DMR quality	Mesh resolution, mm^2	Geometry size in x-direction, mm	Geometry size in y-direction, mm	Surface area of the geometry, mm^2	Maximum time step, s	Convergence time, s
B1	Low	0,200 x 0,200	10	10	100	10^{-5}	5013
B2	Low	0,200 x 0,200	20	10	200	10^{-5}	8375
B3	Low	0,200 x 0,200	20	20	400	10^{-5}	11189
B4	Low	0,200 x 0,200	20	40	800	10^{-5}	21703
B5	Low	0,200 x 0,200	50	10	500	10^{-5}	17822

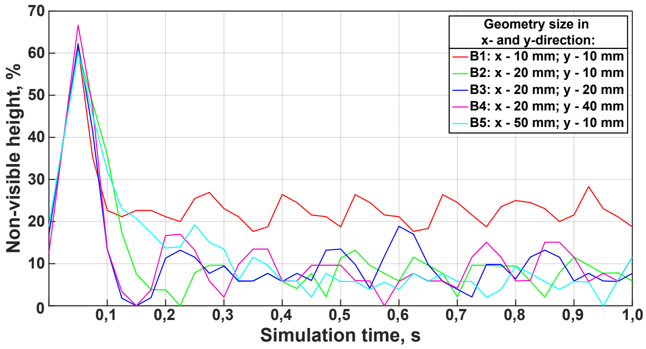

Figure 19: Effect of the geometry size on the non-visible height of slag droplet in the parametric study. The average non-visible height in percent at the steady state (after 0,2 s of simulation time) for each test is: B1 - 22,3; B2 - 7,4; B3 - 9,0; B4 - 8,8; B5 - 7,4.

strate that the slag droplet remains above the interface at relatively high values of interfacial tension (≈1,20 - 1,50 N/m), which promotes better separation of FeMn alloy and slag and therefore less metal losses. The slag droplet begins to sink down below the interface at intermediate interfacial tension (≈0,85 - 1,15 N/m), contributing to emulsification of FeMn and slag.

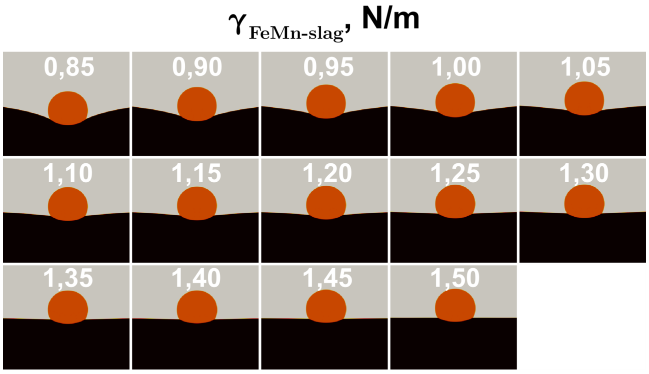

Figure 20: The simulations results, depending on interfacial tension between FeMn alloy and slag from 0,85 to 1,50 N/m.

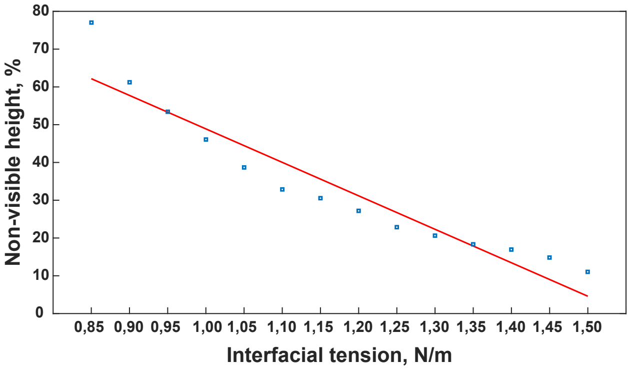

Figure 21: Effect of interfacial tension on the non-visible height in the simulations.

The simulations shown in Fig. 20 were compared to the non-visible part of slag droplets from corresponding experiments, from which the interfacial tension could be estimated under various conditions. Figure 22 shows a comparison of the non-visible surface to that obtained under simulations under similar conditions. The estimated interfacial tension between FeMn alloy and slag at different temperatures and holding time is presented in Fig. 23 and Fig. 24, respectively. According to Fig. 23, the interfacial tension gradually decreases from 1,50 ± 0,05 N/m to 1,15 ± 0,04 N/m when temperature increases. Fig. 24 shows that the holding time of 5 and 10 min has no effect on the interfacial tension; however, interfacial tension slightly decreases to 1,25 N/m when the holding time is 15 min.

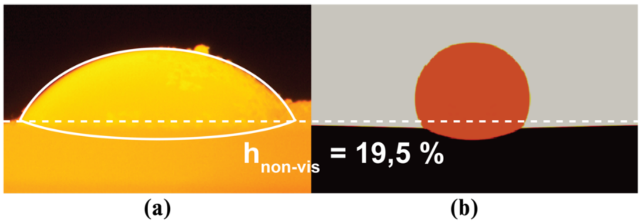

Figure 22: Comparison of the slag surface obtained experimentally at 1673 K (a) and in simulations (b), corresponding to interfacial tension of 1,30 N/m.

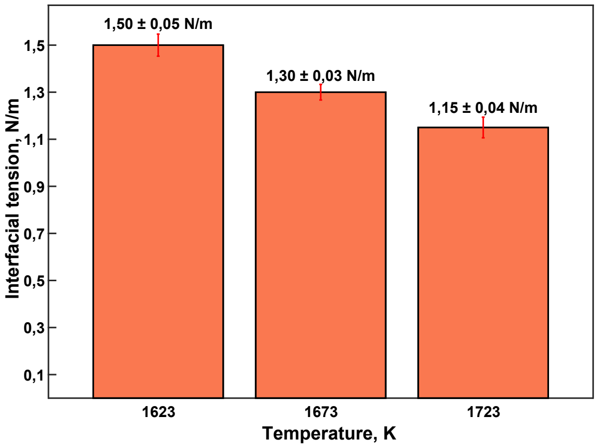

Figure 23: Effect of the temperature on interfacial tension between FeMn alloy and slag. Red lines on top of bars are 95 % confidence intervals.

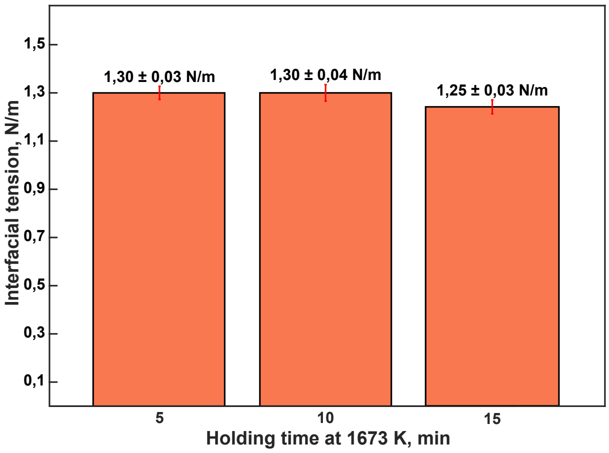

Figure 24: Effect of the holding time on interfacial tension between FeMn alloy and slag at constant temperature. Red lines on top of bars are 95 % confidence intervals.

F. Previous research on surface tension of FeMn alloy and slag

Lee *et al.*, 2011 have reported that the surface tension of FeMn alloys without carbon decreases with increasing the Mn content - from ≈1,90 N/m for a pure Fe-system to ≈1,00 N/m for a pure Mn-system. According to their data, the corresponding value of surface tension is 1,10 N/m for the composition used in this study, assuming that no carbon is present in FeMn alloy (≈84 wt. % Mn, ≈16 wt. % Fe). However, they have not studied the influence of carbon on the Fe-Mn system, which can explain the difference in the surface tension of FeMn alloy - 1,10 N/m in Lee *et al.*, 2011 compared to 1,50 N/m in the present work for high-carbon saturated FeMn alloy. Xin *et al.*, 2019 developed a numerical model for calculation of the surface tension of molten slags which predicts that molten slags generally have surface tension in the range from 0,30 to 0,70 N/m, depending on the composition, again corresponding well to that identified in the current work.

While there to our best knowledge is no data for interfacial tension between FeMn alloy and slag, Park *et al.*, 2009 have reported interfacial tension between molten iron and CaO-SiO_2-MgO-Al_2O_3-FeO slag between 0,72 and 1,44 N/m, depending on slag composition and oxygen content in iron. Surface tension of FeMn slag (0,65 N/m) and interfacial tension between FeMn alloy and FeMn slag (1,15-1,50 N/m), again in the range of that found in the current work.

SUMMARY AND CONCLUSIONS

The current paper presents a method in which images from a sessile drop furnace are combined with multiphase simulations in order to determine material properties which otherwise are not easily accessible. The method is demonstrated for a FeMn-slag system with constant composition.

The proposed method estimates interfacial tensions of 1,50 ± 0,05 N/m, 1,30 ± 0,03 N/m and 1,15 ± 0,04 N/m at temperatures of 1623, 1673 and 1723 K, respectively. Furthermore, it has been found that changing the holding times from 5 to 15 minutes does not affect the interfacial tension significantly. Surface active elements, such as S, can have a considerable impact on interfacial tension. Although it is not addressed in the current work, experiments considering such effects have been carried out recently, and will be published in the near future (Bublik *et al.*, 2021).

The methodology developed here is demonstrated only for FeMn; however, it is expected that it could also be applied for other processes, i.e. metal refining and for other metals, for instance, SiMn, FeSi, Si and Fe. Future work will explore these possibilities as well as the influence of slag composition for the FeMn system.

REFERENCES

ANDERSSON, P. (2010). "Tutorial multiphaseInterFoam". `http://www.tfd.chalmers.se/~hani/kurser/OS_CFD_2010/patrikAndersson/patrikAnderssonReport.pdf`. Accessed: 24.08.2020.

BERBEROVIC, E., VAN HINSBERG, N.P., JAKIRLIC, S., ROISMAN, I.V. and TROPEA, C. (2009). "Drop impact onto a liquid layer of finite thickness: Dynamics of the cavity evolution". *Phys. Rev. E*, **79**, 036306.

BUBLIK, S., BAO, S., TANGSTAD, M. and EINARSRUD, K.E. (2019). "Slag-metal interactions in the FeMn tapping process: Interfacial properties and wetting". *Proceedings of the Liquid Metal Processing & Casting Conference 2019*. Birmingham, UK.

BUBLIK, S., BAO, S., TANGSTAD, M. and EINARSRUD, K.E. (2021). "Influence of sulphur on the interfacial behaviour between FeMn alloy-slag and SiMn alloy-slag". To be presented at MOLTEN 2021.

CFD Online Discussion Forums (2018). "Main Forum". `https://www.cfd-online.com/Forums/openfoam-community-contributions/118870-2d-adaptive-mesh-refinement-2.html#post703369/`. Accessed: 24.08.2020.

CLIFT, R., GRACE, J. and WEBER, M. (1978). *Bubbles, Drops, and Particles*. Academic Press.

DAMIAN, S.M. (2012). "Description and utilization of interFoam multiphase solver". *International Center for Computational Methods in Engineering*.

HERNANDEZ-BALTAZAR, E. and GRACIA-FADRIQUE, J. (2005). "Elliptic solution to the Young–Laplace differential equation". *Journal of Colloid and Interface Science*, **287(1)**, 213 – 216.

HIRT, C. and NICHOLS, B. (1981). "Volume of fluid (VOF) method for the dynamics of free boundaries". *Journal of Computational Physics*, **39(1)**, 201 – 225.

HOLAPPA, L. (2013). "Chapter 2 - Basics of Ferroalloys". M. Gasik (ed.), *Handbook of Ferroalloys*. Butterworth-Heinemann, Oxford.

JAKOBSSON, A., SICHEN, D., SEETHARAMAN, S. and NURNI, V. (2000). "Interfacial phenomena in some slag-metal reactions". *Metallurgical and Materials Transactions B*, **31**, 973–980.

KIM, H., KIM, J. and SASAKI, Y. (2010). "The role of molten slag in iron melting process for the direct contact carburization: Wetting and separation". *ISIJ international*, **50**, 1099–1106.

LEE, J.J.E. (2016). "Droplet formation mechanisms in metallurgical processes".

LEE, J., SHIN, M. *et al.* (2011). "Density and surface tension of liquid Fe-Mn alloys". *Metallurgical and Materials Transactions B*, **42(3)**, 546–549.

LI, Z., ZEZE, M. and MUKAI, K. (2003). "Surface tension and wettability of liquid Fe-16 mass%Cr-S alloy with alumina". *Materials Transactions*, **44(10)**, 2108–2113.

MULLER, J., ZIETSMAN, J. and PISTORIUS, P. (2015). "Modeling of manganese ferroalloy slag properties and flow during tapping". *Metallurgical and Materials Transactions B*, **46**.

OOI, H., NOZAKI, T. and YOSHII, H. (1974). "The effect of chemical reactions on the interfacial tension between iron and CaO-SiO_2-Al_2O_3 slag". *Transactions of the Iron and Steel Institute of Japan*, **14(1)**, 9–16.

PARK, S.C., GAYE, H. and LEE, H.G. (2009). "Interfacial tension between molten iron and CaO–SiO_2–MgO–Al_2O_3–FeO slag system". *Ironmaking & Steelmaking*, **36(1)**, 3–11.

ROWLINSON, J. and WIDOM, B. (2002). *Molecular Theory of Capillarity*. Dover books on chemistry. Dover Publications.

RUEDEN, C.T., SCHINDELIN, J., HINER, M.C., DEZONIA, B.E., WALTER, A.E., ARENA, E.T. and ELICEIRI, K.W. (2017). "ImageJ2: ImageJ for the next generation of scientific image data". *BMC bioinformatics*, **18(1)**, 529.

SARIDIKMEN, H., KUCUKKARAGOZ, C.S. and ERIC, R.H. (2007). "Sulphur behaviour in ferromanganese smelting".

SJALANDER, M., JAHRE, M., TUFTE, G. and REISSMANN, N. (2019). "EPIC: An energy-efficient, high-performance GPGPU computing research infrastructure".

STALDER, A.F., MELCHIOR, T., MULLER, M., SAGE, D., BLU, T. and UNSER, M. (2010). "Low-bond axisymmetric drop shape analysis for surface tension and contact angle measurements of sessile drops". *Colloids and Surfaces A: Physicochemical and Engineering Aspects*, **364(1)**, 72 – 81.

TANGSTAD, M. (2013). *Handbook of Ferroalloys: Chapter 7. Manganese Ferroalloys Technology*. Elsevier Science.

The OpenFOAM Foundation (2016). "OpenFOAM v6 User Guide". `https://cfd.direct/openfoam/user-guide-v6/`. Accessed: 24.08.2020.

VACHAPARAMBIL, K.J. and EINARSRUD, K.E. (2019). "Comparison of surface tension models for the volume of fluid method". *Processes*, **7(8)**, 542.

WELLER, H.G., TABOR, G., JASAK, H. and FUREBY, C. (1998). "A tensorial approach to computational continuum mechanics using object-oriented techniques". *Computers in Physics*, **12(6)**, 620–631.

XIN, J., WANG, N., CHEN, M. and GAN, L. (2019). "Surface tension calculation of molten slag in SiO_2–Al_2O_3–CaO–MgO systems based on a statistical modelling approach". *ISIJ International*, **59(5)**, 759–767.

MODELLING OF MASS TRANSFER IN A STEELMAKING LADLE

Nelson JOUBERT[1,2]*, **Pascal GARDIN**[1†], **Stéphane ZALESKI**[2‡], **Stéphane POPINET**[2•]
[1]ArcelorMittal Maizières Research, BP 30320, Voie Romaine, 57283
Maizières-lès-Metz Cedex, FRANCE
[2]Sorbonne Université, CNRS, UMR 7190, Institut Jean Le Rond d'Alembert,
BP 162, 4, Place Jussieu, 75252 Paris Cedex 05, FRANCE

* E-mail : nelson.joubert@sorbonne-universite.fr
† E-mail : pascal.gardin@arcelormittal.com
‡ E-mail : stephane.zaleski@sorbonne-universite.fr
• E-mail : stephane.popinet@sorbonne-universite.fr

ABSTRACT

Mass transfer between liquid steel and slag is an important point during secondary metallurgy for prediction of the chemical reaction rate and adjustment of liquid steel composition. We want to study this phenomenon in the case of an argon gas bottom blown ladle. To do so we use an experimental and numerical water model at ambient temperature. We measure experimentally the mass transfer of thymol between water and oil when the air flow rate injected is varied. The experimental results show that two mass transfer regimes can be observed. The mass transfer regime change could be correlated to the continuous formation of oil droplets in the water when the air flow rate is above a critical value. The numerical results represent qualitatively well the fluid flow of the water model. But the numerical results cannot reproduce different mass transfer regimes as observed experimentally and, have a tendency to overestimate the mass transfer.

Keywords: CFD, hydrodynamics, multiphase flow, mass transfer.

NOMENCLATURE

Greek Symbols

ρ	Mass density, [kg/m^3].
μ	Dynamic viscosity, [kg/m.s].
ν	Kinematic viscosity, [m²/s].
δ	Boundary layer thickness, [m].
σ	Surface tension, [N/m].
χ	Volume fraction, [-].
ϵ	Rate of dissipation of turbulence kinetic energy, [m²/s].
η	Kolmogorov length scale, [m].
λ_B	Batchelor length scale, [m].

Latin Symbols

L	Width of the ladle, [m].
h	Height, [m].
d	Diameter, [m].
V	Volume, [l].
Q	Gas flow rate, [l/min].
g	Gravitational acceleration, [m/s^2].
J	Mass flux, [kg/m^{2}s].
A	Interfacial area, [m^2].
C	Concentration, [g/l].
D	Diffusion coefficient, [m²/s].
k	Mass transfer coefficient, [m/s].
p	Pressure, [Pa].
u	Velocity, [m/s].
T	Numerical tracer concentration, [g/l].
P	Partition coefficient, [-].
N	Maximum number of grid points in one direction [-].
Fr	Froude number, [-].
Sc	Schmidt number, [-].
Sh	Sherwood number, [-].

Sub/superscripts

a	Air.
w	Water.
o	Oil.
c	Concentration.
0	Initial condition.
th	Thymol.
$'$	Interface value.
ov	Overall.
inj	Injector.
il	Industrial ladle.
ml	Model ladle.
$norm$	Normalized value.
$\bar{\ }$	Time average.
∞	Fluid bulk.

INTRODUCTION

In numerous natural and industrial processes, chemical reaction occurs together with a fluid flow and possibly other physical phenomena. In the steel industry, during the secondary metallurgy step, the adjustment of liquid steel composition at high temperature in a ladle involves several chemical reactions between steel and slag (another liquid phase of variable chemical composition depending on the expected chemical reaction with steel) (Riboud & Vasse, 1985). Chemical reactions can be broken down into three stages: transport by convection of reactive species within the liquid phase toward the interface, transport by molecular diffusion through concentration boundary layer and finally chemical reaction at the interface. The global kinetics is governed by the kinetics of the slowest stage. In the case of a chemical reaction between liquid steel and slag, it is generally accepted that chemical reactions at the interface are very fast. Then, the steps governing the global kinetics are the convective and diffusive transport or mass transfer of reactive species. Therefore, we want especially to characterise the mass transfer of reactive species between the liquid steel and slag phase. Here, for example, the process we are interested in to reproduce is the desulfurization of liquid steel by chemical reaction with slag under argon gas bubbling. Previous studies attempted to model experimentally the process either with a cold model (Kim & Fruehan, 1987; Ishida et al., 1981; Mietz & Oeters, 1991; Wei & Oeters, 1992) or a high-temperature model (Hirasawa et al., 1987a; Hirasawa et al., 1987b). Other studies try to model the process numerically (Lou & Zhu, 2014; Lou & Zhu, 2015). The results showed some change in the mass transfer regime between the two phases when the gas flow rate reaches a particular value. From the studies in the literature several explanations are made to explain the observed mass transfer regime change:

- Change of the steel phase flow behaviour;
- Change of the slag phase flow behaviour;
- Increase of steel-slag exchange area.

This could also be a combination of the three assumptions. But in the literature, it is generally acknowledged that the observed mass transfer regime change is due to the high deformation of the slag layer leading possibly to its fragmentation into droplet in liquid steel (Calabrese et al., 1986; Iguchi et al., 1994; Xiao et al., 1987). Slag droplets formation would increase the exchange area between the two phases. In order to verify this assumption and the mass transfer regime change, we build an experimental water model of the process with its numerical model. We will detail in the following the results obtained experimentally and numerically on the mass transfer characterization.

MODEL DESCRIPTION

We want to establish a model that allows to reproduce the main flow characteristics that can be observed in an industrial ladle especially when the gas flow rate is changed and with the easiest experimental setup as possible.

EXPERIMENTAL MODEL

The main characteristics of the flow consist of a gas bubble plume, and the water-oil layer interaction. Because in this study the gas bubble plume is mostly used to generates agitation of the liquid phase, we will not focus on the gas bubble plume. Nevertheless, the gas flow rate remains an important parameter as it will globally put in motion the fluids. Given the numbers of parameters of the physical model, many dimensionless number quantities can be established. As a result, the choice of similitude to follow is not trivial and depends on the phenomena of interest. In this study, we are interested in the mass transfer characterization between liquid steel and slag. Nevertheless, this mass transfer depends strongly on the fluid flow characteristics. So, in order to reproduce the mass transfer configuration of an industrial ladle, we proceed as in Kim & Fruehan (1987) for the choice of fluids and chemical tracers that will be detailed below. Furthermore, the gas flow rate is a control parameter of the process then it will be used to reproduce the fluid flow with a scaled model of an industrial ladle. So, we proceed again as in Kim & Fruehan (1987) and we choose to follow a similitude based on the Froude number:

$$Fr = \frac{Q}{\sqrt{g h_w^5}} \tag{1}$$

To determine the correspondence between a 200-ton industrial ladle and our model ladle gas flow rate a Fr similitude is used, and we can write:

$$Q_{il} = \lambda^{\frac{5}{2}} Q_{ml} \tag{2}$$

The geometric scale is given by $\lambda = h_{w,il}/h_{w,ml}$ is equal to $\lambda = 1/16.6$.

In this study, we use a cubic water model of length L_x with a water and oil bath height respectively h_w and h_o at ambient temperature based on the one used by Kim & Fruehan (1987). Figure 1 displays a sketch of the experimental setup of the water model and the main geometric parameters of the ladle can be found in Table 1. It is a square section transparent ladle made with acrylic glass, with a single bottom centred circular air injection hole. The ladle is partially filled with water and a layer of oil is floating on top of the water. Air flow within the range of $[0.6L/min : 8L/min]$ is injected from a compressed air network and can be varied through an automate controlling the valve opening.

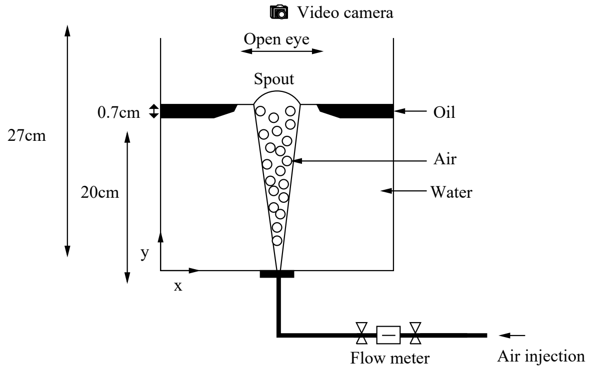

Figure 1: Schematic of the experimental setup of the water model

L	d_{inj}	h_w	h_o	V_w	V_o	h_w/L_x
0.27	$2.5.10^{-3}$ to $7.9.10^{-3}$	0.2	$7.0.10^{-3}$	14.6	0.49	0.7

Table 1: Main geometrical parameters of the model

As in the industrial process, it is a three-phase model where the air phase represents the argon gas, water represents the liquid steel, and the oil mixture layer represents the liquid slag. The choice of fluids follows the one used in Kim & Fruehan (1987) and allows us to study both hydrodynamics and mass transfer with the same fluids. The choice of water can be justified because of its kinematic viscosity $\nu_w = 1.10^{-6}\ m^2.s^{-1}$ which is very close to that of liquid steel $\nu_{steel} = 7.10^{-7}\ m^2.s^{-1}$. The oil phase is a 50-50% in volume mixture of cottonseed oil and paraffin oil. All the fluids physical parameters can be found in Table 2.

	ρ	μ	$\sigma_{a/w}$	$\sigma_{w/o}$	$\sigma_{o/a}$
Air	1.225	$1.85.10^{-5}$	$7.20.10^{-2}$		
Water	998	$1.00.10^{-3}$		$2.55.10^{-2}$	
Oil mixture	920	$7.9.10^{-2}$			$3.17.10^{-2}$

Table 2: Physical properties of fluids used in the water model

In the case of two immiscible liquids at steady-state condition, boundary layers offering resistance to the overall mass transfer are considered for both liquids. The overall mass transfer coefficient at the interface can be computed by equating mass fluxes computed using fluid film approximation of the first law of Fick:

$$J = k_w(C_w - C'_w) \qquad (3)$$
$$-J = -k_o(C_o - C'_o)$$

where $k_w = D_w/\delta_c$ and $k_o = D_o/\delta_c$. At the interface, when the concentration is at chemical equilibrium there is a discontinuity because of chemical tracer solubility difference between the two phases. It can be described by the partition coefficient:

$$P = \frac{C'_o}{C'_w} \qquad (4)$$

Combining the above equations, we can write the following mass flux equations for the water phase:

$$J = k_{ov}\left(C_w - \frac{C_o}{P}\right) \qquad (5)$$

where $k_{ov} = 1/(1/k_w + 1/Pk_o)$, and $1/k_w$, $1/Pk_o$ represent the water and oil phase mass transfer resistance. Depending on the value of Pk_o the mass transfer resistance value can be preponderant in either one of the phases or of equal importance in both phases. In the mentioned literature it is generally acknowledged that in an industrial ladle case the desulphurization reaction of liquid steel with slag has a high Pk_o value. So, the steel phase mass transfer is controlled by the steel phase mass transfer resistance. As in Kim & Fruehan (1987), to reproduce the sulphur behaviour within this assumption we have chosen as chemical tracer thymol in the water model. It has a high partition coefficient between oil and water $P > 350$ assuming that k_o is not too small it leads to a water phase mass transfer controlled by the water phase resistance.

Using (3) and (4) we can write that:

$$C'_o = \frac{P\alpha}{1+\alpha}C_w + \frac{1}{1+\alpha}C_o \qquad (6)$$

where $\alpha = k_w/Pk_o$. The value of C'_o depends on the magnitude of α. In Kim & Fruehan (1987) it is assumed that $\alpha \ll 1$ giving $C'_o \sim C_o$.

Now if we consider unsteady state, we can write that:

$$\frac{V_w}{A}\frac{dC_w}{dt} = k_w(C_w - C'_w) \qquad (7)$$
$$\frac{V_o}{A}\frac{dC_o}{dt} = k_o(C'_o - C_o)$$

And the mass balance for the transferred species give:

$$(C_{w,0} - C_w)V_w = C_oV_o \qquad (8)$$

Considering the same assumption as in Kim & Fruehan (1987) and equilibrium at the interface it is possible to rewrite (7) using (8) and (4) :

$$\frac{1}{\left[C_w(1+\beta) - \beta C_{w,0}\right]}\frac{dC_w}{dt} = \frac{k_wA}{V_w}$$

where $\beta = V_w/V_oP$. After integration we obtain:

$$\frac{ln\left[\frac{C_w}{C_{w,0}}(1+\beta) - \beta\right]}{1+\beta} = \frac{k_wA}{V_w}t \qquad (9)$$

From relation (9), it is possible to compute directly the product of the average mass transfer coefficient with interfacial area per volume unit in function of the measured thymol concentration in water on the left-hand side of (9). This formulation will be used to determine the average mass transfer coefficient in the following experimental results.

Thymol concentration in water is measured every 10 minutes during 3 hours by analysing water samples with a refractometer previously calibrated. Measurements are done with two injection diameters $d_{inj} = 2.35mm$ and $d_{inj} = 7.9mm$, with $14.4l$ of water with a thymol concentration of 0.9g/l dissolved in it and 0.486l of oil mixture atop of it.

NUMERICAL MODEL

To resolve the problem, we solve numerically the partial differential equations with the open-source free code Basilisk. Basilisk is a DNS code with no turbulence model and the possibility to adapt the mesh dynamically following a quad/oc-tree structure. The numerical schemes used in Basilisk are based on its ancestor the Gerris solver and can be found in Popinet (2003), Popinet (2009). The Incompressible Navier-Stokes equations with surface tension term treated by a Continuous Surface Force (Brackbill et al., 1992) can be written:

$$\rho\left(\frac{\partial \boldsymbol{u}}{\partial t} + \boldsymbol{u}\cdot\boldsymbol{\nabla}\boldsymbol{u}\right) = -\boldsymbol{\nabla}p + \boldsymbol{\nabla}\cdot(2\mu\boldsymbol{D}) + \sigma\kappa\boldsymbol{n}\delta_S$$
$$\boldsymbol{\nabla}\cdot\boldsymbol{u} = 0$$

with $\boldsymbol{D}$ the deformation tensor $\boldsymbol{D} = (\nabla\boldsymbol{u} + (\nabla\boldsymbol{u})^T)/2$. Because we are dealing with multiphase flow the variations of density and viscosity inside the domain are described with the help of the Volume Of Fluid method: The fluid fractions are described by:

$$\chi_k(x,t) = \begin{cases} 1 \; if \; x \in phase \; k \\ 0 \; elsewhere \end{cases} \qquad (10)$$

which obeys an advection equation:

$$\frac{\partial \chi}{\partial t} + \boldsymbol{\nabla} \cdot (\chi \boldsymbol{u}) = 0 \qquad (11)$$

Because we are in presence of a three-phase flow, we cannot use the implicit declaration of phase two as in a two-phase flow. Instead, we declare explicitly three fluid fractions corresponding to each phase. To ensure that a cell is not filled with more than one phase the sum of fluid fractions should respect:

$$0 \leq \sum_i^n \chi_k(x,t) \leq 1 \qquad (12)$$

To do so at each time-step we normalize fluid fractions with the sum of fluid fractions:

$$\chi_{norm}(x,t) = \frac{\chi_k(x,t)}{\sum_i^n \chi_k(x,t)} \qquad (13)$$

This way we can follow a one fluid description with variable density and viscosity determined in the domain with arithmetic means:

$$\begin{gathered} \rho(\chi) \equiv \chi_a\rho_a + \chi_w\rho_w + \chi_o\rho_o, \qquad (14) \\ \mu(\chi) \equiv \chi_a\mu_a + \chi_w\mu_w + \chi_o\mu_o, \end{gathered}$$

Surface tension is acting on the interface between two fluids, but here there is more than one possibility of fluid neighbour for one phase. That is why we decompose the physical surface tension into phase-specific surface tension just depending on the phase and not the fluid in contact following K.A. Smith et al. (2002), Chen et al. (2017), Wallmeyer et al. (2018):

$$\begin{gathered} \sigma_w \equiv (-\sigma_{o/a} + \sigma_{a/w} + \sigma_{w/o})/2 \qquad (15) \\ \sigma_o \equiv (\sigma_{o/a} - \sigma_{a/w} + \sigma_{w/o})/2 \\ \sigma_a \equiv (\sigma_{o/a} + \sigma_{a/w} - \sigma_{w/o})/2 \end{gathered}$$

To take into account the concentration variation we need to consider also the generic scalar transport equation of concentration c (amount of passive scalar/unit volume) for an incompressible flow and without sources or sinks:

$$\frac{\partial C}{\partial t} = \boldsymbol{\nabla} \cdot (D \boldsymbol{\nabla} \boldsymbol{C}) - \boldsymbol{u} \cdot \boldsymbol{\nabla} \boldsymbol{C} \qquad (16)$$

We can separate (16) in two parts:

- $\nabla \cdot (D \nabla C)$ described the diffusion of C it measures the influence of molecular diffusion on C value;
- $u \cdot \nabla C$ described convection of C on the domain it measures the influence of the flow on C.

It means that C has no influence on the velocity field determined by solving the Navier-Stokes equation and is only used to consider diffusion, therefore we call it a passive scalar or tracer. We define tracers confined to one VOF phase in the same manner as described in López-Herrera et al. (2015), meaning that tracer cannot cross a VOF interface except through molecular diffusion. This tracer is advected in the flow within the VOF phase to which it is attached. Tracer concentration in a specific phase is given by:

$$T_k = C\chi_k \qquad (17)$$

where C is the amount of chemical species. Because of the formulations used in the Basilisk code, we cannot add easily the equivalent of the partition ratio P at the interface to reproduce the concentration jump. We use instead a Dirichlet condition imposed on the k phase side:

$$if \; \chi_k > 0.5, \qquad T'_k = 0 \qquad (18)$$

Furthermore, to simplify the model we consider constant phase-specific diffusion coefficients with values determined by Sc in water and oil but we set $D_a = 0 \; m^2/s$ in the air phase as we do not consider its influence on the mass transfer.

To have an idea of the smallest scales to be resolved in the simulation we can use the Kolmogorov length scale given by:

$$\eta = \left(\frac{\nu_w^3}{\epsilon/\rho_w}\right)^{1/4} \qquad (19)$$

Pope (2001) postulated that $\Delta \leq 2.1\eta$ as a criterion to determine the minimum mesh size needed to resolve the Kolmogorov length scale in a DNS simulation. Now as we are interested to do a simulation of diffusion, the smallest concentration fluctuation scale has been defined as the Batchelor length scale (Batchelor, 1953) and is given by:

$$\lambda_B = \frac{\eta}{Sc^{1/2}} \qquad (20)$$

where $Sc = \mu/\rho D$ is the Schmidt number characterizing the ratio of momentum diffusivity and mass diffusivity. Using Pope criteria with the Batchelor length scale we can determine the minimum number of grid points in one direction required to resolve λ_B:

$$N_B = Sc^{1/2} L_x/(2.1\eta) \qquad (21)$$

Applying this criteria with the water model properties i.e. a Schmidt number of thymol in water of $Sc_{th,w} = 1.48 \; 10^3$ for the highest gas flow rate $Q = 6l/min$ leads to $N_B = 5.21 \; 10^4$ cells. So, to resolve sufficiently the boundary layer, in this case, a maximum resolution of 2^{16} cells in one direction would be necessary. This estimation of mesh resolution might be too strict but gives a worst-case scenario for the simulation. We see that this estimation of mesh resolution leads to a too high mesh resolution to reasonably do a DNS simulation. Instead of that, we do a simulation with smaller Schmidt number. We consider 4 tracers in water with smaller Schmidt numbers in the range of $Sc_{th,w} \in \{1,4,10,40\}$ by adjusting the value of the diffusion coefficient for each tracer. Then from the numerical results, we expect to do a scaling to extrapolate the Sherwood number values to higher Schmidt values. At low value of Schmidt number, the concentration boundary layer thickness is approximately equal to the hydrodynamic boundary layer thickness. If we consider a maximum mesh resolution in one direction of 2^{10} cells we can describe the oil layer with 26 cells. Now, if we consider an oil droplet of $3mm$ of diameter with the same mesh resolution we end up with 11 cells in its diameter.

RESULTS

EXPERIMENTAL RESULTS

From the evolution of thymol concentration (Figure 2), we can perfectly fit our experimental data at a gas flow rate $Q = 5.5l/min$ with an exponential decay. Taking the slope of the linear fit of the left-hand side of (9) computed from data in Figure 2, we can compute the product of the average mass transfer coefficient with the area. From Figure 3 results the slope of the linear fit is $8.47\ 10^{-5}$ so it gives here $\overline{k_w}A/V_w = 8.47\ 10^{-5}\ s^{-1}$.

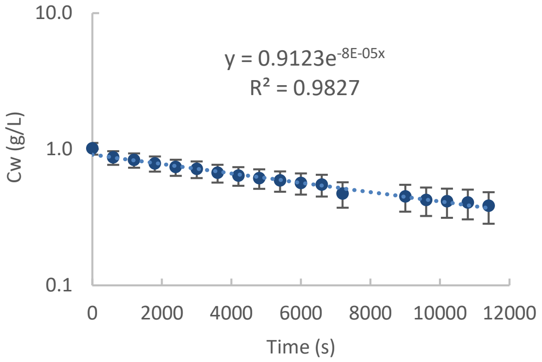

Figure 2: Evolution of thymol concentration for $Q = 5l/min$ and $d_{inj} = 7.9mm$.

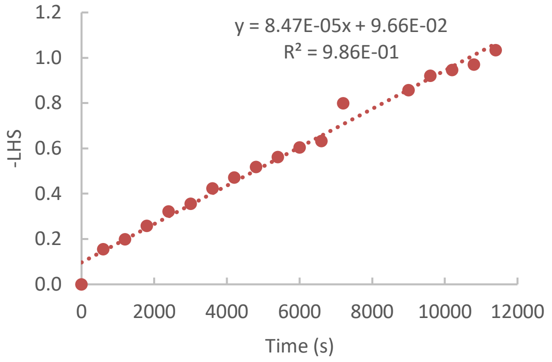

Figure 3: Evolution of - left-hand side of (9) for $Q = 5l/min$ and $d_{inj} = 7.9mm$.

Now, considering the specific water volume for each experiment we can replot the evolution of the product of the mass transfer coefficient with the interfacial area in a log/log scale (Figure 4). From our experimental results (Figure 4) first we can observe that the product of the average mass transfer coefficient with interfacial area increases when the air flow rate is increased for both injection diameters and in agreement with Kim & Fruehan (1987). Even if we have less data for $d_{inj} = 2.35mm$ case it appears that the product of the average mass transfer coefficient with interfacial area varies only a little compared to $d_{inj} = 7.9mm$ results. We can also identify two different mass transfer regimes below and above a critical air flow rate $Q{\sim}5.0\mathrm{l/min}$ for both injection diameters. If we compare the results with the one obtained by Kim & Fruehan (1987), we observe a similar evolution with a critical air flow rate qualitatively the same as the ones we measured with $d_{inj} = 7.9mm$.

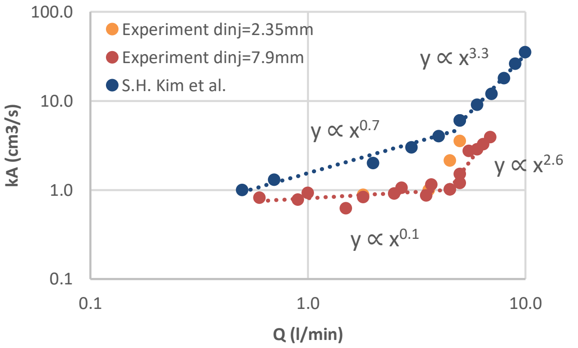

Figure 4: Comparison of the product of the average mass transfer with the interfacial area in function of gas flow rate.

One possible explanation for the mass transfer regime change observed in Figure 4 is the continuous formation of oil droplets of various sizes at high air flow rate. Indeed it can be seen on the top picture of Figure 5 that no oil droplet is visible in water for $Q = 1.0l/min$. As air flow rate increases, we start to see more oil droplets in water only a few minutes after the start of air injection. If we increase air flow rate further, a lot of dark spots which correspond to oil droplets can be identified on the bottom picture of Figure 5 for $Q = 7.5l/min$. Oil droplets of various sizes and shapes are present in water both at the start of air injection and after 3 hours of agitation. These oil droplets could change the interfacial area and the mass transfer mechanism between water and oil droplets.

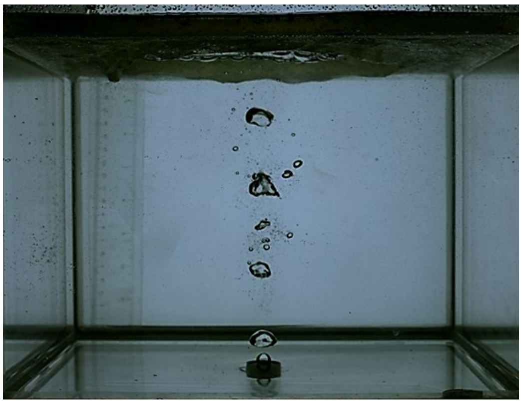

Figure 5: Front view picture of the experimental model.
Top: $Q = 1.1 l/min$, after 3h of gas stirring.
Bottom: $Q = 7.5 l/min$, after 3h of gas stirring.

NUMERICAL RESULTS

We can see on Figure 6 that the numerical model reproduces globally the same flow behaviour as the one that can be seen on Figure 5. We can identify a central bubble plume generating an oil-free region when it reaches the free surface. The oil layer is relatively stable and no oil droplet is observed at low air flow rate on Figure 5 top picture. On the other hand, the free surface seems to be highly perturbated by gravity waves and possibly reflection from the border of the domain at high air flow rate on Figure 5 bottom picture. We can also note that some oil droplets of various sizes can be identified in the water phase on Figure 5 bottom picture.

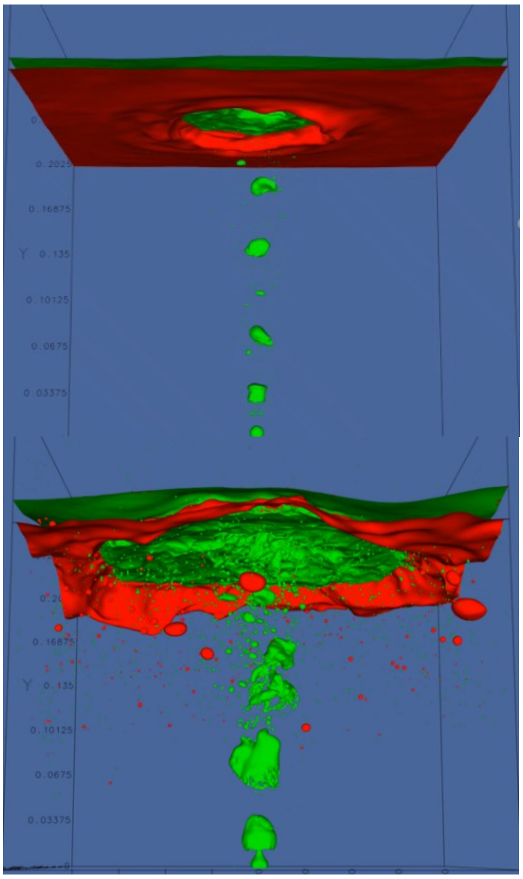

Figure 6: Front view of the numerical model with the air interface coloured in green and the oil interface coloured in red with a maximum mesh resolution in one direction of $\mathbf{2^9}$cells. Top: $\boldsymbol{Q = 0.6 l/min}$; Bottom: $\boldsymbol{Q = 5.5 l/min.}$

We performed simulations for five distinct air flow rates below and around the mass transfer transition observed experimentally. The simulations are started with a maximum mesh resolution in one direction of 2^9 cells. Then when the mass transfer transitory regime is finished, we use the obtained results to restart the simulation with a maximum mesh resolution in one direction increased by a power two. This allows us to save computational time by not recomputing the mass transfer transitory regime for each maximum mesh resolution. From the evolution of the concentration of tracer in water, we can compute the mass transfer coefficient in the water assuming that because of the Dirichlet condition the concentration of tracer at the interface is null. So, we can write:

$$k_w(t)A = \frac{V_w}{C_{w,\infty}} \frac{dC_w}{dt} \tag{22}$$

As we do not know the experimental oil-water interfacial area, we consider the area without gas injection as reference area $A = L^2$. With this we can compute the average water Sherwood number which is the ratio of convective mass transfer to the rate of diffusive mass transport:

$$Sh_w = \frac{\overline{k_w}}{D_w / h_w} \tag{23}$$

First, we have to keep in mind that in order to save computational time the numerical results are obtained for a maximum $Sc_{th,w} = 40$ which is thirty seven times lower than the experimental value $Sc_{th,w} = 1.48\,10^3$. From the results of Figure 7, we can see that for a constant flow rate there is a significative gap in the value of the Sherwood number between a maximum mesh resolution in one direction of $lvl9 = 2^9$ cells and higher mesh resolutions. The difference in the Sherwood number value between a maximum mesh resolution in one direction of $lvl10 = 2^{10}$ and $lvl11 = 2^{11}$ cells is small. This indicates that for an air flow rate of $Q = 0.6 l/min$ the results show a mesh convergence for all the Schmidt numbers with a maximum mesh resolution in one direction of $lvl10 = 2^{10}$ cells. We can also note from Figure 7 that the standard deviation increases with the Schmidt number and decreases when the mesh resolution is increased. Looking now at Figure 8 results we can see that either with the experimental results or the numerical results the Sherwood number in water increases when the air flow rate is increased. The experimental results follow the same behaviour than the experimental results of Figure 4 because of the expression of the Sherwood number (23). For the numerical results in the Figure 8, we do not observe abrupt increase of the Sherwood number and so different mass transfer regime.
We can rewrite relation (23) with the Schmidt number:

$$Sh_w = \frac{\overline{k_w}}{\nu_w / h_w} Sc_w \tag{24}$$

From (24) we can anticipate that when the diffusion coefficient decreases the Schmidt number increases and so the variation of the concentration of tracer decreases too. For a constant fluid flow, it would lead to a smaller mass transfer coefficient. So, the effect on the value of the Sherwood number depends on the ratio between the decrease of $\overline{k_w}$ and the increases of Sc_w. Now, looking more closely at Figure 8 we can see that when the Schmidt number increases the value of the numerical Sherwood number increases too. This indicates that in our numerical results the increase of the Schmidt number is preponderant over the decrease of the mass transfer coefficient. Furthermore, we can also note that the difference between the experimental and numerical results is more important at low air flow rate than at high air flow rate. And that the numerical results the closer to the experimental results are the ones obtained for $Sc_{th,w} = 40$. Now, if we apply relation (21) at $Q = 5.5 l/min$ with $Sc_{th,w} = 40$ it leads to a necessary maximum mesh resolution of 2^{14} cells in one direction. On the other hand applying (21) at $Q = 0.6 l/min$ with $Sc_{th,w} = 40$ leads to a necessary maximum mesh resolution close to 2^{12} cells in one direction. This indicates that at high Schmidt number the concentration boundary layer is possibly not enough well resolved especially at high air flow rate. If we consider the numerical results at $Q = 0.6 l/min$ as the most converged we can see that there is factor three in the Sherwood number between $Sc_{th,w} = 1$ and $Sc_{th,w} = 10$ but a factor ten between $Sc_{th,w} = 1$ and $Sc_{th,w} = 40$. This indicates that we have to consider with caution the results obtained for $Sc_{th,w} = 40$. The observed overestimation of the Sherwood number especially at high Schmidt number may be due to the usage of a too coarse mesh to represent the concentration boundary layer.

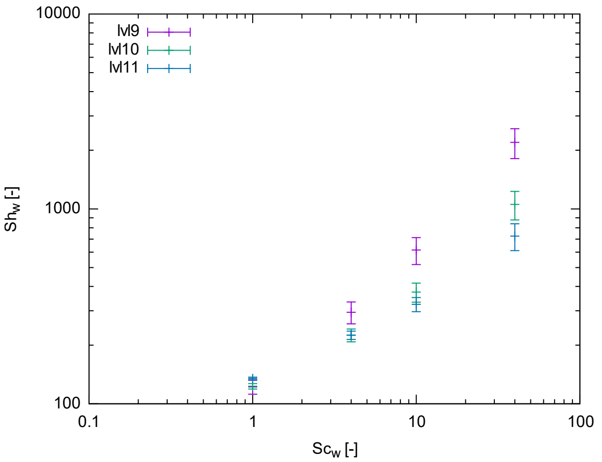

Figure 7: Numerical average water Sherwood number with standard deviation as a function of the Schmidt number in water with different maximum mesh resolution in one direction.

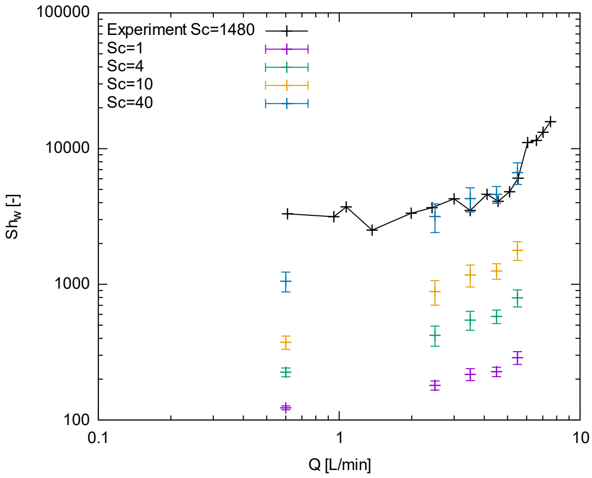

Figure 8: Comparison of experimental (black cross) and numerical average water Sherwood number (colored cross) with standard deviation as a function of gas flow rate. The numerical results are obtained with a maximum mesh resolution in one direction of 2^{10} cells.

CONCLUSION

In this study, we have focused on the mass transfer characterization between water and oil as a model of the industrial process. We have built an experimental model at ambient temperature to reproduce the industrial process. The obtained experimental results show that two different mass transfer regimes of thymol between water and oil phase can be identified in accord with the literature. Furthermore, this change of mass transfer regime seems to be correlated with the continuous formation of oil droplets in water at high air flow rate.

The established numerical model from the experimental water model reproduces qualitatively the same flow behaviour as the one that can be observed in the experimental model. For the mass transfer of the tracer between water and oil we obtained some encouraging results at low Schmidt numbers and for several air flow rates. But the numerical results do not show the abrupt increases of the Sherwood number observed experimentally. Moreover, the numerical results obtained with a much smaller Schmidt number than the experimental one gives similar results than the experimental results. This indicates that the numerical model has a tendency to overestimate the Sherwood number for the high Schmidt number and high air flow rate considered in this study. The fact that numerically no mass transfer regime change is observed may be due to a not sufficiently well described mass transfer around the oil droplets forming at high air flow rate.

ACKNOWLEDGMENTS

This work was supported by ANRT with convention CIFRE N° 2017/0694 and benefited from access to the HPC resources of CINES under the allocations 2018-A0052B07760 and 2019 - A0072B07760 granted by GENCI, and by the ERC ADV grant TRUFLOW.

REFERENCES

BATCHELOR, G. K. (1953), “The theory of homogeneous turbulence*”.*Cambridge university press.

BRACKBILL, J. U., KOTHE, D. B., & ZEMACH, C. (1992), "A continuum method for modeling surface tension" *Journal of computational physics,* **100**, 335–354.

CALABRESE, R. V., CHANG, T. P., & DANG, P. T. (1986). “Drop breakup in turbulent stirred-tank contactors. Part I: Effect of dispersed-phase viscosity”, *AIChE Journal,* **32**, 657–666.

CHEN, X., SUN, Y., XUE, C., YU, Y., & HU, G. (2017), “Tunable structures of compound droplets formed by collision of immiscible microdroplets”, *Microfluidics and Nanofluidics,* **21**, 109.

HIRASAWA, M., MORI, K., SANO, M., HATANAKA, A., SHIMATANI, Y., & OKAZAKI, Y. (1987), “Rate of mass transfer between molten slag and metal under gas injection stirring”, *Transactions of the Iron and Steel Institute of Japan,* **27**, 277–282.

HIRASAWA, M., MORI, K., SANO, M., SHIMATANI, Y., & OKAZAKI, Y. (1987), “Correlation equations for metal-side mass transfer in a slag-metal reaction system with gas injection stirring”, *Transactions of the Iron and Steel Institute of Japan,* **27**, 283–290.

IGUCHI, M., SUMIDA, Y., OKADA, R., & MORITA, Z.-i. (1994), “Evaluation of critical gas flow rate for the entrapment of slag using a water model”, *ISIJ international,* **34**, 164–170.

ISHIDA, J. (1981), “Effects of Stirring by Argon Gas Injection on Metallurgical Reactions in Secondary Steelmaking”, *Denki-Seiko (Electr. Furn. Steel),* **52**, 2–8.

KIM, S.-H., & FRUEHAN, R. J. (1987), “Physical modeling of liquid/liquid mass transfer in gas stirred ladles”, *Metallurgical Transactions B,* **18**, 381–390.

LOPEZ-HERRERA, J. M., GANAN-CALVO, A. M., POPINET, S., & HERRADA, M. A. (2015), ”Electrokinetic effects in the breakup of electrified jets: A Volume-Of-Fluid numerical study”, *International Journal of Multiphase Flow,* **71**, 14–22.

LOU, W., & ZHU, M. (2014, 10 01), “Numerical Simulation of Desulfurization Behavior in Gas-Stirred Systems Based on Computation Fluid Dynamics–Simultaneous Reaction Model (CFD–SRM) Coupled Model”, *Metallurgical and Materials Transactions B,* **45,** 1706–1722.

LOU, W., & ZHU, M. (2015). “Numerical Simulation of Slag-metal Reactions and Desulfurization Efficiency in Gas-stirred Ladles with Different Thermodynamics and Kinetics”, *ISIJ International,* **55**, 961-969.

MIETZ, J., SCHNEIDER, S., & OETERS, F. (1991, 1), “Emulsification and mass transfer in ladle”, metallurgy. *Steel Research,* **62**, 10–15.

POPE, S. B. (2001), “Turbulent flows”. IOP Publishing.

POPINET, S. (2003), “Gerris: a tree-based adaptive solver for the incompressible Euler equations in complex geometries”, *Journal of Computational Physics,* **190**, 572-600.

POPINET, S. (2009), “An accurate adaptive solver for surface-tension-driven interfacial flows”, *Journal of Computational Physics,* **228**, 5838-5866.

RIBOUD, P., & VASSE, R. (1985), “Désulfuration de l'acier en poche: synthèse des résultats théoriques et industriels“, *Revue de métallurgie (Paris),* **82**, 801–810.

SMITH, K. A. (2002), “A projection method for motion of triple junctions by level sets”, *Interfaces and Free Boundaries,* **4**, 263-276.

WALLMEYER, B., TRINSCHEK, S., YIGIT, S., THIELE, U., & BETZ, T. (2018), “Collective Cell Migration in Embryogenesis Follows the Laws of Wetting”, *Biophysical Journal,* **114**, 213-222.

WEI, T., & OETERS, F. (1992), “A model test for emulsion in gas–stirred ladles”, *Steel research,* **63**, 60–68.

XIAO, Z., PENG, Y., & LIU, C. (1987), “Modelling study of the entrapment phenomena at the slag-metal interface in the gas-stirred ladle”, *Chinese Journal of Metal Science and Technology,* **3**, 187–193.

A CFD STUDY ON THE IMPACT OF BARRIERS AND NONUNIFORMITIES ON FURNACE TAPPING

Jan Erik OLSEN
SINTEF Industry, 7465 Trondheim, NORWAY

* E-mail: Jan.E.Olsen@sintef.no

ABSTRACT

Tapping of slag and metal from metal producing furnaces are often inconsistent and it is difficult to predict the outcome of the process. Nonuniformities in the particle bed has been hypothesized as reasons for inconsistent tapping of slag and metal. Examples of nonuniformities are cracks in the particle bed, zones with looser packed particles (weak zone) and barriers in the particle bed. The impact of these nonuniformities on the tapping rate have been studied by CFD. The CFD model and results of the study are presented.

Keywords: CFD, metallurgy, furnace tapping.

NOMENCLATURE

Greek Symbols
ρ Mass density, [kg/m^3].
μ Dynamic viscosity, [kg/m.s].
ε Porosity [ ]

Latin Symbols
d Diameter, [m].
P Pressure, [Pa].
v Velocity, [m/s].

Sub/superscripts
p particle.
pb particle bed
s superficial

INTRODUCTION

Furnace tapping is the removal of liquids produced in a furnace. In metal production the liquids are slag and alloy (hereafter referred to as metal). A wide range of different configurations exist depending on which metal is being produced (Nelson and R. Hundermark 2016). Some metals are tapped by suction through a tube (e.g. aluminium), but most metals are tapped by gravity through a tap-hole at the bottom of the furnace. Our main focus is ferroalloys. They are produced in submerged arc furnaces where gravity is the driving force of the tapping. Slag and metal are tapped through a tap-hole into a ladle for further post-furnace processing as illustrated in Figure 1. The grey diffuse area is the particle bed of mineral ore and coke particles. Three electrodes (darker grey) provide energy to run the carbothermic reduction of mineral ore producing slag and metal.

Consistent tapping is desirable for smooth and predictable downstream processing. This is often not the case. The tapping rate varies between different taps and sometimes slag is tapped before metal even though metal is supposed to be tapped first according to the laws of physics. Model studies (mathematical and experimental) have not been able to reproduce this inconsistency. Since these model studies have been performed with uniform conditions in the particle bed, it is hypothesized that nonuniformities or barriers in the particle bed is the cause of inconsistent behaviour. It is very unlikely that the particle bed has a constant particle size and porosity throughout its domain. It will vary.

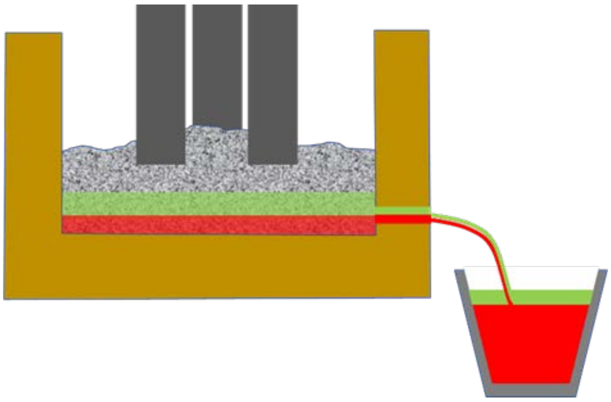

Figure 1: Sketch of furnace with tapping of slag (green) and metal (red).

In this study we apply computational fluid dynamics (CFD) to study tapping rates of slag and metal. CFD has been employed to furnace tapping earlier (Kadhodabeigi, Tveit, and Johansen 2011; Nishioka, Maeda, and Shimizu 2005; Reynolds and Erwee 2017) and validation studies show consistency between model results and experimental results. All of these studies assumed a uniform particle bed in the furnace. This is a reasonable first order approximation, but reality is more complicated. Furnace excavations in connection with furnace shutdown due to maintenance show that the particle bed is not uniform (Ksiazek, Tangstad, and Ringdalen 2016; Ringdalen and Ksiazek 2018). There are regions with an impenetrable material formed by different accumulated elements including graphite, titanium carbide, slag and other. They particularly form around the periphery of the furnace. If they form at the furnace bottom or break off from the furnace periphery and fall to the bottom, they can form barriers for flow of liquid slag and metal. Also, there can be cracks in the particle bed or nonuniform particle distribution close to the tap-hole. This can be caused by the opening and closing of a tap-hole. Tap-holes are closed by injecting tapping clay with a mud gun. It is opened again by drilling through the tapping clay. Both these operations exert a significant force on the materials close to the tap-hole which will reconfigure the particle structure. It is hypothesized that this reconfiguration is significant enough to change the morphology of the particle bed close to the tap-hole which will not be uniform. Such deviations from the assumption of a uniform particle bed may impact the tapping rates of slag and metal. CFD is here applied to furnace tapping with barriers and nonuniformities in the particle bed.

CFD MODEL

Furnace tapping is conceptually similar to drainage of tanks which is often used as modelling examples in introductory classes in fluid mechanics and mathematics. Compared to classic tank drainage, furnace tapping is complicated by the granular material (ore, coke, …) which forms a particle bed in the furnace. The granular material provides resistance to drainage and this needs to be accounted for in mathematical models for furnace tapping. Within the CFD-framework of models, there are three different methods to account for the granular material. These are the coupled Navier-Stoke's and discrete element method (DEM), the Eulerian multiphase model with a granular phase and the porous zone model. Here we have chosen to apply the porous zone model available in the commercial CFD-software ANYS/Fluent r19. The model allows for sharp interface tracking between the different phases which is not possible in the Eulerian multiphase model. The DEM approach is computationally too expensive if a typical number of particles in a furnace needs to be tracked.

The porous zone model solves for conservation of mass and momentum with the continuity equation and the Navier-Stokes equations respectively. The phases are immiscible, and their motion is governed by one common momentum equation which applies material properties according to the phase material present locally. The phases are separated by interfaces which are tracked with the Geo-Reconstruct scheme. The porous zone model accounts for the granular material by adding a sink term in the momentum equation which provides resistance to the flow. This is described as a pressure drop. We apply the Ergun equation (Ergun 1952) for this pressure drop ΔP_{pb} through the particle bed

$$\frac{\Delta P_{pb}}{\Delta L} = \frac{150\,\mu}{d_p^2}\frac{(1-\varepsilon)^2}{\varepsilon^2} v_s + \frac{1.75\,\rho}{d_p}\frac{(1-\varepsilon)}{\varepsilon^3} v_s |v_s| \qquad \text{Eq. 1}$$

Here ΔL is a length increment in the particle bed, μ is liquid viscosity, ρ is liquid density, ε is particle bed porosity, d_p is particle diameter and v_s is the superficial liquid velocity through the particle bed. Such a model can be applied to study how barriers and nonuniformities in the particle bed affects tapping from the furnace. In the following sections we demonstrate how the model compares with experimental results (model validation) and how some nonuniformities and barriers affect the tapping rate.

Model Validation

The model is compared against the drainage experiment of Vångö, Pirker, and Lichtenegger (2018). The experiment was performed in a 400 mm tall tank with a footprint of 330 x150 mm. Wood chips were used as granular material. After a while they became saturated with water and achieved an equivalent radius of 6.5 mm. Water was filled up to a level of 300 mm. The authors did not specify the height up to which the tank was filled with wood particles. By assuming a packing porosity of 0.4, which is quite typical we get a particle bed height of 200 mm. The experiment is illustrated in Figure 2. Two simulations with the model were performed: one with a porous zone up to 200 mm representing the wood particles and one without a porous zone. The simulation accounting for the particle bed (porous zone) produces results on the tapping rate which is very consistent with the experimental measurements. This is seen in Figure 3. Note that the assumption of a packing porosity of 0.4 affects the result. The assumption is reasonable, but it still is an assumption. However, any deviation from 0.4 will not discredit the consistency. The consistency might change from very good to fairly good. The simulation neglecting the particle bed (no porous zone) gives a higher tapping rate and faster tapping. This is as expected since the particle bed is supposed to provide resistance to the flow.

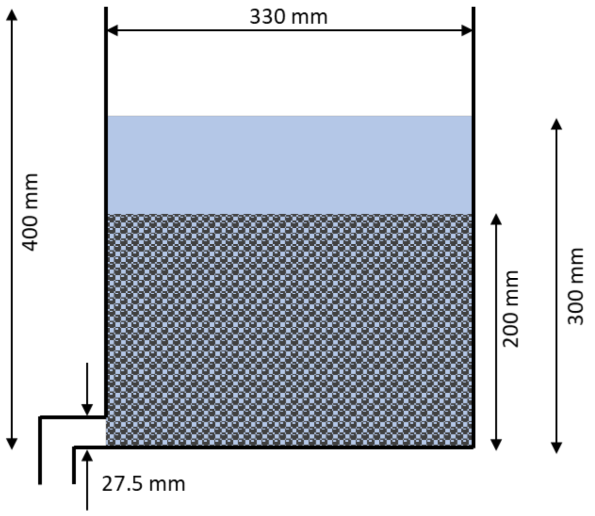

Figure 2: Sketch of drainage experiment

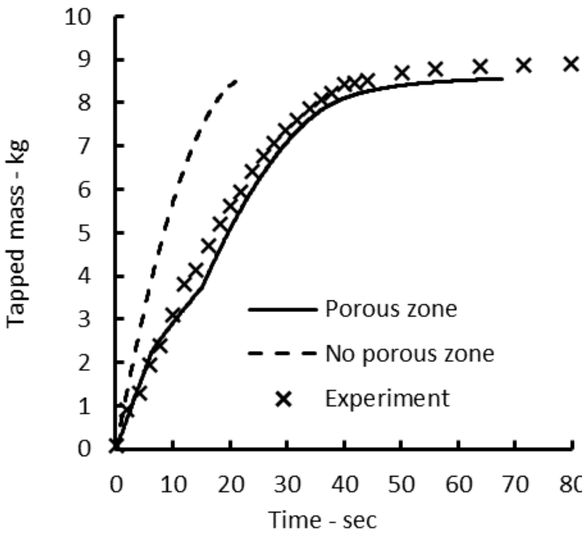

Figure 3: Tapped mass as function of time based on experimental measurements and simulation results with and without a porous zone.

SIMULATIONS OF NONUNIFORM FURNACE CONDITIONS

As mentioned above, nonuniform conditions in the furnace can impact the tapping rates. The effect from some examples are investigated here.

Structural inhomogeneities near tap-hole

When the tap-hole is opened, the structural integrity of the packed bed of materials close to the tap-hole entrance is destabilized. This may lead to cracks in the particle bed or a nonuniform distribution of the particles.

A CFD analysis on two potential nonuniform conditions have been carried out. These have been compared against a base case of uniform condition. In a uniform condition, the particles are evenly distributed inside the container representing a furnace. This volume is described by a constant porosity with particles of constant size. The tap-hole is represented with a cylindrical exit tube where no particles are present. The geometry is illustrated in Figure 4 with boundary conditions. At the top there is a pressure inlet condition where a driving pressure can be applied. At the tap-hole outlet, there is a pressure outlet condition. Three phases are accounted for: metal, slag and gas with properties as listed in Table 1. The CFD model applies the VOF algorithm to account for the interfaces between the faces. For the initial configuration, the amount of metal is varied. This is specified with a height or level of metal above the furnace bottom. The initial slag level (i.e. height of gas-slag interface) is kept constant which due to the varying initial metal level results in a varying initial amount of slag.

Typical results are seen in Figure 5 illustrating the different phases. We see a typical uplift of metal towards the tap-hole due to the driving pressure from the weight of the slag phase and the gas phase pressure. At the outlet of the tap-hole there seem to be a well-defined layer of slag above the metal as seen in Figure 6.

Two types of nonuniformities are defined here. One is a crack in the particle bed where fluids can flow freely without porous resistance. This is illustrated in Figure 7. The other is a weak zone on the upper neighbourhood of the tap-hole. The opening of the tap-hole can cause some collapse in the region which will lead to looser packing of the material. This zone is illustrated in Figure 8 and the weak zone is modelled with a porosity of 0.5 compared to 0.4 elsewhere.

Table 1: Modelling conditions.

Metal density:	6100 kg/m3
Metal viscosity:	0.005 kg/m s
Slag density:	3000 kg/m3
Slag viscosity:	0.1 kg/m s
Gas density:	0.5 kg/m3
Gas viscosity:	0.00005 kg/m s
Tap-hole diameter:	10 cm
Tap-hole length:	1 m
Height of tap-hole centre line:	15 cm
Initial height gas-slag interface:	0.5 m

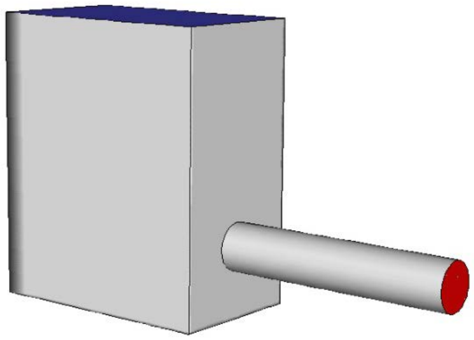

Figure 4: Model geometry with boundary conditions

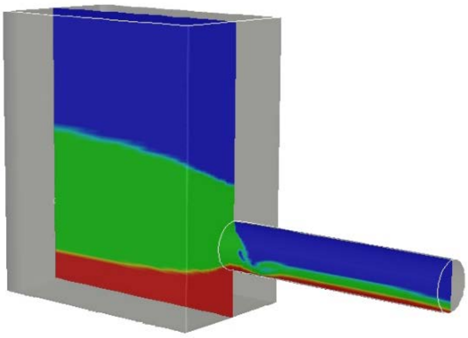

Figure 5: Contours of metal (red), slag (green) and gas (blue) phases during tapping

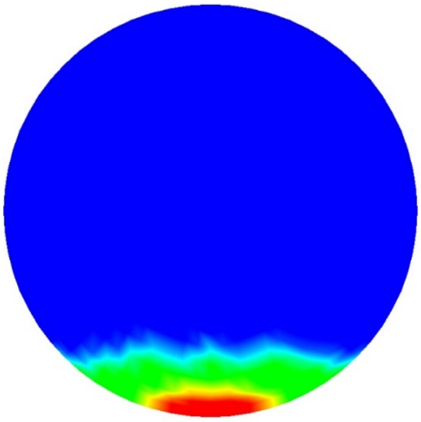

Figure 6: Contours of metal (red), slag (green) and gas (blue) phases at tap-hole outlet

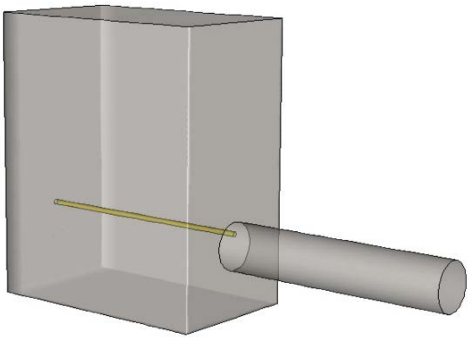

Figure 7: Geometry with crack (yellow)

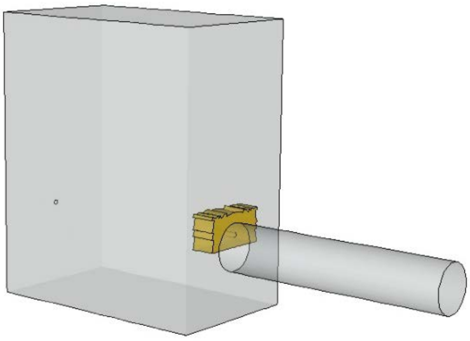

Figure 8: Geometry with weak zone (yellow)

Quantitatively there is some sensitivity on the tapping rates with respect to nonuniformities. A typical evolution of tapping rates as function time is seen in Figure 9. The cases shown are for an initial level of 10 cm of metal which covers up to lower level of the tap-hole. The tapping rates peak shortly after tap-hole opening before it decreases almost linearly with time. In Figure 10 the peak tapping rates are plotted for various values of initial metal levels. We see that the initial metal level has a significant impact on the tapping rates. The impact of a crack is almost insignificant, but a weak (or loose) zone close to the tap-hole affects the tapping rate of the slag phase in particular. Since the weak zone is in the upper part of the inflow towards the tap-hole it is natural that it mostly affects the slag flow. Note that for high levels of metal, the tapping rate of metal is also affected. This is caused by metal now being present in the weak zone.

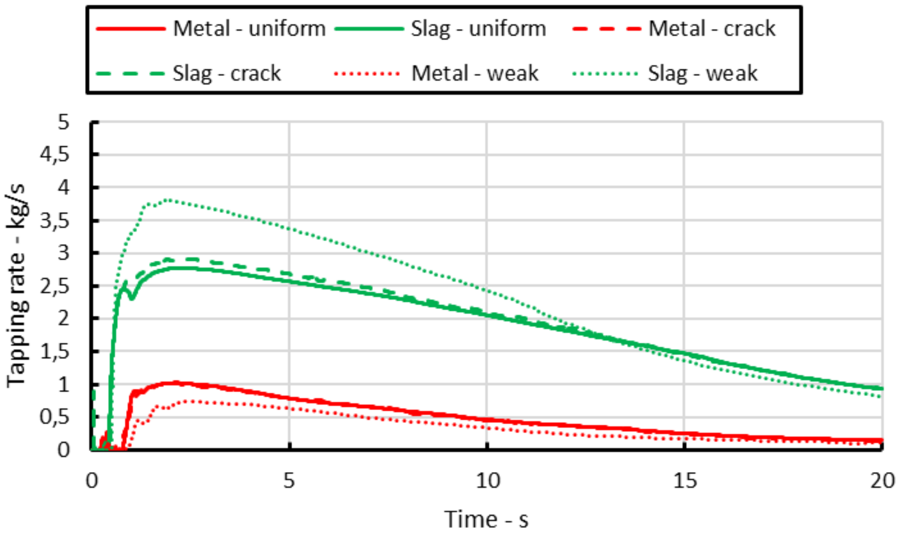

Figure 9: Tapping rates of slag and metal for initial metal height of 10 cm above furnace bottom.

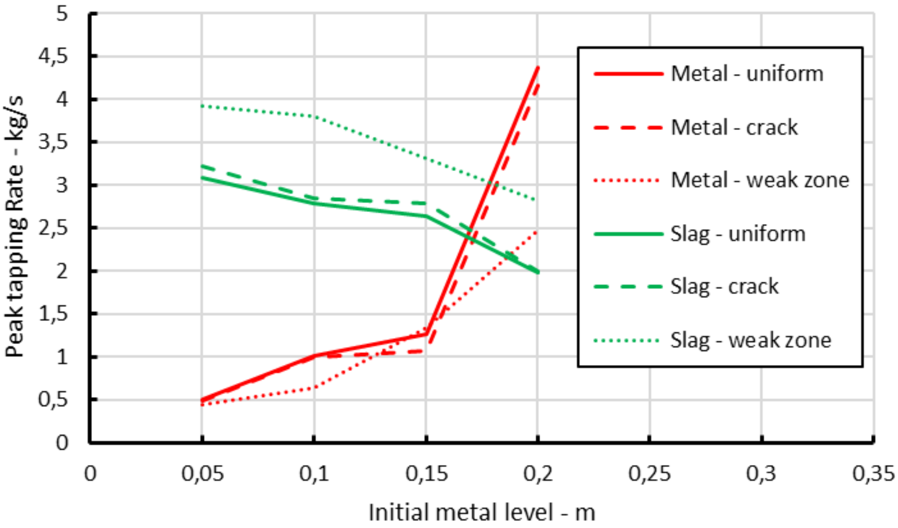

Figure 10: Tapping rates of slag and metal

No barrier

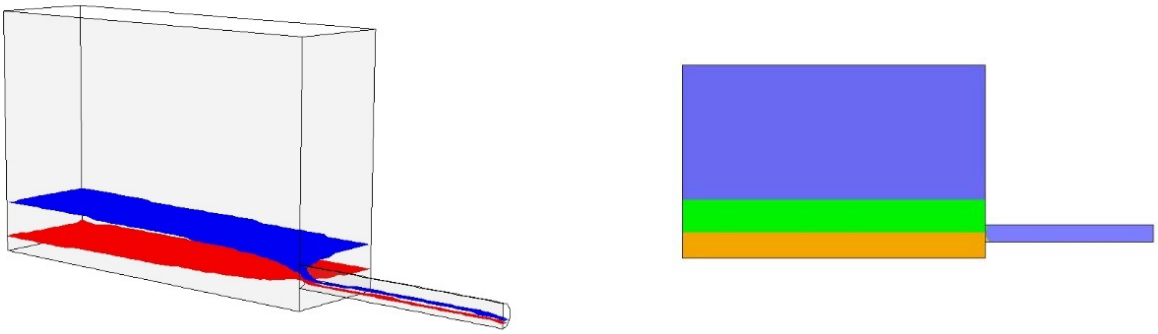

Low barrier

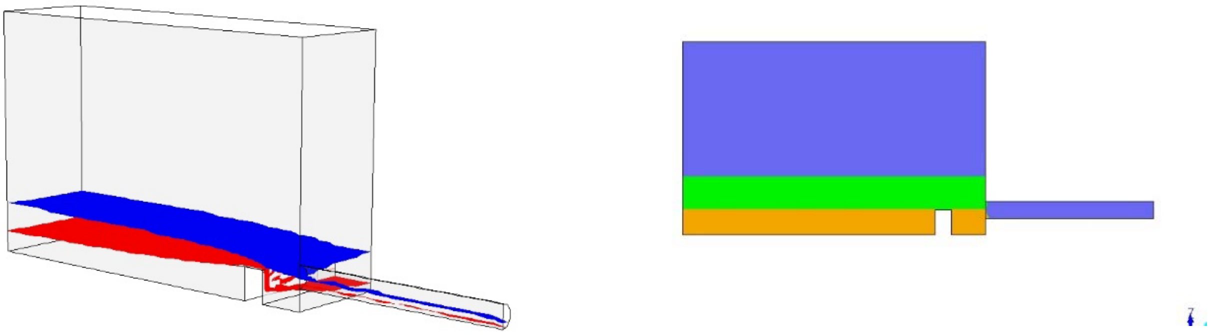

High barrier

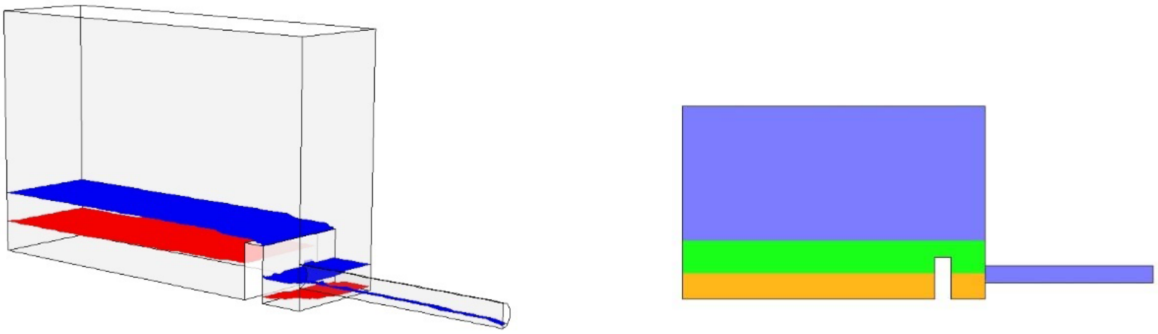

Figure 11: Tapping of slag and metal with and without barriers. Left side shows interface between gas and slag (blue) and metal and slag (red) during tapping. Right side shows initial filling of slag (green) and metal (orange).

Barriers near tap-hole

Barriers near the tap-hole will affect the flow of slag and metal towards the tap-hole and the respective tapping rates of slag and metal.

A CFD study has been conducted where two barriers (one low and one high) have been positioned in front of the tap-hole. This is illustrated in Figure 11. Since the barriers are resting on the floor of the furnace, they mostly affect the flow of the lower liquids which tend to be the metal phase.This can be assessed by analysing the resulting tapping rates of slag and metal.

Tapping rates of slag and metal are plotted in Figure 12. We see that the tapping rates are affected by the barriers. The metal rate is reduced by the barriers and slag rates are increased. The high barrier reduces metal rate more than the low barrier. However, metal has the highest initial peak rate regardless of barriers.

What happens if the barriers also block access to the region in front of the tap-hole for metal to fill up this part prior to opening of the tap-hole? Two simulations were run with such initial conditions. The initial conditions are illustrated in Fig.13 and the results are shown in Fig.14. The results show that for the low barrier, metal tapping is delayed and only slag leaves the tap-hole initially. For the high barrier, no metal leaves the tap-hole. The metal production rate and/or tapping interval needs to be sufficient for the initial metal level to either overflow the barrier or at least be close enough for the driving pressure to lift the metal level above the barrier. As metal accumulates, metal will flow over the barrier and start to tap. Then only the metal beneath a certain level will be disabled for tapping. All metal produced after this level is reached will be tapped.

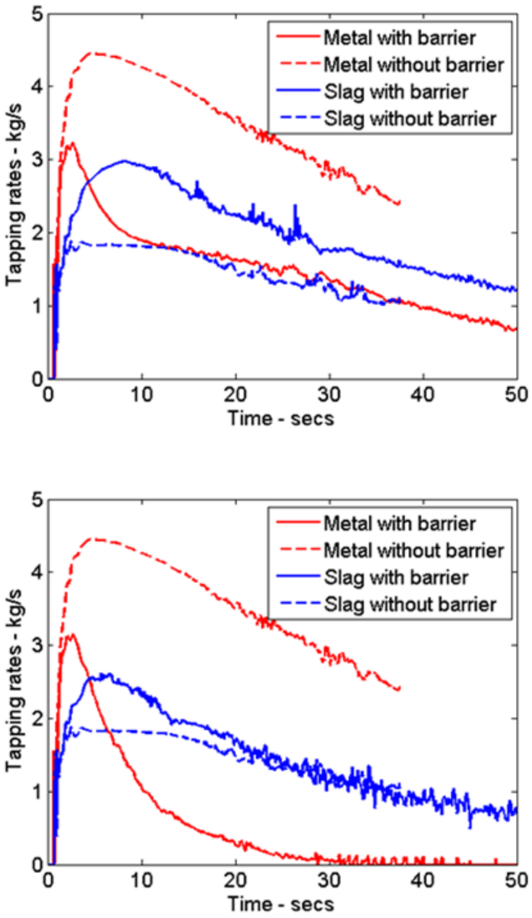

Figure 12: Tapping rates for metal and slag with low barrier (top) and high barrier (bottom) in front of tap-hole compared against tapping rates without barriers.

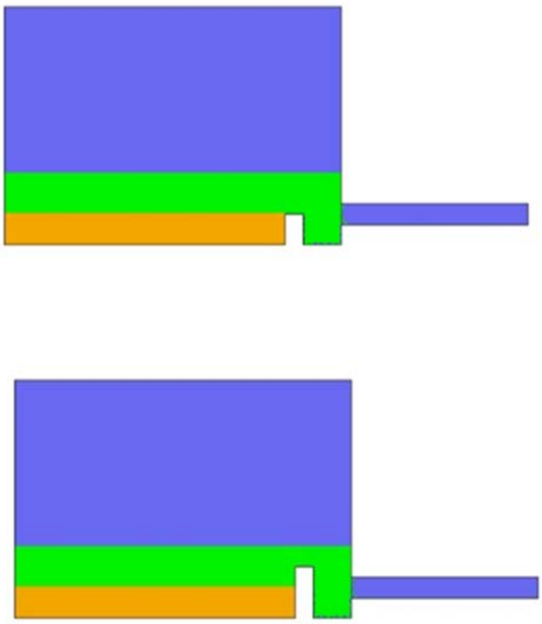

Figure 13: Initial slag and metal filling when barriers block filling of metal in front of tap-hole. Low barrier at the top and high barrier below.

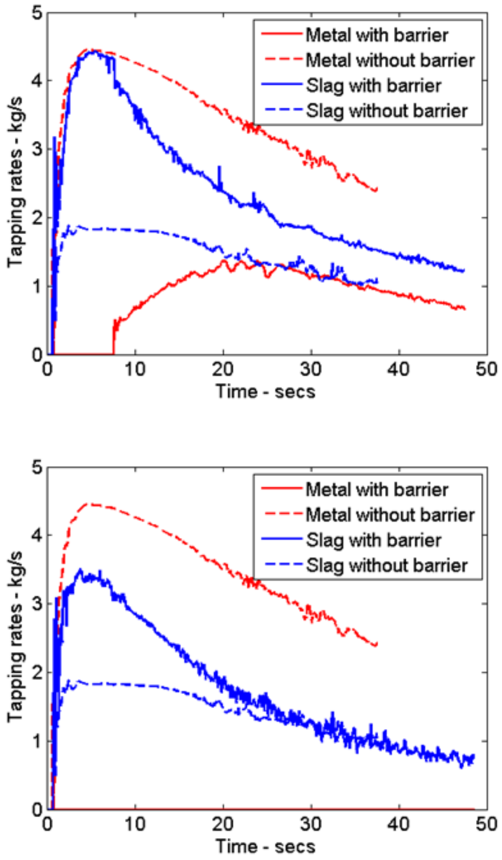

Figure 14: Tapping rates for metal and slag with low (top) and high barrier (bottom) in front of tap-hole when barrier blocks filling of metal in front of tap-hole compared against tapping rates without barriers.

CONCLUSION

Nonuniformities in the particle bed has been hypothesized as reasons for inconsistent tapping of slag and metal. Examples of nonuniformities are cracks in the particle bed, zones with looser packed particles (weak zone) and barriers in the particle bed. The impact of these nonuniformities on the tapping rate have been studied by CFD. A crack (as defined in this study) has little impact on the tapping rates. A zone with looser packed particles (weak zone) close to the tap-hole has a more significant effect on the tapping rate. If a barrier blocks drainage of one or two phases towards the tap-hole, tapping might be hindered or delayed for the phase being blocked. This can cause slag to be tapped before metal, which is unusual, but sometimes observed. A barrier has a significant impact on tapping rates.

The study shows that the nonuniformities studied to different degrees affect the tapping rates of slag and metal. Some of these nonuniformities can easily change between consecutive taps and thus cause inconsistent tapping. Barriers will most likely not change that frequently and are thus probably not the cause for inconsistency between consecutive taps. They may explain inconsistency over longer time spans. More studies on nonuniformities can easily be performed by this method provided insight on particle bed configuration and nonuniformities defines interesting cases. The model complexity and realism can be increased by introducing heat transfer and phase change. This requires a fair bit of extra work. These mechanisms will probably add randomness to the tapping process and strengthen the trend of inconsistent tappings.

REFERENCES

Ergun, S. 1952. 'Fluid flow through packed columns', *Chem. Eng. Prog.*, 48.

Kadhodabeigi, Mehdi, Halvard Tveit, and Stein Tore Johansen. 2011. 'Modelling the tapping process in in submerged arc furnaces used in high silicon alloys production', *ISIJ International*, 51: 193-202.

Ksiazek, M, M. Tangstad, and Eli Ringdalen. 2016. "Five furnaces five different stories." In *Silicon for the Chemical and Solar Industry XIII*, 33-42. Kristiansand, Norway.

Nelson, L.R., and R. Hundermark. 2016. 'The tap-hole - key to furnace performance', *Journal of the Southern African Institute of Mining and Metallurgy*, 116: 465-90.

Nishioka, Koki, Takayuki Maeda, and Masakata Shimizu. 2005. 'A Three-dimensional Mathematical Modelling of Drainage Behavior in Blast Furnace Hearth', *ISIJ International*, 45: 669-76.

Reynolds, Q.G., and M.W. Erwee. 2017. "Multiphase flow modelling of furnace tapholes." In *12th International Conference on Computational Fluid Dynamics in the Oil & Gas, Metallurgical and Process Industries*, edited by Jan Erik Olsen and Stein Tore Johansen. Trondheim, Norway: SINTEF.

Ringdalen, Eli, and Michal Tomasz Ksiazek. 2018. "Excavation of SiMn-Furnace." In *Furnace Tapping*. Kruger, South Africa: Southern African Institute of Mining and Metallurgy.

Vångö, Mathias, Stefan Pirker, and Thomas Lichtenegger. 2018. 'Unresolved CFD–DEM modeling of multiphase flow in densely packed particle beds', *Applied Mathematical Modelling*, 56: 501-16.

CFD modelling of an accidental release of a methane and hydrogen sulfide mixture in an offshore platform

Gianmario Ledda, Alberto Moscatello, Anna Chiara Uggenti, Raffaella Gerboni, Andrea Carpignano
Department of Energy, Politecnico di Torino, corso Duca degli Abruzzi, 24, 10141 Torino, Italy
E-mail: gianmario.ledda@polito.it
E-mail: alberto.moscatello@polito.it
E-mail: anna.uggenti@polito.it
E-mail: raffaella.gerboni@polito.it
E-mail: andrea.carpignano@polito.it

ABSTRACT

Oil & Gas plants are complex systems involving dangerous substances, potential origin of severe accidental scenarios. Therefore, according to Directive 2013/30/EU, a Risk Assessment (RA) is mandatory. A fundamental step of the RA is the accident simulation to evaluate the damage area involved by each accidental scenario.

One of the main issues of natural gas extraction platforms is the presence of traces of hydrogen sulfide (H_2S) in the extracted mixture. When the H_2S is present in the natural gas, the mixture is called sour gas. The presence of H_2S is of great interest since it is flammable, colorless and highly toxic, therefore, highly dangerous to people. Several literature studies demonstrate that it is common to have mixtures with 2 % to 20 % by weight H_2S in Oil & Gas facilities reservoirs, underlying how this problem is of common interest.

In this work a highly pressurized (50 bar) accidental release of a methane-hydrogen sulfide mixture (95 % CH_4 – 5 % H_2S) in the production deck of an Oil & Gas platform is treated. Due to the complexity of the geometry and the need to accurately define the dangerous areas, the Computational Fluid Dynamics (CFD) is chosen to simulate the event instead of the commonest empirical models.

In particular, the multi-scale and multi-physics nature of the involved phenomena represent a real challenge for the CFD simulation implementation. In fact, as the gas is released from high pressures (10 bars or more) into the ambient, a highly under-expanded jet develops: a supersonic velocity is reached (Ma >> 1) near the release point where a Mach disk appears and produces very strong discontinuities in the flow-field variables (pressure, velocity, density, temperature, etc.). As the gas slows down, a subsonic dispersion follows in the main portion of the deck, where the velocity gradients rapidly decrease, and the buoyancy effects become dominant.

This work proposes a CFD two-steps approach implemented on ANSYS Fluent, called SBAM (Source-Box Accident Model) to simulate the accident in order to account for the different physics involved, in order to evaluate the damage areas affected.

Keywords: accidental gas release, risk, safety, CFD fluid dynamics, ANSYS Fluent, Oil & Gas, offshore facilities, hydrogen sulfide

NOMENCLATURE

Greek Symbols

ρ	Mass density, [kg/m^3].

Latin Symbols

d	Diameter, [m].
p	Pressure, [bar].
$\vec{v}$	Velocity, [m/s].
Ma	Mach number, [-].
y^+	Dimensionless wall distance, [-].
Y_i	Local mass fraction of *i*th species, [-].
R_i	Net rate of production of *i*th species, [kg/m^3/s].
S_i	Source term of *i*th species, [kg/m^3/s].
$\vec{J_i}$	Diffusion flux of *i*th species, [kg/m^2/s].
t	time, [s].

INTRODUCTION

Nowadays, the Risk Assessment implementation tools are being continuously improved for risk-relevant industrial applications that involve hazardous substances, e.g. Oil & Gas facilities, chemical plants, nuclear installations (Patè-Cornell, 1993 and Necci et al., 2019). Quantitative Risk Assessment (QRA) is fundamental and mandatory according to European guidelines to guarantee the industrial plant sustainability (Casal, 2007 and Vinnem, 2019). This procedure requires the analysis of numerous accidental scenarios in order to perform an exhaustive consequence analysis. This work takes into account an Oil & Gas offshore platform offering an improvement in the accident simulations to enhance the sustainability of the consequences analysis process. The state-of-practice for onshore facilities involves the use of empirical models (e.g. Chen and Rodi, 1980, Davidson, 1967 and Zamejc, 2014) to estimate the damage areas associated to the accidental events, due to their fast response. Meanwhile, in the offshore applications,

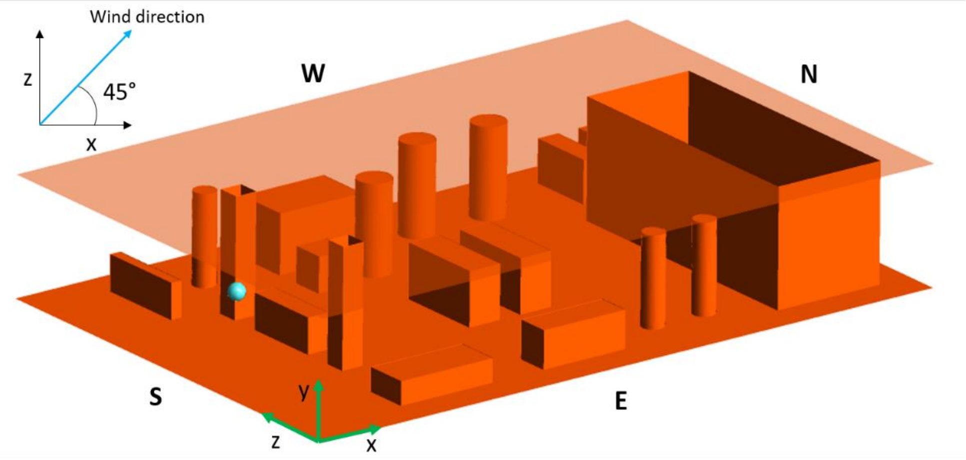

Figure 1: Production deck CAD, wind direction, release point (blue sphere).

characterized by complex geometries and congested environments, the empirical models lead to a large overestimation of the damage areas and to an oversizing of protections, which involve the growth of construction cost and a mechanical overload of the offshore structure. From the last considerations, the necessity to find another approach for consequences' estimation in complex structures arises. The SEADOG Lab Group of Politecnico di Torino, driven by this necessity, proposed a novel CFD method, called SBAM (Source Box Accident Model) aiming at guaranteeing a suitable cost-accuracy trade-off for the simulation of accidental releases of a pressurized gas in congested industrial environments. The SBAM approach splits the phenomenon in two different CFD simulations, realized in ANSYS Fluent, in order to properly treat its multiscale and multi physics nature and to speed-up the simulation for obtaining a computational time compatible with the QRA procedure (detailed description in section 3). Different authors have already proposed this two-steps method (Venetsanos et al., 2008, Choi et al., 2013, Liu et al., 2014 and Deng et al., (2018)), but they used a hybrid empirical-CFD approach to simulate the event, while here a full CFD method is proposed because the congested environment requires to model the first phase of the phenomenon in a reliable way .

This paper would not have been possible without the sponsorship of the Ministry of Economic Development's Directorate General for Safety – National Mining Office for Hydrocarbons and Georesources.

Objective of the work

In this work, a high-pressure sour gas release in an offshore platform production deck is analysed. The SBAM approach is applied to a specific case study to obtain the damage distances useful for flammable and toxic maps of a QRA. The objective of this paper is to show how the method works considering a flammable and toxic gas mixture, its advantages and its flexibility to identify the damage areas consequent to an offshore accidental scenario.

PROBLEM DESCRIPTION

Sour gas in offshore environment

In the offshore extraction platform, the natural gas is mainly composed by methane with traces of other volatile hydrocarbons, carbon dioxide, nitrogen and hydrogen sulfide. The hydrogen sulfide (H_2S) is the major pollutant in natural gas and, when it is present, the natural gas is called sour gas. H_2S is a colourless, flammable and highly toxic gas. Several Oil&Gas extraction facilities observe the presence of hydrogen sulfide in their reservoirs and many studies are performed on the amount of H_2S in natural gas. As suggested by (Worden et al., 2003), in the North Sea the natural gas can contain up to the 2 vol% of H_2S; according to (Zempolich et al.,2002) and (Warner et al., 2007), the Kazakh gas fields of Kashagan and Tengiz can reach contents of 19 vol% and 16 vol% of H_2S respectively; in the Sichuan Basin, the percentage of H_2S in natural gas can vary between 10 vol% and 17 vol% as suggested by (Liu et al.,2010); with reference to (Mi et al., 2017) the natural gas extracted from Eastern Venezuela Basin contains the ~ 5 vol% of H_2S.

An accidental high-pressure release of sour gas can lead to several major hazards like explosions, fires or intoxication. Moreover, the presence of H_2S can cause several damages to the process components due to its corrosive properties, increasing the failure rate due to leakages (Li et al., 2014). The effects of sour gas release can be dramatic for the people and the environment, as observed during the Lodgepole blowout accident in Alberta in 1982 (Layfon and Cederwall, 1987), up to now the biggest release of sour gas.

Case study

The sour gas release in a production deck (shown in Fig. 1) analysed here is defined by a set of relevant parameters:

- Release conditions: $p_0 = 50\ bar, T_0 = 300\ K$
- Release hole diameter: $d_e = 3\ cm$
- Released gas mixture molar composition: $95\ mol\%\ CH_4 - 5\ mol\%\ H_2S$
- Wind velocity: $v = 6\ m/s$
- Wind direction: 0.5x + 0.5z (Fig. 1)
- Ambient temperature: $T_a = 300\ K$

- Release position x = 3 m, y= 2.5 m, z = 10 m and direction x (light blue sphere in Fig. 1);

The release pressure and hole diameter values (a circular hole is assumed) are chosen in agreement with (Vivalda et al., 2018) and are considered representative for Oil & Gas field. The selected wind intensity is typical of Italian platforms installed in the Adriatic Sea. The mixture molar composition is chosen according to the literature review exposed in section 2.1.

METHODOLOGY

In this work, the SBAM method is applied and it is characterised by the splitting of the accidental release in two different simulations.

This necessity arises from the phenomenon multi-physics and multi-scaling nature. In fact, since the gas, in case of accident, is released at high pressure (10 bar or more), a highly under-expanded jet results (Franquet et al., 2015) with strong compressible effects, as the presence of a Mach disk. This phenomenon is confined in a very small portion of the domain, near the release point, where the flow is compressible (Ma>0.3) (Munson et al., 2009). At a certain distance from the release point, the gas flows, it reaches subsonic velocities (Ma<0.3) so that the flow can be assumed incompressible and a gas dispersion occurs in the remaining part of the domain, the biggest one.

Consequently, the splitting of the phenomenon into a supersonic-compressible discontinuous flow (the *release*) and an incompressible-subsonic smooth flow (the *dispersion*) results convenient for modelling purposes.

The SBAM method consists in simulating the *release* in a small domain, the Source-Box (SB), dimensioned to contain all the compressibility effects (see paragraph 3.1.1), and setting the right models to account for these effects and a suitable mesh to capture the discontinuities in the Mach disk region. The results of this *release* model are the profiles of velocity and mass fraction of the pollutant gas on the outer faces of the SB, representing the interface with the domain of the *dispersion* modelling (section 3.2.1); in the latter, the mesh can be rough as no complex fluid dynamic structures are expected.

As shown in the results, this approach permits to have a fast dispersion evaluation. Moreover, the same SB results can be used for many dispersion simulations just changing the release position and direction in the domain. This outcome is relevant especially from a QRA point of view, since this procedure requires the simulation of many scenarios in a relatively short time.

Release simulation (Source-Box)

Design and mesh

The SB presents a cubic shape with dimensions defined to guarantee that all the compressibility effects are exhausted inside its domain. (Crist et al., 1966) suggest that the compressible effects become negligible when the distance from the release point is ten times the distance of the Mach disk (X_m). Several authors, as (Franquet et al, 2015), have conducted numerical and experimental studies to obtain a correlation to define the Mach disk position. (Franquet et al, 2015) suggest the following definition of X_m:

$$X_m = 0.645 \cdot d_e \cdot \sqrt{\frac{p_0}{p_{amb}}} \qquad (1)$$

where p_{amb} is the ambient pressure. Then, according to (Crist et al., 1966), the SB side length (L_{SB}) is:

$$L_{SB} = 10 \cdot X_m \qquad (2)$$

Using the parameters presented in 2.2 the characteristic length of the SB of this case study is L_{SB} = 1.38 m.

Another important feature of the SB is the presence of an obstacle in front of the release point, since it is likely to occur in industrial congested plants. In this case, a cylinder with diameter 30 cm is located at a distance of 45 cm from the release point.

An unstructured tetrahedral mesh is chosen as it better suits complex geometries and it is suggested for non-directional flows (ANSYS Fluent, 2018). A non-uniform mesh with a major refinement in the Mach disk region and near the cylindrical obstacle is created; to assure the solution independence from the chosen grid a convergence study is performed obtaining a ~9.5e4 elements mesh with an average size of computational cell of ~5e-3m and a refinement around the release hole with a cell of ~2e-3m. The Fluent inflation algorithm is used to model the boundary layer near the nozzle wall and the obstacle, the first cell height is chosen in order to obtain $y^+ < 5$ in the wall region (Munson et al., 2009).

Source-Box simulation setup

To model the highly under-expanded jet of CH_4-H_2S mixture, a 3D steady-state simulation is set. This choice is made because the detection time of the safety detectors is longer than the transient time of the phenomenon: the dangerous substance cloud reaches the steady-state configuration before the gas detectors can detect the presence of the hazardous atmosphere. According to (Doroudi et al., 2015), a Pressure-Based Coupled Algorithm is selected (ANSYS Fluent, 2018). A pressure inlet of 50 bar, a CH_4 mole fraction equal to 0.95 and a H_2S mole fraction equal to 0.05 are imposed at the nozzle inlet. A wall with no-slip condition is imposed on the nozzle external surface and the cylinder surface. A pressure outlet set at atmospheric pressure is imposed on all the external SB surfaces to reproduce the open environment around.

Due to the compressible nature of the flow, the temperature field must be evaluated by solving the energy equation in order to calculate the density. The SST k-ω turbulence model, validated for under-expanded jets by (Novembre et al., 2006) and (Liu et al., 2014) against the available experimental data (Eggins and Jackson, 1974), is selected for the purposes of this study. Moreover, since a y+ < 5 is obtained at the walls, the SST k-ω model guarantees a proper boundary layer evaluation. The viscous dissipation term is selected to describe the thermal energy due to viscous shear in the flow, which is relevant for high velocity compressible flows (ANSYS Fluent, 2018). To model the interaction between different chemical species (CH_4-H_2S-Air) the "Species Transport" model is used in order to solve a transport equation without chemical reactions. The "constant dilute approximation" provided by ANSYS Fluent is considered by setting a value ~2e-5 m^2/s in order to take into account the diffusion of the chemical species in the air. The same assumption is made for the dispersion simulation as well.

The local mass fraction of each species (Y_i) is predicted using the transport equation in the following form:

$$\frac{\partial}{\partial t}(\rho Y_i) + \nabla \cdot (\rho \vec{v} Y_i) = -\nabla \cdot \bar{J}_i + R_i + S_i \qquad (3)$$

where R_i is the net rate of production of species and S_i is a source term.

A pseudo-transient model is used in order to relax the solution. This option is a form of implicit under-relaxation that guarantees a better convergence of the solution.

Dispersion simulation

Design and mesh

The simulation domain is shown in Fig. 1. For the dispersion simulation, a simplified CAD of the production deck is considered; in order to simplify the geometry of the study the deck minor equipment is neglected. It should be noticed that the roof and the floor of the deck are plated walls, typical of gas extraction platforms in order to limit the hazardous areas involved in the accidental scenario if a leakage occurs.

Due to the complexity of the geometry, an unstructured tetrahedral mesh is generated. This choice is also due to the fact that the use of structured meshes for the discretization of complex geometries with curves can require high time-consuming processes and low quality meshes (e.g. high skewness, etc.). Coherently, (ANSYS Fluent, 2018) suggests that an unstructured mesh is more efficient in the distribution of the elements, especially when curved objects are present. Finally, also for this simulation a grid convergence study is performed, and the resulting mesh consists of ~3e6 elements with an average computational cell size of ~0.5 m and a face refinement on the obstacles of ~0.15 m and on the SB about of ~1 cm.

Dispersion simulation setup

As the release simulation, also the dispersion simulation is performed in steady-state since the final purpose is the estimation of the cloud dimensions at steady-state conditions because of the flammability and toxicity of the released mixture. In addition, in view of a CFD-QRA integration, a transient simulation will lead to high computational cost.

To describe the assumed boundary conditions, Fig. 1 can be taken as a reference. On the South and East side of the platform, a *velocity inlet* is imposed to reproduce the wind velocity of 6 m/s and the direction explained in the case study explanation in 2.2. On the North and West side a *pressure outlet* is used to impose an atmospheric pressure. In fact, as the deck lateral faces are open, the gas cloud can escape the domain due to its dispersion and the wind effect. The deck floor, the ceiling and all the obstacles inside the deck are modelled as *walls with no-slip* conditions. The results of the SB simulation are used as boundary conditions of the dispersion simulation to simulate the release; for this purpose, a box with the same dimensions of the SB is created in the domain in the release position. On its faces the CH_4 m.f. (mass fraction), H_2S m.f. and velocity profiles are imposed (Fig. 3, Fig. 4, Fig. 5).

The turbulence model employed in the calculation is an SST k-ω as it has been validated for subsonic dispersions of methane in a room by (Li et al., 2016), against the experimental data obtained by (Ivings et al., 2010).

The choice of a RANS model can be justified by considering that a fast evaluation is desirable and, for our purposes (i.e. the evaluation of damage areas and volumes), an average distribution of the variables of interest (such as the CH_4 and H_2S mass fraction, the velocity, etc.) is sufficient.

For this simulation as well as for the SB one, the species transport model (Eq. 3) is used to model the CH_4 – H_2S - air interaction; no chemical reaction is considered in both release and dispersion simulations, therefore no CO_2 and water vapor will form during the event.

Particular attention is paid to the relaxation factors, as the species interaction causes oscillations in the residuals in most of the cases. Therefore, a fine tuning of the species relaxation factors is necessary. For example, at first, very low values of CH_4 and H_2S equations relaxation factors are used, e.g. 0.5; once the residuals began to be smooth, these values are incremented to 0.8 until the simulation converges. The convergence is evaluated looking at some significant indicators like the average velocity at the outlet, the mass integral of CH_4 and H_2S: when they reach a plateau, the simulation is stopped.

RESULTS

Release phase results

A first discussion of the results is made in order to check their physical consistency. The high release pressure (50 bar) causes the formation of a highly under-expanded jet, which structure is very well known and studied in the past (Franquet et al., 2015). Therefore, it is important to check if the fluid-dynamic structure resembles the theoretical one. For this purpose, Fig. 2, which shows the midplane section of the SB, can be considered.

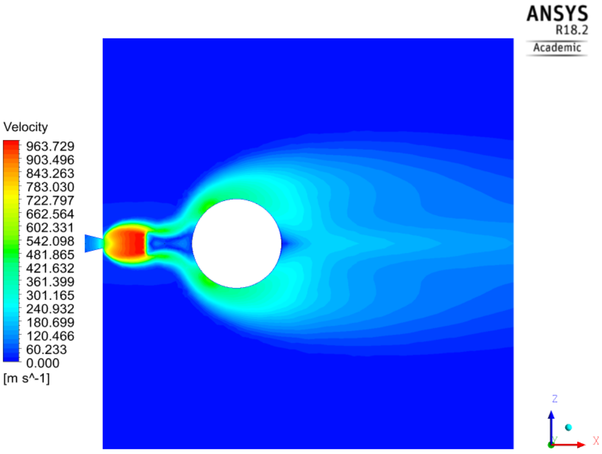

Figure 2: Velocity field in the SB midplane

As expected, the jet presents the typical fluid-dynamic structure: a supersonic core appears near the release point and a normal shock (Mach disk) divides the supersonic core from a subsonic region. Furthermore, the jet obstacle interaction reproduces a strong Coanda effect, as the fluid tends to follow the convex cylinder surface. To assess the accuracy of the solution in the most critical region, i.e. around the Mach disk characterized by strong discontinuities in the flow filed, the distance of the disk is compared to that obtained by using (Eq.1).
In Table 1, the values obtained by CFD and theory are detailed.

Table 1: Mach disk location

X_m (Eq. 1) [m]	X_m (CFD) [m]	Relative error [%]
0.1368	0.1300	4.97

The accuracy of the Mach disk location obtained by CFD can be considered satisfactory and physically consistent as the relative error with respect to the theoretical value is small enough.
At this point, it is important to analyze the important results for the SBAM method; in Fig. 3, Fig. 4 and Fig. 5 the velocity, CH_4 m.f. and H_2S m.f. contours on the external SB surfaces are shown respectively.

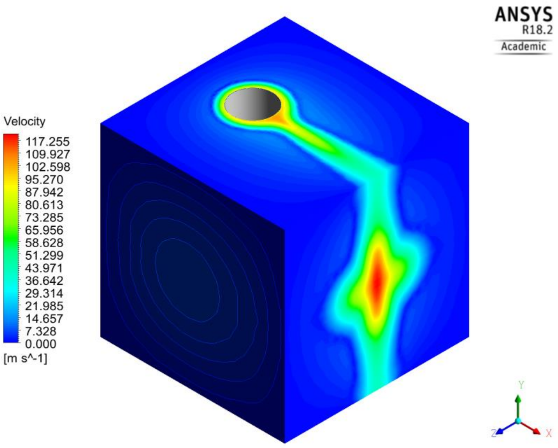

Figure 3: Velocity contours of SB outer surfaces

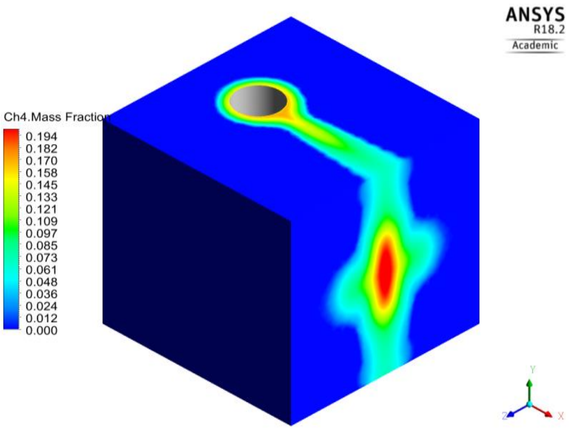

Figure 4: CH_4 mass fraction contours of SB outer surfaces

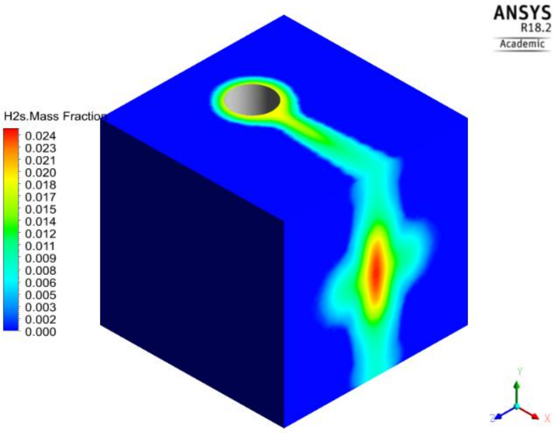

Figure 5: H_2S mass fraction contours of SB outer surfaces

These profiles are crucial, since they represent the input boundary conditions of the dispersion simulation. It can be appreciated that the flow has enough inertia to close after the cylinder. The jet opening is more pronounced in the midplane of the SB, the release plane, since the momentum of the fluid is higher than in the other SB sections. The temperature field analysis is neglected because the released gas and the ambient are at the same temperature. Near the release point, it is possible to observe the temperature of the jet decreasing in correspondence of the Mach disk, but the fast mixing between the jet and the surrounding ambient air maintains the CH_4-H_2S mixture near the ambient temperature. For this reason, also in the dispersion simulation the temperature field is not discussed.

Dispersion phase results

Before discussing the results, some quantities of interest must be defined, as the objective is to estimate the dangerous areas associated to the accident. Both CH_4 and H_2S are flammable, while only H_2S is toxic, therefore it is important to introduce the following quantities:

- LFL: Low Flammability Limit;
- UFL: Upper Flammability Limit;
- IDLH: Immediately Dangerous to Life and Health concentration;
- LC_{50}: lethal dose at which 50% of the population is killed in a given exposition time.

The reference values for each species taken from (NIOSH, 1994, OSHA, 2020 and Zlochower et al., 2009) are presented in Table 2.

Table 2: Flammability and toxicity limits

	LFL [mol. conc.]	UFL [mol. conc.]	IDLH [ppm]	LC_{50} [ppm]
CH_4	0.05	0.16	\	\
H_2S	0.045	0.455	100	713

Since both species of the released mixture are flammable, it is possible to evaluate the LFL and UFL of the mixture using LeChatelier's rule as done in (Liao et al., 2005) remembering that the release mixture has 95% CH_4 – 5 % H_2S composition:

$$\mathrm{LFL_{mix}} = \frac{100}{\sum \mathrm{C_i}/\mathrm{LFL_i}} \tag{4}$$

(Analogous for UFL). By Eq. 4 the following values are obtained:

- $LFL_{mix} = 0.049$
- $UFL_{mix} = 0.17$

First of all, to understand the spatial distribution of the pollutant is fundamental to analyze the velocity flow field. From a qualitative point of view, the velocity field obtained at the release height plane is shown in Fig. 6.

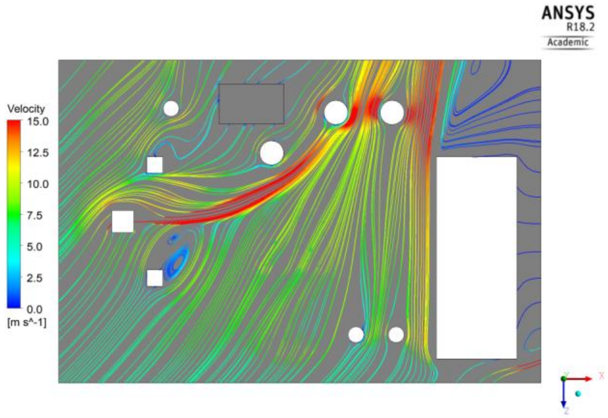

Figure 6: Velocity field in the production deck

The velocity streamlines follow the wind direction near the inlet boundaries b1 and b2, therefore the wind velocity seems to be well reproduced in the deck. The flow becomes quite complex as it interacts with the objects: separation flows appear and secondary vortices are generated. The velocity field analysis is very important because it allows understanding how the pollutants are transported in the domain.

For the purposes of a QRA, it is important to study the flammable and toxic concentration maps. The first one is relevant for people safety and the integrity of the equipment because the ignition of the flammable cloud can lead to a flash fire and a domino effect that involve the equipment integrity. Meanwhile, in the second one, the workers should be subjected to a risk for their health or life.

In Fig. 7 the flammable region, i.e. the region in which the mixture concentration is between LFL_{mix} and UFL_{mix}, is shown in red, while in Fig. 8 the toxic regions with H_2S concentration higher than IDLH and LC_{50} are shown respectively in red and yellow on the same section plane of the velocity field.

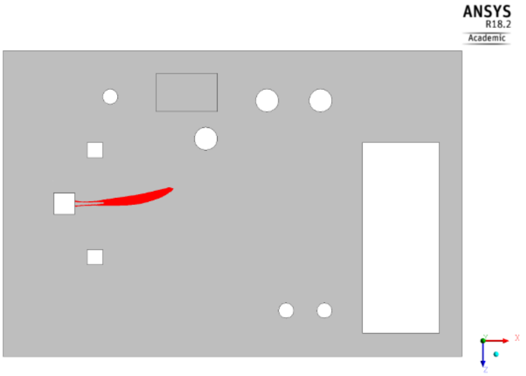

Figure 7: Flammable area

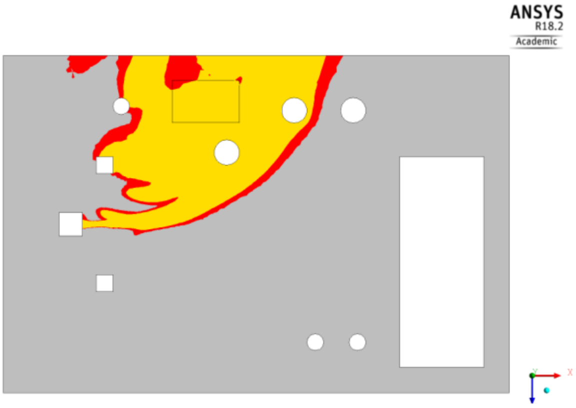

Figure 8: IDHL (red) and LC_{50} (yellow) regions

The flammable area appears as a plume with extension of ~7 m that is slightly deviated by the wind: the velocity of the jet is such that the wind is not affecting too much the plume shape in the first 10 m. The ignition of the mixture can cause an explosion or a fire involving a bigger area of the platform, causing also a possible domino effect depending on the type of components involved in the fire. The toxic area covers a large part of the platform and it is evident that the shape is highly influenced by the wind direction: it can be deduced that the wind condition is a crucial parameter in the assessment of the dangerous areas, and it is the main driver of the pollutant cloud diffusion. It is possible to define the toxic hazardous area and to apply risk control measures for workers. From the comparison of the flammable and toxic areas it can be appreciated that the toxicity is the most dangerous aspect to consider in a release of sour gas to protect the worker health, without considering a possible domino effect due to the flammability. The previous considerations are referred only to a plane section of the platform and it is interesting to see that also the 3D results confirm this trend. In Fig. 9 the flammable cloud is shown, while in Fig. 10 the toxic cloud (IDLH) is shown.

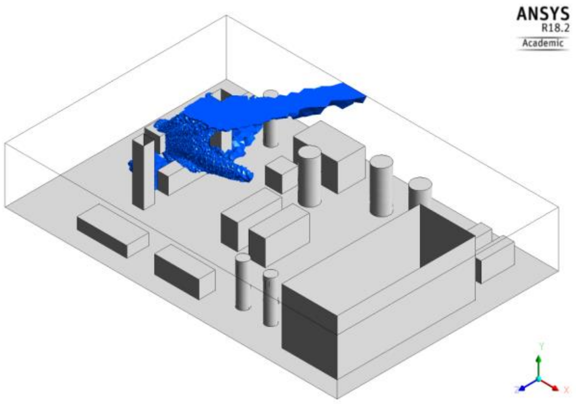

Figure 9: 3D flammable cloud

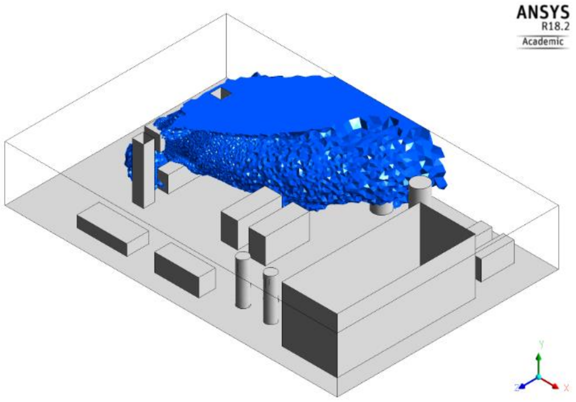

Figure 10: 3D toxic cloud (concentration > IDLH)

The two volumes configurations confirm the considerations made for the 2D results: the toxic cloud involves a larger number of components with respect to the flammable one and it seems to be the most impacting factor on the safety of the system. In addition, the quantities reported in Table 3 give a numerical measure of these differences: it can be noticed that the toxic volume is more than 10 times larger than the flammable one.

Table 3: mass and volume of flammable and toxic cloud

Flammable cloud volume [m^3]	~26
Flammable cloud mass [kg]	~29
Toxic cloud volume [m^3]	~328
Toxic cloud mass [kg]	~369

A final important comment must be made about the simulations time of the SB and dispersion. Both simulations are carried out on the same machine that is a Dell Tower 7810 using the same number of cores (8 cores and 64Gb RAM). The SB simulation takes almost 24 h while the dispersion one takes ~3 h. The big difference in the simulation time can be explained considering that, in the dispersion phase, the phenomena to be simulated are very simple and no complex fluid dynamic structure appears. On the other hand, the complexity of the fluid-dynamic structures characterizing the release makes the SB simulation heavier.

CONCLUSION

In this work, a pressurized sour gas (CH_4-H_2S mixture) release simulation is performed using ANSYS Fluent software.

The SBAM approach provides reliable results for a pressurized flammable and toxic gas mixture leakage accidental scenario. Firstly, the physical consistency of the under-expanded jet is analyzed by comparing the CFD results with the corresponding theoretical references. The comparison shows a good accordance between numerical results and theoretical predictions and it is possible to see the presence of the Mach cell and its correct location as predicted by theory. Secondly, it is possible to see that the velocity field in the entire platform is strongly influenced by the presence of the wind and separation flows appear near the obstacles.

The second phase of the proposed approach is the most relevant for the risk assessment procedure; in fact, it allows defining the damage areas of the accidental scenario:

- a flammable area, where the CH_4-H_2S mixture is inside the flammable range. In this area, it is fundamental to avoid the interaction between the gas mixture and hot surfaces, flames or sparks to prevent the ignition of the gas cloud and the damage for people and the environment.
- a toxic area, where the H_2S concentration is higher than IDLH. The presence of H_2S means a threat for workers: for this reason, safety equipment needs to be adequate to protect workers from the hazards of H_2S.

One of the main outcomes of the work is that the splitting of the phenomenon can reduce dramatically the computational time, since the SB simulation results can be used for several dispersion simulations in which the release position and direction change. In fact, the dispersion simulation time is very low (~3 h) compared to the more complex release one (~24 h). This result can lead to a new approach in QRA, in which several accidental scenarios can be simulated via CFD in a reasonable time.

Finally, a future step deals with the validation. CFD models usually require an experimental validation: for this reason, an experimental campaign is in progress in order to validate the SBAM approach in a novel wind tunnel located in Turin, the SEASTAR wind tunnel, which is presently being calibrated. The experiments using a 1:10 scaled offshore platform mockup can provide significant results for SBAM validation (Moscatello et al., 2020).

REFERENCES

ANSYS Fluent 18.2, User's Guide, 2018.

CARPIGNANO, A., CORTI, T., UGGENTI, A.C. and GERBONI, R. (2017), "Modelling of a supersonic accidental release in Oil&Gas offshore: Characterisation of a source box", *GEAM. Geoingengeria ambientale e mineraria*, 58-64.

CASAL, J., (2007), "Evaluation of the effects and consequences of Major Accidents in industrial plants" *Elsevier, Chapter 11.*

CHEN, C.J. and RODI, W., (1980), "Vertical turbulent buoyant jets*", Pergamon Press*.

CHOI, J., HUR, N., KANG, S., LEE, E. D. and LEE, K.B., (2013), "A CFD simulation of hydrogen dispersion for the hydrogen leakage from a fuel cell vehicle in an underground parking garage", *International Journal of Hydrogen Energy*, Vol. 38, Issue 19, 8084-8091.

CRIST, S., GLASS, D. R., and SHERMAN, P. M., (1966), "Study of the highly underexpanded sonic jet", *AIAA Journal*, 68-71.

DAVIDSON, G. (1967), "Simultaneous trajectory and dilution predictions from a simple integral plume model", *Atmospheric Environment*, Vol. 23, 341-349.

DENG, Y., HU, H., YU, B., SUN, D., HOU, L. and LIANG, Y., (2018), "A method for simulating the release of natural gas from the rupture of high-pressure pipelines in any terrain", *Journal of Hazardous Materials*, Vol. 342, 418-428.

DOROUDI, S., POPHALI, A., BUSSMANN, M., TANDRA, D., TRAN, H., (2015), "Modelling Sootblower jet effectiveness with ANSYS Fluent", *Journal of Science & Technology for Forest Products and Processes* Vol. 4, 30-35.

EGGINS, P. L. and JACKSON, D. A., (1974), "Laser-Doppler velocity measurements in an under-expanded free jet", *Journal of Physics D: Applied Physics*, Vol. 7, N. 14.

FRANQUET, E., PERRIER, V., GIBOUT, S. and BRUEL, P. (2015), "Free underexpanded jets in a quiescent medium: A review", *Progress in Aerospace Science*, Vol. 77, 25-53.

IVINGS, M. J., GANT, S. E., SAUNDERS, C. J., and POCOCK, D. J., (2010), "Flammable gas cloud build up in a ventilated enclosure", *Journal of Hazardous Materials*, Vol. 184 (1), 170-176.

LAYFON, D.W., CEDERWALL, R.T., (1987), "Predicting and managing the health risks of sour-gas wells", *JAPCA*, Vol. 37, 1185-1190.

LI, X. J., ZHOU, R. P. and KONOVESSIS, D., (2016). "CFD analysis of natural gas dispersion in engine room space based on multi-factor coupling", *Ocean Engineering*, Vol. 111, 524-532.

LI, D., ZHANG, L., YANG, J. et al., (2014), "Effect of H2S concentration on the corrosion behavior of pipeline steel under the coexistence of H2S and CO2", *Int J Miner Metall Mater*, Vol. 21, 388–394.

LIAO, S., CHENG, Q., JIANG, D. M. and GAO, J., "Experimental study of flammability limits of natural gas-air mixture", *Journal of Hazardous Materials*, Vol. 119, 81-84.

LIU, X., GODBOLE, A., LU, C., MICHAL, G. and VENTON P., (2014), "Source strength and dispersion of CO2 releases from high-pressure pipelines: CFD model using real gas equation of state", *Applied Energy*, Vol. 126, 56-68.

LIU, W., GAO, B., ZHANG, Z., ZHANG, J., ZHANG, D., FAN, M., FU, X., ZHENG, L., LIU, Q., (2010), "H_2S formation and enrichment mechanisms in medium to large scale natural gas fields (reservoirs) in the Sichuan Basin", *Petroleum exploration and development*, Vol. 37, Issue 5.

MI, J., ZHANG, B., SHEN, Z., HUANG, W., CASALINS, A., LIU C., (2017), "The experimental study on H2S generation during thermal recovery process for heavy oil from the Eastern Venezuela Basin", *Journal of Natural Gas Geoscience*, Vol. 2, Issue 3, 201-208.

MOSCATELLO, A., UGGENTI, A.C., IUSO, G., D'AMBROSIO, D., CAFIERO, G., GERBONI, R., CARPIGNANO, A., (2020), "Scaling procedure for designing accidental gas release experiments", *Engineering Computations*.

MUNSON, B., YOUNG, D., OKIISHI, T., HUEBSCH, W., (2009), "Fundamentals of Fluid Mechanics (VI ed.)", *Wiley*.

NECCI, M., TARANTOLA, S., VAMANU, B., KRAUSMANN, E. and PONTE L., (2019), "Lessons learned from offshore oil and gas incidents in the Arctic and other ice-prone seas", *Ocean Engineering* Vol. 185, 12-26.

NIOSH, (1994), "Documentation for Immediately Dangerous to Life or Health Concentration".

NOVEMBRE, N., PODENZANI, F. and COLOMBO, E., (2006), "Numerical study for accidental gas releases from high pressure pipelines", *Proceedings of the European Conference on Computational Fluid Dynamics*.

OSHA, https://www.osha.gov/SLTC/hydrogensulfide/hazards.html#:~:text=The%20explosive%20range%20of%20hydrogen,much%20higher%20than%20the%20PEL. Available at 6/2020.

PATÉ-CORNELL, M., (1993), "Risk analysis and risk management for offshore platforms: Lessons from the Piper Alpha accident", *Journal of Offshore Mechanics and Arctic Engineering*, Vol. 115, 179-190.

VENETSANOS, A.G., BARALDI, D., ADAMS, P., HEGGEM, P.S. and WILKENING, H., (2008), "CFD modelling of hydrogen release, dispersion and combustion for automotive scenarios", *Journal of Loss Prevention in the Process Industries*, Vol. 21, Issue 2, 162-184.

VINNEM, J.E., (2019), "Offshore Risk Assessment vol 2 – Chapter 14 (Fourth Edition)", *Springer*.

VIVALDA, C., GERBONI, R. and CARPIGNANO, A., (2018), "A practical approach to risk-based gas monitoring system design for oil and gas offshore platforms", *Proceedings of the 14th Probabilistic Safety Assessment and Management Conference*.

WARNER, J.L., BASKIN, D.K., HWANG, R.J., CARLSON, R.M., and CLARK, M.E., (2007), "Geochemical Evidence for Two Stages of Hydrocarbon Emplacement and the Origin of Solid Bitumen in the Giant Tengiz Field, Kazakhstan", *Oil and Gas of the Greater Caspian Area*, Pinar O. Yilmaz, Gary H. Isaksen.

WORDEN R.H., SMALLEY, P.C., BARCLAY, S.A, 2003, "H_2S and diagenetic pyrite in North Sea sandstones: due to TSR or organic sulphur compound cracking?", *Journal of Geochemical Exploration*, Vol. 78 79, 487-491.

ZAMEJC, E. (2014), "API Standard 521 new alternative method to evaluate fire relief for pressure relief device sizing and depressuring system design", *Journal of Loss Prevention in the Process Industries,* Vol. 27, 21-31.

ZEMPOLICH, W., NEGRI, A., LEO, C., VAN OJIK, K. and VERDEL, A., (2002), "Kashagan Discovery: An Example of the Successful Use of a Multi-disciplined Approach in Reducing Geologic Risk", *AAPG Annual Meeting,* March 10-13, 2002 Houston, Texas.

ZLOCHOWER, I. and GREEN, G., "The limiting oxygen concentration and flammability limits of gases and gas mixtures", *Journal of Loss Prevention in the Process Industries*, Vol. 22, 499-505.

PERFORMANCE OF THE BLENDING FACTORS APPROACH FOR MODELING THE INTERFACIAL FORCES IN BUBBLE COLUMNS OPERATING AT HIGH GAS HOLD UP

Francesco MANISCALCO^{1*}, **Mohsen SHIEA**^{1}, **Antonio BUFFO**^{1}, **Daniele MARCHISIO**^{1}, **Marco VANNI**^{1†}

^{1}Department of Applied Science and Technology, Politecnico di Torino, ITALY

* E-mail: francesco.maniscalco@polito.it
† E-mail: marco.vanni@polito.it

ABSTRACT

Gas-liquid bubble columns are commonly used in the process industry due to their ease in construction and their excellent performances. However, the formulation of numerical models of such industrial-scale systems is troublesome especially because of the strong coupling between the phases. In fact, it is crucial to properly describe the phase coupling in the Euler-Euler framework in terms of the drag and other interfacial forces. This is particularly important at high gas superficial velocity, when the global gas fraction is higher and the drag coefficient is very different from that for isolated particles. One way of addressing the problem is coupling a correction for the swarm effect occurring at relatively high gas fractions with a blending approach, which sets a natural transition of the drag force in the phase inversion region.

The numerical simulations were carried out with the CFD code OpenFOAM. While in commercial codes the application of methods of this kind is not always mentioned, in open-source codes, such as OpenFOAM, it is possible to prescribe completely all the settings of the procedure. As a first step of the work, we performed an accurate study on a proper selection of the blending parameters in order to evaluate the impact on the results. Then, a comparison of the proposed model with experimental data and with simulations available in the literature is performed, showing that blending produces accurate results and significantly increases computational speed, since in both homogeneous and heterogeneous regimes the required computational time has been halved.

Particularly interesting is the comparison between simulations carried out in absence and in presence of blending: in the former case the swarm formulation needs an ad hoc correction to capture correctly the gas hold up. It also shows numerical instability due to the phase inversion occurring at the boundary between liquid and head space of the column. Therefore the blending implementation, with a valid selection of parameters, is preferable since it improves the computational speed and numerical robustness.

Keywords: CFD, hydrodynamics, bubble columns, OpenFOAM, multiphase system .

NOMENCLATURE

Greek Symbols

α	Volume fraction, $[-]$.
ε	Turbulent dissipation rate, $[^{m^2}/_{s^3}]$.
ρ	Mass density, $[^{kg}/_{m^3}]$.
μ	Viscosity, $[^{kg}/_{ms}]$.
μ_T	Turbulent viscosity, $[^{kg}/_{ms}]$.
$\mathbf{\Sigma}$	Stress tensor, $[Pa]$.
σ	Interfacial tension, $[^{N}/_{m}]$.

Latin Symbols

C_D	Drag coefficient, $[-]$.
D	Column diameter, $[m]$.
d_b	Bubble diameter, $[m]$.
$\mathbf{g}$	Gravitational acceleration, $[^{m}/_{s^2}]$.
H	Column height, $[m]$.
h	Swarm factor ,$[-]$.
I	Turbulence intensity, $[-]$.
k	Turbulent kinetic energy, $[^{m^2}/_{s^2}]$.
p	Pressure, $[Pa]$.
R	Column radius, $[m]$.
S	Section area, $[m^2]$.
r	radial coordinate, $[m]$.
$\mathbf{u}$	Velocity, $[^{m}/_{s}]$.
$\langle U \rangle$	Superficial gas velocity, $[^{m}/_{s}]$.
z	axial coordinate. $[m]$.

Sub/superscripts

FD	Fully Dispersed.
G	Gas.
in	Inlet.
k	Phase index k.
L	Liquid.
l	Phase index l.
PD	Partially Dispersed.

INTRODUCTION

Bubble column reactors are nowadays fundamental in industrial equipment: the easiness in construction and the excellent performances in heat and mass transfer have provided them a wide diffusion in chemical, petrochemical and biochemical engineering (Ranade, 2002), ranging from Fischer-Tropsch synthesis (Basha *et al.*, 2015) to microbial digestion (Kantarci *et al.*, 2005).

In the most common configuration the gas phase is injected from the bottom of the column through a sparger and rises through the liquid phase, which may often contain solid catalytic particles (slurry bubble column). The gas is thus dispersed into small bubbles through the liquid, therefore the former may be considered as dispersed phase and the latter as continuous. As a consequence of the injection of the gas, the liquid height rises to a new value corresponding to the sum of the liquid and air volumes: this variation corresponds to the global gas hold-up, which is a key feature in the analysis of the column performances.

In particular, low values of hold-up are peculiar of the so-called homogeneous regime, where the bubbles have approximately the same size and the liquid recirculation is moderate. As the gas superficial velocity, namely the velocity the gas would have if it occupied the whole cross-sectional area, increases, the hold-up increases linearly as well and, after a transition area, starts rising again with a lower slope, hitting hence the heterogeneous regime: the bubbles present a broad variation in size and the liquid recirculation patterns become relevant.

Despite its apparent simplicity, the hydrodynamics of such systems is complicated due to the many types of interaction between dispersed and continuous phase which have a relevant impact on the global behavior. These issues worsen in the heterogeneous regime, which is preferred in industrial applications to maximize the mixing: the larger values of gas fraction and the strong dependency on the radial coordinate of the most notable variables (local hold-up, axial velocity, turbulent quantities) (Shu *et al.*, 2019) have caused non-trivial difficulties when a reliable modeling is desired.

To address this crucial matter, recent research has focused on the expression of the major interfacial forces (Tabib *et al.*, 2008). The most relevant is undoubtedly the drag force, which is due to velocity difference between phases. As the heterogeneous regime is approached, the bubbles get closer and the local gas fraction dramatically increases, eventually leading to a wrong prediction of the drag force and, therefore, of the global hydrodynamics. With the aim to solve this issue, some authors proposed a correction of the drag formula considering the impact of bubbles proximity (swarm effect) (Simonnet *et al.*, 2008; Roghair *et al.*, 2011; McClure *et al.*, 2017). The main drawback of these corrections is either their limited operative range (limited to $\alpha_G \leq 0.1$) or, if formulated for heterogeneous regime, the fact that the predicted correction factor approaches to zero as the hold-up is increased, thus canceling out the whole drag force and giving rise to large regions of high gas volume fraction in the dispersion that are not physical.

This point may be addressed by limiting the swarm correction term to avoid the cancellation of the drag swarm at high gas fraction (Gemello *et al.*, 2018). This correction became necessary because in most of commercial CFD solvers the dispersed and continuity phases must be specified *a priori* throughout the domain: when the gas superficial velocity is high, it may occur that in some portion of the domain the gas fraction is high enough to eliminate the swarm correction although the gas is still the dispersed phase. The swarm correction limitation avoids this type of issues, guaranteeing a non-zero drag term even for large gas fraction values. Unfortunately, in this approach the correction factor must be fitted to match the experimental data of hold up.

On the other hand, the open source software OpenFOAM offers an implementation of the so-called blending parameters, which, through an appropriate selection, allow the solver to distinguish locally the dispersed and the continuous phase. To the best of our knowledge an accurate study of this method has not been attempted in the literature so far: the aim of this study is thus providing an insight of the blending implementation in order to find the best set of parameters for gas-liquid and gas-solid-liquid bubbly flows.

MODEL DESCRIPTION

The gas and liquid phases are both modeled as interpenetrating continuous media according to the Euler-Euler description. In this case, the continuity and Navier-Stokes equations are:

$$\frac{\partial}{\partial t}\alpha_k\rho_k + \nabla\left(\alpha_k\rho_k\mathbf{u}_k\right) = 0 \tag{1}$$

$$\frac{\partial}{\partial t}\alpha_k\rho_k\mathbf{u}_k + \nabla\cdot\left(\alpha_k\rho_k\mathbf{u}_k\mathbf{u}_k\right) = \\ = -\alpha_k\nabla p + \alpha_k\rho_k\mathbf{g} + \nabla\cdot\left(\alpha_k\mathbf{\Sigma}_k\right) + \mathbf{F}_{kl}. \tag{2}$$

The turbulence is implemented as a standard k-ε dispersed model, where only the continuous phase is considered turbulent.

The term $\mathbf{F}_{kl}$ denotes the summation of all the interphase forces occurring between generic phase k and l. In this study the only term considered is the drag force, and, denoting liquid phase as L and gaseous phase as G, it may be formulated as:

$$\mathbf{F}^{\infty}_{D,LG} = \frac{3}{4}C^{\infty}_{D}\frac{\alpha_G\rho_L}{d_b}\left(\mathbf{u}_L - \mathbf{u}_G\right)|\mathbf{u}_L - \mathbf{u}_G|. \tag{3}$$

(in the following the subscripts LG are dropped in sake of simplicity). The drag coefficient for isolated bubbles can be evaluated from a wide number of correlations (Naumann and Schiller, 1935; Ishii and Zuber, 1979). In this study the one suggested by Tomiyama was used since it is the most suitable for contaminated bubbly gas-liquid systems (Tomiyama, 1998):

$$C^{\infty}_{D} = \max\left[\min\left(\frac{24}{Re}(1+Re^{0.687}), \frac{72}{Re}\right), \frac{8}{3}\frac{Eo}{Eo+4}\right], \tag{4}$$

being Re and Eo respectively the Reynolds and Eötvös number.

The swarm effect is taken into account multiplying C^{∞}_{D} by a semi-empirical factor h (Simonnet *et al.*, 2008)

$$h = \frac{C_D}{C^{\infty}_{D}} = (1-\alpha_G)\left[(1-\alpha_G)^{25} + \left(4.8\frac{\alpha_G}{1-\alpha_G}\right)^{25}\right]^{-2/25} \tag{5}$$

This correlation is often bounded imposing a minimum value of h, namely h_0 (Gemello *et al.*, 2018):

$$h = \max\left(h_{\text{Simonnet}}, h_0\right) \tag{6}$$

h_0 might range from 0.08 to 0.30 and it should be selected according to the gas superficial velocity and geometry in order to fit the experimental hold up. However, this approach may lead to unrealistic calculations of the liquid velocity and the turbulent quantities when α_k reaches the phase-inversion range and, further on, it generates numerical instability in the head space of the column and at the boundary between liquid and head space. The global outcome is a slow simulation, presenting numerical issues and non-physical results.

A possible approach is the so-called symmetric blending: the drag formula in Eq. (3) is multiplied by the liquid volume fraction α_L in such a way that the drag force approaches to zero in the head space. This solution, despite its straightforwardness, may underestimate the drag force and, consequently, the gas fraction in the two-phase system, where $\alpha_L < 1$.

An improvement of this method is offered by the open-source software OpenFOAM (OpenCFD): in the `twoPhaseEulerFoam` solver, it is possible to specify a blending method, which may be linear or hyperbolic, and some blending parameters. Through the specification of the blending parameters, the solver is capable to detect locally

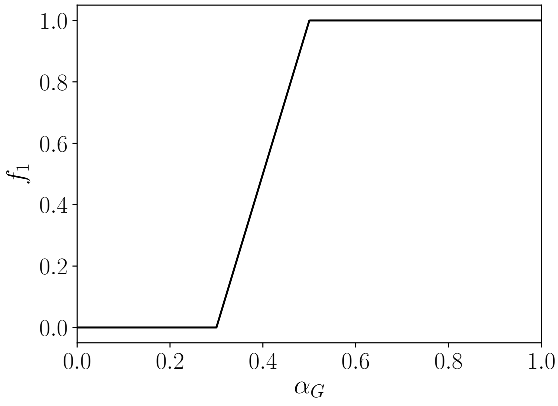

Figure 1: Default linear blending factor f_1.

which phase is dispersed and treat it accordingly. With this aim, two correlations must be specified for every interphase forces coefficient: for phase k dispersed into phase l and vice versa.
In case of linear blending, the code requires 2 parameters per phase:

- `maxFullyDispersedAlpha` (here referred as α_{FD}) defines the gas fraction range $[0, \alpha_{FD}]$ where the phase is modeled as completely dispersed;
- `maxPartialDispersedAlpha` (here referred as α_{PD}), which is the largest value of α_k for the phase to be modeled as dispersed, even if partially.

The blending is achieved by a definition of the blending parameter f for each phase. For the gas phase the blending parameter f_1 is defined as:

$$f_1(\alpha_G) = \min\left[\max\left(\frac{\alpha_G - \alpha_{G,FD}}{\alpha_{G,PD} - \alpha_{G,FD}}, 0\right), 1\right] \tag{7}$$

while, similarly, the blending parameter for the liquid phase is f_2:

$$f_2(\alpha_L) = \min\left[\max\left(\frac{\alpha_{L,PD} - \alpha_L}{\alpha_{L,PD} - \alpha_{L,FD}}, 0\right), 1\right] \tag{8}$$

In the case of $\alpha_{G,FD} = 0.3$ and $\alpha_{G,PD} = 0.5$ (default values in `twoPhaseEulerFoam`) the plot of the blending factor f_1 is provided in Fig. 1.
In the general approach two drag forces and associated blending factors must be computed: bubbles in water (a/w) and drops in air (w/a), respectively. The interphase momentum term is crucial in bubbly flows and in this study it coincides with the drag force. It is blended according to the local air volume fraction through the f_1 factor as it follows:

$$\mathbf{F}_D^{\text{new}} = \mathbf{F}_D^{a/w}(1 - f_1) + \mathbf{F}_D^{w/a}(f_2 - f_1). \tag{9}$$

The formation of aerosol is beyond the scope of this work, a model for the water drop dispersion in air is hence omitted and the second term in the RHS of (9) is dropped.
For each computational node there are three possible scenarios, according to the local value of α_G:

a) $\alpha_G \leq \alpha_{G,FD}$. The air is fully dispersed into water and the whole drag formulation as in Eq. (3) is applied;

b) $\alpha_G > \alpha_{G,PD}$. The air fraction is outside the dispersion range, thus the drag term related to air dispersion in water is null;

c) $\alpha_{G,FD} < \alpha_G \leq \alpha_{G,PD}$. The air is partially dispersed and the drag formula is adjusted according to Eq. (9).

Although the blending was introduced to improve the prediction of the drag force in the two phase region, an additional advantage of the method is the absence of numerical convergence issues in the head space: here, if the blending is not implemented, the solver tries to calculates the drag force for the air-in-water system even if the amount of liquid is completely negligible. That often leads to divergence in the computation of the velocity and turbulence fields. However, through the blending factors specification, in the head space the water switches from being continuous to dispersed and the numerical issues are thus overcome. The final result is a faster and more stable simulation.
It is clear that $\alpha_{k,FD}$ and $\alpha_{k,PD}$ must be chosen wisely in order to obtain physical-sounding results and to maintain the simulations fast and stable. With this aim, a study on a wide range of values was performed and will be discussed in the Results section.

Computational settings

The simulated system in this study is a cylindrical air-water bubble column. The details of the system are provided in Tab. 1 and Tab. 2; the gas density ρ_G is calculated in accordance with the ideal gas law. Experimental data for comparisons are extracted from literature (Raimundo, 2015; Gemello *et al.*, 2018).

Table 1: Properties of the system.

Property	Value	Units
T	25	°C
p	1	bar
μ_L	1.003	mPa s
ρ_L	998.2	kg m^{-3}
μ_G	0.0182	mPa s
σ	0.072	N m^{-1}
d_b	6.5	mm
$\langle U \rangle$	0.03-0.09-0.16	m s^{-1}

Table 2: Geometrical features of the system.

Property	Value	Units
D	0.400	m
H	3.6	m

The domain was discretized in a 45’000 cells mesh depicted in Fig. 2 and Fig. 3: this discretization should guarantee mesh-independent results (Gemello *et al.*, 2018). In particular, at the bottom a thin outer ring was excluded from the inlet section (red area in Fig. 3) to prevent computational issues possible due to gas accumulation at the wall.
Simulations were performed using the `twoPhaseEulerFoam` solver in OpenFOAM 5.0 at various gas superficial velocities in order to investigate both homogeneous and heterogeneous regimes.
The van Leer scheme (van Leer, 1974) was used as discretization scheme for the pressure and velocity equations, while an upwind scheme was used for k and ε. Boundary conditions are summarized in Tab. 3.

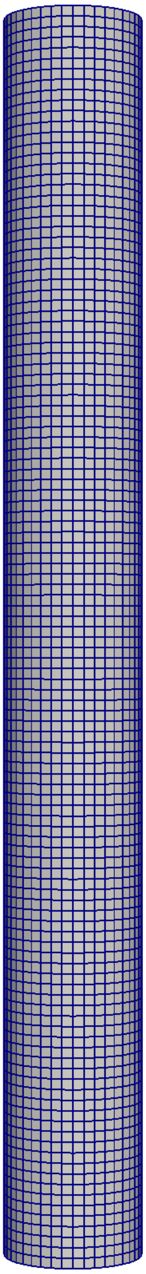

Figure 2: Side view.

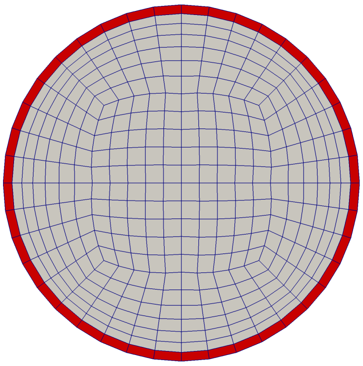

Figure 3: Bottom view. Red area is not included in the sparger.

Transient simulations were performed: each case was simulated for 180 s and it was initialized with the liquid static height equal to 1.6 m and no air dispersion in it. The first order Euler implicit method was used as time-advancement scheme, and an adjustable time step was chosen such in a way that the maximum Courant number was 0.65. The PIMPLE algorithm with 2 inner iterations and a maximum number of 30 outer iterations was adopted for the transient pressure-velocity coupling. The absolute tolerance for every equation was set to $1{\cdot}10^{-7}$.

The results presented in the following sections are obtained through time-averaging the transient data over the last 100 s of simulation.

RESULTS

Impact of input parameters

Firstly a study of the variation impact of $\alpha_{G,FD}$ and $\alpha_{G,PD}$ on the hydrodynamics of the system was performed (in the following the two parameters will always refer to the gas phase: for sake of simplicity, the G subscript will be dropped). This set of simulations was executed for a superficial gas velocity $\langle U \rangle = 0.16$ m s^{-1}: the heterogeneous regime is indeed more complex to simulate and, once the optimal set of parameters is found, they can be easily applied to lower superficial velocity. However, in order to perform a sensitivity study on α_{FD}, it is necessary to set α_{PD} a reasonable value which will we be verified *a posteriori*. In the literature it may be found that for air-in-water dispersion the gas fraction corresponding to the maximum close-packing state of bubbles is approximately 0.75 (Hibiki and Ishii, 2000). Therefore, α_{PD} was set to 0.8 as first value.

Fig. 4 and Fig. 5 present the air fraction and liquid axial velocity profiles for α_{FD} ranging from 0.2 to 0.5 and compare them with experimental data. The effect of the blending factor variation is very small in the prediction of the velocity field, while it becomes more relevant when dealing with the calculation of the air distribution in water. In particular, the wider discrepancies occur in the center of the column where the gas fraction is higher and falls into the $[\alpha_{FD}, \alpha_{PD}]$ interval, with the lowest profile corresponding to α_{FD} equal to 0.2.The increase of this latter parameter causes a shift of the partial dispersion area to higher volume fraction, with a consequent spread of the fully dispersion area. The final outcome is that multiplicative factor $(1 - f_1)$ in Eq. (9) boosts up enlarging α_{FD}, eventually leading to a heavier evaluation of the drag force and, as a final consequence, to a higher local gas fraction. The most effective value for α_{FD} thus seems 0.2, since it both broadens out the partial dispersion region and it provides results closer to experimental data.

Table 3: Boundary conditions.

Var.	Inlet	Outlet	Walls
α_G	0.5	1 for backflow	`zeroGradient`
$\mathbf{u}_G$	$\frac{\langle U \rangle S}{\alpha_{(G,\text{in})} S_\text{in}}$	`pressureInletOutletVelocity`	`slip`
$\mathbf{u}_L$	0	`pressureInletOutletVelocity`	`noSlip`
k	$I = 0.05$	$I = 0.001$	`kqRWallFunction`
ε	μ_T/μ = 10	length scale = $0.7D$	`epsilonWallFunction`

Secondly, after setting α_{FD} to 0.2, the simulations were repeated using 0.7 and 0.8 for α_{PD} to investigate its actual relevance in hydrodynamics of the system: results are shown in Fig. 6 and Fig. 7. The two values provide indistinguishable outcomes, therefore the choice fell on 0.8 since it provides a softer transition between fully dispersion and inversion zones (slope of f_1 in Fig. 1).

In any case, the simulations are not particularly sensitive to the values of α_{FD} or α_{PD}, provided that they are chosen in a reasonable range. From this point of view, the predictions of the blending approach appear quite robust.

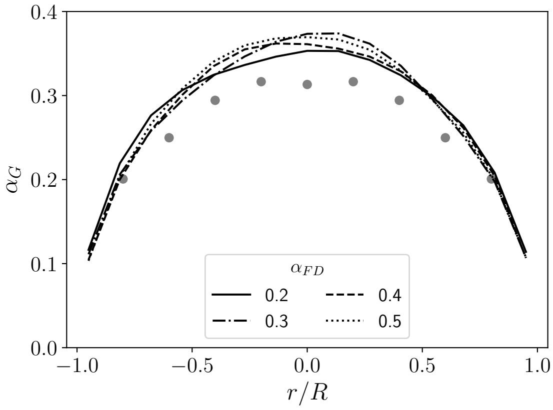

Figure 4: Impact of α_{FD} on gas fraction profiles at height $z/D = 2.5$ and $\langle U \rangle = 0.16\,\mathrm{m\,s^{-1}}$: comparison with experimental data (circles).

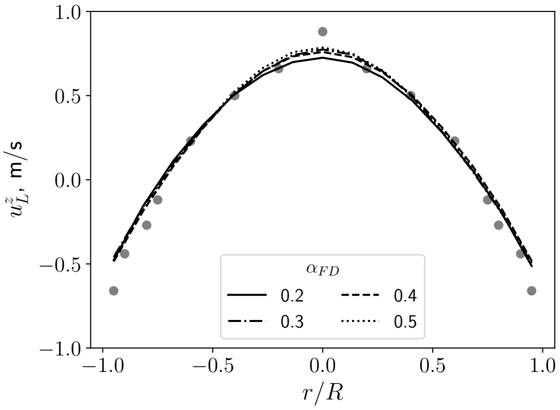

Figure 5: Impact of α_{FD} on liquid z-velocity profiles at height $z/D = 3.75$ and $\langle U \rangle = 0.16\,\mathrm{m\,s^{-1}}$: comparison with experimental data (circles).

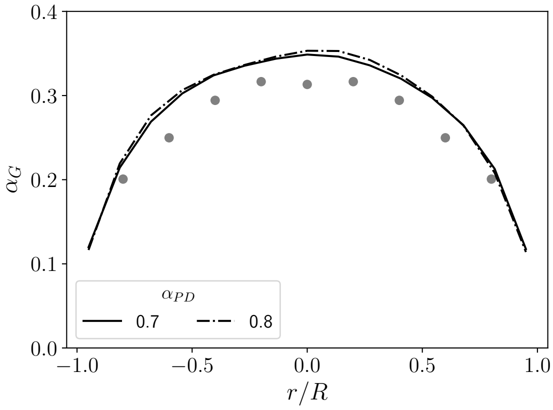

Figure 6: Impact of α_{PD} on gas fraction profiles at height $z/D = 2.5$ and $\langle U \rangle = 0.16\,\mathrm{m\,s^{-1}}$: comparison with experimental data (circles).

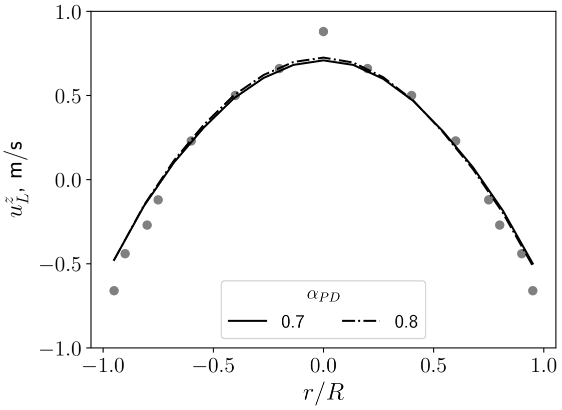

Figure 7: Impact of α_{PD} on liquid z-velocity profiles at height $z/D = 3.75$ and $\langle U \rangle = 0.16\,\mathrm{m\,s^{-1}}$: comparison with experimental data (circles).

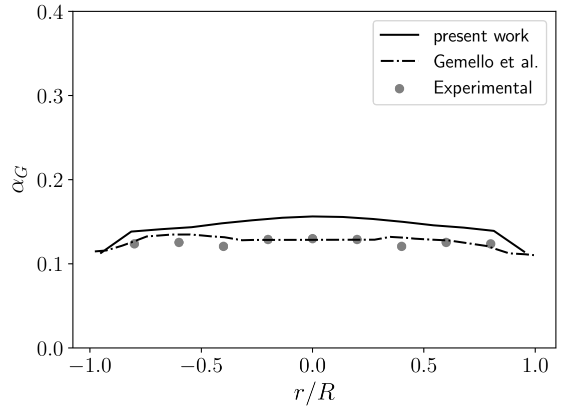

Figure 8: Gas fraction profiles at height $z/D = 2.5$ at $\langle U \rangle = 0.03\,\mathrm{m\,s^{-1}}$ (homogeneous regime): comparison with (Gemello *et al.*, 2018) and experiments.

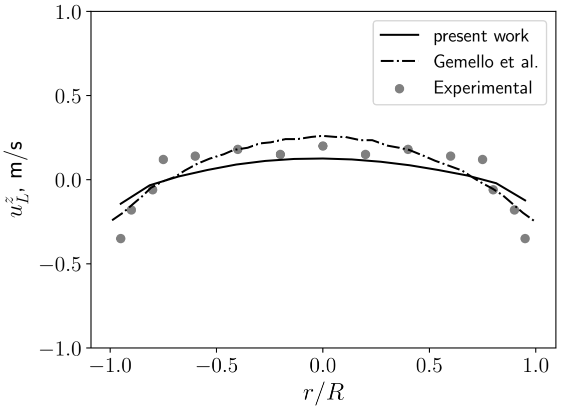

Figure 9: Liquid z-velocity profiles at height $z/D = 3.75$ at $\langle U \rangle = 0.03\,\mathrm{m\,s^{-1}}$ (homogeneous regime): comparison with (Gemello *et al.*, 2018) and experiments.

Results accuracy

The results above-mentioned were then compared to the results obtained by other CFD simulations of the same system (Gemello *et al.*, 2018) executed without the blending factor, but fixing a minimum value of the swarm factor. Computational and modeling settings were set as much as possible identical to the compared work, with the sole exception of turbulence. In accordance with the recent literature, reporting that the RNG k-ε model may provide more realistic results (Syed *et al.*, 2018; Fleck and Rzehak, 2019) for the volume fraction prediction, Gemello et al. modeled the turbulence correspondingly. However, in `twoPhaseEulerFoam` is

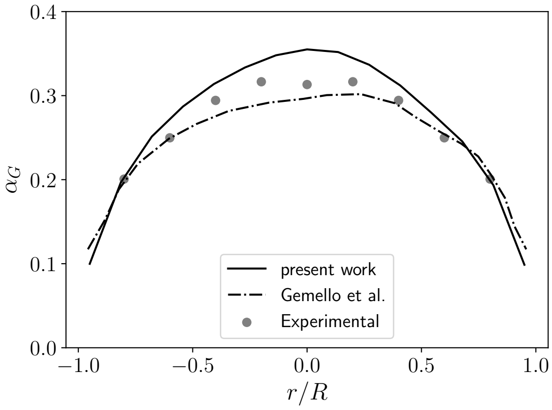

Figure 10: Gas fraction profiles at height $z/D = 2.5$ at $\langle U \rangle = 0.16\ \mathrm{m\,s^{-1}}$ (heterogeneous regime): comparison with (Gemello *et al.*, 2018) and experiments.

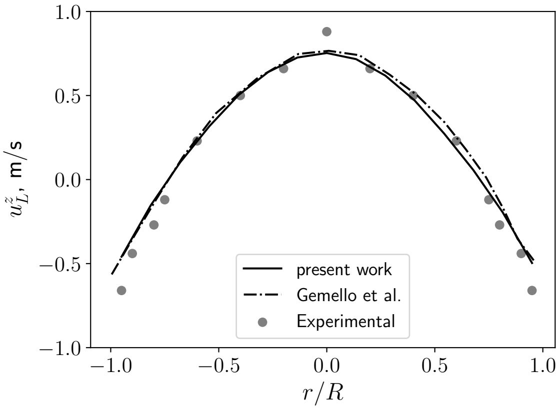

Figure 11: Liquid z-velocity profiles at height $z/D = 3.75$ at $\langle U \rangle = 0.16\ \mathrm{m\,s^{-1}}$ (heterogeneous regime): comparison with (Gemello *et al.*, 2018) and experiments.

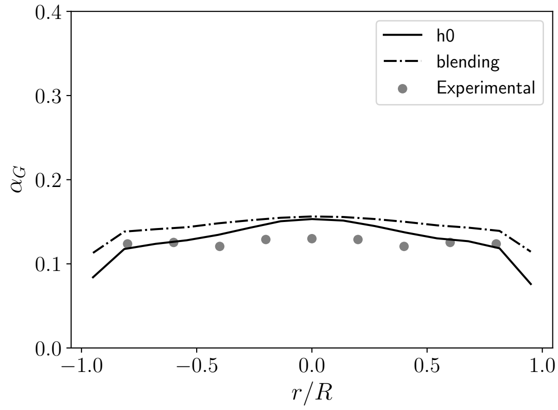

Figure 12: Gas fraction profiles at height $z/D = 2.5$ at $\langle U \rangle = 0.03\ \mathrm{m\,s^{-1}}$ (homogeneous regime): comparison between the usage of $h_0 = 0.15$ and the blending method.

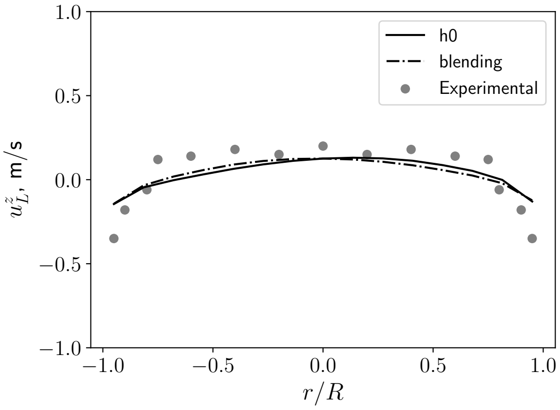

Figure 13: Liquid z-velocity profiles at height $z/D = 3.75$ at $\langle U \rangle = 0.03\ \mathrm{m\,s^{-1}}$ (homogeneous regime): comparison between the usage of $h_0 = 0.15$ and the blending method.

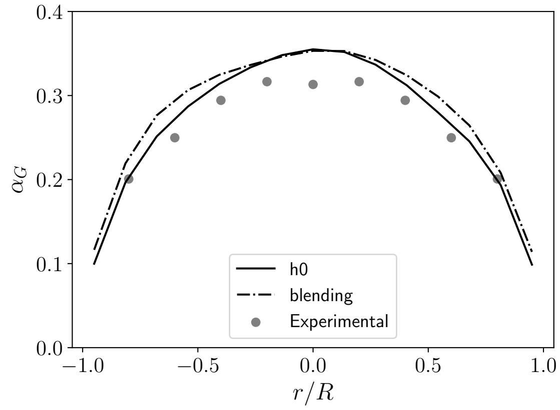

Figure 14: Gas fraction profiles at height $z/D = 2.5$ at $\langle U \rangle = 0.16\ \mathrm{m\,s^{-1}}$ (heterogeneous regime): comparison between the usage of $h_0 = 0.15$ and the blending method.

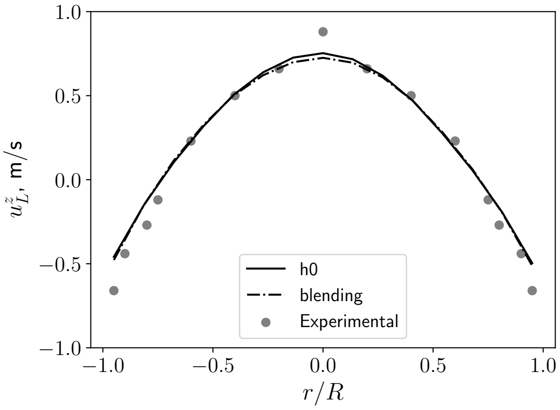

Figure 15: Liquid z-velocity profiles at height $z/D = 3.75$ at $\langle U \rangle = 0.16\ \mathrm{m\,s^{-1}}$ (heterogeneous regime): comparison between the usage of $h_0 = 0.15$ and the blending method.

not available for multiphase systems: therefore the OpenFOAM results in this work are obtained keeping the standard k-ε.

The outcome of the comparison is shown in Fig. 8 and Fig. 9 for the homogeneous regime and in Fig. 10 and Fig. 11 for the heterogeneous one.

Results indicate that our model provides considerable accuracy in predicting the liquid velocity profiles for both hydrodynamical regimes, especially for the prediction of the liquid axial velocity (Figs. 9,11). In this case, the correspondence between both models and experimental data is maximal. In particular, when the superficial gas velocity is lower (Fig. 9) the values provided by experiments are scattered and do not correspond to the usual quasi-parabolic profiles and a rigorous comparison is harder; nevertheless the standard k-ε model combined with blending produced a flatter profile, closer to the experimental trend.

However, the larger discrepancy was detected in the prediction of the gas fraction profiles (Fig. 8,10) and, in particular, when the superficial gas velocity is equal to $0.16\ \mathrm{m\,s^{-1}}$ (Fig. 10). In this case the trends of the two models differ specularly from the experimental data, reaching the maximum deviation at the center of the column. This behavior is not encountered in the homogeneous regime (Fig. 8) where the profiles are flat and the gap between the two models is non-negligible even closer to the walls.

With the aim to isolate the impact of the turbulence model, a set of simulations was run in `twoPhaseEulerFoam` using the standard k-ε turbulence model and the same swarm factor correction as in (Gemello *et al.*, 2018) with $h_0 = 0.15$. What stands out from results (Figs. 12–15) is that the turbulence modeling has a remarkably stronger impact than the usage of the blending method on the final results. The gap displayed by the two models is now considerably reduced, especially for the prediction of the liquid velocity field: this indicates that the gap reported in Fig. 10 was evidently due to the different k-ε turbulence models used, combined with the high gas velocity.

It may be thus suggested that the implementation of the blending method, if performed with a proper choice of parameters as discussed above, does not affect the fluid dynamical description of two-phase systems.

Computational effort

The capability of the blending method to determine cell by cell the dispersed and the continuous phase and to use the corresponding interphase law allows a significant gain in computational speed. Fig. 16 reports the simulation elapsed time at different gas superficial velocities using 4 processing units Intel Xeon E5-2680 v3 2.50 GHz.

In every case the implementation of blending halved the computational time, without any accuracy loss in results. As pointed out above, this impressive speed up may be linked to description of the head space of the column according to the blending method: if not used, the solver still treats any amount of water in it as continuous phase. This generates huge numerical issues in the computation of the drag force, because it is designed for a dispersion of air in water, and consequently of velocity, k and ε. Contrarily, the activation of the blending allows the recognition of the phase inversion and the water is treated as dispersed phase, using the adequate interphase forces correlations.

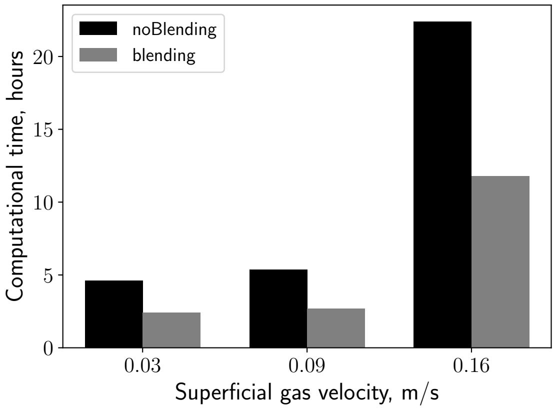

Figure 16: Computational time required by simulations with and without blending implementation.

CONCLUSION

Air-water bubble columns were simulated with OpenFOAM 5.0 using the blending factor approach to model properly interphase forces. After having performed a sensitivity study on the input parameters, an optimal set of them was proposed for the studied system for the investigated superficial velocities. Comparisons with both other models and experimental data shown that the blending factor method is a valid choice for simulating air-water bubbly flows at high gas hold up. Further studies on different geometries and gas velocities may extend the validity of this choice of parameters, with the possibility to increase or reduce the maximum air fully/partially dispersion fraction values. Nevertheless, the upper limit is the maximum close-packing state of bubbles at which, as aforementioned, the air volume fraction is approximately 0.75 for monodisperse bubbles.

The blending approach provides a more physical modeling of the dynamical dispersion phenomena, preventing the usage of semi-empirical correlations to adjust the numerical issues due to miscalculation in the drag force due to high gas hold-up. This matter is addressed through a definition of a partial dispersion zone, where the drag force impact is soften and eventually vanished when the phase-inversion zone is reached.

An insight of the computational time required by the blending method is then reported, showing how its implementation can significantly drop the CPU wall time by more than 50% at any gas superficial velocity.

ACKNOWLEDGMENTS

Computational resources were provided by HPC@POLITO, a project of Academic Computing within the Department of Control and Computer Engineering at the Politecnico di Torino (`http://www.hpc.polito.it`).

REFERENCES

BASHA, O.M., SEHABIAGUE, L., ABDEL-WAHAB, A. and MORSI, B.I. (2015). “Fischer-Tropsch Synthesis in Slurry Bubble Column Reactors: Experimental Investigations and Modeling - A Review”. *International Journal of Chemical Reactor Engineering*, **13(3)**, 201–288.

FLECK, S. and RZEHAK, R. (2019). “Investigation of bubble plume oscillations by Euler-Euler simulation”. *Chemical Engineering Science*, **207**, 853–861.

GEMELLO, L., CAPPELLO, V., AUGIER, F., MARCHISIO, D. and PLAIS, C. (2018). “CFD-based scale-up of hydrodynamics and mixing in bubble columns”. *Chemical Engineering Research and Design*, **136(69)**, 846–858.

HIBIKI, T. and ISHII, M. (2000). “Two-group interfacial area transport equations at bubbly-to-slug flow transition”. *Nuclear Engineering and Design*, **202(1)**, 39 – 76.

ISHII, M. and ZUBER, N. (1979). “Drag coefficient and relative velocity in bubbly, droplet or particulate flows”. *AIChE journal*, **25(5)**, 843–855.

KANTARCI, N., BORAK, F. and ULGEN, K.O. (2005). “Bubble column reactors”. *Process Biochemistry*, **40(7)**, 2263–2283.

MCCLURE, D.D., KAVANAGH, J.M., FLETCHER, D.F. and BARTON, G.W. (2017). “Experimental investigation into the drag volume fraction correction term for gas-liquid bubbly flows”. *Chemical Engineering Science*, **170**, 91–97.

NAUMANN, Z. and SCHILLER, L. (1935). “A drag coefficient correlation”. *Z Ver Deutsch Ing*, **77**, 318–323.

OpenCFD (). “OpenFOAM”. `https://openfoam.org`. [Online; accessed 20-October-2020].

RAIMUNDO, P.M. (2015). *Analysis and modelization of local hydrodynamics in bubble columns*. Thesis, Université Grenoble Alpes.

RANADE, V.V. (2002). *Computational flow modeling for chemical reactor engineering*. Academic Press.

ROGHAIR, I., LAU, Y.M., DEEN, N.G., SLAGTER, H.M., BALTUSSEN, M.W., Van Sint Annaland, M. and KUIPERS, J.A. (2011). “On the drag force of bubbles in bubble swarms at intermediate and high Reynolds numbers”. *Chemical Engineering Science*, **66(14)**, 3204–3211.

SHU, S., VIDAL, D., BERTRAND, F. and CHAOUKI, J. (2019). “Multiscale multiphase phenomena in bubble column reactors: A review”. *Renewable Energy*, **141**, 613–631.

SIMONNET, M., GENTRIC, C., OLMOS, E. and MIDOUX, N. (2008). “CFD simulation of the flow field in a bubble column reactor: Importance of the drag force formulation to describe regime transitions”. *Chemical Engineering and Processing: Process Intensification*, **47(9-10)**, 1726–1737.

SYED, A.H., BOULET, M., MELCHIORI, T. and LAVOIE, J.M. (2018). “CFD simulation of a slurry bubble column: Effect of population balance kernels”. *Computers and Fluids*, **175**, 167–179.

TABIB, M.V., ROY, S.A. and JOSHI, J.B. (2008). “CFD simulation of bubble column-An analysis of interphase forces and turbulence models”. *Chemical Engineering Journal*, **139(3)**, 589–614.

TOMIYAMA, A. (1998). “Struggle with computational bubble dynamics”. *Multiphase Science and Technology*, **10(4)**, 369–405.

VAN LEER, B. (1974). “Towards the ultimate conservative difference scheme. ii. monotonicity and conservation combined in a second-order scheme”. *Journal of Computational Physics*, **14(4)**, 361 – 370.

DIRECT NUMERICAL SIMULATION STUDY ON THE FREE LIQUID AREA IN LIQUID-PARTICLE AGGLOMERATES.

Evan MILACIC^{1*}, **Maike W. BALTUSSEN**^{1}, **J.A.M. KUIPERS**^{1}

^{1}Multiphase Reactors Group, Department of Chemical Engineering and Chemistry,

Eindhoven University of Technology, Postbus, 5600 MB Eindhoven, Netherlands

* E-mail: e.milacic@tue.nl

ABSTRACT

Multiphase flows often occur in intensified industrial processes and understanding these complex processes is instrumental in their design and optimisation. In gas-phase polymerisation reactors, the heat management is improved by injecting an inert liquid. However, the injected liquid also affects the collisional behaviour of the produced particles. The liquid can create agglomerates of particles due to cohesive forces, e.g. surface tension. The formation of these agglomerates can have a drastic effect on the efficiency of the process. To determine the lifetimes of the agglomerates, it is important to predict the evaporation rate of the liquid inside such an agglomerate. The evaporation rate of the liquid is dependent on the gas-liquid interface which can be studied using Direct Numerical Simulations (DNS), specifically a combination of a Volume of Fluid method and an Immersed Boundary method. The effect of contact angle and particle configuration on the interface area is studied in this work.
This study showed that the random particle configuration has a large impact on the interface area. Due to its random nature, the six investigated configurations are not sufficient to provide a meaningful average area. To determine the interface area, more different random configurations need to be investigated in order to provide a conclusive answer.

Keywords: Computational Fluid Dynamics, Direct Numerical Simulations, Combined Volume of Fluid Immersed Boundary Method, Contact angle model, Agglomerates .

NOMENCLATURE

Greek Symbols
ρ Mass density, $[^{kg}/_{m^3}]$
μ Dynamic viscosity, $[^{kg}/_{ms}]$
τ Stress tensor, $[Pa]$
σ Surface Tension, $[^{N}/_{m}]$
ε Fraction, $[-]$
Θ Contact Angle, $[-]$

Latin Symbols
p Pressure, $[Pa]$
$\mathbf{u}$ Velocity, $[^{m}/_{s}]$
t Time, $[s]$
Δt Time-step, $[s]$
g Gravitational acceleration, $[^{m}/_{s^2}]$
F Color function or phase fraction, $[-]$
$\hat{\mathbf{n}}$ Interface normal vector, m
N Number of cells, $[-]$
V Volume, $[m^3]$
D Diameter, $[m]$

Sub/superscripts
g Gas.
l Liquid.
s Solid.
i Index i.
j Index j.
d Droplet.
p Particle.
$*$ Intermediate.

INTRODUCTION

Understanding complex multiphase flows is important for industrial applications, either for the design or optimisation of processes. Studying the behaviour of multiphase flows on industrial scales however, has been challenging as small scale phenomena influence the large scale behaviour. Well known complex multiphase processes are, e.g. fluid catalytic cracking, granulation, spray drying, floatation of metal ores and gas-phase polymerisation.

This work focusses on the liquid injection in fluidized bed reactors under reactive conditions, specifically the condensed-mode operation of the gas-phase polymerisation reaction (Chinh and Dumain, 1991; Havas and Lalanne-Magne, 1994). The gas-phase polymerisation reaction is highly exothermic and the reactor temperature is limited by the melting point of the produced polymer. To increase the production capacity of the reactor, the excess heat is removed by injecting an inert liquid. The role of the liquid in the condensed-mode gas-phase polymerisation reactor is to improve the heat removal capacity through evaporation. The temperature in the reactor is thus controlled by the evaporation rate of the injected liquid.

The liquid in the bed is present under three forms: vapour, droplets and in contact with polymer particles. The vapour in the reactor has a small contribution to the cooling of the reactor compared to the liquid state. The droplets in the reactor have a short life-time as collisions with particles are inevitable due to the vigorous solids mixing.

The remaining liquid is in contact with the particles. The liquid will enable the particles to stick together in a so called agglomerate. These are clusters of particles held together by the cohesion forces of the injected liquid. The heat of reaction will gradually evaporate the liquid and reduce the size of the agglomerate.

Studying the effect of the agglomerates on the condensed-mode polymerisation process experimentally is very costly and does not allow for simple experimentation. An alternative to experiments is numerical modelling. Because computer models are often restricted with respect to either the size of the studied system or the level of detail that is resolved, a the multi-scale modelling approach has to be used to cover all time and length scales. This technique has been applied for many complex cases such as dense bubbly flows in industrial scale bubble columns and dense particle laden flows for fluidized beds (Deen *et al.*, 2004, 2012, 2014; Bauer and Eigenberger, 2001).

For example, a lab scale fluidized bed reactor can be studied using the Discrete Element Method (DEM). However, it is currently computationally too expensive to fully resolve the behaviour of the liquid inside the agglomerates. Thus the main focus of this work is to formulate closures in order to account for the effect of the liquid agglomerates. To include the effect of evaporation in agglomerates in DEM simulations, it is important to understand the time-scale of the liquid evaporation when encased with particles. To this end, Direct Numerical Simulations (DNS) are used to study the gas-liquid interface area in agglomerates for the prediction of evaporation rates. The effect of the number of particles in the agglomerate is studied along side the particle configuration and wetting properties.

MODEL DESCRIPTION

The model used in this work is based on the Volume of Fluid (VOF) method and Immersed Boundary (IB) method reported by (Baltussen *et al.*, 2017). It can accurately model three-phase systems involving fluid and solid interfaces.

Governing equations

The fluids are modelled using the one-fluid formulation, resulting in one set of mass and momentum conservation equations. The fluids are assumed to be Newtonian and incompressible.

Continuity equation:

$$\nabla \cdot \mathbf{u} = 0 \tag{1}$$

Momentum equation:

$$\rho\frac{\partial \mathbf{u}}{\partial t} + \rho\nabla\cdot(\mathbf{u}\mathbf{u}) = -\nabla p + \nabla\cdot\boldsymbol{\tau} + \rho\mathbf{g} + \mathbf{F}_\sigma \tag{2}$$

$\boldsymbol{\tau} = \mu\left[\nabla\mathbf{u} + (\nabla\mathbf{u})^T\right]$ is the fluid stress tensor. The effects of surface tension are included using $\mathbf{F}_\sigma$ as a volumetric source term acting on fluid interface. The density, ρ, and viscosity, μ, are calculated using linear and harmonic averaging, respectively (Prosperetti, 2002). $\mathbf{F}_\sigma$ is calculated using the Contiunum Surface Tension (CSF) method of (Brackbill *et al.*, 1992), equation 3. To reduce the effects of parasitic currents and to increase numerical stability for high density ratio systems, a density scaling is applied for this $\mathbf{F}_\sigma$. This method conserves the surface tension by symmetrically distributing the acceleration due to surface tension over the interface (Yokoi, 2014).

$$\mathbf{F}_\sigma = \frac{\rho}{\langle\rho\rangle}\sigma\kappa\hat{\mathbf{n}} \tag{3}$$

In this CSF method, κ is the surface curvature and $\hat{\mathbf{n}}$ the interface normal vector. The dynamics of the fluid-interface are captured using a VOF method where the fluid phase fractions are tracked with a color function (F). The movement of the interface is captured by advecting the color function with the local fluid velocity (equation 4).

$$\frac{\partial F}{\partial t} + \mathbf{u}\cdot\nabla F = 0 \tag{4}$$

Equation 4 is solved using a geometrical advection scheme based on Piecewise Linear Interface Calculation (PLIC) by Youngs (1982). To reduce numerical diffusion and maintain a high degree of mass conservation, the integration of equation 4 is based on a pseudo-Lagrangian geometric advection scheme, more information on this advection can be found in van Sint Annaland *et al.* (2005).

To calculate the normals, the phase fraction is smoothed using a polynomial proposed by Deen *et al.* (2004). However when the smoothing is performed in close proximity of the solid interface, non-physical results are obtained. This is prevented by extending the phase fraction field into the solid region (Sussman, 2001). In this work, the phase fraction extension is 4 grid-cells, more details on the implementation can be found in Patel *et al.* (2017).

The fluid-solid interactions are represented by an implicit second-order accurate IB method that applies no-slip boundary conditions (Deen *et al.*, 2009; Das *et al.*, 2016). A unidirectional quadratic interpolation polynomial is used to express the velocities near the boundaries to satisfy the no-slip boundary condition at the solid interface. A detailed explanation of this method can be found by Deen *et al.* (2009) and Das *et al.* (2016). To model the interactions of the fluid interface with the solid interface, a contact angle model is used. The contact angle is applied to the normal of the gas-liquid interface as a boundary condition. Due to the low Reynolds range used in this work, the model developed by Voinov (1976) and Cox (1986) is applied for changing the normal at the contact line. A thorough explanation on the method can be found in Patel *et al.* (2017).

Numerical method

The VOF-IB method solves the mass and momentum conservation equations (equations 1 and 2) on a staggered grid. The diffusion term is calculated using a second order central difference scheme, which is treated implicitly except for the mixed derivatives. The convection terms in the momentum equations are discretised using a second order flux delimited Barton scheme and solved implicitly. To solve the momentum equation, a fractional step method for pressure-velocity coupling is used. The intermediate velocity is calculated in the first step based on the momentum equation, excluding the pressure gradient. In the second step, the pressure Poisson equation (equation 5) is solved to compute the pressure correction term which is then used to compute the velocities at the next time step (equation 6).

$$\nabla\cdot\left\{\frac{\Delta t}{\rho}\nabla(\delta p)\right\} = \nabla\cdot\mathbf{u}^* \tag{5}$$

$$\mathbf{u}^{k+1} = \mathbf{u}^* - \frac{\Delta t}{\rho}\nabla(\delta p) \tag{6}$$

Verification and Validation

The model used in this work has been validated and verified in literature. Information on the implementation and performance of the IB method can be found in Deen *et al.* (2009, 2012). An extensive explanation of the VOF method can be found in van Sint Annaland *et al.* (2005) and Baltussen *et al.* (2014). The IBM-VOF coupling was reported by Patel *et al.* (2017). Because this study will use the same methods and code implementations, the model will not be verified and validated again.

SIMULATION AND DATA ANALYSIS

In this work, DNS was used to study the gas-liquid area of a droplet caught between a cluster of particles, by allowing the liquid to reach its stable configuration. The sections below describe the details of the simulations and the calculation of the free liquid area and the wetted solid area.

Simulation set-up

Under normal conditions, the particles in an agglomerate have a random packing. This random configuration was obtained by the creation of a packed particle bed generated with a DEM model. The mono-dispersed particles were deposited into the domain and shaken until a solids fraction of $\varepsilon_s = 0.55$ was obtained. This resulted in a cube of approximately 8000 particles in a close random packing.

To extract the particle positions from this packed bed, a subsection of the bed was taken and the local porosity was calculated. Next, a sphere was inserted into the subsection of which the overlap between the sphere and the particles was subtracted from its shape. By moving the subsection of the bed through the length, width and height, a set of domains was acquired having the same local porosity and volume of the inserted sphere.

The coordinates of these particles and sphere were used to set-up the solid and fluid-interfaces in the simulation domain. This effort was made to ensure that the outcome of the simulations are independent of the liquid volume and the local porosity of the particles.

The simulation time was taken such that the liquid reached a stable configuration, i.e. when the liquid interface is no longer moving. Wetting properties of the system have tremendous impact on the spreading behaviour of the liquid between particles, thus two contact angles (Θ) were used in the simulations. For both the contact angles, six random packings were simulated. The details of the simulations are listed below in table 1, including the particle diameter (D_p) and liquid volume (V_d).

Table 1: Simulation Details.

Property	Value	Unit
N_x, N_y, N_z	400	(-)
dx, dy, dz	5e-6	m
dt	5e-7	s
ρ_g	1	kg/m^3
μ_g	1e-5	Pas
ρ_l	1e3	kg/m^3
μ_l	1e-3	Pas
σ	7.2e-2	N/m
V_d	1e-10	m^3
D_p	2e-4	m
ε_s	0.55	(-)
Θ	30^o & 60^o	(-)

Data Analysis

To retrieve the gas-liquid interface area, the surface area of the interface in each cell is calculated based on the PLIC representation. By calculating the intersections of the PLIC interface with the cell edges, a polygon is formed, which is used to calculate the area. By summing the areas of all the interface cells, the total gas-liquid interface area is obtained. Due to the nature of the IB interface, the wetted area of the solids is not available during the simulations. To obtain the wetted area, the intersection between the solid sphere and cell is approximated using the intersections on the cell edges and IB surface. This method provides an accurate calculation of the sphere surface with less than 1% error with 5 cells per diameter of the particle. To properly model the fluid-solid interactions, 20 cells per particle diameter are used, which results in approximately an error of 0.3 % in the fluid-solid surface area calculation. To obtain the wetted area, the solid surface area per cell is multiplied with the fluid phase fraction. During the calculation of the wetted area, the particles whom are in contact with the droplet are registered, providing the number of wetted particles.

RESULTS

Figure 1 shows the resulting gas-liquid interface area for both contact angles, versus the number of particles in contact with the liquid phase. The gas-liquid area is normalised by the area of a spherical droplet with equivalent volume. The varying colors indicate the different random particle configurations. The interface area seems to increase with increasing number of wetted particles with exception for the cases with 19 wetted particles. The difference in average area between the contact angles is expected: a lower contact angle will spread out further with a thinner liquid layer, resulting in a larger gas-liquid interface area.

Figure 2 shows the contact area between the liquid phase and particles, normalised by the area of a single particle.Similarly to the gas-liquid area, the contact area seems to be slightly dependent on the number of wetted particles, but the configurations with 19 or more wetted particles do not fit the trend. In addition, the contact angle seems to have a well defined effect on the contact area, as the data for the higher contact angle seems to be reduced with a factor 0.83.

In figures 1 and 2, there are two particle configurations with the same amount of wetted particles (19). The figures show that there is a drastic difference in both gas-liquid interface area and wetted contact area between those two different configurations. Figures 3 and 4 show both configurations rotated

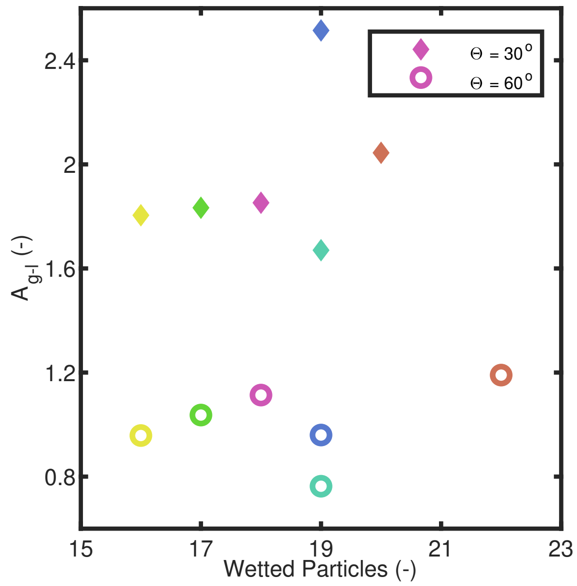

Figure 1: Free liquid area in a cluster of particles.

along an axis. Note that only the particles in contact with the liquid are visualised. Figure 3 has both the highest gas-liquid interface area and the highest contact area. This seems mainly due to the more concave shape of the agglomerate, where a cavity is observed, whereas the shape of the agglomerate from figure 4 is more convex. This suggests that the particle configuration has a strong influence on the wetting outcome of the liquid. To gain insight on this influence, more random particle configurations should be simulated.

In coarse grained models, the gas-liquid interface area is used to predict the evaporation rate. We expected the gas-liquid interface area to be a function of: the liquid to particle volume ratio, the contact angle and the number of particles in the agglomerate. From the figures 1 and 4, it can be concluded that the particle configuration is also an important parameter to take into account. Due to the random nature of the particle configuration, the average gas-liquid interface area is determined by a normal distribution. The normal distribution can be used to provide an average interface area independent on the particle configuration but dependent on the other process parameters, such as the contact angle and liquid to particle volume. However, to determine the mean and variance of the distribution, the sample size needs to be larger.

CONCLUSION

The gas-liquid area in agglomerates is dependent on the con-tact angle of the multiphase system, as expected. However, the random particle configuration seems to dictate the spreading outcome more than the amount of wetted particles. The random nature of this configuration suggests a normal distribution, and thus to extract an average gas-liquid interface area and its variance. With the current number of simulations, it is not possible to determine an average gas-liquid interface area independent of particle configuration.

ACKNOWLEDGEMENT AND AFFILIATION:

This work is part of the Research Programme of the Dutch Polymer Institute (DPI), PO Box 902, 5600 AX, Eindhoven, The Netherlands, project nr. #803.

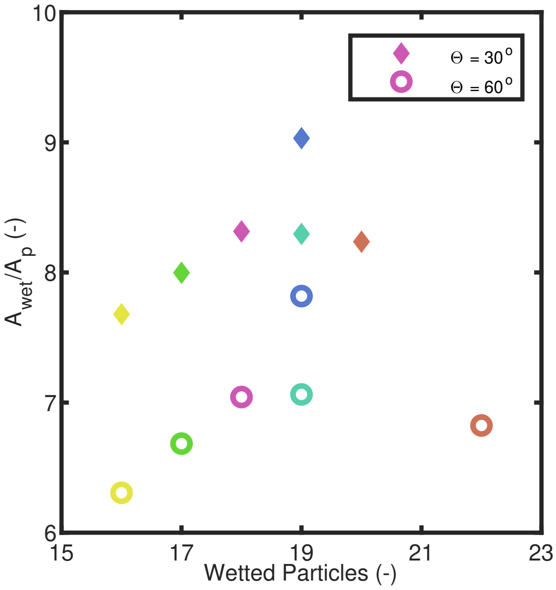

Figure 2: Contact area between the liquid and the particles.

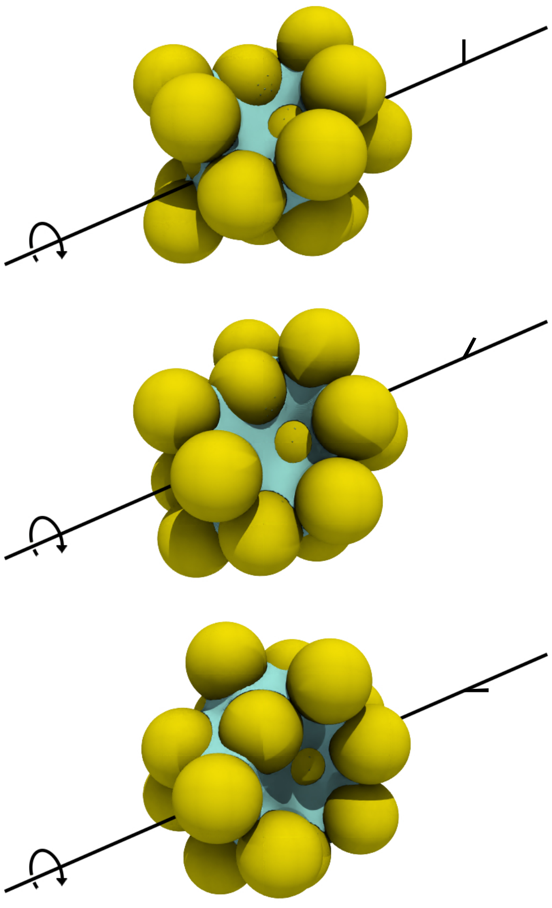

Figure 3: Agglomerate with 19 wetted particles rotated on an axis. This agglomerate show a concave shape, resulting in a larger gas-liquid interface area.

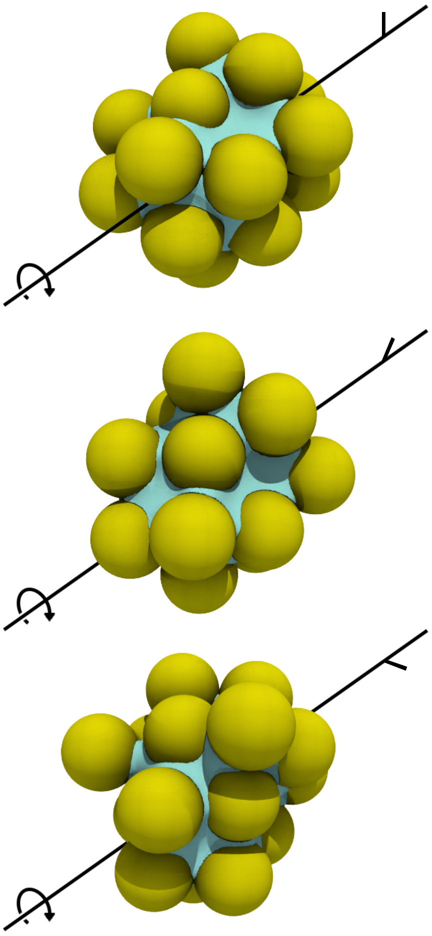

Figure 4: Agglomerate with 19 wetted particles rotated on an axis. This agglomerate show a convex shape, resulting in a smaller gas-liquid interface area.

REFERENCES

BALTUSSEN, M.W., KUIPERS, J.A.M. and DEEN, N.G. (2014). "A critical comparison of surface tension models for the volume of fluid method". *Chemical Engineering Science*, **109**, 65–74.

BALTUSSEN, M.W., SEGERS, Q.I.E., KUIPERS, J.A.M. and DEEN, N.G. (2017). "Cutting bubbles with a single wire". *Chemical Engineering Science*, **157**, 138–146.

BAUER, M. and EIGENBERGER, G. (2001). "Multiscale modeling of hydrodynamics, mass transfer and reaction in bubble column reactors". *Chemical engineering science*, **56(3)**, 1067–1074.

BRACKBILL, J.U., KOTHE, D.B. and ZEMACH, C. (1992). "A continuum method for modeling surface tension". *Journal of computational physics*, **100(2)**, 335–354.

CHINH, J.C. and DUMAIN, A. (1991). "Process for the gas-phase polymerization of olefins in a fluidized-bed reactor".

COX, R.G. (1986). "The dynamics of the spreading of liquids on a solid surface. part 1. viscous flow". *Journal of Fluid Mechanics*, **168**, 169–194.

DAS, S., DEEN, N.G. and KUIPERS, J.A.M. (2016). "Direct numerical simulation for flow and heat transfer through random open-cell solid foams: Development of an ibm based cfd model". *Catalysis Today*, **273**, 140–150.

DEEN, N., PETERS, E., PADDING, J. and KUIPERS, J. (2014). "Review of direct numerical simulation of fluid–particle mass, momentum and heat transfer in dense gas–solid flows". *Chemical Engineering Science*, **116**, 710–724.

DEEN, N.G., VAN SINT ANNALAND, M. and KUIPERS, J.A.M. (2004). "Multi-scale modeling of dispersed gas–liquid two-phase flow". *Chemical Engineering Science*, **59(8-9)**, 1853–1861.

DEEN, N.G., VAN SINT ANNALAND, M. and KUIPERS, J.A.M. (2009). "Direct numerical simulation of complex multi-fluid flows using a combined front tracking and immersed boundary method". *Chemical Engineering Science*, **64(9)**, 2186–2201.

DEEN, N.G., KRIEBITZSCH, S.H.L., VAN DER HOEF, M.A. and KUIPERS, J.A.M. (2012). "Direct numerical simulation of flow and heat transfer in dense fluid–particle systems". *Chemical Engineering Science*, **81**, 329–344.

HAVAS, L. and LALANNE-MAGNE, C. (1994). "Gas phase polymerisation process".

PATEL, H.V., DAS, S., KUIPERS, J.A.M., PADDING, J.T. and PETERS, E.A.J.F. (2017). "A coupled Volume of Fluid and Immersed Boundary Method for simulating 3D multiphase flows with contact line dynamics in complex geometries". *Chemical Engineering Science*, **166**, 28–41.

PROSPERETTI, A. (2002). "Navier-stokes numerical algorithms for free-surface flow computations: An overview". *Drop-Surface Interactions*, 237–257. Springer.

SUSSMAN, M. (2001). "An adaptive mesh algorithm for free surface flows in general geometries". *Adaptive Method of Lines*, 207–231.

VAN SINT ANNALAND, M., DEEN, N.G. and KUIPERS, J.A.M. (2005). "Numerical simulation of gas bubbles behaviour using a three-dimensional volume of fluid method". *Chemical Engineering Science*, **60**, 2999–3011.

VOINOV, O.V. (1976). "Hydrodynamics of wetting". *Fluid Dynamics*, **11(5)**, 714–721.

YOKOI, K. (2014). "A density-scaled continuum surface force model within a balanced force formulation". *Journal of Computational Physics*, **278**, 221–228.

YOUNGS, D.L. (1982). "Time-dependent multi-material flow with large fluid distortion". *Numerical Methods for Fluid Dynamics*.

14th International Conference on CFD in Oil & Gas, Metallurgical and Process Industries
SINTEF, Trondheim, NORWAY
October 12-14, 2020

MODELLING OF WAX DEPOSITION IN OIL PIPES: A DISPERSED MULTIPHASE TURBULENT FLOW APPROACH

Federico MUNICCHI[1]*, **Ismail El MELLAS**[2], **Matteo ICARDI**[1], **Mirco MAGNINI**[2]
[1]School of Mathematical Sciences, University of Nottingham, Nottingham NG72RD, UK
[2]School of Engineering, University of Nottingham, Nottingham NG72RD, UK

* E-mail: federico.municchi@nottingham.ac.uk

ABSTRACT

Crude oils are complex mixtures of hydrocarbons including high molecular weight paraffin waxes. When a "waxy" crude oil flows through a cold pipeline whose temperature is below the wax appearance temperature, e.g. in subsea transportation systems, heavy paraffins separate and deposit on the pipe walls. The available prediction methods for wax deposition are essentially empiric, particularly regarding the description of the fouling deposition and removal processes, which depend on the fluid dynamic interaction between the deposit layer and the bulk flow. In this work, we present a novel theoretical and numerical model for predicting wax deposition in oil pipes and, more generally, coagulation/deposition processes for a wide range of applications. Unlike other models existing in literature, which are mostly based on a separated two-fluid description of the oil/wax-oil flow and phase-change represented as a deposition process, our model is based on a mixture description, where wax is considered as a suspended phase immersed in crude-oil. Coagulation and dissolution phenomena are modelled with an associated first order kinetic reaction which allows to study arbitrarily complex geometries. Wax ageing (hardening) is solved with a dynamic equation for the viscosity. We show how this model can be implemented in the open-source C++ library OpenFOAM and we present key results for deposition in a variety of pipe shapes.

Keywords: CFD, multiphase flows, deposition, asphaltenes .

NOMENCLATURE

Greek Symbols
ϕ Solid volume fraction, $[-]$
ν Kinematic viscosity, $[m^2/s]$
α Heat diffusivity, $[m^2/s]$
ϕ_m Maximum solid volume fraction, $[-]$
τ_s Settling time, $[s]$
τ_c Characteristic coagulation time, $[s]$
τ_d Characteristic dissolution time, $[s]$
β Expansion factor, $[K^{-1}]$
θ Hardening time, $[s^{-1}]$
σ Shear-breaking time scale, $[s]$
$\dot{\gamma}$ Strain rate, $[s^{-1}]$
λ Ageing factor, $[-]$

Latin Symbols
$\boldsymbol{u}$ Velocity, $[m/s]$.
p Pressure, $m^2/s^2]$.
T Temperature, $[K]$.
c Molar concentration, $[-]$.
D_c Diffusion coefficient of c, $[m^2/s]$.
$\dot{S}$ Deposition rate, s^{-1}.

Sub/superscripts
s Solid.
o Oil.
t Turbulent.
eq Equilibrium .
ref Reference .
mix Mixture .

INTRODUCTION

Wax deposition represents a significant flow assurance problem for the oil and gas industry because it can lead to restriction and then blockage of oil reservoir formations, pipelines, and process equipment. Crude oil is a complex mixture of saturates (paraffin/waxes), aromatics, naphthenes, asphaltenes, and resins. Among these components, high molecular weight paraffin (waxes) and asphaltenes are typically the main cause for production and transportation problems in subsea pipeline systems. At reservoir temperatures $(70-150\,^\circ\mathrm{C})$ and pressures $(50-100\,\mathrm{MPa})$, wax molecules can be found dissolved in the crude oil. However, during transportation crude oil flows through pipelines located in cooler environments, e.g. in sub-sea pipelines resting on the ocean floor at temperatures of $4\,^\circ\mathrm{C}$. Owing to the thermal losses to the surroundings, the temperature of oil can quickly decrease below the cloud point temperature (or wax appearance temperature, WAT). The solubility of wax decreases drastically as the temperature decreases, and wax molecules start to precipitate out of the crude oil (Singh *et al.*, 2000). Waxes have long molecular chains and they usually form stable wax crystals and a solid network. The network trapped liquid is like a vector for further diffusion of heavier hydrocarbons molecules that appear with the counter diffusion of the trapped oil out of the deposit. A large number of mechanisms have been suggested to be responsible for the deposition of solids from waxy crude oil mixtures, including molecular diffusion, Soret diffusion, Brownian motion, shear dispersion, and gravity settling (Burger *et al.*, 1981; Azevedo and Teixeira, 2003). Molecular diffusion has been often regarded as the main deposition mechanism and, accordingly, the deposition rate is calculated as proportional to the concentration gradient at the wall (Burger *et al.*, 1981; Svendsen, 1993). Many different models to predict the build-up of the deposit layer on the cold wall of a pipeline have been proposed, with different levels of sophistication, see Magnini and Matar (2019) for a recent review. These models are mainly one-dimensional, and predict the thickness of the wax layer as a function of time along the pipeline, based on a balance of deposition and removal terms. Deposition is usually modelled following molecular diffusion, and therefore calculating the deposition rate according to the gradient of the fluid temperature at the wall. The latter is reconstructed according to simplified fluid dynamics model of the flow in the pipe, assuming laminar or turbulent velocity profiles (Svendsen, 1993; Ramirez-Jaramillo *et al.*, 2001; Singh *et al.*, 2001). The deposit removal is due to the shear exerted by the fluid and is typically modelled empirically, by means of a negative source term with attempts to correlate this to wall shear, deposit thickness or time (Correra *et al.*, 2007; Eskin *et al.*, 2013; Ramirez-Jaramillo *et al.*, 2004; Solaimany Nazar *et al.*, 2005). In particular, time is an important factor in the build-up of the deposit because it makes the deposit harder, a phenomenon known as "ageing". Although one-dimensional models have the great advantage of being little time-consuming to run, their drawback is that the mechanisms of deposition and removal are poorly linked to the actual fluid mechanics and heat transfer characteristics of the flow. Direct numerical simulations promise to be a very effective tool to investigate the fundamental mass, momentum and energy exchanges leading to wax deposition and removal, however the only approach published so far (Magnini and Matar, 2019) utilised interface-resolving simulations using a time-explicit Volume-Of-Fluid method, which dramatically limits the temporal duration of the flow that can be simulated.

This work represents a step forward in the direction of direct numerical simulations of the crude-oil flow and resulting wax deposition, but using a more efficient and less time-consuming technique to deal with the different phases present in the flow. Furthermore, we introduce a novel rheological model for the viscosity of the deposited mass which accounts for ageing effects upon solution of a transport equation for the ageing time.

MODEL DESCRIPTION

In our model, we employ a mixture model similar to the suspension balance model (Nott and Brady, 1994) to describe the suspension of solid particles of coagulated wax in the suspending crude oil as an effective fluid. Therefore, we introduce a phase volume fraction ϕ representing the volume occupied by the solid particles with respect to the total volume of the mixture, that we assume incompressible.

Momentum transport

The mixture velocity is then defined as:

$$\boldsymbol{u} = \phi \boldsymbol{u}_s + (1-\phi)\boldsymbol{u}_o \,, \tag{1}$$

where $\boldsymbol{u}_s$ and $\boldsymbol{u}_o$ are the solid and crude oil velocities respectively. Then, the momentum conservation equation for the whole mixture reads:

$$\frac{\partial \boldsymbol{u}}{\partial t} + \boldsymbol{\nabla}\cdot(\boldsymbol{u}\boldsymbol{u}) = -\boldsymbol{\nabla} p + \boldsymbol{\nabla}\cdot\left[\nu_{\text{mix}}\left(\boldsymbol{\nabla}\boldsymbol{u} + \boldsymbol{\nabla}^T\boldsymbol{u}\right)\right] \,, \tag{2}$$

together with the incompressibility condition;

$$\boldsymbol{\nabla}\cdot\boldsymbol{u} = 0 \,. \tag{3}$$

Notice that in equation 2 we denoted the pressure field as p and the mixture kinematic viscosity as ν_{mix}. Hence, equations 2 and 3 provide a global description of the effective fluid, where phase-specific forces and fluxes like drag and gravity currents cancel out. The only term that really plays a role in representing the multiphase system is the mixture density ν_{mix}, which we express as a linear combination of turbulent and suspension contribution:

$$\nu_{\text{mix}} = \nu_t + \nu_s \tag{4}$$

where ν_t is the usual turbulent viscosity and ν_s is the added viscosity due to the suspended phase. In this work, we employ a RANS standard κ–ϵ model (Launder and Spalding, 1974) to model the turbulence. A key feature of asphaltenes is their tendency to agglomerate resulting in the formation of solid structures that becomes more impermeable with time. This process is called "ageing", and it will be discussed in a later section.

Concerning the solid phase, we are not solving a separate momentum transport equation. Instead, we assume that the settling time of the particles is sufficiently small that its velocity can be directly computed from the mixture velocity, such that the slip velocity is given by (Ferry *et al.*, 2003):

$$\boldsymbol{u}_{\text{slip}} = \tau_s\left(\frac{\partial \boldsymbol{u}}{\partial t} + \boldsymbol{u}\cdot\boldsymbol{\nabla}\boldsymbol{u}\right) \,. \tag{5}$$

Notice that equation 5 is only valid under the assumption that no gravitational forces are present, and its overall effect is that of relaxing $\boldsymbol{u}_{\text{slip}}$ to zero. Consequently, our model considers only small deviations between the velocities of the two phases.

Within this work, we will therefore assume that the oil and solid velocities can be computed from:

$$\boldsymbol{u}_s = \boldsymbol{u}_o + \boldsymbol{u}_{\text{slip}} \,, \tag{6}$$

where $\boldsymbol{u}_{\text{slip}}$ is a small deviation. Hence, the mixture velocity is given by:

$$\boldsymbol{u} = \boldsymbol{u}_s - (1-\phi)\boldsymbol{u}_{\text{slip}} = \boldsymbol{u}_o + \phi\boldsymbol{u}_{\text{slip}} \,. \tag{7}$$

Rearranging leads to the expressions:

$$\boldsymbol{u}_s = \boldsymbol{u} + (1-\phi)\boldsymbol{u}_{\text{slip}} \,, \tag{8}$$

$$\boldsymbol{u}_o = \boldsymbol{u} - \phi\boldsymbol{u}_{\text{slip}} \,. \tag{9}$$

Species transport and thermodynamics

We assume that the transport properties are not depending on the temperature T and that the suspension flow is in thermal equilibrium (i.e., the temperature of the solid and the liquid phases are approximately the same) as is often the case in non-Brownian suspensions (Dbouk, 2018). Thus, we can write the transport equation for the temperature as:

$$\frac{\partial T}{\partial t} + \boldsymbol{u}\cdot\boldsymbol{\nabla} T = \alpha\nabla^2 T \,, \tag{10}$$

Where α is the heat diffusivity of the mixture, which we assume equal to that of crude oil.

As a consequence of mass conservation, an advection equation is employed to evolve the solid volume concentration ϕ:

$$\frac{\partial \phi}{\partial t} + \boldsymbol{\nabla}\cdot(\boldsymbol{u}_s\phi) = \dot{S}(1-\phi) \,, \tag{11}$$

where $\dot{S}$ is the creation-destruction term due to coagulation or dissolution and it is a function of the temperature T and

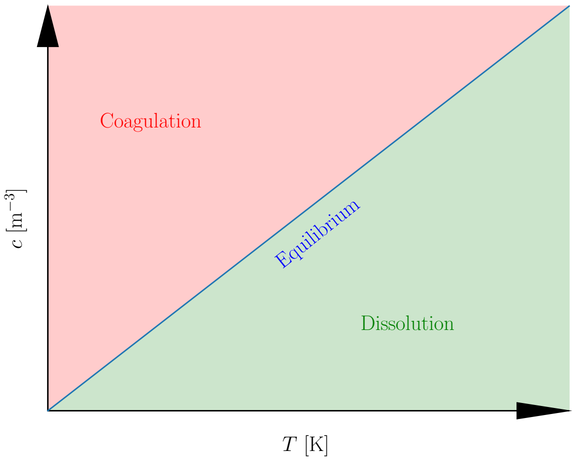

Figure 1: Schematic representation of the equilibrium change as a function of temperature and concentration.

the concentration of asphaltenes c in the crude oil. At the heart of our model, there is the expression for $\dot{S}$:

$$\dot{S}(c,T) = \begin{cases} \dfrac{1}{\tau_c}\left(c - c_{eq}(T)\right) & \text{if } c > c_{eq}(T) \\ \dfrac{\phi}{\tau_d}\left(c - c_{eq}(T)\right) & \text{if } c < c_{eq}(T) \end{cases} \tag{12}$$

where c is the molar concentration of asphaltenes in the crude oil, while τ_d and τ_r are the characteristic time scales associated with coagulation and dissolution. For simplicity, we also assume that the equilibrium concentration can be represented as a linear function of the temperature:

$$c_{\text{eq}} = c_{\text{ref}} + \beta\left(T - T_{\text{ref}}\right), \tag{13}$$

where the subscript ref indicates reference quantities.

As shown in Figure 1, our mathematical model predicts that coagulation occurs at lower temperatures, while the asphaltenes tend to dissolve into the fluid phase at higher temperatures.

Clearly, our model requires the solution of the transport equation for the molar concentration c in the crude oil:

$$\frac{\partial\left(1-\phi\right)c}{\partial t} + \boldsymbol{\nabla}\cdot\left[\left(1-\phi\right)\boldsymbol{u}_o c\right] = \boldsymbol{\nabla}\cdot\left[\left(1-\phi\right)D_c\boldsymbol{\nabla}c\right] - \dot{S}\left(1-\phi\right), \tag{14}$$

where D_c is the diffusion coefficient of asphaltenes in crude oil. Notice that summing Equations 14 and 11 the source term disappears since the total mass transferred between the phases is conserved by our model.

Deposit ageing and hardening

It is well known that wax deposits exhibit non local (in time) phenomena that lead to dramatic changes in their material properties (Hewitt, 2015). The most noticeable of these is hardening. The thermal gradient across the walls and the deposit layer result in an internal mass flux which leads to a continuous increase of the solid particles content. This leads to a significant hardening of the sub layer with time, i.e. the aging process.

Following the approach of Sileri *et al.* (2011), we model the viscosity of the solid phase as the product of the classic Maron-Pierce viscosity for suspensions of spheres (Maron and Pierce, 1956) with an ageing term (Roussel N, 2004):

$$\nu_s = \nu\left(\frac{\phi_m}{\phi_m - \phi}\right)^2\left(1 + \lambda\phi\right), \tag{15}$$

where ν is the laminar kinematic viscosity of crude oil, ϕ_m is the maximum packing fraction of the solid phase (set equal to 1). λ is a structure parameter that describes the iteration of network of wax crystals.

The structure parameter contains the flow history and it is obtained from the rivalry of two opposite behaviours, a structuration process where the crystals are spontaneously formed and a de-structuration process which causes a continued removal of the crystals network.

In our work, we propose a transport equation for the structure parameter:

$$\frac{\partial\lambda}{\partial t} + \boldsymbol{\nabla}\cdot\left(\phi\boldsymbol{u}_s\lambda\right) = \phi\left(\frac{1}{\theta} - \sigma\dot{\gamma}\lambda\right). \tag{16}$$

The last term in equation 16 follows the expression proposed by Huynh *et al.* (2005) and Coussot *et al.* (2005), where the parameters σ and θ control the generation and destruction of λ. Equation 16 allows to properly model the ageing process in a fluid domain, where the information regarding the residence time of the particulate is transported by the mixture.

Numerical solution

We developed an application in the open-source finite volume library OpenFOAM® to solve the governing equations of our model. We employ a PIMPLE algorithm (fundamentally a fixed point iteration) to couple the seven transport equations in a segregated manner. For each time step, the application performs the operations below:

Numerical procedure adopted to solve the model equations:

1. Update the viscosity ν_{mix} using equation 4;
2. Assemble the velocity matrix and solve for p using the PISO algorithm (Issa, 1986);
3. Solve for T using equation 10;
4. Update c_{eq} (equation 13) and compute $\dot{S}$ (equation 12) using the actual value of c;
5. Update $\boldsymbol{u}_{\text{slip}}$ using equation 5 and solve for ϕ using equation 11;
6. Solve for c using equation 14;
7. Solve for λ using equation 16;
8. Proceed to the next time step if the convergence criteria are satisfied. Otherwise, repeat from point 1.

Convergence criteria are specified as thresholds on the residuals for each field equal to 10^{-5}. We found this procedure capable of producing stable solutions in a short time and without convergence issues. Laplace operators are discretised using linear schemes, while divergences are discretised using linear upwind schemes. One noticeable exception is the divergence in the equation for ϕ that we discretised using a van Leer scheme bounded between zero and one to improve the roboustness of the algorithm. All time derivatives where discretised using a second order backward finite difference scheme.

RESULTS

In order to illustrate the usage of the proposed model, we will first calibrate the values of τ_c and τ_d using the experiments of Singh *et al.* (2017). Subsequently, we show how the model can be applied to study the dynamics of deposition in oil pipes. Finally, we will investigate the effects of ageing.

In all simulations, the computational domain consists in a cylinder with diameter D (40 cells) and length L (50 cells). Due to the symmetry of the problem (we assume that gravity does not play a significant role) we employ a structured axial-symmetric grid to represent the cylindrical pipe. In order to resolve the boundary layer and predicting the onset of wall deposition, we graded the mesh spacing such that the grid is finer at the pipe wall.

Boundary conditions

We impose a fixed velocity and temperature, at the inlet, where we also set volume concentration of asphaltenes to 1 and ϕ to zero. We assume fully developed fields (zero gradient) at the outlet. At the wall, we employ a fixed temperature condition and a no slip velocity condition, while a zero gradient condition is imposed for the concentration of asphalthenes. The material properties employed in this work are listed in Table 1.

Table 1: List of material properties employed

Property	Symbol	Units	Value
Kinematic viscosity	ν	[m^2/s]	0.01051
Diffusion coefficient	D_c	[m^2/s]	10^{-7}
Reference temperature	T_{ref}	[K]	319
Initial temperature	T_i	[K]	293
Particle settling time	τ_s	[s]	10^{-32}
Maximum solid volume fraction	ϕ_m	[-]	1
Characteristic coagulation time	τ_c	[s]	$5 \cdot 10^2$
Characteristic dissolution time	τ_d	[s]	10^{-3}
Thermal diffusivity	α	[m^2/s]	0.134
Expansion factor	β	[1/ K]	0.65
Viscosity destruction term	σ	[-]	0.65
Viscosity hardening coefficient	θ	[s]	0.5

Calibration of the coagulation and dissolution rates

Table 2: Initial conditions and parameters for the calibration against Singh *et al.* (2017)

D $[m]$	$\boldsymbol{u}_{in}$ $[{}^m/_s]$	T_{in} $[K]$	T_w $[K]$	σ $[{}^1/_s]$	θ $[-]$
0.0165	1.83	298	289	0	0

To obtain appropriate values for the coagulation and dissolution rates, we investigate a wide range of values of τ_c and τ_d in the absence of ageing. The predicted deposition rate is compared against results from Singh *et al.* (2017) to find the values that give the best matching. Notice that assumption of absence of ageing effects is only justified if we look at the first seconds of the deposition process. Results from Singh *et al.* (2017) show that the deposition rate approaches an asymptotic linear trend after an initial transient. We therefore calibrate τ_c and τ_d to closely match that value, as the nonlinear transient would require a model with multiple time scales, like that proposed by Municchi and Icardi (2020). Here, we are interested in capturing the linear mode only.

In Singh *et al.* (2017), a wax deposition experiment was conducted using a Garden Banks condensate as operating fluid, circulated in turbulent flow conditions. All the relevant parameters they employed are collected in Table 2.

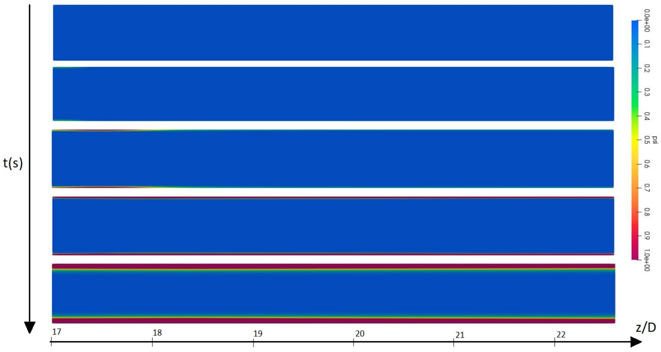

Figure 2: Evolution in time of the deposition

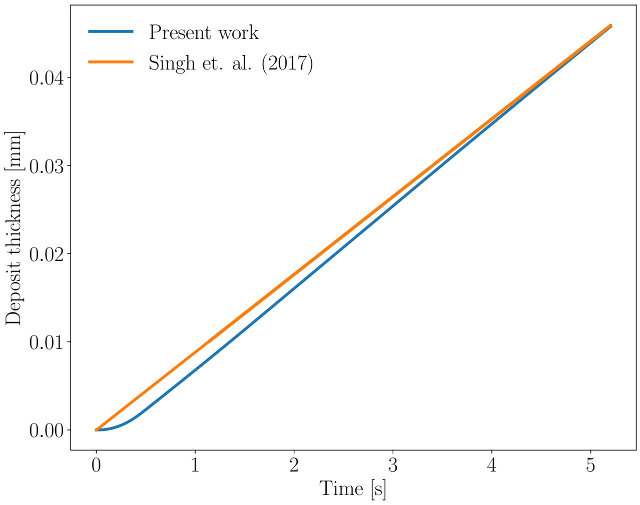

Figure 3: Deposition rate as predicted by our simulation and measured by Singh *et al.* (2017)

Figure 2 shows the evolution in time of the deposit, represented by the field ϕ. We notice that a layer of substantial deposit gradually starts to agglomerate, and attaches to the wall as a consequence of the radial temperature gradient. Therefore, the model predicts the correct physical behaviour of the system.

The dynamics of the model works as follows: particles are forming based on the difference between c and c_{eq}, which is a function of the temperature. Once formed, the particles alter the fluid viscosity increasing the resistance to the flow. Large clusters of particles forming in the middle of the channel will be advected downstream, while layers forming at the wall will continue to grow as they reduce the already small velocity field in that region. On the time-scale of the layer growth, one can observe that a sharp interface is forming between the almost clear fluid in the bulk and the solid formation growing from the wall.

The rate of mass deposition $\dot{S}$ is negligible (compared to the advective flux) everywhere except at the interface between the two phases. After a time $t = 10s$, the average thickness of the deposit layer is approximately persistent, and the flow reaches a steady-state. Notice that this would be different if we included the effect of ageing in this simulation.

The reduction in the cross section of the pipe causes the flow field to accelerate up to five times the inlet velocity. Another phenomenon that occurs, is the formation of small waves when the deposit film becomes sufficiently thick, and can therefore detach from the fluid downstream. However, the flow within the travelling waves exhibits a substantially larger speed depending on the height of the wave, and it may reach values as high as $0.15 m/s$, with the waves “surfing” over an almost sluggish layer of deposit. This is a numerical artifact and not a physical phenomenon (Magnini and Matar, 2019). The growth rate can be defined as the time variation of the deposit height h in the radial direction $\hat{r}$:

$$\dot{h} = (\boldsymbol{u} \cdot \hat{r})(\boldsymbol{\nabla}\phi \cdot \hat{r}). \tag{17}$$

Figure 3 shows the average thickness of wax long the pipe in time, demonstrating that the model is capable to obtain good agreement with experimental results.

Parametric Study

We now explore a limited range of parameters and discuss their repercussions on the wax deposition and detach process. We investigate the effects of the inlet average crude oil velocity, channel diameter, ageing process and inlet crude oil temperature. Table 3 shows the different scenarios we explored.

Table 3: List of operation conditions we probed in the parametric study

Case	D $[m]$	$\boldsymbol{u}_{\text{in}}$ $[^m/_s]$	T_{in} $[K]$	T_{w} $[K]$	σ $[^1/_s]$	θ $[-]$
1	0.0165	0.092	298	289	0	0
2	0.0165	3.66	298	289	0	0
3	0.001	1.83	298	289	0	0
4	0.1	1.83	298	289	0	0
7	0.0165	1.83	298	289	0.1	0.1
8	0.0165	1.83	298	289	1	0.001

Effect of the velocity field

Figure 4 shows that during the early stage of wax deposition the deposition rate decreases with the Reynolds number because of the consequent increase in the Péclet number. Higher velocity fields also increase detachment and transport downstream, leading to the formation of a thinner layer of deposit.

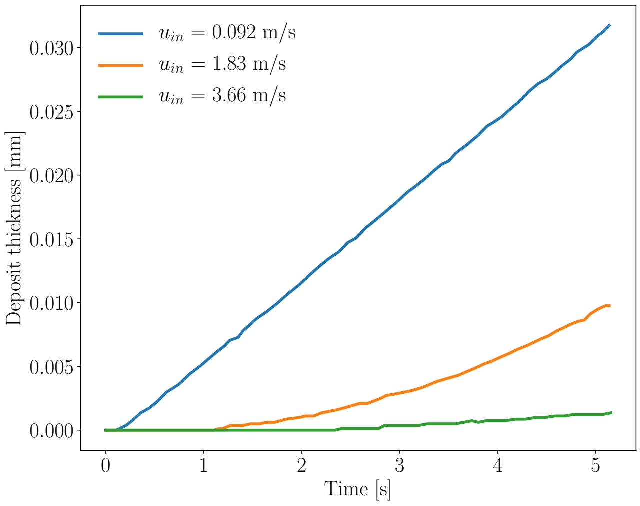

Figure 4: Time evolution of the deposit thickness for different values of the inlet velocity.

Effect of the pipe diameter

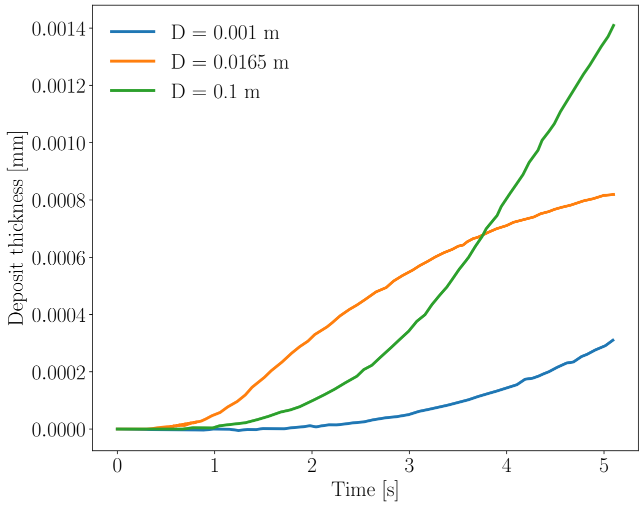

Figure 5: Time evolution of the deposit thickness for different values of the pipe diameter (cases 2, 3, and 4).

In order to compare the absolute values of the film thickness at different diameters, we rescale the film thickness with respect to the pipe radius. The diameter of the pipe appears to have a significant influence on the deposition dynamics as shown in Figure 5. In fact, a steady state flow, characterised by a constant growth of the deposit layer, is reached more quickly in larger pipes. In case 3 the models for asphaltene deposition in the reservoir pores becomes more relevant, and should include capillary forces (Magnini and Matar, 2019; Lawal *et al.*, 2012) due to the low impact of the advective transport compared to viscous forces.

Effect of the ageing λ

We now investigate the effects of ageing processes on the mixture rheology. We simulate two configurations of σ and θ, using parameters similar to those in Sileri *et al.* (2011) for the asphaltene. Figure 6 shows that ageing phenomena exert a strong influence on the flow behavior, affecting the motion of the sub-layer significantly. After a time $t = 50s$ such influence becomes more incisive.

CONCLUSIONS AND OUTLOOK

We proposed a new mathematical model for the coagulation and dissolution of asphaltenes in crude oil, and presented a stable numerical approach to its solution.

Our model possesses several novel aspects as (i) attempts to describe the problem of deposition through coagulation/dissolution using a kinetic approach rather than using a diffusive flux approach and (ii) implements a full non-equilibrium model for the transport of the structure parameter. This allows to model the effects of aging and hardening in complex flows, where transport phenomena are significant.

We demonstrated that the model can be calibrated to obtain reasonably accurate results, and that it is able to provide physically sound predictions in a number of configurations. Specifically, we illustrated how our model can be employed to analyse different scenarios in oil pipes.

Future works will require a combination of experimental and theoretical approaches to identify proper values for the free parameters that are present in the model. Furthermore, ex-

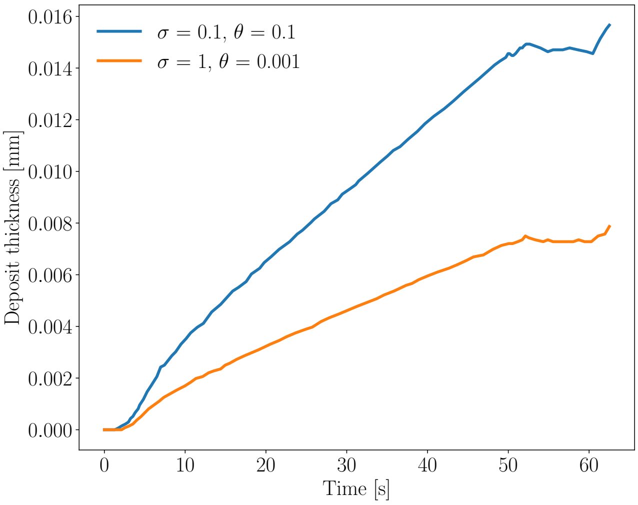

Figure 6: Time evolution of the deposit thickness for different values of the parameters in the transport equation λ.

tension to precipitation applications with gravity and variable density is ongoing.
However, the lack of field data regarding the coagulation and dissolution rates pose significant limits to the current methodology, which strongly relies on calibration.

REFERENCES

AZEVEDO, L.F.A. and TEIXEIRA, A.M. (2003). “A critical review of the modeling of wax deposition mechanisms”. *Petrol. Sci. Technol.*, **21**, 393–408.

BURGER, E.D., PERKINS, T.K. and STRIEGLER, J.H. (1981). “Studies of wax deposition in the trans alaska pipeline”. *J. Petrol. Technol.*, **33**, 1075–1086.

CORRERA, S., FASANO, A., FUSI, L. and MERINO-GARCIA, D. (2007). “Calculating deposit formation in the pipelining of waxy crude oils”. *Meccanica*, **42**, 149–165.

COUSSOT, P., ROUSSEL, N., JARNY, S. and CHANSON, H. (2005). “Continuous or catastrophic solid–liquid transition in jammed systems”. *Physics of Fluids*, **17(1)**, 011704. URL `http://aip.scitation.org/doi/10.1063/1.1823531`.

DBOUK, T. (2018). “Heat transfer and shear-induced migration in dense non-Brownian suspension flows: Modelling and simulation”. *Journal of Fluid Mechanics*, **840**, 432–454.

ESKIN, D., RATULOWSKI, J. and AKBARZADEH (2013). “A model of wax deposit layer formation”. *Chem. Eng. Sci.*, **97**, 311–319.

FERRY, J., RANI, S.L. and BALACHANDAR, S. (2003). “A locally implicit improvement of the equilibrium Eulerian method”. *International Journal of Multiphase Flow*, **29(6)**, 869–891.

HEWITT, G. F.AND COLETTI, F. (2015). “Crude oil fouling”. *Gulf Professional Publishing*.

HUYNH, H.T., ROUSSEL, N. and COUSSOT, P. (2005). “Aging and free surface flow of a thixotropic fluid”. *Physics of Fluids*, **17(3)**, 033101. URL `http://aip.scitation.org/doi/10.1063/1.1844911`.

ISSA, R. (1986). “Solution of the implicitly discretised fluid flow equations by operator-splitting”. *Journal of Computational Physics*, **62(1)**, 40–65. URL `https://linkinghub.elsevier.com/retrieve/pii/0021999186900999`.

LAUNDER, B.E. and SPALDING, D.B. (1974). “The numerical computation of turbulent flows”. *Computer Methods in Applied Mechanics and Engineering*, **3(2)**, 269–289.

LAWAL, K.A., CRAWSHAW, J.P., BOEK, E.S. and VESOVIC, V. (2012). “Experimental Investigation of Asphaltene Deposition in Capillary Flow”. *Energy & Fuels*, **26(4)**, 2145–2153. URL `https://pubs.acs.org/doi/10.1021/ef201874m`.

MAGNINI, M. and MATAR, O.K. (2019). “Fundamental study of wax deposition in crude oil flows in a pipeline via interface-resolved numerical simulations”. *Ind. Eng. Chem. Res.*, **58**, 21797–21816.

MARON, S.H. and PIERCE, P.E. (1956). “Application of ree-eyring generalized flow theory to suspensions of spherical particles”. *Journal of Colloid Science*, **11(1)**, 80–95.

MUNICCHI, F. and ICARDI, M. (2020). “Generalized multirate models for conjugate transfer in heterogeneous materials”. *Physical Review Research*, **2(1)**, 013041. `1906.01316`, URL `http://arxiv.org/abs/1906.01316https://link.aps.org/doi/10.1103/PhysRevResearch.2.013041`.

NOTT, P.R. and BRADY, J.F. (1994). “Pressure-driven flow of suspensions: simulation and theory”. *Journal of Fluid Mechanics*, **275(-1)**, 157. URL `http://www.journals.cambridge.org/abstract_S0022112094002326`.

RAMIREZ-JARAMILLO, E., LIRA-GALEANA, C. and MANERO, O. (2001). “Numerical simulation of wax deposition in oil pipeline systems”. *Petrol. Sci. Technol.*, **19**, 143–156.

RAMIREZ-JARAMILLO, E., LIRA-GALEANA, C. and MANERO, O. (2004). “Modelling wax deposition in pipelines”. *Petrol. Sci. Technol.*, **22**, 821–871.

ROUSSEL N, ROY RL, C.P. (2004). “hixotropy modelling at local and macroscopic scales”. *Non-Newton Fluid Mech*, **117(85)**.

SILERI, D., SAHU, K.C. and MATAR, O.K. (2011). “Two-fluid pressure-driven channel flow with wall deposition and ageing effects”. *Eng Math*, **71**, 109–130.

SINGH, A., PANACHAROENSAWAD, E. and SARICA, C. (2017). “A mini pilot-scale flow loop experimental study of turbulent flow wax deposition by using a natural gas condensate”. *Energy Fuels*, **31**, 2457.

SINGH, P., VENKATESAN, R., FOGLER, H.S. and NAGARAJAN, N. (2001). “Morphological evolution of thick wax deposits during aging”. *AIChE J.*, **47**, 6–18.

SINGH, P., VENKATESAN, R., FOGLER, H.S. and NAGARAJAN, N. (2000). “Formation and aging of incipient thin film wax-oil gels”. *AIChE Journal*, **46(5)**, 1059–1074. `https://aiche.onlinelibrary.wiley.com/doi/pdf/10.1002/aic.690460517`, URL `https://aiche.onlinelibrary.wiley.com/doi/abs/10.1002/aic.690460517`.

SOLAIMANY NAZAR, A.R., DABIR, B. and ISLAM, M.R. (2005). “Experimental and mathematical modeling of wax deposition and propagation in pipes transporting crude oil”. *Energy Sources*, **27**, 185–207.

SVENDSEN, J.A. (1993). “Mathematical modeling of wax deposition in oil pipeline systems”. *AIChE Journal*, **39(8)**, 1377–1388.

MODELING A TWO-PHASE FLOW IN A DEVICE TO REDUCE THE MUSCLE TONE OF THE HANDS

Lenar Akhmetshin [1]*, Andrei Chernyshev[1]†

[1] Bauman Moscow State Technical University, 105005, Moscow, Russia

* E-mail: lenar_akhmetshin_94@mail.ru
† E-mail: av-chernyshev@yandex.ru

ABSTRACT

In this work, a new design of internal channels for a pneumatic mechanical device was proposed to reduce the muscle tone of the hands. The new design uses a two-phase gas-liquid system as a working medium. Numerical modeling was performed, according to the results of which a cumulative distribution of the average diameter of gas bubbles was obtained at different pressure values in the channels. We used the Euler-Euler approach to simulate a two-phase system, the Reynolds Stress turbulence model and the Population Balance model, which is a set of partial differential integral differential equations that allow performing an average behavior analysis for a set of particles based on an analysis of the behavior of a single particle in local conditions. Simulations have been carried out for different bubble breakup and coalescence models. Graphs of the Sauter bubble diameter has been obtained. The results are to be validated with experimental data in the near future.

Keywords: Actuator, manipulator, CFD, two-phase gas-liquid flow, bubble flow.

NOMENCLATURE

Greek Symbols

ρ Mass density, [kg/m^3].

Latin Symbols

p Pressure, [Pa].

$\mathbf{u}$ Velocity, [m/s].

Sub/superscripts

i Index *i.*

INTRODUCTION

Damage to the vessels of the brain leads to the development of a disease called a stroke or cerebral infarction. Most often, an acute violation of cerebral circulation can be of the ischemic type, when there is a sharp spasm of cerebral vessels with blood clots, leading to the death of brain cells. If a vessel ruptures, then a hemorrhagic stroke develops, accompanied by the formation of a hemorrhage.

Depending on the location of the stroke, the corresponding clinical signs develop. When the motor cortex is damaged, paresis (paralysis) of the upper or lower extremities develop. Most often, unilateral damage occurs: left-sided damage with damage to the right half of the brain, right-sided with damage to the vessels of the left half of the brain [1].

When examining such a patient, there is a restriction or absence of movement in the arm or leg. The appearance of a pronounced muscle spasm, leading to the development of joint contractures, is noted, as well as a loss of sensitivity of certain areas of the skin [2].

The treatment of the stroke itself takes place in a hospital setting. Active vascular and metabolic therapy is performed and takes several weeks, but the restoration of lost functions can take months or years.

The main rehabilitation methods for treating paresis and paralysis are methods of physical education, massage, physiotherapy [3]. The patient himself can engage in physiotherapy exercises, but most often the presence of pronounced contractures and weakness interfere with full-fledged exercises.

A breakthrough in the treatment of such patients was the invention of special electrically driven simulators, which make it possible to perform the necessary movements in a given amplitude and intensity.

We considered the advantages and disadvantages in more detail in our previous work [4]. This work is a continuation of the previous one, where, on the basis of the experiments carried out, a solution was chosen – to create a new structure and use a two-phase gas-liquid system as a working fluid. The main advantage of using such a system is to add additional rigidity to the structure, since the pneumatic manipulator in the previous work [4] did not fully fulfill its functions.

MATHEMATICAL MODEL

Having reviewed the existing equipment, having considered all the advantages and disadvantages of the designs of elastomeric manipulators, a diagram of a device with branching internal channels is proposed on Figure 1, in which a two-phase medium is used as a working medium: gas-liquid.

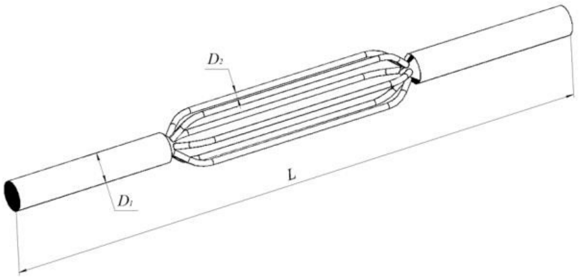

Figure 1: Elastomer manipulator internal channels design.

When the pressure inside the channels changes, the volume of gas bubbles changes, which can cause deformation of the wall material and set the structure in motion. In order to prevent the internal channels from "collapsing", they are completely filled with liquid. Due to the branched channels and changes in the volume of gas bubbles in them, an axisymmetric deformation of the elastomeric manipulator actuator occurs. In order to proceed to modeling the deformation and calculating the force created by the actuator, it is necessary to develop an integrated computational pneumo-hydrodynamic model for horizontal two-phase flows in channels. Modeling a two-phase system is not a trivial task. There are various studies concerning the local distribution of the gas volume fraction and the fluid velocity field in horizontal two-phase flows in channels.

The most interesting are dispersed bubbly flow and buoyant bubbly flow since they are able to provide large interfacial regions for heat and mass transfer in general. In fact, there is a big difference between scattered and buoyant bubble flows. It consists in characterizing the role of buoyancy. In a dispersed bubble flow, buoyancy can be neglected in comparison with the effect of the liquid on the gas phase. In a scattered flow, bubbles move in horizontal tubes with some symmetry about the channel axis. However, in the buoyant bubble mode, buoyancy plays an important role, and the bubble concentration in this mode is asymmetric with respect to the channel axis. Due to the buoyancy effect, bubbles move from the bottom to the top of the channel. Similar studies have already been carried out in many works [5-7], experiments were carried out, and models were described, but for each specific case. It is this mode that is subject to mathematical modeling in this work. The goal of this work is to carry out a numerical simulation of a two-phase gas-liquid system inside three-dimensional channels and obtain complete information about three-dimensional fields in terms of the volume average velocities and volume fraction of the dispersed phase.

The volume-averaged velocity fields are significantly influenced by turbulence, and therefore, it is equally important to know the spatial distribution of turbulent kinetic energy and energy dissipation rates, although they are more difficult to measure experimentally, especially in multiphase flow situations.

The numerical calculations obtained in this work are based on the Euler-Euler two-phase model. This model is based on the combined averaged mass and momentum transfer equations for each phase.

The volume fraction of phase *i* is calculated from the continuity equation [8]:

$$\frac{\partial}{\partial t}(\alpha_i \rho_i) + \nabla \cdot (\alpha_i \rho_i \vec{u}_l) = 0 \tag{1}$$

where α is the void fraction, u is the superficial velocity.

The momentum balance for phase i [8]:

$$\begin{aligned} &\frac{\partial}{\partial t}(\alpha_i \rho_i \vec{u}_l) + \nabla \cdot (\alpha_i \rho_i \vec{u}_l \vec{u}_l) = \\ &= -\alpha_i \nabla p + \nabla \cdot [\alpha_i (\tau_i + \tau_i^t)] + \\ &+ \alpha_i \rho_i \vec{g} + M_i \end{aligned} \tag{2}$$

$$\sum M_i = 0 \tag{3}$$

where τ is the molecular stress, τ^t is the turbulent stress, M_i is the momentum transfer in the interface, $\vec{g}$ is the acceleration due to gravity.

Figure 2 shows a diagram of the forces acting on the bubble.

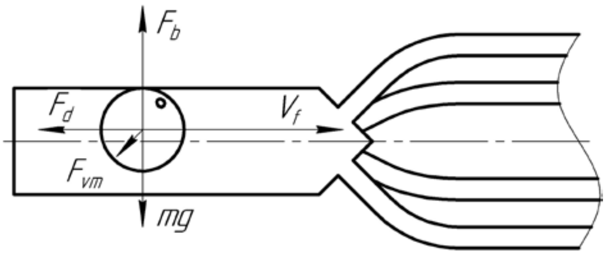

Figure 2: Diagram of the forces acting on the bubble.

The total interfacial force acting between the two phases can result from several independent physical effects:

$$\vec{F} = \vec{F}_d + \vec{F}_L + \vec{F}_{VM} + \vec{F}_b + \vec{F}_{TD} + m\vec{g} \tag{4}$$

The forces indicated above are: the drag force F_d, F_b is the buoyant force, the lift force F_L, the virtual mass force F_{VM}, the wall lubrication force F_{WL} and the turbulent dispersion force F_{TD}. To simplify our model and calculation, we will not take into account the virtual mass force for now.

MODEL DESCRIPTION

The breakup of bubbles in turbulent dispersion flows, the Luo and Svendsen model [9] and Lehr model [10] developed by the respective authors, is used. Different models were taken in order to determine how different the results would be and which model to use in subsequent simulations after validation with experiments.

The coalescence model used for modeling, Prince and Blanch [11], was inserted into the software ANSYS Fluent using a user-defined function (UDF) [12].

The Ishii-Zuber drag model was used as a drag force model [13]. The turbulent dispersion force was obtained using the Lopez de Bertodano model [14]. The Antal et al. [15] model was used as a wall lubrication model.

In this work, we used the Reynolds Stress turbulence model (RSM). Population Balance model has been used [16]. This model makes it possible to obtain the distribution of the dispersed phase over the average diameters, which is obtained in the case of formation, coalescence, destruction and disappearance of the gaseous phase.

Numerical modeling was carried out in three-dimensional horizontal channels with diameters D_1 = 5 *mm* and D_2 = 1 *mm*, channel length L = 100 *mm* (Figure 1). The calculations were carried out using ANSYS Fluent software. The flow of glycerine was considered as the continuous liquid phase, while the air was taken as the dispersed gas phase. The interfacial tension was assumed to be $\gamma = 0.07\ N/m$. The sizes of gas bubbles were set in the range from 0.1 mm to 0.9 *mm*. This range has been subdivided into ten discrete bubble sizes.

The structured mesh in each block is generated using commonly curved coordinates to accurately represent flow boundaries. To select a mesh size, the effect of changing its shape and size was investigated. Several simulations were carried out using a different number of a grid: 112843, 879324, 1299505. The grid with the largest number of cells showed the best convergence. As a result, a grid with the number of cells 1299505 was chosen (Figure 3). The calculations were carried out at the university workstation.

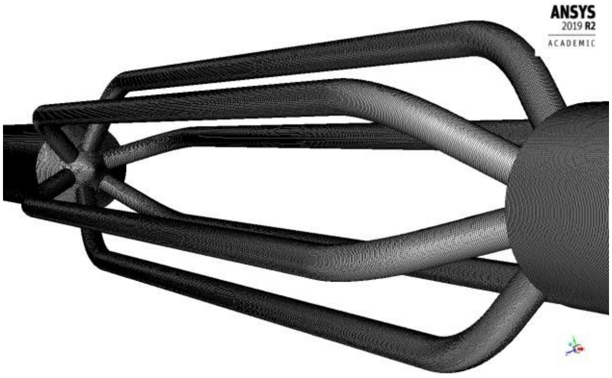

Figure 3: Hexahedral structured mesh selected for the calculation number of cells 1299505.

For calculations, time step 0.01 *s* was used. The Phase Coupled SIMPLE scheme was used. Under-relaxation factors were used. At the pipe inlet, uniform gas and liquid velocities and volume fractions have been specified. At the channel outlet, a relative average static pressure of zero was specified.

RESULTS

Simulations were carried out under fully developed bubble flow conditions for the air-glycerine system. The velocity of liquid (v_g) and gas (v_l) is equal to U_{mean} = 0.5 *m/s*, and the average volumetric gas fraction φ = 30%. The simulation results are the cumulative distribution at the outlet of the channels $D_1 = 5\ mm$, $D_2 = 1\ mm$, respectively (Figure 4). The graph shows that there is a high probability of the presence of air bubbles with a size of ≈ 0.7 *mm*, and it is ≈ 80%.

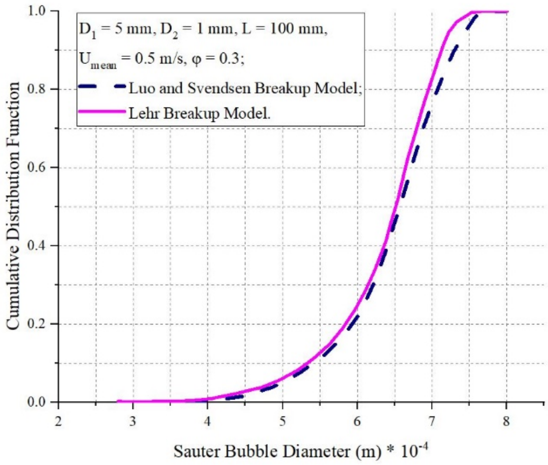

Figure 4: Cumulative Bubble distribution function.

Figures 5-6 show the distributions of bubble concentration along the diameter for different tube diameters for D_1 = 5 *mm*, and D_2 = 1 *mm*.

It should be noted that both models give approximately the same result and do not differ much from each other. It should be concluded that further modeling can use one of these models. When using the Luo and Svendsen [9] breakup model, the convergence of the calculation was carried out faster.

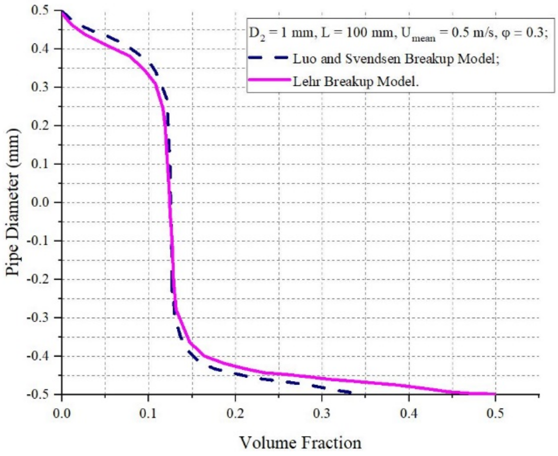

Figure 5: Bubble Volume Concentration Distribution across Pipe Diameter.

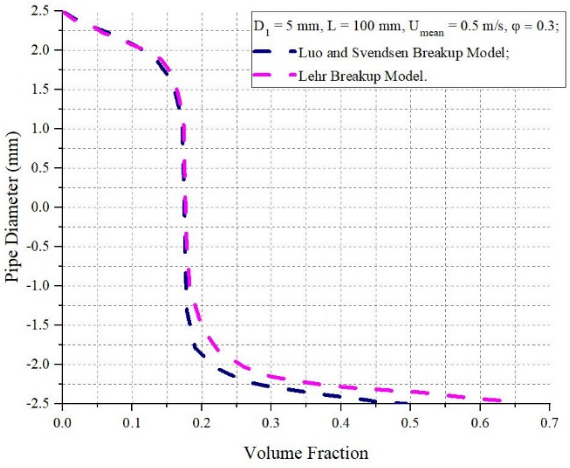

Figure 6: Bubble Volume Concentration Distribution across Pipe Diameter.

Analyzing the graphs, it can be seen that bubbles of large diameters accumulate mainly in the channel with a diameter $D_1 = 5\ mm$.

At the inlet to thin channels with a diameter of $D_2 = 1\ mm$, bubbles are evenly distributed. The main concentration of the gas phase is located in the upper part of the channels, which is explained by the action of the gravitational component. Figure 7 shows the results of the bubble diameter distribution. The scale shows data on bubble diameters d_b, m.

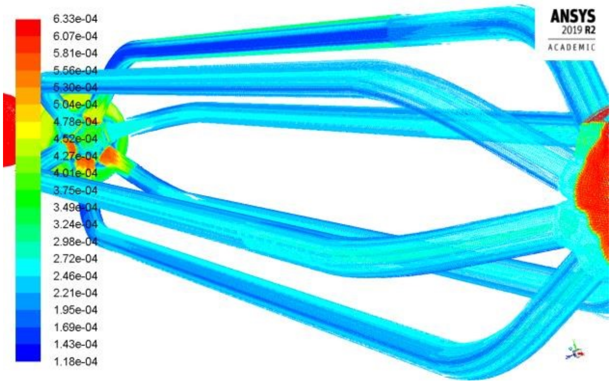

Figure 7: Dispersed phase distribution within the channel, the scale shows the values of the bubble diameters d_b, m.

Thus, we have obtained data in what places of the channel and what sizes of bubbles can be obtained with a given geometry of the channels. The accuracy of the calculated data will be evaluated by experiments in future work.

CONCLUSION

A comprehensive computational pneumo-hydrodynamic model for horizontal two-phase flows in channels has been developed. From the calculated data, a distribution of the dispersed gas phase inside the channel, and cumulative distribution over the diameters of air bubbles, were obtained. Thus, using the developed pneumo-hydrodynamic model, we can predict where in the channel and what size bubbles are formed in the gas-liquid system. This enables the modeling of the deformation and calculation of the forces created by the actuator of the elastomeric manipulator. Calculations were carried out for two different breakup models Luo and Svendsen [9] and Lehr model [10], using a user-defined function in ANSYS Fluent (2019). And a coalescence model was introduced. Data were obtained on the distribution of the Sauter bubble diameter over the entire tubing system and the distribution of the volume concentration of bubbles for different diameters. In the future, it is planned to conduct an experiment and compare the simulated data with the experimental ones. Based on the validation, future decisions creating a hand rehabilitation device.

REFERENCES

[1] B. Peele, T. Wallin, H. Zhao and R. Shepherd, “3D printing antagonistic systems of artificial muscle using projection stereolithography”, Bioinspiration & Biomimetics, 10 (5) (2015), 567-943;

[2] B. Homberg, R. Katzschmann, M. Dogar and D. Rus, “Haptic Identification of Objects using a Modular Soft Robotic Gripper”, Intelligent Robots and Systems (IROS), (2015) IEEE/RSJ International Conference on. IEEE;

[3] R. Deimel and O. Brock, “A compliant hand based on a novel pneumatic actuator,” Robotics and Automation (ICRA), 2013 IEEE International Conference on. IEEE, (2013), 2047-2053;

[4] Meretskaya, E.R., Chernyshev, A.V. “Calculating and theoretical research and determination of the functional parameters of a pneumo-mechanical device actuator”, (2018) AIP Conference Proceedings, № 030045;

[5] A. J. Ghajar and C. C. Tang, “Advances in Void Fraction”, Flow Pattern Maps and Non-Boiling Heat Transfer Two-Phase Flow in Pipes with Various Inclinations, vol. 1. (2009);

[6] R. Brito, “Effect of Medium Oil Viscosity on Two-Phase Oil-Gas Flow Behavior in Horizontal Pipes”, The University of Tulsa, (2012);

[7] H. Matsubara and K. Naito, “Effect of liquid viscosity on flow patterns of gas-liquid two-phase flow in a horizontal pipe”, Int. J. Multiph. Flow, 37 (10) (2011), 1277–1281;

[8] Esteban Guerrero, Felipe Muñoz and Nicolás Ratkovich, “Comparison between Eulerian and VOF Models for two-phase flow assessment in vertical pipes”, CT&F, 7 (1) (2017) 73 – 84;

[9] H. Luo, H. Svendsen, “Theoretical model for drop and bubble breakup in turbulent dispersions”, AIChE J. 42 (1996);

[10]F. Lehr, D. Mewes, M. Millies, Bubble-Size Distribution and Flow Fields in Bubble Columns, AIChE Journal 48(11) (2002) 2426 – 2443;

[11] M.J. Prince, H.W. Blanch, “Bubble coalescence and breakup in air sparged bubble columns”, AIChE J. 36 (1990) 1485–1499;

[12] ANSYS Fluent Theory Guide, ANSYS Fluent Release 15.0: ANSYS (Europe Ltd, 2013) 42 p.;

[13] M. Ishii, N. Zuber, “Drag coefficient and relative velocity in bubble, droplet or particulate flows”, AIChE J. 25 (1979) 843–855;

[14] M.A. Lopez de Bertodano, “Turbulent bubbly two-phase flow in a triangular duct”, Ph.D. dissertation, Rensselaer Polytechnic Institute, 1992;

[15] S.P. Antal, R.T. Lahey, J.E. Flaherty, “Analysis of phase distribution in fully-developed laminar bubbly two phase flow”, Int. J. Multiphase Flow 7 (1991) 635;

[16] Nopens, I., Torfs, E., Ducoste, J., Vanrolleghem, P.A., Gernaey K.V., 2014, “Population balance models: a useful complementary modelling framework for future WWTP modelling”, Water Sci. Technol. 71(2), 159-167.

TO QUANTIFY MIXING QUALITY IN A SINGLE SCREW EXTRUDER SIMULATION

TJ Mateboer*, **C Hummel, DJ van Dijk, J Buist**
Windesheim University of Applied Sciences, Professorship for Polymer Engineering, P.O. Box 10090,
8000 GB Zwolle, The Netherlands

* E-mail: t.j.mateboer@windesheim.nl

ABSTRACT

Polymer mixing with a single screw extruder is a common process in industry. The mixing quality depends (amongst others) on the screw geometry. The main objective of this study was to develop a method for quantifying distributive mixing quality of a single screw extruder with computational fluid dynamics (CFD) simulations.
Tracer particles and Shannon entropy calculations were used to determine the distributive mixing quality as a function of direction, position in the extruder and scale of observation.
This method performed well for making a distinction in mixing quality between different extrusion simulations.

Keywords: CFD, Polymer mixing, distributive mixing, single screw extruder, Non-Newtonian fluid dynamics, Shannon entropy, Numerical simulation, spiral Maddock

NOMENCLATURE

Greek Symbols

$\dot{\gamma}$	Shear rate, [s^{-1}].
η	Viscosity, [Pa·s].
η_0	Viscosity at zero shear rate, [Pa·s].
η_∞	Viscosity at infinite shear rate, [Pa·s].
λ	Relaxation time, [s].
τ	Shear stress, [Pa].

Latin Symbols

c_i	Number of particles in bin *i*, [-].
i	Bin number, [-].
M	Number of bins, [-].
m	Flow consistency index, [Pa·s^{-n}].
N	Total number of tracer particles, [-].
n	Power law index, [-].
p_i	Probability of a particle to flow through bin *i*.
S_{rel}	Relative Shannon entropy, [-].

INTRODUCTION

Polymer mixing with a single screw extruder is a common process in industry. Mixing quality is often divided into dispersive and distributive mixing. With distributive mixing the additive units or the discontinuous phase are/is homogeneously distributed throughout the polymer. Mixing quality depends on (amongst others) the screw geometry. Specialized mixing sections in a screw geometry are necessary for a high mixing quality with a single screw extruder. The spiral Maddock is such a mixing section.

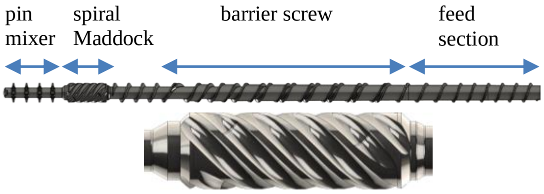

Figure 1: Upper: Extruder screw with four section. Fluid flow is from right to left. Lower: spiral Maddock section.

With computational fluid dynamics (CFD) many different mixing parameters can be simulated, such as different screw geometries. A more efficient mixer may be found by comparing several simulated extruders. Mixing quality has to be quantified in order to find the best mixer. The goal of this study was to find a method of quantifying mixing quality in a single screw extruder using CFD simulation.
Several studies have modeled polymer mixing with CFD (1-13). Distributive mixing behavior in simulations is often quantified with a residence time distribution (RTD) of tracer particles (1, 5, 14-18) and with the Shannon entropy (6, 8, 15, 16, 19, 20). These methods often result in limited information of:

- Mixing quality in different directions (angular and radial directions separately).
- Mixing quality at different positions in the extruder.
- Mixing quality at both a large and small scale of observation.

In this study a method was developed applying the Shannon entropy for calculating distributive mixing quality as function of the position in the extruder, as function of direction and scale. For several extrusion simulations the mixing quality was calculated to determine how well a distinction in mixing quality can be made with this method. These extrusion simulations were only used to test the method of quantifying mixing quality, the study is not focused on finding an optimized screw geometry. Furthermore only the spiral Maddock screw mixing section was included in the simulations, not the whole extruder.

SIMULATION SETUP

To show the effectiveness of the method extrusion simulations with the spiral Maddock were performed. The flight height and the rotational velocity was varied between the simulations. The specifics of the simulations are shown in this section. The simulations were performed with the immersed solid method (ISM) in CFX (Ansys 19.2). All the simulations are steady state and isothermal.

Spiral Maddock geometry

The spiral Maddock is a mixing section of a single screw extruder with a 75 mm diameter, see Figure 1. The spiral Maddock is specifically designed for dispersive mixing, while in this study only distributive mixing quality was calculated. The simulations were created in order to have a data set to test the method for determining mixing quality. Therefore the exact purpose of the screw section was not significant for this study. The spiral Maddock consist of several flights, inflow and outflow channels. The spiral Maddock is discrete rotational sy ong th xis.

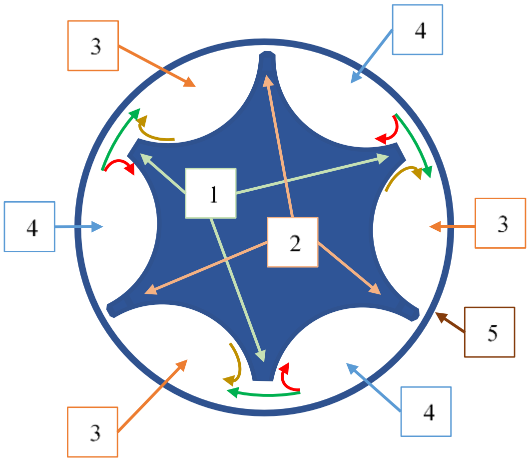

Figure 2: Schematic cross section of a spiral Maddock. 1: barrier flights. 2: main flights. 3: outflow channels. 4: inflow channels. 5: barrel.

The spiral Maddock is designed in such a way that the fluid passes through a gap between the barrier flight and the barrel. The barrier flight height was varied so the gap between the barrier flight and the barrel was varied between 1.74 mm and 0.74 mm.
The gap between the main flight and the barrel wall is very narrow in order to prevent fluid flowing through. The size of this gap makes meshing difficult. Therefore the main flight was extended beyond the barrel wall. With this setup the gap between the main flight and the barrel wall does not exist in the simulations. This simplification of the model was expected to have minor effects on outcome of this study. This is justified since the simulations were used to create a dataset for applying the method to determine mixing quality.

Boundary conditions

A no slip condition was set on both the barrel and screw walls. The screw rotates relative to the barrel wall. The mass flow rate condition was set to $20 \cdot 10^{-6}$ m^3s^{-1}. At the outflow opening the pressure was set to 0 Pa.

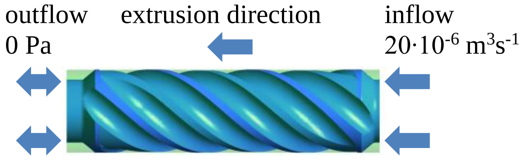

Figure 3: Side view of the spiral Maddock. The screw is in blue, the fluid domain is in green.

Simulations were performed with a screw rotational velocity of both 1.5 rad/s and 4.6 rad/s.

Material parameters

The input of the material parameters were derived from an HDPE grade (Marlex TRB-432, Chevron Phillips Chemical Company). The viscosity as function of shear rate was determined with a capillary rheometer at 200 °C. Measurements were performed in a shear rate range from $\dot{\gamma} = 4\,s^{-1}$ up to $\dot{\gamma} = 500\,s^{-1}$. A power law was fitted onto the rheological measurements with $n = 0.35$ and $m = 3.3 \cdot 10^4$ $Pa \cdot s^{-n}$.

Power law

$$\tau = m\dot{\gamma}^n \tag{1}$$

For numerical stability a Bird-Carreau model was used in the simulations:

Bird-Carreau model

$$\eta = \eta_\infty + (\eta_0 - \eta_\infty)\left(1 + (\lambda\dot{\gamma})^2\right)^{\frac{n-1}{2}} \tag{2}$$

The Bird-Carreau and the power law are almost identical in the shear rate range of $\lambda^{-1} > \dot{\gamma} > \left(\frac{\eta_\infty}{m}\right)^{\frac{1}{n-1}}$. λ and η_∞ were chosen in such a way that the power law and the Bird-Carreau are similar behavior at $10^{-3} > \dot{\gamma} > 10^{7}$. The chosen values were η_∞ = 1 Pa·s, η_0 = 3 MPa·s and λ = 1000 s. These values were chosen since lower and higher shear rates were not expected to have a significant influence on the simulation. Furthermore no rheological measurements were available at those low and high shear rates.

Mesh

A fluid domain and an immersed solid were created.

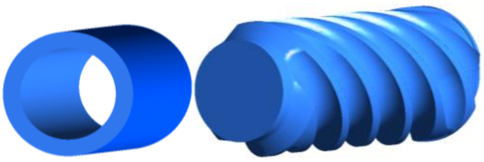

Figure 4: Left: fluid domain. Right: immersed solid domain (spiral Maddock).

The two domains were meshed separately. The fluid domain mesh consists of a part with cubical cells near the barrel wall.

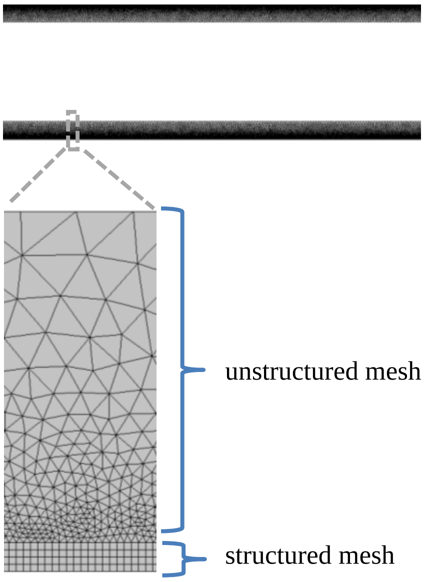

Figure 5: Cross section of a fluid domain mesh.

The height of this structured part is similar in size to the gap between the barrier flight and the barrel. This ensures a minimum number of cells between the barrier flight and the barrel wall. A large aspect ratio in these cells resulted in numerical instabilities, therefore the structured cells are cubical.

The rest of the fluid domain consists of an unstructured mesh. The results of a simulation with a proper mesh density do not change when the mesh cell density is increased. The cell size of the cubical cells was incrementally reduced from an average cell size of 0.15 mm down to 0.05 mm. The unstructured cell was reduced in size accordingly. The total number of cells increased from 58 M up to 479 M.

Simulations with the different meshes were evaluated by comparing the pressure at the inflow of the spiral Maddock.

The immersed screw mesh size does not have a great impact on the computational costs. Therefore a single fine mesh was made of the screw. This unstructured mesh was used in each of the simulations.

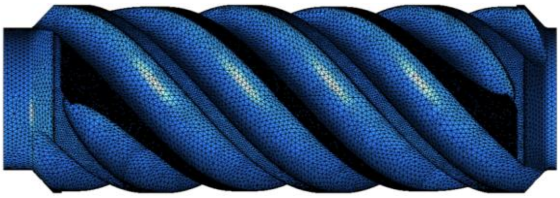

Figure 6: Side view of the immersed solid domain mesh / screw mesh.

It is preferred to have a well-defined gap between the barrel and the barrier flight. Therefore a very fine mesh was chosen for the barrier flight back.

Tracer particles

The flow paths of the fluid determine the quality of the distributive mixing. The flow paths can be determined with tracer particles of zero mass (21). These flow paths were calculated in a post processor (Ansys CFD-Post) with the streamline function. The flow paths consists of a series of points. The fluid velocity and trajectory at a point can be used to calculate the position of the next point. The distance between the points is a factor of 0.01 of the mesh cell size. Therefore a smaller cell size results in more accurate tracer particle path.

In total 10^5 tracer particles were introduced at the inflow boundary. The position of the inflow boundary is shown in Figure 3.

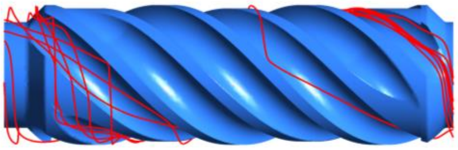

Figure 7: Example of the trajectory of a small number of tracer particles introduced at the inflow boundary into the spiral Maddock simulation.

The particle inflow positions, and a method to determine mixing quality is shown in the next section.

Variation in the simulation setup

3 different simulations were executed. The configurations are shown in Table 1.

Table 1: Modelling conditions.

simulation name	screw rotational velocity	Gap between the barrier flight and the barrel
standard	1.5 rad/s	0.74 mm
high screw velocity	4.6 rad/s	0.74 mm
lowered barrier flight	1.5 rad/s	1.74 mm

The standard setup was used for the mesh study. The mixing quality was calculated for all three setups. The purpose of the different setups was to determine how well a distinction in mixing quality can be made with the Shannon entropy. The setups were not chosen to determine an optimal extrusion setup or screw geometry.

SHANNON ENTROPY FOR DETERMINING THE MIXING QUALITY

Shannon entropy is a single measure to determine a distribution across a number of bins (M). Relative Shannon entropy (S_{rel}) is calculated with the probability (p_i) that a tracer particle flows through a bin and will be referred to from here on as the Shannon entropy.

Relative Shannon entropy

$$S_{rel} = \frac{-\sum_{i=1}^{M} p_i \ln p_i}{\ln M} \qquad (3)$$

p_i is equal to the number of tracers (c_i) in bin i divided by the total number of tracer particles (N).

The Shannon entropy was calculated at the outflow side of the spiral Maddock, see Figure 3. Therefore the outflow was divided into several bins, see the example in Figure 8.

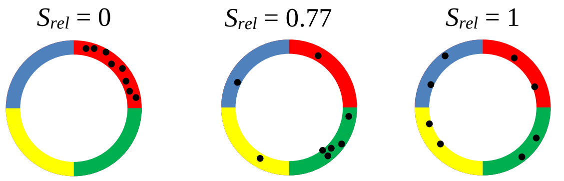

Figure 8: Outflow divided into 4 bins with eight tracer particles. Left low quality mix (S_{rel} = 0), middle: medium quality mix (S_{rel} = 0.77), right: high quality mix (S_{rel} = 1).

The mixing quality is low with a inhomogeneous probability distribution, see the particle distribution in the most left outflow in Figure 8. The mixing quality is high with a homogeneous probability distribution, see the particle distribution in the most right outflow in Figure 8. The Shannon entropy is a measure of probability distribution, therefore the Shannon entropy can be applied as a measure of mixing quality.
A low Relative Shannon entropy corresponds to a low mixing quality. The maximum Relative Shannon entropy and maximum mixing quality is reached when S_{rel} = 1. The Relative Shannon entropy is in the range $0 < S_{rel} \leq 1$, which makes it possible to estimate the mixing quality with the Relative Shannon entropy.
It seems reasonable that a lower number of particles per bin results in an increase in uncertainty in the Shannon entropy. Therefore the average number of particles per bin was kept at a minimum of 30 particles. All the Shannon entropy calculation were performed with GNU Octave.

Bin division schemes

The orientation of the bin division scheme determines the direction of mixing quality that can be calculated with the Shannon entropy. Mixing quality in an angular direction (angular mixing quality) can be calculated with an angular bin division scheme. Mixing quality in a radial direction (radial mixing quality) has to be calculated with a radial bin division scheme.

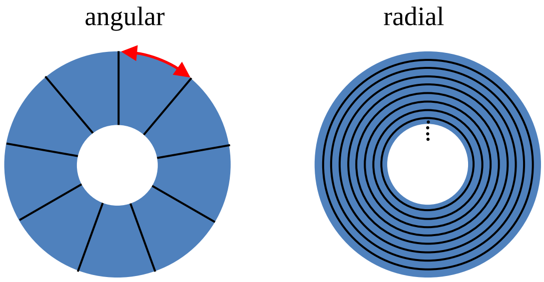

Figure 9: Schematic of bin distribution schemes. Left: angular divisions, the red arrow indicates the typical size for this bin division. Right: radial division.

The above schematic shows two bin division with 8 bins. The typical size of the angular bins is the circumference divided by the number of bins (M), see the red arrow in the above figure. The typical size of the radial bins is the distance between the screw and the barrel divided by the number of bins (M). The bin size defines the scale of observation (6). Mixing quality at a macroscopic level can be determined with a small number of bins. Mixing quality on a microscopic level needs to be determined with a large number of bins. From 3 up to 96 bins were used to calculate a Shannon entropy.

Tracer particle inflow sections

The tracer particles flow from the inflow boundary to the outflow boundary, see Figure 3. The increase in homogeneity of the particle distribution represents the increase in mixing quality. Therefore it is preferred to have a inhomogeneous particle distribution at the inflow. The particles were grouped together in a section of the inflow boundary, see Figure 10.

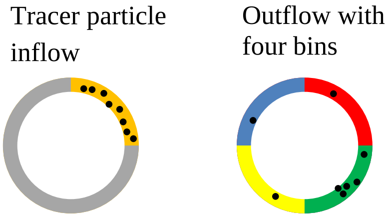

Figure 10: Left: an inflow boundary with, in orange, a section were 8 particles were introduced. Right: an outflow boundary divided into 4 bins.

An inflow sections, such as shown in Figure 10, has the same size and shape as an outflow bin. If there is no mixing in the simulation, than all the particle would end up in 1 bin at the outflow. And the Shannon entropy would be S_{rel} = 0.
Mixing quality as function of position at the inflow can be determined by using several inflow section with different sets of particles. The Shannon entropy can be calculated for each inflow section independently.

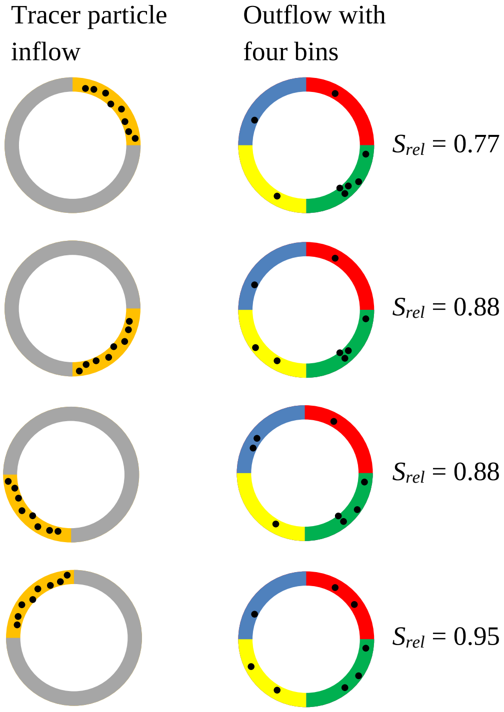

Figure 11: A hypothetical example of four Shannon entropy calculations based on an angular bin division scheme and different section for particle entry.

Figure 11 shows an example for an angular bin division scheme with 4 separate bins. The inflow sections are the same size as the bins, therefore the inflow (in the

example) is divided into 4 section. A different Shannon entropy can be calculated for each inflow section. Multiple inflow sections can also be used with a radial bin division scheme. In that case the inflow is divided in a radial direction. With this method the Shannon entropy as a function of inflow position (angular and radial) can be calculated.
The spiral Maddock consists of 3 rotational symmetric parts, see Figure 2. The Shannon entropy as function of inflow position is also expected to be symmetrical. Therefore only 1/3 of the inflow is divided into section with particles.

RESULTS

Mesh study

Simulations with the different meshes were compared based on pressure at the inflow of the spiral Maddock.

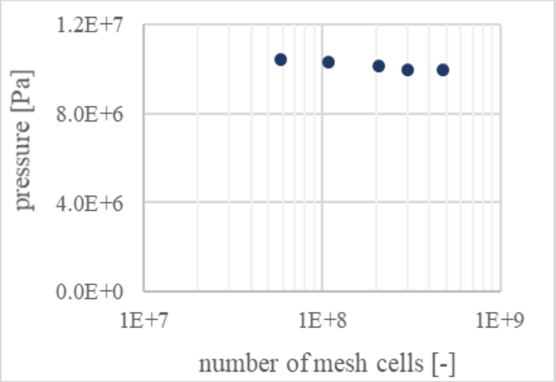

Figure 12: Simulated pressure at the inflow of the spiral Maddock as function of mesh size.

The pressure does not reduce much with increase of mesh size. As can be seen from Figure 12, a limited reduction of the pressure was calculated with increasing mesh size. Therefore the most coarse mesh (58 M cells) was used to determine mixing quality.

Particle distribution

In the next step tracer particles were introduced to determine mix quality. An example of the particle positions at the outflow boundary is shown in Figure 13. In this example the particles were introduced at a section of 1/3 of the inflow boundary. The outflow was divided into 3 bins in an angular direction.

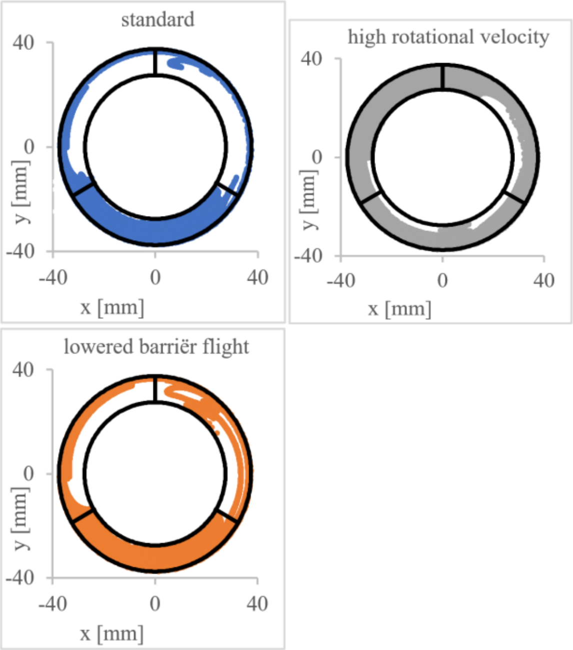

Figure 13: Tracer particle positions (colored dots) at the outflow of the spiral Maddock. The outflow is divided into 3 bins.

The figure allows for a visual evaluation of the mixing quality. The simulation with a high rotational screw velocity shows (visually) a higher mixing quality compared to the other simulations. The standard and lowered barrier flight show a very similar particle distribution.
The outflow was divided, in an angular direction, in 3 bins for the Shannon entropy calculations. The bins were large with a typical size of 79 mm (in angular direction, see Figure 9). The Shannon entropy is 0.95 for the simulation with a high rotational screw velocity, S_{rel} = 0.68 for the lowered flight simulation, and S_{rel} = 0.56 for the standard simulation. A high Shannon entropy corresponds to a high distributive mixing quality in angular direction. Therefore the simulation with a high screw velocity is the better mixer for mixing in angular direction at this large scale (typical bin size is 79 mm).

Angular distributive mixing quality

The mixing quality was visually evaluated in the above paragraph, and quantified for 1 inflow section at 1 scale of observation. This section shows the quantified mixing quality for several scales of observation and several positions at the inflow.
The inflow of the spiral Maddock was divided into sections in an angular direction. The tracer particles were introduced in each section and the Shannon entropy was calculated for each section. Figure 14 shows the Shannon entropy as function of inflow section with an angular bin division scheme.

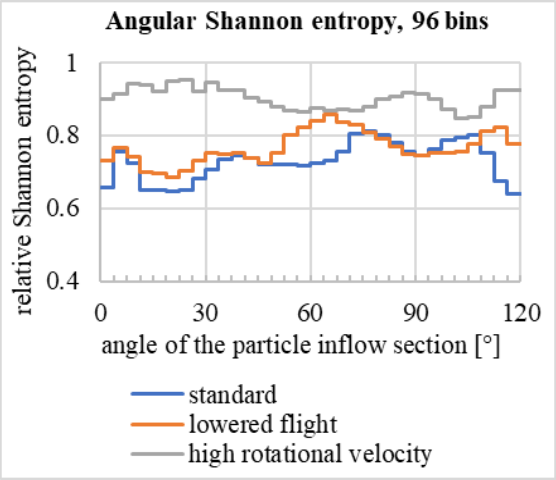

Figure 14: Shannon entropy as a function of inflow section with an angular bin division scheme and a typical bin size of 2.5 mm.

A high Shannon entropy corresponds to a high distributive mixing quality while a low Shannon entropy corresponds to a low distributive mixing quality.
The angular mixing quality depends on the tracer particle inflow section. For example the lowered flight simulation: the mixing quality is better for inflow section at 60.75°-67.50° ($S_{rel} = 0.86$) while the mixing quality is less ($S_{rel} = 0.73$) for the inflow section at 0°-3.75°. The high rotational velocity shows a higher mixing quality. Figure 14 only shows the results with a typical bin width of 2.5 mm. A minimum or an average mixing quality of all inflow section can be used to show mixing quality at other scales of observation.

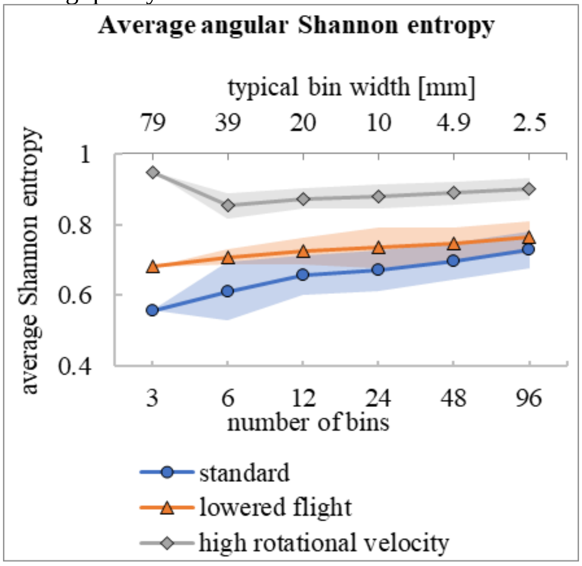

Figure 15: Average angular Shannon entropy as an function of the number of bins (bottom axis) and typical bin width (top axis). The colored bands show the standard deviation. Note: the horizontal axis is on a logarithmic scale.

The high rotational velocity simulation shows a higher average Shannon entropy compared to the other simulations. And therefore the high rotational velocity shows a higher distributive mixing quality. The lowered flight simulation shows a slightly higher average angular mixing quality compared to the standard simulation at each typical bin width. Although there is a certain overlap when the standard deviation is taken into account. The mixing quality of the simulations can also be compared with the minimum Shannon entropy of a simulation at a specific typical bin width.

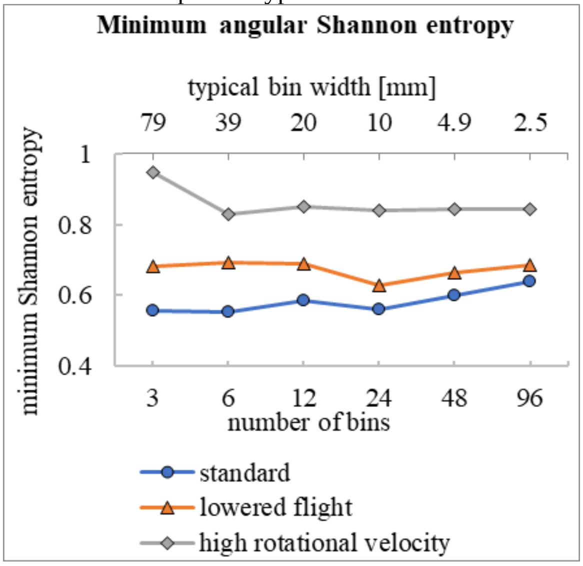

Figure 16: Minimum angular Shannon entropy as function of number of bins (bottom axis) and typical bin width (top axis). The colored bands show the standard deviation. Note: the horizontal axis is on a logarithmic scale.

Comparing the minimum Shannon entropy is useful for a design study when a minimum mixing quality is required. The lowest angular mixing quality of the lowered flight simulation is better than the lowest mixing quality of the standard simulation at all typical bin widths.
The Shannon entropy can be used to make a distinction in angular mixing quality between the extrusion simulations. Furthermore the angular mixing quality was determined as function of angular position and of scale of observation.

Radial distributive mixing quality

Shannon entropy was calculated with a radial bin division scheme. The inflow was divided into radial sections. Figure 17 shows the Shannon entropy as a function of radial inflow section.

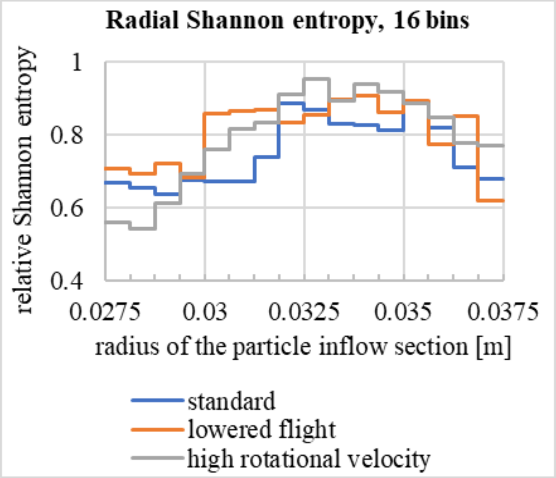

Figure 17: Shannon entropy as a function of inflow section with a radial bin division scheme and a typical bin size of 0.6 mm.

It was found that the distributive mixing quality in the radial direction depends on the radial position of the particle inflow section. The mixing quality shows a dependency on the inflow position rather than on the simulation setups included in this study. Therefore it is not meaningful to compare the average or minimum Shannon entropy as was performed with the angular bin distribution.

CONCLUSION AND RECOMMENDATIONS

With this method tracer particles and Shannon entropy calculations were used to determine the distributive mixing quality as function of:

- radial and angular direction
- scale of observation
- radial and angular inflow position of the tracer particles

For 3 spiral Maddock simulations the mixing quality was calculated to determine how well a distinction in mixing quality can be made with this method. The flight height and the rotational velocity was varied in these simulation. The mixing quality depends on both the angular and radial inflow position of the tracer particles. The different simulations show different mixing quality in angular direction. Therefore this method can be applied to determine which extruder the most efficient angular mixer is.

Recommendation / future work

In this study only a single mixing section of an extruder was included (the spiral Maddock) and the simulations were not verified with experiments. Future work will focus on including the whole screw and the extruder die and verifying the simulations with experiments, specifically the distributive mixing quality of the simulations.

ACKNOWLEDGEMENTS

This study was financially supported by Tech For Future (TFF) and Wavin T&I. The Windesheim University Professorship for Polymer Engineering conducted this study with Wavin T&I. Wavin T&I provided expert advice, essential equipment, materials and experimental data.

REFERENCES

1. Zong Y, Tang H, Zhao L. 3-D numerical simulations for polycondensation of poly(p-phenylene terephthalamide) in twin screw extruder. Polymer Engineering and Science. 2017;57(11):1252-61.
2. Tang H, Zong Y, Zhao L. Numerical simulation of micromixing effect on the reactive flow in a co-rotating twin screw extruder. Chinese Journal of Chemical Engineering. 2016;24(9):1135-46.
3. Zhang XM, Xu ZB, Feng LF, Song XB, Hu GH. Assessing local residence time distributions in screw extruders through a new in-line measurement instrument. Polymer Engineering & Science. 2006;46(4):510-9.
4. Zhang XM, Feng LF, Hoppe S, Hu GH. Local residence time, residence revolution, and residence volume distributions in twin-screw extruders. Polymer Engineering & Science. 2008;48(1):19-28.
5. Zhang XM, Feng LF, Chen WX, Hu GH. Numerical simulation and experimental validation of mixing performance of kneading discs in a twin screw extruder. Polymer Engineering & Science. 2009;49(9):1772-83.
6. Manas-Zloczower I, Kaufman M, Alemaskin K, Camesasca M. Color Mixing in Extrusion: Simulations and Experimental Validation. NSF DMII Grantees Conference; Scottsdale Arizona, USA2005.
7. Alemaskin K, Manas-Zloczower I, Kaufman M. Color mixing in the metering zone of a single screw extruder: numerical simulations and experimental validation. Polymer Engineering & Science. 2005;45(7):1011-20.
8. Alemaskin K, Manas-Zloczower I, Kaufman M. Entropic analysis of color homogeneity. Polymer Engineering & Science. 2005;45(7):1031-8.
9. Alemaskin K. Entropic Measures of Mixing in Application to Polymer Processing: Case Western Reserve University; 2004.
10. Alemaskin K, Camesasca M, Manas-Zloczower I, Kaufman M, editors. Entropic measures of mixing tailored for various applications. AIP Conference Proceedings; 2004: AIP.
11. Alemaskin K, Camesasca M, Manas-Zloczower I, Kaufman M, Kim E, Spalding MA, et al., editors. Entropic mixing characterization in a single screw extruder. SPE ANTEC; 2004.
12. Alemaskin K, Manas–Zloczowe I, Kaufman M. Index for simultaneous dispersive and distributive mixing characterization in processing equipment. International Polymer Processing. 2004;19(4):327-34.
13. Alemaskin K, Manas-Zloczower I, Kaufman M, editors. Simultaneous characterization of dispersive and distributive mixing in a single screw extruder. Proceedings of the Int Conf ANTEC; 2003.
14. Wang W, Zloczower I, editors. Dispersive and distributive mixing characterization in extrusion equipment. Antec 2001 Conference Proceedings; 2001.
15. Tadmor Z, Gogos CG. Principles of Polymer Processing: Wiley; 2006.
16. Xu B, Yu H, Kuang T, Turng LS. Evaluation of Mixing Performance in Baffled Screw Channel Using Lagrangian Particle Calculations. Advances in Polymer Technology. 2017;36(1):86-97.
17. Yamada S, Fukutani K, Yamaguchi K, Funahashi H, Ebata K, Uematsu H, et al. Dispersive mixing performance evaluation of special rotor segments in an intermeshing co-rotating twin-screw extruder by using weighted probability distributions. International Polymer Processing. 2015;30(4):451-9.
18. Chen J, Cao Y, editors. Simulation of 3D flow field of RPVC in twin-screw extrusion under wall slip conditions. Proceedings of 2012 9th International Bhurban Conference on Applied Sciences and Technology, IBCAST 2012; 2012.
19. Wang W, Manas-Zloczower I, Kaufman M. Entropic characterization of distributive mixing in polymer processing equipment. AIChE Journal. 2003;49(7):1637-44.
20. Manas-Zloczower I, Agassant JF. Mixing and Compounding of Polymers: Theory and Practice: Hanser; 2009.
21. Ansys C-P. CFD-Post User's Guide. Ansys Inc.

14th International Conference on CFD in Oil & Gas, Metallurgical and Process Industries
SINTEF, Trondheim, NORWAY
October 12-14, 2020

CFD APPROACH TO SIMULATE TWO PHASE FLOW INLINE-SEPARATOR COUPLING IBM, LES, LAGRANGIAN TRACKING AND VOF METHODS

Hanane ATMANI[1]*, **Rémi ZAMANSKY**[1], **Eric CLIMENT**[1], **Dominique LEGENDRE**[1]
[1]Institut de Mécanique des Fluides de Toulouse (IMFT), Université de Toulouse, CNRS.
2 Allée du Professeur Camille Soula, Toulouse, 31400, France.

* E-mail: hanane.atmani@imft.fr

ABSTRACT

Inline fluid separation using a swirl element is a recent technology for oil/gas processing. Centrifugal forces up to 100 times the gravitational acceleration separate the phases, leaving the heavy phase close to the wall and the light one in the center. The current study is part of a Europeen project TOMOCON aiming at developing CFD methods in the in-house code JADIM to simulate the two-phase flow separation in order to help the development of inline separation control. The objective is to propose a hybrid approach based on Navier Stokes solver that makes possible accurate simulations with coarse spatial resolution. First, Immersed Boundary Method (IBM) is used to simulate both the pipe and the complex geometry of the swirl element on a cartesian regular mesh. Turbulence is modeled by the classical dynamic Smagorinsky sub-grid model in Large Eddy Simulation (LES) with a special stochastic wall law coupled to the IBM allowing to avoid the need for a mesh refinement in the near wall region. A Lagrangian tracking (LT) method is used to solve the dispersed bubbly flow and it is coupled to the Volume of Fluid (VoF) approach once the coalescence takes place and the gas core is formed. The numerical strategy based on the coupling of these different methods is presented and we report some of the simulations used for the verification-validation of the numerical developments.

Keywords: CFD, two-phase flow, Inline fluid separation, Swirl, IBM, LES, Lagrangian tracking, VoF. .

NOMENCLATURE

Greek Symbols

ρ	Density, $[^{kg}/_{m^3}]$
μ	Dynamic viscosity, $[^{kg}/_{ms}]$
ν	Kinematic viscosity, $[^{m^2}/_{s}]$
α_{IBM}	Solid volume fraction , $[-]$
Δt	Time step, $[s]$.

Latin Symbols

p	Pressure, $[Pa]$.
u_i	Velocity, $[^{m}/_{s}]$.
u_b	Bulk velocity, $[^{m}/_{s}]$.
v_b	Bubble velocity, $[^{m}/_{s}]$.
R	pipe radius, $[m]$.
r_b	Bubble radius, $[m]$.
V_b	Bubble volume, $[m^3]$.
C_M	Added mass coefficient, $[-]$.
C_D	Drag coefficient, $[-]$.
C_L	Lift coefficient, $[-]$.
C	Phase fraction, $[-]$.

Sub/superscripts

f	Continuous phase.
b	Dispersed phase: bubble.

INTRODUCTION

Two-phase flow separation is a common process in many industrial applications. In the oil/gas extraction, for instance, the separation can be done using gravity or a centrifugal force. Based on the latter concept, the inline separator (see figure 1), through the swirl element inserted inside the pipe, pushes the heavy phase toward the wall, leaving the light phase in the center of the separator. This type of swirling flow, having complex features, is interesting to investigate especially when experimental studies become constrained to cost and time. CFD methods allow to understand more in details the flow characteristics particulary those influencing on the separation efficiency. Neverthless, considering all the range of flow and interface length scales present in the separator, new CFD approaches need to be developed.

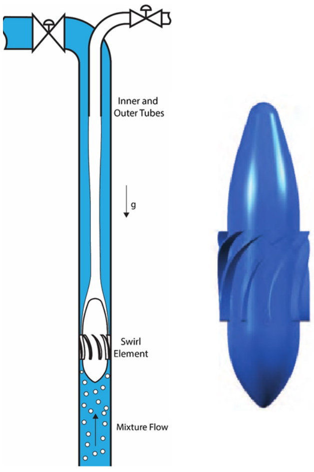

Figure 1: Sketch of the inline separator (left), swirl element (right)

Indeed, the interface scales are typically ranging from 1 m the length of the device (pipe, swirl element) to 10^{-4} m the size of the smallest bubbles and drops. The flow is highly turbulent ($Re = 10^4 - 10^6$), and the swirl element geometry is complex. The numerical strategy proposed here combines the Immersed Boundary Method (IBM) for the complex geometry, the Large Eddy Simulation (LES) for the turbulent flow, the Lagrangian Tracking (LT) for the dispersed phase and the Volume of Fluid (VoF) for the interface of the core formed in the separator wake. To simulate complex geometries, many methods exist for solid/fluid interaction. Peskin (Peskin, 1977) was the first to introduce Immersed Boundary Method (IBM) to study flow patterns around heart valves. This method is based on adding the force applied by the solid on the fluid to Navier Stokes equation and to locate the surface of the solid, Lagrangian markers are defined on the Eulerian grids. Bigot (Bigot *et al.*, 2014) replaced the use of those Lagrangian points by a solid volume fraction which is 0 is the fluid, 1 in the solid and between 1 and 0 through the interface. This enables to reduce the cost of the computation and provides a smooth transition across the fluid and the solid.

Considering the large Reynolds number of the flow in the process, the flow is turbulent. Therefore, performing Direct Numerical Simulation (DNS) becomes computationally impossible as the Reynolds number increases. In fact, to solve all time and 3D spatial scales, DNS requires a small time step and a number of the cell $N = O(Re^{9/4})$. For turbulence modeling we consider the LES method which models only scales below the filter size (the grid size). One of the interesting models in LES and which is suitable to confined flows is the mixed dynamic Smagorinsky model (Calmet and Magnaudet, 1997). This approach has been proved to handle very well the turbulent viscosity next to the wall through the calculation of a local Smagorinsky coefficient instead of using a constant value in the whole domain. However, a resolved LES always demands that 4 to 5 cells should be located in the viscous sub-layer. Therefore, it requires a significant mesh refinement close to the wall because the thickness of the viscous sub-layer decreases with the increase of the Reynolds number. To avoid this constraint, wall models are oftenly used and special treatments of the wall are done when the latter is simulated using IBM. Simplifying the Navier Stokes equations to have the thin boundary layer equation, Ma (Ma *et al.*, 2019) solved this equation on an embedded mesh to get the local wall shear stress at the IB cells and then corrected the SGS viscosity to take into account the IB forcing. In our work, a stochastic model for the velocity imposed inside the IBM boundary layer is used (Atmani *et al.*, 2020). This model makes possible an accurate resolution of both the mean velocity and the rms fluctuations on a coarse mesh in the bulk of a high Reynolds turbulent pipe flow.

Two phases are present in the separator and they are organized as dispersed before the separator and stratified flow in the separator wake. Each phase has to be treated using a specific approach: a LT method for the dispersed phase and a VoF method for the gas core in the separator wake. To take advantage from both methods, hybrid approaches have been recently proposed to make possible a dynamic switch. This kind of model is interesting when the bubbles/droplets are accumulated to form a core or when the VoF core is dispersed into small bubbles/droplets, as observed in two phase flow separation.

MODEL DESCRIPTION

The numerical approach is based on the IMFT-in-house CFD code JADIM. It solves the Navier-Stokes equations for incompressible, unsteady, three dimensional flows (Calmet and Magnaudet, 1997) (Legendre and Magnaudet, 1998):

$$\frac{\partial u_i}{\partial x_i} = 0 \tag{1}$$

$$\frac{\partial u_i}{\partial t} + \frac{\partial u_i u_j}{\partial x_j} = -\frac{1}{\rho}\frac{\partial p}{\partial x_i} + \nu \frac{\partial^2 u_i}{\partial x_j \partial x_j} + f_i \tag{2}$$

with f_i is the sum of any existing volumetric force applied on the fluid.

The diffusive term is solved using a semi implicit Crank Nicolson scheme, while the other terms are treated explicitly by Runge Kutta 3 and the projection method is used to satisfy the incompressibility condition 1.

Large Eddy Simulation

Using the mixed dynamic Smagorinsky model (Calmet and Magnaudet, 1997), the filtered Navier Stokes equations are:

$$\frac{\partial \overline{u}_i}{\partial x_i} = 0 \tag{3}$$

$$\frac{\partial \overline{u}_i}{\partial t} + \frac{\partial \overline{u}_i \overline{u}_j}{\partial x_j} = -\frac{1}{\rho}\frac{\partial \overline{p}}{\partial x_i} + \nu \frac{\partial^2 \overline{u}_i}{\partial x_j \partial x_j} - \frac{\partial \tau_{ij}^{SGS}}{\partial x_j} + \overline{f}_i \tag{4}$$

where $\overline{u}_i$ with (i=1,2,3) is now the filtered velocity, $\overline{p}$ is the filtered pressure, $\overline{f}_i$ is the filtered body force.

$\tau_{ij}^{SGS} = \overline{u_i u_j} - \overline{u}_i \overline{u}_j$ is the sub-grid stress tensor (SGS). It is can be expressed as the sum the following terms:

$$L_{ij} = \overline{\overline{u}_i \overline{u}_j} - \overline{\overline{u}}_i \overline{\overline{u}}_j \tag{5}$$

$$C_{ij} = \overline{\overline{u}_i u'_j} + \overline{\overline{u}_j u'_i} - \overline{\overline{u}}_i \overline{u'}_j - \overline{\overline{u}}_j \overline{u'}_i \tag{6}$$

$$R_{ij} = \overline{u'_i u'_j} - \overline{u'}_i \overline{u'}_j \tag{7}$$

The Leonard term L_{ij} is calculted explicitly.

$$\tau_{ij}^{SGS} - \frac{1}{3}\tau_{kk}^{SGS}\delta_{ij} = -2\nu_T \overline{S}_{ij} + L_{ij} - \frac{1}{3}L_{kk}\delta_{ij} \tag{8}$$

where $\overline{S}_{ij}$ is the strain rate tensor calculated from the resolved velocity field and the turbulent viscosity ν_T is given by:

$$\nu_T = C\overline{\Delta}^2 (2\overline{S}_{ij}\overline{S}_{ij})^{\frac{1}{2}} \tag{9}$$

with $\overline{\Delta}$ is the filter length. C is a local parameter calculated at each time step. By re-filtering eq (4) using $\widetilde{\Delta}$, we define: $T_{ij} = \widetilde{\overline{u_i u_j}} - \widetilde{\overline{u}}_i \widetilde{\overline{u}}_j$. Similary as τ_{ij}^{SGS}, T_{ij} is also expressed in function of C as:

$$T_{ij} - \frac{1}{3}T_{kk}\delta_{ij} = -2C\widetilde{\overline{\Delta}}^2 |\widetilde{\overline{S}}|\widetilde{\overline{S}}_{ij} + L_{ij}^T - \frac{1}{3}L_{kk}^T\delta_{ij} \tag{10}$$

with $L_{ij}^T = \widetilde{\overline{\overline{u}_i \overline{u}_j}} - \widetilde{\overline{\overline{u}}}_i \widetilde{\overline{\overline{u}}}_j$. Both T_{ij} and $\widetilde{\tau^{SGS}}_{ij}$ cannot be calculated explicitly however the difference $l_{ij} = T_{ij} - \widetilde{\tau^{SGS}}_{ij} = \widetilde{\overline{u}_i \overline{u}_j} - \widetilde{\overline{u}}_i \widetilde{\overline{u}}_j$ can be and allows to find the local coefficient C:

$$\begin{aligned} l_{ij} - \frac{1}{3}l_{kk}\delta_{ij} = -2C(\widetilde{\overline{\Delta}}^2 |\widetilde{\overline{S}}|\widetilde{\overline{S}}_{ij} - \overline{\Delta}^2 \widetilde{|\overline{S}|\overline{S}_{ij}}) - \widetilde{\overline{\overline{u}}}_i \widetilde{\overline{\overline{u}}}_j \\ + \widetilde{\overline{\overline{u}}_i \overline{\overline{u}}_j} + \frac{1}{3}(\widetilde{\overline{\overline{u}}}_k \widetilde{\overline{\overline{u}}}_k - \widetilde{\overline{\overline{u}}_k \overline{\overline{u}}_k})\delta_{ij} \end{aligned} \tag{11}$$

C is then:

$$C = -\frac{(l_{ij} - h_{ij})M_{ij}}{2M_{ij}M_{ij}} \tag{12}$$

with $M_{ij} = \widetilde{\overline{\Delta}}^2 |\widetilde{\overline{S}}|\widetilde{\overline{S}}_{ij} - \overline{\Delta}^2 \widetilde{|\overline{S}|\overline{S}_{ij}}$ and $h_{ij} = \widetilde{\overline{\overline{u}}_i \overline{\overline{u}}_j} - \widetilde{\overline{\overline{u}}}_i \widetilde{\overline{\overline{u}}}_j$

Immersed Boundary Method

To simulate the fluid/solid interaction, we use Immersed Boundary Method (IBM) by adding to Navier-Stokes equation a volumetric force $\overline{f}_{IBM}$ (Bigot *et al.*, 2014):

$$\overline{f}^{k}_{IBM,i} = \alpha_{IBM}\frac{\overline{vs}_i^{k-1} - \widehat{u}_i^k}{\Delta t} \tag{13}$$

with vs_i is the local velocity imposed to the solid, $\widehat{u}_i$ is the predictor fluid velocity without considering the solid. α_{IBM} is defined by a mathematical expression allowing to describe the geometry (Yuki and Takeuchi, 2007):

$$\alpha_{IBM}(x) = \frac{1}{2}[1 - \tanh(\frac{(\|\mathbf{x} - \mathbf{x}_p\| - R)}{\sqrt{2}\lambda\eta\Delta})] \tag{14}$$

with $\lambda =\mid n_x \mid + \mid n_y \mid + \mid n_z \mid$ is calculated using the components of **n** the normal outward unit vector at the surface. $\eta = 0.065(1-\lambda^2) + 0.39$ is a parameter controlling the thickness of the transition region. A new stochastic wall model has been developed to enhance the forcing term of IBM through a correction of the solid velocity based on a log law inside the transition from solid to fluid taking into account the spatio-temporal correlation of the wall shear stress for the simulation of turbulent flows (Atmani *et al.*, 2020).

Lagrangian tracking

Lagrangian tracking consists in solving the trajectory equation for each bubble/droplet taking into account the buoyancy force, the drag force, the lift force, the added mass and Tchen forces (Chouippe *et al.*, 2014). Each bubble/droplet trajectory is obtained by solving:

$$\frac{d\mathbf{x}_b}{dt} = \mathbf{v}_b \tag{15}$$

where the bubble/droplet velocity is obtained by integrating the force balance:

$$(\rho_b + C_M\rho_f)V_b\frac{dv_{p,i}}{dt} = (\rho_b - \rho_f)V_b g_i +$$
$$C_D\rho_f\frac{\pi r_p^2}{2}\|u - v_b\|(u_i - v_{b,i}) + C_L\rho_f V_b(u_i - v_{b,i}) \wedge \Omega +$$
$$\rho_f V_b(1 + C_M)\frac{Du_i}{Dt} \tag{16}$$

When considering the LES approach, the fluid velocity $u_{\mathbf{x}_b}$ and acceleration $Du/Dt|_{\mathbf{x}_b}$ at the bubble location $\mathbf{x} = \mathbf{x}_b$ are obtained by a second order interpolation of the filtered velocity $\overline{u}$. A two way coupling approach is also considered to take into account the effect of the bubbles/droplets on the fluid. Moreover, the bubbles/droplets can be in interaction with the solid wall described using the IBM method and a collision model has been introduced to model the rebound on the wall with a restitution coefficient r (is 1 for full restitution):

$$v_{b,i}^{new} = v_{b,i} - (1 + r)(\mathbf{n}.\mathbf{v}_b)n_i \tag{17}$$

where **n** is the solid surface normal oriented to the fluid.

Volume of Fluid

The Volume of Fluid (VoF) approach considered here is an interface capturing method without an interface reconstruction allowing to simulate the break-up and the coalescence. It is based on the VoF volume fraction C which equals 1 in one phase and 0 in the other. The value of C varies between 0 and 1 across the interface and is governed by the transport equation solved using the FCT (Flux Corrected Transport scheme) (Zalesak, 1979) (Bonometti and Magnaudet, 2007):

$$\frac{\partial C}{\partial t} + u_i.\frac{\partial C}{\partial x_i} = 0 \tag{18}$$

The capillarity force is added to Navier Stokes equation and is solved using the classical CSF (Continuum Surface Force) model intoduced by Brackbill(Brackbill *et al.*, 1992):

$$F_\sigma = \sigma\nabla.(\frac{\nabla C}{\|\nabla C\|})\nabla C \tag{19}$$

The hybrid LT/VoF model is activated when the coalescence of the bubbles occurs i.e. after the swirl element. The algorithm for switching from Lagrangian tracking to VoF is decomposed as following:

1- Identify any bubble/droplet verifying the coalescence criteria i.e. inside a cell where $0 < C < 1$.

2- The detected bubbles/droplets are removed from the Lagrangian solver and the phase fraction C is updated by adding the volume of those bubbles/droplets.

RESULTS

The objective of this paper is to present the preliminary results of our approach consisting in coupling the methods IBM, LES, LT and VoF and to report some of the simulations used for the verification-validation of the numerical developments. The numerical domain used for the system considered in this work is of size $L_x \times L_y \times L_z = 0.9m \times 0.104m \times 0.104m$ on a regular cartesian mesh made of $N_x \times N_y \times N_z = 800 \times 92 \times 92$ cells in the x ,y and z directions, respectively. The pipe diameter is $D = 2R$ and its axis is along the x-direction. First, we have to describe the complex geometry of the separator system using the IBM as reported in Figure 2. The flow field has been simulated for different Reynolds number defined using the pipe diameter $D = 2R$ and the pipe mean velocity u_b. Figure 2 represents the streamlines for $Re = \rho D u_b/\mu = 4500$, u_b being the bulk velocity. The velocity field is clearly swirled by the separator and a vortex is formed in the separator wake. The velocity reaches its maximum next to the blades of the swirl element. To characterize the strength of the swirling flow, we introduce the dimensionless swirl number S defined as the ratio of the axial flux of the angular momentum to the axial flux of the axial bulk momentum:

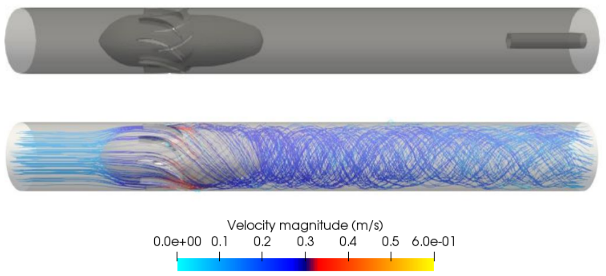

Figure 2: (Top) Description of the pipe, the separator and the pick-up tube using IBM. The contour $\alpha_{IBM} = 0.5$ is shown on the figure. (Bottom) Streamlines of single phase flow in the separator for $Re = 4500$.

$$S(x) = \frac{\int \rho r u_x u_\theta dA}{R\rho u_b^2 A} \tag{20}$$

where u_x is the axial velocity, u_θ is the angular velocity and A is the pipe section. Figure 3 presents the variation of the swirl number S along the pipe. S is maximum at the end of the swirl element and then it decreases following the relation obtained experimentally (Dirkzwager, 1996):

$$S(x) = S_0 \exp(-C_{ds}(x - x_0)/D) \tag{21}$$

where S_0 is the swirl number at the reference point x_0 right after the swirl element, D is the pipe diameter and C_{ds} is a swirl decay coefficient depending on Re, the roughness of the pipe and the swirl intensity. Figure 4 presents the radial distribution of the dimensionless time-averaged axial and azimuthal velocities as well as pressure downstream the swirl element for a distance of D/2, 2D, 3D. The centrifugal force on the fluid, acting towards the wall, is the reason why the pressure drops in the center. In addition we can easily see that the pressure increases with the increase of the azimuthal velocity. The axial velocity profile shows the occurence of a reverse flow behind the swirl element, a phenomenon which characterizes swirling flows in general.

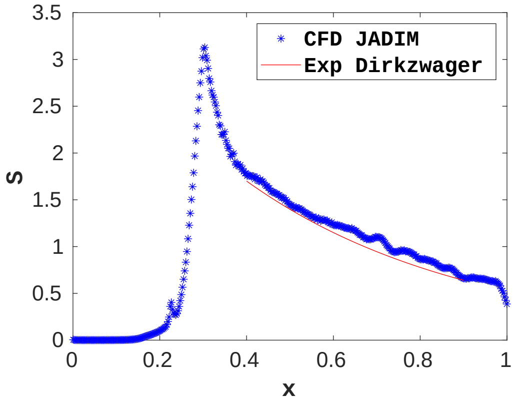

Figure 3: The swirl number S in function of the position x, fitting in red line based on Dirkzwager results where: $x_0 = 0.4$, $S_0 = 1.32$, $C_{ds} = 0.21$.

Now, a set of 10^5 bubbles of radius 1mm are injected at the inlet with the fluid velocity (see figure 5). The simulation shows that a relatively small group of bubbles is accumulated around the center of the pipe. The lift force induced by the swirling flow is expected to induce the migration of the bubbles to the pipe center. The magnitude of the lift force is directly proportional to the magnitude of the vortex generated in the separator wake. Its magnitude is expected to increase with increasing Reynolds number. Simulation of high Reynolds number flow has required the development of a specific wall modeling for LES simulations applied to the IBM wall zone ($0 < \alpha_{IBM} < 1$) (Atmani *et al.*, 2020). The proposed LES-IBM modeling allows an accurate simulation of the mean and rms velocities in the bulk of high Reynolds turbulent pipe flows with a coarse mesh (typically, a grid size of order 100 times the wall unit for $Re = 10^6$). Finally to make possible the global simulation of all the physical mechanisms involved in the separation process, the proposed coupling between the LT and VoF solvers has to be validated. For that purpose, the numerical set up is simplified and we model the velocity fields in the separator wake by considering a Taylor Couette flow generated by the pipe wall rotation. Bubbles are randomly injected. Figure 6 illustrates the bubbles accumulation towards the pipe center resulting in an air core formation.

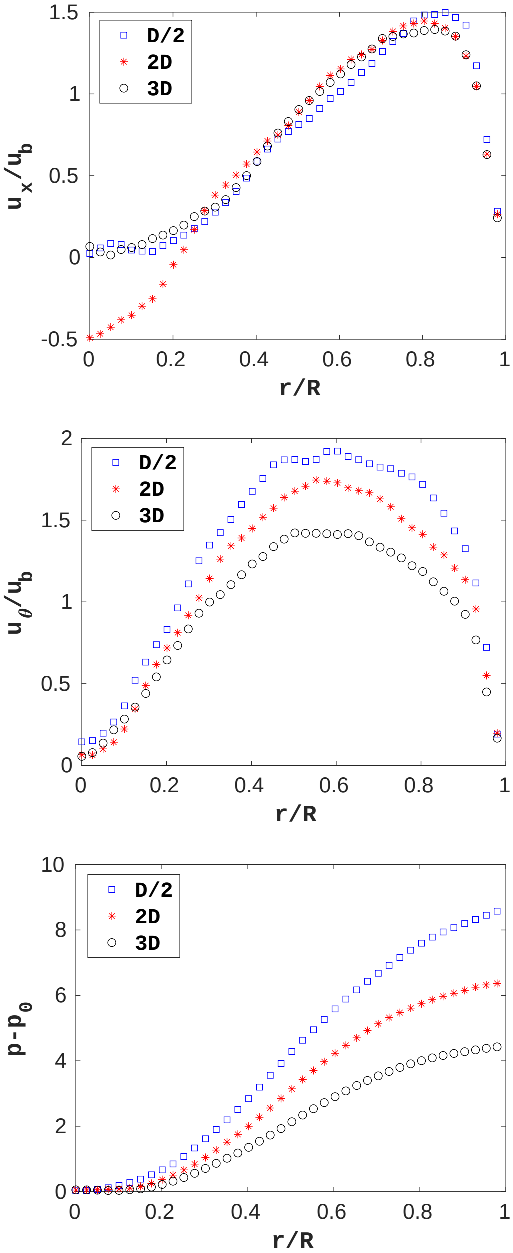

Figure 4: The radial distribution of the axial, the azimuthal velocities and pressure.

Figure 5: Simulation of two phase flow.

CONCLUSION

We have presented the numerical strategy developed to make possible accurate simulations of the inline separation with limited CPU cost. The complexity of the geometry and the large characteristic length scales involved in the process for both the turbulent flow and the interface topology (from dispersed to separated) make the numerical simulation challenging. The numerical strategy proposed here combines the Immersed Boundary Method (IBM) for the separator geometry, the Large Eddy Simulation (LES) for the turbulent flow, the Lagrangian Tracking (LT) for the dispersed phase and the Volume of Fluid (VoF) for the interface of the core formed in

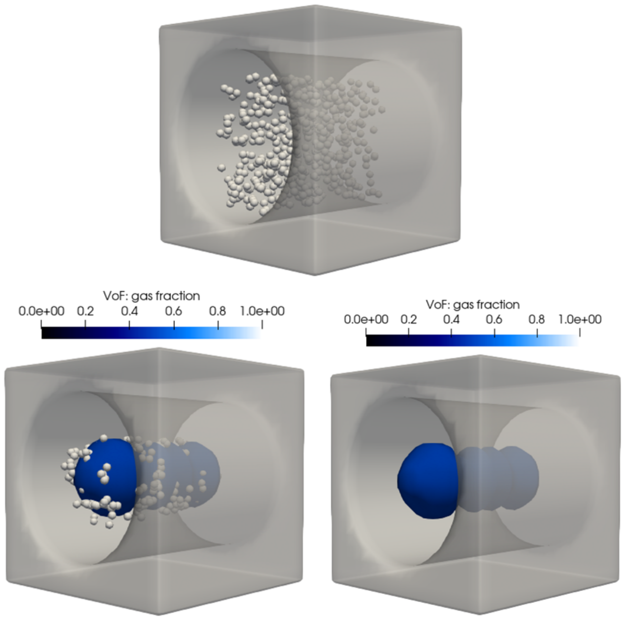

Figure 6: (top): Initial condition for the bubbles position. (bottom left) bubbles are accumulating at the center and are generating the gas core. (bottom right) All bubbles have been captured inside the air core.

the separator wake. The objective of this paper was to present the different steps of validation with a particular attention to the coupling between the methods. Some validations still need to be carried out in particular for the core formation in the separator wake for large Reynolds numbers. Numerical results of the entire process will then be compared to the experimental data produced by our partners TU Delft, TUL and HZDR in the TOMOCON H2020 project.

ACKNOWLEDGMENTS

This work is done within the TOMOCON project which has received funding from the European Union's Horizon 2020 research and innovation programme under the Marie Sklodowska Curie grant agreement No 764902. Numerical simulations were performed using high-performance computing resources from CALMIP Center of the University of Toulouse.

REFERENCES

ATMANI, H., ZAMANSKY, R., PEDRONO, A., CLIMENT, E. and LEGENDRE, D. (2020). "Stochastic wall model for turbulent pipe flow using immersed boundary method and large eddy simulation". *Computers and fluids, (in progress)*.

BIGOT, B., BONOMETTI, T., THUAL, O. and LACAZE, L. (2014). "A simple immersed boundary method for solid fluid interaction in constant and stratified density flows". *J. Computers and fluids*.

BONOMETTI, T. and MAGNAUDET, J. (2007). "An interface capturing method for incompressible two-phase flows. val- idation and application to bubble dynamics". *International Journal of Multiphase Flow*.

BRACKBILL, J., KOTHE, D. and ZEMACH, C. (1992). "A continuum method for modeling surface tension." *J Comput Phys*.

CALMET, I. and MAGNAUDET, J. (1997). "Large eddy simulation of high schmidt number mass transfer in a turbulent channel flow". *Physics of Fluids*.

CHOUIPPE, A., CLIMENT, E., LEGENDRE, D. and GABILLET, C. (2014). "Numerical simulations of bubble dispersion in turbulent taylor couette flow". *Physics of Fluids*.

DIRKZWAGER (1996). *A new axial cyclone design for fluid separation*. Ph.D. thesis, Delft university of Technology.

LEGENDRE, D. and MAGNAUDET, J. (1998). "The lift force on a spherical bubble in a viscous linear shear flow." *J. Fluid Mech.*

MA, M., HUANG, W. and XU, C. (2019). "A dynamic wall model for large eddy simulation of turbulent flow over complex/ moving boundaries based on the immersed boundary method". *Physics of Fluids*.

PESKIN, C. (1977). "Numerical analysis of blood flow in the heart". *J. Comput. Phys*.

YUKI, Y. and TAKEUCHI, S. (2007). "Efficient immersed boundary method for strong interaction problem of arbitrary shape object with the self-induced flow". *Journal of Fluid Science and Technology*.

ZALESAK, S.T. (1979). "Fully multidimensional flux corrected transport algorithms for fluids". *Journal of computational physics*.

TOWARD COMPUTATIONAL MODELS OF ARC DYNAMICS IN SILICON SMELTERS

Quinn Gareth REYNOLDS
Mintek, Private Bag X3015, Randburg 2125, South Africa
University of Stellenbosch, Private Bag X1, Matieland, Stellenbosch 7602, South Africa

E-mail: quinnr@mintek.co.za

ABSTRACT

The production of silicon in electric smelting furnaces is a complex and energy-intensive process. High current plasma arcs are used in such furnaces to generate the temperatures required for the chemical reaction of silica to silicon. In order to facilitate further study of such processes, a computational magnetohydrodynamic model suitable for studying the electrical and dynamic behaviour of alternating current plasma arcs at industrial scales is described. An implementation of the model in the OpenFOAM® computational mechanics framework is developed, tested, and validated. A simulation workflow for prediction of practical aspects of furnace operation is demonstrated with a simple example calculation of the dependence of electrical parameters on electrode position for systems with multiple arcs in the presence of a test gas (Argon). It was found that the nonlinear electrical behaviour of the arc was exaggerated by the presence of multiple arcs, and that control of the furnace's voltage and current parameters by moving the electrodes could be negatively affected as a result.

Keywords: multiphysics, magnetohydrodynamics, plasma, pyrometallurgy .

NOMENCLATURE

Greek Symbols

α_R	Radiative absorption coefficient, $[1/m]$
δ_l	Mesh element size, $[m]$
ϵ_R	Radiative emission coefficient, $[1/m]$
ϕ	Electric potential, $[V]$
κ	Thermal conductivity, $[W/m.K]$
μ	Viscosity, $[Pa.s]$
μ_0	Vacuum permeability, $[N/A^2]$
ρ	Density, $[kg/m^3]$
σ	Electrical conductivity, $[1/\Omega m]$
$\bar{\bar{\tau}}$	Viscous stress tensor, $[N/m^2]$

Latin Symbols

$\mathbf{A}$	Magnetic vector potential, $[T.m]$
$\mathbf{B}$	Magnetic flux density, $[T]$
C_P	Heat capacity, $[J/kg.K]$
e	Elementary charge, $[C]$
$\mathbf{g}$	Gravitational acceleration, $[m^2/s]$
G	Radiative energy intensity, $[W/m^3]$
h	Specific enthalpy, $[J/kg]$
I	Current, $[A]$
$\mathbf{j}$	Current density, $[A/m^2]$
k_b	Boltzmann constant, $[J/K]$
L_a	Arc length, $[m]$
P	Pressure, $[Pa]$
q	Energy flux, $[W/m^2]$
Q	Energy source term, $[W/m^3]$
T	Temperature, $[K]$
$\mathbf{u}$	Velocity, $[m/s]$
V_a	Arc voltage, $[V]$

INTRODUCTION

During industrial production of silicon metal, the first stage in the process is the smelting of quartz ores containing silica (SiO_2) together with a mixture of carbonaceous reductants such as wood chips and metallurgical coke. This is generally performed in alternating current (AC) electric furnaces of circular design, using three vertically-mounted self-baking graphite electrodes. The raw materials are fed through the furnace roof and form a deep porous bed layer inside the containment vessel (the burden). An open cavity or "crater" is formed around the tip of each electrode inside the burden. Inside the crater, an electric arc operates between the tip of the electrode and the surface of the molten process products. High temperatures in the plasma arc (>10000°C) provide the required energy to drive the chemical reactions of SiO_2 to Si metal (Gasik, 2013). An illustration of a typical silicon furnace is shown in Figure 1.

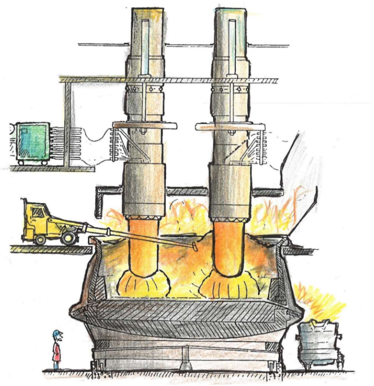

Figure 1: Layout and interior of a typical silicon smelter (image credit: Thorsteinn Hannesson, www.elkem.is).

A diagram of the crater region is shown in Figure 2. A unique feature of silicon processes is that the crater cavity is often surrounded by a shell of solid silicon carbide (SiC) which forms as an intermediate reaction product. The conductive SiC layer provides an alternative current path between the electrode and the molten bath via one or more side arcs, which can operate in the upper part of the crater.

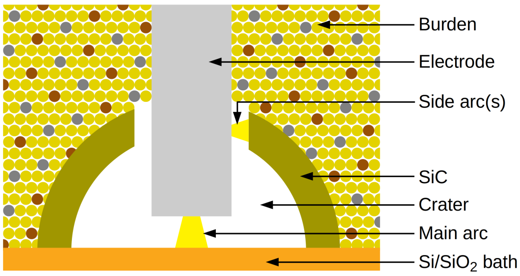

Figure 2: Structure of arc crater and surrounding burden.

Extensive work has been conducted in the development of numerical models for the study of arcs in pyrometallurgical furnaces. These generally fall into two distinct categories: *process models* which use simplified semi-empirical descriptions of the arc to capture observable phenomena such as overall energy balances and voltage-current relationships, and *computational models* which attempt to solve some or all of the fundamental governing equations of the plasma arc system in time and space. Examples of the former include channel arc models (Larsen, 1996) (Sævarsdóttir *et al.*, 1998) (Sanchez *et al.*, 2009), and arc shape models (Bowman and Krüger, 2009). Computational models have been continuously developed since the 1980s and modern multiphysics models may include power supply and transformer interaction effects (Sævarsdóttir *et al.*, 2001) (Reynolds, 2018), sophisticated boundary conditions to account for plasma non-ideality in anode and cathode regions (Lowke *et al.*, 1997) (Sævarsdóttir *et al.*, 2006), and applications to high current industrial systems (Sævarsdóttir *et al.*, 2006). Recent work has also examined the current distribution between main and side arcs in the crater using multi-region models (Tesfahunegn *et al.*, 2018).

Because they are computationally cheap and can often be run in real time or better, process models are most useful in furnace design, operation, and control while computational models are usually reserved for academic research. However with sustained exponential growth in available computer power, it is becoming increasingly feasible to use full-featured computational models in the furnace design and operation space; the present work aims to develop and demonstrate a modelling framework which can form the basis for numerical experiment and virtual prototyping studies in the future.

MODEL DESCRIPTION

Plasma arcs are a coupled physical system arising from interactions between multiple distinct phenomena: fluid flow, heat transfer, electromagnetism, and chemical reactions. Governing equations for each of these phenomena must be described. In the case of fluid flow, this is the compressible Navier-Stokes and continuity equations, including the Lorentz source term for acceleration of the plasma by electromagnetic fields:

$$\frac{\partial\left(\rho\mathbf{u}\right)}{\partial t} + \nabla\cdot\left(\rho\mathbf{u}\otimes\mathbf{u}\right) + \nabla P = \nabla\cdot\bar{\bar{\tau}} + \mathbf{j}\times\mathbf{B} - \rho\mathbf{g} \quad (1)$$

$$\frac{\partial\rho}{\partial t} + \nabla\cdot\left(\rho\mathbf{u}\right) = 0 \quad (2)$$

Heat transfer is described by the energy conservation equation and includes terms describing enthalpy transport by electrons, joule heating, thermal radiation, and mechanical heating. The complete energy equation is given by:

$$\frac{\partial\left(\rho h\right)}{\partial t} + \nabla\cdot\left(\rho\mathbf{u}h\right) = \nabla\cdot\left(\frac{\kappa}{C_P}\nabla h\right) + \nabla\cdot\left(\frac{5k_B h\mathbf{j}}{2eC_P}\right) + \frac{\mathbf{j}\cdot\mathbf{j}}{\sigma} - Q_r + Q_m \quad (3)$$

The enthalpy and pressure determine a unique temperature field, and (3) is therefore effectively an equation in T. The mechanical source Q_m includes standard terms for heating by pressure and kinetic energy changes in compressible flows (viscous dissipation is neglected). The thermal radiation source Q_r is a complex function of temperature, wavelength, and geometry, and must be obtained from an appropriate solution of the radiative transport equation. This is discussed further in the implementation sub-section.

The electromagnetic fields are governed by Maxwell's equations, presented here in the magnetic vector potential formulation using the Coulomb gauge. Significant simplifications are made by discarding second order time derivatives related to high-speed wave propagation dynamics:

$$\nabla\cdot\mathbf{j} = 0 \quad (4)$$

$$\nabla^2\mathbf{A} = -\mu_0\mathbf{j} \quad (5)$$

$$\mathbf{j} = -\sigma\left(\nabla\phi + \frac{\partial\mathbf{A}}{\partial t} - \mathbf{u}\times\mathbf{B}\right) \quad (6)$$

$$\mathbf{B} = \nabla\times\mathbf{A} \quad (7)$$

Here, the expression for the current density vector (6) and the relationship between the magnetic vector potential and the magnetic field (7) must be substituted into (4) and (5) to obtain governing equations for ϕ and $\mathbf{A}$ respectively.

In order to provide a closure for this set of equations, the local thermodynamic equilibrium approximation (Boulos *et al.*, 1994) is used - this is generally valid in plasma arcs away from the anode and cathode surfaces. This approximation assumes that chemical as well as thermal equilibrium exists between the electrons and heavy species (ions, atoms, molecules) and eliminates the need to perform computationally-costly chemical reaction dynamics calculations. With this approximation, plasma chemical compositions and thermophysical properties may be calculated in advance as functions of the thermodynamic state variables only.

Implementation details

For most cases of relevance to industrial furnace operations, equations (1)-(5) must be solved numerically. A variety of modern computational fluid dynamics (CFD) methods are available for this including finite difference, finite volume, and meshless methods such as smoothed particle hydrodynamics and lattice Boltzmann techniques. In the present work a finite volume method implementation was developed using the OpenFOAM$^{®}$ open source computational mechanics framework (OpenFOAM, 2019). Source code from version 7, sub-version 20191118 was used as a basis for the present work.

The implementation is based on the `rhoPimpleFoam` compressible flow solver included with standard releases of OpenFOAM$^{®}$. This solver implements a segregated solution of the $\mathbf{u}$, P, and T fields, with a combined pressure-implicit with splitting of operators (PISO) and semi-implicit method for pressure-linked equations (SIMPLE) algorithm used for the CFD component.

As part of OpenFOAM®'s standard framework a number of interoperable numerical schemes are available for the finite-volume discretisation, together with shock-capturing limiters for transonic or supersonic flow cases. Although turbulence modelling was not applied in the present study a comprehensive framework is also present for this, and investigations into large-eddy simulation (LES) integration in arc models are currently underway.

The base solver was extended with a sub-module implementing solution of equations (4) and (5) for fields $\mathbf{A}$ and ϕ. The sub-module performs a loop solving the components of the magnetic vector potential and electric potential as segregated matrix equations, and iterating until the largest residual is below a specified value. This calculation is executed at each time step in a simulation, and the results are passed back to the CFD model via appropriate source terms in the momentum and energy equations. A simplified pseudo-code description of the electromagnetic solver algorithm is as follows:

```
...
calculate $\sigma(P,T)$
$n_{EM} = 0$
while $n_{EM} < n_{EM,max}$ do
    solve equation (4) for $\phi$
    store $\phi$ residual
    calculate $\mathbf{j}$ using equation (6)
    solve equation (5) for $\mathbf{A}$ components
    store $\mathbf{A}$ component residuals
    calculate $\mathbf{B}$ using equation (7)
    if $\phi$ and $\mathbf{A}$ residuals $<$ specified tolerance then
        exit while loop
    end if
    $n_{EM}$++
end while
if $n_{EM,max}$ reached then
    print convergence warning
end if
...
```

A new thermodynamics sub-module was developed in order to permit the specification of ρ, μ, C_P, κ, and σ as functions of temperature and pressure using lookup tables. For the results shown in the present paper, the properties (with the exception of the plasma density) were approximated as being invariant with pressure. A simple pseudo-compressible formulation was used which scales the density relative to a reference state in accordance with the ideal gas law:

$$\rho(T,P) = \frac{P}{P_0}\rho_0(T) \tag{8}$$

A comparison between the exact and ideal-gas scaled density was calculated for an argon plasma using the open source `minplascalc` Python package (minplascalc, 2018), and is shown in Figure 3. The agreement is very good in the weakly-compressible pressure range, with minor deviations occurring only at high temperatures when multiply-ionised species start to become significant. Although argon gas was used for all the simulations in the present work, it is expected that similar behaviour will be observed in more complex process gas plasmas.

A new absorption/emission sub-module for radiation modelling was also developed in order to allow α_R and ϵ_R to be specified as functions of temperature, pressure, and wavelength via lookup tables. For the work in this paper, the wavelength dependence was integrated out and the pressure dependence neglected in order to obtain total coefficients as functions of temperature only. These are passed as arguments to any of OpenFOAM®'s standard radiation solver sub-models, which at present includes the P_1 (used here), discrete ordinate method, and view factor models. Provided reliable values of the emission and absorption coefficients are available, these sub-models alleviate the need to pre-calculate effective values of Q_R based on fixed geometries such as cylinders or spheres at the expense of some additional computational cost. At user-defined intervals (typically each time step) the chosen radiation model is solved using a segregated matrix solution algorithm, and the results are returned to the CFD model via a radiation intensity field.

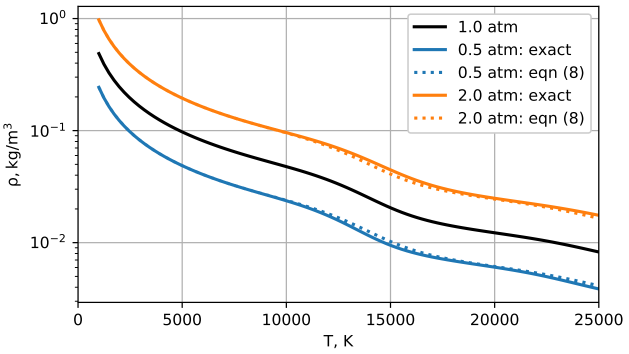

Figure 3: Comparison of ideal and pseudo-compressible density calculations for argon plasma near atmospheric pressure.

Boundary conditions for ϕ

At cathode surfaces it is often expedient to specify a fixed current density in the region where the arc attaches (Bowman and Krüger, 2009). This is complicated in cases of time-varying currents and three dimensions, since the shape, size, and location of the arc attachment zone can vary arbitrarily. In the present model this was implemented by looping over a list of all surface elements on the cathode ordered by surface temperature, and assigning each to the attachment spot until the total required area for the current at that time is reached. The boundary condition per element is then assigned as follows:

$$\frac{\partial \phi}{\partial \mathbf{n}} = \begin{cases} -\frac{j_k}{\sigma} & \text{if } \in \text{attachment zone} \\ 0 & \text{if } \notin \text{attachment zone} \end{cases} \tag{9}$$

It should be noted that more rigorous cathode and anode boundary conditions are possible, such as those developed by Lowke *et al.* (1997) and Sævarsdóttir *et al.* (2006) which directly model the behaviour of the plasma in the near-electrode sheath. It is recommended to consider such approaches in future work, particularly at high currents.

Boundary conditions for $\mathbf{A}$

The solution of the magnetic vector potential equation (5) requires spatial boundary conditions to be specified. In complex geometries these are difficult to determine precisely, although Westermoen (2007) reports that acceptable accuracy may be obtained by setting the derivative in the direction normal to the boundary surface to zero while forcing the tangential components to zero (note that Westermoen's conclusions were based on qualitative comparisons from a sensitivity study using identical models with $\mathbf{A} = 0$ Dirichlet conditions at the boundary). This is equivalent to a "magnetically insulating" boundary:

$$\frac{\partial\left(\mathbf{A}\cdot\mathbf{n}\right)}{\partial\mathbf{n}}=0,\mathbf{A}\cdot\mathbf{t}=0 \qquad (10)$$

In the present implementation of the model this is achieved by pre-computing normal and tangent vector basis sets on each surface element in the geometry at the start of the simulation, and using a linear transformation to extract the required mixed boundary condition for each component of $\mathbf{A}$ in order to satisfy (10) on arbitrarily-oriented surfaces.

Boundary conditions for T

The anode and cathode surfaces in direct contact with the arc can receive extremely high energy fluxes from the hot plasma by conduction, convection, and radiation. This can raise the surface temperature to the point at which materials begin to evaporate. In the present model this is accounted for by numerically limiting the temperature that a surface can reach, with any excess energy assumed to be taken up by the phase change:

$$\begin{cases}-\kappa\frac{\partial T}{\partial\mathbf{n}}=q_b & \text{if } T<T_v\\ T=T_v & \text{if } T\geq T_v\end{cases} \qquad (11)$$

Here, q_b is a combined expression which must account for any additional energy balances in the plasma sheath, surface radiation fluxes, energy of phase change, and energy transport into the surface by conduction or other mechanisms. In the present work this is simplified by assuming the electrode surface is in thermal equilibrium ($q_b\approx 0$) with the neighbouring plasma unless it is over the vaporisation temperature T_v. More rigorous approaches are documented in for example Pálsson *et al.* (2007) and Sævarsdóttir *et al.* (2006), and should be considered in future models.

RESULTS AND DISCUSSION

In silicon smelters, the main and side arcs typically operate at short lengths (< 15 cm) on the surface of very large electrodes (> 1.5 m). To a first approximation the arc is effectively contained between two parallel surfaces serving as cathode and anode. For the present study a simplified three-dimensional geometry was therefore used to represent the region in the immediate vicinity of the arc, and is shown in Figure 4.

The disc-shaped region is bounded by four surfaces: the *anode*, representing the molten bath or SiC surface, the *cathode*, representing the portion of the graphite electrode that the arc is allowed to attach in, the *electrode*, representing the remainder of the electrode surface, and the *open boundary* which permits inflow and outflow from the surrounding gas atmosphere in the crater. The anode, cathode, and electrode boundaries are treated as no-slip walls. The anode is held at ground potential (0 V), while the cathode boundary is specified dynamically during the simulation according to equation (9) taking into account the changing values of σ and $\mathbf{j}$ in time. An average cathode current density of j_k = 10^7 A/m^2 representative of diffuse arc attachments was assumed based on results of simulations by Sævarsdóttir *et al.* (2006). All other boundaries are treated as insulating, with a zero-gradient condition applied to ϕ. The cathode and electrode are limited in temperature to the sublimation temperature of graphite, 4100 K. The anode is similarly regulated to 3000 K representing the vaporisation temperature of either molten silica slag or solid SiC.

In the present work, the arc is assumed to be supplied with a perfectly sinusoidal current at 50 Hz. This is a simplification - in general, there will always be some degree of interaction between the arcs and the three-phase transformer feeding the furnace (Sævarsdóttir *et al.*, 1998). However due to the significant line inductances present the current waveforms generally remain much more sinusoidal than the voltage. There is also a superimposed magnetic field generated by the three electrodes which causes the arcs to be deflected away from the furnace centreline, but the examination of this effect is left for a future study.

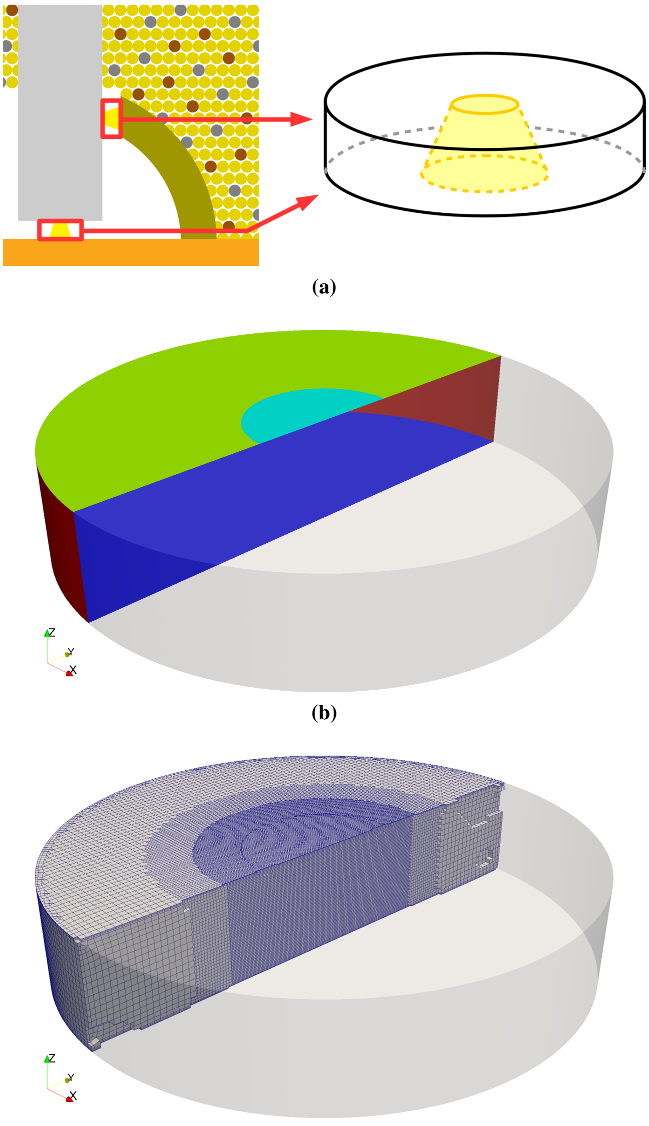

(a)

(b)

(c)

Figure 4: (a) Crater region showing model domains for arcs, (b) model region showing cathode (light blue), electrode (green), anode (dark blue) and open boundaries (red), and (b) example computational mesh showing local refinements.

For all simulations shown in the subsequent sections, argon gas was used as the plasma medium. Argon plasmas are well-studied both experimentally and theoretically, and serve as a good basis for understanding the model's trends and general behaviour before extending to specific Si-C-O atmospheres typical of silicon furnaces. Plasma property data was obtained from Boulos *et al.* (1994) or calculated using minplascalc (2018).

A second-order linear Gauss finite volume discretisation was used for the spatial component of all field variables, with the exception of velocity (limited linear TVD scheme) and enthalpy (upwind scheme). A backward Euler scheme was used for the temporal discretisation, combined with adaptive time-step calculation to limit the Courant number to below 1. The numerical parameters for the field matrix solvers are shown in Table 1, and were used in all simulations unless otherwise indicated.

Table 1: Numerical settings for OpenFOAM® plasma arc simulations

Field variable	Matrix solver	Preconditioner	Residual tolerance
P	PCG	GAMG	10^{-6}
$\mathbf{u}$	smoothSolver	n/a	10^{-7}
G	PCG	GAMG	10^{-5}
ϕ	PCG	GAMG	10^{-6}
$\mathbf{A}$	PCG	GAMG	10^{-5}

Model validation

The computational model was validated against experimental data from Larsen (1996). The current supplied in the experiment was 650 A RMS, and the arc length was 4 cm. A computational model with a volume-element resolution δ_l of 1 mm was used. The model was run for a total of 0.1 s starting from stagnant conditions (zero velocity, uniform temperature of 10000 K), with the experimental data compared against a cycle from the second half of the simulation after the initial conditions had decayed sufficiently. The results are shown in Figure 5.

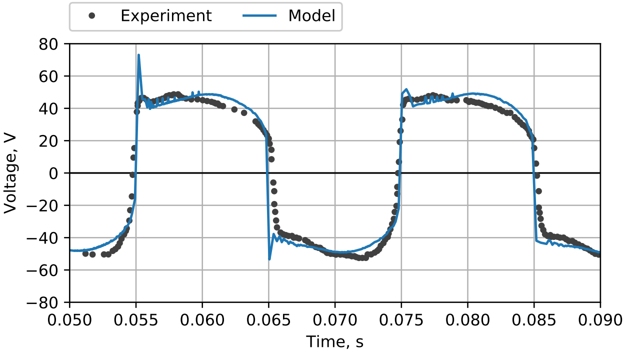

Figure 5: Comparison between experimental and model voltages for a laboratory AC arc in argon gas.

Relatively good agreement was obtained between model and experiment. In particular the RMS voltages (42.7 V for the experiment, 44.2 V for the model) match closely, and the qualitative shape of the voltage waveform is quite well captured. The differences seen are mostly high-frequency disturbances of short duration - it is possible that these are due to numerical noise in the model, or they may be real physical phenomena which are damped out by the experimental system's circuit inductance.

Mesh dependence

In order to investigate the model's accuracy on computational meshes of different resolutions, a series of argon arc simulations was performed using both the validation test case, 4 cm arc length and 650 A current, and a case close to industrial scale, 10 cm arc length and 42 kA current (for comparison, typical silicon smelters operate with arcs < 15 cm in length and between 50 and 100 kA current). The mesh resolution in the central arc region was varied in both cases, and the final two cycles of the 0.1 s simulation period were compared.

Results for the validation case are shown in Figure 6. It can be seen that the voltages predicted by the computational model are fairly insensitive to mesh resolution in this range, with values and qualitative dynamic behaviour being captured reasonably well at all resolutions.

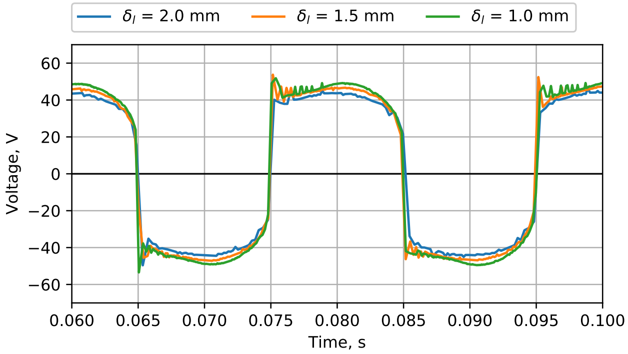

Figure 6: Model voltages at different mesh resolutions for a 4 cm arc at 650 A RMS.

For the industrial-scale case there is a transition in the resolved dynamics as the spatial resolution increases. As seen in Figure 7, although the model voltages are again not particularly sensitive to mesh resolution, there is significantly more high-frequency behaviour in the voltage during the peak current periods on finer meshes. Whether the source of this noise is numerical or physical requires further investigation, however, high-frequency dynamics have been observed in industrial arcs under different conditions (Hockaday *et al.*, 2015).

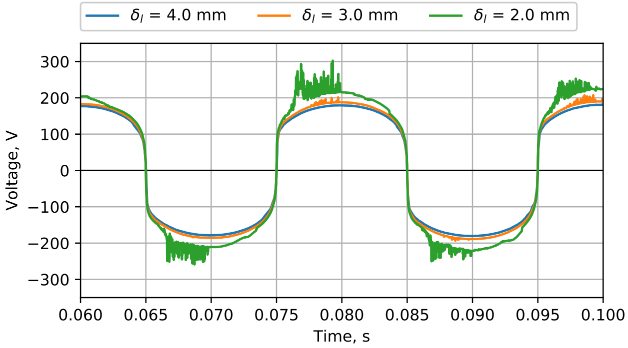

Figure 7: Model voltages at different mesh resolutions for a 10 cm arc at 42 kA RMS.

Industrial-scale arc characterisation

As a simple demonstration of the utility of computational models in studying practical furnace matters, the problem of *arc characteristics* is considered. In industrial silicon smelters the electrodes are typically mounted on mechanical or hydraulic hoists, and their position on the vertical axis is constantly adjusted by automated control systems. The power input to the furnace as well as the electrical balance between the three electrodes is maintained in this fashion in order to ensure consistent operation of the unit.

The relationship between electrode position, current, and voltage can be quite complex for AC arcs. This is further exacerbated if side arcs are present between the electrode and the SiC shell around the crater, since multiple parallel current paths to the neutral point are then possible (Tesfahunegn *et al.*, 2018). Moving the electrode changes the arc length of the main arc but has minimal effect on the side arcs; it is therefore expected that as the electrode is raised the balance of current distribution will shift from main to side arcs. This is shown schematically in Figure 8.

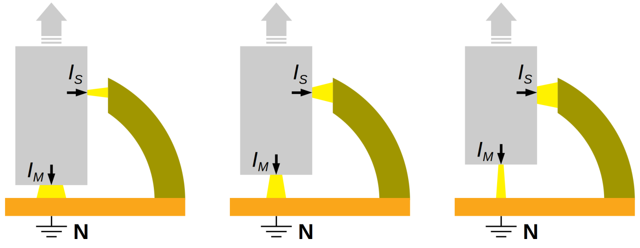

(a) $I_M > I_S$ **(b)** $I_M \approx I_S$ **(c)** $I_M < I_S$

Figure 8: Redistribution of current between main and side arcs as electrode is raised (l to r).

In order to demonstrate a methodology for quantifying such effects, the computational model was used to estimate the voltage response of an argon plasma arc over a range of electrode currents and arc lengths approximating the scale of industrial silicon furnaces - 0 to 71 kA RMS, and 0 to 10 cm. Visualisations of selected simulation results at different extremes of current and arc length are shown in Figure 9. These simulations were performed on meshes with 2 mm resolution in the central arc regions.

The voltage dynamics of the arc are shown in Figure 10 for some example cases. It can be seen that the voltage is strongly dependent on arc length and less sensitive to current, which is in line with predictions from empirical process models. As the arc length decreases, the voltage waveforms also become more rectangular and less sensitive to current. This is related to the shape of the conductive core of the arc, which tends toward cylindrical at higher currents and lower arc lengths.

AC voltages were calculated for each of the 25 cases simulated during the arc characterisation study, and are given in Table 2. In order to facilitate faster processing and use in real-time applications, the voltage results from the computational model were fitted to a simple empirical expression given in equation (12) (for currents in kA and arc length in cm). This expression has a maximum error of 6% relative to the values in Table 2, and is shown graphically in Figure 11.

Table 2: RMS voltages from arc characterisation simulations

	L_a 2 cm	L_a 4 cm	L_a 6 cm	L_a 8 cm	L_a 10 cm
I 14 kA	46.3	74.8	97.3	112.7	125.9
I 28 kA	49.8	84.4	108.3	131.1	151.2
I 42 kA	55.3	88.8	116.6	149.5	175.0
I 57 kA	55.9	92.4	123.4	167.3	194.0
I 71 kA	56.5	93.5	131.9	179.0	208.7

$$
\begin{aligned}
C_1 &= 72.9\left(1 - e^{-0.424L_a}\right) + 4.29L_a \\
C_2 &= \frac{1.45}{1 + e^{-0.755(L_a - 6.47)}} - 0.0109 \\
V_a(I, L_a) &= C_1\left(1 - e^{-0.194I}\right) + C_2 I
\end{aligned}
\tag{12}
$$

When main and side arcs are both present in the system, the total electrode current must divide between them. Assuming that the graphite of the electrode and the SiC of the crater shell are both very conductive, this implies that the arc voltages must all be approximately equal. If I_{tot} (= $I_M + I_S$), $L_{a,M}$, and $L_{a,S}$ as well as the number of separate side and main arcs are known, the current balance can be solved simply by equating the main and side arc voltages $V_{a,M}$ and $V_{a,S}$, both of which are given by equation (12).

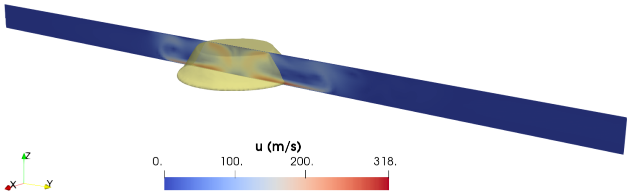

(a) I 14 kA RMS, L_a 2 cm

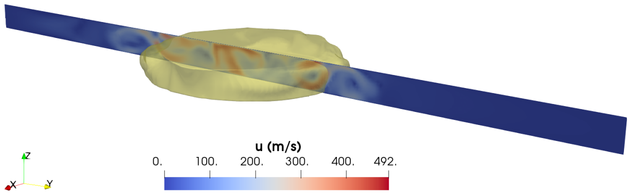

(b) I 71 kA RMS, L_a 2 cm

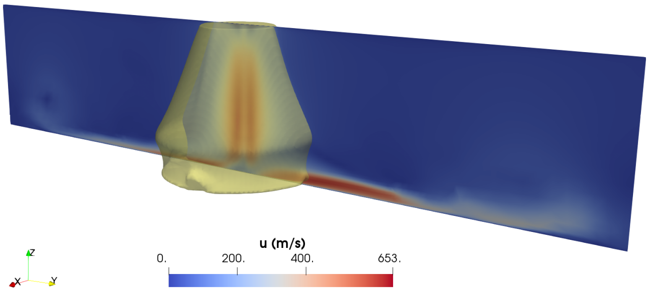

(c) I 14 kA RMS, L_a 10 cm

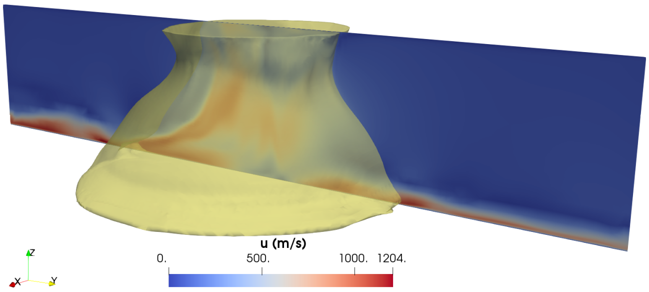

(d) I 71 kA RMS, L_a 10 cm

Figure 9: Velocity magnitude (plane) and temperature (8500 K isotherm) fields visualised at 0.1 s for selected arc characterisation simulations.

An example calculation using the present demonstration case is shown in Figure 12. In this example, only a single main and side arc were assumed to be present. The clearance between the electrode and the SiC shell is $L_{a,S}$ = 5 cm.

Several effects are apparent. Firstly, the arc system in a silicon furnace crater is likely to be a very nonlinear and non-ohmic circuit element. This has implications for the electrical design, scale-up, and operation of furnace plants.

Second, it is clear that there will be a loss of control sensitivity in the region where the main arc is longer than the side arcs. Beyond this point, changing the electrode position has less and less effect on the electrode voltage since the majority of the electrode current is being carried by the side arcs. Such an arrangement has the potential to cause runaway raising of electrodes if naive control implementations are used.

Finally, a simple means of extinguishing any side arcs is available should it become necessary to do so. Lowering the electrode into the molten bath would drop the side arc current close to zero, leaving only the main arc running when the electrode is raised again. Whether the transformers on real furnace plants are able to tolerate dead-shorting a phase to

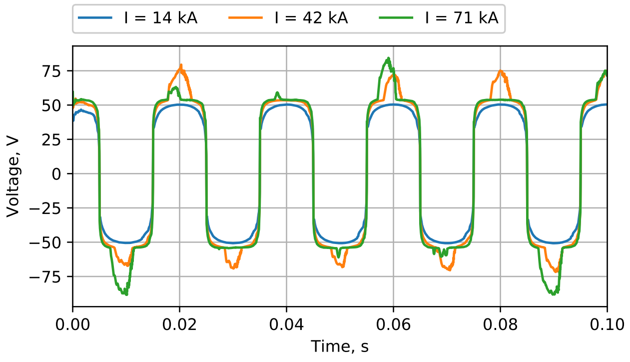

(a) L_a 2 cm

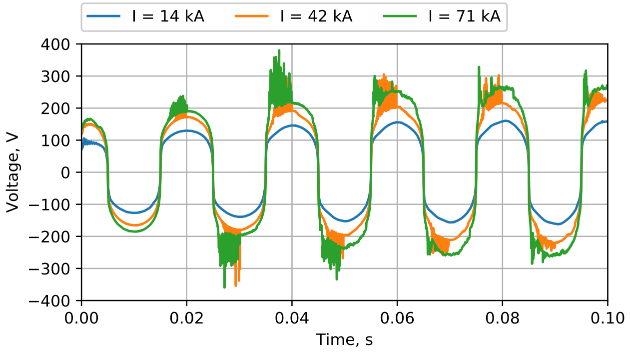

(b) L_a 10 cm

Figure 10: Evolution of arc voltage for selected arc characterisation simulations.

neutral on a routine basis would however need to be considered carefully.

CONCLUSION

A flexible and extensible computational model suitable for studying the dynamic behaviour of AC plasma arcs in silicon smelter environments was successfully developed. A preliminary validation study was conducted against data from small-scale experimental tests, with good agreement. An example workflow for the calculation of arc characteristics at industrial scale was demonstrated using arcs operating in argon gas plasmas, by combining a suite of arc simulations with empirical system modelling to account for the presence of main and side arcs and their influence on the complex non-linear relationships between electrode position, voltage, and current.

This work represents a preliminary step, and of course much remains to be done in order to make the plasma arc model more applicable to industrial systems. The model will need to be tested more thoroughly both for numerical veracity and validity against additional experimental and industrial data, both of which are currently in progress. The assembly of a database of appropriate thermophyiscal properties for Si-C-O plasma mixtures for use in computational simulations is also underway and will be applied in a future study. Improvements in the boundary conditions used, particularly at the conducting surfaces, should be explored to ensure that non-ideality effects in near-surface plasma sheaths are captured correctly. Similarly, the interaction between the arcs and the transformers powering them should be included in the computational model using appropriate three-phase circuit calculations to avoid any errors arising from specifying the current waveform directly. Energy transport and electromagnetic fields in the solid materials comprising the arc crater region should also be accounted for via improved boundary conditions or multi-region models. For large-scale arcs the use of turbulence modelling methods is advisable to optimise computational workloads, and these will require separate verification and validation to determine their applicability to multiphysics plasma arc problems. Finally, the coupling of the plasma arc models with additional relevant physics such as multiphase fluid flow in the molten bath should be considered, as it is expected that these will have an appreciable effect on the system's dynamic behaviour.

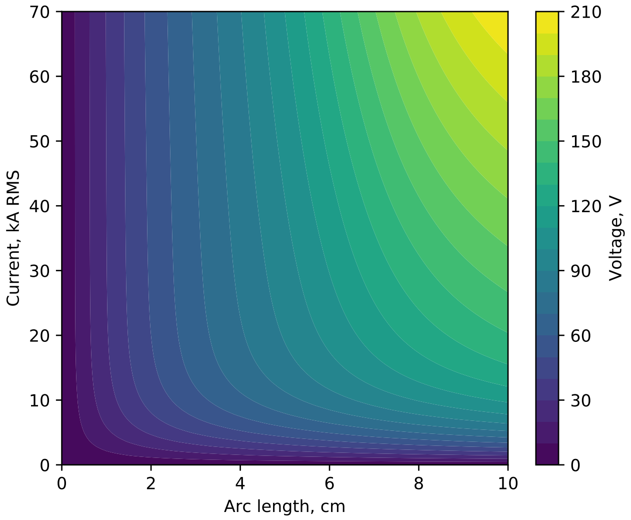

Figure 11: Relationship between current, arc length, and voltage described by equation (12).

ACKNOWLEDGEMENTS

This paper is published by permission of Mintek. The author acknowledges the Centre for High Performance Computing (CHPC), South Africa, for providing computational resources to this research project. Discussions with colleagues at the University of Reykjavík on the subject of computational arc modelling were greatly appreciated.

REFERENCES

BOULOS, M.I., FAUCHAIS, P. and PFENDER, E. (1994). *Thermal Plasmas: Fundamentals and Applications*, vol. 1. Plenum Press, New York, USA.

BOWMAN, B. and KRÜGER, K. (2009). *Arc Furnace Physics*. Verlag Stahleisen GmbH, Düsseldorf, Germany.

GASIK, M. (ed.) (2013). *Handbook of Ferroalloys*. Elsevier Ltd, United Kingdom.

HOCKADAY, C.J., REYNOLDS, Q.G. and JORDAN, D.T. (2015). "Industrial demonstration of arc detection in DC arc furnaces". *Proceedings of the Fourteenth International Ferroalloys Congress: Energy Efficiency and Environmental Friendliness are the Future of the Global Ferroalloy Industry*, 682–688. Public Organization INFACON XIV, Kyiv, Ukraine.

LARSEN, H.L. (1996). *AC electric arc models for a laboratory set-up and a silicon metal furnace*. Dr. Ing., Norwegian University of Science and Technology (NTNU), Trondheim, Norway.

LOWKE, J.J., MORROW, R. and HAIDAR, J. (1997). "A simplified unified theory of arcs and their electrodes". *Journal of Physics D: Applied Physics*, **30(14)**, 2033–2042.

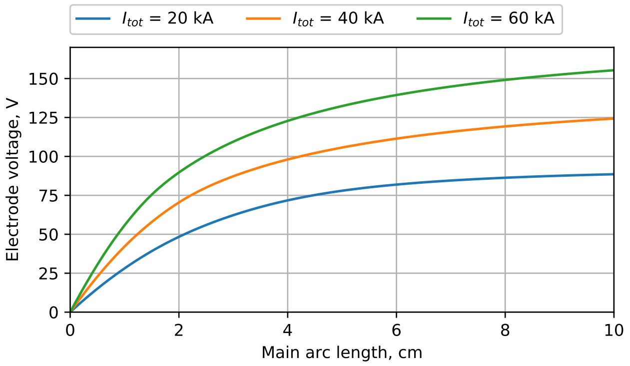

(a) Voltages

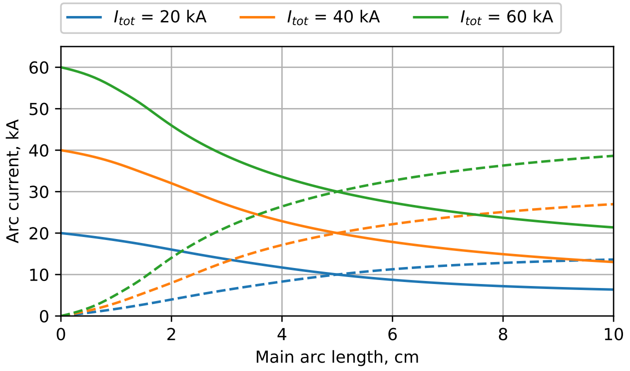

(b) Main (solid lines) and side (dashed) arc currents

Figure 12: Electrical behaviour of example system as a function of main arc length $L_{a,M}$ ($\propto$ electrode position) for different values of I_{tot}.

MINPLASCALC (2018). "minplascalc v0.7 alpha, commit 22a5f5d". URL `https://github.com/quinnreynolds/minplascalc`.

OPENFOAM (2019). "OpenFOAM v7". URL `https://openfoam.org/release/7/`.

PÁLSSON, H., SÆVARSDÓTTIR, G.A., JÓNSSON, M.T. and BAKKEN, J.A. (2007). "Thermal effects on carbon based electrodes close to a high current electric arc". *INFACON XI 2007: Innovations in Ferroalloys Industry*, 695–702. IFAPA, New Delhi, India.

REYNOLDS, Q.G. (2018). "Influence of the power supply on the behaviour of DC plasma arcs - a modelling study". *Journal of the Southern African Institute of Mining and Metallurgy*, **118(6)**, 655–660.

SÆVARSDÓTTIR, G.A., LARSEN, H.L. and BAKKEN, J.A. (1998). "Modelling of AC Arcs in Three-Phase Submerged Arc Furnaces". *8th International Ferroalloys Congress Proceedings*, 317–322. China Science & Technology Press, Beijing, China.

SÆVARSDÓTTIR, G.A., BAKKEN, J.A., SEVASTYANENKO, V.G. and GU, L. (2001). "Arc Simulation Model for Three-Phase Electro-Metallurgical Furnaces". *The Ninth International Ferroalloys Congress and the Manganese 2001 Health Issues Symposium Official Proceedings*, 253–263. The Ferroalloys Association, Quebec City, Canada.

SÆVARSDÓTTIR, G.A., PÁLSSON, H., JÓNSSON, M.T. and BAKKEN, J.A. (2006). "Electrode Erosion due to High-Current Electric Arcs in Silicon and Ferrosilicon Furnaces". *Steel Research International*, **77(6)**, 385–391.

SANCHEZ, J.L.G., RAMÍREZ-ARGAEZ, M.A. and CONEJO, A.N. (2009). "Power Delivery from the Arc in AC Electric Arc Furnaces with Different Gas Atmospheres". *Process Metallurgy*, **(2)**, 113–120.

TESFAHUNEGN, Y.A., MAGNUSSON, T., TANGSTAD, M. and SÆVARSDÓTTIR, G.A. (2018). "Effect of electrode shape on the current distribution in submerged arc furnaces for silicon production - A modelling approach". *Journal of the Southern African Institute of Mining and Metallurgy*, **118(6)**, 595–600.

WESTERMOEN, A. (2007). *Modelling of Dynamic Arc Behaviour in a Plasma Reactor*. Ph. D., Norwegian University of Science and Technology (NTNU), Trondheim, Norway.

CONTROLLING FLUE GAS TEMPERATURE FROM FERRO SILICON SUBMERGED ARC FURNACES (SAF) USING FLUE GAS RECIRCULATION (FGR)

Balram PANJWANI[1*], **Torbjørn PETTERSEN**[1†], **Bernd WITTGENS**[1‡]
[1]SINTEF Industry, 7465 Trondheim, NORWAY

[*] E-mail: balram.panjwani@sintef.no
[†] E-mail: torbjorn.pettersen@sintef.no
[‡] E-mail: bernd.wittgens@sintef.no

ABSTRACT

Flue gas Recycling (FGR) is a well-known method for NOx reduction. A feasibility study is presented on the potential use of FGR in ferro-silicon production. The aim of the study is to illustrate how recycling of flue gas into the furnace for temperature control will affect local temperatures and NOx formation in the furnace hood (the flue gas combustion zone) of a conventional furnace design. Computational fluid dynamic (CFD) simulations using a generic model of a submerged arc furnace (SAF) developed in previously NFR financed projects like ProMiljø are performed. The SAF model consists of seven charging pipes, three electrodes and one flue gas stack. ANSYS FLUENT was used for modelling the interaction between process gas, ambient air, and flue gas. The simulation results show that introduction of recirculated flue gas affects the peak temperatures since the reduced oxygen concentration of flue gas significantly reduce the reaction rates compared to injection of air. A corresponding effect on NOx formation has been demonstrated, results indicate an order of magnitude reduction in NOx formation when recirculated flue gas (6vol% O_2) is used in the combustion zone instead of air (21vol% O_2). Simulations of the rapid increase in NOx production during an avalanche within the furnace is simulated using theoretical flow profiles. The effects of 1) recirculated flue gas, 2) rapid increase in the process gases from charging bed (burst), and 3) effect of radiation on NOx have been studied. The study showed that FGR has significant effect on NOx reduction. The study also showed that accounting for radiation is very relevant for an accurate estimation of NOx. The formation of process gas burst through a charging surface increase the rate of NOx formation.

Keywords: CFD, NOx, radiation, combustion, flue gas recycling (FGR).

INTRODUCTION

Ferroalloys are produced in a submerged arc furnaces (SAF) where ore and carbon (coke, coal, etc.) are mixed inside the furnace and allowed to react. The electric energy for the reaction is supplied through electrodes. Furnace operation and raw material properties determine the metal yield and quality of the metal and how much process gas will be formed. Process gases mainly consisting of CO and metal oxide are formed underneath the charge surface due to the reduction processes and these process gases travel upward through the charge surface into the furnace hood. The liquid metal sink to the bottom where it is collected in ladles through a tapping hole. As the hot process gas rises upwards through the charge surface into a furnace hood, in case of open furnace hood, air is sucked into the hood through various open areas on the furnace walls due to the pressure drop. The air and process gas reacts inside the hood in a combustion process and produces an off-gas containing SiO_2, CO_2, H_2O and other components. In the open furnace, most of the chemical energy of the process gas is lost due to uncontrolled combustion of CO inside the hood. The uncontrolled combustion can be hindered by closing the furnace hood which prevents the reaction between fresh air and process gases. However, closing the Si furnace is a challenge due to many practical and technical constraints and therefore closed Si Furnaces are not in industrial use today. Nevertheless, in the Open furnace usually, temperature and material stream are high enough, and it is possible to produce electricity from the heat. In an open furnace, there are two main potential sources of energy recovery, 1) from the off-gas with a high temperature and 2) from the cooling water used for cooling the SAF. An energy analysis carried out by Kamfjord et al. (Kamfjord, 2012) has shown utilization of hot water obtained from the furnace for other industries including agriculture, sports etc. Some of the Si plant have installed a steam power plant to recover the energy.

One of the major challenges with open SAF is uncontrolled combustion of process gases inside the furnace hood resulting in an excessive NOx formation due to the formation of high temperature zones. There are various kinds of health related issues with NOx once it is released into the atmosphere. NOx can cause breathing problems, chronically reduced lung function, eye irritation, loss of appetite. It mainly contribute to the acid rain and formation of ground-level ozone that can damage the ecosystems. All the metallurgical companies have to follow the governmental regulations on the NOx emission and therefore these companies have been developing many techniques to reduce the NOx emissions. NOx emission can be reduced by primary methods such as water direct injection, water emulsification, flue gas recirculation (FGR) and secondary method such as selective catalytic reduction (SCR). Three main mechanisms have been identified for the NOx formation: the thermal or Zel'dovich mechanism, the Fennimore or prompt mechanism and N_2O intermediate mechanism, corresponding NOx are respectively called thermal, prompt and fuel NOx. Thermal NOx generally dominates in high temperature turbulent diffusion flames. At temperature around 1527 °C, oxygen radicals are formed from the dissociation of atmospheric oxygen. These atoms react with nitrogen molecules and produce NOx and nitrogen atoms. The nitrogen atom again reacts with oxygen molecules and OH radicals and produces NOx. A detailed mechanism of NOx formation have been discussed in this paper.

An improved understanding of the combustion process inside the SAF is essential for minimization of the NOx formation and maximization of energy recovery. In SAF, high temperature processes makes it difficult to perform extensive experiments and most of these experiments are performed on the small pilot scale experiments. Numerical techniques such as Computational fluid dynamic (CFD) is a good alternative to understand the dynamics and functioning of SAF, CFD techniques can be deployed to understand complex solid-gas, liquid-solid, and liquid-gas reactions prevalent in SAF. Many studies have been performed on the modelling of SAF to understand the operational behavior of the furnace (Scheepers *et al.*, 2006a; Darmana *et al.*, 2012; Scheepers *et al.*, 2006b; Panjwani and Olsen, 2013; Kadkhodabeigi *et al.*, 2010). CFD tools validated with experiments enable us to understand the complex reactions between process gas and air taking place inside hood. CFD simulation of furnace hood (Panjwani and Olsen, 2013) indicates, many hot pockets inside the furnace hood which results in excessive NOx formation. The hot pockets are also responsible for radiation losses and reduces the potential for energy recovery. To alleviate this problem, a NOx reduction techniques flue gas recirculation (FGR) have been utilized.

The results from previous techno economical evaluations (Pettersen et al. (Pettersen *et al.*, 2017)) indicated the potential of using recirculated flue gas in silicon production as a mean for both increased energy recovery and simultaneously improved temperature control in a semi-closed submerged arc furnace. This potential has been further explored through the following activities:

- A base case has been defined for silicon production in a semi-closed submerged arc furnace
- Results from a computational fluid dynamics simulation of the combustion zone are presented.
- Some critical design trade-offs are discussed

FGR involves recirculating part of the flue gas back into the furnace or the burners to modify conditions in the combustion zone by lowering the peak flame temperature and reducing the oxygen concentration, thereby reducing thermal NOx formation. FGR has been used commercially for many years at coal-fired units, waste incinerators (WI), gas turbines(Tsiliyannis, 2013; Liuzzo *et al.*, 2007; Chen *et al.*, 2015; Guethe and Burdet, 2009). Flue gas recirculation (FGR) emerges as a promising method for reducing WI atmospheric pollution, mainly NOx and volatile metal emissions by resulting in lower total off gas volumes. In WI plant, a portion of flue gas is recycled back to the incinerator and the secondary combustion air is manipulated by measuring the oxygen concentration of the incineration chamber flue gas. Being a mass recycle, FGR is fundamentally different than the heat integration (exchange of the heat of flue gases with the feed, air or wastes); the latter redirects enthalpy to the WI and raises its temperature, whereas oxygen concentration in both the primary and secondary air are not affected. The application of FGR in new plants has allowed a reduction of the total amount of incineration air and flue gas in the range of 10–15%.

In the present study a CFD model of generic furnace is developed and effect of FGR on the NOx reduction and temperature controlled have bee studied with the help of CFD simulations.

FLUE GAS RECYCLING IN SAF

Figure 1 shows a conceptual design of a semi-closed silicon production process, where recirculated flue gas is used for temperature control in the combustion zone[1] following the submerged arc furnace. Semi-closed in this context means that the amount of ingress air into the SAF is limited and used to actively control the oxygen concentration in the flue gas at the exit of the combustion zone. The ingress air which in current processes are used for temperature control is in this concept replaced by flue gas taken downstream of the hear recovery steam boiler and filter system. The recirculated flue gas which is available at "flue gas stack temperature", typically around 150 °Cand is used to control the flue gas temperature at the exit of the combustion zone up-stream inlet to the convective part of the heat recovery steam boiler.

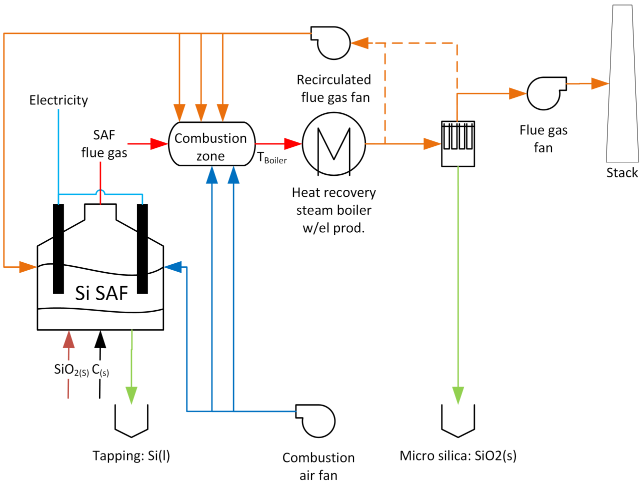

Figure 1: Conceptual design of a semi-closed silicon production process, where recirculated flue gas is used for temperature control in the combustion zone following the submerged arc furnace (SAF

A dedicated flue gas combustion zone is indicated in Figure 1. This corresponds to the staged combustion chamber as described by Wittgens et al. (Wittgens *et al.*, 2018) in the SCORE-project. In this study, we have focused only on the effect of replacing ingress air with recirculated flue gas in a conventional SAF design. Base case conditions are defined in Table 1. The combustion of the SAF process gas (leaving the charge surface) is simplified by merging the content of tar components and SiO (g) into CO on a volumetric basis, nevertheless the overall energy balance is correct and combustion is described properly. The SAF process flow rate correspond to a furnace with around 40 MW electric effect.

DESIGN TRADE-OFFS

The oxygen concentration in the flue gas leaving the combustion zone (and the stack) is the most important design variable in terms of mass and energy balance for a semi-closed silicon process, as outlined in Figure 1. The O_2-concentration in the flue gas will have major impact on both the stack-loss and the gross flue gas flow rate through the SAF combustion zone and the heat recovery steam boiler. The stack loss is affected

---

[1] The combustion zone is defined as the void volume above the charge until flue gas is exiting the furnace hood.

Table 1: Base case conditions used as basis for CFD simulations.

Components	Nm3/h	°C
SAF process gas	11 500	1500
CO=70.3%; H_2=6.4%; H_2O=23.3%; N_2 rest.		
Net flue gas to stack	40 703	150
O_2=6.2%; CO_2=20%; H_2O=9%; N_2 rest.		
Total combustion air	33 583	20
Recirculated flue gas from boiler	94 975	150
Gross flue gas to boiler	135 678	745

through the amount of "excess" air which is heated up from ambient to stack temperature. The lower the oxygen concentration is (less excess air), the lower the stack loss will be. The gross flue gas flow rate is a result of the amount of recirculated flue gas which is needed to meet the desired flue gas temperature at the entrance of the convective part of the heat recovery steam boiler system (another key design parameter). With less excess air available for cooling in the combustion zone, more recirculated flue gas is needed to meet the desired design temperature.

The oxygen concentration of the recirculated flue gas has a significant effect on local peak temperatures within the combustion zone. Figure 2 shows theoretical flue gas temperature (from a simple energy balance model) versus stoichiometric ratio, λ during combustion of the flue gas using mixtures of combustion air and recirculated flue gas. The stoichiometric ratio, λ is here defined as the ratio between the amount of O_2 added to the SAF flue gas and the amount of O_2 needed to completely convert CO and H_2 in the SAF flue gas to CO_2 and H_2O. Thus, $\lambda = 0$ corresponds to the flue gas leaving the SAF charge, $\lambda = 1$ corresponds to completely combusted flue gas (with O_2 = 0 vol in the flue gas) and $\lambda = 1.57$ corresponds to the specified base case O_2 concentration of 6.2 vol% O_2.

Case 1 shows the theoretical flue gas temperature as a function of λ when combustion air is added first to the flue gas leaving the SAF charge. The theoretical flue gas temperature at $\lambda = 1$ is very high - above 2500degC and represents a theoretical peak temperature during combustion of the SAF process gas in air. After combustion to the specified excess air concentration of 6.2 vol% O_2 which corresponds to $\lambda = 1.57$ the flue gas temperature is slightly below 2000 °C. Cooling down to the target temperature at 745 °Cis achieved by injection of recirculated flue gas available at 150 °Cdownstream of the heat recovery steam generation system.

Case 2 shows the corresponding temperature profile if combustion air and recirculated flue gas streams are mixed prior to injection to the SAF combustion zone (which is assumed to start above the SAF charge surface). This mixture of air and flue gas will with the given base case conditions have a concentration of around 10 vol% O_2 which leads to significantly lower temperatures. The theoretical peak temperature (at $\lambda = 1$) is below 1600 °C. Although still above the temperature where thermal NOx formation is likely to dominate the extreme temperatures are avoided when compared to Case 1.

Case 3 shows the temperature profile which can be achieved if the process gas leaving the SAF charge surface is combusted using recirculated flue gas at 6.2 vol% O_2. Where the flue gas temperature drops down to below 1200 °Cat $\lambda = 1$ and the specified exit conditions for the SAF charge represents the peak temperature in this case.

The results from this simple model (energy and mass balances) provides the following insights relevant for implementation of a semi-closed silicon furnace:

- Avoid introducing air to flue gas at sub stoichiometric conditions otherwise extreme peak temperatures may occur.
- Recirculated flue gas with sufficiently low oxygen content is an efficient way of avoiding extreme peak temperatures while ensuring complete burnout of the flue gas.
- Sufficiently low oxygen content for recirculated flue gas is in this case most likely below 10vol% O_2 if significant NOx formation and operational challenges with high temperatures are to be avoided.

The potential in a conventional SAF furnace is explored further using 3D CFD models in the following chapter.

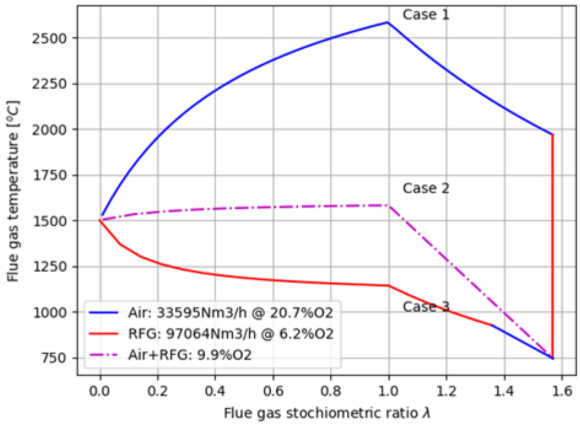

Figure 2: Theoretical flue gas temperature versus stoichiometric ratio for base case conditions outlined in Table 1. **Case 1:** Combustion of process gas with combustion air followed by cooling with recirculated flue gas; **Case 2:** Combustion and subsequent cooling of air using a mixture of combustion air and recirculated flue gas; **Case 3:** Combustion of recirculated flue gas and subsequent cooling using combustion air.

MODELLING

The main objective of CFD simulations was to study the how recirculated flue gases affects the NOx emission during SAF operation. As described in the previous section, when recirculated flue gases are admitted into a combustion system, it primarily reduces the peak temperature which results in NOx reductions. As we know that the NOx formation depends on the local temperature resulting from the reaction between fuel (process gas) and oxygen concentration (air + FGR). In FGR, the oxygen concentration is altered by introducing the additional flue gas with low oxygen concentration and high CO_2 concentration. However, there are many questions which need to be answered before implementing the FGR in the real operating SAF

- Which strategy for recirculation of the gas into the furnace hood need to be adapted is not very clear?
- At what location the flue gas should be injected?
- How "burst" will affect the overall NOx formation?

- How radiation losses will affect both the temperature and NOx formation?

To answer these questions, a CFD model of a SAF is constructed. In the present study, the SAF charge surface is modelled as a wall, where flow of process gas is modelled as a mass flux boundary condition. The escaping of process gas through the charge surface is non-uniform and in the real operation a strong burst of SiO and CO have been observed inside the furnace. These bursts are responsible for increased in a local temperature and also increase in a NOx formation. The other objective of this study is to asses the effect of these burst on the NOx formation.

Geometry

The geometry used for understanding the effect of recirculated flue gases on the NOx formation is shown in Figure 3. This model geometry of furnace hood was developed in two NFR financed projects, namely Promiljø and FUME. The model furnace consists of seven charging pipes, three electrodes, charging surfaces (top surface of the charge bed), simplified single stack, gates, slits and gapes. The charging surface is further divided into three different zones inner, middle and outer.

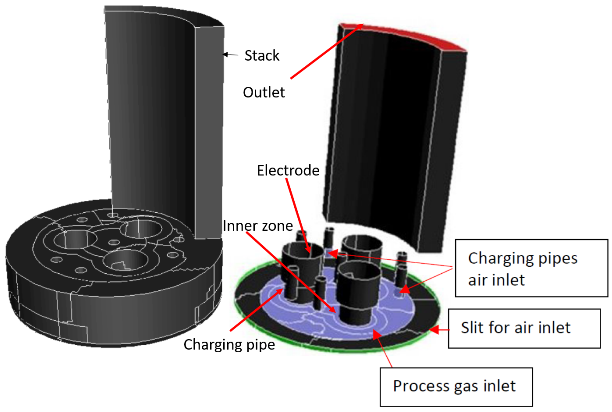

Figure 3: Schematic of the model furnace

Mathematical modeling

ANSYS Fluent was used in the present study. Steady state model solving for continuity, momentum, energy, species balances and radiation equations was used. Flow inside the furnace is turbulent in nature and flow dynamics depend on the initial temperature and turbulence distribution. Fluent solves the Reynolds averaged Navier-Stokes equation (RANS) on the grid scales and turbulence is modeled using an appropriate turbulence model. In the present study we used the RNG k-ϵ model for turbulence modelling and radiation is modelled with Discrete Ordinates (DO) model. Both the k-ϵ model for turbulence and DO model for radiation were chosen based on our previous experience on modelling such kind of furnaces. In DO model, the number of theta and phi divisions were set to 5 and theta and phi pixels were set to 3.

Combustion and kinetics

A variety of combustion models (i.e. Eddy dissipation concept (EDC), Flamelet model, Presumed PDF model) can be used for simulating the combustion related problems with great difference in terms of computational costs, accuracy and complexity. A non-premixed turbulent methane flame was studies by Rohani et al. (Rohani *et al.*, 2012) using EDC model and Presumed PDF model. Their studies revealed that presumed-PDF model shows considerably better agreement with experimental data which is mainly due to implementing a probabilistic approach for relating the turbulence characteristics of the flow field to thermo-chemical properties of the flame. However, the presumed PDF model was computational demanding and very complex and therefore it is very challenging to use this model for simulating the complex geometries such as SAF. Therefore, in the present study, EDC model is applied. The original version of the EDC model was developed by Magnussen (Magnussen and Hjertager, 1977) and after that various version of EDC model have been developed. In the current study the model available in FLUENT have been used in which the chemical reaction rate is governed by the large-eddy mixing time scale and also by the chemical time scale. ANSYS FLUENT provides the finite-rate/eddy-dissipation model, where both the Arrhenius and eddy-dissipation reaction rates are calculated. The net reaction rate is taken as the minimum of these two rates. The EDC model accounts for the chemical kinetics through Perfectly Stirred Reactor (PSR) concept in which each numerical grid is assumed as a stand alone reactor.

Combustion of CO does not take place in a single step, there are many intermediate steps involved in CO combustion. Accounting all the intermediate steps is indeed computationally expensive because many species transport equations need to be solved in CFD framework. Nevertheless, combustion inside the furnace takes place at very high temperatures and therefore a simplified CO mechanism is assumed to be sufficient for our analysis. In the present study, a two-step reaction mechanism for the CO combustion is used. How a detailed kinetic model could affect the NOx formation is presented in our previous publication (Panjwani and Olsen, 2013). The soot formation is not considered in the current paper.

NOx modeling

In present study it is believed that the main source of NOx production is thermal NOx, therefore only thermal NOx is considered. Formation of NOx depends on the instantaneous temperature, species concentration, and radical concentration. NOx is the common notion for the two gases nitric oxide (NO) and nitrogen dioxide (NO_2). For simplification, we only calculate the formation of NO. In combustion system the NO kinetics is very slow, and concentration is generally low, and because of this NO chemistry has negligible influence on the overall flow pattern, temperature field and other species concentration. Therefore, a post processing approach is used for estimation of NO concentration. The post processing approach implemented in FLUENT solves the transport equation for NO concentration with a source term expressed as an Arrhenius rate of law. With post processing-based approach we expect to capture trends based on different furnace hood designs, but we do not expect to find the correct overall emission of NO.

First, the fundamental equations of mass, momentum and energy were solved. Once the chosen convergence criteria were fulfilled, then the post processing tool was used for modeling the NO. The principal reactions governing the formation of thermal NOx from molecular nitrogen are as follows:

$$O + N_2 \Leftrightarrow N + NO \tag{1}$$

The forward and backward coefficient for above reaction were $1.8 \times 10^8 e^{-38370/T}$ and $3.8 \times 10^7 e^{-425/T}$ respectively.

$$N + O_2 \Leftrightarrow O + NO \tag{2}$$

The forward and backward coefficient for above reaction were $1.8 \times 10^4 e^{-4680/T}$ and $3.8 \times 10^3 e^{-20820/T}$ respectively.
A third reaction has been shown to contribute, particularly at near-stoichiometric conditions and in fuel-rich mixtures:

$$N + OH \Leftrightarrow H + NO \tag{3}$$

The forward and backward coefficient for above reaction were $7.1 \times 10^7 e^{-450/T}$ and $1.7 \times 10^8 e^{-24560/T}$ respectively.
The net rate of NOx formation now depends on the above mentioned forward and backward reaction rates and also N_2 and O_2 concentration

Boundary conditions and case description

In Figure 3, some of the boundary conditions are illustrated. The inlet of process gases is divided into three zones and most of the gas comes from the center (zone 1) near the electrodes. The zone 1 (inner) gets 60 % of the fuel (process gas), Zone 2 gets 30 % and Zone 3 gets 10 % of the fuel. The fuel consists of 77 % CO and 23 % of H_2O (mass basis). The flow rates, temperature and species concentration at various inlets were specified based on the value provided in Table 1. In total four simulation were carried out and description of these simulations are provided in Table 2 In all the simulations, it was assumed that all the gates of SAF were closed. In Case-1, 25% fresh air (O_2=21%, N_2=79%) was supplied at charging pipes and 75% fresh air (O_2=21%, N_2=79%) was supplied through gaps and slits. In Case-2, 75% fresh air was supplied at charging pipes and 25% fresh air was supplied through gaps and slits. In Case-3, 75% recirculated flue gas (O_2=6%, CO_2=20%, H_2O=9%, N_2=65%) was supplied at charging pipes and 25% fresh air was supplied through gaps and slits. In Case-4, 25% fresh air was supplied at charging pipes and 75% recirculated flue gas supplied through gaps and slits.

Table 2: Simulation description

Simulation	Flow rate charging pipes (Nm3/h)	Flow rate gaps (Nm3/h)
Case-1	Fresh air: 33 583	Fresh air: 94 953
Case-2	Fresh air: 94 953	Fresh air: 33 583
Case-3	Flue gas: 94 953	Fresh air: 33 583
Case-4	Fresh air: 33 583	Flue gas: 94 953

RESULTS

Steady state simulations

The above mentioned model has been validated with pilot furnace and the results from this validation has been presented in a previous conference (Panjwani and Olsen, 2013). FGR can be a highly effective technique for lowering NOx emissions and it is relatively inexpensive to apply. The recirculation ratio R, as a key parameter in gases combustion system, was defined as mass ratio between the amounts of recycled and total flue gases, as expressed:

$$R = \frac{MRFG}{MRFG + MTFG} \tag{4}$$

where MRFG is the recycled flue gas mass flow rate and MTFG is the total produced flue gas mass flow. For example, $R = 0$ means that there is no flue gas that was recycled back to the hood, and in extreme case, $R = 1$ represents that total flue gas was recycled back to the hood. The effect of FGR on NOx is shown in Table 3. In Case-1, NOx is around 150 g/s but by replacing the fresh air with flue gases on the slits and other opening(Case-4), the NOx was reduced to 17 g/s. Similarly, in Case-2 and Case-3, when fresh air through charging surface was replaced with flue gas NOx was reduced from 90 g/s to 10 g/s.

Table 3: CFD simulation results

Simulation description	NOx [g/s]	T_{out} degC	O_2	R
Case-1 (without FGR)	150	640	16.5%	0
Case-2 (without FGR)	90	560	17%	0
Case-3 (with FGR)	10	640	6.2%	0.75
Case-4 (with FGR)	17	720	5.8%	0.75

Thermal NOx is produced by the reaction of atmospheric oxygen and nitrogen at elevated temperatures, and is considered to be the dominant mechanism. ISO clip temperature of the furnace for Case-1 (without FGR) and Case-4 (with FGR through the gaps) are shown in Figure 4, and 5 respectively to understand the effect of FGR on temperature.

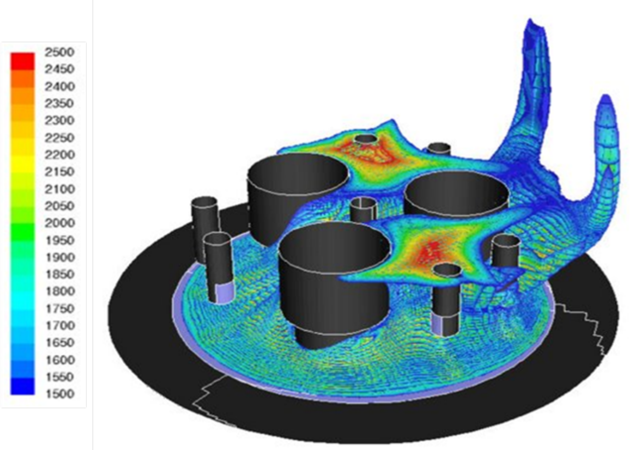

Figure 4: Case-1: Iso-clip of temperature °C

High temperature pockets responsible for thermal NOx formation are clearly visible in CASE-1 (see Figure 4). The number of hot pockets has been reduced with FGR (see Figure 5).

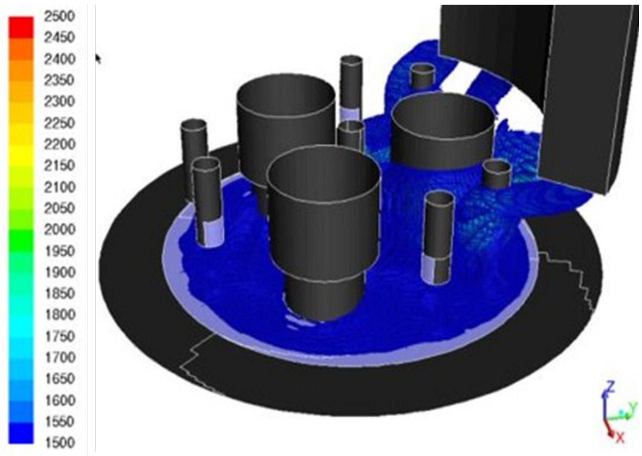

Figure 5: Case-4: Iso-clip of temperature °C

The effect of temperature on the NOx is exponential and small reduction in temperature causes significant reduction in NOx formation and thus concentration of NOx in the furnace off-gas. The amount of thermal NOx formed not only depends on the temperature of the flame but also the residence time. Both higher temperature and the longer residence time result in more NOx production. However these simulations have been performed assuming steady state conditions and therefore the effect of residence time is not shown in the current calculations. The prediction of temperature in a turbulent flame is important because the temperature affects the chemical kinetics considerably (i.e. reaction rates of all intermediate reactions) and therefore the combustion behavior. If the temperature is poorly predicted a realistic estimation of the pollution (i.e soot, NOx) is less likely to be achieved.

Effect of radiation

Due to the high temperatures involved in combustion processes, e.g. 2000 °C, radiation heat transfer appears as an important heat transfer mechanism in many combustion devices including combustion inside the furnace hood. Infrared (IR)-active species such as CO_2, CO and H_2O are often present in the products of combustion of fuel consisting of Carbon and Hydrogen. The combustion products such as CO_2, CO and H_2O are responsible for the non-luminous radiation.

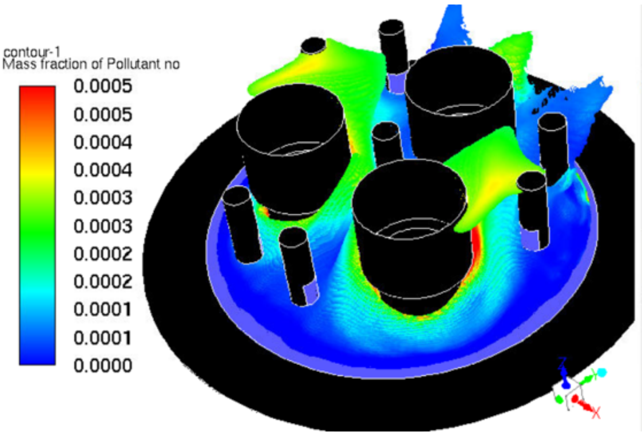

Figure 6: Iso-clip of NOx without Radiation

In fuel-rich flames, soot is also formed and, as a consequence, a significant amount of radiation is emitted in the luminous region of the spectrum (Pessoa-Filho, 1999). In industrial furnaces, there are many hot particles such as dust and soot and because of these hot particles a significant amount of radiation is emitted in the luminous region of the spectrum. Many studies have indicated that radiation is found to reduce the flame temperature with a consequent reduction of the overall reduction in NOx concentration. Radiation is the dominant mechanism of energy transfer in combustion systems like furnaces, turbines, engines, combustion chambers, etc. Many studies have shown that heat transfer by radiation should be considered in the CFD combustion simulation.

The radiation effects proved to have a great influence on the velocity and temperature profiles. Although in many combustion calculation effect of radiation is neglected assuming combustion gases as a transparent. However, the combustion gas inside the furnace contain H_2O and CO_2 and both these gas components are not transparent to the radiation. The effectiveness of CO_2 addition in reducing flame temperature and NOx emission have been studied widely and CO_2 primarily increase the heat capacity and radiation loss (Park *et al.*, 2008).

The previous simulations as given in Table 3 were carried out with radiation model but it was assumed that gas is transparent to the radiation. This had resulted in higher temperature and therefore higher NOx formation. These assumptions were modified and additional simulations with and without radiation were performed. WSGGM-domain-based model was used for estimating the absorption coefficient. Although scattering also affects the radiation intensity along the path for purposes of simplicity, here scattering is neglected. The simulations results with and without radiation are shown in Table 4. The NOx formation rate without radiation is 90 (g/s) and with radiation the rate of NOx formation is 2.44 (g/s). The results from this study without radiation and with radiation are shown in Figure 6 and Figure 7. The figures 6 and Figure 7 show the iso-clip of the local NOx concentration without and with radiation. A peak in the NOx corresponding to the high temperature zone are quite visible. In absence of the radiation, the heat losses to the surrounding is extremely small which results in higher temperature inside the furnace and therefore many pockets with a larger concentration of NOx (as shown in Figure 6) are observed. However, the temperature became much lower when simulations were repeated with radiation and therefore the larger NOx concentration disappear see Figure 7.

Table 4: The effect of radiation model on NOx formation

Case	Charge pipes (Nm3/h)	Gaps (Nm3/h)	Radiation	NOx (g/s)
Case-2	94 953 (F)*	33 583 (F)*	NO	90
Case-2A	94 953 (F)*	33 583 (F)*	YES	2.44

Effect of gas burst

One of the challenging issue with the submerged arc furnace used in the silicon and high silicon alloy industries is the existence of high gas pressure condition inside the crater zone of the furnace. Crater zone is formed as cavity in the bulk of charge materials around the electrodes tip. In fact due to the existence of chemical reactions inside the charge materials, there is always a high gas pressure situation in the furnace heart. Because of reduced permeability of charge materials and melting of charge materials in the region near by the electrode tips (the crater walls), the gas pressure in the crater zone increases to higher levels than what can be expected from a porous bed. Furthermore, a submerged-arc

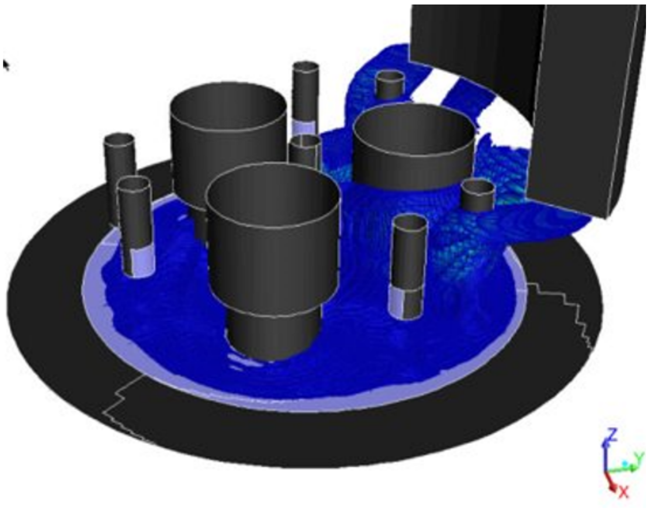

Figure 7: Iso-clip of NOx with Radiation (scales are given in Figure 6)

Table 5: Base case conditions used as basis for CFD simulations.

Case	Charge pipes (Nm3/h)	Gaps (Nm3/h)	burst	NOx (g/s)
Case-2A	94 953 (F)*	33 583 (F)*	NO	2.44
Case-5	94 953 (F)*	33 583 (F)*	Inner	2,73
Case-6	94 953 (F)*	33 583 (F)*	Outer	2.94
Case-7	94 953 (FGR)*	33 583 (F)*	Inner	0.026
Case-8	94 953 (FGR)*	33 583 (F)*	Outer	0.286

furnace is continually fed with carbon and quart to produce liquid metal which is tapped from the base of the furnace). To maintain the continuous production of liquid metal, the raw material such as ore and carbon sources (coke, coal, and wood chips) are injected in an regular intervals. During the reduction process, gas cavities are formed underneath the charge surface and a solid crust region builds up above a gas cavity. This crust is composed of a mixture of carbon, molten quartz, silicon carbide, and condensate. (Sloman *et al.*, 2017). During the furnace operation, the cavity pressure becomes so high that gas escapes rapidly to the charge surface and the rapid release of the gas are known as a burst (Schei *et al.*, 1998; Kadkhodabeigi *et al.*, 2010).

Burst of high velocity hot gases from the furnace charging is one of phenomena which seems to be related to the existence of the high pressure crater zone of the furnace. A 2D view of the inside of the silicon furnace is presented in Figure 8. Results of furnace excavations confirm the formation of the cavities around the electrodes tips. Normally these burst consist of the process gases with a high concentration of SiO and CO gas. These gases reacts with air and produces high temperature zone responsible for NOx formations. The proposed CFD model of the furnace with burst allows better understanding of the burst effects on the NOx formation.

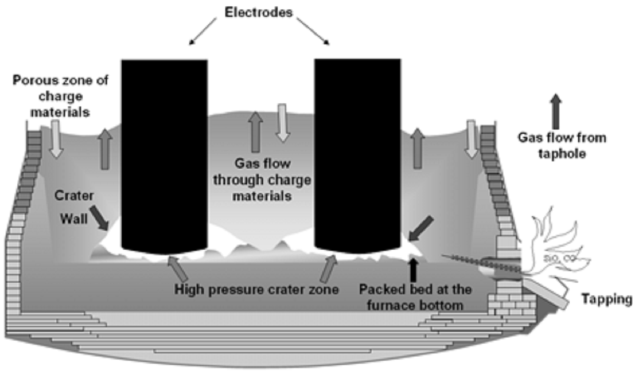

Figure 8: Schematic of the inside conditions of a submerged arc furnace used for Silicon production (Kadkhodabeigi *et al.*, 2010)

In the present study, CFD simulations of the submerged arc furnace with and without burst were performed. The simulations and corresponding results for burst simulations are given in Table 5. In Table 5, (F)* Means fresh air and (FGR)* Means Flue gas recirculation

In total, four simulations were performed to establish the effect of burst and FGR on the temperature and NOx distribution. The burst results in a higher rate of process gas formation and the combustion of additional process gases from the burst results in an increased temperature and therefore increase in thermal NOx formation. The process gas in silicon furnace consist of both CO and SiO and the combustion of SiO results in micro-silica (SiO_2) formation. The heat of formation of SiO_2 is approximately three times higher than CO_2. In practice, the burst results in more SiO formation and this SiO will react with air resulting in an increase flame temperature. However, the SiO reaction is not considered in the present calculations instead equivalent CO reactions are considered. Again to model the burst, mass flow rate boundary condition was used at the charge surface. For burst, the process gas mass flow rate was provided as an input. Case-5 is a baseline case where the fresh air is injected through charging pipes and also through other openings. The process gas was released from the charging surfaces and burst at inner location of charging surface was considered. The Case-6 is similar to the Case-5 except the burst was considered at the outer location of the charging surface. In case-7, flue gas was injected equally through the seven charging pipes and fresh air was injected through other openings. The burst was considered at the inner location of the charging surface. The Case-8 is similar to the Case-6 but with FGR through charging pipes. The effect of burst on the NOx can be seen in Table 5. The NOx without burst is 2.44 g/s (Case-2A) and with burst at outer location (Case-6) is 2.94 g/s. With FGR and with burst, the NOx production rate was decreased from 2.93 g/s (Case-6) to 0.286 g/s (Case-8). The Iso-clip of Case-6 and Case-8 are shown in Figures 9 and 10.

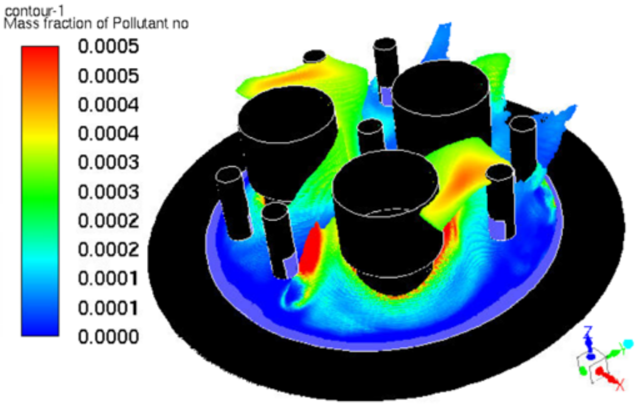

Figure 9: Iso-Clip of NOx concentration with radiation, without FGR, and with burst

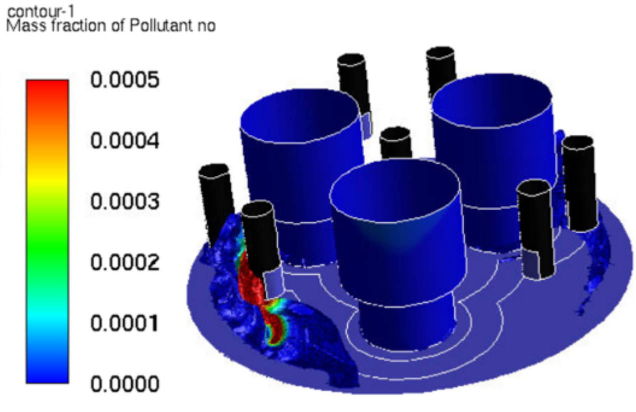

Figure 10: Iso-Clip of NOx concentration with radiation, with FGR, and with burst

A localized pocket of NOx at the burst location can be seen that indicates the localized high temperature zone resulting from the reaction between burst gases and ambient air. However, with FGR, with a reduced amount of fresh air the rate of NOx formation is also reduced. The location of burst also affects the NOx formation, the rate of NOx formation is higher when burst occurs at the outer location of the charge surface. Therefore, the effect of location of burst has a prominent effect on the rate of NOx formation with FGR.

CONCLUSIONS

It is demonstrated how the use of recirculated flue gas in the flue gas combustion zone of a ferro-silicon furnace affects the peak temperatures. The reduction in peak temperature is achieved because recirculated flue gas with reduced oxygen concentration has a significantly lower adiabatic flame temperature than air. The corresponding effect on NOx formation has been demonstrated through computational fluid dynamics simulations. The results indicate an order of magnitude reduction in NOx formation when recirculated flue gas (6vol% O_2) is used in the combustion zone instead of air (21vol% O_2). The recirculation ratio (R) has significant influence on both peak temperature and NOx rate. Furthermore, the studies also indicated that the accounting of radiation model is extremely important for modeling the combustion related problems. The studies show that both the burst and its location play a significant role in the NOx production.

ACKNOWLEDGMENT

The research work carried out in this article is funded by FME HighEff supported by Norwegian research council and many industrial partners. Funding from the FME HighEff project is greatly acknowledged

REFERENCES

CHEN, Q., ZHANG, X., ZHOU, J., SHARIFI, V.N. and SWITHENBANK, J. (2015). “Effects of Flue Gas Recirculation on Emissions from a Small Scale Wood Chip Fired Boiler”. *Energy Procedia*, **66**, 65–68.

DARMANA, D., OLSEN, J.E., TANG, K. and RINGDALEN, E. (2012). “Modelling concept for submerged arc furnaces”.

GUETHE, F. and BURDET, A. (2009). “Flue gas recirculation in gas turbine: Investigation of combustion reactivity and nox emission”. *ASME Turbo Expo*, **2**, 179–191.

KADKHODABEIGI, M., TVEIT, H. and JOHANSEN, S.T. (2010). “CFD modelling of the effect of furnace crater pressure on the melt and gas flows in the submerged arc furnaces used for silicon production”. *Progress in Computational Fluid Dynamics, An International Journal*, **10(5/6)**, 374.

KAMFJORD, N.E. (2012). *Mass and Energy Balances of the Silicon Process:-Improved Emission Standards*. Ph.D. thesis, Noregs teknisk-naturvitskaplege universitet.

LIUZZO, G., VERDONE, N. and BRAVI, M. (2007). “The benefits of flue gas recirculation in waste incineration”. *Waste Management*, **27(1)**, 106–116.

MAGNUSSEN, B. and HJERTAGER, B. (1977). “On mathematical modeling of turbulent combustion with special emphasis on soot formation and combustion”. *Symposium (International) on Combustion*, **16(1)**, 719–729.

PANJWANI, B. and OLSEN, J.E. (2013). “Combustion and mechanisms for NOx formation in ferrosilicon electric arc furnaces”. *European combustion meeting, ECM 2013*, 7.

PARK, J., BAE, D.S., CHA, M.S., YUN, J.H., KEEL, S.I., Chang Cho, H., KIM, T.K. and HA, J.S. (2008). “Flame characteristics in h2/co synthetic gas diffusion flames diluted with co2: Effects of radiative heat loss and mixture composition”. *International Journal of Hydrogen Energy*, **33(23)**, 7256 – 7264.

PESSOA-FILHO, J.A.B. (1999). “Thermal radiation in combustion systems”. *Journal of the Brazilian Society of Mechanical Sciences*, **21**, 537 – 547.

PETTERSEN, T., WITTGENS, B. and BERGLIHN, O.T. (2017). “Technical and economical evaluations of selected concepts: SCORE”. Tech. Rep. D4.1._2017.04, SINTEF, Trondheim Norway.

ROHANI, B., WAHID, M.A., SIES, M.M. and SAQR, K.M. (2012). “Comparison of eddy dissipation model and presumed probability density function model for temperature prediction in a non-premixed turbulent methane flame”. 384–391. Melaka, Malaysia.

SCHEEPERS, E., ADEMA, A., YANG, Y. and REUTER, M. (2006a). “The development of a cfd model of a submerged arc furnace for phosphorus production”. *Minerals Engineering*, **19(10)**, 1115 – 1125. Selected papers from Computational Modelling â€™05, Cape Town, South Africa.

SCHEEPERS, E., YANG, Y., REUTER, M. and ADEMA, A. (2006b). “A dynamic-cfd hybrid model of a submerged arc furnace for phosphorus production”. *Minerals Engineering*, **19(3)**, 309 – 317. Selected papers from Pyrometallurgy â€™05, Cape Town, South Africa, March 2005.

SCHEI, A., TUSET, J. and TVEIT, H. (1998). *Production of High Silicon Alloys*. 1st ed. TAPIR Forlag, Trondheim, Norway.

SLOMAN, B.M., PLEASE, C.P., VAN GORDER, R.A., VALDERHAUG, A.M., BIRKELAND, R.G. and WEGGE, H. (2017). “A Heat and Mass Transfer Model of a Silicon Pilot Furnace”. *Metallurgical and Materials Transactions B*, **48(5)**, 2664–2676.

TSILIYANNIS, C.A. (2013). “Flue Gas Recirculation and Enhanced Performance of Waste Incinerators under Waste Uncertainty”. *Environmental Science & Technology*, **47(14)**, 8051–8061.

WITTGENS, B., PANJWANI, B., PETTERSEN, T., JENSEN, R., RAVARY, B. and HJERTENES, D.O. (2018). “SCORE: Staged Combustion for Energy Recovery in Ferroalloy Industries â€“ Experimental Validation”. *Infacon XV: International Ferro-Alloys Congress*.

14th International Conference on CFD in Oil & Gas, Metallurgical and Process Industries
SINTEF, Trondheim, NORWAY
October 12-14 , 2020

DIRECT NUMERICAL SIMULATION OF MASS TRANSFER FROM A SINGLE BUBBLE VIA AN IMPROVED SUBGRID SCALE MODEL

Claire M.Y. CLAASSEN[1]*, **Shafiul ISLAM**[1], **E.A.J.F. PETERS**[1], **Niels G. DEEN**[2], **J.A.M. KUIPERS**[1],
Maike W. BALTUSSEN[1]†

[1]Multiphase Reactors Group, Department of Chemical Engineering and Chemistry, Eindhoven University of Technology, Eindhoven, The Netherlands

[2]Power and Flow Group, Department of Mechanical Engineering, Eindhoven University of Technology, Eindhoven, The Netherlands

* E-mail: c.m.y.claassen@tue.nl
† E-mail: m.w.baltussen@tue.nl

ABSTRACT

Hydrogenation, oxidation and alkylation are just some of the processes which are performed in bubble columns. One of the reasons to use a bubble column for these processes is the high interfacial mass transfer coefficients. Trying to simulate the mass transfer around the bubbles is however challenging due to the typically high Schmidt numbers of liquids, meaning that the mass boundary layer is very thin compared to the momentum boundary layer. To resolve this thin mass boundary layer, a subgrid scale model can be used. This work focuses on improving the subgrid scale model that we have embedded in our in-house front tracking framework of Claassen et al., AIChe J 2019. In the current implementation the unphysical numerical back diffusion at the grid into the bubble has been prevented with a staircase immersed boundary implementation. A verification has been performed by comparing the simulated, local and global Sherwood number with the analytical solution in creeping and potential flow regimes. Furthermore, the model was validated for 20 free rising bubbles of different shapes at industrial relevant Schmidt numbers (10^3-10^5). The model was able to correctly predict the Sherwood numbers.

Keywords: Computational Fluid Dynamics, bubble columns, Front Tracking, mass transfer, subgrid scale modeling, boundary layer, Direct Numerical Simulation .

NOMENCLATURE

Greek Symbols

δ	Boundary layer thickness, $[m]$
γ	Strain rate ($-\frac{\partial u_n}{\partial n^2}$), $[{}^{1}/_{s}]$
κ	Viscosity ratio
ρ	Density, $[{}^{kg}/_{m^3}]$
$\boldsymbol{\tau}$	Stress tensor, $[{}^{kg}/_{ms^2}]$
θ	Angle from the top of the bubble to the bottom, $[rad]$

Latin Symbols

c	Concentration, $[{}^{kg}/_{m^3}]$
D	Diffusion coefficient, $[{}^{m^2}/_{s}]$
$\mathbf{F}$	Force density, $[{}^{kg}/_{m^2s^2}]$
$\mathbf{g}$	Gravity constant, $[{}^{m}/_{s^2}]$
M_0	Total mass density in the model boundary layer region of a marker, $[{}^{kg}/_{m^2}]$
n	Normal coordinate from the interface, $[m]$
p	Pressure, $[{}^{kg}/_{ms^2}]$
Pe	Peclet number, $[-]$
Re	Reynolds number, $[-]$
Sh	Sherwood number, $[-]$
t	Time, $[s]$
$\mathbf{u}$	Velocity, $[{}^{m}/_{s}]$

Sub/superscripts

δ_0	At the model boundary layer thickness
σ	Surface tension
n	Normal direction from the interface
0	Model/bubble

INTRODUCTION

Bubbly flows are frequently encountered in many industries such as in the metallurgical, biochemical and chemical industry. In these industries, the bubbles are used to introduce mixing and/or supply reactants or remove reaction products. The efficiency of the last two processes depends on the mass transfer characteristics which are not thoroughly understood in bubbly flows. One of the reasons is the high Schmidt numbers typically found in gas-liquid systems. As the Schmidt number is high, the mass boundary layer is very small compared to the momentum boundary layer making it difficult to capture experimentally and to resolve numerically. Nevertheless, the subject has still been heavily studied in the past two decades.

For numerical studies, four different techniques have been used to resolve the boundary layer. The first technique uses the same uniform grid for solving the momentum equation and the advection-diffusion equation which ensures an easy coupling between the two equations. The disadvantage, however, is that both equations are solved with the grid size that is required to resolve the smallest boundary layer of the two. With this approach Bothe *et al.* (2004); Bothe and Warnecke (2005); Onea *et al.* (2009); Alke *et al.* (2009) and Hayashi and Tomiyama (2011) studied the mass transfer from single (deformable) bubbles, Taylor bubbles or bubble trains. Because the computational costs are high in this approach, several simplifications are made: the Schmidt number was kept low (Onea *et al.*, 2009; Alke *et al.*, 2009), an axisymmetric domain was used (Bothe *et al.*, 2004; Bothe and Warnecke, 2005; Alke *et al.*, 2009; Hayashi and Tomiyama, 2011), and/or the simulations were performed in 2D (Bothe and Warnecke, 2005; Alke *et al.*, 2009; Hayashi and Tomiyama, 2011).

The disadvantage of this first technique is reduced when two separate grids are used. The two grids are uniform and regular but have the size required for resolving the boundary layer of the solved field. Since both grids are regular and uniform, interpolating the value of one grid to the other grid is still easy. With this technique, Davidson and Rudman (2002) investigated the mass transfer of deformable bubbles. Koynov *et al.* (2005) and Radl *et al.* (2007, 2008) also investigated the mass transfer of deformable bubbles with this technique, but they included a reaction. Whereas these studies used 2D domains, Darmana *et al.* (2006) simulated a single bubble in full 3D, but with a low Schmidt number of unity. Roghair *et al.* (2016) simulated a bubble swarm in 3D with the Schmidt number equal to unity.

This second technique only refines the field which requires refinement. However, refinement is only required at specific locations. The most important location is the boundary layer at the interface (although the concentration wake might also benefit from refinements). The refinement at the interface can be imposed by unstructured grids or techniques such as Adaptive Mesh Refinement (AMR). Unstructured grids have been used by Jung and Sato (2001, 2005); Dani *et al.* (2006); Wylock *et al.* (2011); Colombet *et al.* (2013); Deising *et al.* (2016) and Hayashi and Tomiyama (2011). Most of these researches simulated fixed bubble shapes due to the difficulty of moving the unstructured mesh with the bubble oscillations. Panda *et al.* (2020) showed the potential of AMR with simulations of forced-convection mass transfer from single bubbles at high Prandtl numbers ($\mathcal{O}(10^2)$). Mass transfer of moving deformable bubbles with industrial relevant Schmidt numbers in the range of $\mathcal{O}(10^3)$ - $\mathcal{O}(10^5)$ is however still a challenge, due to the high level of refinement that is required.

The last approach that is being used for the simulation of mass transfer from bubbles is different from the previous approaches. This approach does not resolve the boundary layer with a small enough grid size, but uses a subgrid scale (SGS) model to approximate the concentration boundary layer. So far two different SGS models for the mass transfer of bubbles have been developed. The Center of Smart Interfaces and the Institute for Mathematical Modeling and Analysis groups in Darmstadt have worked on a SGS model which is implemented in the Volume of Fluid framework. Their first model uses an analytical solution to the advection-diffusion equation which is simplified by assuming curvature effects to be negligible, convection to be dominant parallel to the interface and diffusion to be dominant tangential to the interface. The mass boundary layer thickness, used as a free model parameter, is then fitted from the simulation data and with that the convective and diffusive fluxes in interface cells are corrected (Alke *et al.*, 2010; Bothe and Fleckenstein, 2013; Gründing *et al.*, 2016; Weiner and Bothe, 2017). In one of the most recent publications, the analytical solution is no longer used. It is replaced by a solution provided by a machine learning method. With the result from the machine learning model the fluxes are corrected (Weiner *et al.*, 2019).

The other subgrid scale model has been developed at the University of Notre Dame by Aboulhasanzadeh *et al.* (2012). This subgrid scale model has been implemented in the Front Tracking (FT) framework. It makes use of the same assumptions as the other subgrid scale model to simplify the advection-diffusion equation. The advection-diffusion equation in a specific region normal to a FT marker is solved with an approximate boundary layer model. If the surface concentration in the boundary layer passes a certain threshold only then the mass is transferred to the grid that deals with the species transport in the remainder of the domain.

In this research, we chose to improve this latest model. First of all, we ensure species conservation in the SGS model during the crucial remeshing operations. Secondly, we make use of the exact analytical solution in the form of the error function instead of the second order polynomial that is used by Aboulhasanzadeh *et al.* (2012). And lastly, we prevent the numerical diffusion back into the bubble.

This article will first explain the details of the Front Tracking method. Next, the subgrid scale model and the made improvements will be elaborated on. Subsequently, the correctness of the improved model is shown with verification and validation of the method.

MODEL DESCRIPTION

Front Tracking

In Direct Numerical Simulations (DNS), two types of interface representations are encountered. The first are so-called front capturing methods in which the interface is not explicitly tracked but reconstructed from other quantities such as a color function for Volume of Fluid and a distance function for Level-Set. The second type are so-called front tracking methods in which the interface is explicitly tracked via Lagrangian points. One of these methods is the FT method in which the Lagrangian points are connected to form a closed triangular mesh. This method is used in this study.

In FT, the bubble moves by advecting the Lagrangian marker points with the local velocity, which is calculated via piecewise cubic spline interpolation of the Eulerian velocity field. As a result of the individual advection of the marker points, the mesh quality decreases. To correct this a remeshing algorithm is performed after the point positions are updated (Roghair *et al.*, 2016). When the distance between two marker points is too long and/or the edge shows local undulations, a point is added to give a high point concentration in curved parts (edge splitting). On the other hand, when the distance between two marker points is too short and/or the mesh is locally very flat, a point is removed which leads to a lower resolution in flat parts (edge collapsing). To ensure a good mesh quality (preferably equal lateral triangles), the connection between two markers might change from an edge between two points to an edge between the opposite two points (edge swapping). Lastly, to reduce the amount of remeshing operations that are needed all the marker points are evenly distributed over the interface while any volume changes due to the remeshing operations are corrected via the volume restoration/conservation method described by Kuprat *et al.* (2001) (edge smoothing). These crucial remeshing operations are graphically shown in Figure 1.

In FT, the Navier-Stokes equation and the continuity equation, given in equations 1 and 2, are then solved on a staggered Cartesian grid with a one-fluid formulation where the density is obtained via volume weighing averaging and the viscosity via harmonic averaging with the phase fraction.

$$\rho\frac{\partial\mathbf{u}}{\partial t} = -\nabla p - \rho\nabla\cdot(\mathbf{u}\mathbf{u}) - \nabla\cdot\boldsymbol{\tau} + \rho\mathbf{g} + \mathbf{F}_\sigma \quad (1)$$

$$\nabla\cdot\mathbf{u} = 0 \quad (2)$$

The connection between the interface representation and the Cartesian grid is made via the surface tension force inside the incompressible Navier-Stokes equation. The surface tension is calculated at every FT marker as the sum of the tensile forces the marker exerts on its neighboring markers, i.e. the pull force method (Tryggvason *et al.*, 2001). This force is mapped to the nearby Eulerian cells using a mass-weighing function (Deen *et al.*, 2004).

To solve the equations, a projection-correction method is used to first solve for the velocity with equation 1 and then correct the velocity with equation 2. The convective term in the Navier-Stokes equation is discretized via a second order flux-delimited Barton scheme and treated explicitly. The diffusive term, on the other hand, is discretized using a second order central difference scheme and treated semi-implicit such that the velocities in all three directions can be solved separately. Further numerical details can be found in Dijkhuizen *et al.* (2010) and Roghair *et al.* (2016).

Mass Transfer

For the mass transfer, the advection-diffusion equation, given in equation 3, is solved on the same Cartesian grid as the hydrodynamics. The diffusion term is discretized with a second order central difference scheme and treated implicitly, while the convection term is discretized with the Van Leer scheme and treated explicitly. Since the SGS model deals with the mass transfer from the bubble interface to the liquid, the whole concentration field on the Eulerian grid is uniformly initialized to the initial concentration in the liquid. The concentration is assumed to not influence the fluid properties.

$$\frac{\partial c}{\partial t} + \mathbf{u} \cdot \nabla c = D \nabla^2 c \tag{3}$$

Subgrid-scale model

The subgrid-scale model describes the concentration profile close to the bubble interface, in a region of width δ_0, by means of a boundary layer approximation. The advection-diffusion equation in the boundary layer is simplified by assuming negligible curvature effects, dominant convection parallel to the interface and dominant diffusion tangential to the interface. Next to that, a Taylor expansion of the velocity is applied. This leads to the following simplified equation for each marker (Aboulhasanzadeh *et al.*, 2012):

$$\frac{\partial c}{\partial t} = n\gamma \frac{\partial c}{\partial n} + D \frac{\partial^2 c}{\partial n^2} \tag{4}$$

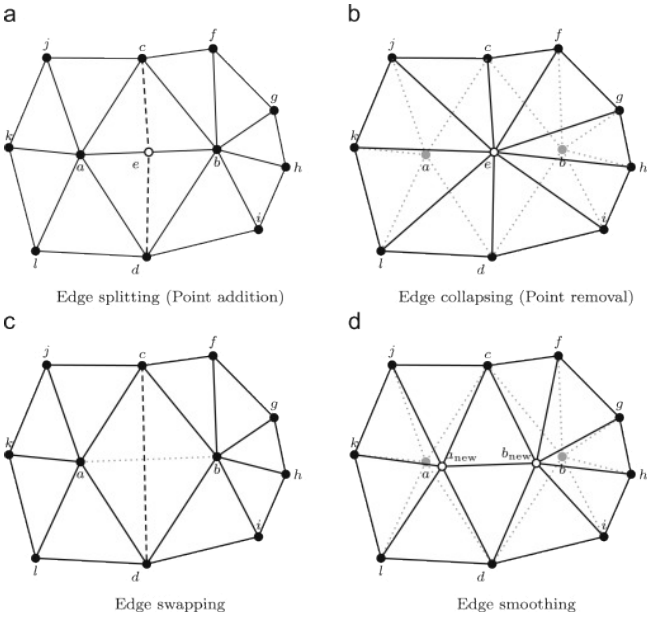

Edge splitting (Point addition)

Edge collapsing (Point removal)

Edge swapping

Edge smoothing

Figure 1: The remeshing operations that are used to maintain a good mesh quality.

The first term on the right hand side indicates the concentration change as a result of compression or expansion of the boundary layer due to the flow field and the second term indicates a concentration change as a result of diffusion normal to the interface.

Equation 4 is solved for every marker via the zeroth moment of the concentration in the model boundary layer region, i.e. $M_0 = \int_0^{\delta_0} c(n)\mathrm{d}n$. The evolution of the zeroth moment over time is given in equation 5.

$$\frac{dM_0}{dt} = -\gamma M_0 - D \left.\frac{\partial c}{\partial n}\right|_0 + \gamma c_{\delta_0} \delta_0 + D \left.\frac{\partial c}{\partial n}\right|_{\delta_0} \tag{5}$$

Aboulhasanzadeh *et al.* (2012) assumed a second order concentration profile to evaluate this equation explicitly. We will use the concentration profile given by the error function (equation 6). The concentration profile depends on the (real) boundary layer thickness (δ). When assuming a second order concentration profile the boundary layer thickness can easily be calculated from the total mass and the concentration profile. For the error function profile, this is however not the case as the error function can not be inverted. Therefore Newton-Rapson's method is used to calculate the real boundary layer thickness.

$$\frac{c(n)}{c_0} = \mathrm{erfc}\left(\sqrt{\pi}\frac{n}{\delta}\right) \tag{6}$$

The above given concentration profile only holds in the region close to the bubble interface. The Eulerian grid should solve the remainder of the concentration field. Note that equation 6 is the analytical solution of equation 4 for an semi-finite domain with concentration zero at infinity. As mentioned before the whole concentration field in initialized uniformly. The Eulerian grid only gets a concentration when the boundary layer thickness at a marker becomes larger than the model boundary layer thickness. When this happens the latter two terms in equation 5 are added to the Eulerian grid as a source term in equation 3 via polynomial weighing (Darmana *et al.*, 2006). There is a one-way coupling between the boundary layer SGS model and the bulk concentration field: the SGS model determines the molar flux into the fluid bulk, but the concentration in the bulk fluid does not influence the boundary layer development.

Remeshing

This subgrid scale model is implemented at the individual FT markers where the markers should store the mass density (M_0) to evaluate the change over time. When markers are removed, added or reshaped as a result of remeshing, the mass density of the changed markers should be adjusted accordingly to prevent numerical mass gain or loss. For every remeshing operation, we have implemented an algorithm to restore the total mass.

The first considered remeshing operation is edge splitting that occurs when an edge becomes too long and/or is not capable to capture the local curvature (Figure 1a). When an edge is split two markers are divided into two new markers each. These new markers will have the same mass density as the marker they originated from.

For edge swapping, a similar algorithm is used. With edge swapping two markers change how they are connected (Figure 1c). In this case, the average mass density is calculated and the mass density of both markers will be equal to this average after the remeshing.

For edge collapsing the algorithm is a little less straightforward as there are more markers involved. Edge collapsing is performed when an edge is too short and/or the local curvature is very low. This means the resolution can be reduced by removing an edge and hence removing two markers (Figure 1b). All the markers with one point connected to the to be removed edge will consequently change shape. To correct for the removed mass from the two markers the total mass before and after removal is calculated. The difference in mass is then distributed over all markers that have grown in size weighted by their size increase.

The last remeshing operation, edge smoothing, follows the same algorithm as for edge collapsing. Edge smoothing slightly changes the position of the two edge endpoints to yield a better local node distribution (Figure 1d). As a result, all markers that contain one of those nodes will slightly change in size, similar to what happens for edge collapsing. Hence the algorithm here is again: calculate the total mass before and after smoothing and distribute the difference over all involved markers that increased in size weighted by their size increase.

IBM

In our previous work (Claassen *et al.*, 2019) as well as in the work of Aboulhasanzadeh *et al.* (2012) an unphysical mass flux into the bubble was found. On the grid the convection-diffusion equation, equation 3, is solved using a one-fluid approximation. This means the concentration can diffuse from the fluid to the gas phase without a problem. A concentration gradient appears into the bubble at δ_0 when mass is transferred from the SGS model to the Eulerian grid on which the concentration inside the bubble is initialized to zero. A source is thus introduced close to the bubble interface resulting into a flux to the bubble. To prevent this flux, we have further improved the model by implementing an immersed boundary at the end of the boundary layer. At this boundary a Neumann boundary condition is enforced using a staircase Immersed Boundary Method (IBM) (Tseng and Ferziger, 2003; Mizuno *et al.*, 2015; Seo and Mittal, 2011) to prevent molar fluxes into the bubble. Before the IBM can be implemented, the cells that are outside the bubble and boundary layer region should be determined. Only to these cells, the source term from the SGS model should be forced.

To determine the cells outside the bubble and boundary layer region, we adopted the approach of Mittal *et al.* (2008) in which for every cell the vector to the closest marker is identified. The dot product of this vector and the marker's normal vector determines where the cell center is located. To take into account the mass boundary layer, the marker's center is temporary transposed a distance of δ_0 in its normal direction. Performing this procedure for every cell at every time step will result in quite some computational overhead. However, since markers move maximally one grid cell in one time step, the computational time can be reduced significantly by only considering the eight cells neighboring a marker.

To map the mass flux that comes out of the SGS model the polynomial weighing procedure Darmana *et al.* (2006) is slightly adapted. The flux is only mapped to the cells that lay outside the model boundary layer. The same polynomial weighing is used but corrected by the total weight of the cells that lay outside the boundary layer.

To prevent the unphysical flux into the bubble, the implicit matrix coefficients and the explicit source vector are adjusted for cells outside of the bubble and the boundary layer that have a neighbor inside the bubble or boundary layer and for all cells inside the bubble or boundary layer. This last step is not necessary but is expected to speed up the computation. For cells outside the bubble and boundary layer that have a neighbor inside the bubble or boundary layer the implicit diffusive flux between those cells are set to zero. The explicit convective flux, discretized with the Van Leer scheme, depends on four cells: the cell at which the flux is calculated (i), the neighboring cell on one side ($il = i - 1$) and the two neighboring cells on the other side ($ih = i + 1$, $ihh = i + 2$). In case the cell at which is being calculated (i) is inside the bubble or the boundary layer, the flux is set to zero. If the $i - 1$ cell is inside the bubble or the boundary layer, the flux is calculated with the concentration of i at the place of il. If ih is inside the bubble or the boundary layer, then the flux is set to zero. Lastly, if ihh is inside the bubble or the boundary layer, the flux is calculated with ih at the place of ihh. The procedure for il and ihh is analogous to the flux calculation when those cells would be outside of the domain. All cells inside the bubble or boundary layer are always forced to have a zero concentration (although this is not strictly necessary as the IBM will already prevent mass from going there).

RESULTS

Verification

To check the implementation of this new model we used a test where a bubble is placed in Stokes flow and a test where the bubble is placed in potential flow. For these tests the velocity field is not solved but imposed from the Hadamard-Rybczynski solution (Hadamard, 1911; Rybczynski, 1911) and Clift *et al.* (1978), respectively. Since we use a moving frame of reference (Deen *et al.*, 2004) the velocity and pressure field are only set at initialization. Further simulations settings are given in Table 1.

Table 1: Settings used for the verification tests.

Bubble diameter	3.2	mm
Bubble resolution	40	Grid cells
Domain size	$2.5 \times 2.5 \times 2.5$	d_e
Time step	0.000001	s
Simulation time	6.0	s
Viscosity ratio	0.185	-
Velocity	0.05	m/s
Peclet number	160,000	-

To verify the correct implementation the local and global Sherwood number obtained in the simulations are compared with the analytical solution. In the simulations the Sherwood number is calculated as $\frac{dc}{dn}\Big| = -\frac{2c_0}{\delta}$ at every marker. The analytical local and global Sherwood number are obtained from equation 7 and 8 for Stokes flow and equation 9 and 10 for potential flow.

$$\frac{Sh(\theta)}{\sqrt{Pe}} = \sqrt{\frac{3}{\pi}}\frac{1+\cos\theta}{\sqrt{2+\cos\theta}}\sqrt{\frac{1}{1+\kappa}} \qquad (7)$$

$$\frac{Sh}{\sqrt{Pe}} = \sqrt{\frac{4}{3\pi}\frac{1}{1+\kappa}} \qquad (8)$$

$$\frac{Sh(\theta)}{\sqrt{Pe}} = \sqrt{\frac{3}{\pi}}\frac{1+\cos\theta}{\sqrt{2+\cos\theta}}\sqrt{3} \qquad (9)$$

$$\frac{Sh}{\sqrt{Pe}} = \sqrt{\frac{4}{\pi}} \qquad (10)$$

In Figure 2, the computed local Sherwood number averaged over the last 2s of the Stokes flow simulation are plotted together with the analytical solution. Figure 3 shows the same plot but for potential flow. For comparison, we also performed a simulation with our improved SGS model with the second order profile as described by Aboulhasanzadeh *et al.* (2012). The results of these simulations are also included in the graphs. As can be seen, in both cases our SGS model predicts the local Sherwood number correctly especially at the top of the bubble. At the bottom of the bubble, there's a small mismatch both with the erf function profile as well as with the second order profile. This is attributed to the fact that at the bottom of the bubble the model boundary layer is almost completely saturated which makes it difficult to correctly fit the concentration profile. Nevertheless, the global Sherwood number prediction is still accurate. With our SGS model with the error function, the Sherwood number was underestimated by 0.9% and 0.6% in Stokes flow and potential flow, respectively. This is almost half the error compared to the second order profile which overestimated the Sherwood number by 1.6% and 1.7%, respectively.

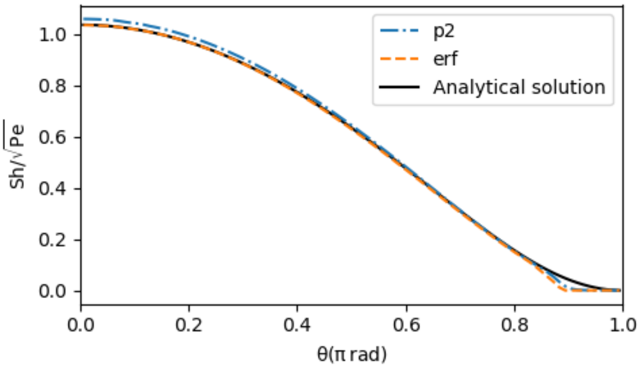

Figure 2: Local Sherwood number in the Stokes flow test. Averaged over the last 2s of the simulation.

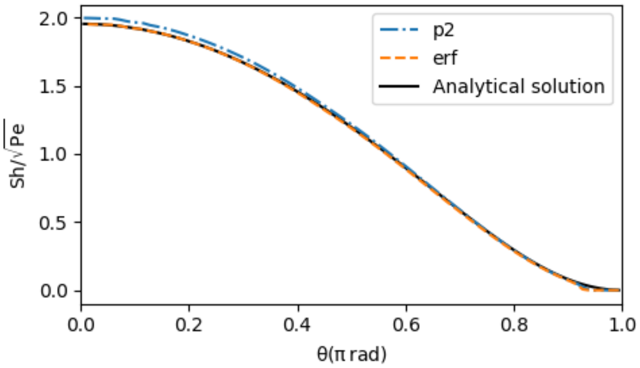

Figure 3: Local Sherwood number in the potential flow test. Averaged over the last 2s of the simulation.

Validation

To validate our code, we have performed the same set of simulations as in Claassen *et al.* (2019). The cases are indicated in the Grace diagram in Figure 4. The simulations have been performed with a moving frame of reference (Deen *et al.*, 2004). The simulations settings are the same as in our previous work and are summarized in Table 2.

Table 2: Simulations settings for the 20 cases depicted in Figure 4. Z is the domain height in the rise direction and is case dependent.

Bubble diameter	$1.5 - 6.9$	mm
Bubble resolution	20	Grid cells
Initial bubble shape	Spherical	
Domain size	$100 \times 100 \times Z$	Grid cells
Initial bubble position	$50 \times 50 \times 60$	%
Interface concentration (c_0)	1.0	kg/m^3
Time step	$10^{-6} - 10^{-5}$	s
Dimensionless simulation time	100	-
Viscosity ratio	$48 - 66$	-
Density ratio	$640 - 908$	-
Eötvos number	$0.2 - 60$	-
log Morton	-11 – 1	-

Since the hydrodynamics of the code was already validated in Claassen *et al.* (2019), the focus here is only on the mass transfer. To validate the mass transfer the time-average global Sherwood number calculated from the simulations is compared with literature correlations. For spherical and slightly ellipsoidal bubbles the correlation of Takemura and Yabe (1998) (equation 11) and of Lochiel and Calderbank (1964) (equation 12) are used. For wobbling bubbles the correlation of Brauer and Mewes (1971) (equation 13) and of Anderson (1967) (equation 14) are used. The simulation results together with predictions from these correlations are shown in Figure 5 and Figure 6 for spherical/ellipsoidal bubbles and wobbling bubbles, respectively. For spherical/ellipsoidal bubbles the Sherwood number is always within 10% of the literature correlations that have an accuracy of 7% and 12% for Takemura and Yabe (1998) and Lochiel and Calderbank (1964) respectively. It may appear as if our simulations are constantly lower than the correlations, this is, however, due to the fact that our bubbles or not all perfectly spherical as the correlations assume. Figueroa-Espinoza and Legendre (2010) showed that for low Reynolds numbers ($<\sim 100$) the Sherwood number decreases with a slightly increased aspect ratio which supports our results. For the wobbling bubbles the accuracy is always within 15% of the literature correlations. For this regime the literature correlations mismatch between one another (this is even more visible in Claassen

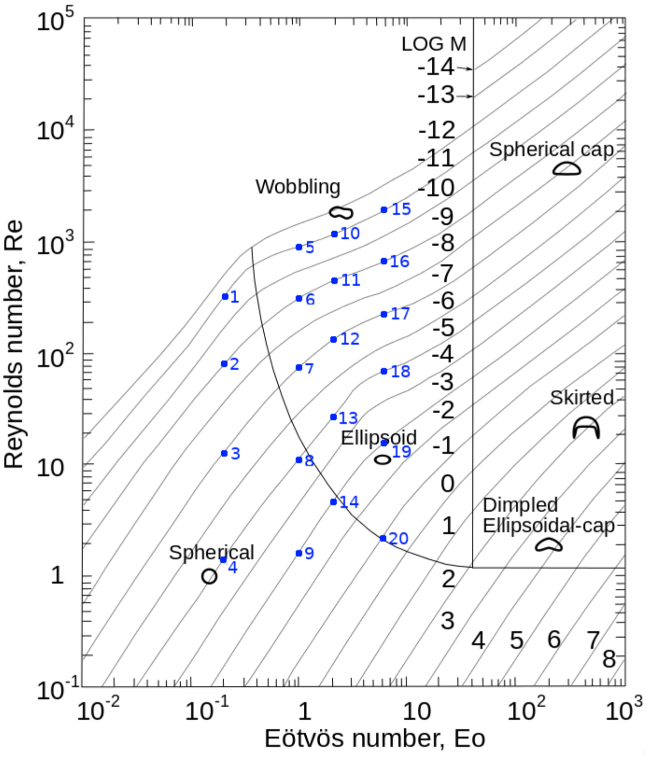

Figure 4: 20 simulations of different bubble shapes that have been performed.

et al. (2019) where more correlations are included), it is therefore harder to make a statement about the precise accuracy of our method.

$$Sh = \frac{2}{\sqrt{\pi}} \sqrt{1 - \frac{2}{3\left(1 + 0.09 Re^{2/3}\right)^{3/4}}} \left(2.5 + \sqrt{Pe}\right) \quad (11)$$

$$Sh = \frac{2}{\sqrt{\pi}} \sqrt{Pe\left(1 - \frac{2 + 3\kappa}{1 + \sqrt{\kappa\lambda}} \frac{1.45}{Re^{1/2}}\right)} \quad (12)$$

$$Sh = 2 + 0.015 Re^{0.89} Sc^{0.7} \quad (13)$$

$$Sh = 1.2\sqrt{\frac{d_e f_N}{D}} \text{ with } f_N = d_e \sqrt{\frac{48\sigma}{\pi^2 d_e^3 \rho_l (2 + 3\lambda)}} \quad (14)$$

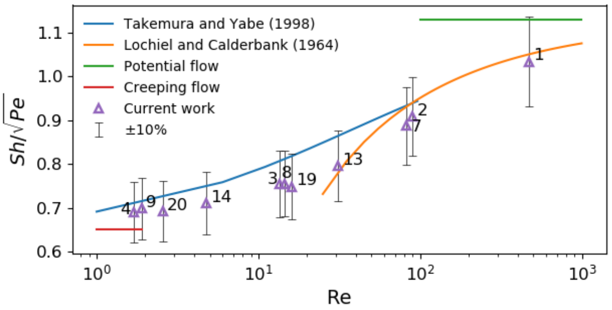

Figure 5: Calculated Sherwood number for the spherical/ellipsoidal cases (markers with errorbars) together with literature correlations (lines).

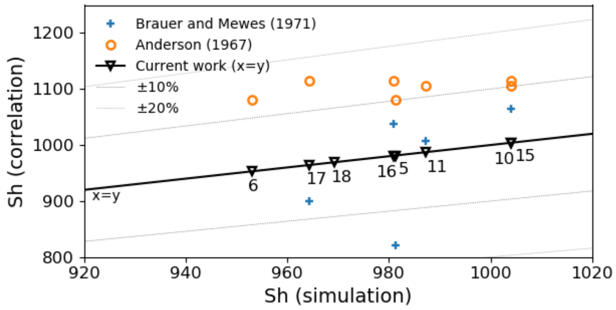

Figure 6: Calculated Sherwood number for the wobbling cases together with literature correlations.

The above-mentioned Sherwood results agree with the results of our previous work (Claassen *et al.*, 2019). The local concentration on the Eulerian grid, however, is different due to the here implemented IBM. Figure 7 shows the concentration on the grid with and without IBM for case 1. The figure shows the diffusion back into the bubble when IBM is not used, while the model with IBM clearly shows that there is no diffusion in the bubble. Due to the use of a log scale for the concentration, a difference in the wake predicted by the two models becomes visible. The wake of our new model has the expected thin shape, while the other wake is broader due to the diffusion back into the bubble and even outside the top of the bubble.

CONCLUSION

In this paper, the SGS model initially developed by Aboulhasanzadeh *et al.* (2012) is improved by including an algorithm for the SGS model upon remeshing, using the exact erf function and implementing an IBM to prevent numerical diffusion into the bubble. To check the implementation, the predicted Sherwood number of the model is verified for a bubble in Stokes flow and a bubble in potential flow. The computed Sherwood number was slightly under-predicted at the bottom of the bubble, but the global Sherwood number was still within 1% of the analytical solution. Furthermore, we validated the new model with 20 free rising bubbles. For the spherical and ellipsoidal bubbles, the Sherwood number deviated maximally 10% from literature correlations that mostly have an accuracy of roughly 10%. For the wobbling bubbles, the deviation was maximally around 15%, which is still good considering the accuracy of the correlations in this regime. We attribute the deviation between our results and the literature results to the fact that the correlations are rather strict and only applicable in very specific conditions such a potential or creeping flow and/or perfect sphericity. New, more broadly applicable correlations should be developed for which potentially this model could be used. Lastly, we compared the concentration profile on the grid predicted by a model with and without IBM implemented and found that the numerical diffusion into the bubble also leads to an incorrect wake which is broader than it should be. While the numerical diffusion into the bubble could be considered as negligible as is done in our previous work and the work of Aboulhasanzadeh *et al.* (2012), the broader wake is not neglectable.

REFERENCES

ABOULHASANZADEH, B., THOMAS, S., TAEIBI-RAHNI, M. and TRYGGVASON, G. (2012). "Multiscale computations of mass transfer from buoyant bubbles". *Chemical Engineering Science*, **75**, 456 – 467.

ALKE, A., BOTHE, D., KRÖGER, M., WEIGAND, B., WEIRICH, D. and WEKING, H. (2010). "Direct numerical simulation of high schmidt number mass transfer from air bubbles rising in liquids using the volume-of-fluid-method". *Ercoftac Bulletin*, **82**, 5–10.

ALKE, A., BOTHE, D., KROEGER, M. and WARNECKE, H.J. (2009). "Vof-based simulation of conjugate mass transfer from freely moving fluid particles". *Computational Methods in Multiphase Flow V*, 157–168.

ANDERSON, R.A. (1967). *Fundamentals of vibrations*. Macmillan.

BOTHE, D. and WARNECKE, H. (2005). "Vof-simulation of rising air bubbles with mass transfer to the ambient liquid".

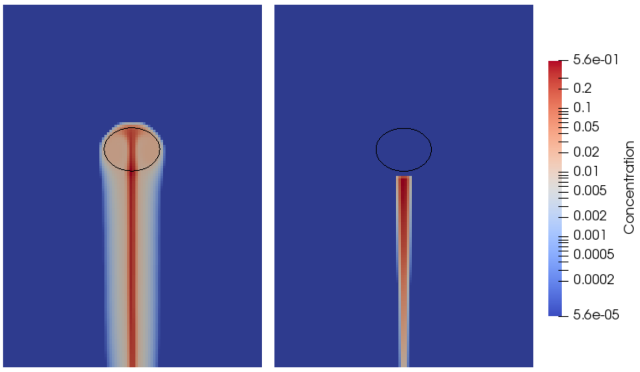

Figure 7: Slice of the concentration profile for case 1 with our previous work (Claassen *et al.*, 2019) without IBM (left) and our current work with IBM implemented (right). The black circle is the bubble contour.

10th Workshop on Transport Phenomena in Two-phase Flow, Bothe & Warnecke, Sunny Beach, Bulgaria, 61–72.

BOTHE, D. and FLECKENSTEIN, S. (2013). “A volume-of-fluid-based method for mass transfer processes at fluid particles”. *Chemical Engineering Science*, **101**, 283 – 302.

BOTHE, D., KOEBE, M., PRUSS, J. and WARNECKE, H.J. (2004). “Direct numerical simulation of mass transfer between rising gas bubbles and water”. *Sommerfeld, M. ed., Bubble Flows: Analysis, Modelling and Calculation*, 159–174.

BRAUER, H. and MEWES, D. (1971). *Stoffaustausch einschließlich chemischer Reaktionen*. Sauerländer.

CLAASSEN, C.M.Y., ISLAM, S., PETERS, E.A.J.F., DEEN, N.G., KUIPERS, J.A.M. and BALTUSSEN, M.W. (2019). “An improved subgrid scale model for front-tracking based simulations of mass transfer from bubbles”. *AIChE Journal*.

CLIFT, R., GRACE, J.R. and WEBER, M.E. (1978). *Bubbles, drops and particles*. Academic Press, New York.

COLOMBET, D., LEGENDRE, D., COCKX, A. and GUIRAUD, P. (2013). “Mass or heat transfer inside a spherical gas bubble at low to moderate reynolds number”. *International Journal of Heat and Mass Transfer*, **67**, 1096 – 1105.

DANI, A., COCKX, A. and GUIRAUD, P. (2006). “Direct numerical simulation of mass transfer from spherical bubbles: the effect of interface contamination at low reynolds numbers.” *International Journal of Chemical Reactor Engineering*, **4**, A2.

DARMANA, D., DEEN, N.G. and KUIPERS, J.A.M. (2006). “Detailed 3D modeling of mass transfer processes in two-phase flows with dynamic interfaces”. *Chemical Engineering & Technology*, **29**, 1027–1033.

DAVIDSON, M.R. and RUDMAN, M. (2002). “Volume-of-fluid calculation of heat or mass transfer across deforming interfaces in two-fluid flow”. *Numerical Heat Transfer B*, **41**, 291–308.

DEEN, N.G., VAN SINT ANNALAND, M. and KUIPERS, J.A.M. (2004). “Multi-scale modeling of dispersed gas-liquid two-phase flow”. *Chemical Engineering Science*, **59(8-9)**, 1853–1861.

DEISING, D., MARSCHALL, H. and BOTHE, D. (2016). “A unified single-field model framework for volume-of-fluid simulations of interfacial species transfer applied to bubbly flows”. *Chemical Engineering Science*, **139**, 173–195.

DIJKHUIZEN, W., ROGHAIR, I., VAN SINT ANNALAND, M. and KUIPERS, J.A.M. (2010). “DNS of gas bubbles behaviour using an improved 3D Front Tracking model–model development”. *Chemical Engineering Science*, **65(4)**, 1427–1437.

FIGUEROA-ESPINOZA, B. and LEGENDRE, D. (2010). “Mass or heat transfer from spheriodal gas bubbles rising through a stationary liquid”. *Chem. Eng. Sci.*, **65**, 6296–6309.

GRÜNDING, D., FLECKENSTEIN, S. and BOTHE, D. (2016). “A subgrid-scale model for reactive concentration boundary layers for 3d mass transfer simulations with deformable fluid interfaces”. *International Journal of Heat and Mass Transfer*, **101**, 476 – 487.

HADAMARD, J. (1911). “Movement permanent lent d’une sphere liquide et visqueuse dans un liquide visqueux”. *Comptes Rendus*, **152**, 1735.

HAYASHI, K. and TOMIYAMA, A. (2011). “Interface tracking simulation of mass transfer from a dissolving bubble”. *The Journal of Computational Multiphase Flows*, **3(4)**, 247–261.

JUNG, R.T. and SATO, T. (2001). “Direct numerical simulation on single-droplet flow with mass transfer”. *Chem. Eng. Technol.*, **24**, 1071–1075.

JUNG, R.T. and SATO, T. (2005). “Numerical simulation of high schmidt number flow over a droplet by using moving unstructured mesh”. *Journal of Computational Physics*, **203(1)**, 221–249.

KOYNOV, A., KHINAST, J.G. and TRYGGVASON, G. (2005). “Mass transfer and chemical reactions at dynamic interfaces”. *AIChE J.*, **51**, 2786– 2800.

KUPRAT, A., KHAMAYSEH, A., GEORGE, D. and LARKEY, L. (2001). “Volume conserving smoothing for piecewise linear curves, surfaces, and triple lines”. *Journal of Computational Physics*, **172**, 99–118.

LOCHIEL, A.C. and CALDERBANK, P.H. (1964). “Mass transfer in the continuous phase around axisymmetric bodies of revolution”. *Chemical Engineering Science*, **19(7)**, 471–484.

MITTAL, R., DONG, H., BOZKURTTAS, M., NAJJAR, F.M., VARGAS, A. and VON LOEBBECKE, A. (2008). “A versatile sharp interface immersed boundary method for incompressible flows with complex boundaries”. *Journal of computational physics*, **227(10)**, 4825–4852.

MIZUNO, Y., TAKAHASHI, S., NONOMURA, T., NAGATA, T. and FUKUDA, K. (2015). “A simple immersed boundary method for compressible flow simulation around a stationary and moving sphere”. *Mathematical problems in Engineering*, **2015**.

ONEA, A., WÖRNER, M. and CACUCI, D.G. (2009). “A qualitative computational study of mass transfer in upward bubble train flow through square and rectangular mini-channels”. *Chemical Engineering Science*, **64(7)**, 1416–1435.

PANDA, A., PATEL, H., PETERS, E.A.J.F., BALTUSSEN, M.W. and KUIPERS, J.A.M. (2020). “A multiple resolution approach using adaptive grids for fully resolved boundary layers on deformable interfaces at high schmidt numbers”. *Submitted to Chemical Engineering Science*.

RADL, S., TRYGGVASON, G. and KHINAST, J.G. (2007). “Flow and mass transfer of fully resolved bubbles in non-newtonian fluids”. *AIChE journal*, **53(7)**, 1861–1878.

RADL, S., KOYNOV, A., TRYGGVASON, G. and KHINAST, J.G. (2008). “DNS-based prediction of the selectivity of fast multiphase reactions: Hydrogenation of nitroarenes”. *Chem. Eng. Sci.*, **63**, 3279–3291.

ROGHAIR, I., VAN SINT ANNALAND, M. and KUIPERS, J.A.M. (2016). “An improved front-tracking technique for the simulation of mass transfer in dense bubbly flows”. *Chemical Engineering Science*, **152**, 351–369.

RYBCZYNSKI, W. (1911). “Über die fortscheitende bewegung einer flüssigen kugel in einem zählen medium”. *Bull. Acad. Sci. Cracovie*, **A**, 40.

SEO, J.H. and MITTAL, R. (2011). “A sharp-interface immersed boundary method with improved mass conservation and reduced spurious pressure oscillations”. *Journal of computational physics*, **230(19)**, 7347–7363.

TAKEMURA, F. and YABE, A. (1998). “Gas dissolution process of spherical rising gas bubbles”. *Chemical Engineering Science*, **53(15)**, 2691 – 2699.

TRYGGVASON, G., BUNNER, B., ESMAEELI, A., JURIC, D., AL-RAWAHI, N., TAUBER, W., HAN, J., NAS, S. and JAN, Y.J. (2001). “A Front-Tracking method for the computations of multiphase flow”. *Journal of Computational Physics*, **169(2)**, 708–759.

TSENG, Y.H. and FERZIGER, J.H. (2003). “A ghost-cell immersed boundary method for flow in complex geometry”. *Journal of computational physics*, **192(2)**, 593–623.

WEINER, A. and BOTHE, D. (2017). “Advanced subgrid-scale modeling for convection-dominated species transport at fluid interfaces with application to mass transfer from rising bubbles”. *Journal of Computational Physics*, **347**, 261–289.

WEINER, A., HILLENBRAND, D., MARSCHALL, H. and BOTHE, D. (2019). “Data-driven subgrid-scale modeling for convection-dominated concentration boundary layers”. *Chemical Engineering & Technology*, **42(7)**, 1349–1356.

WYLOCK, C., LARCY, A., COLINET, P., CARTAGE, T. and HAUT, B. (2011). “Direct numerical simulation of bubble-liquid mass transfer coupled with chemical reactions: Influence of bubble shape and interface contamination”. *Colloids ans Surfaces A: Physicochem. Eng. Aspects*, **381**, 130–138.

14th International Conference on CFD in Oil & Gas, Metallurgical and Process Industries
SINTEF, Trondheim, NORWAY
October 12-14, 2020

COMBINING AN IMPLICIT SOLUTION WITH AN EXPLICIT CORRECTOR STEP FOR THE SOLUTION OF THE CONTINUITY EQUATIONS IN A TWO-FLUID SOLVER

Eva-Maria WARTHA[1*], **Markus BÖSENHOFER**[12], **Michael HARASEK**[1]
[1]Technische Universität Wien - Institute of Chemical Environmental and Bioscience Engineering, 1060
Vienna, Austria
[2]K1-MET GmbH, Area 4 - Simulation and Analyses, Linz, Austria

[*] E-mail: eva-maria.wartha@tuwien.ac.at

ABSTRACT

To model two-phase flows in industrial applications, for example the raceway zone in a blast furnace, an Eulerian two-fluid model is usually the method of choice. It has proven to predict the behavior of gas-solid flows well and has a justifiable computational demand. Although, it is already widely used, there are still some deficiencies which arise from the averaged equations. Especially the continuity equation needs some special care compared to single phase flows. The consistency and boundedness need to be ensured, which is not straightforward. One widely used approach to target this problem is to use the relative velocities in the continuity equation. A drawback is, that this modified equation is non-linear in the phase fraction and therefore needs to be solved iteratively if solved implicitly. We propose to solve the discretized equation by combining an implicit solution step with (an) explicit corrector step(s). This new approach was implemented in the open source software OpenFOAM® and compared with the standard implementation. The new algorithm gives good prediction results for several test cases and this implicit approach could lead to larger time steps through better stability of the solution procedure.

Keywords: Two-Fluid Flow, Euler-Euler Approach, Raceway Simulation .

NOMENCLATURE

Greek Symbols

α	Phase fraction, $[-]$
η	Constant = 2 $[-]$
κ	Solid conductivity $[^{kg}/_{ms}]$
λ	Blending coefficient $[-]$
ξ	Coupling term, $[s^{-1}]$
ρ	Density, $[^{kg}/_{m^3}]$
τ	Stress tensor, $[^{kg}/_{ms^2}]$
ϕ	Angle of internal friction $[\circ]$
φ	Velocity, $[^{m}/_{s}]$

Latin Symbols

p	Pressure, $[Pa]$.
t	Time, $[s]$
A	Diagonal contributions
F	Flux $[m/s]$
Fr	Constant = 0.05 $[-]$
K	Drag coefficient $[^{kg}/_{m^3s}]$
P	Constant = 5 $[-]$
S	Source term
V	Cell volume$[-]$
$(I_{2D})^{-1/2}$	2nd-order deviatoric shear stress tensor
$\mathbf{g}$	Gravitational acceleration $[^{m}/_{s^2}]$
$\mathbf{S}$	Surface normal vector $[-]$
$\mathbf{U}$	Velocity, $[^{m}/_{s}]$

Sub/superscripts

e	Explicit
f	Face value
g	Gas
i	Implicit
n	Time step
p	Center value
r	Relative value
s	Solid
C	Convective
H	High order
L	Low order
$fric$	Frictional
$ktgf$	Kinetic theory of granular flows
min	Minimum for frictional effects
max	Maximum (packing) limit
$*$	Quantity enlarged with decoupling terms

INTRODUCTION

Industrial processes often incorporate two- or multi-phase flows, for example: fluidized beds for pyrolysis (Papadikis *et al.*, 2008) or the blast furnace for pig iron production (Abhale *et al.*, 2020). The simulation of such processes using computational fluid dynamics (CFD) helps to understand and improve them. To accurately and efficiently predict the phenomena dominating the operation, well calibrated models and numerical procedures are essential.

In general, the solid phase in a two-phase flow could be described by using Lagrangian or Eulerian models. The Lagrangian models offer more detail, since they are able to resolve particle interactions on a per particle basis (van der Hoef *et al.*, 2008; Agrawal *et al.*, 2001). Although, computer power is and has been increasing, the computational demand is still limiting. Therefore, this approach is usually only applied to small scales or low solid concentrations. For the many two-phase flows in industry, which incorporate dense solid flows, the Eulerian models are the way to go, (van der Hoef *et al.*, 2008). Here, both (gas and solid) phases are treated as interpenetrating continua. Particle interactions can not be resolved using those models but the models have proven to correctly predict phenomena in two-phase flows.

Compared to single-phase flows, the coupled equations are more difficult to solve and need special treatment, (Passalacqua and Fox, 2011; Weller, 2005). To further speed-up simulations the community is constantly trying to improve the algorithms to solve the equations. In this paper we suggest an alternative algorithm for the solution of the continuity equation in two-phase flows.

The algorithmic approach is described in the following section. The new approach was implemented in OpenFOAM® and tested on several test cases. The results are presented and provide promising results for the application of the new algorithm.

THEORY

Two-Fluid solvers are widely used for dense gas-solid systems. They treat both the phases as interpenetrating continua and use the Navier-Stokes equations for their description. Compared to a single-fluid system, the phase fraction is added to the descriptive equations. The phase-averaged equations for the solid phase are given in the following. Eq. 1 shows the continuity equation and Eq. 2 the momentum equation, where α_s is the solid phase volume fraction, $\mathbf{U}_s$ the solid velocity and $\mathbf{U}_g$ the gas velocity, ρ_s the solid density, τ_s the solid stress tensor, p the pressure, p_s the solid pressure, $\mathbf{g}$ the gravitational acceleration and K_{sg} the drag interaction coefficient. The solid pressure p_s is modeled based on the Kinetic Theory of Granular Flows, which is shortly described in a following section.

$$\frac{\partial}{\partial t}\left(\alpha_s \rho_s\right) + \nabla \cdot \left(\alpha_s \rho_s \mathbf{U}_s\right) = 0 \tag{1}$$

$$\begin{aligned}\frac{\partial}{\partial t}\left(\alpha_s \rho_s \mathbf{U}_s\right) + \nabla \cdot \left(\alpha_s \rho_s \mathbf{U}_s \mathbf{U}_s\right) &= \nabla \cdot \left(\alpha_s \tau_s\right) \\ -\alpha_s \nabla p - \nabla p_s + \alpha_s \rho_s \mathbf{g} &+ K_{sg}\left(\mathbf{U}_g - \mathbf{U}_s\right)\end{aligned} \tag{2}$$

The equations for the gas phase are formulated similarly by using the quantities of the gas phase (gas volume fractionα_g, gas density ρ_g and gas stress tensor τ_g):

$$\frac{\partial}{\partial t}\left(\alpha_g \rho_g\right) + \nabla \cdot \left(\alpha_g \rho_g \mathbf{U}_g\right) = 0 \tag{3}$$

$$\begin{aligned}\frac{\partial}{\partial t}\left(\alpha_g \rho_g \mathbf{U}_g\right) + \nabla \cdot \left(\alpha_g \rho_g \mathbf{U}_g \mathbf{U}_g\right) &= \nabla \cdot \left(\alpha_g \tau_g\right) \\ -\alpha_g \nabla p + \alpha_g \rho_g \mathbf{g} &+ K_{sg}\left(\mathbf{U}_s - \mathbf{U}_g\right)\end{aligned} \tag{4}$$

The two phases are coupled through the momentum exchange terms. In Eq. 2 and Eq. 4 only the drag term is considered ($K_{sg}\left(\mathbf{U}_g - \mathbf{U}_s\right)$). Furthermore, the following condition links the phases:

$$\sum \alpha_i = \alpha_s + \alpha_g = 1 \tag{5}$$

With the phase-averaged equations, some problems arise in the solution procedure, because the conservativeness of the solution and the boundedness of the phase volume fraction need to be ensured. Rusche (2002) and Oliveira and Issa (2003) recap different approaches of the discretization of the continuity equation. Here (and in OpenFOAM®) we use an approach presented by (Weller, 2005) and (Passalacqua and Fox, 2011) where the equation is reformulated in the following way:

$$\frac{\partial}{\partial t}\left(\alpha_s\right) + \nabla \cdot \left(\alpha_s \mathbf{U}\right) + \nabla \cdot \left(\alpha_g \alpha_s \mathbf{U}_r\right) = 0 \tag{6}$$

using the average phase velocity $\mathbf{U}$

$$\mathbf{U} = \alpha_s \mathbf{U}_s + \alpha_g \mathbf{U}_g \tag{7}$$

and the relative phase velocity $\mathbf{U}_r$

$$\mathbf{U}_r = \mathbf{U}_s - \mathbf{U}_g \tag{8}$$

The derivation of the coupling terms and the phase pressure yields the modified phase continuity equation, derived by (Passalacqua and Fox, 2011):

$$\begin{aligned}&\frac{\partial \alpha_s}{\partial t} + \nabla \cdot \left(\alpha_{s,f} \varphi^*\right) + \nabla \cdot \left(\alpha_g \alpha_s \varphi^*_{r,s}\right) \\ &-\nabla \cdot \left[\alpha_{s,f} \xi_{s,f} \left(\frac{1}{\rho_s} \frac{\partial p_s}{\partial \alpha_s}\right)|_f \left|\mathbf{S}\right| \nabla^{\perp} \alpha_s\right] = 0\end{aligned} \tag{9}$$

Where $\mathbf{S}$ is the surface normal vector and the averaged flux (φ) (Eq. 11) and the relative flux ($\varphi_{r,s}$) (Eq. 13) are used. The fluxes (φ^* and $\varphi^*_{r,s}$) are modified by a term resulting from the decoupling of the momentum equations:

$$\varphi^* = \varphi + \alpha_{s,f} \xi_{s,f} \left(\frac{1}{\rho_s} \frac{\partial p_s}{\partial \alpha_s}\right)_f \left|\mathbf{S}\right| \nabla^{\perp} \alpha_s \tag{10}$$

$$\varphi = \alpha_s \varphi_s + \alpha_g \varphi_g \tag{11}$$

$$\varphi^*_{r,s} = \varphi_{r,s} + \xi_{s,f} \left(\frac{1}{\rho_s} \frac{\partial p_s}{\partial \alpha_s}\right)_f \left|\mathbf{S}\right| \nabla^{\perp} \alpha_s \tag{12}$$

$$\varphi_{r,s} = \varphi_s - \varphi_g \tag{13}$$

$$\xi_{s,f} = \frac{1}{A_s + \frac{K_{sg}}{\rho_s}} \tag{14}$$

The partially implicit algorithm (explained by (Weller, 2005) and (Venier *et al.*, 2018)) is used for the decoupling. The term $\xi_{s,f}$ results from this decoupling of the momentum equations - in Eq. 14 only the drag term (K_{sg}) is mentioned, but also the implicit part of the virtual mass force term can be added to $\xi_{s,f}$. A_s is the coefficient matrix arising from the discretisation of the momentum equation.

Boundedness can only be ensured, if a fully implicit solution algorithm is chosen (Rusche, 2002; Passalacqua and Fox, 2011), but the non-linearity in α (Eq. 9) requires subiterations when using an implicit approach.

An upwind differencing scheme can also ensure the boundedness of the solution of Eq. 9. A drawback from the upwind schemes is numerical diffusion and consequently unsatisfying results. Therefore, an algorithm, called MULES (Multidimensional Universal Limiter with Explicit Solution) for blending high-order and upwind solution has been introduced in OpenFOAM® . The MULES algorithm is described in the next section.

Since this MULES algorithm requires quite small time stepping, ≤ 0.25 (Wardle and Weller, 2013), we wanted to suggest a new algorithm to possibly combine the benefits of a fully implicit and the MULES algorithm. This suggested and newly implemented algorithm, named ICMULES, is introduced afterwards and tested on several benchmark cases.

MULES Algorithm

MULES is the abbreviation for "Multidimensional Universal Limiter with Explicit Solution" and is an iterative algorithm to solve hyperbolic equations (Tacconi, 2018). The method explicitly integrates in time and uses a blending of first-order upwind and high-order schemes for the calculation of the fluxes. This ensures the boundedness while keeping the influence of numerical diffusion low.

In the OpenFOAM® Code the *MULES:explicitSolve* function is used to partly solve the modified continuity Eq. 9. The function solves Eq. 9 without the consideration of the last term, see Eq. 15. F_{Cf}^n denotes the convective fluxes, which correspond to the second and third term in Eq. 9. The fluxes are calculated with consideration of the lower ($\alpha = 0$) and upper (α_{max}) limits of the phase fraction. S_i and S_e represent the source terms of the continuity equation arising from f.ex. phase change or compression.

$$\frac{\alpha_{sp}^{n+1} - \alpha_p^n}{\Delta t} V_p + \sum_f F_{Cf}^n = \alpha_{sp}^{n+1} S_i + S_e \qquad (15)$$

The fluxes are blended by fluxes calculated with a low order discretisation scheme F_C^L and fluxes calculated with a high order discretisation scheme F_C^H. The low order and an antidiffusive flux A are summed up, see Eq. 17. The antidiffusive flux is calculated as:

$$A = \left(F_C^H - F_C^L\right) \qquad (16)$$

A limiter function λ, based on the limits of α_s and the neighboring cell values is computed, which determines the degree of blending.

$$\frac{\alpha_{sp}^{n+1} - \alpha_{sp}^n}{\Delta t} V_p + \sum_f F_{Cf}^{n,L} + \sum_f \lambda_f A = \alpha_{sp}^{n+1} S_i + S_e \quad (17)$$

More details on the computation of the limiter λ are given in (Tacconi, 2018).

ICMULES Algorithm

The suggested new algorithm combines an implicit solution step with a corrector step using MULES. Therefore, it will be called ICMULES (Implicit Corrected by MULES) in the following. The implicit step solves Eq. 9. In the present paper the following discretization schemes are used: implicit Euler in time, limited linear for the convective term with the relative flux, pure upwind for the other flux, a linear scheme for the gradient and linear with correction for the laplacian term.

The MULES algorithm is used in the next step to calculate an antidiffusive flux A, as previously, to ensure the boundedness of the solution. This antidiffusive flux is used to correct alpha similarly to Eq. 17:

$$\frac{\alpha_{sp}^{corr} - \alpha_{sp}^i}{\Delta t} V_p + \sum_f \lambda_f A = \alpha_{sp}^{n+1} S_i + S_e \qquad (18)$$

If the corrector step is used multiple times, an underrelaxation factor of 0.5 for all but the first iteration is introduced. It is usually applied three times in the following test cases.

Kinetic Theory Models

The solid phase fraction and its movement are modeled by the Kinetic Theory of Granular Flows (KTGF) (Gidaspow, 1994). A granular temperature Θ_s is used to model the solid phase viscosity and the particle pressure. Usually, a partial differential equation (PDE) for the granular temperature is constructed and solved (see (Gidaspow, 1994) or (Venier *et al.*, 2018) for further details).

If dissipation is assumed to be equal to production of the granular temperature, an algebraic equation is derived and solved instead of the PDE. (This is denoted in the OpenFOAM® settings by equilibrium=on).

For the solid viscosity $\mu_{s,ktgf}$ and the solid conductivity κ_s different models using the radial distribution function g_0, the granular temperature Θ_s and the restitution coefficient e_s exist.

Different models were proposed in literature for the calculation of the granular pressure, the frictional stress and the radial distribution function. A short recap of the used models is given below:

Granular Pressure Models

(a) Lun

$$p_s = \rho_s \alpha_s \Theta_s + 2\rho_s \alpha_s^2 g_0 \Theta_s \left(1 + e_s\right) \qquad (19)$$

For the granular pressure the relation presented by (Ding and Gidaspow, 1990) is used, which is derived based on Lun's velocity relations in a collision (Lun *et al.*, 1984).

Frictional Stress Models

The kinetic theory of granular flows does not model particle interactions with multiple neighboring particles near the packing limit, (Srivastava and Sundaresan, 2003; Venier *et al.*, 2018). Therefore, models to account for friction, frictional stress models, were introduced near the packing limit (when $\alpha_s > \alpha_{min}$). A frictional pressure and a frictional viscosity are added to the solid pressure and the solid viscosity:

$$p_s = p_{s,ktgf} + p_{s,fric} \qquad (20)$$

$$\mu_s = \mu_{s,ktgf} + \mu_{s,fric} \qquad (21)$$

Passalacqua and Fox (2011) and Venier *et al.* (2018) compare different frictional stress models and their influence on the simulation. Commonly used models are:

(a) Johnson Jackson (Johnson *et al.*, 1990)

$$p_{s,fric} = Fr \frac{\left(\alpha_s - \alpha_{min}\right)^\eta}{\left(\alpha_{s,max} - \alpha_s\right)^P} \qquad (22)$$

$$\mu_{s,fric} = 0.5 p_{s,fric} \sin(\phi) \qquad (23)$$

(b) Schaeffer (Schaeffer, 1987)

$$p_{s,fric} = 10^{25} \left(\alpha_s - \alpha_{s,min}\right)^{10} \qquad (24)$$

$$\mu_{s,fric} = 0.5 p_{s,fric} \left(I_{2D}\right)^{-1/2} \sin\left(\phi\right) \qquad (25)$$

The angle of internal friction Φ was set to 28 for the Schaeffer model and to 28.5 for the Johnson Jackson model in the simulations.

Radial Models

Different models to calculate the radial distribution function g_0 used in the granular pressure formulation (Eq. 19) have been proposed: (a) Carnahan Starling (Carnahan and Starling, 1969)

$$g_0 = \frac{1}{1-\alpha_s} + \frac{3\alpha_s}{2\left(1-\alpha_s\right)^2} + \frac{\alpha_s^2}{2\left(1-\alpha_s\right)^3} \tag{26}$$

(b) Lun Savage (Lun and Savage, 1986)

$$g_0 = \left(1 - \frac{\alpha_s}{\alpha_{max}}\right)^{-2.5\alpha_{max}} \tag{27}$$

(c) Sinclair Jackson (Lun and Savage, 1986; Sinclair and Jackson, 1989)

$$g_0 = \left(1 - \left(\frac{\alpha_s}{\alpha_{max}}\right)^{1/3}\right)^{-1} \tag{28}$$

It has to be noted, that the Carnahan Starling model does not take the maximum packing limit α_{max} into account, also emphasized by (Venier *et al.*, 2016). Therefore, the choice of the frictional stress model in conjunction with this model is essential, which will also be shown in the Results section.

RESULTS

Common test cases for two-fluid models are chosen to test the stability of the newly proposed algorithm. The results are compared to simulations with MULES. Furthermore, the influence of different frictional stress and radial models was tested to ensure the applicability of the ICMULES with different settings.

The test cases and the corresponding models used are summarized in Table 1. The abbreviations there correspond to the test cases: falling block=f.b., settling suspension=s.s., bubble growth=b.g. and raceway=r.w.. The letters (a)/(b)/(c) correspond to the models described in the section about the kinetic theory.

In the following subsections the chosen test cases are described and their results are presented.

Table 1: Models for the kinetic theory used for the different test cases and the chosen parameters

Model	f.b.	s.s.	b.g.	r.w.
equilibrium	off	off	off	off
viscosity	(a)	(b)	(b)	(b)
conductivity	(a)	(b)	(b)	(b)
granular pressure	(a)	(a)	(a)	(a)
frictional stress	(a)	(a)/(b)	(b)	(b)
radial	(a)	(c)	(a)/(b)	(c)
Parameters				
packing limit	0.63	0.60	0.63	0.63
α_{min}	0.60	0.55	varying	0.6
restitution coeff.	0.80	0.80	0.95	0.95

Falling Block (f.b.)

The falling block test case is chosen to check the stability of the algorithm. It was also used by (Passalacqua and Fox, 2011) and (Venier *et al.*, 2013). A block (dimensions: 0.026 m x 0.08 m) with a solid volume fraction of 0.58 is introduced at a height of 0.012 m in a 2D-domain with 0.05 m width and 0.2 m height. It falls down solely by gravity. A hexahedral mesh with 10 x 40 cells is used for the simulation in OpenFOAM® .

The particles have a diameter of 0.4 mm and a density of 2000 kg/m^3. The fluid phase viscosity is 1.84·10^{-5} Pa·s and a Prandtl Number of 0.7 is used. No virtual mass effects are taken into account and the drag is modeled as suggested by (Gidaspow, 1994), blending the Ergun and the Wen-Yu drag models.

The velocity boundary conditions are set as Dirichlet boundary conditions at the bottom and top for particle velocity and at the walls and the bottom for the air velocity. A Neumann boundary condition is set for the air velocity at the top and the particle velocity at the walls.

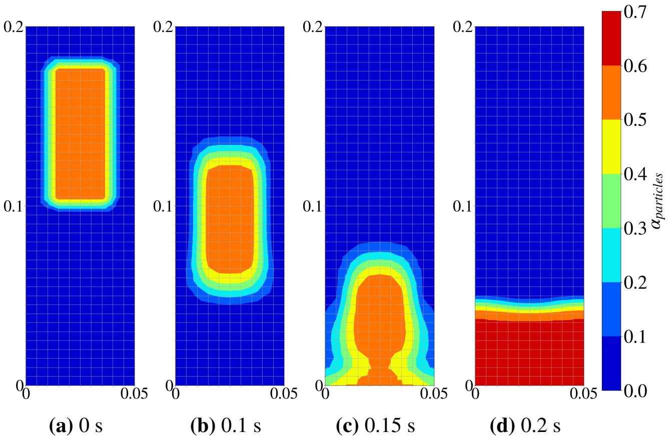

(a) 0 s **(b)** 0.1 s **(c)** 0.15 s **(d)** 0.2 s

Figure 1: Falling block using MULES algorithm

The results using MULES and ICMULES are shown in Figure 1 and Figure 2, respectively. The results are very similar for the both algorithms. The particles are slightly denser packed when using the ICMULES algorithm. The snapshot at 0.2 s is not the finally settled bed.

The difference in the maximum packing could be related to the chosen radial and frictional stress model. The used radial model (Carnahan Starling) does not take the maximum packing limit into account. It is also discussed by (Schneiderbauer *et al.*, 2012), that the maximum packing limit is ensured by the divergence of the frictional stresses, when the Carnahan Starling or a similar model is used for the radial distribution function. The MULES algorithm is still enforcing the packing limit by accounting for it in the flux reconstruction. The correction step in the ICMULES is not enforcing this limit. The question remains if this property is related to a physical model or it is a "numerical" trick in the MULES algorithm. Probably, one should anyways aim to choose a physically valid combination of radial model and frictional stress model, which ensures the packing limit.

Settling Suspension (s.s.)

The settling supension case uses also a 2D-setup with 0.05 m width and 0.3 m height and is discretized by 8 x 40 hexahedral cells. The whole column is initialized with a solid volume fraction of 0.3. Through gravity, the particles settle after time until they reach the packing limit ($\alpha_{max} = 0.6$). Passalacqua and Fox (2011) use this case to test an implicit solution. Venier *et al.* (2016) use it to compare partial elimination with partially implicit approach for the decoupling of the momentum equations.

The properties of the solid and fluid fraction are the same as for the falling block case, except that the Prandtl number was

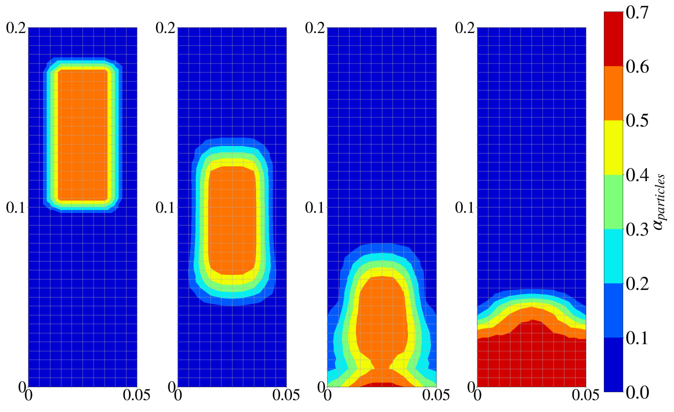

(a) 0 s **(b)** 0.1 s **(c)** 0.15 s **(d)** 0.2 s

Figure 2: Falling block using ICMULES

set to unity for both phases. The boundary conditions as well as the virtual mass and drag effects are treated in the same way as for the falling block case.

The solid void fraction profiles after different settling times are shown in Figure 3. The two algorithms are compared to the literature data from (Passalacqua and Fox, 2011) and (Venier *et al.*, 2016). Here, two different frictional stress models, the Johnson and Jackson (a) and the Schaeffer (b) model were applied.

Figure 3 shows, that the MULES and ICMULES case agree very well at the later settling times. In the beginning, at t = 0.1 s, there is a difference at the top of the column. We are not entirely sure, what is causing those differences between the MULES and ICMULES results. Because the ICMULES algorithm fits better to the presented literature data the presented algorithm seems valid. One reason for the differences at the beginning and the top of the column could be that numerical diffusion is more pronounced when applying the MULES algorithm.

At later times, the major difference between the solutions results from the different frictional stress models. The Schaeffer (b) model limits the phase fraction already to the α_{min} value. The results from the JohnsonJackson (a) model agree well with the results from literature and the results from ICMULES and MULES are virtually identical for the later time steps (t = 0.6 seconds).

Bubble Growth (b.g.)

The 2D bubble growth case checks the bubble growth in a fluidised bed with a central jet. Venier *et al.* (2018) studied the influence of the third dimension and did not find a significant impact, therefore, we only use the 2D case here. The geometry is 0.57 m wide and 1 m high and is discretized by 112 x 200 cells, which was determined to be the "best" mesh regarding the trade-off between calculation time and accuracy (Venier *et al.*, 2018).

First, the bubble formation with no frictional stress - or more precisely $\alpha_{min} > \alpha_{max}$ to avoid the contribution of frictional stresses was studied, see previous section about the frictional stress models. This was done to eliminate the influence of the chosen frictional stress model on the test results and solely study the influence of the radial model.

When using the ICMULES algorithm, the choice of the radial model determines if the packing limit is ensured, as discussed in the previous section. The ICMULES can enforce the packing limit when using the radial distribution models of Lun

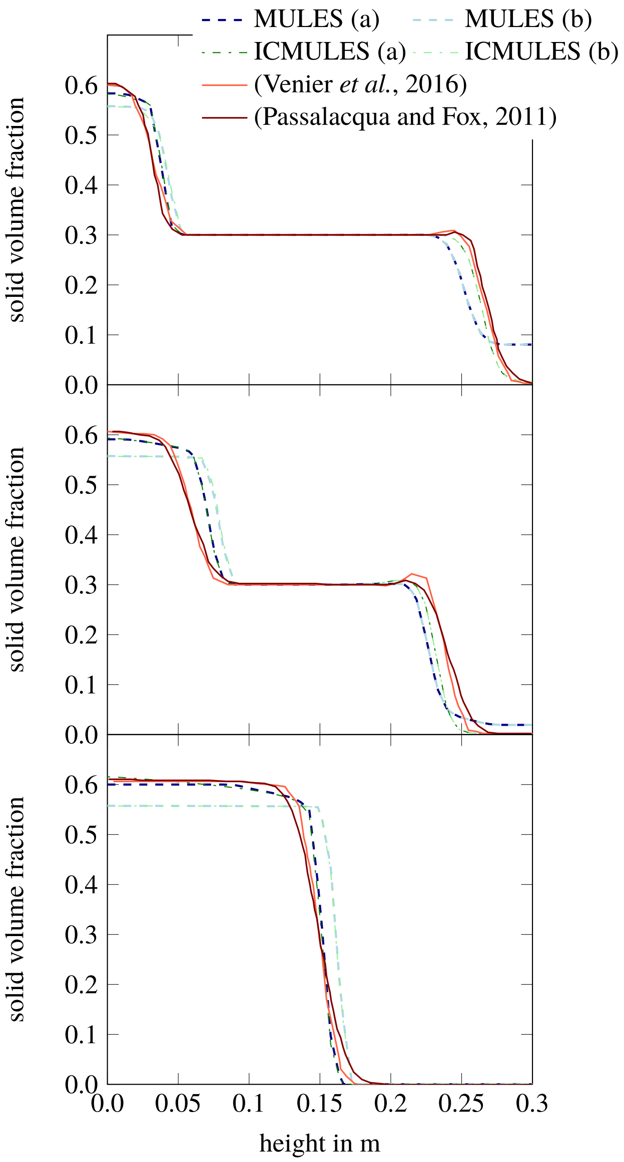

Figure 3: Solid volume fraction α_s after t = 0.1, 0.15 and 0.6 seconds settling time (from top to bottom), (a) and (b) refer to the frictional stress model

Savage or Sinclair Jackson, because there α_{max} is used in the formulations. The contribution of the radial function g_0 has a singularity at the packing limit and avoids overpacking in that way. When the Carnahan Starling model is used, the ICMULES cannot enforce the packing limit, see Figure 4 (d). The results in Figure 4 (d) show clearly, that the ICMULES is not applicable without a proper frictional stress model near the packing limit.

The MULES algorithm can always enforce the packing limit, because α_{max} is given as an input parameter for the flux calculation and ensures α values between 0 and α_{max} through the algorithmic implementation.

When the results without frictional stress with the Lun Savage radial model are compared, they are identical for the explicit and implicit algorithm, see Figure 4. The agreement with the experiments seems though to be best for the Carnahan Starling model using the explicit algorithm. Comparing the simulated and measured bubble detachment time, Table 2 indicates that the Lun Savage model agrees better with the experiments.

Table 2: Bubble detachement time in seconds. Experimental values from (Kuipers *et al.*, 1991). Simulations without frictional stress model

Exp.	**MULES**		**ICMULES**		
	(a)	(b)	(a)	(b)	radial model
0.17	0.19	0.15	0.31	0.15	

The simulations without frictional stress model were conducted to highlight the differences of the algorithmic approaches. For simulations near the packing limit it is usually not advised to ignore the frictional stresses, because the kinetic theory can not account for multiple particle interactions. Therefore, we also studied the bubble formation with a frictional stress model. We chose the Schaeffer frictional stress model, because it can be applied with the Carnahan Starling radial model. The results of the bubble formation at t = 0.1, 0.14 and 0.18 s are also shown in Figure 4. The minimum frictional packing was set to $\alpha_{min} = 0.6$.

Kuipers *et al.* (1991) presented also the bubble diameter ratio of the experiments. Figure 5 compares those ratios with the ones from the simulation without frictional stress. In the simulation the bubble was measured as the region with a void fraction below 0.2. The bubble shape with the Lun Savage radial model and no frictional stresses is predicted in line with the experiments for the first 0.15 seconds. Then, the vertical stretch is over and/or the longitudinal stretch under predicted. The same comparison was made for the bubble prediction using the Schaeffer frictional stress model, see Figure 6. Here the longitudinal stretch of the bubble seems way overpredicted. This is already visible in Figure 4. Nevertheless, the bubble diameter ratio shows, that the algorithm is not influencing the results. The deviations between simulation and experiments are most likely related to the models and settings chosen therein.

2D Raceway (r.w.)

The last studied test case in this paper is a 2D Raceway formation test case. The test case was first presented by (Feng *et al.*, 2003). They studied the raceway formation in a simple 2D-setup by DEM simulation. Here, we test the applicability of an Euler-Euler algorithm in the prediction of the raceway formation in comparison with those DEM results. Furthermore, we test the proposed algorithm ICMULES and study the simulation time in comparison with the original algorithm.

Experiments from (Kuipers *et al.*, 1991)

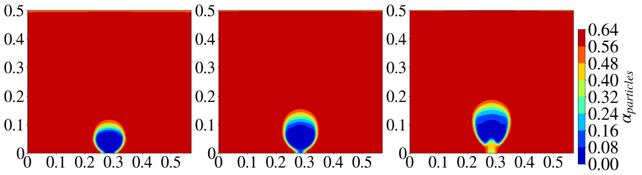

(a) MULES algorithm without frictional stress, Lun Savage model

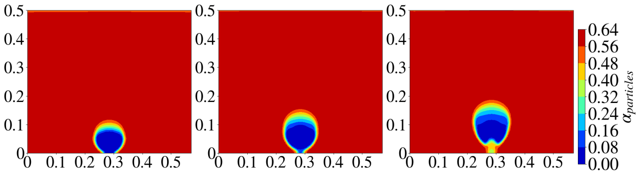

(b) ICMULES algorithm without frictional stress, Lun Savage model

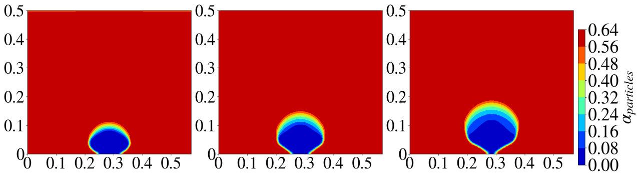

(c) MULES algorithm without frictional stress, Carnahan Starling model

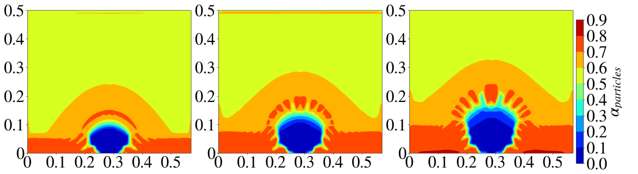

(d) ICMULES algorithm without frictional stress, Carnahan Starling model

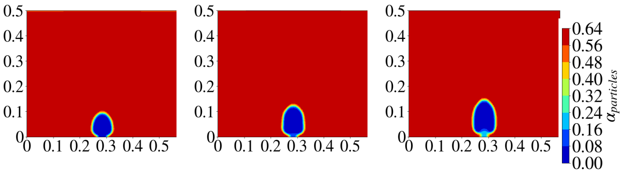

(e) MULES algorithm with Schaeffer frictional stress model, Carnahan Starling model

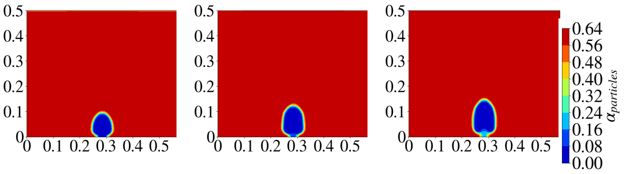

(f) ICMULES algorithm with Schaeffer frictional Stress model, Carnahan Starling model

Figure 4: Single Bubble after 0.1, 0.14 and 0.18 seconds (columnwise).

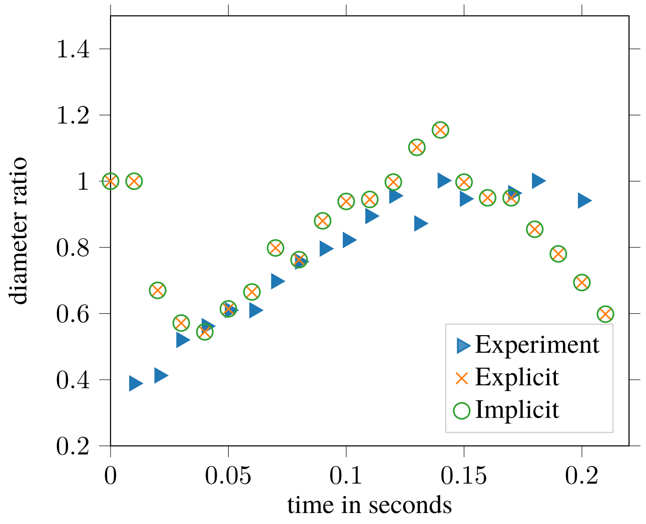

Figure 5: Comparison of the diameter ratio for the experiments from (Kuipers *et al.*, 1991) and the simulations using No Frictional Stress and Lun Savage radial model

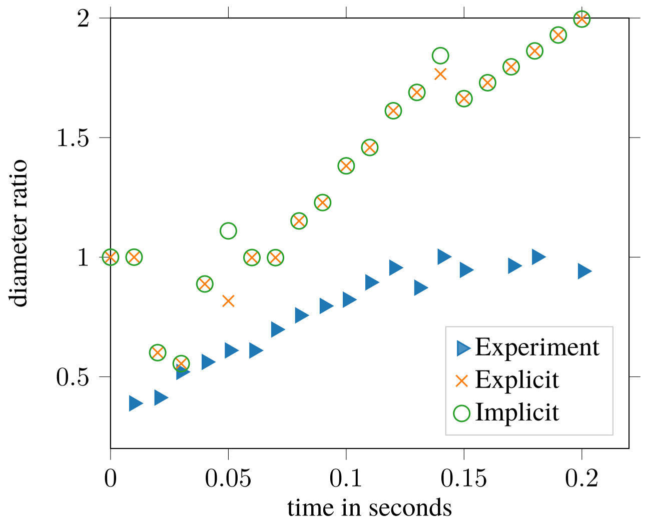

Figure 6: Comparison of the diameter ratio for the experiments from (Kuipers *et al.*, 1991) and the simulations using Schaeffer and Carnahan Starling model

The raceway is simulated as a 2D raceway, same as by (Feng *et al.*, 2003). The bed is 1 m high and 0.3 m wide. It was discretized by a uniform mesh using 200x60 cells. The jet inlet is positioned 0.1 m above the bottom of the bed and is 0.02 m wide. Table 3 lists the physical parameters for solid and gas phase used in the simulation.

Neumann boundary conditions for the air velocity are set at the walls and bottom. The inlet velocity is set to 20, 25 and 30 m/s for the different cases studied. At the top, the air pressure is fixed and no inflow is allowed. The particle velocity is set to zero at the inlet and outlet and a partial slip condition is used at the wall and bottom (Johnson and Jackson, 1987) with a specularity coefficient of one. The specularity coefficient defines the degree of frictional interaction between walls and particles (specularity coefficient = 0 corresponds to frictionless walls). The velocity at the boundary is calculated based on this interaction coefficient. The granular temperature at the walls and bottom is also treated by the JohnsonJacksonParticleTheta conditions, described in (Johnson and Jackson, 1987), using the same specularity coefficient and a restitution coefficient of 0.95.

Table 3: simulation parameters for the raceway case

Solid phase		
diameter	m	0.004
density	kg/m^3	2500
Gas phase		
density	kg/m^3	1.205
viscosity	kg/(ms)	$1.8{\cdot}10^{-5}$

As a result of the previous test cases, we decided to use the Schaeffer frictional stress model and the Carnahan Starling radial model for the simulations. The maximum packing limit was set to $\alpha_{max} = 0.63$ and the minimum frictional velocity to $\alpha_{min} = 0.6$.

Figure 7 and Figure 8 show the results from the raceway formation for two different inlet velocities: 25 and 30 m/s. For the 20 m/s practically no raceway is formed, which qualitatively agrees with the presented results in (Feng *et al.*, 2003). For the case with 25 m/s inlet velocity, the raceway is reaching a steady state after some time. For 30 m/s inlet velocity the bed performs more like a bubbly bed and the raceway does not seem to reach a steady state. The MULES and ICMULES algorithms give the same results for the raceway formation. For these cases a fixed time step of 10^{-5} s was used.

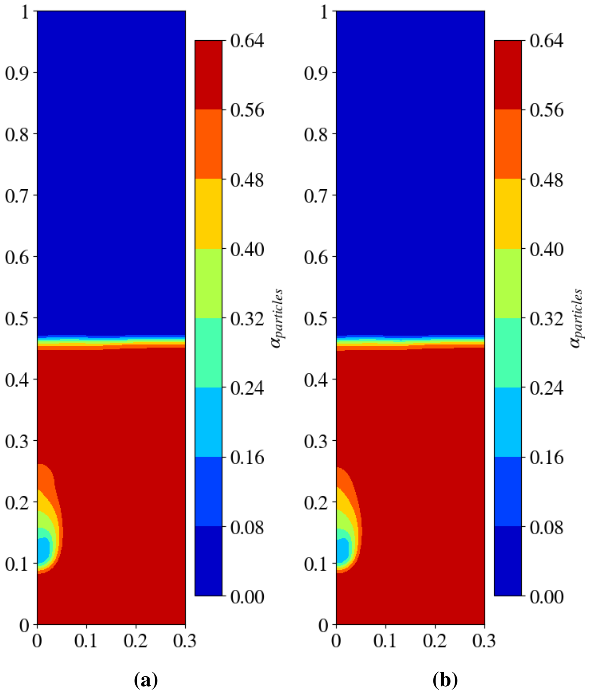

(a) **(b)**

Figure 7: Raceway formation for 25 m/s inlet velocity after 1 s simulation time for the different algorithms: (a) MULES (b) ICMULES

We also compare the raceway penetration depths from (Feng *et al.*, 2003) and the simulations. It is not entirely clear, how the raceway penetration depth is defined by Feng *et al.* (2003). Here it was calculated as the distance from the air inlet to the region with a void fraction above 0.3. Table 4 shows the results from the simulation and literature. The penetration depth agrees well for the cases of high velocity (30 and 25 m/s). For 20 m/s no raceway is formed in the

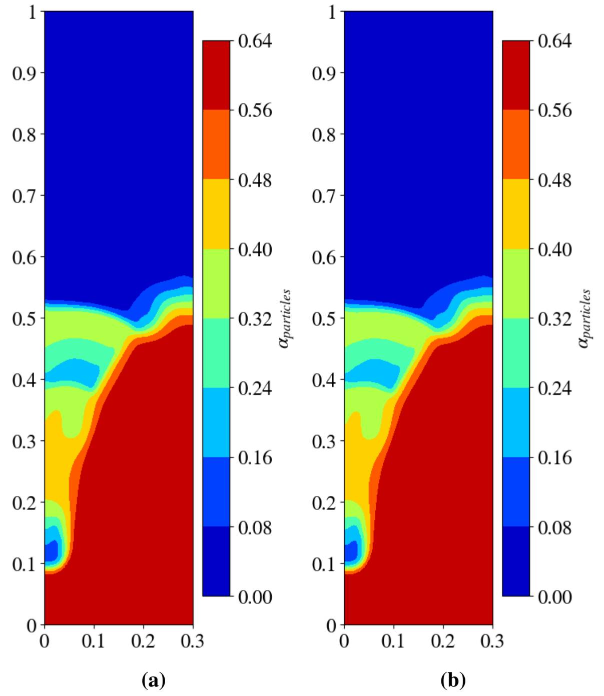

(a) **(b)**

Figure 8: Raceway formation for 30 m/s inlet velocity after 1 s simulation time for the different algorithms: (a) MULES (b) ICMULES

OpenFOAM® simulations. Better agreement might be obtained, by also accounting for virtual mass effects, which were neglected here.

Table 4: Raceway penetration depth in mm in comparison

	paper	explicit	implicit
0.30 m/s	42	41	41
0.25 m/s	30	32	32
0.20 m/s	25	-	-

The above test cases were all tested with the same time step sizes for MULES and ICMULES and consequently resulted in approximately the same computational time. To give an indication on the possible computational improvements through the ICMULES, we also tested the Raceway case with variable time step using a maximum Courant number of 0.6. The computational time of the two cases yields 13805 s using MULES and 4008 s using ICMULES.

Figure 9 shows the results of the simulations with bigger time steps. This reveals, that the results from MULES with a bigger time step are not consistent with the results with lower time step. Contrary, the results from ICMULES agree well with the results in Figure 8.

CONCLUSION

In nearly all the test cases the newly introduced algorithm ICMULES gave similar results as the MULES algorithm. Only for certain model combinations, where the packing limit is not ensured through the radial or frictional stress model, the results differ significantly. There, the ICMULES algorithm fails to enforce the packing limit. This might be a limitation of the newly proposed algorithm. On the contrary, the question remains, if the packing limit should be enforced purely by numerical treatment, if the frictional or the radial model does not depict this packing limitation.

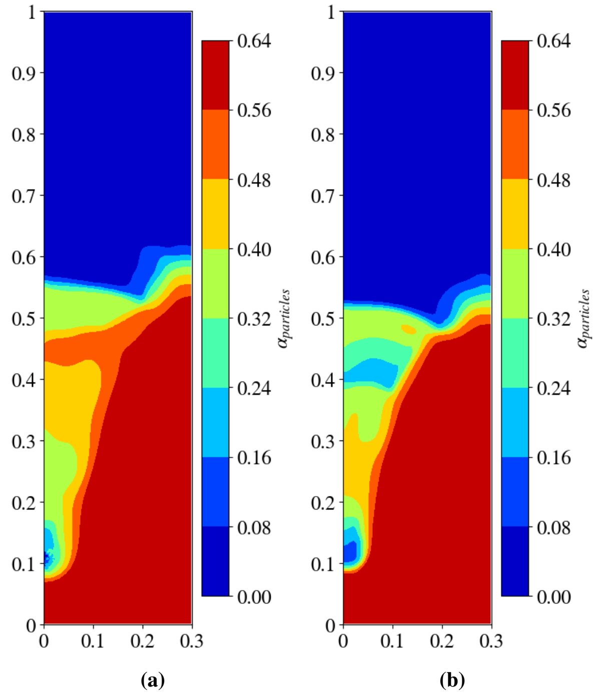

(a) **(b)**

Figure 9: Raceway formation for 30 m/s inlet velocity after 1 s simulation time for the different algorithms using variable time stepping with maxCo = 0.6: (a) MULES (b) ICMULES

First results were presented, showing that the ICMULES enables considerable speed-up, since it produces consistent results also for higher Courant numbers, i.e. time steps.

In conclusion, the introduced algorithm can be used for the simulation of gas-solid systems, also near the packing limit, if suitable frictional and radial models are chosen.

ACKNOWLEDGMENT

The authors gratefully acknowledge the funding support of K1-MET GmbH, metallurgical competence center. The research program of the competence center K1-MET is supported by COMET (Competence Center for Excellent Technologies), the Austrian program for competence centers. COMET is funded by the Federal Ministry for Transport, Innovation and Technology, the Federal Ministry for Digital and Economic Affairs, the province of Upper Austria, Tyrol, and Styria. Apart from funding, the project activities are financed by the industrial partners Primetals Technologies Austria, voestalpine Stahl and voestalpine Stahl Donawitz.

REFERENCES

ABHALE, P.B., VISWANATHAN, N.N. and SAXEN, H. (2020). “Numerical Modelling of blast furnace – Evolution and recent trends”. *Mineral processing and Extractive Metallurgy*, **129(2)**, 166–183.

AGRAWAL, K., LOEZOS, P.N., SYAMLAL, M. and SUNDARESAN, S. (2001). “The role of meso–scale structures in rapid gas–solid flows”. *J. Fluid Mech.*, **445**, 151–185.

CARNAHAN, N.F. and STARLING, K.E. (1969). “Equation of state for nonattracting rigid spheres”. *The Journal of Chemical Physics*, **51(2)**, 635–636.

DING, J. and GIDASPOW, D. (1990). “A bubbling fluidization model using kinetic theory of granular flow”. *AIChE Journal*, **36(4)**, 523–538.

FENG, Y.Q., PINSON, D., YU, A.B. and ZULLI, P. (2003). "Numerical Study of Gas-Solid Flow in the Raceway of a Blast Furnace". *Steel research*, **74(9)**, 523–530.

GIDASPOW, D. (1994). *Multiphase Flow and Fluidization - Continuum and Kinetic Theory Descriptions*. Academic Press, Inc.

JOHNSON, P. and JACKSON, R. (1987). "Frictional-collisional constitutive relations for granular materials, with application to plane shearing". *J. Fluid Mech.*, **179**, 67–93.

JOHNSON, P., NOTT, P. and JACKSON, R. (1990). "Frictional–Collisional Equations of Motion for Granular Materials and Their Application to chutes". *Journal of Fluid Mechanics*, **210**, 501–535.

KUIPERS, J., PRINS, W. and VAN SWAAIJ, W. (1991). "Theoretical and Experimental Bubble Formation at a Single Orifice in a Two-Dimensional Gas-Fluidized Bed". *Chemical Engineering Science*, **46(11)**, 2881–2894.

LUN, C.K. and SAVAGE, S.B. (1986). "The effects of an impact velocity dependent coefficient of restitution on stresses developed by sheared granular materials". *Acta Mechanica*, **63(1-4)**, 15–44.

LUN, C.K., SAVAGE, S.B., JEFFREY, D.J. and CHEPURNIY, N. (1984). "Kinetic theories for granular flow: Inelastic particles in Couette flow and slightly inelastic particles in a general flowfield". *Journal of Fluid Mechanics*, **140**, 223–256.

OLIVEIRA, P.J. and ISSA, R.I. (2003). "Numerical aspects of an algorithm for the Eulerian simulation of two-phase flows". *International Journal for Numerical Methods in Fluids*, **43(10-11)**, 1177–1198.

PAPADIKIS, K., BRIDGWATER, A. and GU, S. (2008). "CFD modelling of the fast pyrolysis of biomass in fluidised bed reactors, Part A: Eulerian computation of momentum transport in bubbling fluidised beds". *Chemical Engineering Science*, **63**, 4218–4227.

PASSALACQUA, A. and FOX, R.O. (2011). "Implementation of an iterative solution procedure for multi- fluid gas–particle flow models on unstructured grids". *Powder Technology*, **213**, 174–187.

RUSCHE, H. (2002). *Computational Fluid Dynamics of Dispersed Two-Phase Flows at High Phase Fractions*. Ph.D. thesis, Imperial College of Science, Technology & Medicine.

SCHAEFFER, D.G. (1987). "Instability in the evolution equations describing incompressible granular flow". *Journal of Differential Equations*, **66(1)**, 19–50.

SCHNEIDERBAUER, S., AIGNER, A. and PIRKER, S. (2012). "A comprehensive frictional-kinetic model for gas-particle flows: Analysis of fluidized and moving bed regimes". *Chemical Engineering Science*, 279–292.

SINCLAIR, J.L. and JACKSON, R. (1989). "Gas particle flow in a vertical pipe with particle particle interactions". *AIChE Journal*, **35(9)**, 1473–1486.

SRIVASTAVA, A. and SUNDARESAN, S. (2003). "Analysis of a frictional-kinetic model for gas-particle flow". *Powder Technology*, **129**, 72–85.

TACCONI, Z. (2018). *Feasibility analysis of a two-fluid solver for cavitation and interface capturing as implemented in OpenFOAM*. Tesi di laurea, Politecnico Di Milano.

VAN DER HOEF, M., VAN SINT ANNALAND, M., DEEN, N. and KUIPERS, J. (2008). "Numerical Simulation of Dense Gas–Solid Fluidized Beds: A Multiscale Modeling Strategy". *Annu. Rev. Fluid Mech.*, **40**, 47–70.

VENIER, C., DAMIAN, S.M., RAMAJO, D. and NIGRO, N. (2013). "Numerical analysis of Multiphase Solid-Gas Flow with Eulerian Models and Kinetic Theory Closure". *Mecánica Computacional*, **XXXII**, 1849–1862.

VENIER, C.M., MARQUEZ, S. and NIGRO, N.M. (2016). "Numerical aspects of Eulerian gas – particles flow formulations". *Computers and Fluids*, **133**, 151–169.

VENIER, C.M., Marquez Damian, S. and NIGRO, N.M. (2018). "Assessment of gas–particle flow models for pseudo-2D fluidized bed applications". *Chemical Engineering Communications*, **205(4)**, 456–478.

WARDLE, K.E. and WELLER, H.G. (2013). "Hybrid Multiphase CFD Solver for Coupled Dispersed/Segregated Flows in Liquid-Liquid Extraction". *International Journal of Chemical Engineering*, 1–13.

WELLER, H. (2005). "Derivation, Modelling and Solution of the Conditionally Averaged Two-Phase Flow Equations". Tech. rep.

14th International Conference on CFD in Oil & Gas, Metallurgical and Process Industries
SINTEF, Trondheim, NORWAY
October 12-14, 2020

SIMULATION OF ENTRAINMENT OF DROPLETS IN NON-RESOLVED WIND-WAVE FLOWS

Son Tung DANG[1 2 *], **Lim Chi HO**[3 †], **Stein Tore JOHANSEN**[2 ‡]
[1]SINTEF Industry, 7034, Trondheim, Norway
[2]NTNU Department of Energy and Process Engineering, 7491 Trondheim, NORWAY
[3]Delft University of Technology, Mekelweg 5, 2628 CD Delft, Netherlands

* E-mail: son.tung.dang@ntnu.no
† E-mail: limchi_ho@hotmail.com
‡ E-mail: stein.t.johansen@sintef.no

ABSTRACT

In this study we focus on a generic method to model the generation of droplets from a non-resolved simulation of free surface flow. The application is entrainment of droplets from the large-scale interface of waves interacting with a wind field. At first, the droplets generation rate will be calculated based on the local shear stress and other interface properties. Then, a special method is applied to detach liquid droplets from the continuous phase such that the total mass and momentum are conserved. Droplets trajectories will be computed using Lagrangian tracking method. Droplets that collide with the large-scale interface will again become continuous water and are removed from the computation. The interaction between droplets and surrounding gas will be accounted by adding a source term in momentum equations. In order to achieve a stable result, the source term will be handled implicitly. The model suggestions are explored and verified through simulations. The prospects of this modelling approach is discussed.

Keywords: Droplets, interface tracking, Shield number .

NOMENCLATURE

Greek Symbols

ρ	Mass density, $[{}^{kg}/_{m^3}]$
ν	Kinematic viscosity, $[{}^{m^2}/_{s}]$
κ	Surface curvature, $[{}^{1}/_{m^2}]$
λ	Wave length, $[m]$
σ	Surface tension constant, $[{}^{J}/_{m^2}]$
τ	Shear stress, $[Pa]$
ϕ	Level set function, $[m]$
α	Volume fraction,

Latin Symbols

p	Pressure, $[Pa]$.
$\mathbf{u}$	Velocity vector, $[{}^{m}/_{s}]$.
$\mathbf{g}$	Gravity vector, $[{}^{m^2}/_{s}]$.
D	Particle diameter, $[m]$.
c	Wave speed, $[{}^{m}/_{s}]$.
k	Wave number.

Sub/superscripts

f	fluid.
g	gas.
w	gas.
p	particle.
D	Drag.

INTRODUCTION

Liquid entrainment is a phenomenon by which parts of the liquid are injected into the gas field in the form of droplets. A good example of this phenomenon is shown when waves clash against marine vessels and off-shore structures. Due to the waves breaking, droplets will be generated and most likely end up on the dock of the vessel. Combine this with cold climates and these droplets will freeze onto the structure, which will cause mass accumulation on the vessel. Mass accumulation may cause big damages and even sink the vessel or structure in a small time period. This happens only in the most extreme cases, but still, a good physical understanding of droplet entrainment can help predict the movement of droplets and optimize designs of these vessels and offshore structures. Several experimental studies (Koga; Mestayer and Lefauconnier) have been performed to study wind-wave interaction and address the source of droplets generation. Numerical methods (Richter and Sullivan, a,b) are applied to study droplet particles transport in the turbulent Couette flow. Druzhinin et al. (Druzhinin *et al.*, 2017) examined the effect of droplets movement to turbulent airflow over the surface wave. The droplets are introduced to the simulation by injecting mechanism based on experimental knowledge. All computations are performed using the Direct Numerical Simulation (DNS) method. Tang et al. (Tang *et al.*) to studied the droplets generation due to the wind-wave interaction. In their work, the DNS method is performed to resolve various droplet scales. The droplet production will be handled by the interface tracking method. Therefore, there is no need for the droplet breakup model. However, DNS requires a lot of computational resources due to small grid sizes. As a result, it is not suitable for fast and large-scale simulation. In this study, we will develop a numerical model to generate a droplet spray from a surface wave in a coarse grid. Therefore, there is no need to use the DNS method.

MODEL DESCRIPTION

Governing equation and numerical implementation

The mass and momentum equation for incompressible flow accounting the interaction with paritcles are written as follows

$$\begin{aligned} &\nabla \mathbf{u} = 0, \\ &\frac{\partial \mathbf{u}}{\partial t} + \nabla(\mathbf{uu}) = -\frac{\nabla p}{\rho}\mathbf{I} + \nu \nabla^2 \mathbf{u} + \mathbf{g} + S_{m,p}. \end{aligned} \tag{1}$$

Where, $S_{m,p}$ is the source term which represents the exchange between discrete particles and continuous phase. In our study, we assume that the particle density is much larger than fluid density. Therefore, the source term can be computed as follows,

$$S_{m,p} = \frac{1}{V_f} \sum_{i=1}^{n_p} -\frac{m_{p,i}}{t_{p,i}} |\mathbf{u}_f - \mathbf{u}_{p,i}| [\mathbf{u}_f - \mathbf{u}_{p,i}], \tag{2}$$

where, n_p is the number of particles and

$$t_p = \frac{4}{3}\frac{\rho_p d_p}{\rho_f C_D}, \tag{3}$$

To conserve mass and the momentum equations, the cut-cell method based on the finite volume method (Dang *et al.*) is used. To prevent problems with pressure-velocity coupling, a staggered grid is introduced in this model. The source term is treated implicitly to ensure the stability for the numerical solution. To make the sharp interface between the two phases, a combination of the Level Set(LS) function and the Volume of Fluid(VOF) method was used to represent the free surface(Dang *et al.*; Wang *et al.*, 2009). The advantage of combining these two methods is that it uses the advantages of both methods. The advantage of VOF type models is that mass conversation can be simulated accurately. The disadvantage of using a VOF type model is that the surface normal vector is estimated less precisely based on the spatial derivatives, however, the level-set method can calculate these normal vectors more accurately. Thus by combining these two methods, both the mass conservation as well as the curvature of the free surface can be simulated accurately. The transport equations for the level set function ϕ and volume of fluid α are given as,

$$\begin{aligned} &\frac{\partial \alpha}{\partial t} + \mathbf{u} \cdot \nabla \alpha = S_\alpha, \\ &\frac{\partial \phi}{\partial t} + \mathbf{u} \cdot \nabla \phi = S_\phi, \end{aligned} \tag{4}$$

where, S_α and S_ϕ are source terms which represent the generation of droplets. The source term for volume fraction can be evaluated as.

$$S_\alpha = -\frac{\alpha_p}{\Delta t_d}, \tag{5}$$

where, α_p is a particle volume fraction which indicates the amount of Eulerian liquid that is converted to Lagrangian particles inside a given control volume, and where Δt_d is then time scale for droplet generation. In this work, we assume that the droplets are generated in an one time step. Firstly, we will solve the Eq. 4 without the source term. After extracting liquid volume fraction to form droplets the level set and liquid volume fraction in the continuous field will be updated accordingly. Equation 4 will be solved numerically without source term based on the interface reconstruction method. The details are given in the work of Griebel and Klitz(Griebel and Klitz). After droplets are produced they are considered as Lagrangian particles. The movement of Lagrangian particles is described as follows (Dehghani *et al.*),

$$\frac{\mathrm{d}\mathbf{x}_p}{\mathrm{d}t} = \mathbf{u}_p, \tag{6}$$

$$\begin{aligned} m_p \frac{\mathrm{d}\mathbf{u}_p}{\mathrm{d}t} =& \rho_p V_p \mathbf{g} - C_D \frac{\pi d_p^2}{8} \rho_f |\mathbf{u}_p - \mathbf{u}_f| (\mathbf{u}_p - \mathbf{u}_f) + \\ & \frac{\rho_f V_p}{2} \frac{\mathrm{d}(\mathbf{u}_f - \mathbf{u}_p)}{\mathrm{d}t} + \rho_f V_p \Big(\frac{\mathrm{d}\mathbf{u}_f}{\mathrm{d}t} - \mathbf{g} \Big). \end{aligned} \tag{7}$$

where, $\mathbf{x}_p(x, y)$ is the location of particle, $\mathbf{u}_p$ is the particle velocity vector. ρ_p is particle density, ρ_f is fluid density. d_p is the particle diameter. V_p is the particle volume. u_f is fluid velocity. C_D is drag coefficient

Model for droplets generation

Primary droplets

The Shields number is normally used to estimate the onset of movement in sedimentation in slurry-like streams. This number is based on the shear stress between particles and made dimensionless with the gravitational force by the following equation

$$Sh = \frac{\tau}{(\rho_p - \rho)\, gD}, \tag{8}$$

where, τ denotes the shear force, ρ_p is the particle density, ρ is the fluid density at the location where the particle is located, g is the gravitational constant, and D is particle diameter. The Shield number is modified for droplet entrainment in the gas field as,

$$Sh = \frac{\tau}{2\pi\sqrt{(\rho_w - \rho_g)\, g\sigma}}, \tag{9}$$

where, ρ_w is the water density, ρ_a is the gas density, and σ is the surface tension. The curved Shields number is computed based on shield number by

$$Sh_{curved} = \kappa \cdot Sh. \tag{10}$$

where, κ is surface curvature which can be computed as

$$\kappa = \nabla \cdot \left(\frac{\nabla \phi}{|\nabla \phi|} \right). \tag{11}$$

When the curved Shield number is larger than the critical Shield number ($Sh_c = 1.7.10^{-3}$) droplets will be generated from a wave. The number of droplets will be determined by

$$n_{droplets} = f(x).n_{droplets,max}, \tag{12}$$

where, $n_{droplets,max}$ is the maximum number of droplets generated at one time step and $f(x)$ is the scaling factor which is evaluated by

$$f(x) = \frac{e^{\left(\frac{Sh_{curve} - Sh_c}{Sh_c}\right)^n} - 1}{e^{\left(\frac{Sh_{curve} - Sh_c}{Sh_c}\right)^n} + 1} \tag{13}$$

The droplet diameter can be determined based on the breakup mechanism presented in the work of Marmottant and Villermaunx (MARMOTTANT and VILLERMAUX, 2004).

RESULT AND DISCUSSION

Wave equation

The initial wave geometry is given by the analytical solution of the third-order Stokes wave as

$$\eta(x) = a_0 \cos\left[k(x-ct)\right] + \frac{1}{2} a_0 \epsilon_0 \cos\left[2k(x-ct)\right] + \frac{3}{8} a_0 \epsilon_0^2 \cos\left[3k(x-ct)\right], \tag{14}$$

where, η is the wave surface height, a_0 is the wave amplitude, $k = 2\pi/\lambda$ is the wave number, $\epsilon_0 = ka_0$ is the initial wave steepness, and $c = \omega/k$ is the wave phase speed. In our study, ω is evaluated by,

$$\omega = \sqrt{gk(1+\epsilon^2)}. \tag{15}$$

The values of parameters are given in table 1. The water velocities corresponding to the wave are defined by

$$\begin{aligned} u &= a_0 \omega \frac{\cosh(ky)}{\sinh(ky_{water})} \cos\left[k(x-ct)\right] \ \text{ for } y \leq y_{water} \\ v &= a_0 \omega \frac{\sinh(ky)}{\sinh(ky_{water})} \sin\left[k(x-ct)\right] \ \text{ for } y \leq y_{water}, \end{aligned} \tag{16}$$

where, y is the water height regarding to the bottom of the computational domain.

Table 1: Computational parameters for the wave equation

λ	c	T	ϵ_0
5	3.19	1.57	0.55

Wind equation

In strong wind conditions, the wind can be described by the logarithmic law (Holmes) as

$$u_a = \frac{u_*}{\kappa}\left[ln\left(\frac{y-d}{y_0}\right)\right] \ \text{ for } y > y_{water} \tag{17}$$

where, u_* = 0.27m/s is the friction velocity, $\kappa \sim 0.41$ is the Von Karman constant, $d = 0$ is the zero plane displacement, and $y_0 = 0.0002$ is the surface roughness (Holmes). The wave interface is depicted in figure 1. The blue and the red interfaces are the air and water phases respectively. Due to blowing wind, the wave tip becomes unstable over time. As result, the interface breaks at the t=0.6015 in figure 2e and t=0.722 in figure 2f. Since this study is only interested in droplet generation at the surface, only grid points at the liquid interface will be given a value for the Shields number. This way, the structure of the wave was visible as well as the values of the Shields number. To prove that the theory of using the Shields number to create droplets would work, the highest values of the Shields number should be at the top of the wave. This is due to the fact that spume droplets are being generated at the wave crest in real scenarios if the velocity difference between the two phases is big enough. Figure 2 shows the highest values of curved Shield number are being created at the wave crest which fits with our assumption. Since the highest values were found at the wave crest, it was fairly easy to determine the critical Shields number ($Sh_c = 0.0017$).The value where the Shields number was higher at the wave crest and lower everywhere else in the domain would be equal to the critical Shields number. As depicted in figure 3, the grid points that exceed the critical Shields number (depicted in white) are indeed at the location of the wave crest. In figure 4, particles are generated at the wave interface. From figures 3 and 4, it can be seen that at the grid points where the local Shields number surpasses the critical Shields number, particles are being generated.

CONCLUSIONS

Numerical simulations were carried out by using an in-house CLS-VOF model (Simcoflow) to describe droplet entrainment in breaking-wave scenarios. The wave in this study follows the analytical of the third-order Stokes wave. The shear force will play a significant role when the velocity difference between the air- and water stream is sufficient enough. This causes the wave to deform and liquid sheets will be developed. These liquid sheets will split up in smaller liquid fragments that are called ligaments. If the shear force is big enough, small globes of liquid will be sheared off the ligament top and droplets are being generated. The criterion for primary droplet entrainment was based on the curved Shields number. Currently, the critical Shields number is a constant value, however, with new insights, this could or maybe should be altered. A good starting point could be to develop a function that is affected by different variables, such as the turbulent properties (fluctuating velocities at local disturbances), wave properties (wavelength, wave height, or amplitude), the velocity at the wave tip, or what is used now in the model, implementing a curvature in the Shields number. When particles are being generated, the liquid fractions that are sheared off will turn into Lagrangian particles, where it will use the two-way coupling model until the particles are out of the computational domain or back in the liquid stream.

ACKNOWLEDGEMENT

We would like to thank the Norwegian Research Council for funding our works through researcher program SprayIce (project 244386) and ICELOAD (308780)

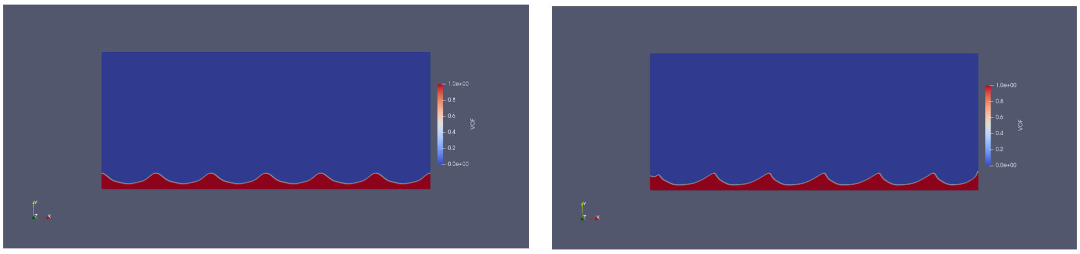

(a) t=0 **(b)** t=0.155

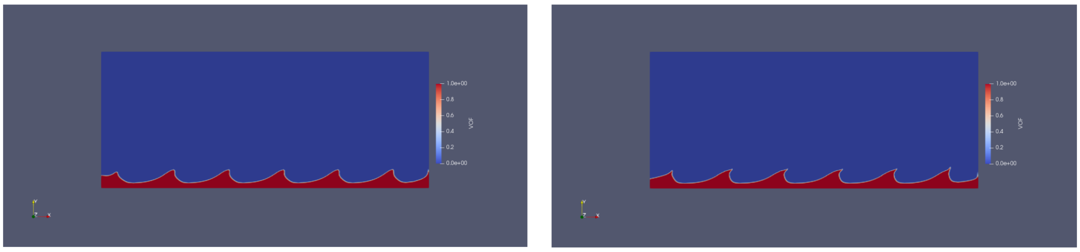

(c) t=0.3109 **(d)** t=0.4667

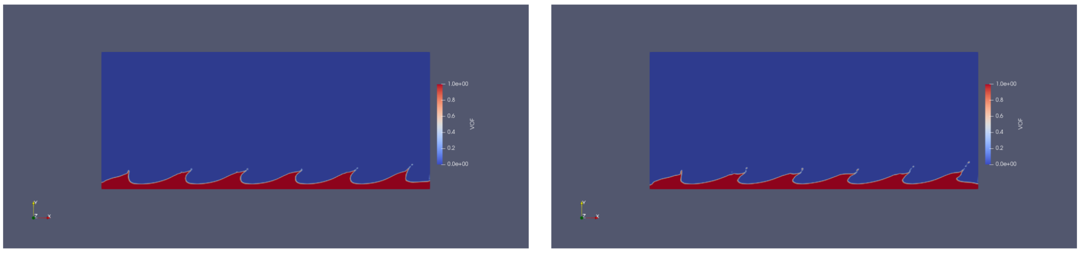

(e) t=0.6015 **(f)** t=0.722

Figure 1: Wave interface at different time steps

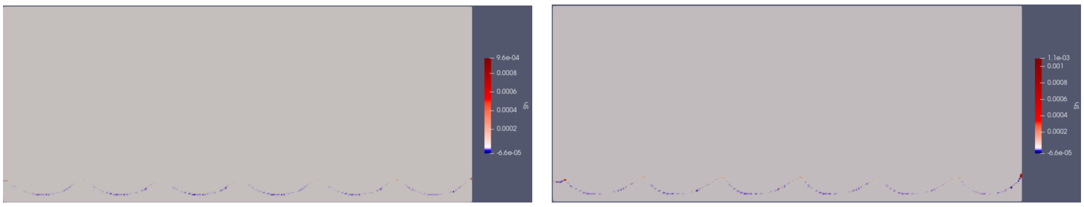

(a) t=0 **(b)** t=0.155

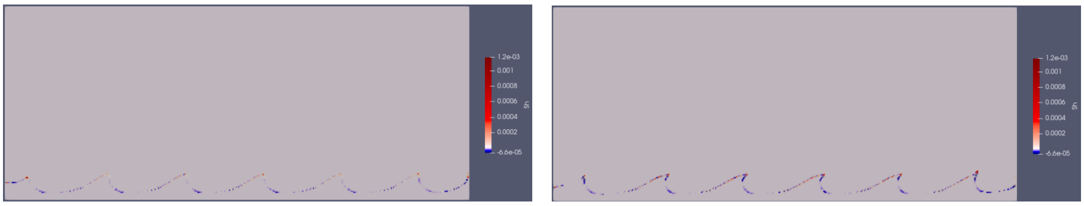

(c) t=0.3109 **(d)** t=0.4667

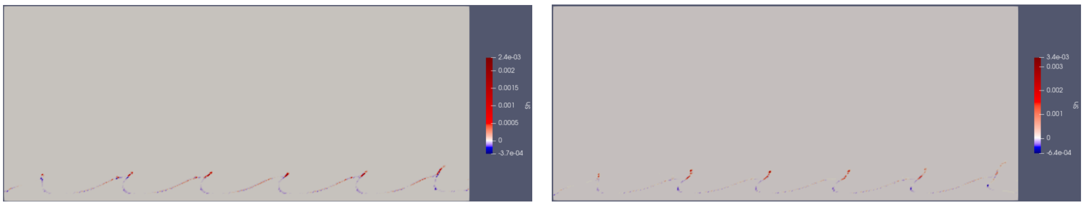

(e) t=0.6015 **(f)** t=0.722

Figure 2: The values of the curved Shields number

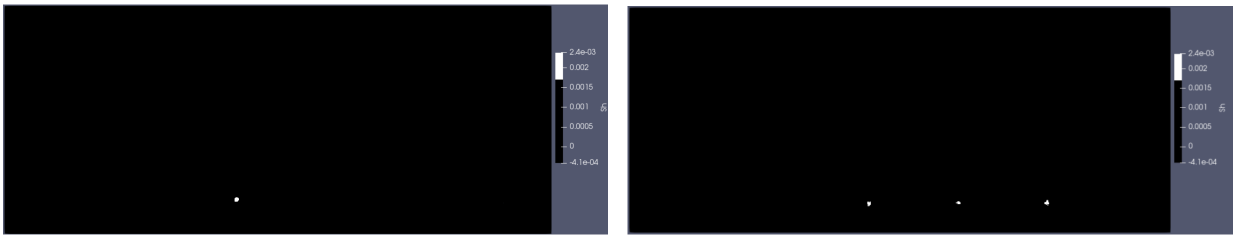

(a) t=0.4667 **(b)** t=0.6015

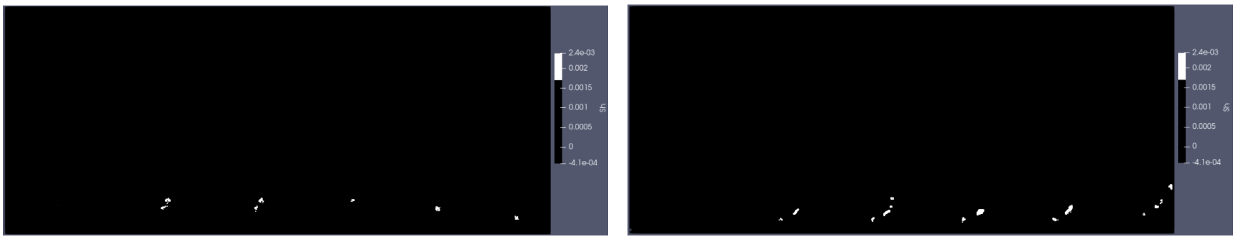

(c) t=0.722 **(d)** t=0.835

Figure 3: The values that are above the critical Shields number

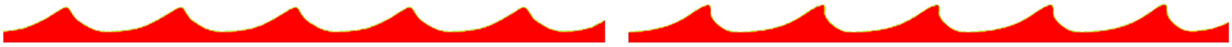

(a) t=0 **(b)** t=0.155

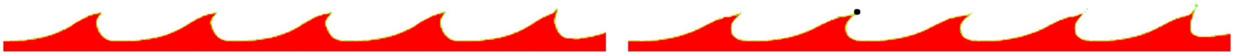

(c) t=0.3109 **(d)** t=0.4667

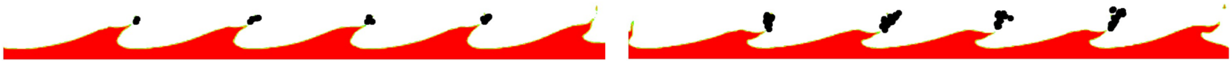

(e) t=0.6015 **(f)** t=0.722

Figure 4: Particle generation at different time steps

REFERENCES

DANG, S.T., MEESE, E.A., MORUD, J.C. and JOHANSEN, S.T. (). “Numerical approach for generic three-phase flow based on cut-cell and ghost fluid methods”. **91(9)**, 419–447.

DEHGHANI, S.R., MUZYCHKA, Y.S. and NATERER, G.F. (). “Droplet trajectories of wave-impact sea spray on a marine vessel”. **127**, 1–9.

DRUZHININ, O., TROITSKAYA, Y. and ZILITINKEVICH, S. (2017). “The study of droplet-laden turbulent airflow over waved water surface by direct numerical simulation”. *Journal of Geophysical Research : Oceans*, **122(3)**, 1789–1807.

GRIEBEL, M. and KLITZ, M. (). “CLSVOF as a fast and mass-conserving extension of the level-set method for the simulation of two-phase flow problems”. **71(1)**, 1–36.

HOLMES, J.D. (). *Wind Loading of Structures*. CRC Press.

KOGA, M. (). “Direct production of droplets from breaking wind-waves -its observation by a multi-colored overlapping exposure photographing technique”. **33(6)**, 552–563.

MARMOTTANT, P. and VILLERMAUX, E. (2004). “On spray formation”. *Journal of Fluid Mechanics*, **498**, 73â€“111.

MESTAYER, P. and LEFAUCONNIER, C. (). “Spray droplet generation, transport, and evaporation in a wind wave tunnel during the humidity exchange over the sea experiments in the simulation tunnel”. **93(C1)**, 572–586.

RICHTER, D.H. and SULLIVAN, P.P. (a). “Momentum transfer in a turbulent, particle-laden Couette flow”. **25(5)**, 053304.

RICHTER, D.H. and SULLIVAN, P.P. (b). “Sea surface drag and the role of spray”. **40(3)**, 656–660.

TANG, S., YANG, Z., LIU, C., DONG, Y.H. and SHEN, L. (). “Numerical Study on the Generation and Transport of Spume Droplets in Wind over Breaking Waves”. **8(12)**, 248.

WANG, Z., YANG, J., KOO, B. and STERN, F. (2009). “A coupled level set and volume-of-fluid method for sharp interface simulation of plunging breaking waves”. *International Journal of Multiphase Flow*, **35(3)**, 227–246.

Numerical simulation of bubble transport and splitting dynamics for varying bifurcation angle

Mahesh S. Nagargoje[1]*, **Raghvendra Gupta**[1‡]
[1] IIT Guwahati, 781039 Guwahati, India

* E-mail: nmahesh@iitg.ac.in
‡ E-mail: guptar@iitg.ac.in

ABSTRACT

Gas embolotherapy is a recent potential cancer treatment. The technique is based on starving the tumors by cutting off the blood supply using perfluorocarbon (PFC) bubbles. The volatile PFC droplets are injected in the circulatory system, and in the region of the tumor, these droplets are made to vaporize using high-intensity ultrasound pulses. As the bubbles are expected to encounter bifurcation during its flow in the vessels, it is imperative to develop an understanding of bubble splitting at the bifurcations to avoid nonhomogeneous splitting, undesirable bioeffects. Splitting dynamics has been studied for symmetric bifurcation angle.

In this work, we investigate the splitting dynamics of a gas bubble at the symmetric, two-dimensional (2D) bifurcation. The volume of fluid method, which employs a single fluid formalism to solve for two-phase flow by considering an additional advection equation for a color function to identify the phases, is used to model the flow. The pressure jump caused by surface tension is modeled by approximating the surface tension force as a body force in the vicinity of the interface. Initially, the entire domain is filled with the liquid phase, i.e., blood. As the flow Reynolds number is 10-100, blood is considered to be a Newtonian fluid. Once a steady solution for liquid-only flow is obtained, a bubble is introduced in the channel having a capsular shape. The bubble takes a steady shape after a few ms.

The results show that at the higher capillary number (Ca = 0.0231), homogenous splitting occurs for all bifurcation angles. Similarly, at lower capillary number (Ca = 0.00231) and low bifurcation angle ($\alpha = \beta = 15°$, $30°$, and $45°$), bubble split homogenously. In contrast, at a higher bifurcation angle ($\alpha = \beta = 60°$) bubble does not split and is pushed in the daughter vessel. The critical bifurcation angle exists between $\alpha = \beta = 45°$-$60°$, where capillary forces become dominant and the bubble does not split.

Keywords: CFD, multiphase flow, gas embolotherapy.

NOMENCLATURE

Greek Symbols

ρ Mass density, [kg/m^3].
μ Dynamic viscosity, [kg/m.s].
σ Surface tension force, [N/m]
$\boldsymbol{\tau}$ Shear stress tensor, [N/m^2]

Latin Symbols

p Pressure, [Pa].
$\mathbf{u}$ Velocity, [m/s].
κ Curvature, [m^{-1}]

INTRODUCTION

Gas embolotherapy is a potential cancer treatment, in which intra-arterial blood supply to cancer tumor is cut off using gas bubbles (Bull, 2007). In this treatment, the perfluorocarbon (PFC) microdroplets (~6 μm in diameter) are passed through the arteries and selectively vaporized at the desired tumor location using high-intensity ultrasound (Kripfgans, O. D., Fowlkes, J. B., Miller, D. L., Eldevik, O. P., & Carson, 2000; Kripfgans et al., 2005; Qamar et al., 2010). Due to ultrasound, these droplets get vaporized, and the bubble formation (~150 times volume expansion) takes place to occlude the blood flow covering an entire cross-section of the blood vessel (Kang, S. T., Huang, Y. L., & Yeh, 2014; Kang et al., 2014; Kripfgans et al., 2004). For effective treatment, a large number of these bubbles should pass through tumor affected vessels. The generated bubbles travel into smaller capillaries and eventually occlude the capillaries with a sausage-shaped configuration (Samuel, S., Duprey, A., Fabiilli, M. L., Bull, J. L., & Brian Fowlkes, 2012). The capillaries are more likely to damage because of its fragile structure, thin vessel wall, and lower blood velocity. Due to acoustic droplet vaporization (ADV) occurred in the capillaries, the expansion of droplets takes place with a higher wall velocity in the order of hundreds of meters per second (Kripfgans et al., 2004; Qamar et al., 2010; Wong et al., 2011). The bubble dynamics in capillaries lead to undesired bioeffects, such as endothelial damage and rupture of the capillaries (Bull, 2005; Wong and Bull, 2011). This work of Embolotherapy has started with experiments of bubble transport in bifurcation models to predict the bubble lodging and occlusion of vessels (Calderón et al., 2006, 2005; Eshpuniyani et al., 2005).

In the past decade, the number of researchers has been explained the various parameters in the gas embolotherapy process. Recently, it has been adopted for the model of hepatocellular carcinoma in mice, which proved that tumor growth had been halted using a gas embolotherapy technique (Harmon et al., 2019). The multiphase flow at bifurcation and control of ADV remains an active topic of research for experimental (Fabiilli et al., 2009; Lo et al., 2007; Wong et al., 2011) and numerical work (Poornima and Vengadesan, 2012; Qamar et al., 2017; Ye and Bull, 2006, 2004), which analyzes the splitting behavior and lodging of bubbles in the capillaries. The present study focuses on bubble behavior at bifurcation after vaporization and before lodging in smaller vessels. For a successful treatment, at least 78% of blood supply to the tumor needs to be occluded (Di Segni, R., Young, A. T., Qian, Z., & Castaneda-Zuniga, 1997). Various factors, such as blood flow rate, gravity, bubble size, and vessel geometry, affect the splitting behavior of the bubble at the bifurcation. Different regimes and splitting behavior were observed at bifurcations. Faster flow rates and weaker gravitational effects result in even splitting in daughter vessels, whereas at lower flow rates, the splitting is uneven, depends on roll angle/gravity, the angle made by horizontal plane with mother vessel axis (Eshpuniyani et al., 2005). Numerical simulations observed homogenous, non-homogenous splitting, and no splitting. For constant inlet droplet size, droplet splits at the higher capillary number, and no splitting observed at the lower capillary number (Carlson et al., 2010). Similar behavior was observed for bubble splitting. With the decrease in capillary number, non-homogenous splitting behavior increases, and at below critical value of a capillary number, the bubble does not split (Calderón et al., 2005). At higher Reynolds number (low capillary numbers) bubble does not split, while at low Reynolds number (higher capillary numbers) bubble splits at bifurcation into two daughter tubes (Qamar et al., 2017). For symmetric bifurcations, the splitting ratio is one, while asymmetric bifurcation ratios show a splitting ratio of less than one (Poornima and Vengadesan, 2012). Boundary element computations of bubble splitting found that bubble splitting ratio increases with increasing bubble driving pressure while it decreases with increasing bifurcation angle (Calderon et al., 2010).

Most of the studies available in the literature were focused on the splitting of the bubble in a fixed bifurcation angle. At the same time, human vascular arterial networks do not have a symmetric angle everywhere. Our previous work studied the flow behavior of single-phase flow in various bifurcation angle combinations (Nagargoje and Gupta, 2020). Successful treatment needs to understand the bubble splitting behavior in the bifurcation to occlude the tumorous vessel. This work addresses this gap by investigating the steady blood flow and PFC bubble in two-dimensional, symmetric bifurcating networks using commercial computational fluid dynamics (CFD) package ANSYS Fluent 19.2 for symmetric bifurcation angles varying in the range 30^{O}-120^{O}. A recent study shows that the splitting ratio does not change for pulsating and constant flows (Valassis et al., 2012). So we have considered the inlet flow to be steady for all simulations.

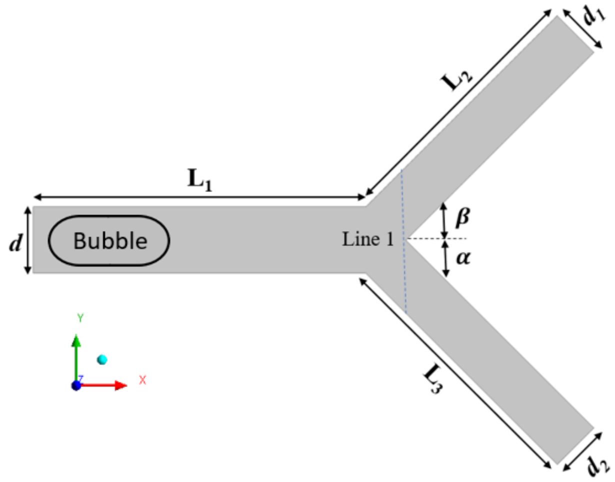

Fig. 1 Schematic of the bifurcation geometry where: $d = 1$ mm; d_1, $d_2 = 0.78$ mm; L_1, L_2, $L_3 = 5d$; α, β are angle made by daughter vessels in-plane with mother vessel.

METHODOLOGY

A two dimensional arterial model with mother vessel (d) and two daughter vessels (d_1 and d_2), as shown in Fig. 1, is used for modeling the bubble splitting in the present study. The diameter of the mother vessel is 1mm, and that of daughter vessels is 0.78 mm each. The values of the bifurcation angles (α, β) are varied symmetrically $(\alpha = \beta)$ from 30^{O}-120^{O}. Blood (Newtonian) is modeled as a primary phase (liquid) with a viscosity of 0.0035 Pa. s and a density of 1060 kg/m^3. The secondary phase (gas) is a perfluorocarbon (PFC) gas with a viscosity of 2×10^{-5} Pa. s and a density of 12 kg/m^3 (Poornima and Vengadesan, 2012).

Numerical modeling

The transport of the PFC bubble through a blood-filled arterial bifurcation model is a multiphase (gas-liquid) problem. Blood is modeled as a Newtonian fluid. We have used a commercial CFD code finite volume based ANSYS Fluent 19.2 and inbuilt continuum surface force (CSF) based volume of fluid (VOF) method to track the gas-liquid interface, in which a single set of momentum equations is solved. VOF approach is used widely due to its high accuracy, flexibility, and excellent stability.

The governing equations of the VOF formulation are as follows:

Equation of Continuity

$$\nabla . \boldsymbol{u} = 0 \tag{1}$$

Equation of momentum conservation:

$$\rho\left(\frac{\partial \boldsymbol{u}}{\partial t} + (\boldsymbol{u}.\nabla)\boldsymbol{u}\right) = -\nabla P + \nabla . \boldsymbol{\tau} + \boldsymbol{F} \tag{2}$$

$$\boldsymbol{\tau} = \mu(\nabla \boldsymbol{u} + \nabla \boldsymbol{u}^T) \tag{3}$$

Volume fraction equation:

$$\frac{\partial \alpha_G}{\partial t} + \boldsymbol{u}.\nabla \alpha_G = 0, \tag{4}$$

At the interfacial cells, the mixture density, and viscosity have been evaluated as the average values of the two phases weighted by their volume fraction,

$$\rho = \alpha_L \rho_L + \alpha_G \rho_G \tag{5}$$

$$\mu = \alpha_L \mu_L + \alpha_G \mu_G \tag{6}$$

The body force term "F" on RHS of equation of eq. (2) includes the surface tension force (σ), which has been modeled by the continuum surface force (CSF) proposed by Brackbill et al.(Brackbill et al., 1992) and it can be written as follow,

$$\boldsymbol{F} = \sigma\kappa\boldsymbol{n} \tag{7}$$

Where κ is the curvature and can be written by following equation:

$$\kappa = \nabla.\hat{\boldsymbol{n}} \tag{8}$$

Where, η is the normal vector given by

$$\boldsymbol{n} = \boldsymbol{\nabla}\alpha \tag{9}$$

And unit normal vector(n) is given by

$$\hat{\boldsymbol{n}} = \frac{\boldsymbol{n}}{|\boldsymbol{n}|} \tag{10}$$

The arterial model is meshed using ANSYS meshing. After the mesh independence study, the model is imported to ANSYS Fluent for further simulations. Blood is considered as the primary phase (liquid) and PFC bubble (gas) as the secondary phase in VOF formulation. The bubble is patched initially 1 mm away from the inlet having length 1.5 times mother vessel diameter. The different Reynolds number, based on mother tube diameter, is used as 10, 100. Surface tension between the PFC bubble and blood is taken as 0.05 N/m. For the unsteady-state simulations, a fully developed parabolic velocity profile with constant velocity is used at the inlet. At the outlet pressure, the outlet boundary condition is imposed with gauge pressure equal to zero. The PISO scheme is used for the pressure velocity coupling. The body force weighted scheme is used for pressure interpolation, and the quadratic upwind interpolation for convection kinetics (QUICK) scheme is used to discretize the terms in the momentum equations. For interpolating the interface between fluids, the modified HRIC scheme is used to get a sharp interface. The first-order implicit time marching scheme with non-iterative time advancement is used for discretization of the unsteady term. The simulations are advanced with a time increment of 1×10^{-7} s.

RESULTS

Figure 2 shows the pressure distribution and bubble shape variation at various time instances during the splitting process. Initially, the pressure at the inner wall of bifurcation is high while low near to the outer wall. The pressure value in the mother tube suddenly increases as the bubble reaches the bifurcation. The bubble occupies entire cross-section of vessel and creates obstruction to fluid flow through the small film thickness around the bubble after reaching at bifurcation.

The effect of the symmetric bifurcation angle on the dynamics of the bubble neck during the final stage of the breaking of the bubble is shown in Fig. 3. Throughout the rupture process, the shape of the bubble head does not change due to the presence of a gap between the bubble and channel wall. However, the bubble neck width changes continuously and is highly deformed. It can be seen as time passes, the neck width gradually decreases to zero at the bifurcation, and then the bubble is pinched-off. The bubble neck is flat for lower bifurcation angle i. e. $\alpha = \beta = 15°$, but as the bifurcation angle increases, the neck of the bubble becomes more concave. For a higher bifurcation angle, there is more possibility of retaining small satellites of the PFC bubble due to the presence of a thin tail between the neck of the bubble and the wall of bifurcation. These small satellites may contribute to unexpected bio-effects such as endothelial suffocation or acoustic cavitation. These satellites may affect the splitting behavior of the next train of bubbles.

Figure 4, and 5 shows the splitting behavior of the PFC bubble at the bifurcation point for $\alpha = \beta = 15°$, and 45° at Re = 10, respectively. Initially, the bubble is close to the wall, separated by a thin film (δ) using Bretherton's correlation(Bretherton, 1961). The shape of the bubble starts to change at bifurcation due to resistance to flow around the bubble, and the concave shape of the bubble takes place at trailing end. After the bubble neck reaches a bifurcation, the thin film stretches, and the bubble splits into two equal-size daughter bubbles in a homogenous way, as shown in Fig. 4, and 5 (t_3). The x-component of velocity at the bifurcation point is parabolic along line 1 at time instance t_1 and t_3, as shown in Fig. 4, 5(a). The maximum velocity is skewed towards the inner wall of bifurcation. The volume of the fluid method was used, which shown the velocities of gas and liquid depending on its position. During the pinch-off stage of bubble break up (t_2), the velocity profiles along line 1 are symmetric along both sides of daughter vessel, and the deviations of velocity are very small from steady-state (t_1 and t_3). Due to symmetry in the velocity profile during pinch-off, the bubble splits in a homogenous fashion. The symmetry in the velocity profile is observed for the y-velocity component as well, as shown in Fig. 4, 5(b). Once the bubble passed into the daughter vessels, flow regains the steady-state at line 1, as shown in Fig. 4, 5(a, b) (t_1 and t_3).

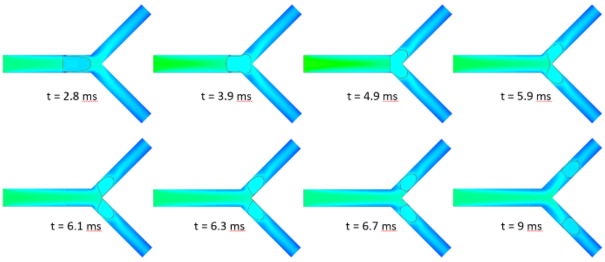

Fig. 2 Pressure contours and bubble shape at various time instance for $\alpha = \beta = 45°$ (Re = 100 and Ca = 0.0231).

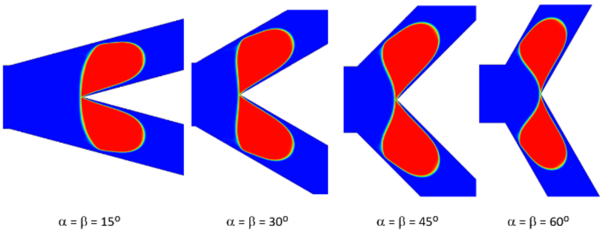

Fig. 3 Splitting behavior of PFC bubble at the bifurcation point for varying symmetric bifurcation angle at Ca = 0.0231.

For the larger bifurcation angle ($\alpha = \beta = 60°$), the bubble does not split and goes into the lower daughter vessel, as shown in Fig. 6 (t_3). The bubble enters the bifurcation in the usual manner as explained earlier, but the portion in the lower channel remains close to the vessel wall, while the portion in the upper channel separates and swings downward. This phenomenon of bubble behavior is called no splitting behavior. At lower Capillary number, the surface tension dominates over the inertial force, and the bubble reverses back into the lower vessel and completely pass through it. A similar kind of reversal splitting was observed for liquid droplets (Calderon et al., 2010; Carlson et al., 2010). Due to stronger capillary force, a larger curvature is observed at the bubble neck, resulting in a larger radius of the gas-liquid interface. As the perturbation grows, the bubble migrates into the lower daughter vessel. The stronger recirculation's observed in the upper daughter vessel, which increases the pressure difference between the upper and lower daughter vessel. The velocity profiles at the bifurcation point along line 1 reveal much about the reversal splitting. The bubble remains stable before reaching to the bifurcation. Once it reaches the bifurcation, the x-component of velocity shows a very high speed and high-velocity gradient between two daughter vessels at the pinch-off stage, as shown in Fig. 6(a). The same phenomena are observed for the y-velocity component and can be seen in Fig. 6(b). From the discussion of bubble splitting in symmetric bifurcation, it was observed that the homogenous splitting of the bubble is observed for higher Reynolds numbers at all bifurcation angles. Whereas no splitting is observed at low Reynolds number (Re = 10) and high bifurcation angle ($\alpha = \beta = 60°$). For higher bifurcation angle ($\alpha = \beta = 60°$) and small Reynolds number (Re = 10), we found the bubble does not split and passes into the lower daughter vessel.

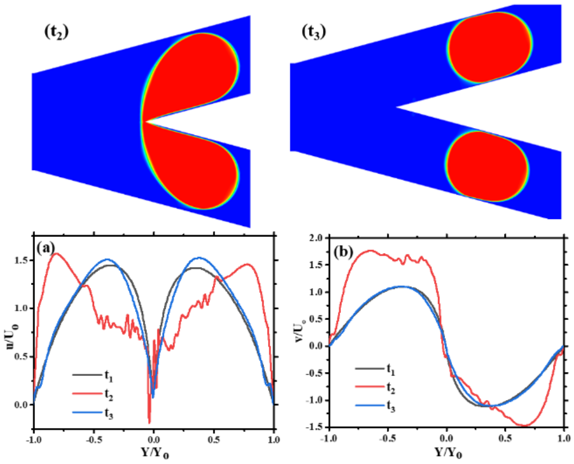

Fig. 4 Splitting behavior of PFC bubble at the bifurcation point for $\alpha = \beta = 15°$ (Re = 10 and Ca = 0.00231)) at different time instance, top: bubble volume fraction (Red colour), bottom: (a) x-velocity and (b) y-velocity profiles along line 1.

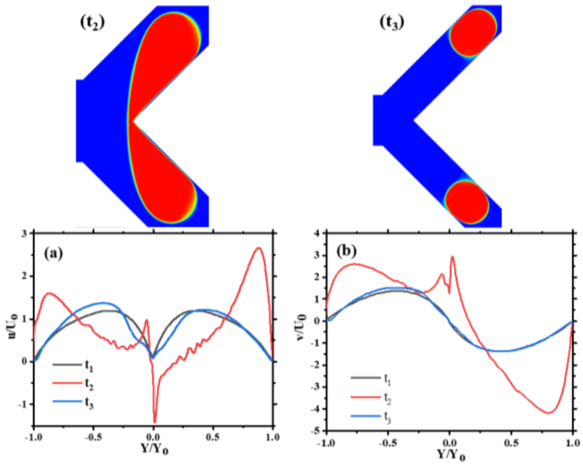

Fig. 5 Splitting behavior of PFC bubble at the bifurcation point for $\alpha = \beta = 45°$ (Re = 10 and Ca = 0.00231 at different time instance, top: bubble volume fraction (Red colour), bottom: (a) x-velocity and (b) y-velocity profiles along line 1.

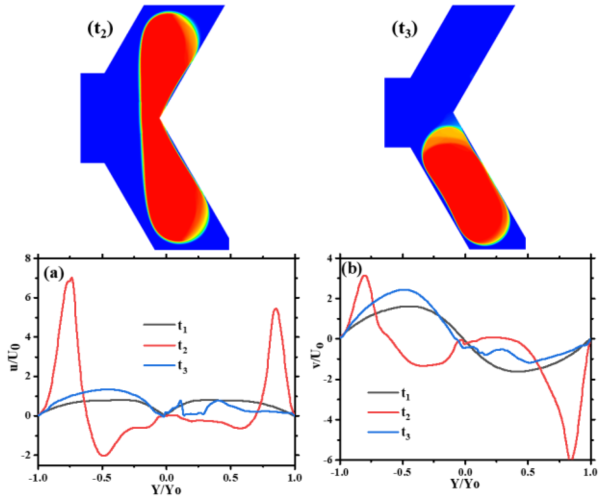

Fig. 6 Splitting behavior of PFC bubble at the bifurcation point for $\alpha = \beta = 60°$ (Re = 10 and Ca = 0.00231 at different time instance, top: bubble volume fraction (Red colour), bottom: (a) x-velocity and (b) y-velocity profiles along line 1.

STUDY LIMITATIONS

The present study's major limitation is the assumption of blood as a Newtonian fluid and two-dimensional arterial geometry. The blood should be modeled as a non-Newtonian fluid in the capillaries. The bubble shape may vary in three-dimensional vessel geometry due to the presence of secondary flow. Future studies should include the influence of asymmetry in bifurcation angle, multiple droplet splitting effect, and bubble splitting in three-dimensional bifurcating vessels for non-Newtonian blood flow.

CONCLUSIONS

The present paper reports on two-dimensional numerical simulations of droplet dynamics in a bifurcating channel for varying bifurcation angles symmetrically. The splitting and non-splitting flow regimes have been observed. We showed the effect of the capillary number on the bifurcation angle.

The PFC bubble split homogenously at a higher value of the capillary number (Ca = 0.0231), where viscous force dominates over the surface tension force, and the bubble splits equally. Similarly, in the lower bifurcation angle ($\alpha = \beta < 60$) and at the lower capillary number (Ca = 0.00231) observed a splitting behavior. But, for a higher bifurcation angle ($\alpha = \beta = 60$), and lower capillary number (Ca = 0.00231) bubble does not split and goes into a lower daughter vessel. In non-splitting behavior, surface tension force dominates over viscous force.

REFERENCES

ANSYS Academic Research Fluent, Release 19.2, Help System, Theory Guide, ANSYS, Inc., 2019.

Brackbill, J.U., Kothe, D.B., Zemach, C., 1992. A continuum method for modeling surface tension. J. Comput. Phys. 100, 335–354.

Bretherton, F.P., 1961. The motion of long bubbles in tubes. J. Fluid Mech. 10, 166–188.

Bull, J.L., 2007. The application of microbubbles for targeted drug delivery. Expert Opin. Drug Deliv. 4, 475–493.

Bull, J.L., 2005. Cardiovascular bubble dynamics. Crit. Rev. Biomed. Eng. 33, 299–346.

Calderon, A.J., Eshpuniyani, B., Fowlkes, J.B., Bull, J.L., 2010. A boundary element model of the transport of a semi-infinite bubble through a microvessel bifurcation. Phys. Fluids 22, 1–11.

Calderón, A.J., Fowlkes, J.B., Bull, J.L., 2005. Bubble splitting in bifurcating tubes: A model study of cardiovascular gas emboli transport. J. Appl. Physiol. 99, 479–487.

Calderón, A.J., Heo, Y.S., Huh, D., Futai, N., Takayama, S., Fowlkes, J.B., Bull, J.L., 2006. Microfluidic model of bubble lodging in microvessel bifurcations. Appl. Phys. Lett. 89, 2004–2007.

Carlson, A., Do-Quang, M., Amberg, G., 2010. Droplet dynamics in a bifurcating channel. Int. J. Multiph. Flow 36, 397–405.

Di Segni, R., Young, A. T., Qian, Z., & Castaneda-Zuniga, W.R., 1997. Embolotherapy: agents, equipment, and techniques. Interv. Radiol. 3.

Eshpuniyani, B., Fowlkes, J.B., Bull, J.L., 2005. A bench top experimental model of bubble transport in multiple arteriole bifurcations. Int. J. Heat Fluid Flow 26, 865–872.

Fabiilli, M.L., Haworth, K.J., Fakhri, N.H., Kripfgans, O.D., Carson, P.L., Fowlkes, J.B., 2009. The role of inertial cavitation in acoustic droplet vaporization. IEEE Trans. Ultrason. Ferroelectr. Freq. Control 56, 1006–1017.

Harmon, J.S., Kabinejadian, F., Seda, R., Fabiilli, M.L., Kuruvilla, S., Kuo, C.C., Greve, J.M., Fowlkes, J.B., Bull, J.L., 2019. Minimally invasive gas embolization using acoustic droplet vaporization in a rodent model of hepatocellular carcinoma. Sci. Rep. 9, 1–11.

Kang, S. T., Huang, Y. L., & Yeh, C.K., 2014. Characterization of acoustic droplet vaporization for control of bubble generation under flow conditions.

Kang, S.T., Lin, Y.C., Yeh, C.K., 2014. Mechanical bioeffects of acoustic droplet vaporization in vessel-mimicking phantoms. Ultrason. Sonochem. 21, 1866–1874.

Kripfgans, O. D., Fowlkes, J. B., Miller, D. L., Eldevik, O. P., & Carson, P.L., 2000. Acoustic droplet vaporization for therapeutic and diagnostic applications. Ultrasound Med. Biol. 26, 1177–1189.

Kripfgans, O.D., Fabiilli, M.L., Carson, P.L., Fowlkes, J.B., 2004. On the acoustic vaporization of micrometer-sized droplets. J. Acoust. Soc. Am. 116, 272–281.

Kripfgans, O.D., Orifici, C.M., Carson, P.L., Ives, K.A., Eldevik, O.P., Fowlkes, J.B., 2005. Acoustic droplet vaporization for temporal and spatial control of tissue occlusion: A kidney study. IEEE Trans. Ultrason. Ferroelectr. Freq. Control 52, 1101–1108.

Lo, A.H., Kripfgans, O.D., Carson, P.L., Rothman, E.D., Fowlkes, J.B., 2007. Acoustic droplet vaporization threshold: Effects of pulse duration and contrast agent. IEEE Trans. Ultrason. Ferroelectr. Freq. Control 54, 933–945.

Nagargoje, M., Gupta, R., 2020. Effect of asymmetry on the flow behavior in an idealized arterial bifurcation. Comput. Methods Biomech. Biomed. Engin. 23, 232–247.

Poornima, J., Vengadesan, S., 2012. Numerical simulation of bubble transport in a bifurcating microchannel: A preliminary study. J. Biomech. Eng. 134, 1–10.

Qamar, A., Warnez, M., Valassis, D.T., Guetzko, M.E., Bull, J.L., 2017. Small-bubble transport and splitting dynamics in a symmetric bifurcation. Comput. Methods Biomech. Biomed. Engin. 20, 1182–1194.

Qamar, A., Wong, Z.Z., Fowlkes, J.B., Bull, J.L., 2010. Dynamics of acoustic droplet vaporization in gas embolotherapy. Appl. Phys. Lett. 96, 1–4. https://doi.org/10.1063/1.3376763

Samuel, S., Duprey, A., Fabiilli, M. L., Bull, J. L., & Brian Fowlkes, J., 2012. In vivo microscopy of targeted vessel occlusion employing acoustic droplet vaporization. Microcirculation 19, 501–509.

Valassis, D.T., Dodde, R.E., Esphuniyani, B., Fowlkes, J.B., Bull, J.L., 2012. Microbubble transport through a bifurcating vessel network with pulsatile flow. Biomed. Microdevices 14, 131–143.

Wong, Z.Z., Bull, J.L., 2011. Vascular bubbles and droplets for drug delivery. J. Drug Deliv. Sci. Technol. 21, 355–367.

Wong, Z.Z., Kripfgans, O.D., Qamar, A., Fowlkes, J.B., Bull, J.L., 2011. Bubble evolution in acoustic droplet vaporization at physiological temperature via ultra-high speed imaging. Soft Matter 7, 4009–4016.

Ye, T., Bull, J.L., 2006. Microbubble expansion in a flexible tube. J. Biomech. Eng. 128, 554–563.

Ye, T., Bull, J.L., 2004. Direct numerical simulations of micro-bubble expansion in gas embolotherapy. J. Biomech. Eng. 126, 745–759.

14th International Conference on CFD in Oil & Gas, Metallurgical and Process Industries
SINTEF, Trondheim, NORWAY
October 12-14, 2020

VOLUME-OF-FLUID SIMULATION OF GAS DISSOLUTION IN LIQUID: RISING BUBBLES AND CO_2 TRAPPING

Alexandros PATSOUKIS-DIMOU[1], **Julien MAES**[1]*
[1]Institute of GeoEnergy Engineering, Heriot-Watt University, Edinburgh EH14 4AS, UK

* E-mail: j.maes@hw.ac.uk

ABSTRACT

Multiphase multispecies transport is an essential field of study for a wide range of applications including bubble reactors and CO_2 storage in the subsurface. Modelling of these processes is challenging due to the discontinuity of material properties, making accurate modelling of mass transfer at reactive interface difficult. Maes and Soulaine (2020) have recently developed a numerical model based on a single-field formulation for Volume-Of-Fluid simulation of interfacial mass transfer with local volume changes. This model was validated by comparison with a semi-analytical solution for the dissolution of a rising bubble of gas in liquid in the creeping (or spherical) flow regime. However, this model is only first-order accurate, and will therefore depend strongly on the discretization scheme used. In this work, we consider two different numerical schemes for the discretization of species interfacial fluxes. Convergence and accuracy are compared for dissolution of a rising bubble of gas in liquid at various regimes (spherical, ellipsoidal shape and dimpled ellipsoidal shaped). The model is then applied to simulate the dissolution of trapped bubble of CO_2 in a cavity.

Keywords: Interface, mass transfer, Volume-Of-Fluid, rising bubbles, CO_2 .

NOMENCLATURE

Greek Symbols

α	phase volume fraction $[-]$
κ	interface curvature $[m^{-1}]$
μ	viscosity $[Pa.s]$
Φ	flux $[{}^{kg}/{}_{m^2 s}]$
ρ	Mass density, $[{}^{kg}/{}_{m^3}]$
σ	interfacial tension $[{}^{N}/{}_{m}]$
τ	viscous stress $[{}^{kg}/{}_{m.s^2}]$

Latin Symbols

A	area $[m^2]$
c	concentration $[{}^{kg}/{}_{m^3}]$
D	molecular diffusivity $[{}^{m^2}/{}_{s}]$
F	advective flux $[{}^{kg}/{}_{m^2.s}]$
f	interior force $[{}^{N}/{}_{m^3}]$
g	gravity accelaration $[{}^{m^2}/{}_{s}]$
H	Henry constant $[-]$
J	molecular diffusion flux $[{}^{k}/{}_{m^2.s}]$
L	reference length $[m]$
p	pressure $[Pa]$
t	time $[s]$
u	velocity $[{}^{m}/{}_{s}]$
U	reference velocity $[{}^{m}/{}_{s}]$

Sub/superscripts

Σ	fluid/fluid interface
g	gas phase.
l	liquid phase.

INTRODUCTION

Interface species transfers are present in a wide range of applications such as bubble column reactors and geological storage of CO_2 in aquifers. Experimental investigations can provide insights into the physics of these processes (Francois *et al.*, 2011; Roman *et al.*, 2016, 2019). However, it is often difficult to investigate a wide range of physical conditions experimentally, due to time and safety constraints. In addition, quantities (e.g. concentration, pH, interfacial flux) are difficult to measure during the course of the experiment. Computational Fluid Dynamics can be an essential tool to complement experiments and perform sensitivity analysis with physical parameters (Deising *et al.*, 2018; Maes and Geiger, 2018; Soulaine *et al.*, 2018).

Numerical simulation of two-phase flow can be performed using the algebraic Volume-Of-Fluid method (Ubbink and Issa, 1999) for which the interface between the two fluids is captured using an indicator function, which is a phase volume fraction. This indicator function is transported by numerically solving an advection equation.

Interface transfer can be modelled within the VOF method by using the single-field approach, developed by (Haroun *et al.*, 2010) and at the base of the Continuous Species Transfer (CST) method, later developed by (Marschall *et al.*, 2012). In the single-field approach, a mixture quantity, obtained by volume averaging of species concentration, is transported by solving an algebraic equation (Haroun *et al.*, 2010; Deising *et al.*, 2016).

The method has recently been extended to include local volume change in order to simulate gas dissolution in liquid, and has been applied to simulate the dissolution of a rising gas bubble in liquid (Maes and Soulaine, 2020). However, this model is only first-order accurate, and will therefore depend strongly on the discretization scheme used. In this work, we consider two different numerical schemes for the discretization of species interfacial fluxes, which require an interpolation of the concentration in each phase from the center of computational cells to the center of cell faces. In the Gauss linear scheme, the concentration in each phase is obtained by linear interpolation. In the phase upwinding scheme, the concentrations are calculated using upwinding based on the normal of the interface, so that each concentration is calculated in its own phase. Convergence and accuracy are compared for dissolution of a rising bubble of gas in liquid at various regimes (spherical, ellipsoidal shape and dimpled ellipsoidal shaped). The model is then applied to simulate the dissolution of a trapped bubble of CO_2 in a cavity.

MODEL DESCRIPTION

The model is described in detail in Maes and Soulaine (2020) and is summarized here.

The Volume-Of-Fluid Method

In the Volume-Of-Fluid method, the location of the interface is given by the indicator function α, which is equal to the volume fraction of one phase (here the liquid phase) in each grid cell. The density ρ and viscosity μ of the fluid are given by volume-averaging

$$\rho = \rho_l \alpha + \rho_g \left(1-\alpha\right), \tag{1}$$

$$\mu = \mu_l \alpha + \mu_g \left(1-\alpha\right), \tag{2}$$

where the subscripts l and g refer to the liquid and gas phase, respectively. The indicator function obeys

$$\frac{\partial \alpha}{\partial t} + \nabla \cdot \left(\alpha \mathbf{u}\right) + \nabla \cdot \left(\alpha \left(1-\alpha\right) \mathbf{u}_r\right) = \frac{\dot{m}}{\rho_l}, \tag{3}$$

where $\dot{m}$ is the phase mass transfer rate and where $\mathbf{u}_r = \mathbf{u}_l - \mathbf{u}_g$ is the relative velocity, often assumed equal to zero. However, in order to reduce the smearing of the interface due to numerical diffusion, it is often replaced by a compressive velocity $\mathbf{u}_{comp}$, normal to the interface and with an amplitude based on the maximum of the single-field velocity (Rusche, 2002)

$$\mathbf{u}_r \equiv \mathbf{u}_{comp} = \overline{\mathbf{n}}_\Sigma \left[\min\left(c_\alpha \frac{|\phi_f|}{A_f}, \max_f\left(\frac{|\phi_f|}{A_f}\right)\right)\right], \tag{4}$$

where c_α is the compression constant (generally between 0 and 4) and ϕ_f is the volumetric flux across f. In all our simulations, we choose $c_\alpha = 1.0$.

The two fluids are assumed to be Newtonian and incompressible. Under isothermal condition and assuming constant interfacial tension, the single-field volume-averaged velocity field $\mathbf{u}$ and pressure p satisfies the single-field Navier-Stokes equations (Fleckenstein and Bothe, 2015)

$$\nabla \cdot \mathbf{u} = \dot{m}\left(\frac{1}{\rho_l} - \frac{1}{\rho_g}\right). \tag{5}$$

$$\frac{\partial \rho \mathbf{u}}{\partial t} + \nabla \cdot \left(\rho \mathbf{u}\mathbf{u}\right) = -\nabla p + \nabla \cdot \boldsymbol{\tau} + \rho \mathbf{g} + \mathbf{f}_\Sigma, \tag{6}$$

where $\mathbf{g}$ is the gravity vector, $\boldsymbol{\tau}$ is the viscous stress tensor and $\mathbf{f}_\sigma$ is the surface tension force. The viscous stress tensor can be expresses as

$$\boldsymbol{\tau} = \mu\left(\nabla \mathbf{u} + \nabla \mathbf{u}^T\right). \tag{7}$$

The Reynolds number is defined as the ratio of inertial to viscous forces

$$R_e = \frac{\rho_l L U}{\mu_l}, \tag{8}$$

where L and U are the reference length and velocity in the domain, and ρ and μ are the density and viscosity of the invading phase. The Reynolds number is used to characterise different flow regimes, such as laminar flow, where viscous forces are dominant, and turbulent flow, where inertial forces are dominant. The surface tension force can be modelled using the Continuum Surface Force (CSF) formulation introduced by Brackbill *et al.* (1992)

$$\mathbf{f}_\Sigma = \sigma \kappa \nabla \alpha. \tag{9}$$

where σ is the interfacial tension between the two fluids and κ the mean interface curvature, which can be computed as

$$\kappa = -\nabla \cdot \mathbf{n}_\Sigma, \tag{10}$$

where $\mathbf{n}_\Sigma$ is the interface normal vector, defined as

$$\mathbf{n}_\Sigma = \frac{\nabla \alpha}{||\nabla \alpha||}. \tag{11}$$

The relative importance of viscous forces, gravity and surface tension force is characterised using the Eötvös Eo and Morton Mo numbers,

$$\mathrm{Eo} = \frac{\Delta \rho g L^2}{\sigma}, \tag{12}$$

$$\mathrm{Mo} = \frac{g \mu_l^4 \Delta \rho}{\rho_l^2 \sigma^3}. \tag{13}$$

In case gravity has no impact, the relative importance of viscous and surface tension forces is characterised using the capillar number Ca

$$\mathrm{Ca} = \frac{\mu_l U}{\sigma}. \tag{14}$$

The Continuous Species Transfer Method

In this work, the gas phase is always assumed pure. In addition, we assume that the gas component dissolves in the liquid phase with Henry's constant H and remains diluted. In this case, the single-field concentration in the domain satisfies an advection-diffusion equation given by the Continuous Species Transfer (CST) formulation (Haroun *et al.*, 2010; Marschall *et al.*, 2012; Deising *et al.*, 2016)

$$\frac{\partial c}{\partial t} + \nabla . \mathbf{F} + \nabla . \mathbf{J} = 0, \tag{15}$$

where $\mathbf{F}$ is the advective flux and $\mathbf{J}$ is the diffusive flux. In order to maintain consistency between advection operators, the advective flux of the species is also modelled with a compressive velocity, using the normal Compressive CST (C-CST) formulation (Maes and Soulaine, 2020)

$$\mathbf{F} = c\mathbf{u} + \alpha\left(1-\alpha\right)\frac{\nabla c \cdot \nabla \alpha}{||\nabla \alpha||^2}\mathbf{u}_{comp}. \tag{16}$$

For the diffusive flux, Maes and Soulaine (2020) showed that it can be written as

$$\mathbf{J} = -D^{SF}\nabla c + \mathbf{\Phi}, \tag{17}$$

where

$$\mathbf{\Phi} = (1-H)D^{SF}\frac{c}{\alpha + H\left(1-\alpha\right)}\nabla \alpha. \tag{18}$$

and D^{SF} is the single-field diffusion coefficient. The debate regarding the best formulation for the single-field diffusion coefficient was initiated in the original work of Haroun *et al.* (2010) and pursued in Marschall *et al.* (2012) and Deising *et al.* (2016). Indeed, Haroun *et al.* (2010) first proposed an arithmetic mean for the diffusion coefficient

$$D^{SF} \equiv D^{a} = \alpha D_l + (1-\alpha)\, D_g . \tag{19}$$

However, Deising *et al.* (2016) performed a rigorous derivation of the single-field formulation with an arithmetic coefficient and show that additional terms arise, resulting from the discontinuity and curvature effect at the interface. They also show that Equ. (17) is correct if using a harmonic mean for the diffusion coefficient

$$D^{SF} \equiv D^{h} = \frac{1}{\frac{\alpha}{D_l} + \frac{1-\alpha}{D_g}}, \tag{20}$$

provided the additional assumption that the concentration in the gas bubble remains approximatively constant. However, this formulation can not be applied when $D_g = 0$, for example when the gas phase is pure. Instead, Maes and Soulaine (2020) shows that Equ. (17) is equivalent to the rigorous single-field formulation based on the arithmetic mean derived by Deising *et al.* (2016) if using the equilibrium-based mean diffusion

$$D^{SF} \equiv D^{e} = \frac{\alpha D_l + H\,(1-\alpha)\, D_g}{\alpha + H\,(1-\alpha)}. \tag{21}$$

The equilibrium-based mean diffusion has two advantages compared to the harmonic mean. First, it does not require the additional assumption that the concentration in the gas bubble remains approximatively constant, and second, it can be applied when $D_g = 0$.

Finally, the phase mass transfer rate at the interface where $0 < \alpha < 1$ can be calculated as (Maes and Soulaine, 2020)

$$\dot{m} = -\frac{D^{e}\nabla c - \boldsymbol{\Phi}}{1-\alpha} \cdot \nabla\alpha. \tag{22}$$

Numerical implementation

The numerical method has been implemented in GeoChemFoam (https://julienmaes.com/geochemfoam), our OpenFOAM®-based (OpenCFD, 2016) reactive transport solver. The full solution procedure is presented in Maes and Soulaine (2020). The standard VOF solver of OpenFOAM®, so-called *interFoam*, has been extended for this purpose into another solver called *interTransferFoam*. *interFoam* solves the system formed by Eq. (5), (3) and (6) on a collocated Eulerian grid. A pressure equation is obtained by combining the continuity (Eq. (5)) and momentum (Eq. (6)) equations. The system is then solved with a predictor-corrector strategy based on the Pressure Implicit Splitting Operator (PISO) algorithm (Issa *et al.*, 1985). Three iterations of the PISO loop are used to stabilise the system. An explicit formulation is used to treat the coupling between the phase distribution equation (Eq. (3)) and the pressure equation. This imposes a limit on the time-step size by introducing a capillary wave time scale described by the Brackbill conditions (Brackbill *et al.*, 1992).

In *interTransferFoam*, the concentration equation (Eq. (15)) is solved sequentially before the phase conservation. The interfacial mass transfer (Eq. (22)) is then computed and re-injected in the continuity (Eq. (5)) and phase equations (Eq. (3)). The space discretization of the convection terms is performed using the second-order *vanLeer* scheme (van Leer, 1974). For the compression terms, the interpolation of $\alpha_d \alpha_c$ is performed using the *interfaceCompression* scheme (OpenCFD, 2016). The diffusion term $\nabla.\left(D^{e}\nabla c\right)$ is discretized using the Gauss linear limited corrected scheme, which is second order and conservative. For the discretization of the CST flux, two different schemes are considered, the Gauss Linear (GL) scheme

$$\Phi_{GL} = D^{e}_{f}(1-H)\frac{c_f}{\alpha_f + H\,(1-\alpha_f)}\nabla\cdot\alpha \tag{23}$$

where D^{e}_{f},c_f and α_f are the molecular diffusion, species concentration and phase volume fraction at face center obtained by linear interpolation, respectively and the Gauss Phase Upwinding scheme (GPU)

$$\Phi_{GPU} = \Phi_U - \Phi_D \tag{24}$$

where

$$\Phi_{Up} = D^{e}_{f}\frac{c_{Up}}{\alpha_{Up} + H\,(1-\alpha_{Up})}\cdot\nabla\alpha, \tag{25}$$

and

$$\Phi_{Dw} = H D^{e}_{f}\frac{c_{Dw}}{\alpha_{Dw} + H\,(1-\alpha_{Dw})}\cdot\nabla\alpha, \tag{26}$$

and c_{Up}, α_{Up}, c_{Dw} and α_{Dw} are the species concentration and phase volume fraction from the upstream and downstream cell in the direction of $\nabla\cdot\alpha$.

For the computation of the mass transfer $\dot{m}$, we define

$$\boldsymbol{\Phi}_D = \frac{D^{e}_{f}\nabla c - \boldsymbol{\Phi}}{1-\alpha} \tag{27}$$

and then we use

$$\boldsymbol{\Phi}_D \cdot \nabla\alpha = \nabla\cdot\left(\boldsymbol{\Phi}_D \alpha_{Dw}\right) - \alpha\nabla\cdot\boldsymbol{\Phi}_D. \tag{28}$$

This is only first-order accurate (Maes and Soulaine, 2020), but all second-order discretization schemes available in OpenFOAM® have shown strong instabilities. Due to this, the numerical results will be strongly impacted by the discretization scheme used for $\boldsymbol{\Phi}$. In this work, we will compare results obtained with the Gauss Linear and the Gauss Phase Upwinding schemes. The linear scheme is available in OpenFOAM® and the phase upwinding scheme has been implemented in GeoChemFoam (https://julienmaes.com/geochemfoam).

RESULTS

Rising bubbles

The objective of this section is to compare convergence and accuracy of the numerical model when using the linear or the phase upwinding schemes. For this we consider the dissolution of a rising single-component gas bubble immersed in liquid for three different regimes. The fluid roperties are summarized in Table 1.

For test case 1, a bubble with initial radius $R = 2$ mm is immersed in liquid 1 (Table 1) in a computational domain of dimension 1.2 cm × 2.4 cm × 1.2 cm. Symmetry conditions are applied to the plane x=0 and z=0, so only a quarter of the bubble is simulated. The other boundary conditions are free-flow. The flow properties correspond to an Eötvös number Eo=3.25 and a Morton number Mo=1.63. For these values, Clift's diagram describing the shape regime (Clift *et al.*, 1978) predicts a spherical shape. Initially, the centre of the bubble is placed at (0 mm, 3 mm, 0 mm). In order to compare

	Density (kg/m^3)	Dynamic viscosity (Pa.s)	Diffusivity (m^2/s)	Interfacial tension (liquid-gas) (mN/m)	Henry's constant (no unit)
Gas	1.2	1.8×10^{-5}	0		
Liquid 1	1245	0.46	1.48×10^{-6}	60	5
Liquid 2	1200	0.024	2×10^{-5}	65	5
Liquid 3	1200	0.46	3.83×10^{-4}	65	20

Table 1: Fluid properties for mass transfer for rising of single-component gas bubble

with the semi-analytical solution proposed by Fleckenstein and Bothe (2015), mass transfer from a rising bubble with no volume change and while forcing the species concentration in the bubble, and therefore the density, to remain constant is simulated until the barycentre of the bubble reaches (0 cm, 1.2 cm, 0 cm). The simulations are then restarted with local volume change taken into account.

For test case 2, the bubble size and computational domain remain the same, but the fluid properties are modified (Table 1) so that Eo=3 and Mo=10^{-5}. For these values, Clift's diagram (Clift *et al.*, 1978) predicts an ellispoidal shape. The bubble is initially at capillary equilibrium in the absence of gravity and interface mass transfer, with centre placed at (0 cm, 0.3 cm, 0 cm).

For test case 3, the domain considered and the gas bubble are five time larger (R=10 mm), and the bubble is immersed in liquid 3 (Table 1). The Eötvös and Morton numbers are 70 and 1.3, respectively. For these values, Clift's diagram (Clift *et al.*, 1978) predicts a dimpled ellipsoidal-cap shape. The bubble is initially at capillary equilibrium in the absence of gravity and interface mass transfer, with centre placed at (0 cm, 1.5 cm, 0 cm).

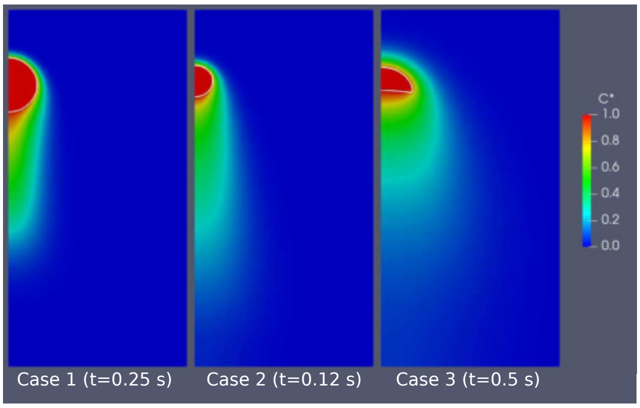

Figure 1: Numerical simulation of the dissolution of a rising bubble in liquid in the spherical regime (case 1), the ellipsoidal regime (case 2) and the dimpled ellipsoidal-cap regime (case 3). The colour represents the dimensionless solute component concentration and the white line the gas/liquid interface.

For each case, we perform eight simulations with four different mesh resolutions (75×150×75, 90×180×90, 120×240×120 and 150×300×150) and using the linear and the phase upwinding scheme. In Fig. 1, the color shows the dimensionless concentration of gas component in the domain, defined as

$$c^{*} = \frac{c}{\rho_g} \frac{H}{\alpha + H\,(1-\alpha)}. \tag{29}$$

at the end of the simulation, while the white line represents the gas bubble contour. In each case the bubble shape corresponds to the one predicted in Clift's diagram (Clift *et al.*, 1978).

Fig. 2, 3 and 4 show the evolution of the bubble mass for each simulation. For the spherical case (Fig. 2), the simulations are also compared with the semi-analytical solution (Fleckenstein and Bothe, 2015). We observe that the phase upwinding method always predicts more dissolution than the linear method. For the spherical bubble, both methods are first-order accurate, but the phase upwinding method seems

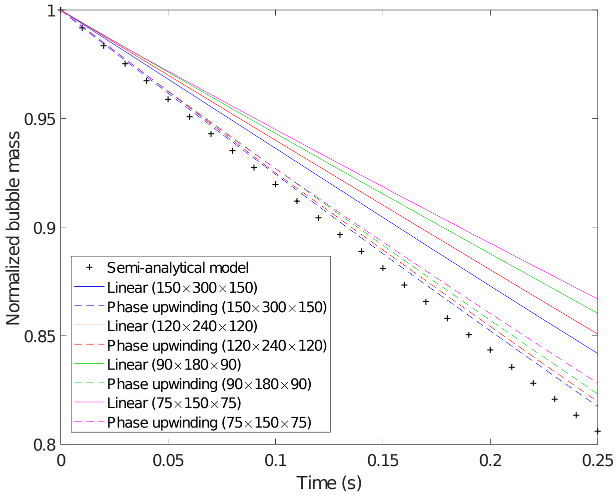

Figure 2: Evolution of bubble size obtained by semi-analytical solution and numerical simulations with various grid sizes and numerical schemes for test case 1 (spherical regime).

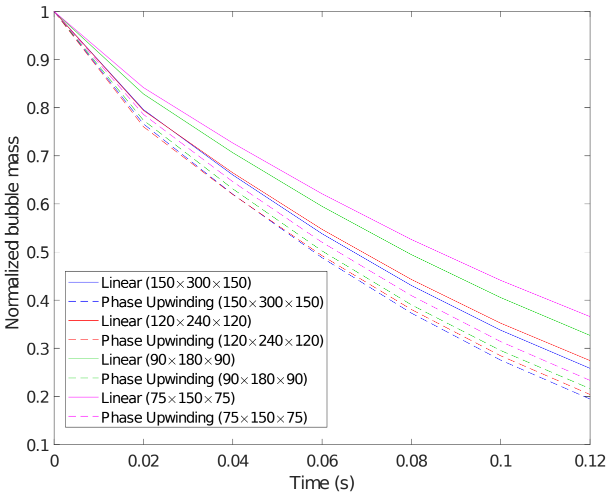

Figure 3: Evolution of bubble size obtained by numerical simulations with various grid sizes and numerical schemes for test case 2 (ellipsoidal regime).

to be further in its convergence toward the semi-analytical solution. This suggests that the phae upwinding method is more accurate for all cases, so we will only use this method in the next example.

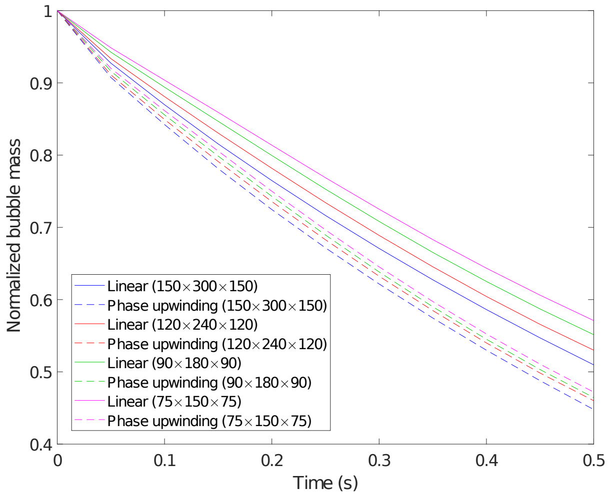

Figure 4: Evolution of bubble size obtained by umerical simulations with various grid sizes and numerical schemes for test case 3 (dimpled ellispoidal-cap regime)

CO_2 trapping

During Carbon Capture and Storage (CCS), clusters of CO_2 may remain trapped in the asperities of the solid surface after the pores are invaded by the water phase (Roman *et al.*, 2016). In this case, molecular diffusion, interface transfer, capillary forces and viscous dissipation all play a role in controlling the time-scale at which the CO_2 bubbles will dissolve in the water phase (Maes and Geiger, 2018; Roman *et al.*, 2019), a process known as solubility trapping.

In this part, we use our simulation framework to investigate mass transfer and dissolution in a pocket of residual CO_2 trapped in a cavity after water injection. The goemetry is a 6mm×1mm×1mm channel, with a 2mm×2mm×1mm cavity inserted in the middle (Fig. 5). Initially, CO_2 gas is trapped in the cavity and the rest is filled with water. The fluid properties are summarized in Table 2. At t=0, we inject water from the left boundary at two different speeds, 0.1 mL/min and 0.01 mL/min. These flow rates correspond to Peclet numbers Pe=104 and Pe=10.4, respectively.

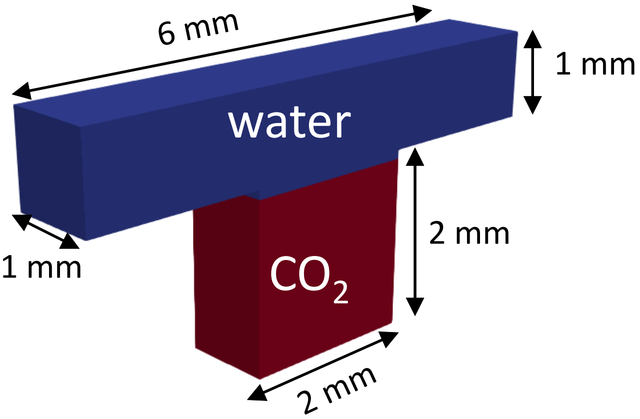

Figure 5: Schematic diagram of the cavity geometry and initial conditions

Fig. 6 shows a screenshot from the middle plan z=0 at different time for the two injection flow rates. The colour represents the single-field concentration of CO_2 and the white line the gas/liquid interface. We observe that at Pe=104, the transport of CO_2 in the water is mostly controlled by the advection, and the concentration of CO_2 follows a streamline around the bottom of the channel. However, for Pe=10.4, diffusion plays a more important role and the concentration of CO_2 is relatively large at any point dowmstream of the cavity.

Fig. 7 shows the evolution of the mass of the CO_2 bubble during the simulation for each Peclet number. For Pe=104, the slope of the curve does not change much and the dissolution remains close to linear. This is characteristic of an advection-dominated process, where the CO_2 in the water phase is flushed out of the domain rapidly and so does not impact the dissolution significantly. However, for Pe=10.4, we observe a transition between advection-dominated and diffusion-dominated regime, as the CO_2 accumulated at the interface by dissolution is not transported sufficiently fast and slow down the process. We conclude that CFD simulation using the VOF-CST metod can be applied to bring insights into the process of CO_2 solubility trapping during CCS in subsurface reservoir.

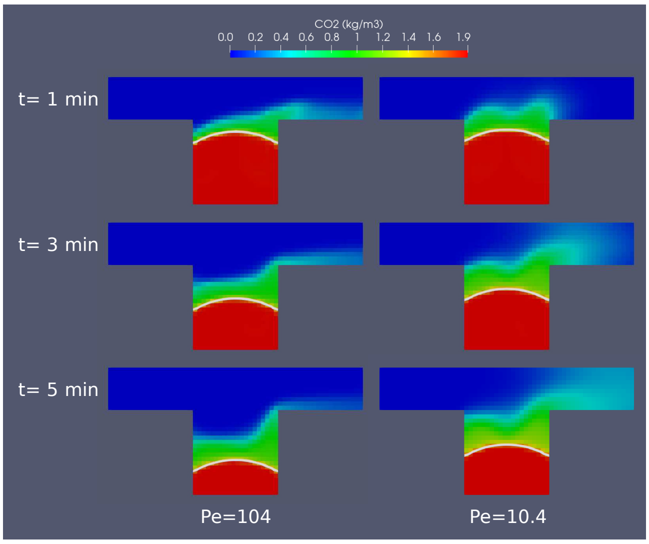

Figure 6: Numerical simulation of CO_2 dissolution in a cavity at two different Peclet numbers. The colour represents the single-field concentration of CO_2 and the white line the gas/liquid interface.

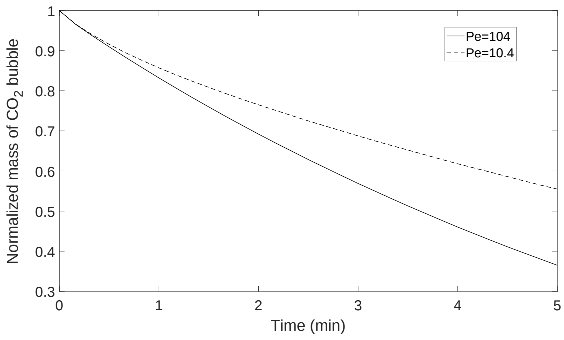

Figure 7: Evolution of the mass of a CO_2 bubble trapped in a cavity at two different Peclet number, obtained by numerical simulation.

	Density (kg/m^3)	Dynamic viscosity (Pa.s)	Diffusivity (m^2/s)	Interfacial tension (liquid-gas) (mN/m)	Henry's constant (no unit)
Gas	1.87	0.8×10^{-5}	0		
Liquid 1	1000	10^{-6}	1.6×10^{-9}	50	1.25

Table 2: Fluid properties for CO_2 dissolution in a cavity

CONCLUSION

In this paper, we used the VOF-CST method to numerically investigate the dissolution of a rising bubble in water at various regimes and the dissolution of a CO_2 bubble trapped in a cavity during injection of water in the subsurface. We compared results obtained with two different numerical discretizations of the interfacial fluxes for dissolution of a rising bubble in the spherical, ellipsoidal and dimpled ellipsoidal-cap regimes, and we concluded that the phase upwinding scheme was more accurate. We then emploied our simulation framework to investigate mass transfer and dissolution in a pocket of residual CO_2 trapped in a cavity after water injection at different flow rates and a transition from advection-dominated regime to diffusion-dominated regime was observed.

We conclude that our simulation framework can be used to investigate multiphase multicomponent reactive transport processes, and bring new insights into engineering application such as bubble reactors and CCS. In future work, we will employ the method to investigate the sensitivity of the process with respect to cavity sizes, shapes and number, as well as investigating the occurence of salt precipitation, a process known as mineral trapping.

REFERENCES

BRACKBILL, J.U., KOTHE, D.B. and ZEMACH, C. (1992). "A continuum method for modeling surface tension". *J. Comput. Phys.*, **100(2)**, 335–354.

CLIFT, R., GRACE, J.R. and WEBER, M.E. (1978). *Bubbles, drops, and particles*. New York; London: Academic Press.

DEISING, D., MARSCHALL, H. and BOTHE, D. (2016). "A unified single-field model framework for Volume-Of-Fluid simulations of interfacial species transfer applied to bubbly flow". *Chem. Eng. Sci.*, **139**, 173–195.

DEISING, D., BOTHE, D. and MARSCHALL, H. (2018). "Direct numerical simulation of mass transfer in bubbly flows". *Computer and Fluids*, **172**, 524–537.

FLECKENSTEIN, S. and BOTHE, D. (2015). "A volume-of-fluid-based numerical method for multi-component mass transfer with local volume changes". *J. Comput. Phys.*, **301**, 35–58.

FRANCOIS, J., DIETRICH, N., GUIRAUD, P. and COCKX, A. (2011). "Direct measurement of mass transfer around a single bubble by micro-plifi". *Chemical Engineering Science*, **66**, 3328–3338.

HAROUN, Y., LEGENDRE, D. and RAYNAL, L. (2010). "Volume of fluid method for interfacial reactive mass transfer: Application to stable liquid film". *Chem. Eng. Sci.*, **65(10)**, 2896–2909.

ISSA, R., AHMADI-BEFRUI, B., BESHAY, K. and GOSMAN, A. (1985). "Solution of the implicitly discretised reacting flow equations by operator-splitting". *J. Comput. Phys.*, **93(2)**, 388–410.

MAES, J. and GEIGER, S. (2018). "Direct pore scale reactive transport modelling of dynamic wettability changes induced by surface complexation in carbonate rocks". *Adv. iWater Resour.*, **111**, 6–19.

MAES, J. and SOULAINE, C. (2018). "A new compressive scheme to simulate species transfer across fluid interfaces using the volume-of-fluid method". *Chem. Eng. Sci.*, **190(23)**, 405–418.

MAES, J. and SOULAINE, C. (2020). "A unified single-field volume-of-fluid-based formulation for multi-component interfacial transfer with local volume changes". *J. Comput. Phys.*, **402(109024)**.

MARSCHALL, H., HINTERBERGER, K., SCHÜLER, C., HABLA, F. and HINRICHSEN, O. (2012). "Numerical simulation of species transfer across fluid interfaces in free-surface flows using OpenFOAM". *Chemical Engineering Science*, **78**, 111–127.

OPENCFD (2016). *OpenFOAM, the open source cfd toolbox, User Guide*. OpenCFD Ltd.

ROMAN, S., SOULAINE, C., ALSAUD, M.A., KOVSCEK, A. and TCHELEPI, H. (2016). "Particle velocimetry analysis of immiscible two-phase flow in micromodels". *Advances in Water Resources*, **95**, 199–211.

ROMAN, S., SOULAINE, C. and KOVSCEK, A. (2019). "Pore-scale visualization and characterization of viscous dissipation in porous media". *Journal of Colloid and Interface Science*, **558(269-279)**.

RUSCHE, H. (2002). *Computational fluid dynamics of dispersed two-phase flows at high phase fraction*. Ph.D. thesis, Imperial College London.

SOULAINE, C., ROMAN, S., KOVSCEK, A. and TCHELEPI, H.A. (2018). "Pore-scale modelling of multiphase reactive flow. application to mineral dissolution with production of co2". *J. Fluid Mech.*, **855**, 616–645.

UBBINK, O. and ISSA, R.I. (1999). "A method for capturing sharp fluid interfaces on arbitrary meshes". *J. Comput. Phys.*, **153**, 26–50.

VAN LEER, B. (1974). "Towards the ultimate conservative difference scheme. II. Monotonicity and conservation combined in a second-order scheme". *J. Comput. Phys.*, **14(4)**, 361–370.

COMPREHENSIVE MODEL FOR BLAST FURNACE USING OPENFOAM®

P. B. ABHALE[1*] , S. NAG[1], Y. BAPAT[2+], A. KULKARNI[2‡], N. N. VISWANATHAN[3#]**
[1] Tata Steel Ltd., Jamshedpur, INDIA
[2] Tridiagonal Solutions Pvt. Ltd., Pune, INDIA
[3] Centre of Excellence in Steel Technology, IIT Bombay, Mumbai, INDIA

***** E-mail: prakash.abhale@tatasteel.com
****** E-mail: samiknag@tatasteel.com
[+] E-mail: yogesh.bapat@tridiagonal.com
‡ E-mail: ashish.kulkarni@tridiagonal.com
[#] E-mail: vichu@iitb.ac.in

ABSTRACT

Blast furnace is a complex, multi-phase and high temperature reactor involving multiple reactions between phases, heat transfer and phase change. Limited options are available to know internal state of the furnace through measurements using instruments or sensors. Hence, mathematical and numerical models play an important role in prediction of blast furnace performance.

Considering the complex nature of equations to model flow, heat transfer, phase change, reaction kinetics and coupling between them a robust framework is required. In this context, to take advantage of new computational paradigms in terms of flexibility offered through open source codes, OpenFOAM® is selected as the primary platform. It offers generic field operations and manipulation solvers for partial differential equations in conjunction with excellent scalability across multiple CPUs. A Comprehensive blast furnace model has been developed using OpenFOAM® with axi-symmetric solver.

The model is in implementation stage in the plant and typical simulation results compared with the field data are presented. In addition, the model can be used for scenario analysis, trend prediction, identification of shape and size of cohesive zone over range of process parameters.

Keywords:

Blast furnace, simulation and modelling, process model, OpenFOAM solver, process diagnostics, cohesive zone, CFD application to metallurgical process industry

NOMENCLATURE

Greek Symbols

ρ	Mass density, [kg/m^3].
φ	Velocity potential, [N/m^2].

Latin Symbols

M	Molecular weight, [kg/kmol].
K	Conductance in flow, [m^4/N s].
R	Universal gas constant, [J/kmol K].
$\dot{R}$	Reaction source term, [kg/m^{3}s].
T	Temperature, [K].
$\dot{V}$	Melting source term, [s^{-1}].
$f1$	Viscous resistance, [kg/m^{3}s].
$f2$	Inertial resistance, [kg/m^4].
p	Pressure, [Pa].
$\boldsymbol{v}$	Velocity, [m/s].

Sub/superscripts

g	Gas.
s	Solid.

INTRODUCTION

Blast furnace is a complex, multi-phase and high temperature reactor involving multiple reactions between phases, heat transfer and phase change. Depending on capacity of the furnace it can produce 2000 to 12000 tons of iron per day. In terms of size blast furnace can be as high as 60m and 15m in diameter. Iron ore and coke are charged from the top of the blast furnace to form a desired layered burden. At the periphery of the hearth top, wind and oxygen are blown through number of tuyeres at 1000^{0}C -1200^{0}C. The pulverized coal at ~80^{0}C is injected into tuyeres through lance. Temperature of gases reach to ~2200^{0}C due to partial combustion of coal and coke descending from the top. The resultant mixture of gas contains mainly CO, H_2 and N_2. The gas mixture acts as a reducing agent for ore, resulting in the production of iron ore. The measurements are mainly available at the periphery due to high temperatures inside the blast furnace. These are insufficient to know the internal state of the blast furnace. Hence, mathematical and numerical models play an important role in the prediction of blast furnace performance.

Several models were developed in the past and are reported in the literature (OMORI (1987)). A two dimensional gas flow model to predict gas distribution in the blast furnace was developed by (YAGI (1982)). In further improvements a comprehensive model involving three phases namely gas, solid and liquid was developed (CHEN (1993)). The model demonstrated that gas flow is mainly governed by layered burden and cohesive zone. The model was further refined by (AUSTIN (1997a)) and (AUSTIN (1997b)) by considering the effect of suspended fine particles as fourth phase and was thus named '*Four-Fluid*' model.

Nippon Steel developed '*BRIGHT*' model (MATSUZAKI (2006)), which used three interface model for ore reduction reaction. CRM Belgium in collaboration with then Arcelor and Corus developed another process model '*MOGADOR*' (DANLOY (2008)) to simulate the effect of gas distribution on ore reduction and also to predict the location of the cohesive zone. The model was validated for one of the European blast furnaces using multi-point vertical probing. Existence of another isothermal zone was found in the top region of the blast furnace due to burden moisture evaporation. A detailed review for numerical modelling of blast furnace is available in literature (P. B. ABHALE (2020)).

At IIT Bombay, India researchers have been working on modelling of the blast furnace using first principles with the financial support from NML Jamshedpur, Tata Steel Jamshedpur, and Gov. of India. In their approach, different sub models were developed from scratch using C programming language and were integrated to develop comprehensive mathematical model of blast furnace (P. B. ABHALE (2011)). However, the comprehensive model had bottlenecks in terms of computation time, robustness, and parallel execution. Thus, it was decided to look at the whole modelling exercise afresh and explore the possibilities of using some of the well-established CFD codes to be used for the modelling exercise.

In view of this, Tata Steel Ltd., Jamshedpur in collaboration with the Centre of Excellence in Steel Technology, IIT Bombay and Tridiagonal Solutions, Pune has developed 2-D comprehensive simulation system for the blast furnace. The model has been developed using OpenFOAM® platform. The model consists of multiple sub-models like layer descent, solid flow, gas flow, liquid flow. It also simulates heat transfer, reaction kinetics and species transport in all three phases. The model can predict different zones in blast furnace like lumpy zone, cohesive zone, dripping zone and deadman. The model has been named as '***BlaSim®***' (***Bla**st furnace **Sim**ulator*).

OpenFOAM® is an open source CFD framework for '*Field Operations And Manipulations'*. The OpenFOAM® provides generic framework for solution of PDEs in Finite Volume Framework (FVM) with operators for divergence, laplacian and gradient operations. It also provides easy adaptation for parallel computing environment.

MODEL DESCRIPTION

BlaSim® is a mathematical model assuming 2-D axisymmetric behaviour of a blast furnace. The assumption is reasonable as effect of discrete injection points for gas disappears after height of 3-4 m from tuyere the level (YAGI (1982)), (Y. G. SHEN (2015)) and (P. B. ABHALE (2009)) (P. B. ABHALE (2010)). The model limitation is accepted considering significant mesh count reduction leading to less computational time. It has multiple sub-models to describe different physical processes in blast furnace viz. layer descent, solid-gas-liquid flow models, enthalpy balance models of all phases, etc. To consider effects of mass and heat transfer among various phases due to reactions and melting, rate equations governing them are coupled with species balance equations of gas-solid-liquid phases through source terms. The formation of raceway due to blowing of air and its hysteresis was studied by (SARKAR (2007)). Similarly, 3-D raceway shape was obtained by detailed CFD model by (Y. S. SHEN (2011)). For the present model raceway shape is assumed and is used as a boundary for the domain. The is due to more fine grid requirements for combustion modelling, instead, simple mass and heat balance of the raceway is performed separately, and various boundary conditions are obtained for the comprehensive model.

Solution algorithm

The model is run in two steps. During the first step layer profiles in the blast furnace are predicted. The prediction is done using lagrangian tracking of layer profiles using predicted solid velocity field, which is obtained by solving solid flow equations Eq. (1) and Eq. (2) without melting term. The motion of solids is modelled using potential flow theory.

Solid flow equations (OMORI (1987))

$$\nabla.(K_s \nabla \varphi_s) = -\dot{V}_{melting,s} \qquad (1)$$

$$\vec{v}_s = -K_s \nabla \varphi_s \qquad (2)$$

Top repeating profiles of layers of ore and coke are represented by the massless particles (at given co-ordinates) which are then tracked using kinematic cloud solver of the OpenFOAM® till raceway. Further the points representing the final predicted layer profiles are converted into separate STL file for each layer. Generated STL files are then used to patch the layer structure on the mesh, which means that the each cell in the computation domain will either bear a ore, a centre coke, or a surface coke material, having distinct properties. The solution algorithm is as show in Figure 1.

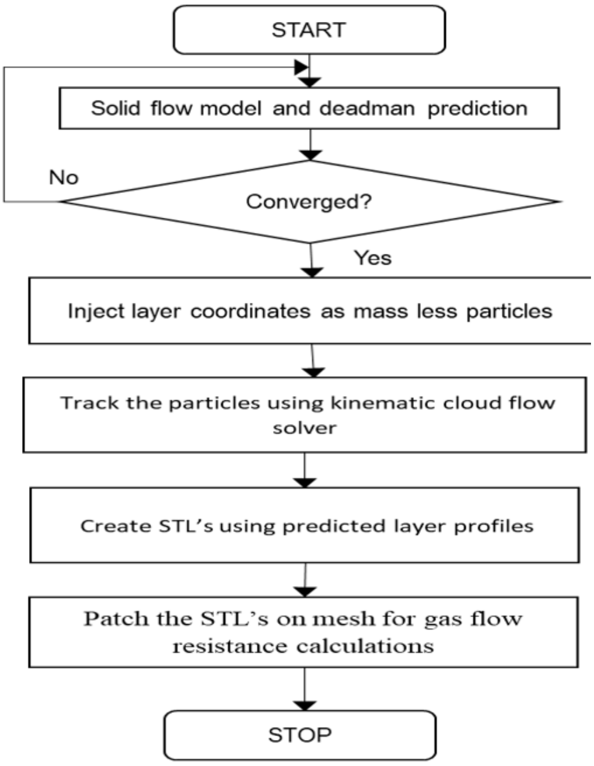

Figure 1: Solution algorithm

In the second step, layer profiles obtained are frozen and the information is mainly used to solve gas velocity fields. For all other models, layers are assumed to be well mixed for the calculation of average properties of the mixed burden. This is required to obtain the steady state results.

The flow of gas through a packed bed is modelled using Ergun equation, continuity and equation of state given by Eq. (3), (4), and (5).

Gas flow equations (OMORI (1987))

$$\left(f1 + f2\,\left|\vec{v}_g\right|\right)\vec{v}_g = -\nabla p \qquad (3)$$

$$\nabla.\left(\rho_g \vec{v}_g\right) = \dot{R}_g \qquad (4)$$

$$\rho_g = \frac{PM_g}{RT_g} \qquad (5)$$

The terms $f1$ and $f2$ in Eq. (3) are standard in chemical engineering to represent viscous, and inertial resistances, respectively to model gas flowing through a packed bed of particles.

As the gas flow is very sensitive to pressure drop within ore and coke layers, which offer widely varying resistances, it is important to get the correct estimates of the resistances in the blast furnace. There are number of ways available in the literature to get the correct estimates for a coarser orthogonal mesh (20x120), (P. B. ABHALE (2009)). However, this involves complex geometrical calculations for knowing layer intersections with the mesh and its inclinations for calculating representative anisotropic resistances.

In the present work much finer non-orthogonal mesh (~10000) is used for its simplicity and take advantage of high-performance CPU's with parallel compute environment provided by OpenFOAM®. The layer profile mapped on the mesh in the first step using STL is used to identify a type of material present in each mesh. Then using the material properties such as mean particle diameter, shape factor and voidage in each zone, resistances $f1$ and $f2$ are estimated. The

Eq. (3), (4), and (5) are solved to obtain gas velocity and pressure distribution.

Three step shrinking core model for ore reduction and homogeneous reaction model for coke gasification reactions are considered in solid phase. Water gas shift reaction, liquid wustite reduction, carbon dissolution and silicon transfer reactions are also considered. Details of all reactions are available in literature (OMORI (1987)). Source terms arising due to reactions and melting are applied to all the continuity equations involving volume, mass, and heat of all three phases. All the equations are solved to obtain steady state results. The complete solution algorithm for second step is given in Figure 2.

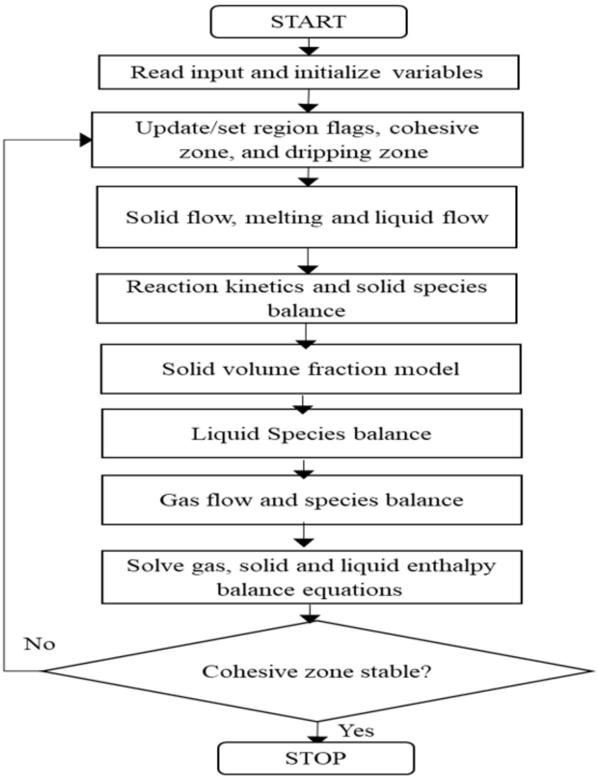

Figure 2: Solution algorithm

Geometry and mesh

The geometry of 'H' blast furnace of Tata Steel, Jamshedpur is used for the simulation. Mesh is created in Ansys such that it is one cell thick in the third direction. Cell count for the mesh is 9932. The mesh is converted to 'polyMesh' format used by OpenFOAM®. In OpenFOAM® axisymmetric simulation is performed by modifying mesh instead of modifying equations. 'extrudeMesh' utility available in OpenFOAM® is used to rotate the 'polyMesh' to create an axisymmetric mesh.

Boundary condition

Inputs required for the model are operating parameters, burden profile, burden properties, reaction kinetics parameters, boundary conditions, etc. First all operating and model parameters are provided in excel sheet. A python code is written to perform heat and mass balance of raceway to obtain raceway gas flow rate, temperature, and composition. Then another python utility is used to convert inputs in the format required by the model in OpenFOAM® format. The inputs provided below are from H blast furnace at Tata Steel, Jamshedpur

- Solid velocity at the top boundary = 0.002 m/s
- Solid temperature at the top = 303 K
- Top gas pressure =2.35 bar (abs)
- Gas mass flow rate for 2^o=0.8735 kg/s
- Flame temperature at raceway boundary = 2498 K
- Gas species mass fraction specified at raceway boundary
    - $CO = 0.4617$, $H_2 = 0.0057$, $N_2 = 0.5326$
- Softening temperature = 1373 K, Melting temperature = 1673 K

Thermodynamic data required for the model are obtained by fitting a polynomial to a data obtained from FactSage® for the required temperature range.

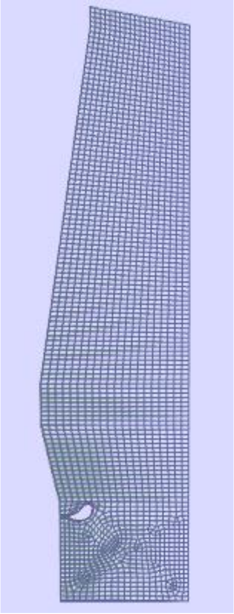

Figure 3: Mesh

Convergence check

As solution is steady state, monitors of important physical variables are used to monitor the convergence. When steady state is achieved, monitors become flat and solution can be stopped. Two such monitors are shown in Figure 4 and Figure 5. Volume weighted value of zone flags is used to plot the monitor. Definition of zone flag is given in Figure 6.

Results

As the model developed is complex and number of assumptions are made during mathematical modelling, to run the model some tuning is required. Tuning is performed by adjusting reaction kinetic parameters and heat transfer coefficients. The tuning is performed by matching results of the model for a particular date with plant measured Key Performance Indicators (KPIs). Once the tuning is done for a particular date the model is used to predict and match results. Results are presented in Table 1.

Simulations can be performed using parallel computations. Typical run time for 9932 cell mesh is about 40 minutes on four processors.

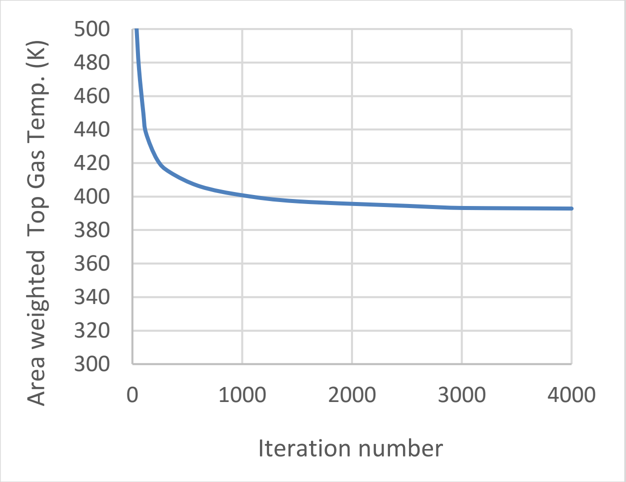

Figure 4: Monitor of top gas temperature

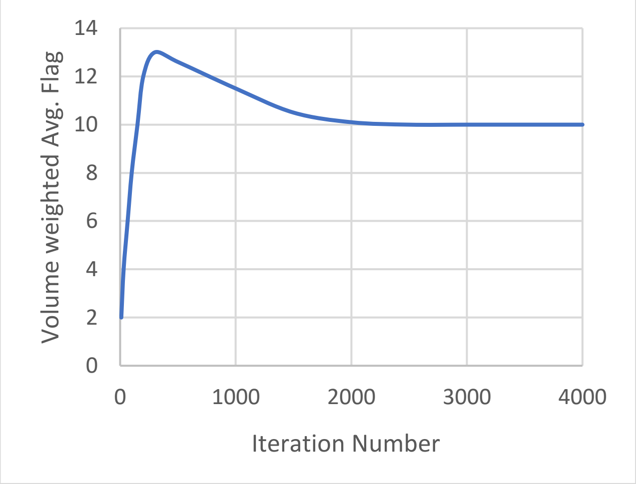

Figure 5: Monitor of flag variable

Following is the list of important output provided by the model

- Velocity, temperature profile for all liquid-gas-solids
- Pressure profile
- Gas-solid-liquid species profiles, ore reduction profiles
- Different zone locations and shapes
- Layer profiles
- Top gas and hot metal composition

Heat and mass balances are also performed to ensure solution satisfies the overall balances. Error in mass balance is 0.003%, whereas, that in heat balance is 0.08%.

Table 1: Comparison between plant and predicted data

Variable	Actual Value	Predicted Value
Dry coke rate (kg/thm)	320	306.6
Delta P (bar)	1.50	1.66
TG Temp (C)	100.0	120.0
Dry TG CO (vol. %)	23.4	23.6
Dry TG CO2 (vol %)	24.0	23.8
Eta CO = CO2/(CO+CO2) (-)	0.5063	0.5016
Dry TG H2 (vol %)	5.0	4.8
Overall heat loss (MJ/thm)	220	200
Hot Metal Cast Temp= Texit -20 (C)	1500	1490

In Figure 6 lumpy, cohesive, dripping and deadman zones can be observed. Location and shape of cohesive zone is a very important output parameter to understand working of blast furnace.

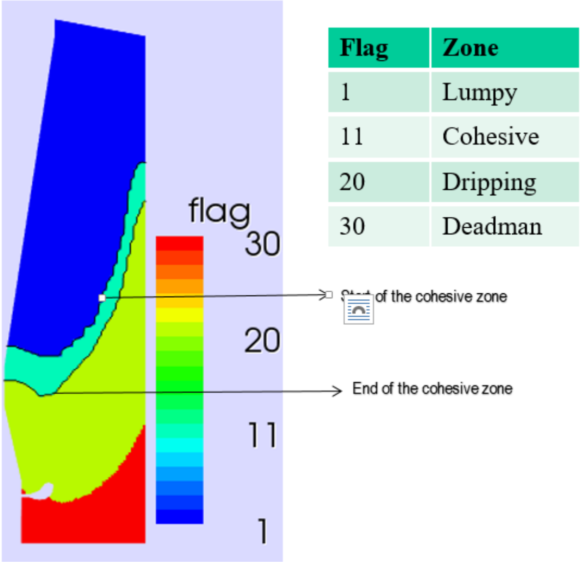

Flag	Zone
1	Lumpy
11	Cohesive
20	Dripping
30	Deadman

Figure 6: Different zones predicted by BlaSim®

In Figure 7 solid velocity streamlines and predicted layer structure are shown. In the layer structure three distinct layers of ore (blue), coke (green) and central coke (red) can be observed.

In the Figure 8, ore volume fraction and gas velocity streamlines are shown. Radial distribution of ore and coke volume fractions is an input to the model and is obtained from burden distribution model (RADHAKRISHNAN (2001)) (NAG (2014)). Ore volume fraction is high at the mid-radius due to practise of charging high amount of ore at the location for better gas distribution and minimizing heat losses. The ore volume fraction is reduced to 0 at the end of cohesive zone due to melting. Gas streamlines show strong impact of cohesive zone on gas flow. Streamlines show that gas flows away from centre through coke layers as mushy ore in the cohesive zone offers very high resistance to gas flow.

Temperature profiles are plotted in Figure 9. Liquid (hot metal + slag) temperature profiles are relevant only below start of cohesive zone as liquid is not present above the cohesive zone. High gas temperature is observed in the centre of the blast furnace indicating strong central flow of gases.

Gas composition and distribution in the blast furnace is shown in Figure 10. Higher CO consumption is clearly visible in the region of maximum ore loading and it is lowest in the central region where ore fraction is very low.

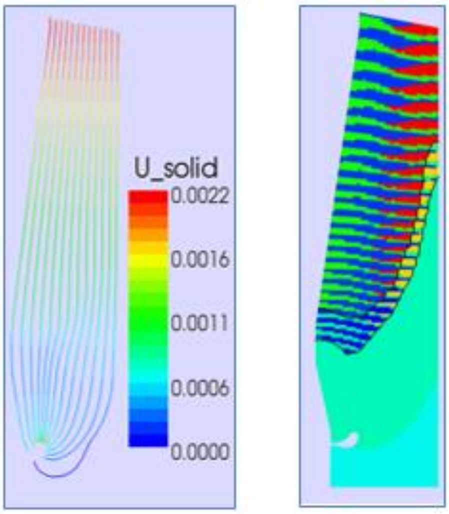

Figure 7: Solid velocity streamlines and predicted layer structure

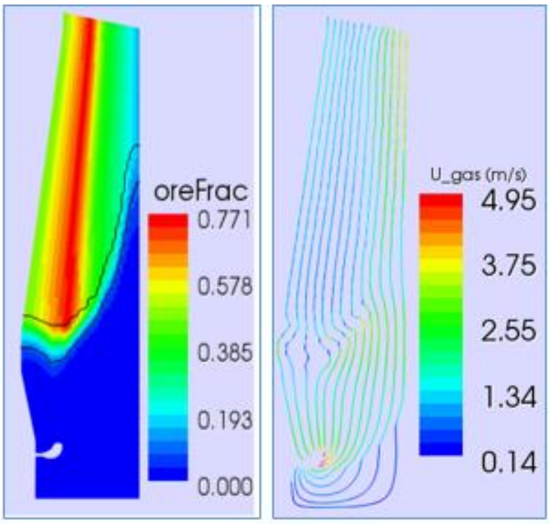

Figure 8: Ore fraction and Gas velocity streamlines

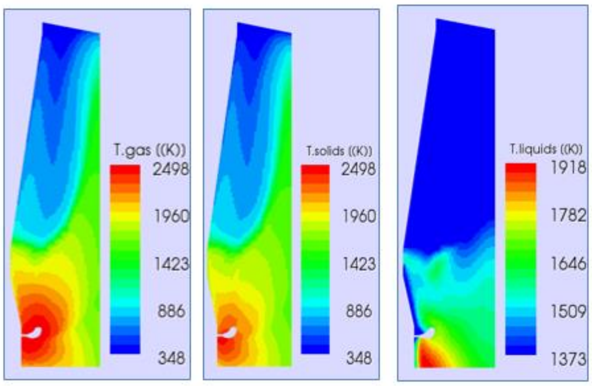

Figure 9: Temperature profiles in gas, solid and liquid

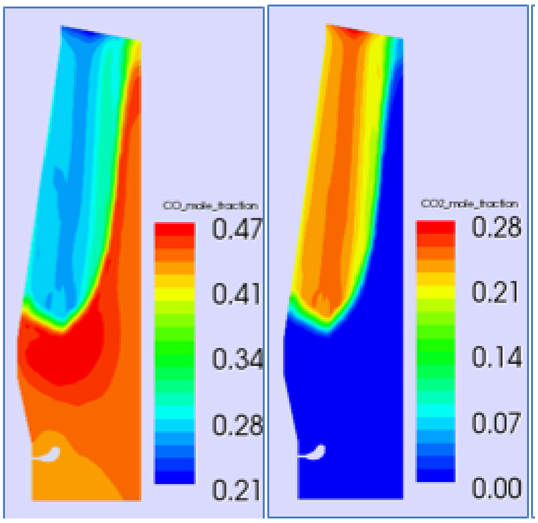

Figure 10: Gas composition, CO and CO2 profiles

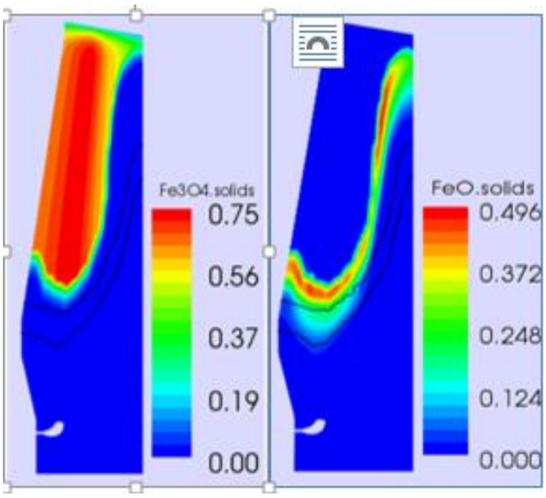

Figure 11: Solid composition magnetite and wustite profiles

Solid composition of magnetite and wustite is shown in Figure 11. Hematite reduction is very fast and occurs in the top region. Magnetite reduction happens deeper into the blast furnace. Thereafter, wustite reduction is quicker and happen in a depth of 1-2 meters at all radius except mid-radius where ore burden is maximum.

Parametric study

Prediction of blast furnace performance with change in operating conditions is an important aspect of the model. Below two such cases are presented in which effect of top gas pressure and effect of central coke burden diameter is predicted. All other inputs are same as that of base case.

Effect of top gas pressure

To study the effect of top gas pressure two additional cases are run with top gas pressure of 1.85 bar and 2.85 bar. The base case is with top gas pressure of 2.35bar. Predicted gas pressure drop is 1.84, 1.66 and 1.48 bar for top gas pressure of 1.85, 2.35 and 2.85 bar. Effect on pressure profiles is shown in Figure 12. As top gas pressure is increased from 1.85bar to 2.85 bar overall pressure drop decreases due to lower gas velocities. Decrease in velocity is due to higher gas density at higher pressure. Note that pressure drop, and square of velocities are directly proportional as per gas flow Eq. (3).

Effect of central coke

In general, coke with larger diameter is charged from centre. This produces central chimney where gas flow is higher.

Similar central coke is used in the base case presented above. To check the impact, a new case is run in which central coke is replaced with same coke as used in surface coke layer. Typical surface coke diameter is around 30 mm and for central coke it is around 50 mm. Cohesive zone is shifted down near the centre, whereas it is shifted up near wall. Other effects observed are

- Eta CO is also increased from 49.37 to 50.03 when same diameter central coke is used due to better gas distribution.
- Top gas temperature decreases from 393K to 389K when same diameter central coke is used indicating higher efficiency.

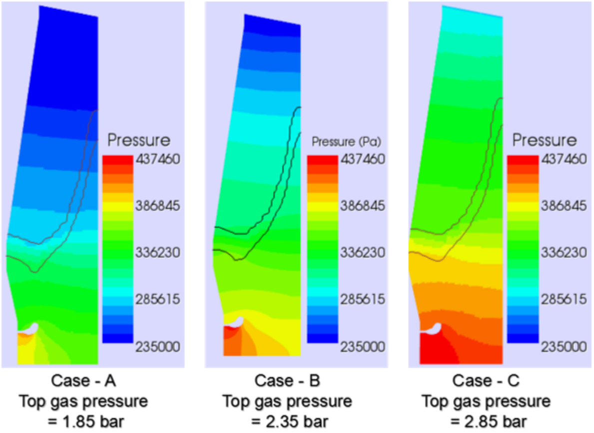

Figure 12: Effect of top gas pressure

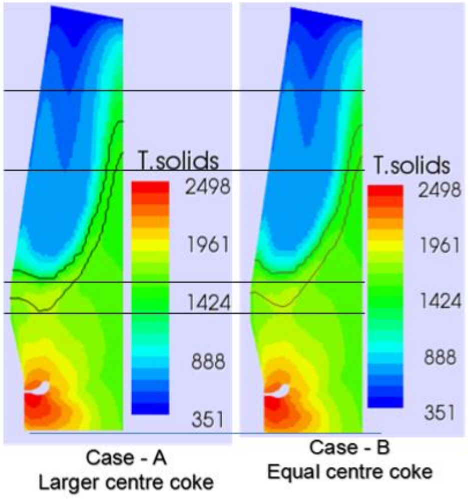

Figure 13: Effect of central coke size on solid temperature and cohesive zone

Conclusion

A comprehensive, steady state model has been developed for blast furnace process analysis using OpenFOAM®. The tool is tuned to predict the performance of 'H' blast furnace of Tata Steel, Jamshedpur. After tuning the model is ready to be used to predict the performance of the blast furnace with different operating conditions.

Parametric studies are performed by changing process conditions. Results predicted by parametric study agree with expected trends as per working of blast furnace and plant conditions.

The model developed can be used for predictive analysis and efficiency improvement of the BF process. This can result in significant cost saving of blast furnace operation and reduce carbon footprint of the process.

REFERENCES

ABHALE, P. B. (2011). *Mathematical modeling of iron blast furnace.* Ph.D. Thesis, IIT Bombay, INDIA.

ABHALE, P. B., VISWANATHAN, N.N., and SAXEN, H. (2020). "Numerical modelling of blast furnace – Evolution and recent trends,." *Mineral Processing and Extractive Metallurgy* 129 (2): 166-183.

ABHALE, P. B., VISWANATHAN, N.N., BALLAL, N.B. (2009). "Efficient simulation of gas flow in blast furnace." *Computers, Materials & Continua* 10 (2): 195.

ABHALE, P. B., YADAV, V. K., VISWANATHAN, N.N., and BALLAL, N.B (2010). "Investigation of mal-distribution in blast furnace aerodynamics using a three dimensional simulation model." *International Conference on Computational & Experimental Engineering and Sciences (ICCES 2010).* Las Vegas, USA.

AUSTIN, P. R., NOGAMI, H., and YAGI, J. (1997a). "A mathematical model for blast furnace reaction analysis based on the four fluid model." *ISIJ Inter.* 748-755.

AUSTIN, P. R., NOGAMI, H., and YAGI, J. (1997). "A mathematical model of four phase motion and heat transfer in the blast furnace." *ISIJ Inter.* 458-467.

AUSTIN, P. R., NOGAMI, H., and YAGI, J. (1997b). "A mathematical model of four phase motion and heat transfer in the blast furnace." *ISIJ Inter.* 458-467.

CHEN, J., AKIYAMA, T., NOGAMI, H., YAGI, J., and TAKAHASHI, H. (1993). "Modeling of solid flow in moving bed." *ISIJ Int.* 33: 664-671.

CHEW, S., ZULLI, P., and YU, A. B. (2001). "Modelling of liquid flow in the blast furnace application in a comprehensive blast furnace model." *ISIJ Inter.* 1122-1130.

DANLOY, G. (2008). "Modelling of the blast furnace internal state with MOGADOR." *Proceedings of the 4th Ulcos Seminar.*

DONG, X.F., YU, A. B., and BURGRESS, A. B. (2009). "Modelling of multiphase flow in ironmaking blast furnace." *Ind. Eng. Chem. Res.* 214-226.

MATSUZAKI, S., NISHIMURA, T., SHINOTAKE, A., KUNITOMO, K., NAITO, M., and SUGIYAMA, T. (2006). *A development of mathematical model of blast furnace.* Japan: Nippon Steel Technical Report.

NAG, S., GUPTA, A., PAUL, S., GAVEL, D., and AICH, B. (2014). "Prediction of heap shape in blast furnace burden distribution." *ISIJ Int.* 54: 1517-1520.

OMORI, Y. (1987). *Blast furnace phenomena and modelling.* Elsevier Applied Science: London.

RADHAKRISHNAN, V. R., and RAM, K.M. (2001). "Mathematical model for predictive control of the bell-less top charging system of a blast furnace." *J Process Control.* 11: 565-586.

SARKAR, S., GUPTA, G. S., and KITAMURA, S. (2007). "Prediction of Raceway Shape and Size." *ISIJ Inter.* 47 (12): 1738-1744.

SHEN, Y. S., GUO, B. Y., YU, A.B., AUSTIN, P. R., and ZULLI, P. (2011). "Three-dimensional modelling of in-furnace coal/coke combustion in a blast furnace." *Fuel* 90: 728-738.

SHEN, Y.S., GUO, B.Y., CHEW, S., AUSTIN, P. R., and Yu, A.B. (2015). "Threedimensional modelling of flow and thermochemical behaviour in a blast furnace." *Metall Mater Trans B.* 46B: 432-448.

YAGI, J.,TAKEDA, K., and OMORI, Y. (1982). "Two dimensional simulation of gas flow and heat transfer in the blast furnace." *ISIJ International* 22: 884.

14th International Conference on CFD in Oil & Gas, Metallurgical and Process Industries
SINTEF, Trondheim, NORWAY
October 12-14, 2020

TOWARDS UNDERSTANDING WIND IMPACT FOR DRONE OPERATIONS: A COMPARISON OF WIND MODELS OPERATING ON DIFFERENT SCALES IN A NESTED MULTISCALE SET-UP.

Mandar V TABIB[1*], **Knut Helge MIDTBØ**[2], **Tor SKASLIEN**[2†], **Adil RASHEED**[13‡], **Trond KVAMSDAL**[14]

[1]SINTEF Digital, 7465 Trondheim, NORWAY
[2]Meteorologisk institutte, Oslo
[3]Department of Engineering Cybernetics, NTNU,Trondheim, Norway
[4]Department of Mathematical Sciences, NTNU, Trondheim, Norway

[*] E-mail: mandar.tabib@sintef.no
[†] E-mail: torhs@met.no
[‡] E-mail: adil.rasheed@ntnu.no

ABSTRACT

The application of Unmanned Aircraft Systems (UAS) in health services is increasing, with a large variety of objectives: delivering medicines and vaccines, transporting blood samples and providing care technology in emergency situations. However, for use in emergency medical purposes, the expectations are a drone should be available at most times. Severe wind conditions are considered to be one of the prime factor that can hamper this expected drone availability. Most of these drone operations are expected to be linked to urban hospitals and understanding urban micro-scale weather patterns are important. The current work tries to develop a methodology for obtaining wind fields in an urban landscape. The multi-scale methodology involves coupling three models operating on different scales namely an operational meso-scale numerical weather prediction model HARMONIE, a micro-scale model that captures terrain-induced wind influence and a super-micro scale Computational Fluid Dynamics code to capture building-induced wind influence. Existence of a large variation in the spatio-temporal scales in an atmospheric flow necessitates such a coupling between different models each of which handles a particular range of scales. In this article, we describe the multi-scale methodology and present a qualitative comparison of the wind velocity predicted by different numerical models with the measured experiment data and then explain the potential of the tool for drone operations.

Keywords: CFD, drones, wind, urban climate.

NOMENCLATURE

Greek Symbols
ρ Mass density, $[{}^{kg}/_{m^3}]$
μ Dynamic viscosity, $[{}^{kg}/_{ms}]$
θ Temperature, $[K]$

Latin Symbols
p Pressure, $[Pa]$.
$\mathbf{u}$ Velocity, $[{}^{m}/_{s}]$.

Sub/superscripts
s hydrostatic part.

INTRODUCTION

Health services are beginning to explore the use of Unmanned Aircraft Systems (UAS) for diverse applications, like for delivering medicines and vaccines, transporting blood samples and providing care technology in emergency situations. However, for use in emergency medical purposes, the expectations are a drone should be available for at-least 95% of the time (if not 24-by-7 a year) to be deemed reliable. The weather challenge is likely to be the factor that threatens the UAS service availability the most. Low cost and small, reliable systems have not yet been developed to be used in all-weather conditions with a high level of safety and availability. The current knowledge of the impact of wind and turbulence on drone flight safety is scarce. For development of this knowledge, tools that can predict urban micro-scale climatology accurately are needed. This has been attempted in different ways, for example, the urban meteorological conditions have been simulated using state-of-the art meso-scale codes with urban parameterizations. These parameterizations are based on the assumption that a city can be represented by regular arrays of cuboids (Kondo *et al.*, 2008). As shown by (Rasheed *et al.*, 2011), this assumption is not valid for European cities. While it is possible to derive statistical information regarding the visibility, temperature and precipitation using these models in combination with measurement data, the coarseness of the model's horizontal resolution (finest being 500m) makes it impossible to model flow induced by buildings or other structures which may have a profound impact on the operating of UAVs.Recently, micro-scale modelling using conventional CFD code has come up with an alternative and researchers have been able to simulate full cities (Ashie and Kono, 2011; Tabib *et al.*, 2017) with promising results. However, such micro-scale models need accurate boundary conditions to work. In this direction, the objective of the present work is to develop a multi-scale coupling to enable computation of urban wind conditions. The next section describes the multi-scale methodology:

MULTI-SCALE METHODOLOGY DESCRIPTION

The multi-scale methodology here consists of unidirectionally coupled HARMONIE-SIMRA-CFD multiscale system (as shown in figure 1). There have been other multi-scale approaches ((Kunz *et al.*, 2000; **?**) but they have been mostly devoted to wind energy requirements. The current work involves a multi-scale approach with the level at finest scale being able to resolve the impact of buildings on wind. HARMONIE (Seity *et al.*, 2011) is a meteorologicial program used for weather forecasting in Norway and SIMRA is a program specially designed to model terrain-induced wind and turbulence in complex terrain at high horizontal spatial resolution, and is capable of resolving important terrain features. Both these programs are based on the mass, momentum and energy conservation principles of fluid mechanics. Earlier a multi-scale methodology was developed for wind farms (details regarding these models can be found in (Rasheed *et al.*, 2017), this multi-scale methodology has been extended to account for buildings by incorporating additional refined-CFD model for building-scale. For sake of completeness, the models are described below as well:

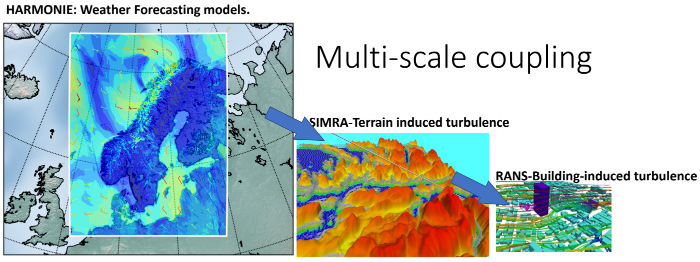

Figure 1: Multi-scale methodology

HARMONIE - a meso- scale numerical weather model

The atmospheric modelling component in the coupled system is a meso-scale model named HARMONIE that can simulate weather phenomena that spans over 100s of kilometers of distance and lasts until days (hence called meso-scale in metereology). based basically on the equations presented below albeit in a slightly modified form to suit meteorology. The model is a non-hydrostatic model, in which the dynamical core is based on a two-time level semi-implicit semi-Lagrangian discretization of the fully elastic equations, using a hybrid coordinate system in the vertical direction ([2]). The surface model Surface Externalise (SURFEX) is used for the calculations of fluxes in the surface layer. One-hourly boundary and initial data comes from the global model called ECMWF (http://www.ecmwf.int/). Although the model captures large scale phenomena (as will be shown later), it does not account for micro-scale flow phenomena driven by terrain complexities. The model has a variety of parameterization schemes for sub-grid scale physical processes. At the upper boundary a condition of zero vertical velocity is imposed.

SIMRA- A micro-scale terrain induced turbulence

SIMRA (Semi IMplicit Reynolds Averaged) model (Utnes, 2007a,b), which is based upon the RANS equations with a standard $k-\epsilon$ turbulence closure (Rodi, 1997; Mohammadi and Pironneau, 1994), is a fully three-dimensional model for anelastic flow. From metereological perspective, it has the capability of predicting micro-scale flows with separation, attachment, hydraulic transition, internal wave breaking and mountain waves, and phenomena occurring from minutes up to an hour and cover small distances such as less than 10 kilometers (hence, it is called micro-scale model). It has finer resolution and near wall boundary conditions that ensures that it is able to resolve the impact of terrain and ocean surfaces. It makes use of the Boussinesque approximation. The governing equations of mass, momentum, energy, turbulent kinetic energy and dissipation are discretized using a finite element method and solved by a projection method. Thus, the model solves prognostic equations for all velocity components, potential temperature and pressure (Eqn. 1 and 2). Turbulence is modeled using two equations: one for turbulent kinetic energy (Eqn. 4) and another for turbulent dissipation (Eqn. 5). A projection method is used for the solution of the Reynolds equations, and a mixed finite element formulation is used for space discretization. Since the effects of Coriolis force at this scale is negligible this is ignored in the model. A Taylor-Galerkin method is used for time discretization. A special feature of this model is the use of logarithmic element interpolation at the near-ground location in order to satisfy logarithmic boundary conditions accurately. This model has been tested against various data, from two-dimensional flow over a single hill in neutral and stratified flow to three-dimensional flow over different hill shapes (Eidsvik, 2005; Eidsvik and Utnes, 1997; Eidsvik *et al.*, 2004). The code has been parallelized using Message Passing Interface (MPI). The code computes wind, temperature and turbulent kinetic energy and dissipation. More details, description and validation results can be found in (Utnes, 2007a,b). SIMRA is designed to be used at the micro-scale level (this scale in metereological parlance covers terrain induced turbulence) with an efficiency of real-time simulation. Hence, simra employs orthogonal structured mesh to resolve the terrain at that scale and the solvers suited to such mesh are efficient and enable real-time analysis. SIMRA is well validated at this scale. However, SIMRA will not work at super-micro scale level as in order to resolve the terrain and buildings at such finer mesh, the resultant volumetric mesh needs to consider non-orthogonal unstructured cells. This helps to avoid Jacobian from being non-negative during the mesh generation process, and such unstructured non-orthogonal meshes need different kind of solvers that have ability to deal with sparse non-diagonally dominant matrices. Hence, we use OpenFOAM to develop the super-micro scale model as it has in-built solvers to work with the finer unstructured non-orthogonal mesh (with non-orthogonal corrections employed). The OpenFOAM can be employed both at micro and super-micro scale, but on the micro-scale level, Simra is expected to be more computationally efficient due to its solvers and physics. Hence, the choice of models at different levels in the multi-scale set-up has been done keeping in view their ability and balance between accuracy and efficiency. The definition and segregation of scales (meso,micro,super micro) is as per the norms used in Metereology.

CFD for urban simulation: A super-microscale phenomena.

The solver is created in OpenFOAM-2.3.0 (OF) (http://www.openfoam.com/) using the finite volume discretization of the equations presented below. To ensure continuity, OF uses an elliptic equation for the modified pressure which involves combining the continuity equation with divergence of momentum equation. This elliptic equation along with the momentum equation, energy equation and turbulence equation are solved in a segregated manner using the SIMPLE algorithm for steady state or using PISO-SIMPLE algorithm (PIMPLE algorithm) for unsteady state. The solver can be run using both steady state and unsteady state manner. For this work, a steady state solver is used with turbulence modelled using realizable k-epsilon model. As compared to standard k-epsilon model, the realizable k-epsilon turbulence model is known to provide better predictions for turbulent flows in regions pertaining to flows involving boundary layers separations, re-circulation and boundary layers with strong adverse pressure gradient that are expected in hilly regions. This is owing to use of a variable turbulent viscosity (C) in realizable k-epsilon as compared to a constant viscosity value that standard k-epsilon uses and use of a new transport equation for the dissipation rate, , that is derived from an exact equation for the transport of the mean-square vorticity fluctuation. The realizable k-epsilon model ends up satisfying certain mathematical constraints on the Reynolds stresses, consistent with the physics of turbulent flows. Authors are aware that there are better performing turbulence models like Shear Stress Transport (SST), but the choice of realizable k-epsilon model had also to do with its ability to be computationally efficient while predicting the statistical mean properties of turbulent flows.

All the equations (except k and turbulence equations) use second order linear discretization scheme, while the turbulent equations use liner-upwind convection schemes. Similarly, the diffusion term involving Laplacian operator (the divergence of the gradient) is simplified to compute the gradient of variables at the faces. The gradient term can be split into contributions from the orthogonal part and the non-orthogonal part, and both these contributions have been accounted for.

The next section describes the governing equations:

Governing Equations

Atmospheric flow at any scale (global, meso or micro) like any other fluid flow is governed by the conservation of mass, momentum, energy and scalars like humidity. The general equations of motion for incompressible flow may be adapted to atmospheric flows by the use of so-called anelastic approximation. This formulation is often applied in meteorological models, and may be written in the following conservative form :

$$\nabla \cdot (\rho_s \mathbf{u}) = 0 \tag{1}$$

$$\frac{D\mathbf{u}}{Dt} = -\nabla\left(\frac{p_d}{\rho_s}\right) + \mathbf{g}\frac{\theta_d}{\theta_s} + \frac{1}{\rho_s}\nabla\cdot\tau + \mathbf{f} \tag{2}$$

$$\frac{D\theta}{Dt} = \nabla\cdot(\gamma\nabla\theta) + q \tag{3}$$

Here $(\mathbf{u}, p, \theta, \rho)$ represent velocity, pressure, potential temperature and density, respectively. Furthermore, τ is the stress tensor, $\mathbf{f}$ is a source term that may include rotational effects, $\mathbf{g}$ is the gravitational acceleration, γ is the thermal diffusivity and q is the energy source term. Subscript s indicates hydrostatic values and subscript d the deviation between the actual value and its hydrostatic part, i.e. $p = p_s + p_d$, $\theta = \theta_s + \theta_d$, $\rho = \rho_s + \rho_d$, where the hydrostatic part is given by $\partial p_s/\partial z = -g\rho_s$. In addition, the following expression for hydrostatic density may be derived from the state equation and the definition of potential temperature:

$$\rho_s = \frac{p_s}{R\theta_s}\left(\frac{p_o}{p_s}\right)^{R/C_p} \tag{4}$$

where R is the gas constant and C_p is the specific heat at constant pressure. Hence, once the hydrostatic (potential) temperature profile is given, the hydrostatic pressure and density may be calculated, and then substituted into Equations 1 and 2.

It may be noted that the Boussinesq approximation is obtained from the system of Equations 1 and 2 by assuming constant values (ρ_o, θ_o) instead of the hydrostatic values, and that formulation may well be used for incompressible flow and ordinary temperature.

In a mesoscale context like HARMONIE , the external force $(\mathbf{f})$ in momentum equations include the Coriolis forces. These forces are neglected in microscale models SIMRA and CFD. Further, the thermal diffusivity (γ) can be used to model the radiative heating of the atmosphere.

The aim of the present study is to solve these equations for high Reynolds-number flows. For this purpose we apply an Reynolds-averaged modelling of the equation system, together with a turbulence model. Presently a standard high-Reynolds $(k-\epsilon)$ turbulence model is used for this purpose in the micro-scale models. The equations are shown below :

$$\frac{DK}{Dt} = \nabla\cdot(\nu_T\nabla K) + P_k + G_\theta - \epsilon \tag{5}$$

$$\frac{D\epsilon}{Dt} = \nabla\cdot\left(\frac{\nu_T}{\sigma_e}\nabla\epsilon\right) + (C_1 P_k + C_3 G_\theta)\frac{\epsilon}{k} - C_2\frac{\epsilon^2}{k} \tag{6}$$

where turbulent viscosity is given by $\nu_T = C_\nu\frac{k^2}{\epsilon}$. The Reynolds stress tensor is given by

$$R_{ij} = \nu_T\left(\frac{\partial u_i}{\partial x_j} + \frac{\partial u_j}{\partial x_i}\right) - \frac{2}{3}k\delta_{ij} \tag{7}$$

while the eddy diffusivity appearing in the energy equation is $\gamma_T = \nu_T/\sigma_T$, σ_T being the turbulent Prandtl number. The production and stratification terms in the turbulence model are given by

$$P_k = \nu_T\left(\frac{\partial u_i}{\partial x_j} + \frac{\partial u_j}{\partial x_i}\right)\frac{\partial u_i}{\partial x_j}, \quad G_\theta = -\frac{g}{\theta}\frac{\nu_T}{\sigma_T}\frac{\partial\theta}{\partial z} \tag{8}$$

Conventional constants for the high-Reynolds $(k-\epsilon)$ model are given by

$$(C_\nu, C_1, C_2, \sigma_e) = (0.09, 1.44, 1.92, 1.3) \tag{9}$$

The value for C_3 is more uncertain. In the present study we assume $C_3 G_\theta = \max(G_\theta, 0)$, i.e. $C_3 = 0$ in stably stratified flows, else $C_3 = 1$

While the microscale and supermicroscale models utilize a two equation turbulence model (one for turbulent kinetic energy given by Eqn. 5 and another for dissipation given by Eqn. 6), the mesoscale model uses a one equation model consisting of the Eqn. 5. The turbulent dissipation is estimated from $\epsilon = (C_\mu^{1/2}K)^{3/2}/\ell_t$. ℓ_t is computed using the relationship

$$\ell_t \approx \frac{\min(\kappa z, 200m)}{1 + 5Ri} \tag{10}$$

where

$$Ri = \frac{(g/\theta)\partial\theta/\partial z}{(\partial u/\partial z)^2} \approx -\frac{G}{P} \tag{11}$$

In convective conditions the stability correction $(1 + 5Ri)$ is replaced by $(1-40Ri)^{-1/3}$. The gradient Richardson number Ri is supposed to be smaller than $1/4$. The coefficients are $(C_\mu, C_1, C_2, C_3) = (0.09, 1.92, 1.43, 1)$ and the coefficients $\kappa, \sigma_K, \sigma_\epsilon$ are $0.4, 1, 1.3$, respectively.

Coupling different codes

The coupling of different codes is shown in 1. For Harmonie-SIMRA, basically three velocity components, temperature, turbulent kinetic energy and dissipation are interpolated from the coarser to the finer grid. The wind, temperature, turbulence kinetic energy and dissipation fields computed by the meso-scale model are interpolated onto the SIMRA mesh to initialize the domain. Such a coupled system is being used for forecasting turbulence at many Norwegian airports and wind power production for a wind farm. For coupling SIMRA with micro-scale OpenFoam solver, a simplified approximation is used with only vertical profiles of variables computed from SIMRA (velocity components, turbulent kinetic energy and dissipation) being used as input for openfoam. A more comprehensive mapping of variables from SIMRA to OpenFoam is being developed.

Application of multi-scale methodology: Case Study of Oslo University Hospital

For studying the impact of multi-scale method, a realistic case study of Oslo University Hospital (OUS) is selected. OUS comprises of four hospitals (Rikshospitalet, Ullevål University Hospital, Radium Hospital and Aker University Hospital) that plans to research an implementation of Unmanned Aircraft Systems for a fast, secure and predictable transport of biological material and blood products between these hospitals. The location of terrain and buildings from where the drones are expected to operate have been shown in figure 2. The drone operations are expected to be impacted by local turbulence and wind shear and hence understand wind conditions is essential to establish safe drone flight trajectories. For validating the multi-scale methodology, an experimental measurement campaign involving mast has been conducted. The mast location at a height of 6 m above the building D4 (marked in figure 2 and shown in figure 3). The simulations are done for two wind cases as described in next section.

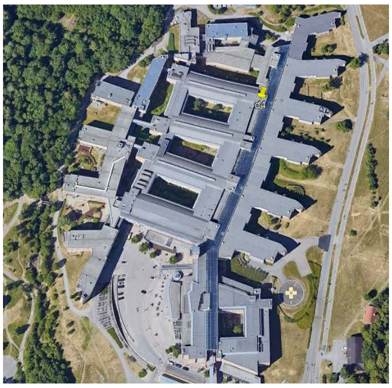

Figure 2: Oslo University Hospital with measurement location marked

COMPUTATIONAL SET-UP

Meshing Details and computational domain

The following domain sizes and grid sizes are used for the models: HARMONIE was operated at a horizontal resolution of 2.5 km × 2.5 km shown in Fig. 1. HARMONIE model covers Norway and runs on a computational domain of size 1875km × 2400km × 16km. The model is run on 1840 cores and it takes 87 minutes to complete a 48 hours forecast. SIMRA was operated at a horizontal resolution with finest grid size of about 112 m × 112 m with a domain size of 18 Km × 18 Km × 4 Km.the number of cells is about 1.28 milion. The SIMRA domain covers the oslo region surrounding the hospitals. Running on 48 cores, SIMRA generally takes 15 minutes to complete steady state simulations for the next 12 hours. For each hour, SIMRA takes the boundary conditions from HARMONIE. The super-micro scale CFD model has a much smaller computational domain size of 760 m × 660 m × 357 m with finest mesh resolution near buildings and terrains being at 0.15 m. A refinement zone is used in the vicinity of terrain and buildings to capture terrain induced flows . Using three different zones of different refinement levels, the mesh grid spacing is slowly increased away from terrain to reach 10 m grid resolution in upper regions of domain where the flow is expected to be uniform and without velocity gradients. The building heights are generally upto around 13m so the building is refined by nearly 80 grid points vertically . Figure 4 shows the mesh used for simulation. The mesh is dominated by hexahedral cells and mesh size is 5.9 Million cells.

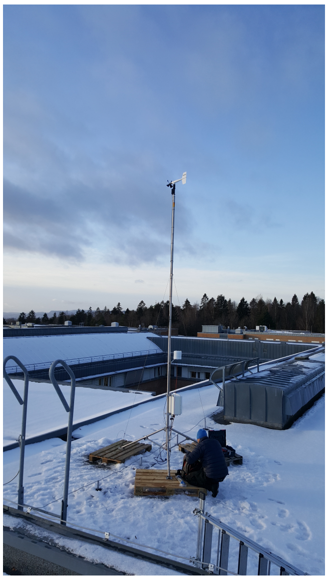

Figure 3: Experimental measurements at 6m above building D4

Boundary conditions and Initial conditions

The inlet and outlet boundaries change with wind directions. Outlet boundaries generally assumes fully developed flow with zero gradient for all variables (except pressure). The terrain and buildings have no-slip boundary with fixed velocity of zero.

Choice of wind direction and Case Studies

Two realistic cases are selected to be simulated for comparison with experimental measurements : (a.) Case 1: Simulating the scenario of 9th February,2020 at 1000 UTC time with wind direction of 180 degrees and (b) Simulating the scenario of 13th February, 2020 at 15 UTC with wind direction of 344 degrees (i.e north westerly flow). The choices are made based upon considerations of dominant wind from the wind rose (like 184 degrees wind direction - South westerly flow, see figure 5) and wind profile considered challenging to drone operations due to gusty nature (wind direction 344).

Experimental measurements using Mast for reference comparison of models

An experimental wind measurement mast was setup at a vertical distance of 6m above the D4 building at the Rikshospitalet to validate the CFD models. For the wind below 4.9 m/s, the measurements are seen to be capturing noise (50Hz noise) due to presence of fan below the roof that is inducing voltage disturbance affecting the sensor signals. Hence, the measured observation is now used only as reference for a qualita-

[SIMRA surface mesh]

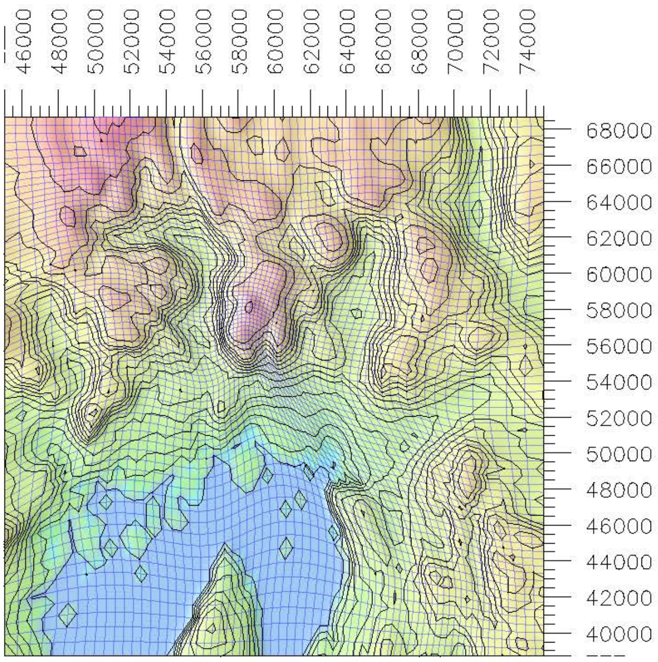

[SIMRA domain 18kmsx18kms]

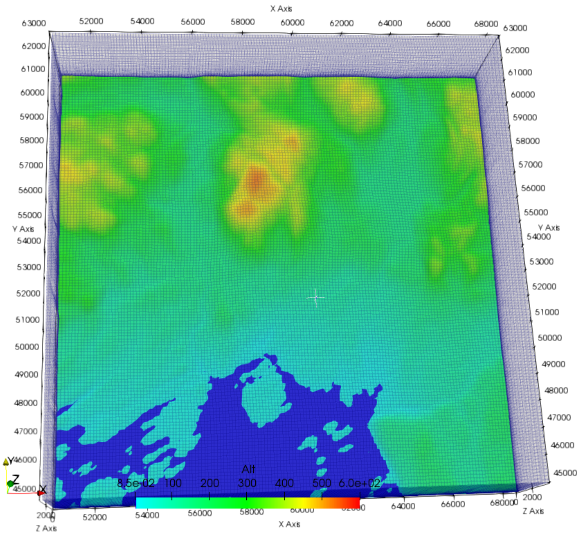

[CFD domain mesh]

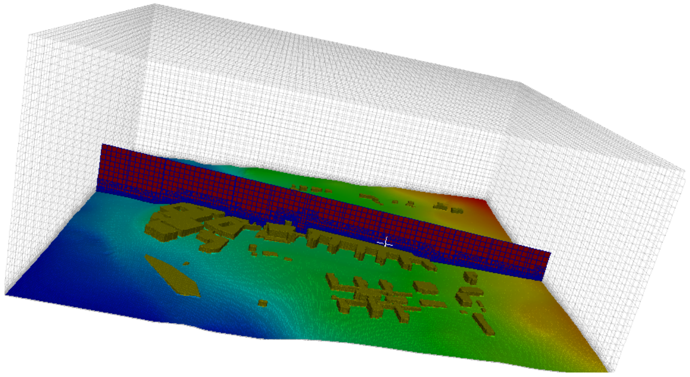

Figure 4: Mesh and domain used in SIMRA and CFD scales

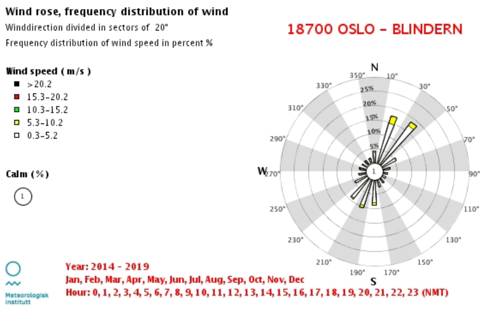

Figure 5: Wind rose to determine wind direction for study

tive comparison between SIMRA and local-micro-scale CFD model, rather than for quantitative validation.

RESULTS

The results presented here compares the simulated and experimental measurements:

Comparison between experiments and model predictions

Figure 6 shows the vertical profile of mean wind speed at a vertical line passing through the D4 measurement point obtained from the SIMRA and super-microscale CFD simulations. The experimental measurement results from the mast at D4 has been plotted as points on the same graph to enable comparison. Currently, only the mean wind speed are compared while the observed gusts (max mean wind speed) are not compared as a steady state simulation is done with steady inlet profile. The figures shows that SIMRA (which does not incorporate building impact) has higher deviations that the super-microscale CFD model. Here, the deviations are measured as: $Deviation = \frac{U_{measurement}-U_{CFD}}{U_{measurement}} * 10$.

For the case 1 of 13April2020 (figure 6), SIMRA deviates with around 32% over-prediction while micro-scale CFD underpredicts by about 24% . For the case 2 of 9thFebruary2020 (figure 6), SIMRA deviates highly with around 72% over-prediction while super micro-scale CFD underpredicts by about 20%. The reasons for CFD to predict closer to measured data is due to the fact that it is accounting for impact of buildings - which is influencing the measurements (as shown in figure 9 and discussed in later section) It is important to note that these comparisons (validations) are being attempted in realistic conditions over which we have little control (as is possible in the case of wind tunnel where we can control inlet wind conditions and thus enable proper validation). The observed deviations reported below are attributed to factors related to both experimental and computational things, 1. The incorporation of unavoidable external noise in the signal collected by the mast has introduced measurement errors in wind below 5 m/s. 2. The measurements at nearby hours at 11UTC and 9UTC (as shown in figure 6) Case 2 reveals that the wind is highly dynamic within the measurement period. While the steady state solver in this work uses a steady inlet profile for the given hour (i.e at 10UTC - the hourly period of comparison) as we do not have information on change in wind conditions within the hour (10UTC). 3. Currently, a simple RANS turbulence model has been used. 4. The approximation considers only vertical variation for inlet profile and a full mapping may help to improve the model further.

So, the comparison with experiments and deviation could be used only for qualitative purposes and shows results along expected lines and known lines - that is the super-microscale CFD is able to account for building wake effects and hence shows lower wind speeds than SIMRA at regions up-to which the building has influence. So, such micro-scale models will be able to more accurately capture the wind conditions experienced by the drones.
Next, we qualitatively define the influence of different models:

Qualitative capabilities of models in the multi-scale framework

Figures 7-9 below shows qualitative capabilities of different models for the case 2 study. HARMONIE (figure 7) is able to capture the large scale meso-scale effects happening at an altitude of thousands of meters . It captures a major wind shift when crossing the frontal surface above Oslo and the associated jet stream in troposphere height is from the North-west. The figure shows wind tangent to the cross-section for both the W-E and S-N together with potential temperature. Here, the frontal zone is seen aloft (a few thousand meters) and it is associated with a potential temperature gradient and a wind shear. This meso-scale model can be used to provide boundary profiles for the micro-scale models - which then can capture the local wind conditions around the urban hospital. The wind conditions in an urban location are impacted by buildings and urban landscape, and a meso-scale model such as HARMONIE that is operating at a resolution in scale of kilo-meters can not capture this. The impact of terrain and buildings are shown in figures below (figure 8-9) from the results of micro-scale models (SIMRA and CFD). As compared to the meso-scale Harmonie predictions, the

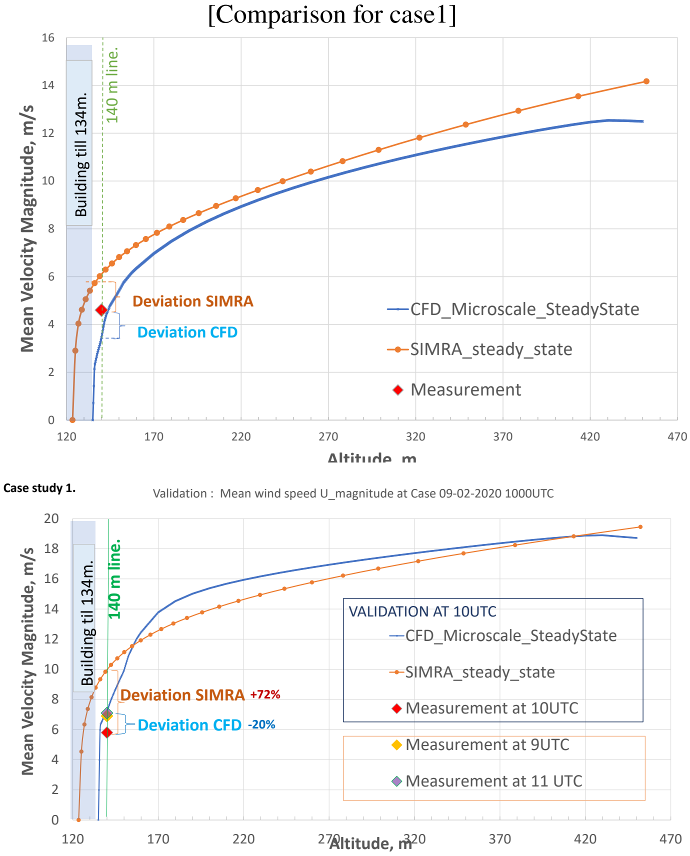
[Comparison for case1]

Case study 1.
Validation : Mean wind speed U_magnitude at Case 09-02-2020 1000UTC

Figure 6: Comparison of models with measurement data

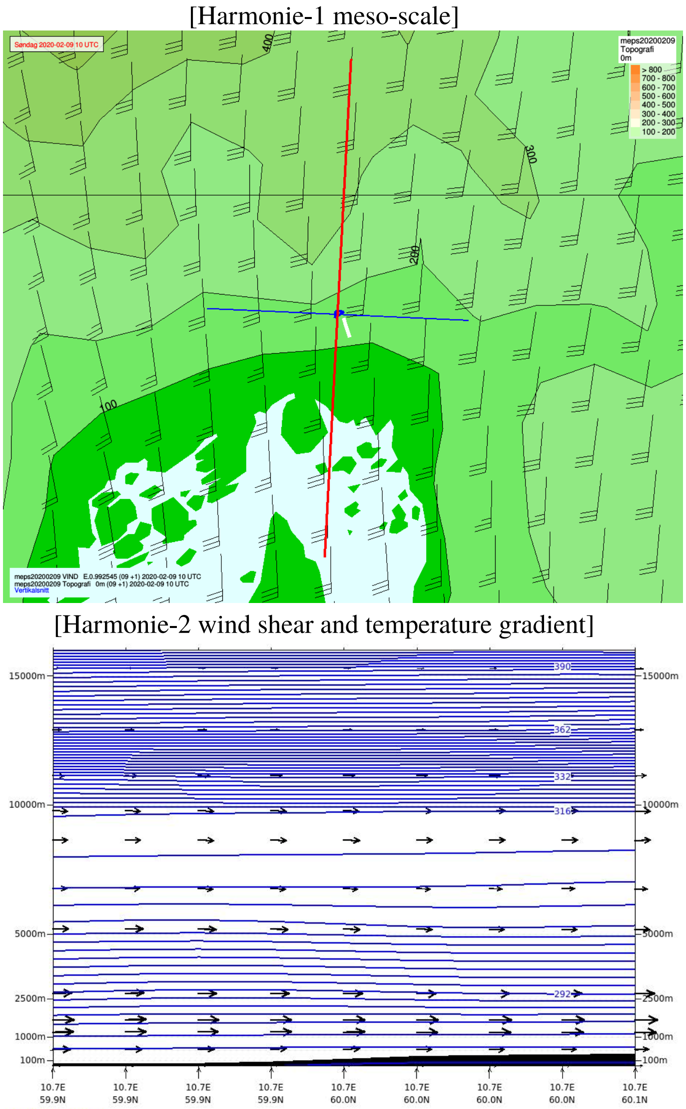
[Harmonie-1 meso-scale]

[Harmonie-2 wind shear and temperature gradient]

Figure 7: Harmonie meso-scale predictions

micro-scale SIMRA model shows that it is able to capture the impact of terrain (figure 8). This result is along expected lines. The terrain in north of Rikshospital, Oslo is hilly with elevation up-to 500m high. This can have an impact on the wind experienced at the hospital. HARMONIE owing to its coarse resolution (in kms) won't be able to capture this terrain impact. The figures shows that the wind vectors at different heights (300m, 140m) are impacted by terrain, and the turbulence emanating from the hilly terrain (terrain-induced turbulence) for the case 2 scenario (i.e. the south-westerly wind) can also been seem in the figure. At height D4 (140 m above sea-level, i.e. about the same height as the location of mast), the figure shows that SIMRA is not able to capture the impact of buildings as this needs grid resolutions to be below atleast a tenth-of a meter so as to explicitly resolve the buildings, while SIMRA operates at a resolution that is about two orders of magnitude higher (112 m resolution). For the cases of wind blowing from other directions (like northerly, north-easterly (NE) and north-westerly (NW)), the terrain-induced turbulence and wakes should impact the local-wind conditions on downstream of hill around the hospital.

As compared to the meso-scale Harmonie and to the micro-scale SIMRA, the super-refined micro-scale CFD model shows that it is able to capture the impact of buildings (figure 9). The figures shows the wind velocity vectors at 10m above ground level and at a vertical plane across the D4 measurement point (D4 represented by a white cross in the figures). The figures show that the D4 measurement location is influenced by the building. Super-micro scale CFD shows that the D4 mast location lies in the building-induced wake region thus experiencing higher turbulence and lower velocity, and hence, the super micro-scale CFD predictions are closer to the mast observations with lower velocity than those predicted by SIMRA (as seen in figure 6).

Thus, the current work qualitatively shows the utility of using a multi-scale approach to obtain wind conditions around an hospital in urban landscape. The quantitative accuracy of this multi-scale approach could not be checked as the experimental data from MET masts has significant noise from external source, and hence the measurement data has been used only for verification purposes.

CONCLUSION

The work shows the utility of the multi-scale tool for generating urban-scale wind conditions. The multi-scale tool in the form presented in this paper is capable of creating a micro scale wind atlas taking into account different combinations of meteorological parameters (like wind directions, building designs etc). However, we do admit that there is scope for a more detailed study and better validation studies (by obtaining better experimental data). In the near future, we intend to develop a more comprehensive coupling between the micro-scales codes and investigate influence of micro-scale turbulence on the drones under unsteady conditions.

ACKNOWLEDGMENT

The authors acknowledge the financial support from the Norwegian Research council for the project "Aerial Transport of biological material (ATB) - Helsevel project call" under which this work is carried out. We would also like to thank the personnel from FFI (especially Hannibal Fossum) for providing the building data for this study, and Vegar Kristiansen from MET for information on wind data.

[SIMRA-1]

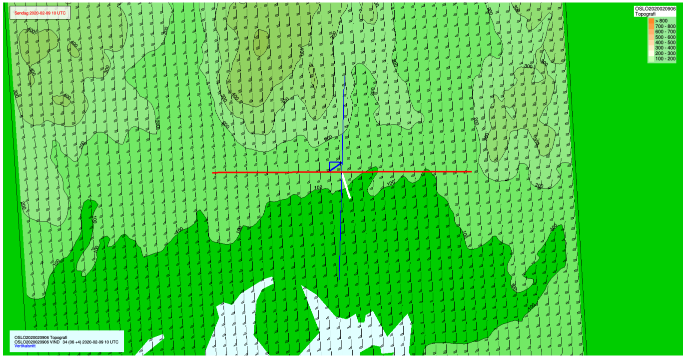

[SIMRA-2 300m above sea level]

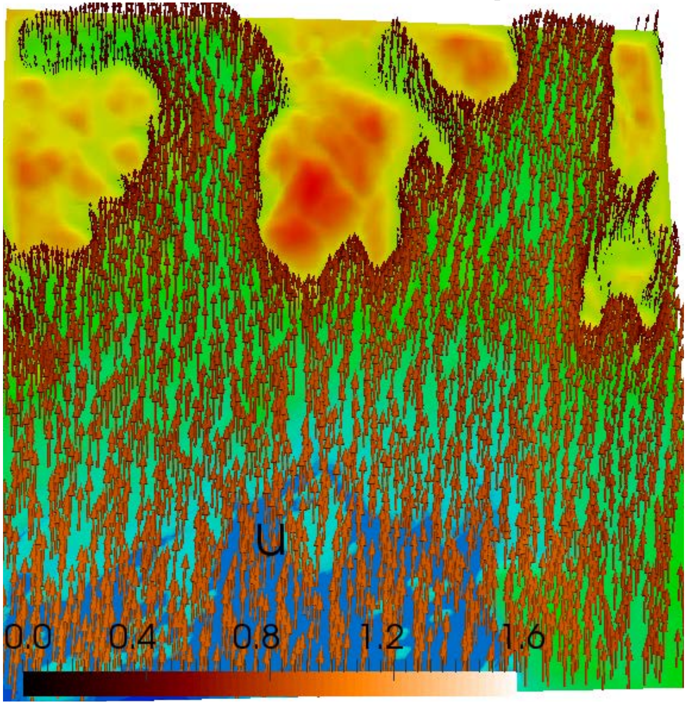

[SIMRA-3 140m above sea-level D4 measurement]

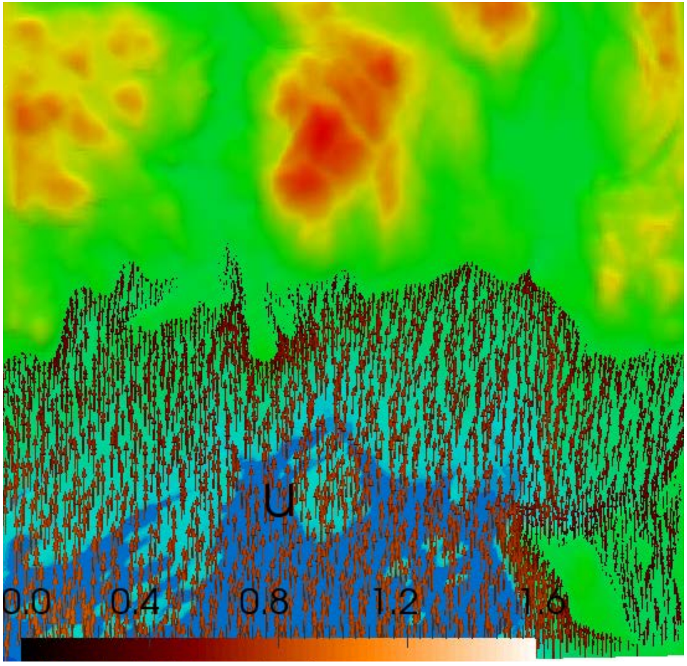

Figure 8: SIMRA wind vectors 10 UTC and terrain induced effects

[CFD velocity]

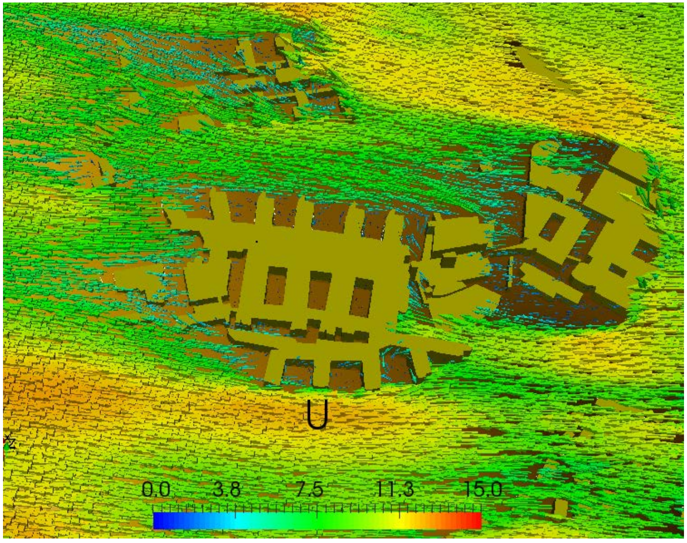

[CFD velocity]

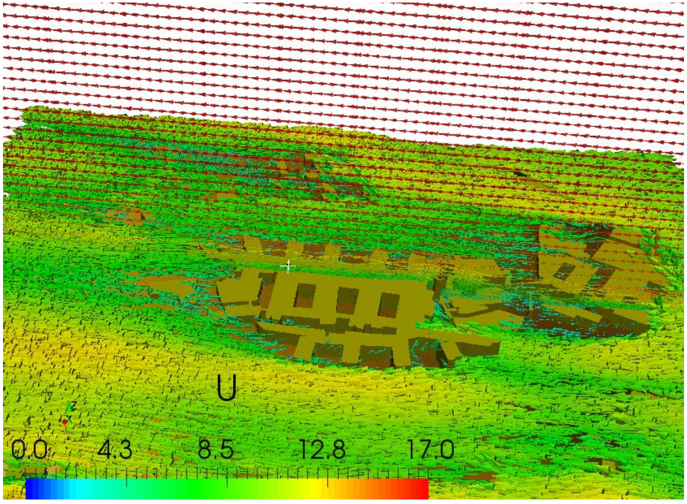

[CFD turbulence]

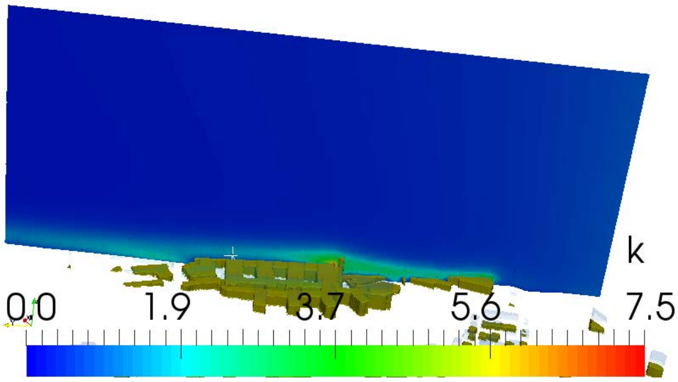

Figure 9: super micro-scale CFD for building-induced effects

REFERENCES

ASHIE, Y. and KONO, T. (2011). “Urban-scale cfd analysis in support of a climate-sensitive design for the tokyo bay area”. *International Journal of Climatology*, **31**, 174 – 188.

Eidsvik, K.J. (2005). “A system for wind power estimation in mountainous terrain. Prediction of Askervein hill data”. *Wind Energy*, **8(2)**, 237–249.

EIDSVIK, K. and UTNES, T. (1997). “Flow separation and hydraulic transitions over hills modelled by the reynolds equations”. *Journal of Wind Engineering and Industrial Aerodynamics*, **67-68**, 403 – 413. Computational Wind Engineering.

EIDSVIK, K., HOLSTAD, A., LIE, I. and UTNES, T. (2004). “A prediction system for local wind variation in mountainous terrain”. *Boundary Layer Meteorology*, **112**, 557–586.

KONDO, H., TOKAIRIN, T. and KIKEGAWA, Y. (2008). “Calculation of wind in a tokyo urban area with a mesoscale model including a multi-layer urban canopy model”. *Journal of Wind Engineering and Industrial Aerodynamics - J WIND ENG IND AERODYN*, **96**, 1655–1666.

KUNZ, R., KHATIB, I. and MOUSSIOPOULOS, N. (2000). “Coupling of mesoscale and microscale models—an approach to simulate scale interaction”. *Environmental Modelling Software*, **15(6)**, 597 – 602.

MOHAMMADI, B. and PIRONNEAU, O. (1994). *Analysis of the K-Epsilon Turbulence Model*. Wiley, New York and Massson, Paris.

RASHEED, A., TABIB, M. and KRISTIANSEN, J. (2017). “Wind farm modeling in a realistic environment using a multiscale approach”. **Volume 10: Ocean Renewable Energy**.

RASHEED, A., ROBINSON, D., CLAPPIER, A., NARAYANAN, C. and LAKEHAL, D. (2011). “Representing complex urban geometries in mesoscale modeling”. *International Journal of Climatology*, **31**.

RODI, W. (1997). “Comparison of LES and RANS calculations of the flow around bluff bodies”. *Journal of Wind Engineering and Industrial Aerodynamics*, **69-71**, 55–75.

SEITY, Y., BROUSSEAU, P., MALARDEL, S., HELLO, G., BéNARD, P., BOUTTIER, F., LAC, C. and MASSON, V. (2011). “The arome-france convective-scale operational model”. *Monthly Weather Review*, **139(3)**, 976–991.

TABIB, M.V., RASHEED, A. and UTENG, T. (2017). “Methodology for assessing cycling comfort during a smart city development”. *Energy Procedia*, **122**, 361 – 366. CISBAT 2017 International ConferenceFuture Buildings Districts – Energy Efficiency from Nano to Urban Scale.

UTNES, T. (2007a). “Modelling of Stratified Geophysical Flows over Variable Topography”. *Geometric Modelling, Numerical Simulation and Optimization*, **ISBN 978-3-540-68782-5**, 361–390.

UTNES, T. (2007b). “A segregated implicit pressure projection method for turbulent flows”. *SINTEF Applied Mathematics*, **Report A1686**.

CFD SIMULATIONS OF AN ADDITIONAL H_2 COMBUSTOR FOR IMPROVING EFFICIENCY IN CHEMICAL LOOPING COMBUSTION POWER PLANTS

Tijmen Scharff[1], Schalk Cloete[2,*], Jan Hendrik Cloete[2], Rob Bastiaans[1]

[1] Eindhoven University of Technology, 5600 MB Eindhoven, THE NETHERLANDS

[2] SINTEF Industry, 7465 Trondheim, NORWAY

* E-mail: schalk.cloete@sintef.no

ABSTRACT

Chemical looping combustion (CLC) is a promising technology for hydrocarbon fuel combustion with integrated CO_2 capture. The CLC process imposes almost no direct energy penalty for separating CO_2, but a large indirect energy penalty is encountered when CLC reactors are integrated into a combined cycle power plant due to the maximum reactor operating temperature that is far below the inlet temperature of modern gas turbines. Previous works have shown that additional fuel combustion after the CLC reactors can almost eliminate this energy penalty, although more expensive hydrogen fuel must be used to avoid CO_2 emissions. This study conducts CFD simulations of an added combustor fired with hydrogen, focusing mainly on mechanisms to reduce NOx formation. Three mechanisms are explored: 1) a greater number of fuel injectors, 2) increased turbulence, 3) and lower O_2 content of the air stream due to flue gas recirculation. Option 2 proved the most effective at reducing NOx, followed by Option 3. When combined, these mechanisms could result in NOx emissions below 50 ppm using a very compact combustor. In conclusion, low-NOx operation of the added combustor appears to be feasible and it is recommended for inclusion in future studies of CLC combined cycle power plants.

Keywords: Combustor, Chemical looping combustion, CFD, Gas turbine, Power production

INTRODUCTION

Urgency is building behind the global effort to combat climate change, with targets of 1.5-2 °C of warming now more broadly accepted [1]. Low-carbon technologies such as chemical looping combustion (CLC) [2] will be needed to reach such targets in a cost-effective manner.

CLC combusts hydrocarbon fuels with the aid of an oxygen carrier material to inherently avoid the mixing of nitrogen from air and CO_2 from fuel combustion. Two fluidized reactors are used for this purpose, with the oxygen carrier powder circulating between them. In the air reactor, the oxygen carrier is oxidized by air in a highly exothermic reaction. The outlet flow of this reactor consists of hot depleted air that can be used to drive a downstream power cycle. Oxidized oxygen carrier from the air reactor is then transferred to the fuel reactor where it is reduced by a hydrocarbon fuel gas (natural gas or syngas), producing an exhaust containing only CO_2 and H_2O. After simple condensation of the H_2O, the CO_2 stream is ready for storage or utilization. The reduced oxygen carrier is then circulated back to the air reactor to complete the cycle.

Gaseous fuel CLC must be coupled with a combined power cycle to achieve competitive electric efficiencies. Modern natural gas combined cycle (NGCC) power plants achieve very high efficiencies (~64%), mainly due to advances in gas turbine technology to facilitate high turbine inlet temperatures (>1600 °C). The primary challenge facing CLC in this respect is that the maximum CLC operating temperature will be around 1200 °C, limited by the stability of the oxygen carrier, as well as material constraints related to the reactors and downstream particle filters. With a turbine inlet temperature of only 1200 °C, the efficiency of a CLC combined cycle power plant is lower than that of a conventional NGCC plant with post-combustion CO_2 capture, rendering the CLC technology uncompetitive [3].

To overcome this fundamental limitation, a combustor can be deployed downstream of the CLC reactors to increase the temperature of the depleted air stream to the level that can be tolerated by modern gas turbines. This method has been shown to virtually eliminate the energy penalty of CO_2 capture in both NGCC [3] and integrated gasification combined cycle [4] power plants. The drawback of this solution is the release of additional CO_2, if natural gas is used for extra firing, or higher fuel costs, if hydrogen is used. Despite this drawback, however, added firing greatly reduces the CO_2 avoidance cost of CLC combined cycles, also outperforming NGCC with post-combustion CO_2 capture [3].

Given these promising results related to the added firing configuration, this paper sets out to study the combustion behaviour in the added combustor after the CLC reactors. A distinguishing feature of this combustor is that the hot depleted air stream is far above the fuel autoignition temperature. This means that lean premixed combustion for low NOx emissions is impossible. When hydrogen fuel is used, however, lean premixed combustion is problematic in any case [5], mainly due to the extremely high flame speed of hydrogen and the risk of flashback. Instead, the fuel must be injected directly into the hot air stream where it will spontaneously combust. Technically, lean premixed combustion performance can also be approached in this case in the limit of perfect mixing (e.g., infinite turbulence or an infinite number of small fuel injectors). Alternatively, flame temperatures and the associated thermal NOx formation can be reduced by diluting the hydrogen fuel with steam or reducing the air oxygen content by recirculating some of the flue gas. Previous work has indicated that the former imposes a small energy penalty, whereas the energy penalty is negligible in the latter case [6].

For these reasons, the present work will investigate the NOx mitigation potential of increasing the number of fuel injectors, increasing the amount of turbulence, and reducing the O_2 content of the air via flue gas recirculation. The modelled combustor is based on the H-class gas turbine modelled in a prior study [3] where hydrogen added firing was used to increase the depleted air temperature from 1160 °C after the CLC reactors to 1648 °C at the combustor outlet.

Given the lack of experimental data for this type of combustor, the present model has not been thoroughly validated. Thus, it should be viewed as a first qualitative numerical investigation of this novel combustor concept, illustrating the potential of different mechanisms to achieve low-NOx combustion. This initial study can pave the way for a more elaborate future project including dedicated experiments and more detailed modelling.

MODEL DESCRIPTION

The simulation campaign was completed in ANSYS Fluent v19.3 using a one-sixth pie-slice of a simple cylindrical combustor geometry – 0.4 m in diameter and 1 m in length. As shown in Figure 1, the geometry features multiple fuel injectors injecting hydrogen into a large stream of hot air from the CLC reactors. The geometry is sized based on an H-class gas turbine with 18 combustors and a flow velocity inside the combustors of ~80 m/s.

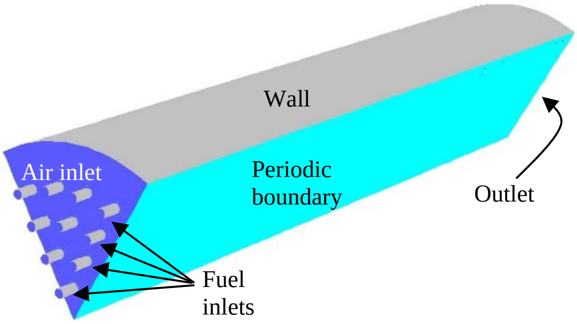

Figure 1: The simulated geometry.

Mesh

Meshes, consisting primarily of hexagonal cells with a cell length of 0.6 cm, were created in ANSYS Meshing. Smaller cells are used in the vicinity of the nozzles to ensure a minimum of 6 cells across each nozzle, but the cell length of 1 cm is maintained in the axial direction.

To increase numerical accuracy without making the solution computationally unaffordable, one level of adaptive refinement was performed according to temperature gradients, in order to only refine on the edges of the flames where the highest gradients in temperature and species concentrations must be resolved. In cases with a long flame, this refinement doubled the number of cells in the domain up to approximately 500 000. In cases with shorter flames, a much smaller volume was adapted, leading to meshes with as low as 280 000 cells. Refining the mesh caused virtually no change in the temperature and conversion profiles in the combustor, but it did change the predicted NOx emissions by about 6%. This moderate solution change on refinement was deemed acceptable for the present study where the primary aim is to compare cases to each other for studying the relative attractiveness of various NOx reduction mechanisms. Hence, a single level of adaptive refinement to the mesh is used in all the cases presented in this study.

Model setup

Steady state simulations were completed using standard combustion modelling settings in Ansys Fluent [7]. The combustion of hydrogen in air was modelled using a single-step, global reaction mechanism, and the reaction rate was described using the eddy dissipation concept (EDC) [8]. In the EDC, it is assumed that the reaction occurs within small turbulent structures, accounting for the mass transfer limitation to small eddies due to limited turbulent mixing. The default Fluent values were used for the reaction kinetics of hydrogen combustion, based on a reaction that is first order with respect to hydrogen and oxygen, and an Arrhenius temperature dependency. Turbulence was modelled according to the realizable k-ε model [9] and radiation according to the P1 model [10].

NOx formation was modelled using standard functionalities in Ansys Fluent [11]. Considering that hydrogen without any hydrocarbons is used as fuel, only thermal NOx formation was included, based on the extended Zeldovich mechanism and using rate expressions from the evaluation of Hanson and Salimian [12]. The equilibrium approach is followed for O radicals and the partial-equilibrium approach for OH radicals.

Turbulence interaction during NOx formation is modelled in Ansys Fluent using a probability density function (PDF) approach to account for the effect of the variance in temperature and species concentrations on the mean reaction rates. In this study, a beta function is used for the probability distribution and the algebraic form of the variance transport equation is used for both temperature and species. This approach requires a maximum limit for the temperature used in the integration of the PDF to be set, in this case as the local temperature multiplied by a factor, T_{max}. It was found in the present study that, although the default value of $T_{max} = 1.1$ was used, the amount of NOx formation predicted was highly sensitive to this parameter. Due to this uncertainty, future combined simulation and experimental work will be required for solutions of high quantitative accuracy.

Boundary conditions

Inlet conditions were chosen to match our prior techno-economic assessment study [3], assuming that the flows are divided equally between 18 combustors feeding the H-class gas turbine. The outlet pressure was set to 22 bar. As shown in Table 1, three different turbulent intensities and O_2 mole fractions were explored. For simplicity, uniform velocity profiles were specified at all inlets. This assumption should be refined in future studies. In addition, inlet turbulence is another important assumption that merits further investigation. In the present study, this uncertainty is investigated via a sensitivity analysis on three turbulent intensities.

Table 1: Summary of boundary conditions.

	Air inlet	Fuel inlet
Flow rate (kg/s)	6.653	0.0389
Turbulent intensity (%)	4, 6, 8	4
Turbulent length scale (m)	0.4	0.01
Temperature (°C)	1160	289
Species mol %	15.6, 12.6, 9.6 O_2; balance N_2	100 H_2

RESULTS

Results will be presented in four sections. The first three sections present the effects of the number of injectors, the inlet turbulent intensity, and the degree of flue gas recirculation, whereas the final section investigates the effect of changing the turbulent intensity and the flue gas recirculation simultaneously. All four sections share a common base case with 60 fuel injectors, 4% turbulent intensity, and no flue gas recirculation (15.6% O_2)

Effect of the number of injectors

Three cylindrical combustor geometries with equally spaced injectors numbering 18, 36 and 60, were simulated with 4% turbulent intensity and no flue gas recirculation. The effect on the cross-sectionally averaged NO concentration and fuel conversion profiles is illustrated in Figure 2.

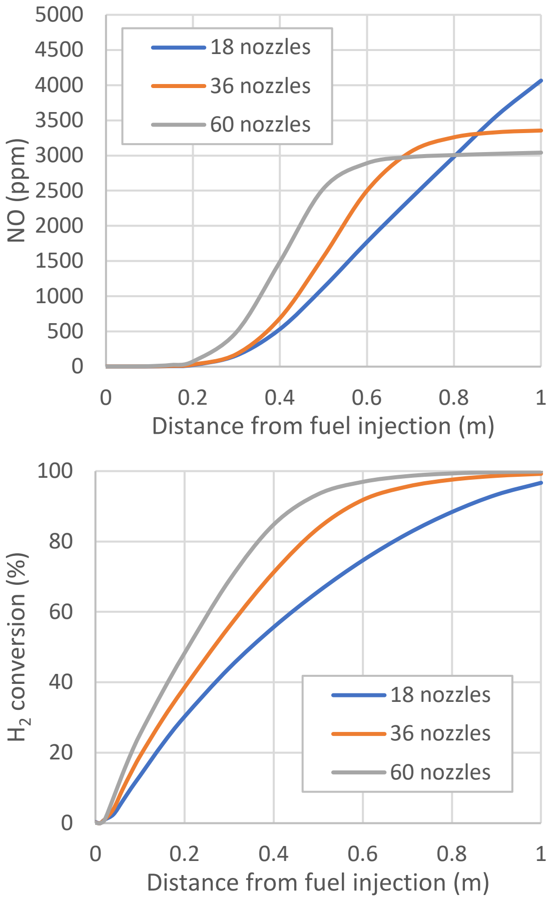

Figure 2: Cross-sectionally averaged profiles of NO concentration and fuel conversion along the length of the combustor for different numbers of nozzles.

Increasing the number of injectors causes a mild reduction in the amount of NO present at the combustor outlet, but it is clear that an impractically large number of injectors will be required to reduce NO below 100 ppm as required in many regions around the world. The figure also shows that a larger number of nozzles has a large positive impact on the rate of fuel conversion. In the case with only 18 injectors, a significant amount of fuel remains unconverted at the combustor outlet, whereas virtually complete conversion is achieved in the other two cases. This is the result of better contact between the air and the fuel when the fuel is injected more uniformly through many injectors.

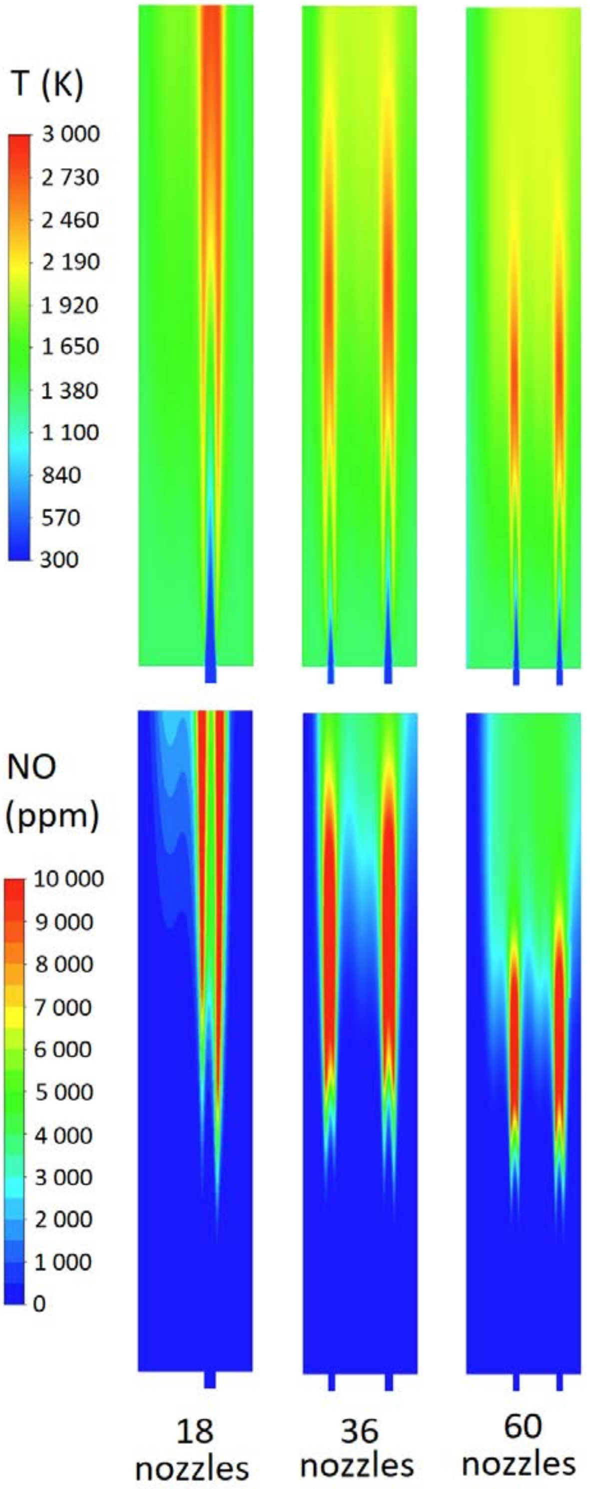

Figure 3: Temperature and NO concentration contour plots on the central plane in the three different geometries.

The high NOx formation is the result of very high flame temperatures (>2700 K) that are observed in this case (Figure 3). Clearly, the injection of pure H_2 into a greatly pre-heated oxidant stream with excess O_2 will require additional measures to reduce the flame temperature and suppress the formation of thermal NOx. Figure 3 also shows how the flame length increases when fewer injections are used. This slower fuel conversion is due to the increased mass transfer limitation created by the larger surface to volume ratios of the larger fuel jets injected in cases with fewer injectors.

Effect of inlet turbulent intensity

Three air inlet stream turbulent intensity values of 4%, 6%, and 8% were investigated in the case with 60 injectors and no flue gas recirculation. The lower bound is representative of a case with no added measures for increasing turbulence, whereas the upper bound represents additional measures to enhance mixing, such as swirl blades.

The inclusion of greater turbulence at the inlet of the combustor had a large positive influence on NOx reduction and significantly increased the rate of fuel conversion. Greater mixing in the combustor allows high flame temperatures to dissipate more rapidly and increases fuel-O_2 contact. The case with 8% turbulent intensity showed only 134 ppm of NO at the combustor outlet, which is close to meeting emissions limits.

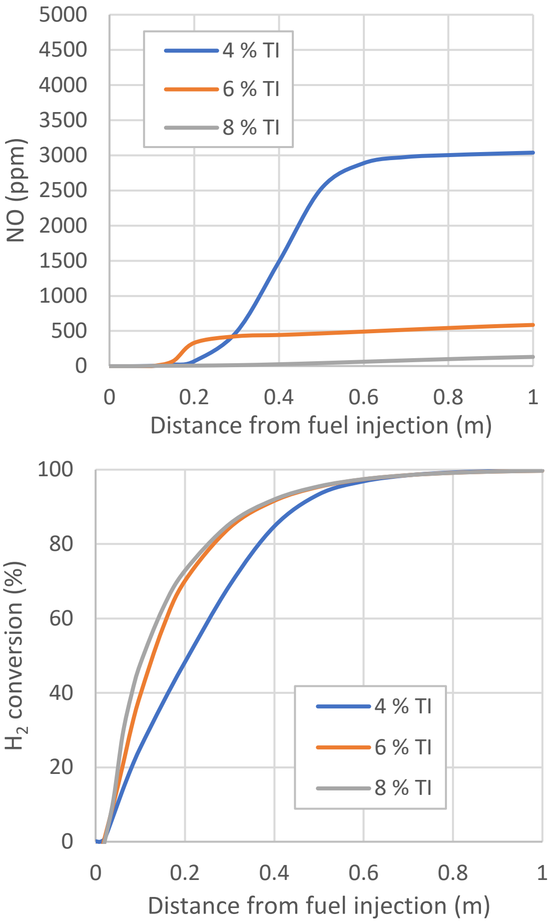

Figure 4: Cross-sectionally averaged profiles of NO concentration and fuel conversion along the length of the combustor for different turbulent intensities (TI).

The large dispersive influence of increased inlet turbulence is clearly illustrated in Figure 5. In the case with 8% turbulent intensity, the temperature field becomes essentially uniform before the half-way point along the combustor length. Most importantly, the maximum flame temperature is greatly reduced by the diffusive effect of turbulence. These results also show that the combustor length could be shortened substantially for the cases with high turbulence, minimizing the combustor cost.

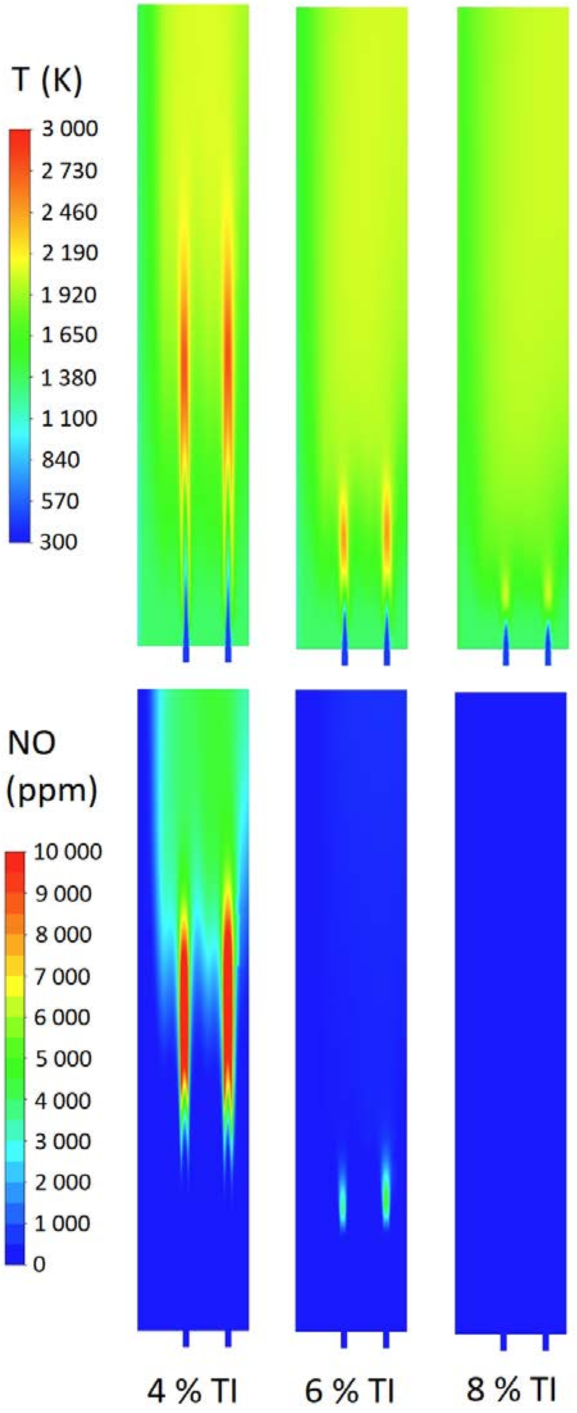

Figure 5: Temperature and NO concentration contour plots on the central plane for the three different inlet turbulent intensities.

These results also indicate the large effect that uncertainties related to inlet boundary conditions can have. For example, the assumption of a uniform inlet velocity profile could significantly impact results. In future work, more upstream details should be included in the geometry to ensure a reasonable flow profile at the start of the combustion zone.

Effect of flue gas recirculation

Flue gas recirculation was represented by reducing the amount of O_2 in the inlet air stream. Hence, three O_2 mole fractions of 15.6%, 12.6% and 9.6% were investigated in the case with 60 injectors and 4% turbulent intensity. The combustion process reduces the O_2 mole fraction by about 4.6 %-points, implying that the lowest case investigated still supplies considerable excess oxygen to the combustor, resulting in an outlet O_2 mole fraction of 5%.

Figure 6 shows that flue gas recirculation strongly reduces NOx formation by creating a shortage of O_2 in the highest temperature regions of the flame. Even so, the rate of fuel conversion is only reduced marginally, suggesting that greater flue gas recirculation should be practically achievable, potentially reducing NOx below 100 ppm, even without any measures to increase mixing.

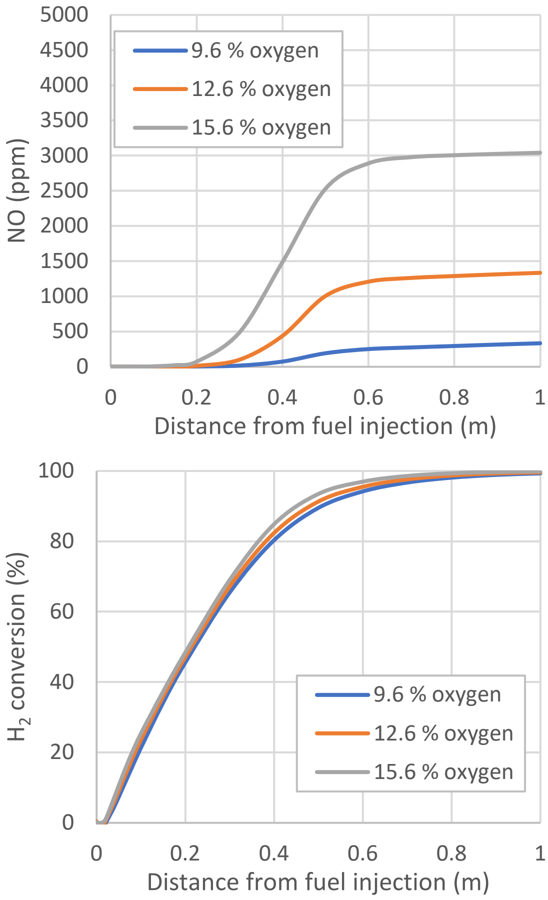

Figure 6: Cross-sectionally averaged profiles of NO concentration and fuel conversion along the length of the combustor for different O_2 mole fractions from flue gas recirculation.

Figure 7 illustrates the effect of reduced O_2 mole fractions more clearly. An increasing shortage of O_2 is observed in the highest temperature regions when the O_2 inlet concentration is reduced. This both avoids additional exothermic reactions in the hottest regions to reduce flame temperatures and causes a greater shortage of O_2 required for NO formation.

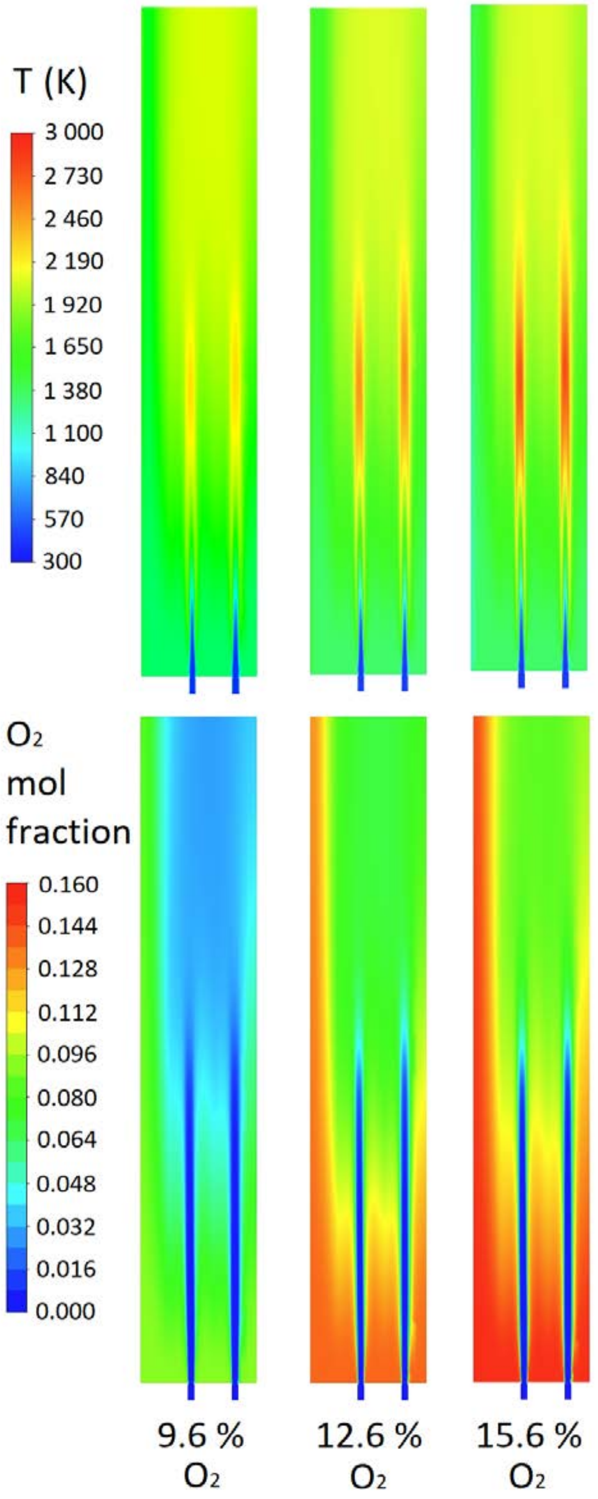

Figure 7: Temperature and O_2 mole fraction contour plots on the central plane for the three different O_2 inlet mole fractions.

Combining turbulence and flue gas recirculation

The optimal design of this combustor will most likely feature a combination of the three NOx reduction mechanisms investigated here. To investigate the potential of such a strategy, the two most influential factors (turbulent intensity and flue gas recirculation) were increased simultaneously in the case with 60 nozzles.

As illustrated in Figure 8, adding flue gas recirculation to the cases with more inlet turbulence further reduces NOx formation without significantly reducing the rate of fuel conversion. Outlet NO is reduced as low as 87 ppm in the case with the most turbulence and lowest O_2 content. However, it is likely that the linear increase in NOx observed in this case will continue between the outlet of the combustor and the inlet of the turbine, leading to an increase relative to the 87 ppm value reported above. The pathway between the combustor outlet and turbine inlet should therefore be as short as possible.

On the other hand, this result may be pessimistic, given that almost all the NOx is formed after more than 90% of the fuel has been converted and the mixture of air and remaining fuel is almost uniform. As mentioned in the model description section, the T_{max} factor of 1.1, describing the sub-scale temperature distribution, is an important uncertainty in this simulation. It is likely that the sub-scale temperature is virtually uniform in the well-mixed latter regions of the combustor with high turbulence, suggesting that the T_{max} factor should be closer to unity. For perspective, a case was run with Tmax = 1, halving the outlet NO concentration to only 46 ppm. Alternatively, the last 0.4 m of the combustor can be removed, leaving the final 1% of fuel conversion to happen in the turbine. In this case, the NOx emissions halve again to 43 ppm for T_{max} = 1.1 and 20 ppm for T_{max} = 1. Such low emissions will ensure compliance with future regulations.

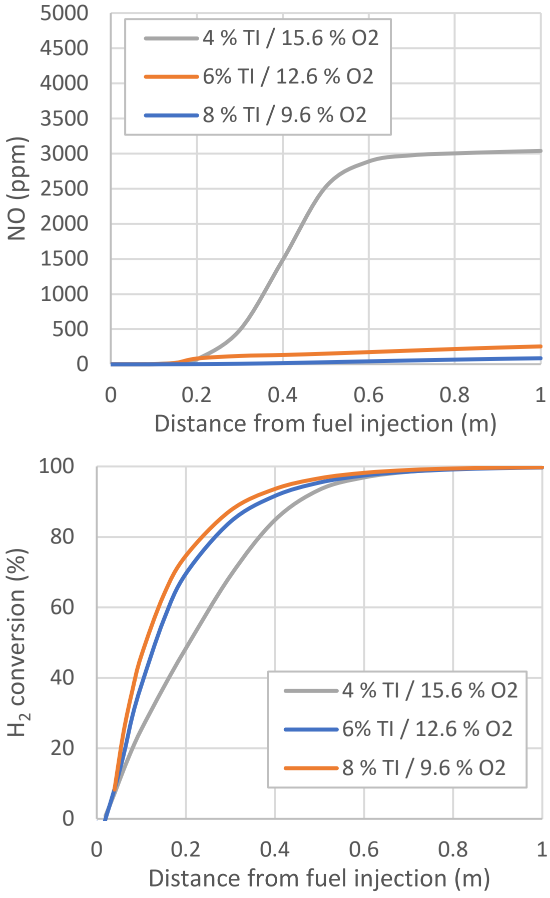

Figure 8: Cross-sectionally averaged profiles of NO concentration and fuel conversion along the length of the combustor for a combined increase in inlet turbulence and flue gas recirculation.

DISCUSSION

All three NOx-reduction mechanisms explored above have some drawbacks. There will be a limit to the number of fuel injectors that can be practically accommodated in the combustor. Turbulence generators like swirl blades impose additional pressure drop and, with a CLC outlet temperature of 1160 °C, might need some blade cooling. Flue gas recirculation will impose some added complexity to divert part of the flue gas back to the main compressor. More detailed combustor design studies will be required to find the optimal combination of these measures for ensuring practical and economical NOx mitigation.

Another interesting possibility that can be explored in future work is further simplification of the combustor. As shown in the results with higher turbulence above, 90% of the reaction happens spontaneously in as little as 30 cm after the fuel is injected with no need for separate combustion zones or premixing. This means that the fuel could be injected close to the gas turbine blades in a simplified combustion zone. Such an arrangement also opens the possibility for simplified multistage combustion and expansion where such a simple combustion zone can be inserted shortly before different stages of the turbine for increasing the inlet temperature of downstream turbine stages to increase turbine power output and overall cycle efficiency.

Future work should also investigate part-load operation of the added combustor. In this case, the ability of the CLC reactors to maintain a constant temperature of the depleted air being fed to the combustor could be advantageous. Since the turbine inlet temperature reduces under part-load operation, the amount of added H_2 combustion required after the CLC reactors will reduce under part-load operation, improving economics and potentially reducing NOx. The sensible heat storage capacity in the CLC oxygen carrier will also be beneficial for start-up after a short shutdown period.

CONCLUSION

This study investigated the feasibility of an added combustor for raising the CLC reactor outlet temperature to the level of modern gas turbines for highly efficient power production with integrated CO_2 capture. The focus was mainly on NOx reduction.

Out of the three NOx mitigation measures investigated, increased turbulence showed the largest effect. It also increased the rate of fuel conversion in the combustor. Using flue gas recirculation for reducing the O_2 content in the depleted air stream fed to the combustor also caused large reductions in NOx emissions with only minimal reductions in the fuel conversion rate. Increasing the number of fuel injection nozzles only had a mild NOx mitigation effect, but substantially increased the rate of fuel conversion by improving air-fuel contact. Combining these measures could achieve NOx emissions well below 100 ppm. However, more detailed studies (including dedicated experimental validation work) are required to draw quantitative conclusions, given uncertainties in the model, particularly regarding the highly sensitive NOx-turbulence interaction model.

In conclusion, this study showed that the concept of adding a H_2-fired combustor after CLC reactors holds promise and merits further investigation. Future work should aim to capitalize on the simplicity that can be achieved by this concept where fuel can simply be injected into the hot air stream to rapidly achieve complete and clean combustion.

REFERENCES

1. IPCC, *Global Warming of 1.5 °C*. 2018, Intergovernmental Panel on Climate Change.
2. Ishida, M., D. Zheng, and T. Akehata, *Evaluation of a chemical-looping-combustion power-generation system by graphic exergy analysis.* Energy, 1987. **12**(2): p. 147-154.
3. Khan, M.N., et al., *Integration of chemical looping combustion for cost-effective CO2 capture from state-of-the-art natural gas combined cycles.* Energy Conversion and Management: X, 2020: p. 100044.
4. Arnaiz del Pozo, C., et al., *The potential of chemical looping combustion using the gas switching concept to eliminate the energy penalty of CO2 capture.* International Journal of Greenhouse Gas Control, 2019. **83**: p. 265-281.
5. García-Armingol, T. and J. Ballester, *Operational issues in premixed combustion of hydrogen-enriched and syngas fuels.* International Journal of Hydrogen Energy, 2015. **40**(2): p. 1229-1243.
6. Khan, M.N., S. Cloete, and S. Amini, *Efficiency Improvement of Chemical Looping Combustion Combined Cycle Power Plants.* Energy Technology, 2019. **7**(11): p. 1900567.
7. Ansys Fluent, *Chapter 7: Species Transport and Finite-Rate Chemistry*, in *Fluent Theory Guide*. 2020.
8. Magnussen, B.F. *On the Structure of Turbulence and a Generalized Eddy Dissipation Concept for Chemical Reaction in Turbulent Flow*. in *Nineteenth AIAA Meeting*. 1981. St. Louis.
9. Shih, T.-H., et al., *A new k-ϵ eddy viscosity model for high reynolds number turbulent flows.* Computers & Fluids, 1995. **24**(3): p. 227-238.
10. Ansys Fluent, *Chapter 5: Heat Transfer*, in *Fluent Theory Guide*. 2020.
11. Ansys Fluent, *Chapter 14: Pollutant Formation*, in *Fluent Theory Guide*. 2020.
12. Hanson, R.K. and S. Salimian, *Survey of Rate Constants in the N/H/O System*, in *Combustion Chemistry*, W.C. Gardiner, Editor. 1984, Springer New York: New York, NY. p. 361-421.

PROCEEDINGS FROM THE 14TH INTERNATIONAL CONFERENCE ON CFD IN OIL & GAS, METALLURGICAL AND PROCESS INDUSTRIES

This book contains manuscripts from the 14th International Conference on Computational Fluid Dynamics in the Oil & Gas, Metallurgical and Process Industries. The conference was organized by SINTEF in collaboration with NTNU, MINTEK and CSIRO. The conference series was initiated by CSIRO and Phil Schwarz in 1997. So far, the conference has been alternating between CSIRO in Melbourne and SINTEF in Trondheim.

The conferences focus on the application of CFD in the oil and gas industries, metal production, mineral processing, power generation, chemicals and other process industries. 2020 was a remarkable year with a worldwide pandemic due to the Covid-19 virus. This led to travel restrictions and a decision to host the conference as a virtual conference. The conference was hosted online through Microsoft Teams on October 12–14, 2020.

SINTEF Academic Press